Biomechanics of Shaken Baby Syndrome

by David R. Wolfson, BEng(hons)

Thesis submitted to the University of Nottingham for the degree of Doctor of Philosophy, September 2006

Contents

1 Introduction **1**

2 Background **3**

2.1 Shaken Baby Syndrome 3

2.2 Anatomy of the Head and Neck 4

2.2.1 Skull 4

2.2.2 Brain 5

2.2.3 Meninges 6

2.2.4 Neck 7

2.3 Techniques for Biomechanical Investigation 11

2.3.1 Anthropometric Test Dummies 11

2.3.2 Rigid Body Modelling 12

2.3.3 Physical Modelling 13

2.4 Brain Injury Mechanisms 14

2.4.1 Penetration Injuries 14

2.4.2 Contact Injuries 14

2.4.3 Acceleration Injuries 15

2.5 Analytical Methods 15

2.5.1 Motion Tracking 16

2.5.2 Green-Lagrange Strain by Tensor Algebra 19

3 Literature Review **21**

3.1 Shaken Baby Syndrome 21

3.1.1 Historical Origins 22

3.1.2 Clinical Reviews 22

3.1.3 Case Studies 25

3.1.4 Biomechanical studies of SBS 26

3.1.5 Controversies in SBS 28

3.2 Infant Neck Stiffness 30
3.3 Brain Injury Studies 31
3.3.1 Biological Studies 31
3.3.2 Physical Models 33
3.4 Discussion 35

4 Investigation of Torso Acceleration **38**
4.1 Materials and Methods 38
4.2 Results 39
4.3 Discussion and Conclusion 41

5 Rigid Body Modelling of Head Kinematics **42**
5.1 Preliminary Investigations 43
5.1.1 Methods 43
5.1.2 Results 46
5.1.3 Discussion 46
5.2 H1 - Neck Stiffness Study 46
5.2.1 Methods 48
5.2.2 Results 49
5.2.3 Discussion 50
5.3 H2 - Head-Torso Impact Study 50
5.3.1 Methods 50
5.3.2 Results 52
5.3.3 Discussion 52
5.4 Conclusions 54
5.4.1 Acceleration Inputs 54
5.4.2 Preliminary Studies 55
5.4.3 H1- Neck Stiffness 55
5.4.4 H2 - Head-Torso Impact 55

6 Physical Continuum Modelling **56**
6.1 Materials 57
6.1.1 Surrogate Brain Tissue Material 57
6.1.2 Test Rig 57
6.1.3 Specimen Containers 57
6.1.4 High Speed Video Equipment 60
6.2 Methods 61

6.2.1 Specimen Preparation 61
6.2.2 Experimental Procedure 61
6.3 Analysis 62
6.3.1 Motion Tracking 62
6.3.2 Strain Calculation 63
6.3.3 Acceleration 63
6.4 Results 64
6.4.1 Acceleration 64
6.4.2 Strain 65
6.5 Discussion 78
6.5.1 Materials 78
6.5.2 Methods 79
6.5.3 Analysis 80
6.5.4 Results 82
6.5.5 Tissue Damage 85
6.6 Conclusions 86
6.7 Recommendations and Future Work 86

7 Thesis Discussion **88**
7.1 Head Kinematics 89
7.1.1 Acquisition of Torso Acceleration Data 89
7.1.2 Computational Study of Neck Stiffness 90
7.1.3 Computational Study of Head-Torso Impact 91
7.2 Brain Injury Criteria 92
7.2.1 Physical Continuum Modelling 92
7.3 Future Work 95
7.3.1 Rigid Body Modelling of Head Kinematics 95
7.3.2 Physical Modelling 95
7.4 Thesis Conclusions 96

Bibliography **97**

A ATD Torso Acceleration Traces **103**

B Results from Preliminary RBM Simulations **109**

C RBM Parametric Neck Stiffness Data **116**

D Results from Parametric Study of Neck Stiffness: Max. rms Acceleration Input **121**

E Results from Parametric Study of Neck Stiffness: Max. peak Acceleration Input **147**

F Results from Study of Head-Torso Impacts **173**

G Rheometric Study of Surrogate Brain Tissue **177**

G.1 Introduction 177

G.2 Materials and Methods 177

G.3 Results and Conclusion 177

H Acceleration Traces **180**

I Principle Strain Traces **185**

J Shear Strain Traces **190**

K Normalised Peak Principle Strain Traces **195**

L Normalised Peak Shear Strain Traces **200**

M Peak Strain Maps **205**

List of Figures

2.1 Adult human skull 4
2.2 Human infant skull 5
2.3 Lateral view of human adult brain 6
2.4 Meningeal layers covering the brain 7
2.5 Examples of cervical vertebrae 9
2.6 Posterior musculature of the neck 10
2.7 Green-Lagrangian strain determination 20

3.1 Chronology of appearance of developmental defects after SBS 25

4.1 ATD equipment 39
4.2 Example torso acceleration trace 40
4.3 Summary of characteristics of ATD shake testing 41

5.1 Preliminary rigid body models 44
5.2 Results of preliminary RBM modelling of SBS. 47
5.3 Parametric RBM model 48
5.4 Parametric neck stiffness study design 49
5.5 Results of parametric neck stiffness study. 51
5.6 End-stop neck stifness charactersitcs 52
5.7 Results of chest impact study. 53

6.1 Rheometric comparison of Q-Gel 310 and previous studies 58
6.2 Diagram of oscillation test rig 59
6.3 Sample High-Speed Video Frames 60
6.4 Video camera positioning 62
6.5 Example of motion tracking from A2 test 64
6.6 Example angular acceleration trace from A3 test 66
6.7 Summary of test frequencies and corresponding accelerations 66

6.8 Example of strain distribution analysis 67
6.9 Strain distribution plot 69
6.10 Example strain-time plots 70
6.11 Example normalised strain-acceleration plot 71
6.12 Peak average strain vs time plots 72
6.13 Peak average strain vs frequency summary plots 74
6.14 Factorial Analysis of Principle Strain 75
6.15 Factorial Analysis of Shear Strain 76
6.16 Interaction Plots 77
6.17 Common imaging problems leading to track errors 81
6.18 Irregular edge meshing leading to strain peaks. 82
6.19 Individual principle strain peak from A3 87

List of Tables

4.1 Body segment masses of ATD 38

4.2 Summary of results of shaking episodes 40

5.1 Description of preliminary computational models 45

6.1 Test configuration names used in physical modelling of SBS 63

6.2 Maximum strain data for selected tests. 73

6.3 Findings from trials of high-speed video cameras. 79

6.4 Acceleration - strain data from previous studies 84

Abstract

In the first part of this work, an Anthropometric Test Dummy (ATD) was used to obtain torso acceleration data for Shaken Baby Syndrome (SBS). These data were used to drive computational simulations of SBS, in studies of the effect of neck stiffness and head-torso impact on injury risk. Finally, physical models were used to investigate the strain induced in brain tissue during shaking.

Clinical literiture describes victims of Shaken Baby Syndrome (SBS) as young infants with life-threatening brain injuries, and poor long-term outcome. However, biomechanical studies using ATDs to study head motion during shaking have been inconclusive about the capacity for shaking alone to cause these injuries [1, 2]. This work comprises a series of investigations into these conflicting findings.

Torso acceleration data for SBS, obtained using a specially constructed ATD, were found to be consistent with previous findings. The data were used to simulate shaking in computational studies of SBS, using Rigid Body Models (RBM) of the infant head and neck. Parametric studies were used to investigate the importance of neck stiffness in assessing the injury capacity of SBS, and showed that in order to exceed current injury criteria for SBS, impact was required. Head-torso impact was then simulated, and although this resulted in higher injury risk than shaking alone, criteria for injuries associated with SBS were not reached.

Since these investigations did not predict brain injury in cases of SBS without impact, the origins of injury criteria were reviewed. It was found that they are derived from single high-energy events, which is distinct from the type of motion in SBS. In order to establish if cyclic, low-energy motion contributes to brain injury in SBS, Physical Continuum Modelling was used to study strain in brain tissue during shaking.

A test rig was constructed to shake silicone gel models, and high-speed video used to capture the motion of optical markers with in the gel. Their movement was tracked using optical flow methods, and Green-Lagrangian strain derived by tensor algebra. No evidence was found to indicate a build up in strain between cycles, but published critical strains for damage to neural tissue were exceeded.

Abstract

Although shaking alone was not found not induce head motion in excess of brain injury criteria, tissue damage criteria were exceeded. The application of current brain injury criteria to SBS maybe therefore be inappropriate.

Acknowledgements

I would like to thank my supervisors, Donal McNally and Mike Clifford for the opportunity to carry out this work and for their support throughout its course. It is only possible to understand the nature of research by having the freedom to take responsibility for its direction, but occasional words of guidance are essential. I would also like to thank Mike Vloeberghs for his clinical guidance and realising the opportunity for this work.

This research required help and expertise from a number of groups and individuals; Drs Mills, Pridmore, Parry and Hammersley helped to turn many thousands of video frames into meaningful engineering data, and the faculty technicians, particularly Mark, Paul and Roger were a huge help in developing both equipment and techniques. It would not have been possible to carry out this work without their help, and I wish to offer them all my thanks.

Funding for this research was provided by the Engineering and Physical Sciences Research Council and video equipment was borrowed from their Engineering Instrument Pool. Also, the nameless masses of the Open Source Software community provided software, guidance and time without asking for anything in return. I am grateful to both these groups, and hope that their work continues to thrive.

On a personal note, I would like to thank all my family and friends for their support and humour during this work, without which I might have taken myself far too seriously. Most of all I would like to thank Jackie for her patience and love throughout, and never questioning that *"After the thesis"* would come.

Chapter 1

Introduction

This thesis presents an exploratory series of biomechanical studies, that investigate various aspects of SBS and its associated brain injuries. Direction is taken from clinical and engineering literature in an effort to progress an area in danger of stagnating in an important field of research. A wide range of techniques are described, including ATD testing and computation and physical modelling. Studies of head kinematics are found to contribute little new knowledge, but cyclic low-acceleration loading is shown to be a potential mechanism for brain injury that has previously been discounted.

In Chapter 2, background information relevant to the following work is presented. A brief overall description of SBS is given in order to provide readers who are unfamiliar with the syndrome some terms of reference. The anatomy of the human head and neck, including the brain and its membranous coverings is described and compared to that of the infant. Various techniques used to carry out biomechanical investigations are described, with particular reference to those employed later, namely ATDs, Rigid Body Modelling (RBM) and physical modelling. This is followed by an introduction to brain injury mechanisms and their classification. Finally, some detail is given on the computational techniques used in Chapter 6; motion tracking using a Kalman Filter and Green-Lagrangian strain calculation by tensor algebra.

Having given an overview of the background to SBS and the methods employed here, the relevant literature that precedes this work is reviewed in Chapter 3. The historical origins of SBS are given, before details of clinical reviews and case studies. The small body of work on the biomechanics of the syndrome is reviewed, and its limitations and other controversies about the syndrome described. Available publications on the kinematics of the infant neck are presented, before biological and physical studies of brain injury are reviewed.

Chapter 4 describes how torso acceleration data were obtained for shaking episodes. The construction of a custom ATD is described, which was fitted with a uni-axial accelerometer.

Acceleration was recorded whilst a number of volunteers shook the dummy. The data were found to be consistent with previous studies and used as input data for computational simulation in Chapter 5.

Here, the development of a RBM of the infant head and neck from a standard ATD model is described and used in a parametric study to investigate the effect of neck stiffness on head motion. Through some simple adaptation of this existing model, the effect of head-torso impact was also studied. Neck stiffnesses within a biofidelic range were not found to lead to injurious motion. Results from stiffnesses outside this range, in conjunction with the findings of the head-torso impact studies supported the assertion that impact is required to exceed injury criteria. However, study of the origins of injury criteria in the literature review suggest that their application in assessment of SBS may be inappropriate, and that shaking should be studied as a distinct injury mechanism.

The methods used to construct, test and analyse idealised silicone models of the infant brain are presented in Chapter 6. High speed video was used to capture the motion of optical markers placed within the gel, whilst being shaken in a specially constructed oscillatory test machine. Kalman filtering was used to track the movement of the markers, and changes in their relative position used to determine the strain induced in the gel. No change in strain response was found between cycles, but shear and principle strain levels in excess of published tissue damage criteria were achieved. The geometry and boundary conditions of the model were altered during development of the model, and their effects determined using factorial analysis. Since these were novel techniques, some of the difficulties encountered in their development are also described, in order to better explain the development process and to aid future research.

In the final chapter, the research findings are discussed in the context of the whole work. The research presented here was carried out as an exploration of the biomechanics of shaken baby syndrome, with one piece of research leading to the next. The progression from the initial literature review of SBS and head kinematic studies to the investigation of brain injury criteria and physical modelling is explained. The implications of the findings of each study are discussed, and suitable areas for further research described. Finally, the conclusions of this thesis are summarised.

Chapter 2

Background

In addition to the engineering techniques applied in Chapters 5 and 6, the research carried out here relied upon understanding of various other subjects; the anatomy of the human infant, mechanisms of brain injury, clinical characteristics of SBS, computer vision and strain tensors. Where there is relevant ongoing research into a subject, the current literature is reviewed in Chapter 3. Here, a general overview is presented in order to provide the reader with the necessary background information to place the following material in context.

2.1 Shaken Baby Syndrome

The specific causes of injury in SBS are contentious and are discussed in chapter 3, but its clinical characteristics as a distinct form of child abuse are generally accepted. Victims tend to be less than two years old, and present with symptoms which range from the apparently trivial, such as digestive complaints or lethargy, to the life threatening such as respiratory distress or unconsciousness[3, 4, 5, 6]. Further examination often shows no obvious sign of head impact, and there may be a wide range of other injuries such as bruising to, or fracture of, the ribs or arms and retinal haemorrhages. The specific combination of Subdural Haematoma (SDH), Diffuse Axonal Injury (DAI) and retinal haemorrhage has commonly been used as the strongest diagnostic indicator of the syndrome.

In addition to clinical findings, the history provided by the caretaker is generally not consistent with the injuries, and there may be evidence of previous injuries or abuse [7]. Treatment is dependent on the type and severity of injuries, but in severe cases is normally focused on stabilising raised intracranial pressure. Outcome is described in one study as dismal, with mortality of 27% and morbidity of 60%, ranging from a persistent vegetative state, to visual and hearing impairment or developmental delay [4].

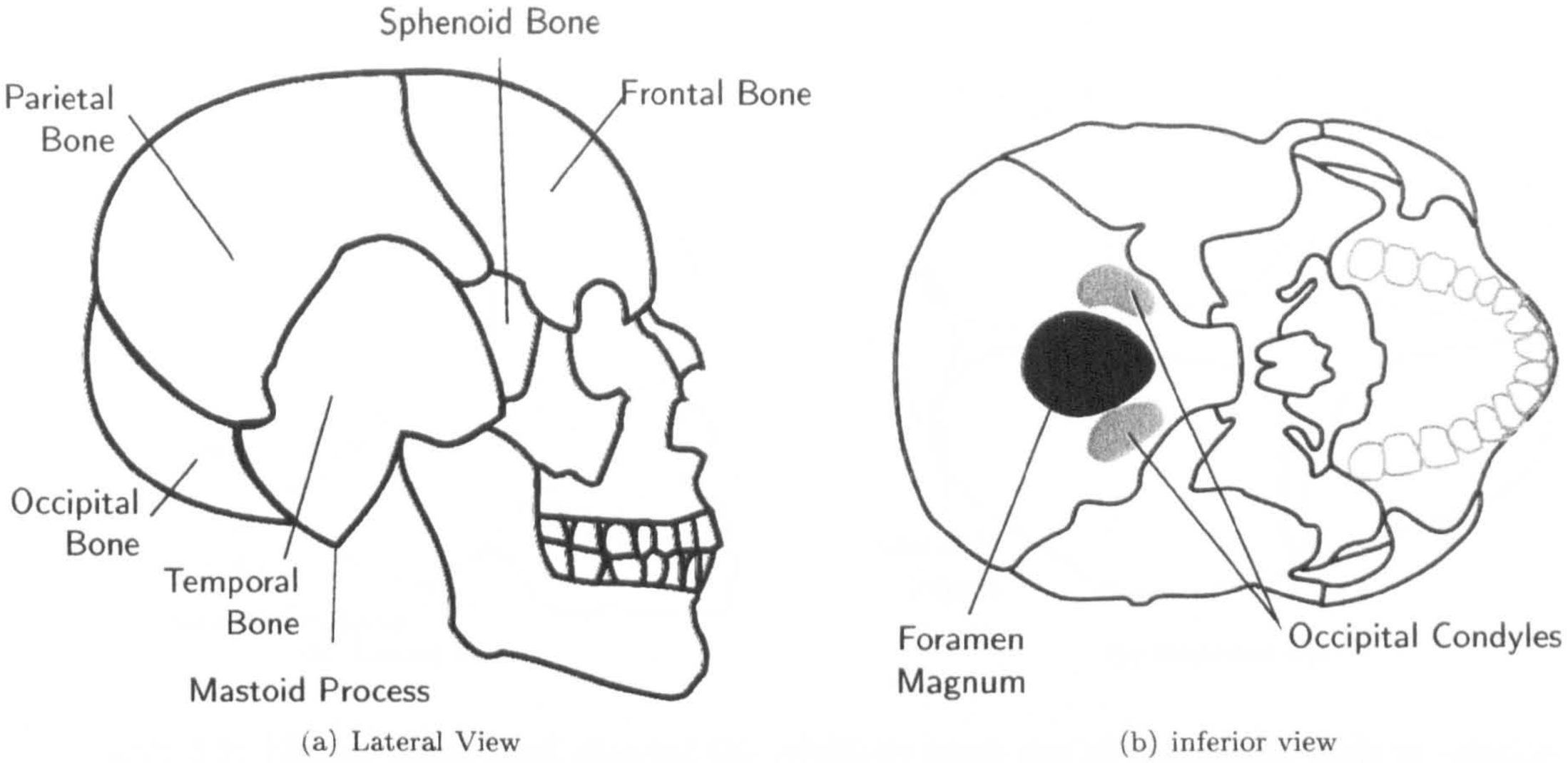

(a) Lateral View

(b) inferior view

Figure 2.1: Adult human skull a) lateral view showing the facial bones and major bones of the cranial vault; frontal bone, parietal bones, temporal bones, occipital bone and sphenoid bones b) inferior view showing foramen magnum and occipital condyles.Adapted from [8].

2.2 Anatomy of the Head and Neck

While the anatomy of the neck determines the type and range of the motion of the head, the structures of the brain and skull incorporate features that affect their vulnerability to injury. Since the infant is born at an early developmental stage there are many anatomical differences to both the head and neck, that are important when considering head kinematics and brain injury. In order to understand these differences and their implications it has been necessary to gain some understanding of the anatomy of the head and neck, and its development in the infant.

2.2.1 Skull

The human skull comprises twenty-eight bones, in two distinct regions; the face and cranial vault [8]. The facial bones provide protection for sensory organs such as the nose and eyes, whilst the eight flat bones of the cranial vault contain and protect the brain. Where they meet, the bones of the cranial vault are knitted together by inflexible joints called sutures. The spinal cord exits the skull via the foramen magnum, a large hole in the inferior occiput lying between the occipital condyles which articulate with the first cervical vertebra. The general layout of these bones, and the foramen magnum is shown in Figure 2.1. Also shown is the mastoid process, one of the main points of muscular attachment between the head and neck.

Although the layout of the infant skull is similar to that of the adult, the cranial vault is large relative to the rest of the body and the facial bones disproportionately small. As with other infant bones, the paper-thin flat bones of the cranial vault are not fully ossified, allowing

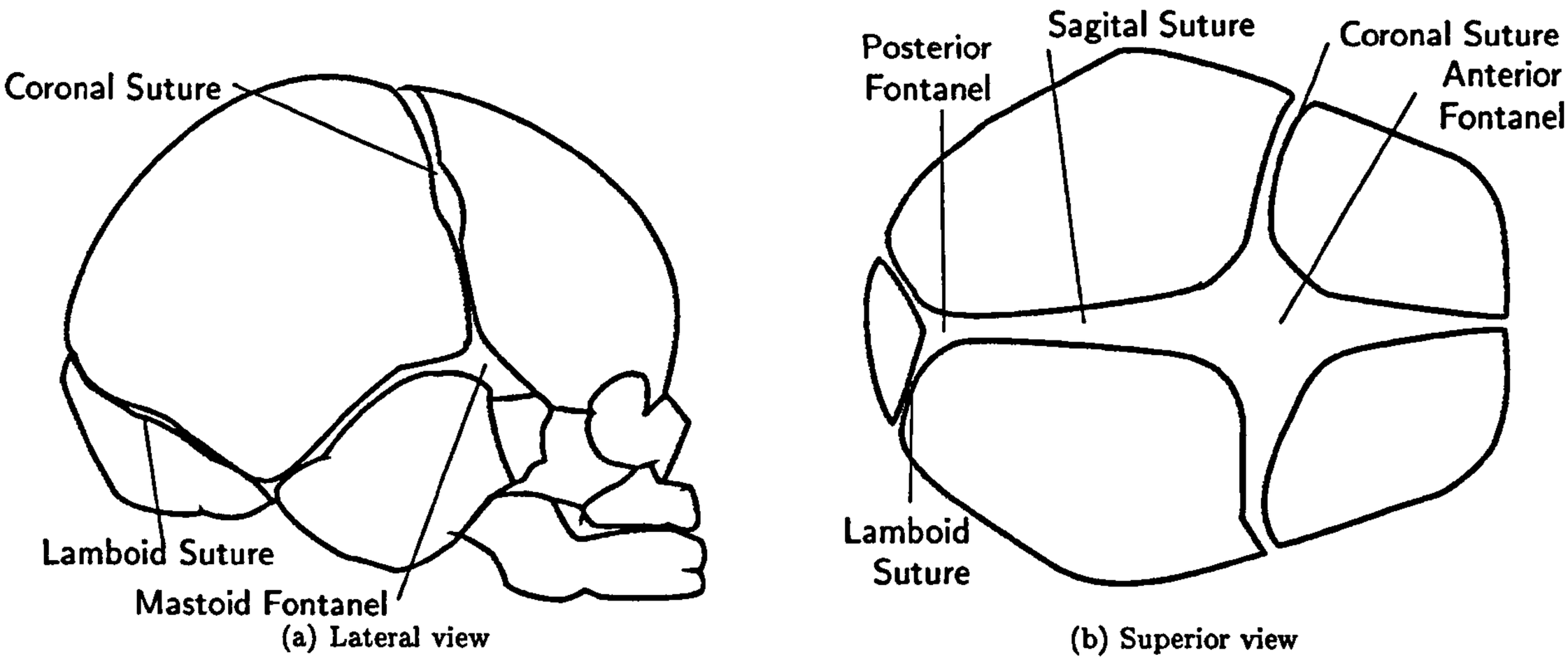

(a) Lateral view (b) Superior view

Figure 2.2: Human infant skull showing the relatively large size of the cranial vault in relation to the face, and the unfused sutures and fontanels.

them to flex and bend. In addition, the sutures are unfused with the resulting gaps between the bones joined by fibrous tissue; where sutures meet, large gaps in the cranium called fontanels are formed. Although these anatomical differences reduce the protection of the brain provided by the cranial vault they allow relative motion of the bones and ease passage through the birth canal. These anatomical differences can be seen in Figure 2.2, where it should also be noted that the mastoid process is undeveloped in the infant.

2.2.2 Brain

Figure 2.3 shows the three main areas of the brain; the cerebrum, the cerebellum and the brain stem. The major mass of the brain is the cerebrum, a complex structure, divided into the left and right hemispheres by the longitudinal fissure. Its surface is covered in numerous folds and grooves (gyri and sulci), which greatly increase its surface area. Each hemisphere is divided into a number of lobes, each named according the over-lying bone of the skull (i.e frontal, parietal, occipital and temporal). These lobes are associated with specific functional activity, for example the frontal lobes control voluntary motor function, the temporal lobes hearing and smell and the occipital lobe vision. In addition to functional control, the cerebrum also hosts memory and reasoning activity. Within the cerebrum is a network of fluid filled spaces or ventricles through which Cerebrospinal Fluid (CSF) circulates.

The cerebellum, or "little brain" lies beneath the posterior cerebrum, and is again divided into two hemispheres. The cerebellum is involved in balance, maintaining muscle tone and fine motor control. Both the cerebrum and cerebellum are connected to the spinal cord via the brain-stem.

The brain-stem is made up of the medulla oblongata, the pons and the mid-brain. As well

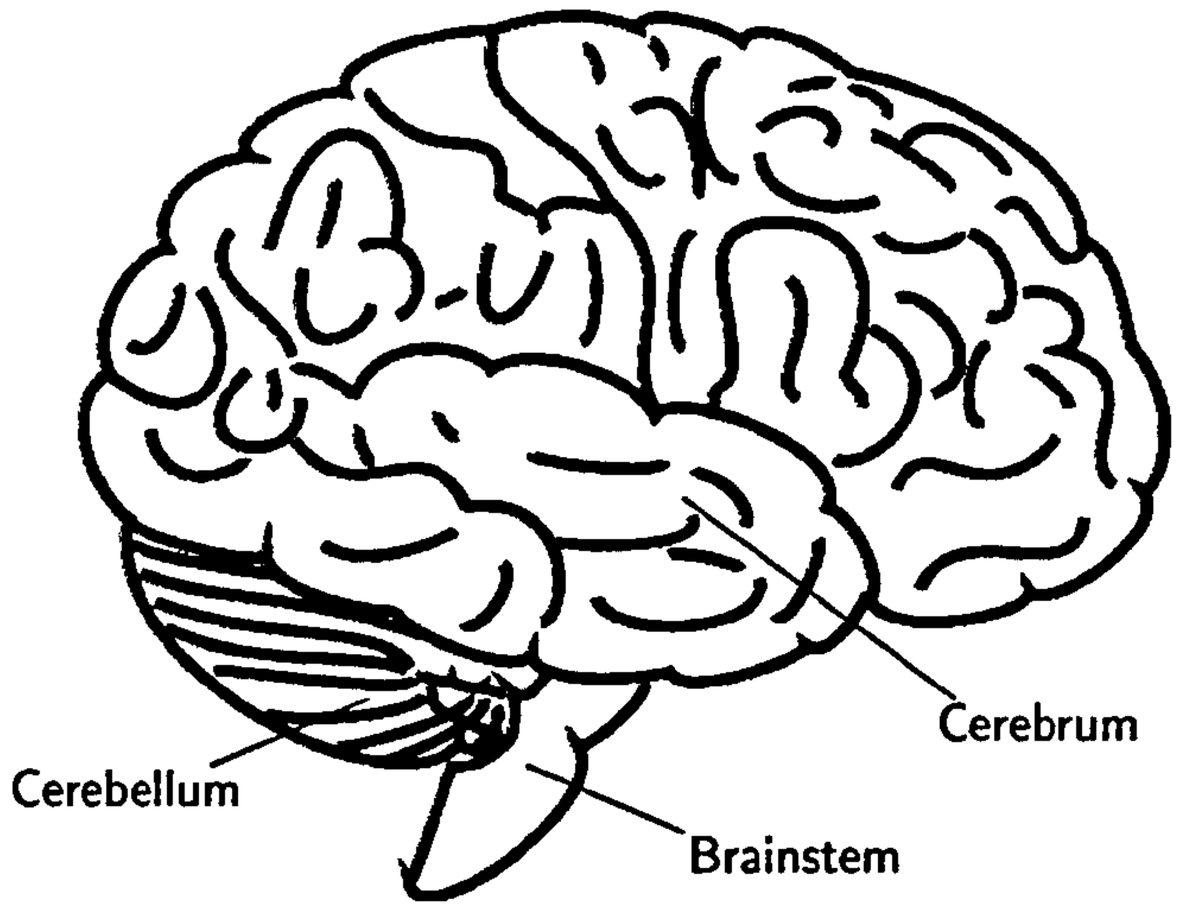

Figure 2.3: Lateral view of human adult brain showing Cerebrum, Cerebellum and Brain-Stem.

as passing signals to and from the spinal cord and the rest of the brain, the mid-brain conducts various basic functions including reflexes such as swallowing and vomiting. Most significantly it controls actions necessary for maintaining life, such as breathing and heart rate, so damage to a small part of the brain-stem can be life-threatening, whereas large portions of the cerebrum may be damaged with relatively small effect.

The infant brain is relatively small, and surrounded by a greater volume of CSF which allows a greater degree of movement within the skull. The neural cells of which the brain is comprised have not yet formed the fatty mylin sheath that act as an electrical insulator (improving conduction speeds) and provide mechanical strength.

2.2.3 Meninges

Between the surface of the brain and the interior of the skull are a series of membranous layers called the meninges, shown in Figure 2.4. Firmly attached to the surface of the brain, and following all the contours of the sulci and gyri is the vascularised pia mater. Outside this is the thin, delicate layer of the arachnoid, so called because of its delicate cobweb appearance. Between these layers, the sub-arachnoid space is filled with CSF providing nutrition and oxygen to the brain, and acting as both a protective cushion and lubricating layer. Finally, the thick layers of the dura mater are firmly attached to the interior of the skull with deep three folds into the cerebral fissures. These help to hold the brain in place within the skull; the falx ceribri lies in the longitudinal fissure, the tentorium cerebelli between the cerebrum and cerebellum and the falx cerebelli between the two hemispheres of the cerebellum. The dura mater has two layers, which are normally firmly attached but divide at the junctions of the dural folds to form the dural sinuses. These sinuses drain CSF and blood from the brain to veins which rejoin the vascular system. Blood passes from the pia mater through the sub-arachnoid space to the dural

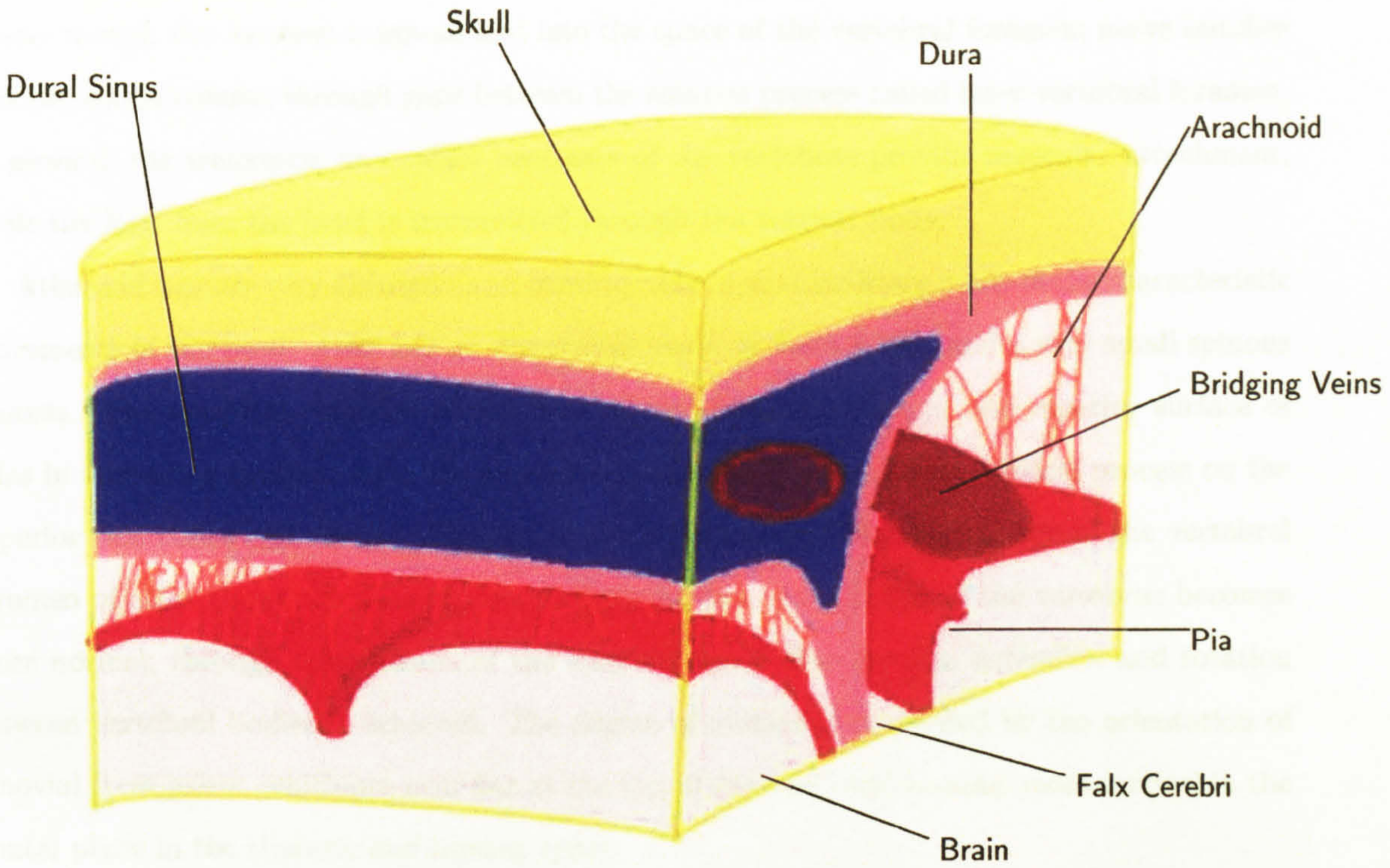

Figure 2.4: Meningeal layers covering the brain; the pia mater, arachnoid and dura mater. Also shown; the falx ceribri with dural sinus and bridging veins.

sinuses via bridging veins. Normally, there is no gap between the arachnoid and dura, but since these layers are not firmly attached there is a potential space called the sub-dural space. Brain injury may cause areas of this space to fill with blood, resulting in a SDH.

2.2.4 Neck

The human head has a large range of motion made possible by the elegant anatomy of the neck. Neck kinematics have been studied in great detail, and the development of biofidelic neck forms had been one of the greatest challenges in ATD design. As with the head, the anatomy of the infant neck is different to that of the adult, and so has bearing on head motion in SBS.

Skeletal

The neck has seven cervical vertebrae, which support the head and provide protection to the spinal cord as it exits the skull. These are the smallest vertebrae in the spinal column, as they have least weight to bear (the vertebrae of the lumber spine must carry the weight and muscular load of the entire torso, as well as the head and upper limbs), but must allow the passage of the spinal cord at its greatest diameter, so have the largest vertebral foramen.

Figure 2.5 shows the general anatomy of three cervical vertebrae; C5 and C1 or *"Atlas"* and C2 or *"Axis"* which have distinct anatomy from the rest of the cervical spine. The spinal cord

passes though the foramen magnum and into the space of the vertebral foramen; nerve bundles exit the spinal column through gaps between the spinous process called inter-vertebral foramen. In general, the transverse and spinal processes of the vertebrae provide muscular attachment, while the load from the head is transmitted through the vertical body.

Atlas and axis are very different to all other vertebrae, and facilitate many of the characteristic movements of the head. Atlas has no discernible body, or facet joints, and a very small spinous process. The occipital condyles of the base of the skull articulate at the superior surface of atlas in a nodding motion. Axis has a small vertebral body with a large vertical process on the superior side called the *"dens"*. Shaking of the head rotates the anterior face of the vertebral foramen of atlas about the dens of axis. Inferior to this, articulation of the vertebrae becomes more normal; through compression of the inter-vertebral discs flexion, extension and rotation between vertebral bodies is achieved. The degree of motion is controlled by the orientation of synovial facet joints, which are near flat at the top of the neck, and become more vertical in the frontal plane in the thoracic and lumbar spine.

Vertebral bodies are joined by inter-vertebral discs, which have a fibrous outer ring called the *annulus fibrosis*, which is filled the by the gelatinous *nucleus pulposus*. As well as allowing motion in six degrees-of-freedom, these discs act as shock absorbers, protecting the the spinal column and head from axial loads.

In the vertebrae of the infant there are several areas of unossified cartilage which reduce strength and stiffness. As with the mastoid process many of anatomical features associated with muscular attachment, such as the spinous and transverse processes, are immature and the facet joints are smooth and flat. These anatomical differences mean that the infant neck has a far greater range of motion, reducing support for the head, and protection of the spinal cord.

Musculature

The musculature of the neck is not only powerful, supporting the full weight of the head, but also provides fine motor control to keep the head steady during motion. Figure 2.6 shows a small selection of the posterior muscles of the neck, largely responsible for extension. For example Trapezius and Semispinalis attach at the occipital bone, and abduct and extend the neck. Sternocleidomastoid, attaches at the mastoid process and may either extend the head when both left and right muscles act together, or rotate the head when acting on one side only. The undeveloped musculature of the infant neck means that it is weak, and the head cannot be held upright without support until after the age of about three months [9].

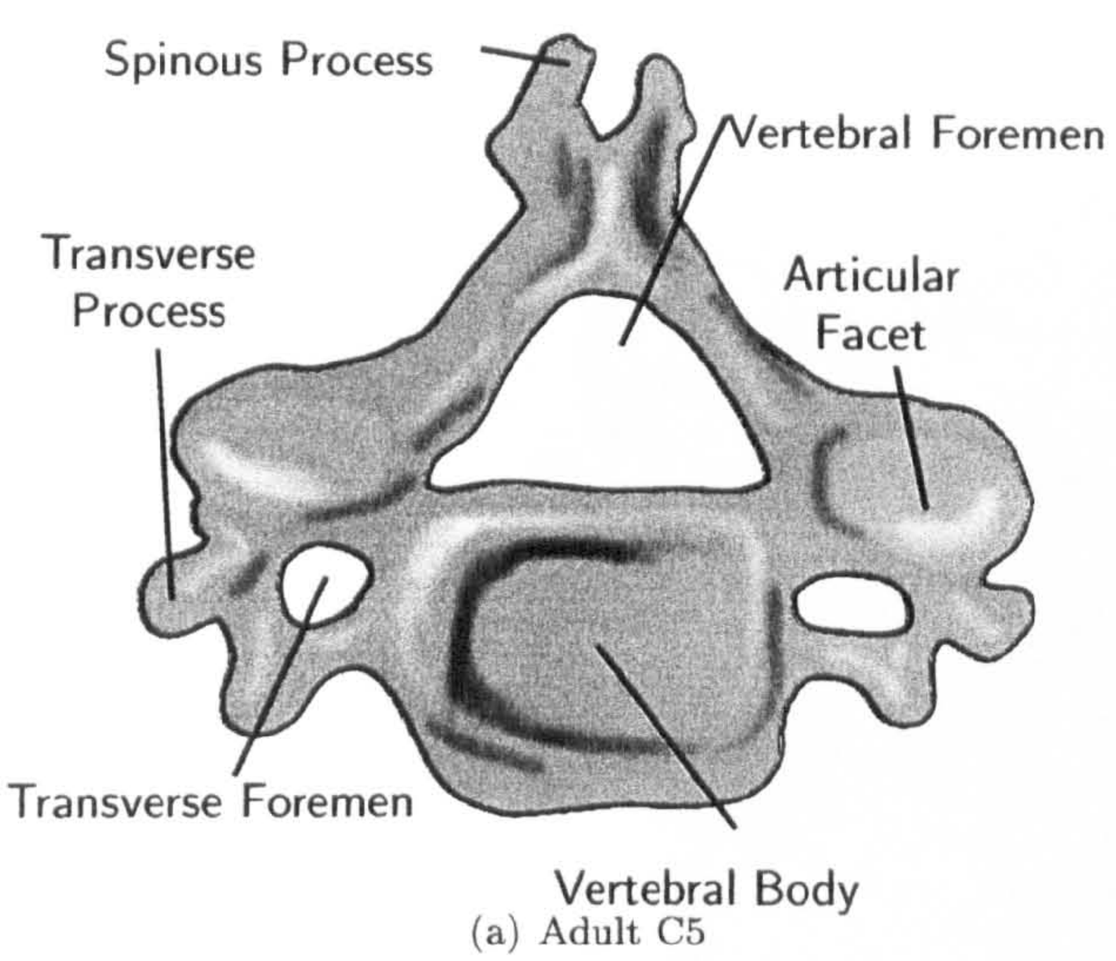

(a) Adult C5

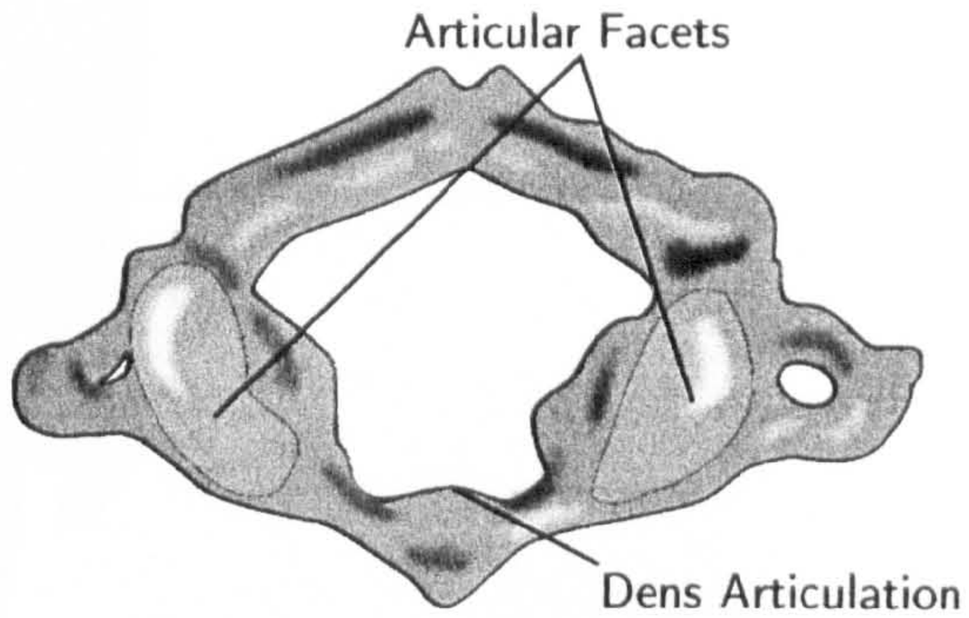

(b) Atlas

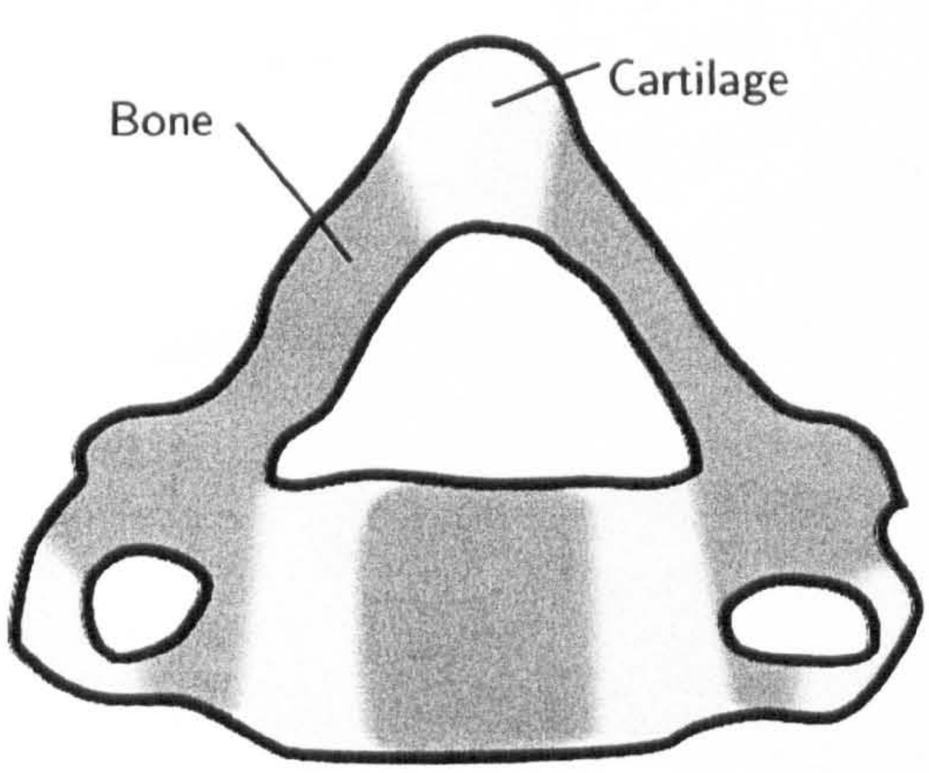

(c) Infant C5

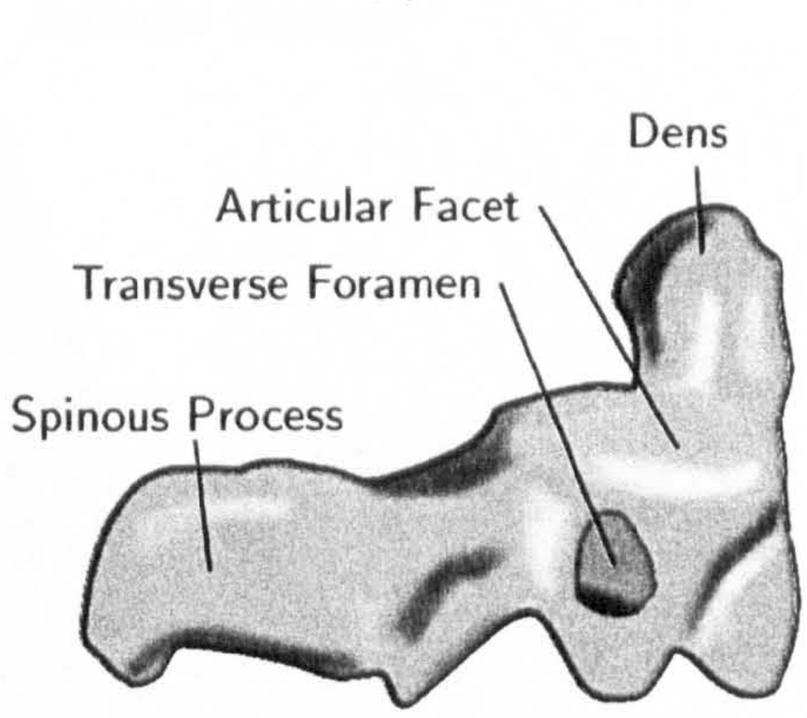

(d) Axis

Figure 2.5: Examples of cervical vertebrae, showing the articulation surfaces of axis and atlas, and general layout of C5 in the adult and areas of cartilage in C5 of the infant. Adapted from [8].

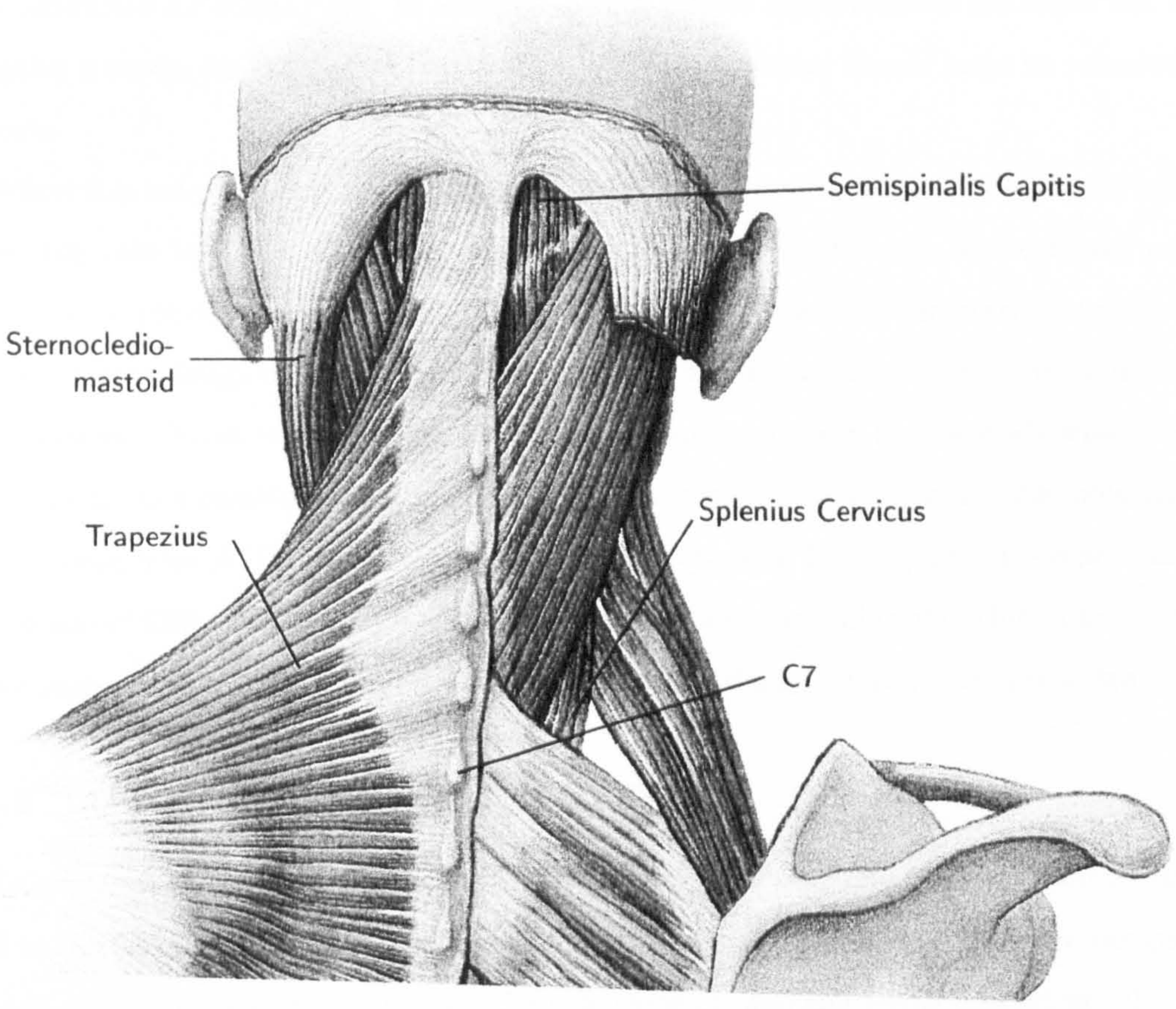

Figure 2.6: Posterior musculature of the neck, showing both strong surface muscles and deep muscle groups providing fine control. Adapted from [8].

2.3 Techniques for Biomechanical Investigation

In order to study biological systems in terms of engineering mechanics, it is necessary to isolate systems or factors of interest. A wide variety of techniques are employed to this end, ranging from volunteer testing to mechanical testing of cadaveric or animal tissue specimens. In each case consideration must be made of the effects of the method of investigation, and the resulting validity of the application of data obtained. For example, fixation and preservation of tissue samples is likely to result in changes in their mechanical properties so it is important that the techniques used should be accurately reported enabling them to be repeated in any subsequent tests conducted for comparison. In addition to this, ethical considerations are important when designing a study, for example no physical of psychological harm should come to volunteers or patients.

Where it is not possible to conduct direct testing on a subject, surrogates may be used instead. These may take the form of physical, computational or analytical models and normally rely on findings from previous material tests. Although the result obtained from surrogate studies are indirect, careful design of methodology and interpretation of results can provide valuable insight into a system. Direct testing on infants or infant tissue specimens in this study would clearly be unethical, so a combination of surrogate techniques were used to examine the biomechanics of SBS. Data from ATD testing was used in combination with RBM to produce computational simulations of SBS. This was followed by physical continuum modelling of the infant brain. Some of the background principles, and examples of these modelling techniques are presented here.

2.3.1 Anthropometric Test Dummies

ATDs were first developed to test ejector seats for early jet planes; today they are most commonly used in the automotive industry to study occupant responses to impact. They are designed to provide repeatable, calibrated data on the behaviour of, and the forces exerted on, the body in hazardous situations. These data are then used in conjunction with known injury criteria to establish the potential for harm of the scenario under investigation. The dummies are not intended as a universal biofidelic representation of the human body, but provide good approximations for specific loading conditions. For example, the Hybrid III dummy is used in frontal automotive impact studies, where the BIO-RID and BIO-SID are Rear Impact Dummies and Side Impact Dummies respectively. It is therefore important that the appropriate dummy is used for each test, and that the approximations and assumptions associated with it are understood when interpreting data.

Understanding the approximations made in ATD design is even more important when using

infant dummies. Although anthropometric data are available for children and infants, ethical considerations make obtaining dynamic response and injury data very difficult. Infant ATDs and their associated injury criteria are therefore scaled from adult data and as such undergo a further level of approximation. Despite this, ATDs provide valuable insight into the crash-worthiness of vehicles, as long as care is taken in interpreting results obtained in test conditions outside the scope of their design.

2.3.2 Rigid Body Modelling

Computational modelling has become a mainstay of engineering design and analysis; finite element (FE) methods allow detailed simulation of engineering components and systems through use of accurate geometric and material data. However, the costs of this method in terms of computational time and required input data are high. As already discussed there is a paucity of data available on the biomechanics of the human infant, so the implied level of assumption and approximation required in producing FE simulations of SBS are great.

Rigid body modelling offers an alternative method of computational simulation, using simplified geometry and component joint and interaction characteristics. Again, there is a high level of approximation, but the computational and data costs are much lower. Through careful validation, the technique has been increasingly used in the study of larger systems, such as full automotive vehicle simulations where incorporation of ATD models has added further functionality. The use of this technique in simulating SBS is described in Chapter 5, but the basic theory of its implementation is given here.

As the name suggests, rigid body models are constructed from a series of individual bodies whose interaction simulates the characteristic of the system under investigation. Each body is defined in terms of its mass and inertial properties. Interaction between bodies occurs in a variety of ways, the simplest of which is through joints.

Joints determine the way bodies move relative to one another, and depending on their type they may be fixed with no degrees of freedom (in effect fixing two bodies together) or slide or rotate with up to six degrees of freedom. Since the body is modelled as a point mass, the relative position and orientation of a joint must also be defined. The way in which the joint moves and its range of motion is described by its stiffness at any given position (e.g. the angle of a hinge joint) and other characteristics such as hysteresis or conditional locking may be used to create complex movement between bodies. In this way a chain of bodies is joined together to create a framework for the model. However, this framework has no volume or surfaces, so no interaction is possible between bodies which are not directed linked.

In a similar manner to joints, surfaces are attached to a body and must be defined by a relative

position and orientation as well as by their geometry. Although FE style meshed surface can be used, the geometric definition need not be detailed and simple ellipsoids are more commonly used; by using multiple ellipses, complex surface approximations can be constructed. By defining their reaction to contact with other surfaces, interaction between separate bodies or systems, such as an ATD model and the interior of a car, can be simulated.

Once a complete model has been constructed, different external forces are applied to simulate its reaction to different scenarios. Gravitational acceleration, a simulated impact load or a velocity impulse could be applied to any body within the model; in Chapter 5 an acceleration pulse is applied to the torso of simple infant models to simulate shaking. The response of the model is studied by defining selected outputs, which act like sensors in ATD tests. They are defined in terms of their position, attachment to bodies or surfaces, the type of output and their sampling rate. In Chapter 5 acceleration and velocity output recorded from sensors in the head are used to asses the risk of injury.

2.3.3 Physical Modelling

Although often superseded by computational modelling, physical surrogates can be useful in studying the characteristics of biomechanical systems. While their design and construction is less flexible, idealisation of a system into a simple physical model can provide more tangible insight into the interactions of a system than a complex computational simulation. Their bio-fidelity need not always be high; a simple geometric approximation of an expensive or rare specimen (such as human cadaveric tissue) might be used during preliminary testing in order to validate an experimental setup or procedure. In other cases, they might be used to isolate a factor in a complex system, or to directly simulate the characteristics of a biological specimen that is not available for testing.

In Chapter 6, silicone gels are used to simulate infant brain tissue under cyclic load. Although these simplified models do not incorporate the full complexity of the anatomy of the brain, such as the shape of the surface gyri or the different material properties of grey and white matter, they provide a good overall approximation of the movement and distortion of the brain. As discussed in chapter 3, this method has given insight into brain injury mechanisms, and and allowed the influence of specific anatomical features such as the ventricular system to be better understood.

2.4 Brain Injury Mechanisms

Although rarely occurring in isolation, brain injury mechanisms are divided into a number of categories each of which are associated with a distinct pattern of injury. The danger to the patient is often dependent not on the apparent severity of the injury, but the region of tissue which is damaged. Whereas injury to relatively large areas of the cerebrum may result only in loss of specific functions associated with that region, damage to very small areas of the brain stem can present a serious threat to life.

While the complex combination of injuries considered diagnostic of SBS described in Section 2.1 includes both SDH and DAI, evidence of impact to the head suggest that shaking has not occurred in isolation. These cases of so called "shaken impact syndrome", have been one of the major points of clinical and academic debate in the literature, and are discussed in some detail in Chapter 3. An understanding of the characteristic injuries of the syndrome and their causal mechanisms is necessary in this work, and this is described in the following section.

2.4.1 Penetration Injuries

Any object with enough force to break through the strong bone of the skull is clearly capable of destroying the soft brain tissue inside. However, if this damage is localised its effect on overall brain function may be surprisingly slight. A classic case of a penetrating brain injury is that suffered of Phineas Gage, a railway construction foreman working in Vermont USA. On 13th September 1848 an explosion blew a tamping iron, 3 feet 7 inches long, through his left cheek bone, and out of the top of his head . Despite what was clearly a major trauma, the injury caused was highly localised and although Gage's personality changed significantly (he was subsequently described as "fitful, irreverent, and grossly profane"), he regained full physical fitness and returned to work, though never again as a foreman [10]. This historic tale reveals the counter-intuitive nature of brain injury, and the resilience of the neurological system.

2.4.2 Contact Injuries

As with penetration injuries, pure contact injuries sustained, for example by slow crushing, can be highly localised, and surprisingly benign. They might include skull fractures and localised contusions, with mechanical damage caused directly by the penetrating object. Concussion is rarely associated with contact injuries and in many cases these injuries are of little danger to the patient who may even be asymptomatic, and make a full recovery in time. However, instances of pure contact injuries are rare, and are more likely to be accompanied by acceleration, following for instance, a blow to head.

2.4.3 Acceleration Injuries

Often more occult than penetration injuries, acceleration injuries can occur with little or no external damage to the head, and are due to relative motion of the brain within the skull, and deformation within the brain itself. They are caused by rapid acceleration or deceleration of the head such as might occur in an automotive impact, or a blow to the head with a soft object. Acceleration injuries are further subdivided into translational, rotational and angular injuries.

Translation: Caused by linear acceleration of the head, this type of injury is characterised by localised areas of tissue damage resulting from contact between the brain and interior of the skull. Although localised, damage may be found in more than one area of the brain. This can be due to coup, contre-coup mechanisms, where motion of the brain lags behind that of the skull both on acceleration and deceleration, or high-strain due to interference of reflected pressure waves within the skull.

Rotation: Considered the most injurious of mechanisms, movement of the brain again lags behind that of the skull, but in rotation the relative displacements of the brain and skull are greater, tearing bridging veins and causing SDH. In addition to this, differences in the stiffnesses of the grey and white matter within the brain result in high shear strain, leading to DAI throughout the brain. This widespread damage can be the most dangerous of brain injuries, leading to widespread neurological impairment, with poor recovery.

Angular: Pure translational or rotational acceleration of the head is unlikely to occur in isolation. In fact, in order for the head to undergo pure rotation, the entire body would have to move about a centre of rotation in the centre of the skull. Due to the anatomy of the neck, angular motion of the head at the atlanto-occiputal joint in a whiplash type of mechanism is far more realistic. This results in a mixture of injury types, for example DAI superimposed over localised coup, contre-coup contusions. It is this type of motion that is associated with SBS.

Whatever the mechanism, the danger of any of the injuries described above can be greatly increased by clinical complications. Increased intracranial pressure caused by bleeding or swelling of brain tissue can lead to reduced blood flow and ischemic hypoxia. This in turn leads to further swelling of the brain and a lethal cycle of increasing pressure within the skull.

2.5 Analytical Methods

In Chapter 6, physical models are used to investigate shaking as a brain injury mechanism: silicone models of the brain are shaken, and their movement captured using high-speed video.

By tracking the motion of optical markers within these models, changes in their relative positions can be used to determine the strain induced within the gel during shaking. Here, the background to the computational methods used to track the markers and determine strain is given.

2.5.1 Motion Tracking

In order to use optical methods to determine strain, it is necessary to know the position of a grid of markers at any time. The position of each marker must be found in each video frame, and its motion tracked using computer vision methods. These computer vision methods are increasingly used to automate the interaction between computers and the real world, and a variety sophisticated techniques are used for both object recognition and motion tracking.

Optical flow relies on the movement of objects between frames being small, so that temporal differences can be used to determine motion. Where the motion is too large for optical flow to be used, correspondence, which derives motion by explicitly matching features in subsequent frames, may be used. These enable large movements to be tracked, but require sophisticated object recognition. Here, implementation of a Simple Kalman Filter suitable for use in tracking two-dimensional motion of optical markers by optical flow is described.

The Kalman filter is a mathematical method to predict changes in a system state using information about its previous conditions; a good description of its use is given by Welch and Bishop [11]. It operates as a feedback loop, making an estimate of state, before taking a measurement of the actual state. Both the estimate and the measurement have an associated Gaussian noise, and by evaluating the relative noise terms a final estimate of the state, and its accuracy can be made. The details of its implementation depend on the complexity of the system being measured, in this case the state s of an object is described by its position (x, y) and motion (u, v). The state update equation is used to estimate the position of the object at time t. If the motion of the object is constant then:

$$s_t = As_{t-1}$$

$$\begin{bmatrix} x \\ y \\ u \\ v \end{bmatrix} = \begin{bmatrix} 1 & 0 & 1 & 0 \\ 0 & 1 & 0 & 1 \\ 0 & 0 & 1 & 0 \\ 0 & 0 & 0 & 1 \end{bmatrix} \begin{bmatrix} x_{t-1} \\ y_{t-1} \\ u_{t-1} \\ v_{t-1} \end{bmatrix}$$

At any time, the position of the object in the image may be found using the measurement equation:

$$m_t = Hs_t$$

$$\begin{bmatrix} x_t \\ y_t \end{bmatrix} = \begin{bmatrix} 1 & 0 & 0 & 0 \\ 0 & 1 & 0 & 0 \end{bmatrix} \begin{bmatrix} x_{t-1} \\ y_{t-1} \\ u_{t-1} \\ v_{t-1} \end{bmatrix}$$

The Kalman filter is initiated with an estimate of the state. From the first frame it is possible to estimate the initial position of the object, for example it may be close to (100, 170), but since its velocity cannot be found from a single time it is estimated to be stationary, i.e.:

$s_0 = [100, 170, 0, 0]^T$

This estimate is noisy, and this noise is expressed in a covariance matrix P. If the initial position measurement is accurate to within 3 pixels, and the velocity to within 5, the initial covariance in noise is given as:

$$P_0 = \begin{bmatrix} 9 & 0 & 0 & 0 \\ 0 & 9 & 0 & 0 \\ 0 & 0 & 25 & 0 \\ 0 & 0 & 0 & 25 \end{bmatrix}$$

By assuming these are independent, the off diagonal terms are zero. In a similar manner the predictions will be noisy as the motion may not be constant, or other factors such as image distortion may affect the position. This is expressed in the update covariance, or process noise and if assumed to be less than a pixel, say $\sigma = \frac{1}{2}$ is:

$$Q = \begin{bmatrix} 0.25 & 0 & 0 & 0 \\ 0 & 0.25 & 0 & 0 \\ 0 & 0 & 0.25 & 0 \\ 0 & 0 & 0 & 0.25 \end{bmatrix}$$

Finally, the measurements themselves are considered noisy, but probably not more than by a pixel, therefore the measurement, or state update covariance may be given as:

$$R = \begin{bmatrix} 1 & 0 \\ 0 & 1 \end{bmatrix}$$

Having defined the process parameters, a prediction of the state in the next frame $t = 1$ is made from the state at $t = 0$.

$s_1^- = As_0$

so in this example:

$$s_1^- = \begin{bmatrix} 1 & 0 & 1 & 0 \\ 0 & 1 & 0 & 1 \\ 0 & 0 & 1 & 0 \\ 0 & 0 & 0 & 1 \end{bmatrix} \begin{bmatrix} 100 \\ 170 \\ 0 \\ 0 \end{bmatrix}$$

the prediction covariance is given by:

$P_1^- = AP_0A^T + Q$

$$P_1^- = \begin{bmatrix} 1 & 0 & 1 & 0 \\ 0 & 1 & 0 & 1 \\ 0 & 0 & 1 & 0 \\ 0 & 0 & 0 & 1 \end{bmatrix} \begin{bmatrix} 9 & 0 & 0 & 0 \\ 0 & 9 & 0 & 0 \\ 0 & 0 & 25 & 0 \\ 0 & 0 & 0 & 25 \end{bmatrix} \begin{bmatrix} 1 & 0 & 0 & 0 \\ 0 & 1 & 0 & 0 \\ 1 & 0 & 1 & 0 \\ 0 & 1 & 0 & 1 \end{bmatrix} + \begin{bmatrix} 0.25 & 0 & 0 & 0 \\ 0 & 0.25 & 0 & 0 \\ 0 & 0 & 0.25 & 0 \\ 0 & 0 & 0 & 0.25 \end{bmatrix}$$

$$P_1^- = \begin{bmatrix} 34.25 & 0 & 25 & 0 \\ 0 & 34.25 & 0 & 25 \\ 25 & 0 & 25.25 & 0 \\ 0 & 25 & 0 & 25.25 \end{bmatrix}$$

From this prediction, the object is expected to be at $(100, 170)$, and it is 95% certain to be within 2σ of this position. A measurement can therefore be taken within a circle of radius $\sigma = \sqrt{34.25} \approx 5.85$ pixels of the predicted position, for this example $m_1 = [103, 163]^T$. The relative certainties of the prediction and measurement are combined into the Kalman gain:

$$K_1 = P_1^- H^T (H P_1^- H^T + R)^{-1}$$

$$K_1 \approx \begin{bmatrix} 0.972 & 0 \\ 0 & 0.972 \\ 0.709 & 0 \\ 0 & 0.709 \end{bmatrix}$$

This provides a weighting for which estimate is more certain, in this case the upper elements are closer to one, therefore the measurement is more certain. A final estimate of state of the system can now be made:

$$s_1 = s_1^- + K_1(m_1 - H s_1^-)$$

$$s_1 \approx \begin{bmatrix} 100 \\ 170 \\ 0 \\ 0 \end{bmatrix} + \begin{bmatrix} 0.972 & 0 \\ 0 & 0.972 \\ 0.709 & 0 \\ 0 & 0.709 \end{bmatrix} \left(\begin{bmatrix} 103 \\ 163 \end{bmatrix} - \begin{bmatrix} 1 & 0 & 0 & 0 \\ 0 & 1 & 0 & 0 \end{bmatrix} \begin{bmatrix} 100 \\ 170 \\ 0 \\ 0 \end{bmatrix} \right)$$

$$s_1 \approx \begin{bmatrix} 102.9 \\ 163.2 \\ 2.13 \\ -4.96 \end{bmatrix}$$

Finally, the state covariance is determined:

$$P_1 = P_1^- + K_1 H P_1^-$$

$$P_1 = \begin{bmatrix} 34.25 & 0 & 25 & 0 \\ 0 & 34.25 & 0 & 25 \\ 25 & 0 & 25.25 & 0 \\ 0 & 25 & 0 & 25.25 \end{bmatrix} +$$

$$\begin{bmatrix} 0.972 & 0 \\ 0 & 0.972 \\ 0.709 & 0 \\ 0 & 0.709 \end{bmatrix} \begin{bmatrix} 1 & 0 & 0 & 0 \\ 0 & 1 & 0 & 0 \end{bmatrix} \begin{bmatrix} 34.25 & 0 & 25 & 0 \\ 0 & 34.25 & 0 & 25 \\ 25 & 0 & 25.25 & 0 \\ 0 & 25 & 0 & 25.25 \end{bmatrix}$$

$$P_1 \approx \begin{bmatrix} 0.971 & 0 & 0.71 & 0 \\ 0 & 0.971 & 0 & 0.71 \\ 0.71 & 0 & 7.52 & 0 \\ 0 & 0.71 & 0 & 7.52 \end{bmatrix}$$

This process is repeated for each frame in the sequence, and if the motion model is accurate the predictions will become more certain, meaning that a smaller area can be used to take the measurement thus reducing computational time.

2.5.2 Green-Lagrange Strain by Tensor Algebra

In Chapter 6 strain distributions in a physical model of SBS are determined by relative positions of optical markers. Strains are calculated for a two-dimensional continuum relative to the initial unstrained condition through use of the Lagrangian Strain Tensor, as described by Ivarsson *et al.* [12]. Any point within the continuum has a unique vector label x, with material coordinates:

$\xi = [\xi_1, \xi_2]$.

The position vector $\mathbf{x}$ of any point at time t given by:

$\mathbf{x} = \mathbf{x}(\xi, \mathbf{t})$,

So that in the initial state, the reference vector is:

$\mathbf{x_0} = \mathbf{x}(\xi, \mathbf{t_0})$.

Consider three points P, Q and R in Figure 2.7. The strain at point P is determined by the relative positions of points Q and R, with vectors $d\mathbf{x}_{01}$, $d\mathbf{x}_{02}$ respectively at t_0 and $d\mathbf{x}_{11}$, $d\mathbf{x}_{12}$ in some strained position at t_1. If the relationship between the reference and strained states is described by the deformation tensor $\mathbf{F}$, then:

$[d\mathbf{x}_{11}, d\mathbf{x}_{12}] = \mathbf{F} \star [d\mathbf{x}_{01}, d\mathbf{x}_{02}]$,

where:

$\mathbf{F} = (\nabla_0 \mathbf{x})^T$,

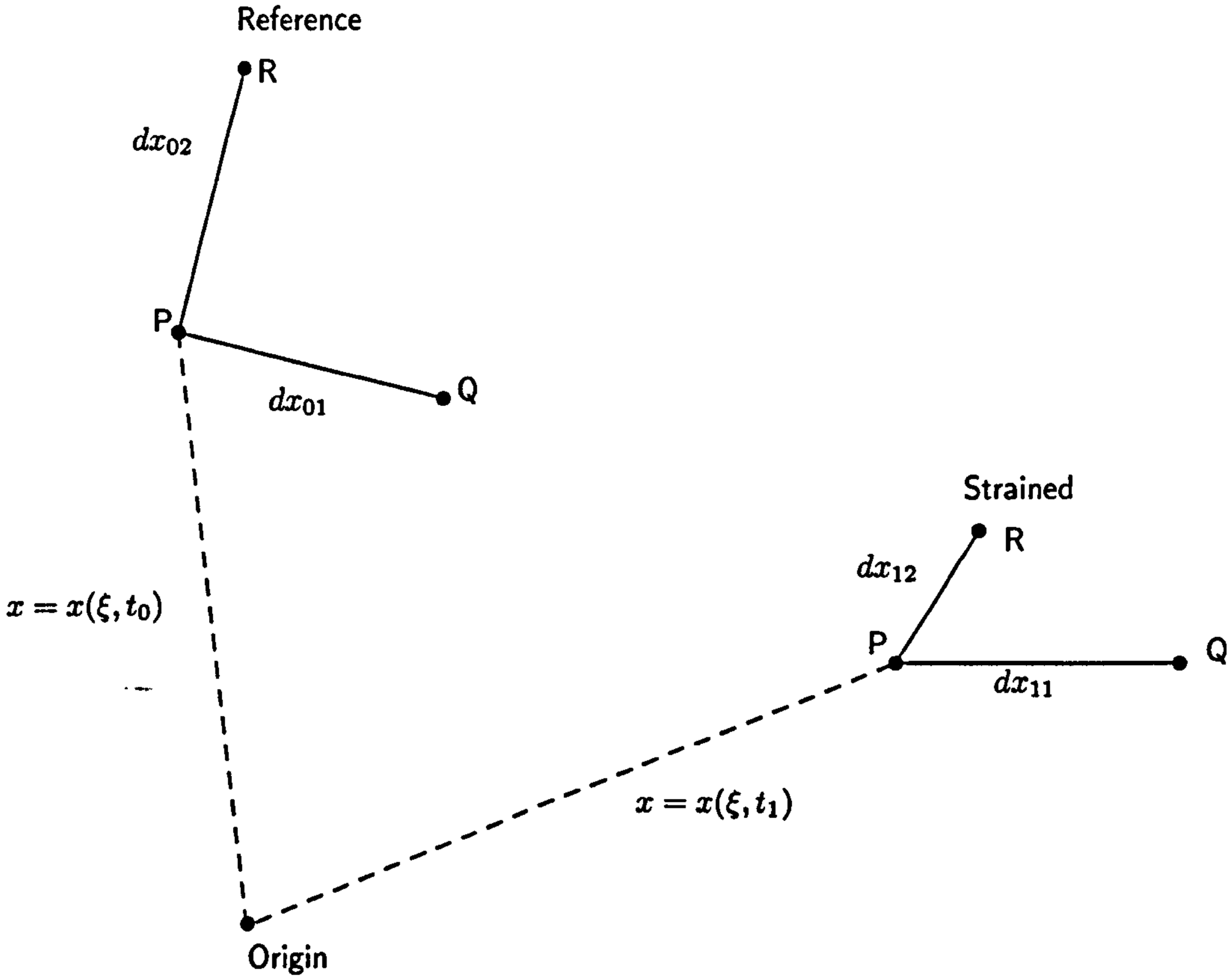

Figure 2.7: Reference and strained state for Green-Lagrangian strain determination. Adapted from[12].

and$\nabla_0$is the gradient operator relative to the reference state. The deformation tensor describes not only the transformation of the point, but also its real and rotational deformation, thus the Green-Lagrangian strain tensor, can be described as:

$\mathbf{L} = \frac{1}{2}(\mathbf{F}^T \star \mathbf{F} - \mathbf{I})$.

where $\mathbf{I}$ is the unit tensor. The various elements of $\mathbf{L}$ have physical meaning. The eigen-values are the principle or maximum and minimum strains at the point. The direction of these principle strains are naturally perpendicular, and given by the eigen-vectors. In addition to the principle strain, the shear strain can be derived from the rotation of the points. In this way the strains at any point within the continuum at time t may be found.

Chapter 3

Literature Review

There is a large body of clinical case studies and reviews of SBS that describe young infants with severe, life-threatening injuries. These studies contain victims both with, and without, evidence of external head impact. The few biomechancial studies that have been reported are inconclusive as to the capacity for shaking alone to cause the injuries associated with the syndrome. Other theories, such as clinical cascades, have been presented as possible causes for the syndrome but they are unable to explain the mechanical injuries associated with SBS.

Biomechanical studies have been restricted by the paucity of data on the biomechanics of the infant. Both Duhaime *et al.* and Cory *et al.* have used infant ATDs to study head acceleration in SBS, but were unable to assess the biofidelity of their neck forms [1, 2]. These studies were unable to demonstrate that shaking alone could exceed brain injury criteria, and indicate that impact is necessary. However, the criteria used to assess the risk of injury in these studies originate from single high-acceleration impact studies, and their use in studying brain injury in SBS is questionable. Of the alternative techniques available to studying brain injury, physical modelling can be carried out with relatively little background data, provides good control of experimental variables and has no ethical constraints.

3.1 Shaken Baby Syndrome

Most of the literature on SBS is clinical in origin and largely consist of analysis of case reviews or individual case studies. It is usual to describe presenting symptoms and physical, radiological and pathological findings from further investigations. The often fatal nature of brain damage in infants and difficulties in tracing survivors mean that there are few long term studies of victim outcome.

SBS has been described as "suffused with dogma and short on hard science" [13], and this is

no more the case than for the debate about the necessity for impact to cause the head injuries associated with the syndrome. In contrast to the large body of clinical literature there has been little scientific research into the mechanisms of injury in SBS. Whilst it is a compelling hypothesis that violent shaking of young infants might lead to retinal haemorrhages, brain damage and inter-cranial bleeding, biomechanical studies have been unable to prove that this is possible without impact.

When reviewing the literature it is also important to bear in mind that the death or serious injury of an infant is a highly emotive event. This is reflected in the strong views and opinions sometimes expressed in the literature, which should not be mistaken for scientific research. Although incorrect allegations of child abuse greatly increase the suffering of the parents, child welfare is of paramount importance. While there continues to be doubt about the mechanisms of injury in SBS, balancing these powerful ethical contradictions continues to be a difficult responsibility for all those involved.

3.1.1 Historical Origins

In 1971 Guthkelch described a number of cases of battered children with inter-cranial bleeding, but no external signs of head impact [14]. He suggested that these might be caused by shear strains within the skull, a theory taken up by Caffey in 1972 when he first proposed that "whiplash shaking and jerking" might be a cause of skeletal and cerebro-vascular lesions [15]. He presented twenty-seven cases comprising a variety of unexplained intracranial bleeding, and long bone injury. Significant in Caffey's description was the absence of "suggestive signs of head injury", and an eventual confession of shaking in several cases.

Caffey further described what he now termed the *"whiplash shaken infant syndrome"* in 1974 as an *"extraordinary diagnostic contradiction"* of intracranial and intraocular haemorrhages without external signs of head trauma [16]. Since these first reports the *"Shaken Baby Syndrome"* has been reported frequently and challenged often, but efforts to understand it have proved inconclusive. An overview of these reports and challenges highlights the current problems with diagnosis and prosecution of cases of Shaken Baby Syndrome.

3.1.2 Clinical Reviews

Since diagnosis of a syndrome relies on recognising a combination of seemingly unrelated symptoms, clinical reviews of groups of cases have been useful in defining the what is meant by SBS. Many of these reviews have been published, some simply describing findings from a specific hospital or time period, others looking at specific aspects of the syndrome such as incidence or abuse history.

General Reviews Reviews of SBS show that victims are young infants, who present with non-specific symptoms, but severe injuries. The combination of SDH and retinal haemorrhage is characteristic, but not diagnostic of, SBS, which as discussed in more detail in Section 3.1.5 may also be accompanied by external head trauma (Shaken Impact Syndrome). Bruising and fractures of ribs and long bones are also common and, as with other forms of abuse, presenting histories are inaccurate. The outcome for victims cannot be expected to be good, with high mortality and morbidity including neurological, sensory and physical impairment.

A typical paper is that of Ludwig *et al.* who carried out a review of all official child abuse reports from the Children's Hospital of Philadelphia between 1977 and 1982 [5]. Of 1250 cases reviewed, 20 children were identified as having been only shaken (i.e. no signs of external head trauma, skull fracture, burns etc.). Fourteen of these were male and six female, and their ages ranged from 1 to 15 months (mean 5.8 months). The most common presenting complaint was respiratory distress, but CNS disorders (i.e. lethargy, irritability, seizure, limpness) and gastrointestinal disorders (i.e. diminished appetite, vomiting, constipation) were also common. A trauma history was obtained in only 11 of the 20 cases, 8 of which were of minor accidents; only three mentioned shaking. Physical findings included bradicardia, apnea and hypothermia as well as a bulging anterior fontanel. Amongst the 18 cases in which ophthalmic examinations were carried out 12 had retinal haemorrhages. Neurological signs ranged from irritability and lethargy to seizures and posturing. Positive findings from radiological examination by cranial CT were considered diagnostic for SBS and included 8 cerebral contusions and 10 subdural and 5 subarachnoid haemorrhages. Three of the children died, and ten of the survivors had significant morbidity including blindness, motor impairment, seizures and developmental delay.

In a similar study Alexander *et al.* identified 24 cases of infants with inter-cranial injuries attributed to shaking between 1984 and 1989 [17]. Half were male, half female and their ages were between 3.5 and 59 weeks with a median of 8 months; 6 died from their injuries. Half the patients had suffered direct head trauma (inferred from physical examination, x-ray or autopsy), but there was no difference between the injuries recorded in this group and those that had only been shaken. This is presented as a challenge to the assertion that impact is required to cause the inter-cranial injuries of SBS, discussed in Section 3.1.5.

A ten year review of SBS in Canada was conducted by King *et al.* for cases of under fives with intracranial, intraocular or cervical spine injuries and suspected or substantiated shaking between 1988 and 1998 [18]. Cases with and without impact were included. 364 cases of SBS were identified, aged between 7 days and 58 months (median 4.6 months), 56% of whom were male. The most common presenting complaint was seizure (45%), with decreased consciousness (43%) and respiratory distress (34%) also common; other complaints included lethargy, irritability,

vomiting and apnea. Historically 47% had previous maltreatment, and prematurity (14%), excessive crying (10%) and feeding difficulty (9%) were also listed. The most common injuries were SDH (86%) and retinal haemorrhage (76%), but bruising (46%), cerebral edema (42%) and subarachnoid haematoma (37%) were also common. There was no sign of external trauma in 40% of cases. The perpetrator was identified in 240 cases (66%), and was most likely to be the biological father (50%) or stepfather/male partner (20%). 69 (19%) children died, and only 65 (22%) of the 295 survivors had no health or developmental impairment. 162 (55%) had neurological deficit, and 192 (65%) had visual impairment.

Serial Abuse SBS is a form of child abuse that may occur as an isolated incident, or as part of a series of abuse. In a review of children seen in Iowa hospitals between 1984 and 1988, twenty-four were identified by a multidisciplinary team as having been shaken [7]. Of these, twelve had sustained external head trauma and were eliminated from the study, but of those remaining seven (58%) had indications of previous physical abuse.

Incidence Few studies look directly at the population incidence of Shaken Impact Syndrome as it is reported by the separate injuries received rather than as a single incident. Barlow and Minns looked at cases of Non-Accidental Head Injury (NAHI) in Scotland during 1998-1999 and report annual incidence of SBS as 24.6 per 100 000 [19]. The median age was 2.2 months, and cases were more common in urban areas during winter. No information is given on the methods used to distinguish Shaken Impact Syndrome from other cases of NAHI.

Long-term Outcome General review papers tend to be based up the clinical notes available following the incident leading to admission which only provide information on the patient up to discharge. Since victims are at an early stage of neurological development, assessment of deficits resulting from their injuries cannot be comprehensive. It is therefore difficult to asses the true damage of SBS at discharge, and long-term followups of victims have revealed higher morbidity than indicated by reviews of medical notes.

Between 1979 and 1985, 25 patients admitted to Children's Hospital of Michigan were classified as having been shaken without impact [20]. In 1994 Fisher traced ten of the 17 those who had not died or been re-injured and reviewed their current condition. Of the three classified as "normal" on discharge only one was still normal on follow-up, the other two having a variety of neurological, cognitive, sensory or behavioural impairment.

A long term follow up of 13 Whiplash Shaken Infants was published by Bonnier *et al.* in 1995 [21]. The children had common SBS injuries, including SDH and retinal hemorrhages, and were reviewed annually for between four and fourteen years. The findings were summarised in a

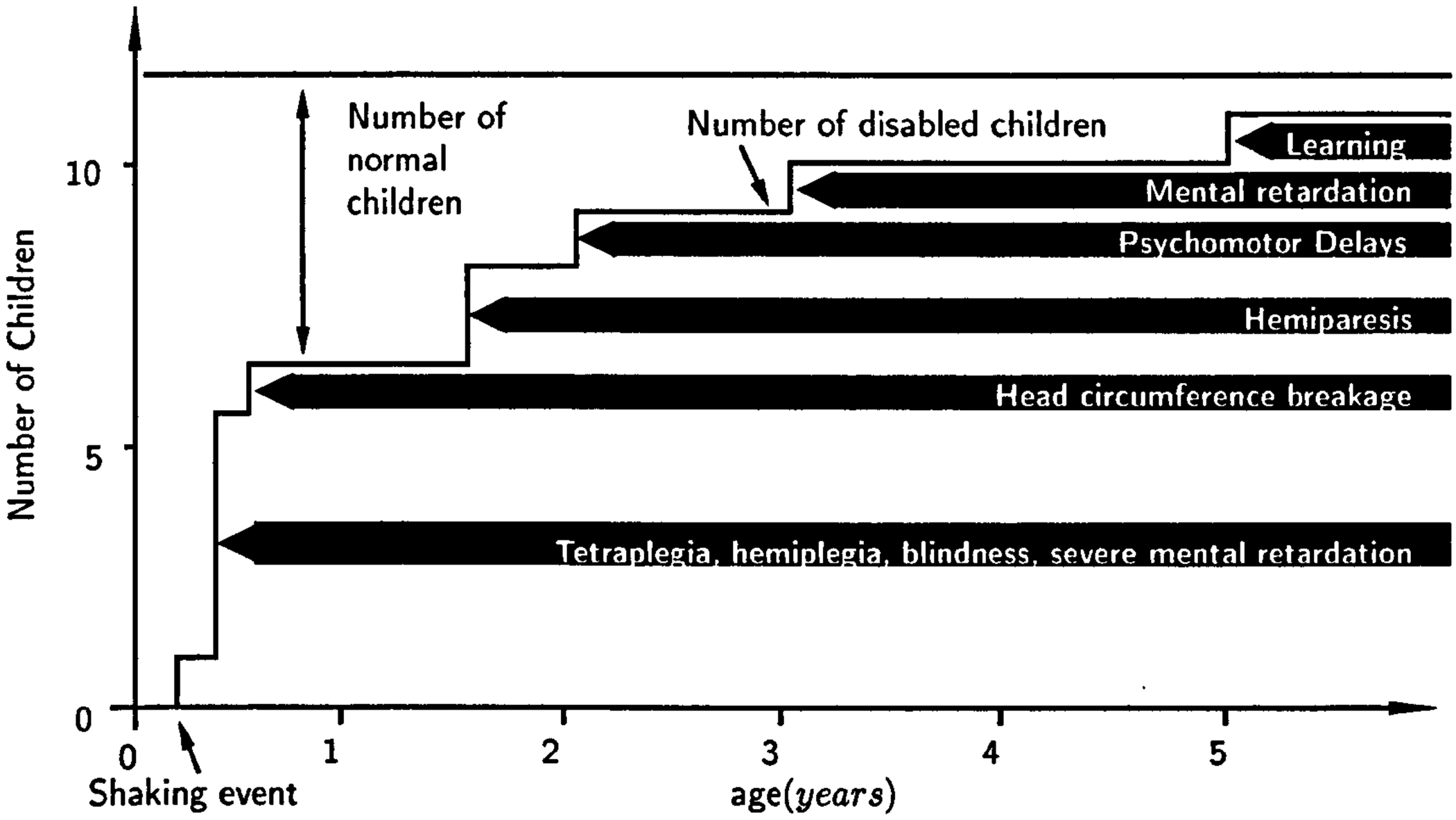

Figure 3.1: Chronology of appearance of developmental defects after SBS. Horizontal upper line represents total number of childeren. Step curve corresponds to number of disabled children; this number increases incrementally with time. Difference between upper horizontal line and step curve corresponds to number of unaffected children remaining. Psychomotor delays and mental retardation are specifically indicated when they were the first disability to appear; they were also conspicuous when other neurological disabilities appeared earlier. Adapted from [21].

figure which has been reproduced here in Figure 3.1. One infant died and six suffered impairment including tetraplegia and blindness within the first year. Other physical and mental impairment did not manifest until 18 months to three years after shaking. At five years there was a further case of learning disability. Only one patient showed no impairment at the time of publication.

Another long term follow-up study tried to trace 84 infants with "Shaken-Impact Syndrome" admitted to a single hospital between 1978 and 1988 [22]. 62 of these infants survived, but only 14 could be traced at an average of nine years after the shaking incident. Seven were severely disabled or vegetative, 2 were moderately disabled and 5 had good outcome but had repeated school years or required tutoring. The worst outcomes were associated with unresponsiveness on admission, age less than 6 months, and diffuse hypo-density on CT scan.

3.1.3 Case Studies

Numerous case studies of SBS are available in clinical literature, but that described by Spaide is a classic example [23]. A 10-week-old female twin presented with deep lethargy and suffering frequent seizures, but with no signs of trauma. Various histories were given, such as bouncing and accidental head impact, but the caregivers eventually admitted that they may have shaken her because she was not breathing well. CT scans showed bilateral haemorrhages over the surface of the brain, and extensive retinal haemorrhages were found in both eyes. Although the

retinal haemorrhages had healed by two weeks, CT scans repeated at ten days showed beginning cerebral atrophy. She was discharged after 13 days and after one month had severe mental and motor delays. The patient was lost to clinical follow-up after two months. Although many other cases such as this are available, there are a few that describe specific characteristics of interest.

Hadley *et al.* described neck injuries in their 1989 review paper [24]. In a note from 1977 McGrory and Fenichel describe a case where a healthy infant aged about four weeks was forcibly shaken after he stopped breathing [25]. He recovered, but became irritable upon manipulation of the neck. At four months old radiological examination revealed a fracture of the second cervical vertebra, also known as a *"Hangman's Fracture"*. It is suggested that this fracture was cased by hyper-flexion/extension during the shaking episode.

Although it is sensible to suggest that SBS is restricted to young infants due to their anatomical vulnerability (i.e. large relative head size, weak neck musculature and unmylinated brain) it is also true that to shake an older child or adult would require much greater strength and would be beyond the capability of most people. There is however one documented case of suspected *"Shaken Adult Syndrome"* [26]. In 1997 Pounder reported on the death of a 30-year-old man following violent interrogation. Autopsy examination found a pattern of injury classic of SBS: extensive bruising to the shoulders, SDH, DAI, oedema of the brain and retinal haemorrhages. There was no sign of external injury to the head and no skull fracture. When confronted with the theory that the man had been shaken, this was confirmed by security personnel involved with the interrogation.

3.1.4 Biomechanical studies of SBS

Probably the most significant publication in relation to this work is that of Duahime *et al.* in 1987 [1]. This comprehensive study of SBS comprised clinical and pathological findings as well as the first biomechanical assessment of the syndrome. Fifty-seven cases of SBS were identified, of which only twelve (25%) of the forty-four (73%) survivors were found to have no signs associated with blunt trauma to the head (e.g. scalp contusion or skull fracture). At autopsy all thirteen fatalities were found to have signs of blunt head trauma.

In addition to these findings, tests were conducted using a specially constructed infant ATD. Since data were not available to develop a biofidelic neck form three conditions were used, incorporating a range of characteristics; a free hinge, a stiff rubber hose, and a flexible rubber hose. The dummy was ballasted, and head accelerations recorded during vigorous shaking, and impact against a rigid bar. Peak angular acceleration was plotted against peak angular velocity and these results assessed against injury thresholds for concussion, SDH and DAI. Shaking alone did not exceed any of these thresholds, whilst all impacts (n=60) were found to exceed

concussion levels, and most to exceed SDH and DAI. The authors concluded that fatal brain injury is unlikely to result from shaking alone, but that impact of some kind is required.

This comprehensive study of Duhaime's has been the foundation for the principle challenge to SBS i.e. that impact is required to caused the injuries associated with the syndrome. There has not yet been a biomechanical study carried out to dispute theses findings, and there is therefore no *"scientific"* proof that the injuries seen in cases of SBS *without* evidence of head impact could have been caused by an act of violence. Cory and Jones recently used a replica of the dummy used by Duhaime to test the validity of these conclusions [2]. This study examined the effect of various parameters including the centre of gravity of the dummy, the neck insertion point and torso material. Although some factors such as head-torso impact were found to lead to increase head acceleration, levels for SDH and DAI were not reached. However the authors go on to question some of the assumptions used in assessing these data such as methods of scaling injury criteria for human infants and the use of single impact injury criteria. Given the low biofidelity of Duhaime's dummy and uncertainty in the application of injury criteria, they conclude that there is reasonable doubt about the assertion that *"pure shaking"* cannot cause fatal brain injuries in human infants.

Finite Element Methods have been used by Prange and Marguilles to study injury potential from shakes, falls and impacts [27]. A model of the head of a one-month-old infant was developed from MRI images, and porcine brain tissue tests, and subjected to loads derived from custom dummy tests. The resulting tissue deformations were assessed for axonal injury risk using thresholds from inertial porcine studies. Falls and shakes were found to be insufficient to damage more than 1% of the brain volume, where impacts were found to be sufficient to damage up to 30% of the brain volume. The authors concede that the study may be limited by the use of a rigid skull model, and no information is provided on the methods used to simulate the infant neck or on the derivation of injury thresholds.

The same group also published the findings of ATD simulations of fall, shakes and impacts[28]. A custom ATD was used with a hinged neck form and angular rate sensor attached to the top of the head. Falls were from a variety of heights (0.3m, 0.9m and 1.5m) and both hard and padded surfaces used for impacts. Accelerations were found to increase with increasing fall height, and shaking was found to result in similar levels of acceleration to falls. However, accelerations achieved during impacts against a hard surface were significantly greater than for falls or shakes, leading the authors to conclude that this leads to a greater brain injury risk. The results are not assessed in relation to any new, or previously published injury criteria.

3.1.5 Controversies in SBS

As with other syndromes, SBS is a collection of symptoms whose causes are not well understood. This naturally leads to debate and controversy within the scientific and medical communities, particularly since the outcome of case decisions relate to child welfare. In the past, issues such as racial predominance in incidence have been discussed and discounted [29], but debate as to mechanisms of injury has been ongoing for nearly twenty years. As well as biomechanical studies of infant brain injury, clinical causes for the syndrome have been explored and present valuable topics for study.

"Shaken Impact Syndrome"

Following the Duhaime's 1987 conclusion that shaking alone could not cause the injuries of SBS, several clinical reviews were published in presenting cases of SBS with no sign of impact [1]. However, the cases of combined of shaking and impact are still documented, so the term *"Shaken Impact Syndrome"* came into use [30, 31, 32, 33].

Gilliland and Folberg presented of a clinical review of 169 child postmortems in a seven year period from 1982 to 1989 [34]. Of eighty deaths by head injury, nine (11.3%) were classified as due exclusively by shaking (the absence of skull or scalp injury, in addition to two or more of: finger marks/rib fractures, subdural/subarachnoid hemorrhage (SAH), history of shaking). A further thirty (37.50%) were found to have signs of direct impact in addition to two or more signs of shaking, and forty-one (51.3%) head impact alone. In addition, the authors go on to cite a series of other studies where examples of apparent SBS without evidence for impact are given, including Hadley (1989) and Alexander (1990) [24, 17]. As well as reinforcing the significance of ocular haemorrhage as an indicator of abusive shaking of infants, the Duahime model is challenged for its inadequacy in providing an explanation for cases of SBS with no impact injuries.

In a rare report from Japan, Asamura presents the case of a 3 month old infant who died after being vigorously shaken during play [35]. The child suffered a sudden loss of appetite, after three days began vomiting and lost consciousness and was hospitalised after four days. CT revealed a small SDH, and the child died 18 hours after admission. At autopsy the child was found to have SDH and SAH, but no sign of head impact was observed.

In a review of 36 cases of Non-Accidental Injury (NAI) over a six year period Hadley *et al.* [24] identified 13 as SBS without impact, 7 boys and 6 girls with a median age of 3 months (range 1.5 to 14 months). All presented with decreased consciousness, seizures and retinal haemorrhages, and had signs of SDH and/or SAH on CT scans. Eight of the 13 patients died, and autopsy was performed on six of these; five had epidural/subdural haematoma of the spinal cord at the

cervical medullary junction, and four had ventral spinal contusions at high cervical levels. These cervical spinal cord injuries had not previously been identified.

Current Controversies

While mechanisms of injury continue to be poorly understood, recent debate has focused on clinical causes for the syndrome, its diagnosis and the strength of evidence relating to it. Respiratory distress or apnea is a common symptom in SBS, and hypoxic brain injuries are often a significant factor in fatalities. Geddes *et al.* compared neurological autopsy findings of 37 infants with inflicted head injury to 14 controls who died of other causes [36]. Craniocervical injury was found in 11 of the subjects, but none of the controls. Since this area of the brain-stem is responsible for breathing control it was hypothesised that if these injuries were caused by hyper-flexion/extension of the neck, this could lead to apnea and the hypoxic injuries associated with SBS.

Geddes *et al.* also studied the occurrence of SDH in three fatal cases diagnosed as SBS and 50 cases with no head injury including a number of inter-uterine deaths [37]. Sections of dura from paediatric autopsy were reviewed and Inter-dural haemorrhages (IDH) found in 36/50. These included 11/17 cases of inter-uterine death, so delivery was excluded as a possible cause. It is suggested that SDH seen in NAI may be caused not by damage to bridging veins, but as a result of hypoxic leakage of blood from within the dura into the subdural space.

Although there is a natural paucity of scientific research into SBS, the available literature from clinical sources should still be view objectively. Using criteria of Evidence Based Medicine, Donohoe assessed the available literature on the syndrome published between 1966 and 1998; 54 articles were evaluated, recording 307 cases [38]. Five studies used control groups, but only two of these were considered valid. All but one were retrospective, and only one was a randomised controlled trial. The available literature is described as an *"inverted pyramid"* with a large volume of opinion based on a small database of poor-quality studies. The author concluded that there was *"inadequate scientific evidence to come to a firm conclusion on most aspects of causation, diagnosis, treatment, or any other matters pertaining to SBS"*.

Since there is still conjecture relating to the details of the abusive syndrome, suspicion of SBS should be carefully considered, and all aspects of each case considered carefully. A case study presented by Lantz *et al.* describes a worrying situation where misinterpretation of literature following the death of an infant led to the removal of siblings and criminal investigations [39]. A healthy 14 month old suffered extensive head injuries after pulling a large television onto himself while at home with his father and younger brother. Injuries included soft tissue swelling of the scalp, SDH, skull fracture, cerebral contusions, and extensive retinal haemorrhaging. The

history given was appropriate to the injuries, corroborated by the other child and consistent with findings at the scene. However, the retinal injuries included perimacular folds, which the attending ophthalmologist believed to be diagnostic of NAI by shaking. The authors carried out a literature search to confirm this, and found that although it had been hypothesised and discussed, there was no scientific evidence to support this view.

3.2 Infant Neck Stiffness

As described in Section 3.1.4, previous biomechanical studies of SBS have measured head acceleration using infant ATDs with simplified neck forms. Since head motion is determined by the stiffness characteristics of the neck, this is a potential source of error. However, accurate information on the biomechanics of the infant neck is not readily available, so it has not been possible to assess the biofidelity of these neck-forms. Some efforts have been made to demonstrate how anatomical differences might change the characteristics of the human infant neck, but validating these data with biological data has not been possible. In Chapter 5, a parametric study of the effect of varying neck stiffness on head motion during shaking is conducted using computational methods. This allowed the significance of neck biomechanics in SBS to be assessed without the need for accurate data, or scaled estimates.

Normally, data on neck mechanics might be obtained through testing of cadaveric or animal specimens, for example; Nightingale *et al.* tested the relative strength of the upper and lower cervical spine of 52 cadaveric specimens in airbag deployment. Here, the upper spine was found to be stronger, but as with other areas of paediatric biomechanics, it is unethical to test human infant specimens, making testing of this sort impossible. In order to estimate what the characteristics of the infant cervical spine might be, comparative animal and computational tests have been used.

Much of this work has been carried out by Kumaresan, Yodanandan *et al.* and is described in a comprehensive collection of papers [40, 41, 42, 43]. Based on a validated FE model of the adult cervical spine, the authors investigated the effects of structural differences in models of one, three and six-year-old children. This comprised three separate studies; scaling, material properties and their combined effects. Scaling was found to increase flexibility by up to 188%, but inclusion of soft and hard tissue areas (as described in Section 2.2.4) increased flexibility by up to 465%. In combination flexibility was not considerably higher than this, with a maximum increase of 534%. Although direct validation of these findings was not possible, they clearly demonstrate that the characteristics of the infant cervical spine are significantly different to those of the adult.

Yodanandan has also utilised animal tests to examine the difference in neck mechanics between adults and infants. Working with Mayer *et al.* caprine specimens of ages equivalent to human one-year-old, three-year-old, six-year-old, twelve-year-old and adults were subjected to mechanical testing. Stiffness and strength were again found to increase with age, and the authors suggest that infant injury criteria estimates should be more conservative.

Although these tests have demonstrated that infant neck characteristics are likely to be significantly different to those of adults, they have not provided validated data suitable for computational modelling. Therefore in Chapter 5 a parametric computational study is used to establish if this lack of data is significant in studying head acceleration during shaking.

3.3 Brain Injury Studies

The results of previous biomechanical studies of SBS by Cory and Duhaime were assessed using brain injury criteria developed for use in the study of automotive collisions. In order to critically evaluate the findings of these studies, and investigate injury mechanisms in SBS, it is important to understand the origins of these criteria and the various techniques used in their derivation.

Through biological studies, levels of forces and types of motion capable of inducing specific injuries in primates have been established and used to estimate corresponding injury levels in humans. Scaling factors, again derived from animal models, are then applied to estimate injury criteria in infants. In conjunction with these biological models, physical continuum modelling of brain injury can provide better insight into the movement and deformation of brain tissue during injury. Using materials with comparable visco-elastic properties to brain tissue, high speed video can be used to record the motion of markers in simple geometric shapes during motion. This has helped to establish the importance of factors such as anatomical geometry, and intracranial membranes on brain injury. As the computational modelling of biological tissues has improved, it has become increasing possible to carry out this type of study using methods such as FE modelling.

3.3.1 Biological Studies

Although animal studies have become ethically less acceptable in recent times, their contribution to early work on brain injury is undeniable. An early breakthrough came from Pundez and Shelden who, by replacing a section of primate skull with a clear Lucite window was able to demonstrate that rapid acceleration of the head caused the brain to move within the skull [44]. This showed that brain injuries could be caused by acceleration of the head alone, and that an impact was not always required. Subsequent studies also involved primates, subjected to rapid

head acceleration through loads either applied directly to the head or through sled tests.

As the number of cars and their speed increased during the 50s and 60s, so the type of injury resulting from crashes changed. The rapid flexion-extension motion of the neck resulting from the unrestrained motion of drivers heads became known as whiplash, and Ommaya *et al.* led research into brain injuries caused by the phenomenon. Anaesthetised rhesus monkeys were secured into a sled and subjected to rapid forward acceleration, causing whiplash of the head [45]. Injuries recorded included SDH, and surfaces haemorrhages of the cervical spine. The severity of these injuries was related to the applied acceleration, providing an early basis for injury criteria.

At about the same time Unterharnscheidt and Higgins firmly fixed the heads of squirrel monkeys into a rigid helmet with a fixed range of angular motion [46]. Controlled accelerations were applied in a sagital plane, inducing injuries including SDH and spinal haemorrhages, as well as SAH and damage to bridging veins. These injuries were found to be predictable from the applied motion, and their pattern and severity dependant on the type of motion, be it translational or angular.

This technique of direct head acceleration was used in another study by Ommaya *et al.* to investigate the different effects of translational and rotational accelerations [47]. Occurrence of concussion, SDH, SAH, and inter-cerebral petechial haemorrhage and brain stem haemorrhage were found to be much higher following rotational rather than translational acceleration. It was hypothesised that while translational acceleration leads to focal brain injuries, rotational acceleration cause diffuse injuries and concussion. The increased rotational shear at the periphery of the brain and at *"sites of structural inhomogeneity"* (i.e. grey-white matter boundary) was also identified.

The effect of direction of head motion on brain injury and concussion was studied by Gennarelli *et al.* in the early 1980s [48]. Subjects were fitted in a helmet which allowed 60°of motion in a sagittal, lateral or oblique plane, during a time of between 11 to 22ms. The resulting period of unconsciousness was recorded and neurological examination conducted post-mortem. The severity of injury (i.e. duration of coma and quality outcome) was found to be directly proportional to the amount of DAI induced. Sagittal acceleration was found to result mostly in cerebral concussion (i.e. coma $\leq 15min$), and oblique acceleration in mild coma (i.e. $16-199min$), but only lateral acceleration caused severe or persisting coma (i.e. $> 6hr$). Lateral motion also resulted in the greatest amount of DAI, and it is concluded that lateral acceleration presents the greatest risk of DAI and prolonged coma.

Research to this point had identified that motion of the brain within the skull could result in brain injury from acceleration alone, and that while translational motion caused focal injuries,

rotational motion caused diffuse injury, which was most severe following lateral motion. However, the investigations described so far have applied only a single acceleration pulse to each subject. In a study by Raghupathi *et al* neonatal piglets (age 3-5 days) were anaesthetized and subjected to either a single or double non-impact rapid axial rotation of the head [49]. The period between double rotations was 15min, and at 6 hours post injury the number and density of axonal injury foci in each group we compared.The density of injury axons did not change in the double acceleration group, but the number of foci increase from ~2.2 per animal to ~15 per animal. Although the period between insults was much larger than during shaking, this demonstrated the graded response and vulnerability of the immature brain to mild but repeated loading.

These biological studies have greatly increased the understanding of brain injury mechanisms. It has been shown that the relative motion of the brain within the skull can lead to injury through acceleration alone, and that impact is not required. The type and severity of injury has been linked to the type of acceleration, with linear translation causing localised injury and rotation causing diffuse injury. Threshold levels for particular injuries have also been derived, enabling the risk of injury to be estimated for different levels of acceleration. In ATD testing, this allows acceleration data from specific test to be meaningfully assessed in terms of human injury.

3.3.2 Physical Models

In Chapter 6 silicone gel is used as a surrogate brain tissue to study strain distribution during shaking. From early investigations of brain injury, physical models have been a valuable tool for simulating the deformation of the brain within the skull. Not only have they offered an opportunity to apply loads that would normally be injurious, but also the ability to control factors such as anatomical features and geometry and skull-brain boundary conditions.

In the first such study in 1943 Holbourn discussed the significance of shear strain in different mechanisms of brain injury; impact, translational acceleration and rotational acceleration [50]. He constructed a gelatin model of the brain in a paraffin wax skull, and subjected it to *"sudden forwards rotation"* inside a circular polaroscope, allowing the distribution of strain within the gelatin to be visualised. Areas of high strain were seen along the vertex, and in the temporal lobe, corresponding to areas of injury autopsy findings. This early work not only demonstrated a link between shear strain and brain injury, but also showed the value of physical modelling in the investigation of brain injury.

Later physical models used silicone gels selected for having physical characteristics close to that of brain tissue, resulting in comparable strain levels. Margullies used physical models with idealised geometry to study the effects of the shape and size of the brain on strain induced under high energy translational or rotational loads from a HYGE kinematic linkage [51]. Again,

regions of high strain were found to correspond with greater incidence of injury; where increased angular acceleration led to a linear increase in strain, increased brain size lead to an exponential increase in strain. In a later continuation of this work, baboon and human skulls were used as gel containers, and the strain induced by lateral acceleration compared [52]. By relating these strains to injuries induced in baboons at corresponding loads, a scaled injury criteria for DAI in man was developed.

Prior to this, Aldman conducted two series of tests using silicone gel physical models to study specific anatomical characteristics [Alderman *et al.* 1981 in [53]]. The first test compared the strain response of semi-circular coronal head models with and without substitute falx-cerebri to acceleration pulses. The falx was found to alter the strain not only in locally, but throughout the substitute brain. In the second series of tests the effect of slip at the brain-skull boundary was studied using parasagittal models. In one model the silicone gel was cast directly into the skull and adhered to its internal surface. In the second model, the gel was cast into a plastic bag slightly smaller than the skull, and water introduced to simulate CSF and create a slip condition. While this reduced strain at the interface of the skull and brain, it increased the strain in the centre of the brain.

These physical modelling techniques are used extensively to further investigate inter-cranial anatomical features in the doctoral thesis of Ivarsson [53]. Following a comprehensive review of current literature on brain injury the main body of work is presented as a series of five published papers, four of which used physical models to investigate the significance of various anatomical features (lateral ventricles, irregular skull base - anterior and middle fossae, flax and sulci) on strain induced in the brain during impact [12, 54, 55, 56, 57]. All the models used a layer of paraffin to create a slip interface between the skull container and silicone brain surrogate. They were then subjected to centroidal acceleration (i.e. pure rotation) by means of a pendulum impacting a cam at a distance of 250mm, and decelerated by impact with an aluminium crush tube after 100^{o}. The motion of optical markers placed with brain was tracked from high-speed video (1000fps), and Green-Lagrangian strain calculated by tensor algebra. The final study in this thesis investigates the effect on head kinematics of various types of padding in Free Head-form Motion (FMH) test for Federal Motor Vehicle Safety Standard No. 201[57].

Each of the anatomical features studied was found to influence strain within the brain material. During sagittal plane motion, the lateral ventricles were found to provide strain relief to the superior and inferior cerebral structures. Whilst the anterior and middle fossae reduce relative motion along the cranial floor, they also influenced deformation throughout the brain. It is suggested that they may also be responsible for local contusions found in this region. During coronal plane motion, the presence of sulci increased the risk of ASDH, but as minimum princi-

ple strains were in the direction of fibre orientation it is suggested that this provides protection from DAI. The FMH test concluded that minimum peak angular acceleration, and peak change in angular velocity correspond to the lowest HIC_{36}.

Physical modelling is now an established technique for investigating brain injury mechanisms. Strain distribution has been consistently shown to correlate with areas of injury, and the inclusion of anatomical features such as inter-hemispheric membranes, ventricles and slip boundaries have a significant effect on these distributions. These techniques provide valuable insight into the likely behavior of tissue within the brain during motion, and allow experimental control of physical variables not possible in biological testing.

3.4 Discussion

The clinical characteristics of SBS are clear. Young infants, normally less than six-months-old, present with symptoms ranging from the apparently benign, such as lethargy or vomiting, to fitting and unconsciousness. On examination, they are likely to have inter-cranial and retinal haemorrhages, combined with injury to the brain itself (DAI) and bruising to the arms or torso from being held. The presenting history (e.g. a short fall) is unlikely to be consistent with the severity of these injuries and there is no clinical cause such as a clotting disorder to explain them. There may also be a history of abuse, perhaps indicated by fractures of varying ages on x-ray.

Rates of mortality and morbidity are high, and survivors may have severe physical or sensory deficit such as blindness or paralysis. Where they have been traced, the long term outcome for those victims who survived the initial insult apparently unscathed is less severe, but incidence of learning or behavioural impairment is still high. What is unclear at this time is mechanism of injury in these infants.

Recent work by Geddes looked at clinical cascades arising from hypoxia caused by small injuries to the brain-stem. While this has contributed to the understanding of the dangers of these injuries, research into mechanical causes of brain injuries has been relatively scarce. To date only two ATD studies and a small number of preliminary computational simulations have been carried out and these have been unable to demonstrate that shaking without impact can exceed criteria for the brain injuries of SBS. The work presented in the following chapters examines aspects of two possible sources of error in these studies; infant neck characteristics and the inappropriate application of injury criteria.

The complex anatomy of the spine means that biomechanical studies of the neck are reliant on testing of biological specimens. While it has been possible to characterise the adult neck in

this manner, the infant neck is anatomically different in more than just its size. Since biological testing of the infant neck is not ethical, estimates of its biomechanical characteristics have to be made by other means. Scaling factors have been derived by relating human neck kinematics to animal neck kinematics, and looking at the effects of age in these animal models. These relationships are then used to make an estimate of infant neck characteristics. Alternatively, detailed computational models, based on validated adult models, have been used to study the effect of specific anatomical differences in the infant neck. However, these methods are only able to provide estimates of infant neck stiffness, and are not able to account for their rapid rate of change at this age of development.

Since validated data on the kinematics of the infant neck are not available, the ATD studies of head motion in SBS used a few simplified neck forms to look at a range of characteristics. Whilst the use of different neck forms recognises that neck stiffness is an important factor in determining head motion, the practical restrictions of physical modelling only allowed three forms to be used; free, stiff and flexible. Although it is still not possible to produce a validated neck-form, computational modelling makes testing a large number of neck models much easier. In Chapter 5 the significance of neck stiffness is studied using a parametric study to test 50 different neck form models with a wide range of stiffness characteristics. In addition to this, the type of head-torso impact hypothesised by Cory as a potential cause of injury was simulated.

Regardless of any limitation due to the restrictions of creating biofidelic infant neck models, the application of injury criteria in assessing the findings of SBS studies needs to be better understood. Although understanding of brain injury mechanism has greatly improved in the last fifty years, only specific types of loading have been studied. Research to date has almost exclusively focused on the type of high-energy impacts resulting from blows to the head or the type of single high-energy acceleration observed in automotive crashes. The motion of shaking in SBS is demonstrably different to this and so may constitute a distinct injury mechanism. In addition to this, where multiple impacts have been studied, results indicate that injuries subsequent to the initial impact may be more injurious than the first. It is therefore reasonable to suggest that shaking may constitute a distinct injury mechanism and that this should be investigated in trying to understand injury in SBS.

The derivation of injury criteria has been largely based on biological, or primate studies. In addition to the added experimental complexities of using animal models, ethical developments have greatly restricted this type of testing. Although it may be appealing to use computational modelling, it requires accurate material models and validation to be used effectively. Again, these type of data are not available for infant materials, but physical modelling offers an established technique for studying brain injury. Variables such as geometry and boundary conditions can

be simply controlled, and data on strain within brain models can be correlated with injury distributions. These methods are used in Chapter 6 to study the response of surrogate brain tissue to cyclic loading.

Chapter 4

Investigation of Torso Acceleration

In order to determine the acceleration characteristic of a shaking episode, torso acceleration data were obtained through used of an ATD. Previously, Duhaime, Cory and Prange have studied infant head acceleration during shaking using ATDs with a range of flexible neck forms [1, 2, 28]. As discussed in Chapter 3 validation of this type of neck forms is not possible, but their properties will clearly effect on the motion of the head. The aim of this study was to obtain the torso acceleration data necessary to simulate shaking in Chapter 5, where computational methods are used to study the significance of neck stiffness on brain injury. Unlike previous studies a rigid neck form was used, and torso acceleration, rather than head acceleration was recorded.

4.1 Materials and Methods

An ATD was constructed by adapting an infant resuscitation training doll (Resusci Baby, Laerdal - Kent, UK) which was freely available for this project. The various body segments were ballasted with a combination of lead blocks and sand, to approximate a 6-month-old infant [58, 59, 60]; details of this ballast, including total segment masses, are given in Table 4.1. The head of the dummy was fitted with a solid aluminium neck form, that acted both as ballast, and to rigidly fix the head to the torso, preventing head motion.

Table 4.1: Body segment masses of ATD

Segment	Ballast	Mass (Kg)
Head	solid aluminium neck form	1.03
Torso	lead	3.62
Upper Limb	lead/sand	2 x 0.39
Lower Limb	lead/sand	2 x 0.78
Total		*6.99*

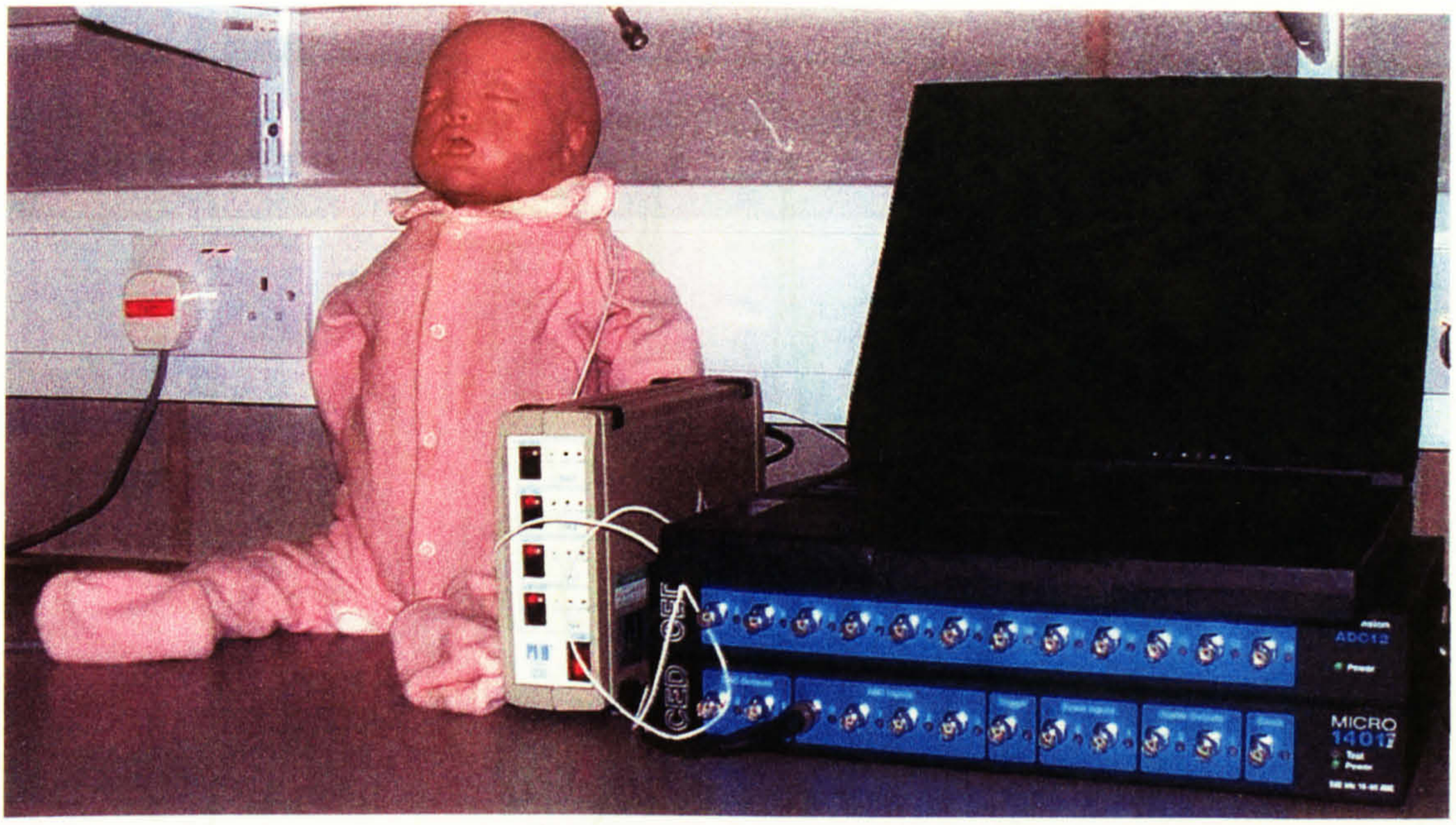

Figure 4.1: Custom built ATD, with data logger, signal conditioner for accelerometer, and laptop computer.

A uni-axial accelerometer (PCB - New York, USA) was placed in the mid-line of the thorax, and its output recorded at 100Hz by a data-logger (Micromark 1401, Cambridge Electronic Design, Cambridge, UK). This was exported on a laptop computer from the data-loggers recording software (Micromark, Spike2) to a CSV file and analysed using Microsoft Excel. The dummy and recording equipment, including signal conditioning unit, are shown in Figure 4.1.

Ten volunteers (7 male, 3 female) were each asked to perform a single shaking episode with the dummy; they were instructed to shake the dummy for as long and as violently as they were able. In each case, the dummy was held by the thorax, facing the volunteer and shaken in an anterio-posterior plane. Torso acceleration was recorded throughout the duration of the shaking episode.

4.2 Results

An example portion from an acceleration trace is shown in Figure 4.2, from which an approximate frequency of 4-5Hz and peak acceleration of 9g can be observed; full traces from each shaking episode can be found in Appendix A. It is interesting to observe the distinctive double or triple acceleration peaks in Figure 4.2, which may be due to differences in the inertia of the dummy and the timing of forces applied by the volunteer. As the volunteer reaches the full extension of their arms they will begin to try and pull the dummy back towards the body. However, this is also the point at which the strength of the arms is weakest, and the momentum of the dummy greatest. This could lead to a double peak, firstly from the volunteer stopping the motion, then

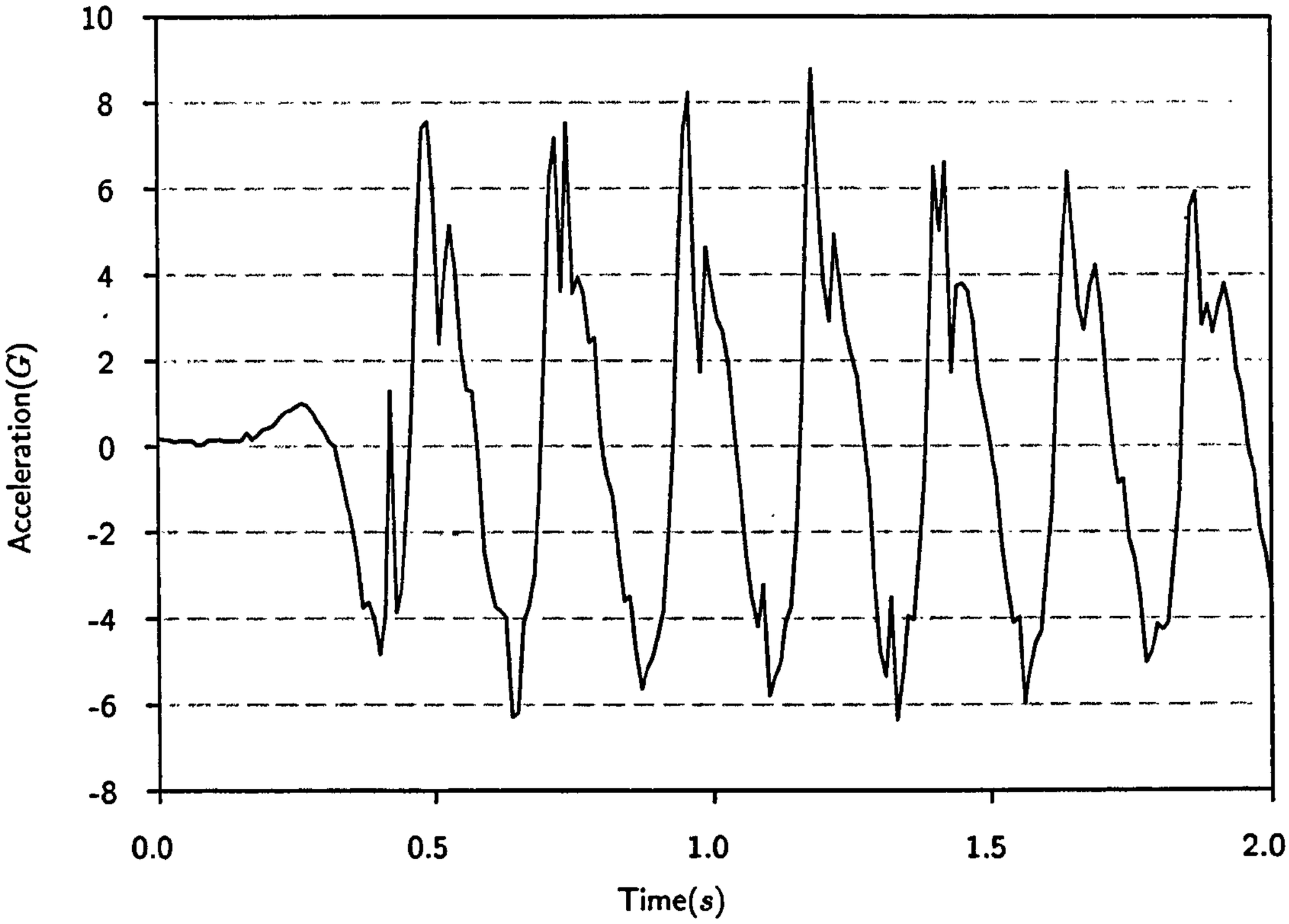

Figure 4.2: Example torso acceleration trace

Table 4.2: Summary of results of shaking episodes

	1	2	3	4	5	6	7	8	9	10
gender	♂	♂	♂	♂	♀	♀	♂	♂	♀	♂
Duration (s)	16.5	2.6	9.3	8.3	6.0	6.9	11.8	10.4	9.9	10.5
peak acc (G)	9.0	11.1	6.1	5.4	3.3	4.3	4.3	0.5	0.4	1.0
rms acc	2.9	2.4	1.6	1.1	0.6	1.0	1.0	0.2	0.1	0.3
sd	2.9	2.7	2.4	1.8	1.1	1.8	1.4	0.2	0.1	0.2
F(Hz)	3.9	3.9	3.5	4.3	2.5	2.7	3.1	3.7	3.0	4.8

from the inertia of the dummy forcing a small hyper-extension before the arms begin to flex. In order to investigate this further it would be necessary to correlate high-speed video of shaking with acceleration data.

For each of these shaking episodes, peak and rms accelerations were calculated, and the frequency of shaking determined by FFT. These findings are given in Table 4.2, and summarised in Figure 4.3. The duration of shaking ranged from 6 to 22s (mean 11.2s, sd 4.95) and the frequency of shaking ranged from 2.5 to 4.8Hz (mean 3.5Hz, sd 0.72). The maximum peak acceleration was achieved in shake 2, and measured 11.1G (mean 4.6G, sd3.57). The highest average acceleration was 2.9G (mean 1.1G, sd 0.94) and achieved in shake 1. Both these maximal shakes were achieved by male volunteers.

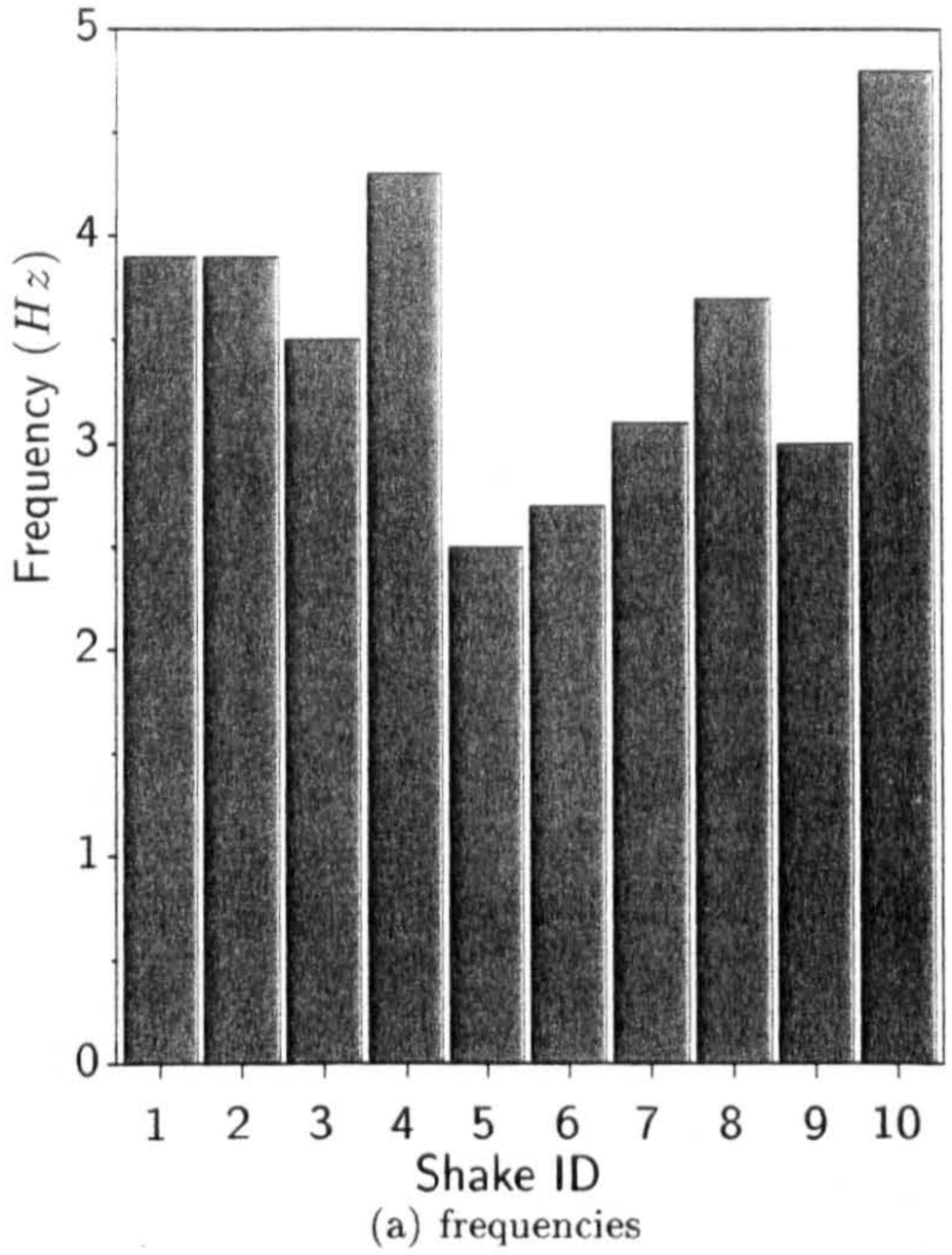

(a) frequencies

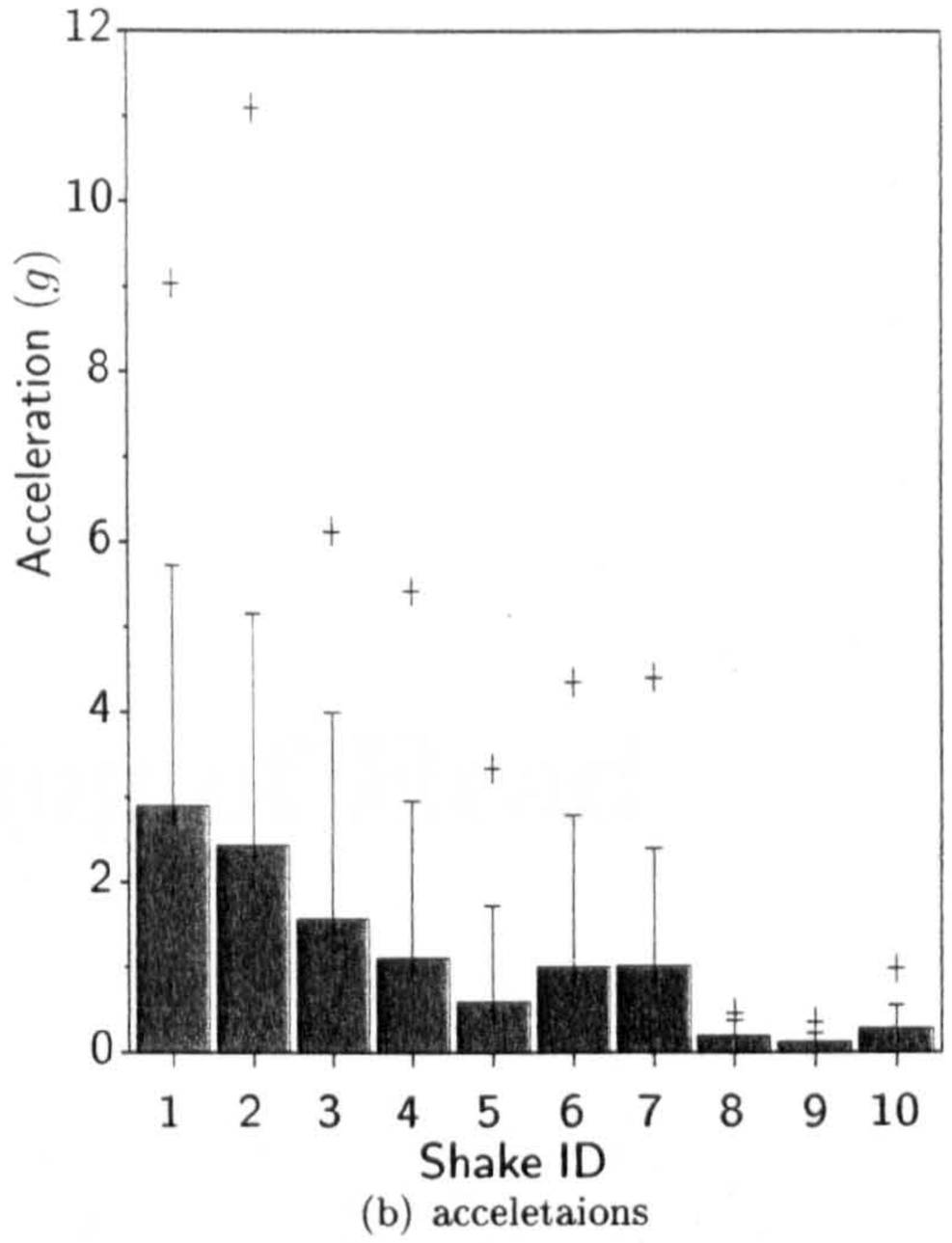

(b) acceletaions

Figure 4.3: Summary of characteristics of ATD shake testing a) frequency b) rms acceleration, with one standard deviation and maximum accelerations shown.

4.3 Discussion and Conclusion

As described in Chapter 2, ATDs are commonly used to obtain data about human responses in automotive impact tests. Specially designed dummies have been used to study infant head motion during shaking, but it has not been possible to validate the characteristics of the neck forms used. In Chapter 5 computational models are used to study the significance of these neck characteristics on head motion. Here, an ATD was used to obtain realistic data on torso motion in SBS, which could be used to simulate shaking. Since only the motion of the torso was to be recorded, a rigid neck form was used, preventing any motion of the head.

The maximum peak torso acceleration achieved in these tests was 11.1G, and the maximum average torso acceleration was 2.9G. This maximum acceleration is a little higher, but consistent with, the findings of Cory *et al*, who reported a maximum peak torso acceleration of 9.8G (mean 7.5G, SD 1.3) [2]. It was therefore reasonable to use these data for the simulation of shaking in Chapter 5 and shakes 1 & 2 were used to this end; further detail about the selection of these traces is given in Section 5.1.1.

Chapter 5

Rigid Body Modelling of Head Kinematics

In this chapter, torso acceleration data obtained from ATD tests in Chapter 4 is used to simulate shaking in a series of studies of head kinematics in SBS. Previous studies using physical models to investigate head kinematics in shaken baby syndrome have been inconclusive about the mechanisms of brain injury [1, 2]. They have, however, been limited in the range of neck forms used; a free hinge, and two rubber hoses, one thin or "*flexible*"(i.e. unable to support the head-form) and the other thick or *"stiff"* (i.e. able to support the head-form). The kinematics of the neck are clearly critical in determining motion of the head, and the significance of this clearly warranted further investigation. Further to this, Cory *et al.* have reported observing impact of the head against the torso and suggest that this may be an additional mechanism of injury[2].

As discussed in Chapter 2, computational modelling techniques offer the opportunity to study an significance of specific factors without the complication of constructing biofidelic physical models. The aims of this work were therefore to:

- Create a suitable computational infant head and neck model
- Simulate shaking of this model to test the two hypotheses:

  H1 Neck stiffness characteristics have a significant effect on the capacity of shaking to produce head motion exceeding injury criteria

  H2 Head-torso impact leads to head motion exceeding injury criteria

As such, this chapter is divided into three parts; a preliminary investigation to establish the modelling technique, a study into the effect of of neck stiffness on head motion and a study into

the effect of head-torso impact on head motion. In each study, torso acceleration data obtained from ATD tests in Chapter 4 were directly applied to the torso of the model in order to simulate shaking.

5.1 Preliminary Investigations

In carrying out these studies, Rigid Body Modelling offered several advantages over FE methods more commonly using in engineering investigations. FE methods require detailed material characteristics and accurate geometry to be defined for every component, but one of the main restrictions in simulations of SBS is the paucity of data available about the material properties of human infant tissues. RBM allowed simple approximations of joint and material characteristics to be used instead. Further to this, ellipsoid surfaces were used to represent body geometry, requiring little input data and computation time. Since this method had not previously been used to study SBS, a series of preliminary studies were carried out to verify that reasonable data could be obtained, and to establish how the model would respond to cyclic loading.

5.1.1 Methods

The modelling environment used in these studies was TNO Automotive's MADYMO 6.1(TNO Automotive Safety Solutions, Delft, The Netherlands), more commonly used for automotive simulations. Rigid body modelling was used, the principles of which are described in Section 2.3.2, and results were generated as text files that could be used to view model motions using Altair HyperView (Altair Engineering, Inc., MI, USA). Further analysis was carried out using MATLAB (The MathWorks, Inc., MA, USA) and the open source perl programming language.

Model Design

All the models used in these studies were based upon the head and neck of the standard MADYMO one-year-old CRABI ATD model. As with the ATD used in Chapter 4, body segment masses were adjusted to that of a 6-month-old infant, as described in Table 4.1. Since only the motion of the head and neck were important, the model could be greatly simplified to reduce the computational demands. The joints and surfaces of the limbs were removed, and their masses included in the single point mass of the torso. The final model therefore comprised only three bodies: the torso, neck and head.

The first model tested had a neck form formed from a simple ellipsoid surface, which was joined to the torso at the level of the first thoracic vertebra and to the head-form at the atlanto-occipital joint. To restrict motion to the sagittal plane, hinge joints were used in the neck, and

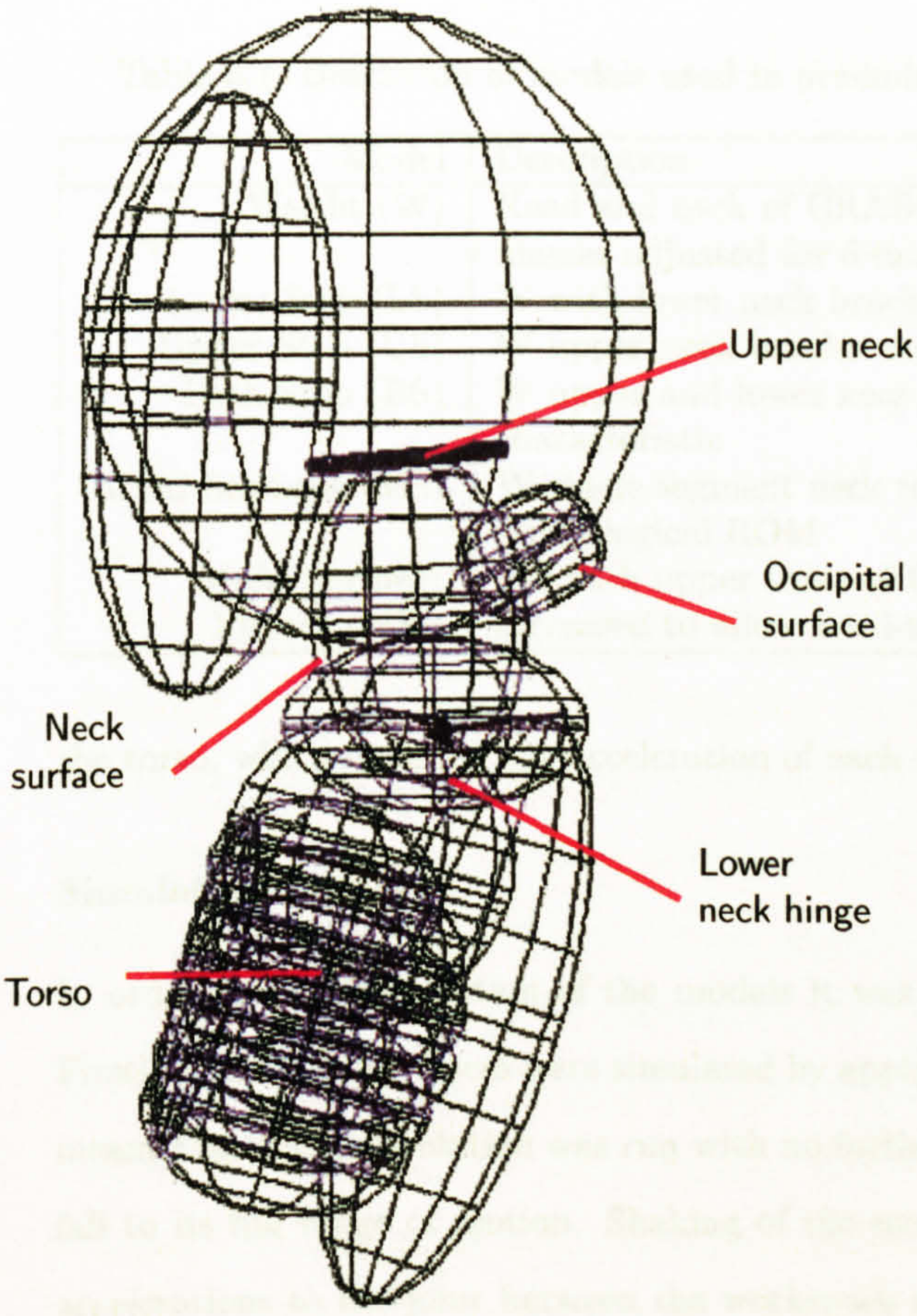

(a) CRABI head, neck and upper torso

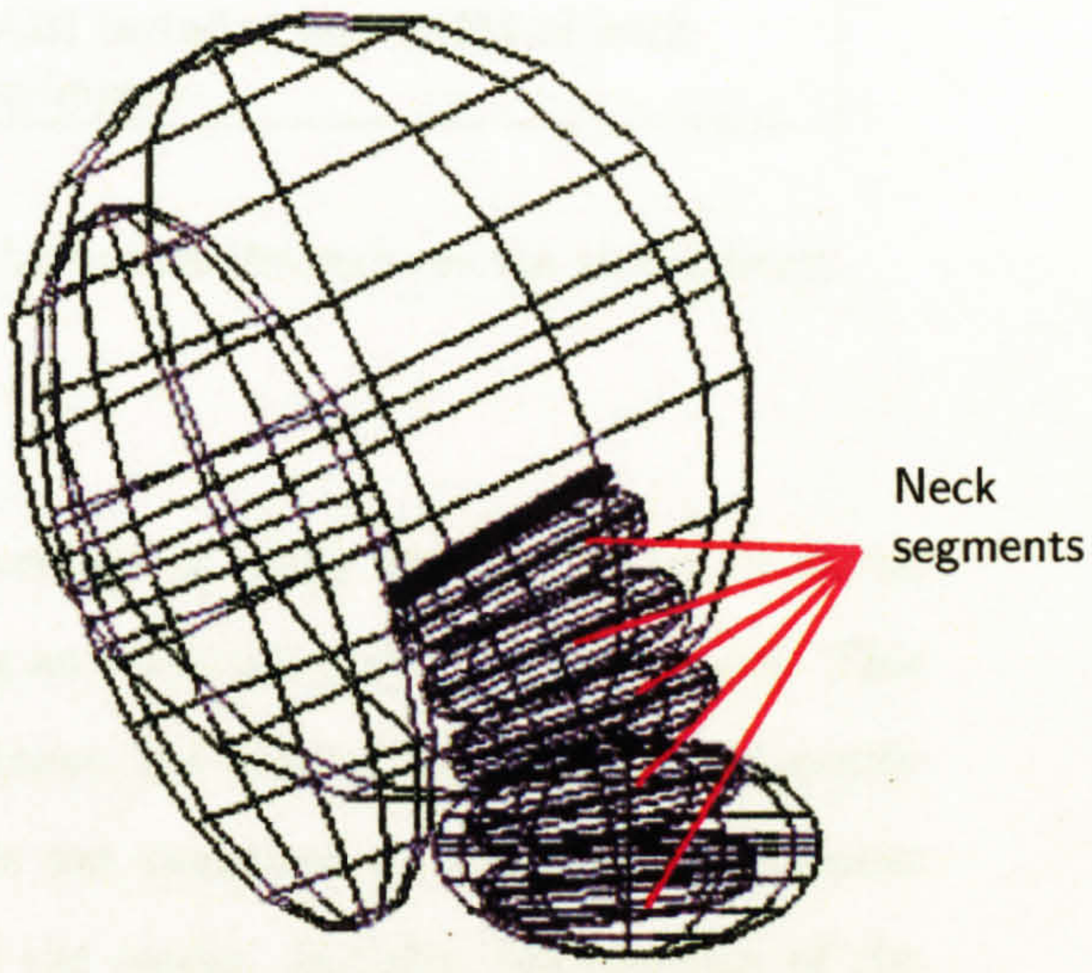

(b) Multi-segmented neck form

Figure 5.1: Wireframe views of models used in preliminary studies of rigid body modelling of SBS

the torso was joined to the workspace by a translational joint. A second model with five vertebral bodies, each separately jointed, was also tested. Diagrams of these two models are shown in 5.1.

By altering the characteristics of the various neck joints, different head kinematics could be achieved.In this manner, the basic head and neck models were adapted to investigate the effect of changing overall neck-form design and how to configure head-torso impact. Six different combinations were used, and are described in Table 5.1.

The first model (W) consisted of the standard two-joint, single ellipsoid neck of the CRABI model, with the model masses adjusted for a 6-month-old infant. In the next three models, the characteristics of each joint were altered in turn, to an impact style end-stop (i.e. free movement within over a small range, but rigid beyond this): first the lower joint (LS), then the upper joint (US) and finally both joints (BS). In the last two models the segment neck form was used, firstly with the same stiffness characteristics as the CRABI model (MS), and finally with increased ROM to allow impact with the torso, which was also included in this model (MSI).

For each model, a sensor element was placed at the centre of gravity of both the head and

Table 5.1: Descrition of models used in preliminary investigation of shaking simulations.

Model	Description
Weight (W)	Head and neck of CRABI 12 month-old dummy model with masses adjusted for 6 month-old
Lower Stop (LS)	W with lower neck bracket set with end stop characteristic
Upper Stop (US)	W upper neck bracket set with end stop characteristic
Both Stop (BS)	W upper and lower neck brackets set with end stop characteristic
Multi Segment (MS)	W single segment neck replaced with cervical segments with physiological ROM
Multi Segment Impact (MSI)	MS with upper torso of CRABI included and ROM of neck increased to allow head-torso impact

the torso, which recorded the acceleration of each of the bodies throughout the simulations.

Simulation Inputs

In order to simulate motion of the models it was necessary to apply external forces to them. Firstly, gravitational forces were simulated by applying an acceleration of 1G to the model. This meant that if the simulation was run with no further input, the head of the model would gently fall to its full range of motion. Shaking of the models was simulated by applying cyclic linear accelerations to the joint between the workspace and the model. Initially, the function of the system was confirmed using small sine wave accelerations, but these were replaced with torso acceleration data obtained from ATD testing in Chapter 4.

Ten acceleration traces were recorded in Chapter 4, but it was not considered necessary to simulate shaking with each of these. Since the aim of this study was to test the capacity for shaking to cause injury, it was decided that only the worst-case motion (i.e. most injurious) should be tested. Although it was apparent that this should be the shake with the greatest acceleration, it was not clear if the data with the greatest single acceleration peak, or the data with the greatest average acceleration would be the most injurious. As described in Section 4.2, these were achieved in different test; the maximum peak acceleration in shake 2, and maximum average in shake 1. Therefore, shaking was simulated twice with each model: once with the acceleration data from shake 2, and once with the acceleration data from shake 1. Graphs of these data can be seen in Figures A.1 and A.2 in Appendix A. From these Figures it can be seen that the duration of shake 1 was approximately 16 seconds and shake 2, 22 seconds. Since the maximum peak acceleration in shake 2 occurred during the third second, shaking was simulated for 16 seconds (around 70 shaking cycles) with each shaking trace.

5.1.2 Results

Acceleration traces from the centre of gravity of the head is given in Appendix B. The results of other biomechanical studies of SBS have been assessed using injury criteria based on the relationship between the peak angular velocity and peak angular acceleration achieved during each test [1, 2]. The results from this study are therefore presented in a similar manner. Peak acceleration for each trace was read from the data in Appendix B, and the peak angular velocity derived by differentiation of the same data.

Figure 5.2 shows separate plots of the results for simulations using the maximum peak acceleration and maximum r.m.s. acceleration; previously reported results and injury thresholds (scaled for a 500g brain mass) are also shown. In each case, the head motion achieved in the weighted (W) and multi-segment (MS) models was low, not reaching the levels found in physical models. The multi-segment with impact model (MSI) was closest to these previous findings, and close to the lower levels for concussion. The upper and lower end-stop models (LS and US) were higher than previous findings, and also exceeded injury thresholds for concussion. The model with both upper and lower end-stops (BS) achieved the highest peak motions exceeding all injury thresholds, and levels associated with impact in physical tests.

Overall, there it is no obvious distinction difference between those simulations driven by different acceleration data. The highest individual result and most number of injurious results were from achieved from maximum r.m.s acceleration, but, more of the results from maximum peak acceleration were above the highest SDH threshold.

5.1.3 Discussion

These preliminary tests showed that RBM could successfully be used to produce reasonable results when modelling SBS. Changes to neck form stiffness characteristics produced a suitable variation in results, with end-stop type characteristics resulting in more injurious head kinematics. Although more physiological, the segmented neck form was more complex, requiring greater assumptions about stiffness characteristics, and resulting in less injurious motion. The two-hinge neck-form was therefore used in the following studies.

5.2 H1 - Neck Stiffness Study

In this study, the significance of neck stiffness on the capacity for shaking to cause brain injury was assessed using parametric RBM. Since direct validation of any infant neck model is not possible, 50 neck forms were tested with a range of stiffness characteristics. The results of these simulations were used to establish if an improved neck model could provide further insight into

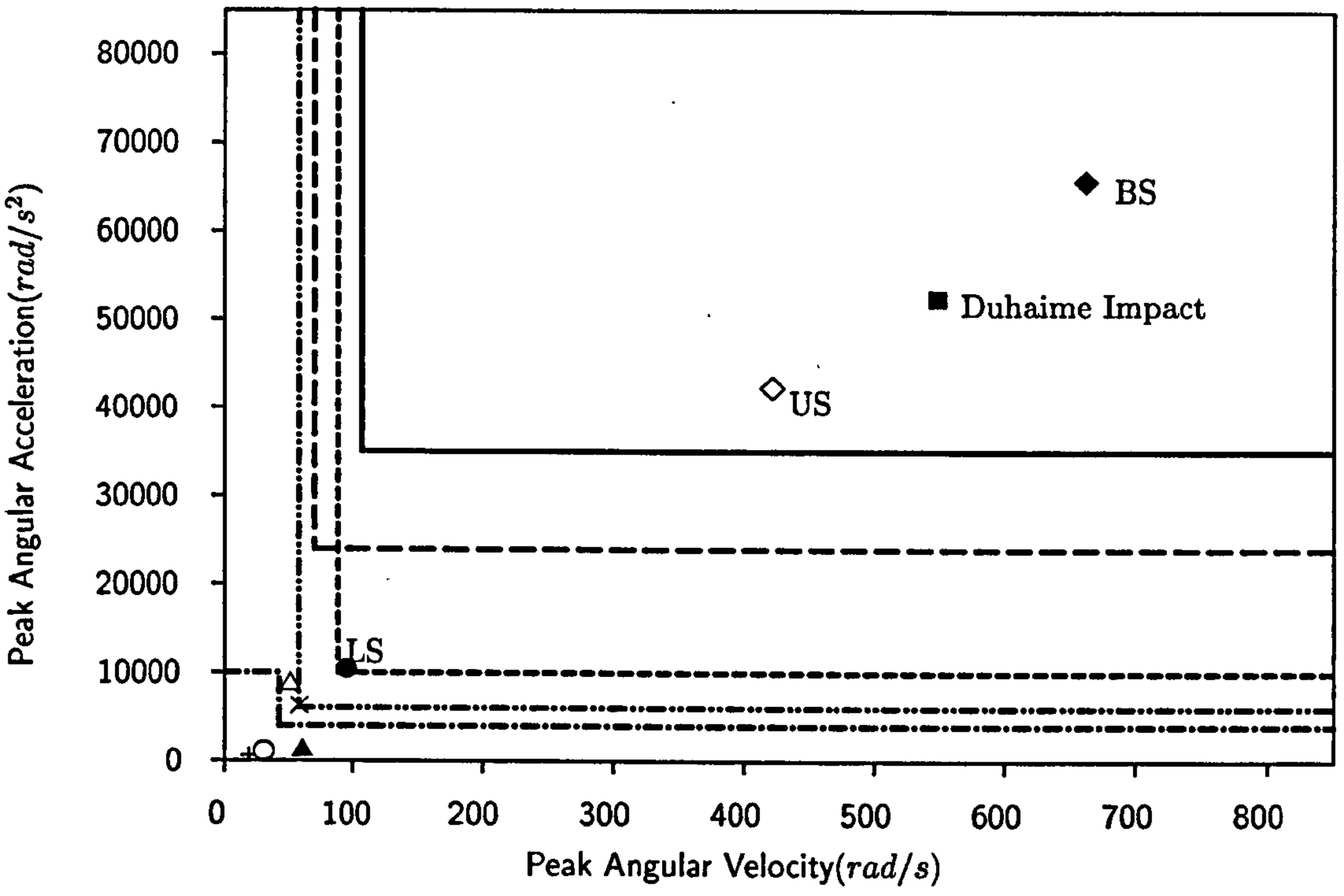

(a) Max. rms accerleration

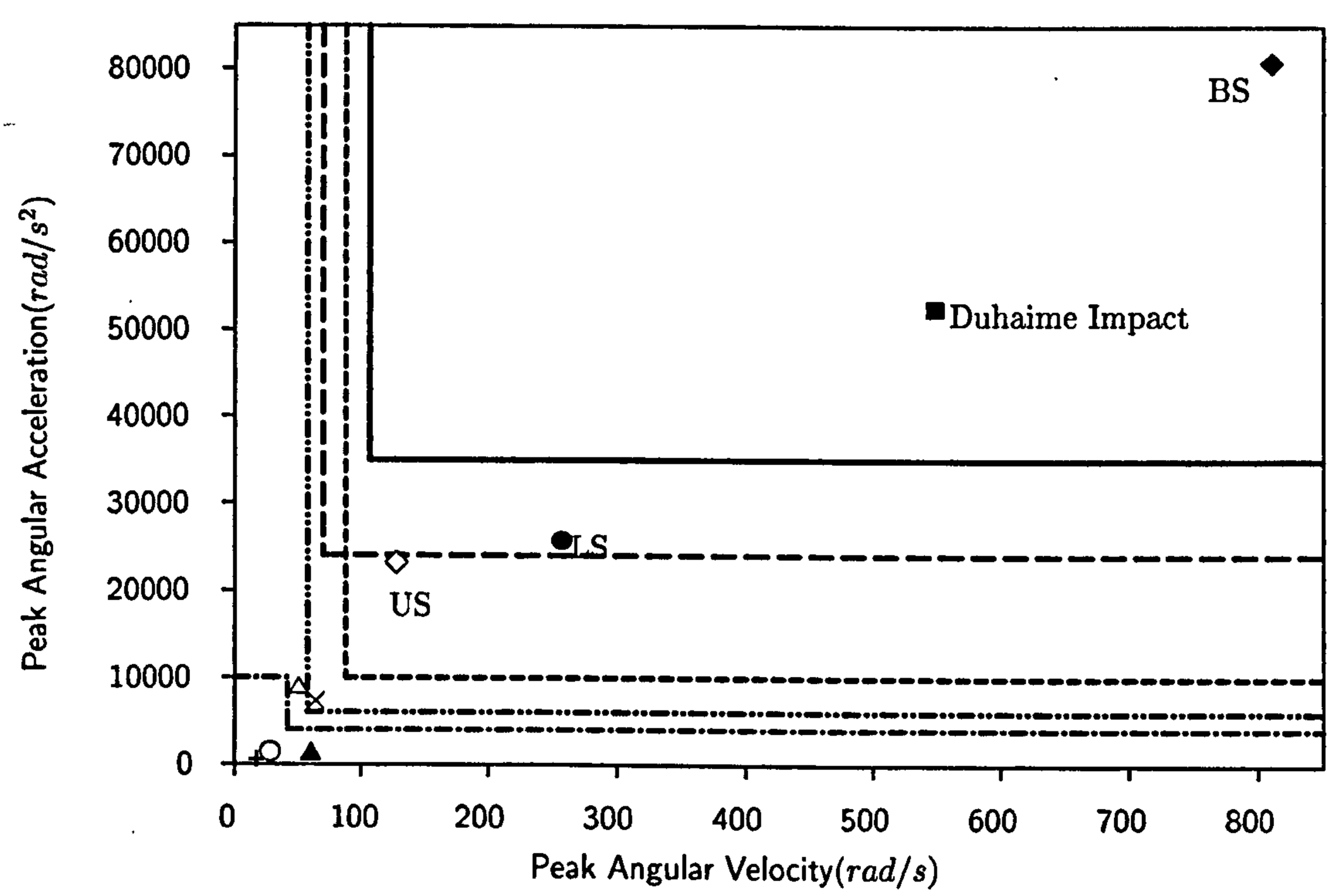

(b) Max. peak accerleration

Figure 5.2: Results of preliminary RBM modelling of SBS. + W, ○ MS, × MSI, ◇ US, ● LS, ◆ BS, ▲ Duhaime shake average [1], ■ Duhaime impact average [1], △ Cory shake average [2]. ——— SDH from [1], - - - - SDH scaled from [61] in [2], ... Concussion from[1], -.-.-. 50% concussion probability from[9] in [2], -..-..- Concussion scaled from [61] in [2].

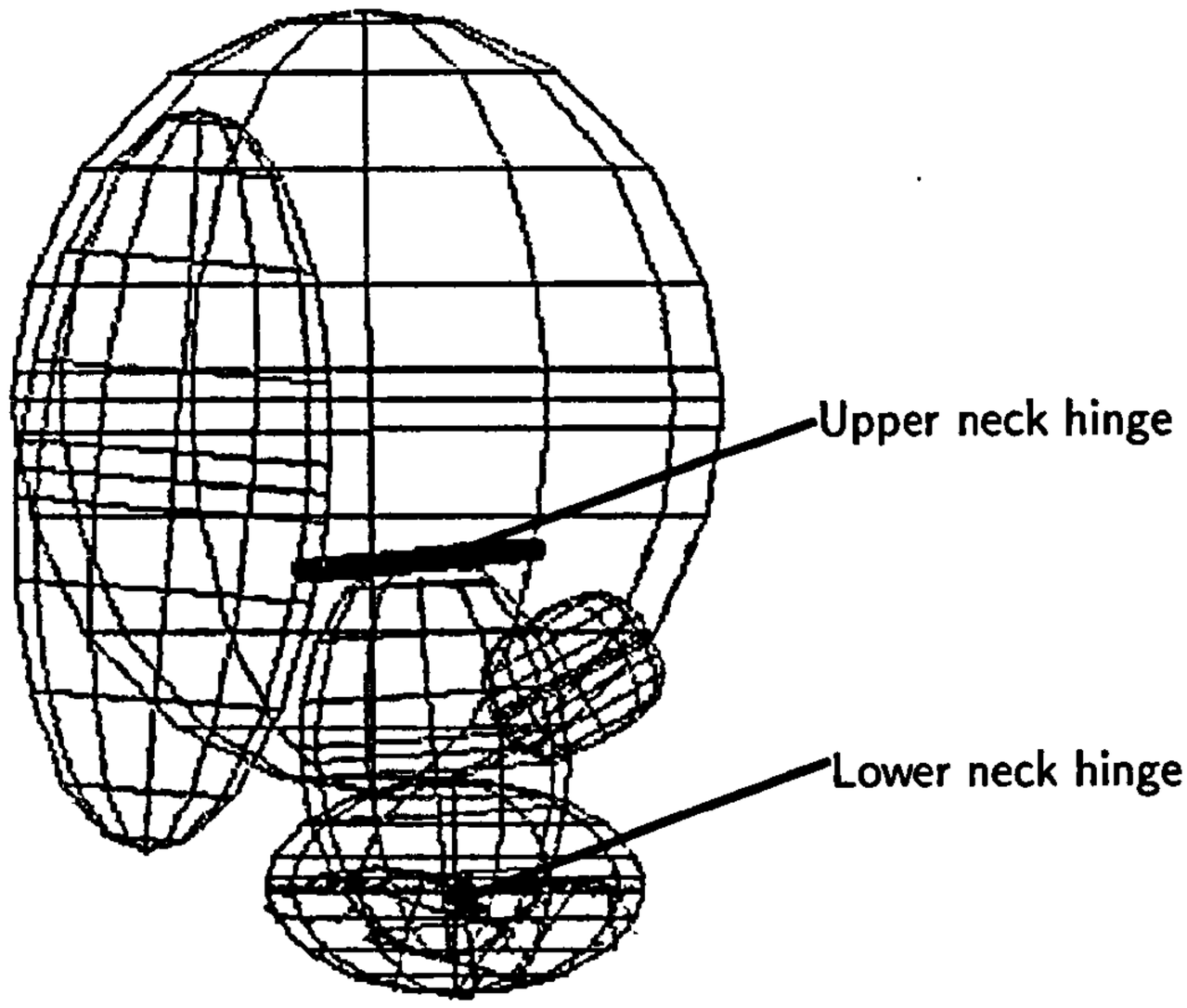

Figure 5.3: Wireframe view of model used in parametric study of neck stiffness

brain injury mechanisms in SBS.

5.2.1 Methods

The basic two-hinge neck form from the parametric study was used as the basis for these simulations. Since head-torso impact was not being studied, the model was further simplified by removing the torso surfaces, to give the basic form shown in Figure 5.3, and matching stiffness characteristics applied to both the upper and lower neck hinges.

Study Design

The MADYMO input format defines joint stiffness by angle-torque relationships. Neck joint characteristics were therefore defined in flexion and extension by their range of free motion, and their full range of motion. In this way the 50 different neck stiffness characteristics comprising the parametric study were designed, based around the standard MADYMO CRABI neck stiffness. Details of these characteristics are given in Appendix C, and summarised in Figure 5.4; the characteristic curve for the standard MADYMO CRABI model, and the range of characteristics, from free and *"floppy"* to stiff end-stops, can be seen.

As in the preliminary study, shaking was simulated for 16 seconds, by applying acceleration data from shakes 1 and 2 in Chapter 4 to the torso of the model.

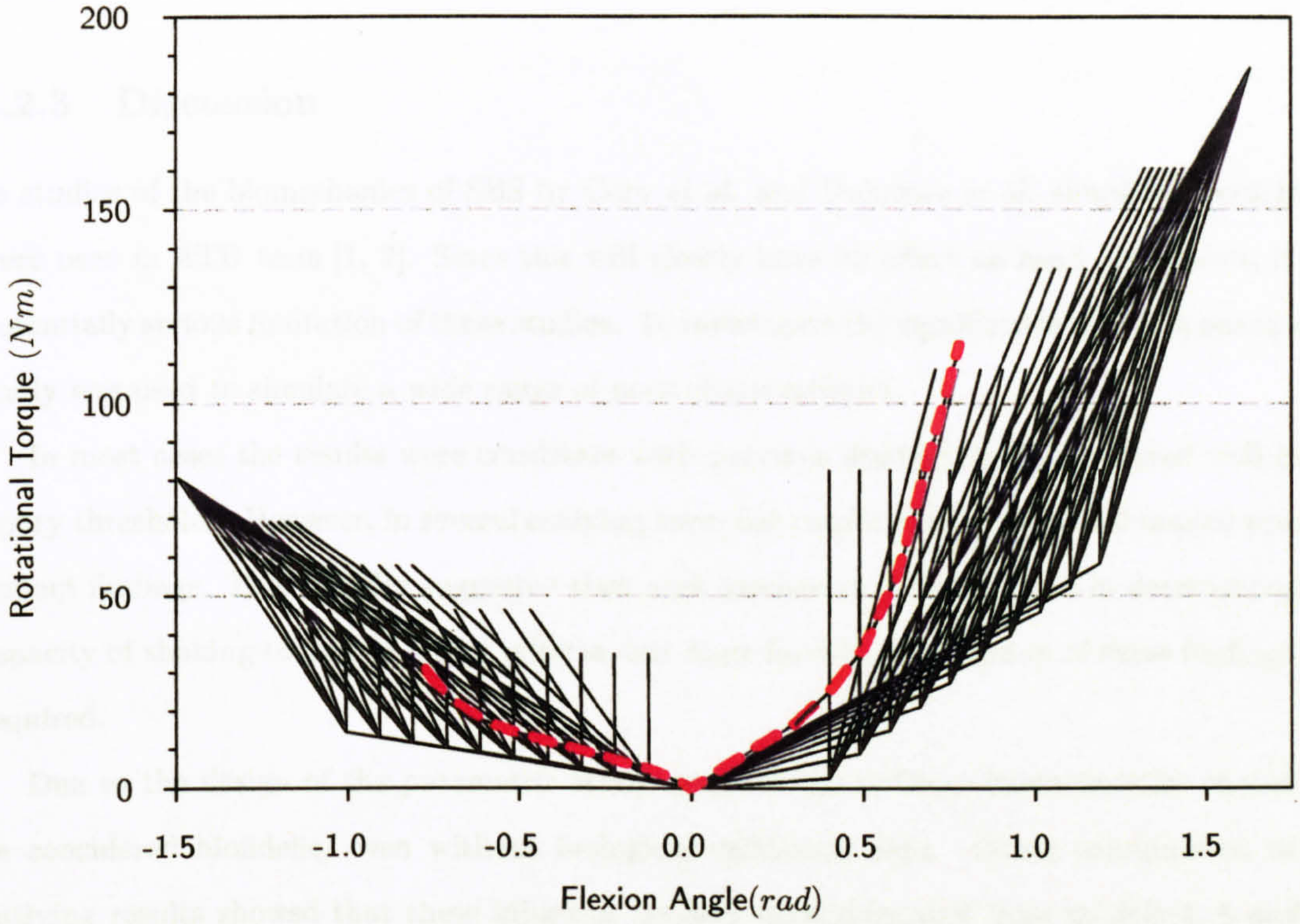

Figure 5.4: Parametric neck stiffness study design. Heavy dashed line is standard MADYMO CRABI characteristic, other lines describe characteristics used in parametric study.

5.2.2 Results

The acceleration traces from the centre of gravity of the head for these simulations are given in Appendix D for the maximum rms acceleration input, and in Appendix E for the maximum peak acceleration input. These have been summarised in Figure 5.5, again with results from the different acceleration pulses plotted separately.

In each case, there were a cluster of results about a peak angular velocity of around 20 rad/s, and a series of outliers from this group. From the simulations using the maximum rms acceleration input, the average result was a velocity of was $24 rad/s$ and acceleration of $1034 rad/s^2$; outliers were at$(27 rad/s, 2530 rad/s^2)$, $(90 rad/s, 9163 rad/s^2)$and $(132 rad/s, 13326 rad/s^2)$. For the simulations with maximum peak acceleration input, the average velocity was $22 rad/s$, with an acceleration of $915 rad/s^2$; outliers were at $(47 rad/s, 4724 rad/s^2)$, $(59 rad/s, 5862 rad/s^2)$ and $(91 rad/s, 9546 rad/s^2)$.

In each case, the main cluster and average results were lower than previous findings, and did not exceed any injury thresholds. The outliers however, show a trend above thresholds and towards the findings of impact studies; the causes of these outliers are discussed in Section 5.2.3. As with the preliminary findings, there is little difference between the results from the two acceleration pulses; the maximum rms input had a slightly higher average and the greatest

outlier.

5.2.3 Discussion

In studies of the biomechanics of SBS by Cory *et al.* and Duhaime *et al.* simplified neck forms were used in ATD tests [1, 2]. Since this will clearly have an effect on head kinematics, it is a potentially serious limitation of these studies. To investigate the significance of this, a parametric study was used to simulate a wide range of neck characteristics.

In most cases the results were consistent with previous findings, being clustered well below injury thresholds. However, in several outlying cases the results were greater and tended towards impact findings. This initially suggested that neck mechanics are significant in determining the capacity of shaking to exceed injury criteria, but some further examination of these findings was required.

Due to the design of the parametric study, some of the stiffness characteristics should not be considered biofidelic, even without biological validation data. Closer examination of the outlying results showed that these injurious outliers were generated from models 1, 6 and 11. The stiffness characteristic for these models are shown in Figure 5.6 and all have short, end-stop type stiffnesses. They are not only at the unrealistic extremes of the study, but also result in motion more that is like a series of impacts than shaking. Rather than demonstrating that neck properties are significant in modelling SBS, these outlying results reinforce the findings of Duhaime, that impacts are required to exceed injury criteria [1].

5.3 H2 - Head-Torso Impact Study

In their ATD study of SBS, Cory *et al.* observed impact between the head and torso during shaking, and suggested that this may be an additional injury mechanism[2]. In this study the hypothesis that head-torso impact results in head motion exceeding injury criteria was tested.

5.3.1 Methods

The ellipsoid surfaces forming the upper torso of the CRABI model were reintroduced to the basic head and neck model, restoring the model to the form shown in Figure 5.1a. Some further adjustment was required, as the torso of the standard CRABI model includes a joint to simulate compression of the chest. The dynamic characteristics of this joint were found to cause the head to spring back violently under its own weight, so joint was fixed, and the interaction of the head and torso restricted to the normal surface interactions.

In order to enable impact, greater freedom of motion of the neck was necessary. This was

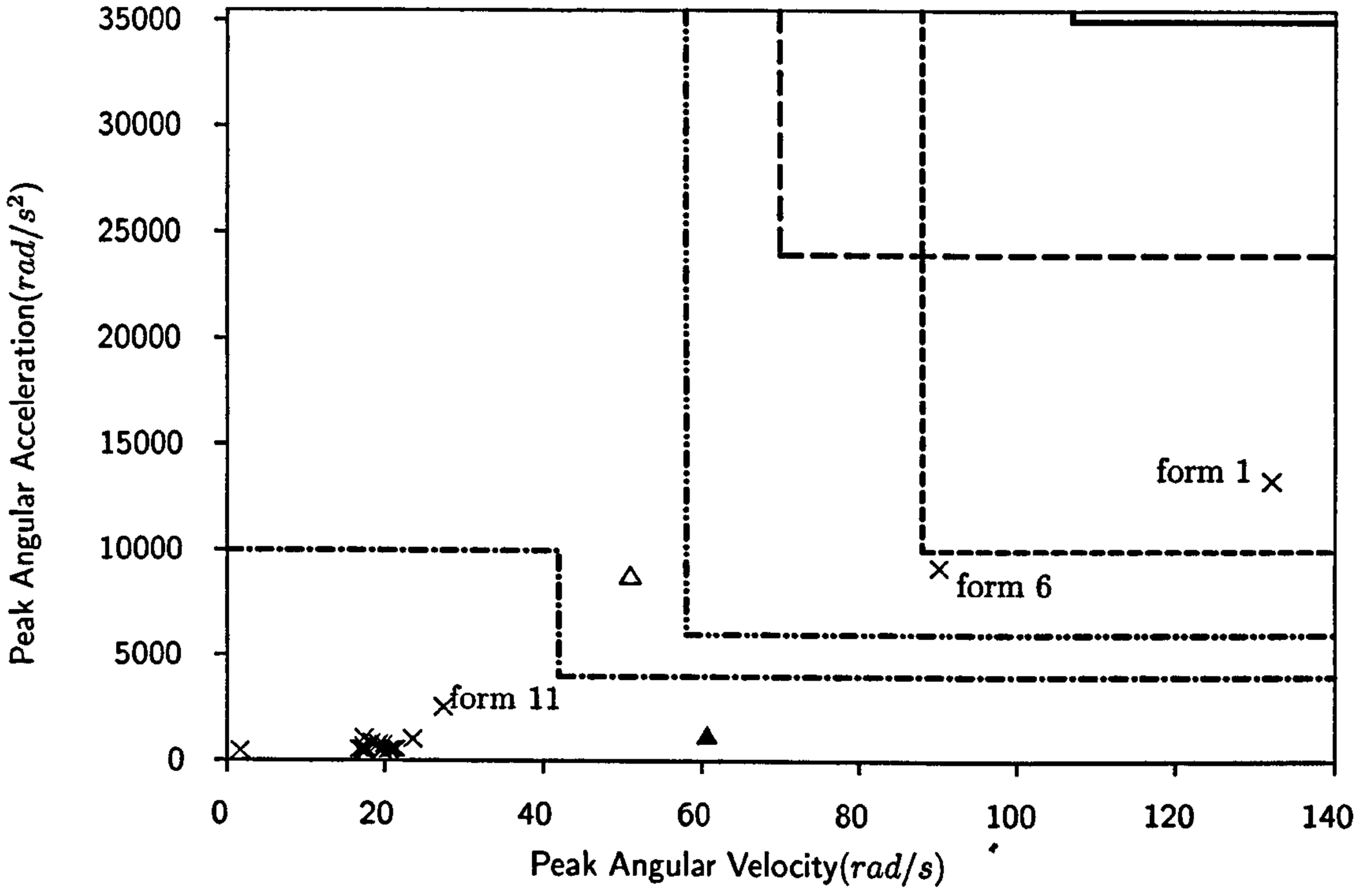

(a) Max. rms accerleration

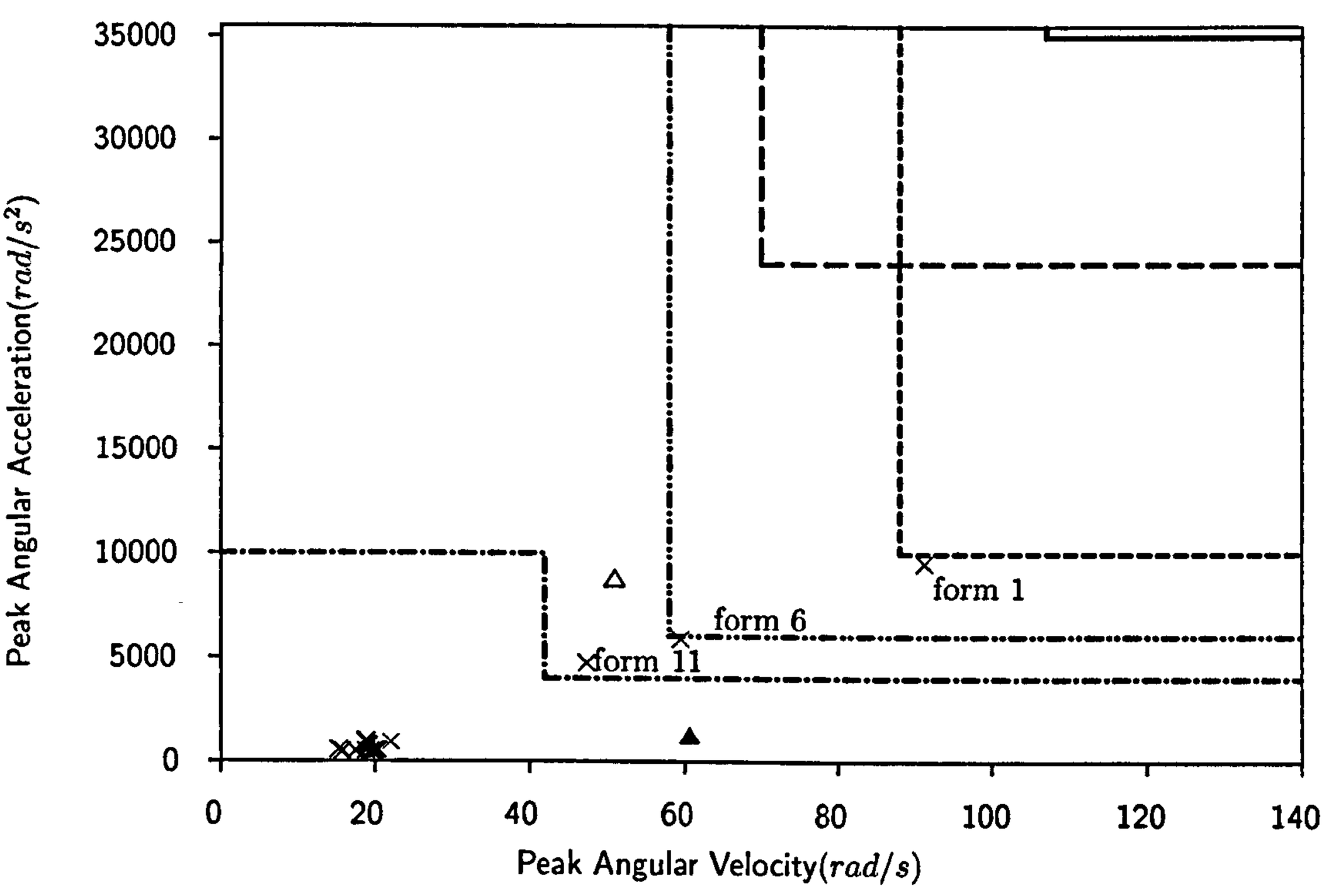

(b) Max. peak accerleration

Figure 5.5: Results from parametric study of neck stiffness. × Parametric Study Results, ▲ Duhaime shake average [1], △ Cory shake average [2].
——— SDH from [1], - - - - SDH scaled from [61] in [2], ... Concussion from[1], -.-.-. 50% concussion probability from[9] in [2], -..-..- Concussion scaled from [61] in [2].

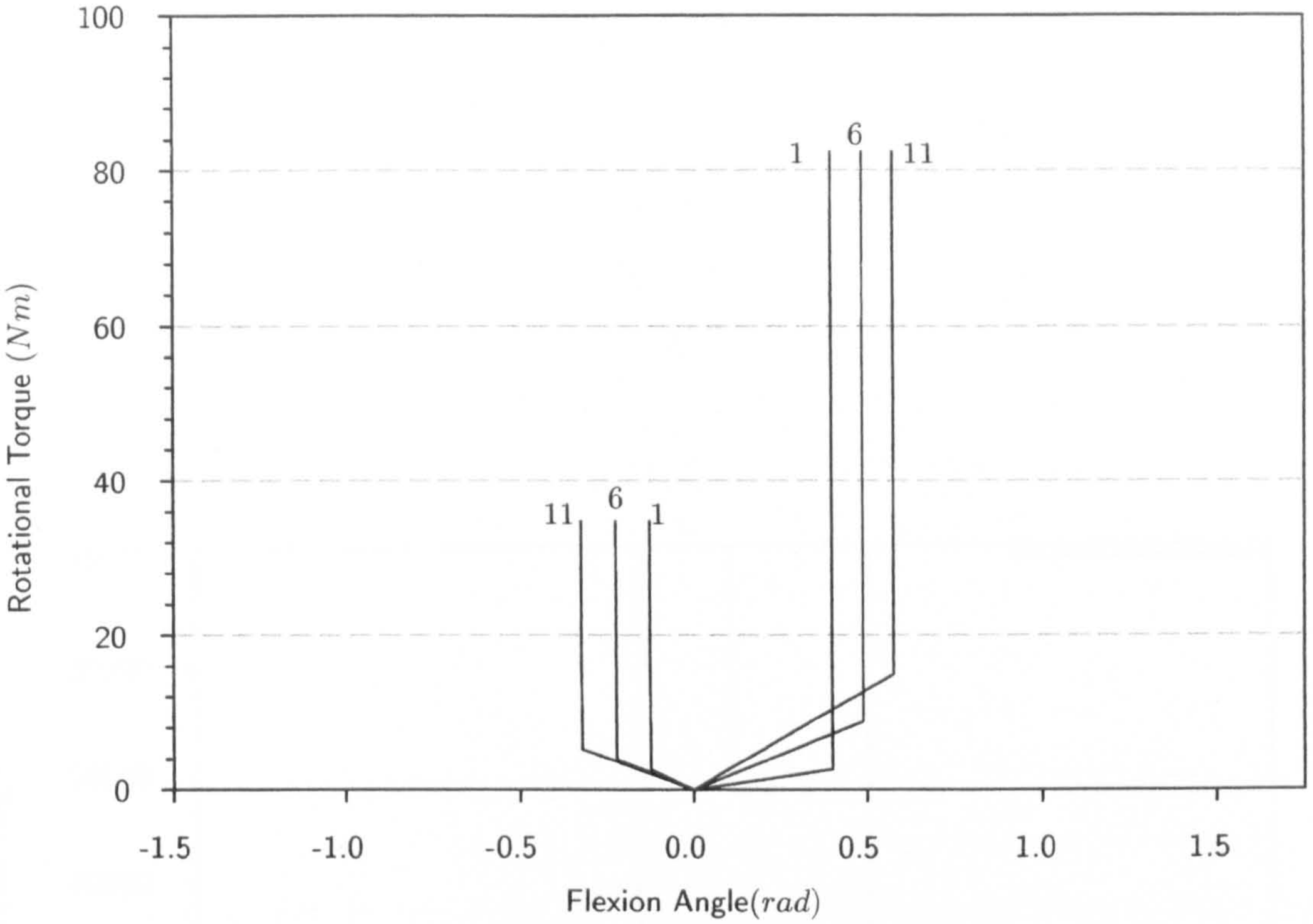

(a) Max. peak accerleration

Figure 5.6: End-stop neck stiffness characteristics from models 1, 6 and 11, leading to outlying peak acceleration - velocity results.

achieved in one of three ways; free motion at the upper neck joint, free motion at the lower neck joint, or increased range of motion at both the upper and lower neck joints. Each of these scenarios was simulated, and are subsequently described as *"up-hinge"* (UH), *"low-hinge"* (LH) and *"two-hinge" (2H)* respectively. Once again, shaking was simulated for 16 seconds, with acceleration data from shakes 1 and 2 in Chapter 4 applied to the torso of the model.

5.3.2 Results

The head center of gravity acceleration data obtained in this study are given in Appendix F, and are collated in Figure 5.7. The lowest results, below all thresholds, are from the two hinge model. The low hinge model lies closest to the averages of previous physical models and upper hinge models are greatest, exceeding concussion levels.

5.3.3 Discussion

Although contact between a victim's head and a hard object is the most obvious source of impact, the head striking against the chest and back has also been described but not been studied [2]. In this study, the range of motion of the head was increased to allow head-torso impact, and

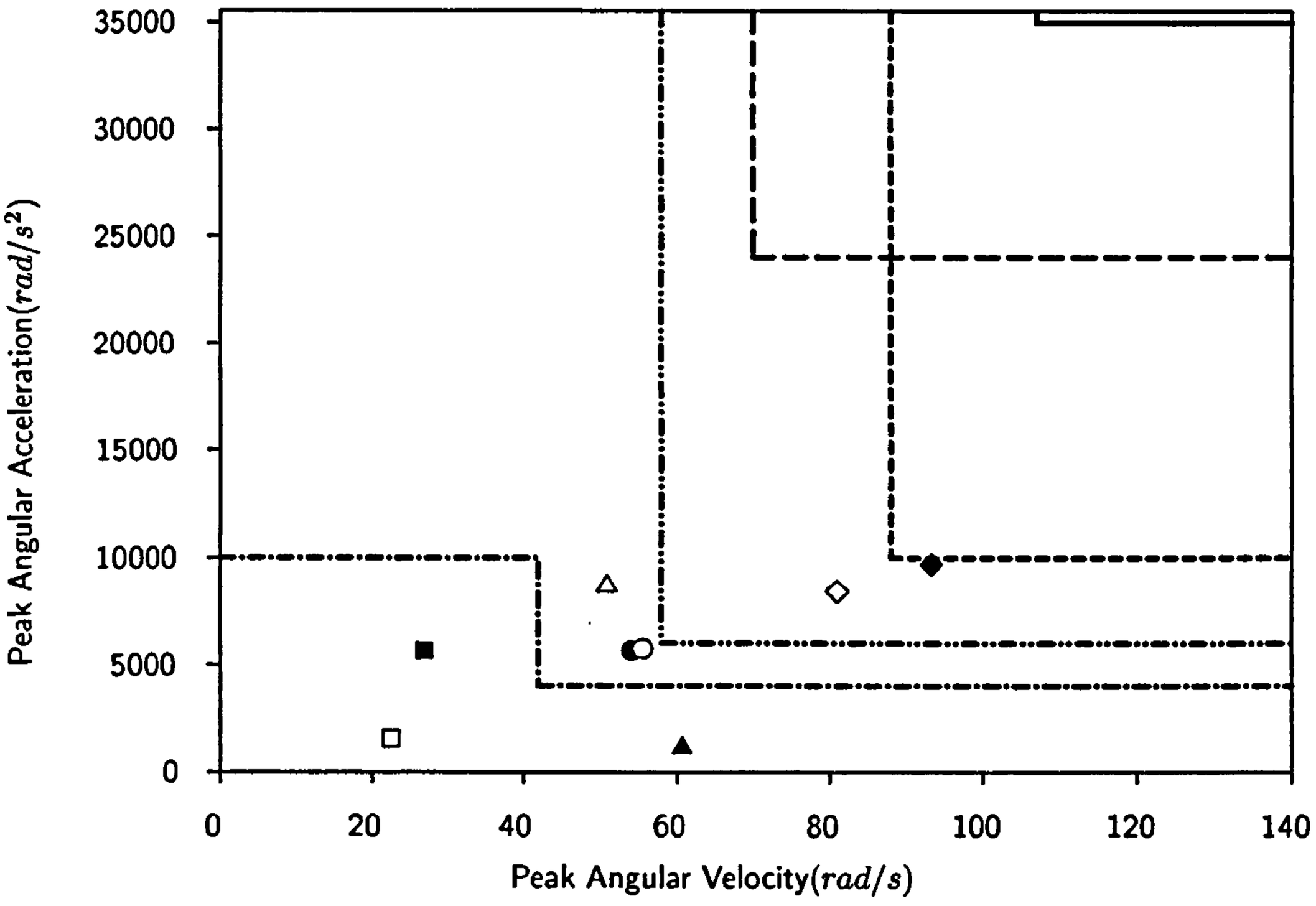

Figure 5.7: Results from study of chest impact. □ 2H max r.m.s. acceleration, ■ 2H max peak acceleration, ○ UH max r.m.s. acceleration, ● UH max peak acceleration, ◇ LH max r.m.s. acceleration, ◆ LH max peak acceleration, ▲ Duhaime shake average [1], △ Cory shake average [2].
——— SDH from [1], - - - - SDH scaled from [61] in [2], ... Concussion from[1], -.-.-. 50% concussion probability from[9] in [2], -..-..- Concussion scaled from [61] in [2].

the injury capacity of the motion assessed. The configuration of the model used was such that three different simulations were carried out; free movement at the lower hinge, free movement at the upper hinge, and increased range of motion at both hinges. Of these three configurations, freedom at both the lower and upper hinge exceeded the lower thresholds for concussion, but higher levels for injuries such as SBS, such as SDH, were not reached. Torso impact in the two hinge model appeared to have little significance, achieving motion comparable to that found in the majority of neck stiffness simulations.

It is likely that the effective centre of rotation of the head is important here, as the greater the arc through which the head moves, the greater the angular velocity achieved. In the low-hinge model, the centre of rotation of the head is greatest with the head and neck moving as a single body about the base of the neck. This results in a greater angular velocity than the upper-hinge model, where the rotation of the head occurs about the top of the neck. In the case of the two-hinge model, the primary motion is of the head and neck together, but unlike the low hinge model, when the limit of motion of the neck is reached, the head then goes through a secondary rotation about the top of the neck. Since only a small movement is achieved before the torso impact occurs, the velocity of the head, and resulting acceleration on impact is small.

5.4 Conclusions

Computational modelling of biological systems generally requires detailed data such as material properties and joint behaviour, often derived and validated from animal, cadaveric or volunteer testing. In the case of the human infant these data are not available, so RBM offered a good opportunity to investigate specific factors using the limited information available. In this series of studies, a computation model of the infant head and neck was successfully used to simulate shaking using acceleration data obtained from ATD tests.

5.4.1 Acceleration Inputs

There was little distinction between the different acceleration pulses from Chapter 4 used to simulate shaking in these simulations; in each study the results were slightly higher from the pulse with the higher peak acceleration then the higher mean acceleration. However, other than extreme simulations in the preliminary tests this difference was not enough to exceed any but the lowest of threshold levels. There is therefore no reason to suggest that repeated, low-acceleration shaking presents any more injury risk than a single, high-acceleration event.

5.4.2 Preliminary Studies

The preliminary tests showed that the model set up was suitable for these studies, and that the acceleration data from Chapter 4 could be applied to simulate shaking. The two-hinge, single ellipsoid model was found to be most suitable, and used in the studies that followed.

5.4.3 H1- Neck Stiffness

Outlying results from a parametric study of 50 neck forms initially appeared to demonstrate that neck kinematics could help to explain brain injury in SBS. However, further examination revealed that the injurious results were from neck models with impact type characteristics, confirming that impact was necessary to exceed injury criteria. It can therefore be concluded that neck form stiffness does not effect the capacity of shaking to exceed injury criteria in biomechanical studies of SBS. This indicates that further work into creating a bio-fidelic neck form is unlikely to provide insight into brain injury in SBS, and that resources should focus on other avenues of research.

5.4.4 H2 - Head-Torso Impact

By allowing free motion at the neck joints, impact of the head against the torso during shaking could be studied. These simulations exceed injury criteria for concussion, but not for injuries associated with SBS. It is unlikely that this is the mechanism of brain injury in SBS, and again, further research should be directed elsewhere.

Chapter 6

Physical Continuum Modelling of Oscillatory Brain Injury Mechanisms

The findings of the computational models carried out in Chapter 5 showed that studies of neck stiffness, and head-torso impacts were unlikely to provide insight into brain injury in SBS. It was therefore necessary to review the subject before progressing with further research.

In the literature review in Chapter 3 it was noted that the injury criteria used to asses the results of biomechanical studies of SBS are derived from single impact tests; their use in this application may therefore be inappropriate. Since cyclic loading had not previously been investigated as a distinct brain injury mechanism, it was decided that it would be of value to study as a potential brain injury mechanism in SBS. The aim of this investigation was therefore to develop experimental techniques to study and evaluate this mechanism to investigate whether cyclic loading constitutes a distinct brain injury mechanism from series of single loads.

Simple sagittal plane models of the infant brain were contructed using visco-elastic silicone gel. Optical markers were placed in a two-dimensional plane within the gel, and their motion during shaking captured using high-speed video. Their movement between frames was tracked using optical-flow methods and the strain induced in the plane of interest during shaking was then calculated.

In developing the model, the effects of geometry and boundary conditions were investigated; the geometry was changed from a full cylinder to a half cylinder and a slip boundary conditions was introduced between the skull and brain. Testing was conducted using pure rotation and angular motion, at a range of nominal speeds.

6.1 Materials

The injury criteria used to asses the findings of the biomechanical studies of SBS by Duhaime *et al.* were derived in part from the work of Margulies on primate brain injury. This included the use of physical continuum models, and the design of the following equipment was guided by descriptions of this work [1, 51].

6.1.1 Surrogate Brain Tissue Material

The use of clear silicone gels as surrogate brain tissue in kinematic studies of brain damage is well documented [12, 53, 55, 56, 62, 63]. The silicone gel used here was Q-Gel 310 (ACC Silicones, Bridgewater, UK), which is a two part silicone compound, which cures at room temperature in about twenty-four hours. In order to validate its use oscillatory rheometric testing was carried out as described in Appendix G. A summary plot of comparisons with other rheometric studies of brain tissue and brain tissue surrogates is given in Figure 6.1. This shows that the complex modulus (G*) of Q-Gel 310 lies within the range of brain tissue and other surrogate materials findings, and as such its use in this study would be appropriate.

6.1.2 Test Rig

A custom designed oscillating mechanism was constructed to subject the specimens to two modes of acceleration; pure rotation (i.e. about its own axis), and angular rotation (i.e. about a centre of rotation not coaxial with its own centre). This comprised a four-bar linkage, powered by an electric motor with separate speed controller. The range of motion of the rocker was ~65°, and the distance from the centre of the specimen to the centre of rotation in the angular configuration was 73mm. These are similar values to those used by Margulies[51] and approximate the length of the infant neck and range of motion of the head. Schematic diagrams of the test rig are shown in Figure 6.2.

6.1.3 Specimen Containers

Specimens were contained in clear acrylic cylinders of internal diameter 102 mm and height 60mm. This approximated the size of the infant skull, and given a density of $0.97 g/cm^3$ for gel, a brain weight of 500g as used by Duhaime *et al.* [1]. Initially steel pots were used but they proved too heavy, and were not only difficult to handle but also affected the movement of the test rig. The exterior of the bottom and sides of the pots were painted matt black, in order to improve the contrast of optical markers. The containers were sealed with silicone sealant and closed with six threaded bars.

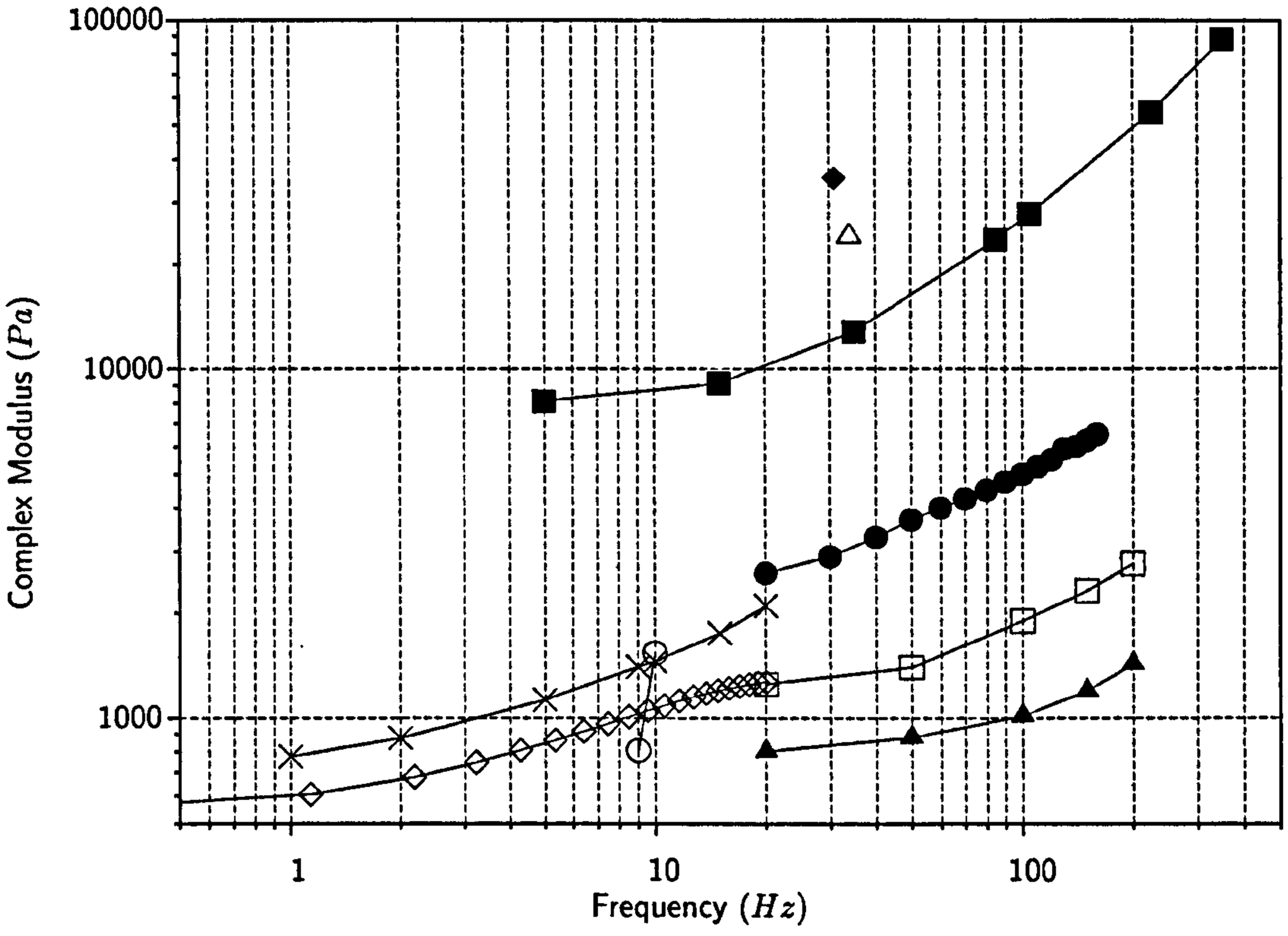

Figure 6.1: Comparison of G* from rheometric testing of Q-Gel 310 and previous studies of brain tissue and brain tissue surrogates.
◇ Q-Gel 310 - pressent study, × Sylgard 527 silicone gel from [12], ▲ Infant porcine brain tissue from [61], □ Adult porcine brain tissue from [61], ● Sylgard 527 silicone gel from [64], ■ Human brain tissue from [65], ◆ Rhesus monkey brain tissue from [66], △ Human brain tissue from [66], ○ Human brain tissue from [67].

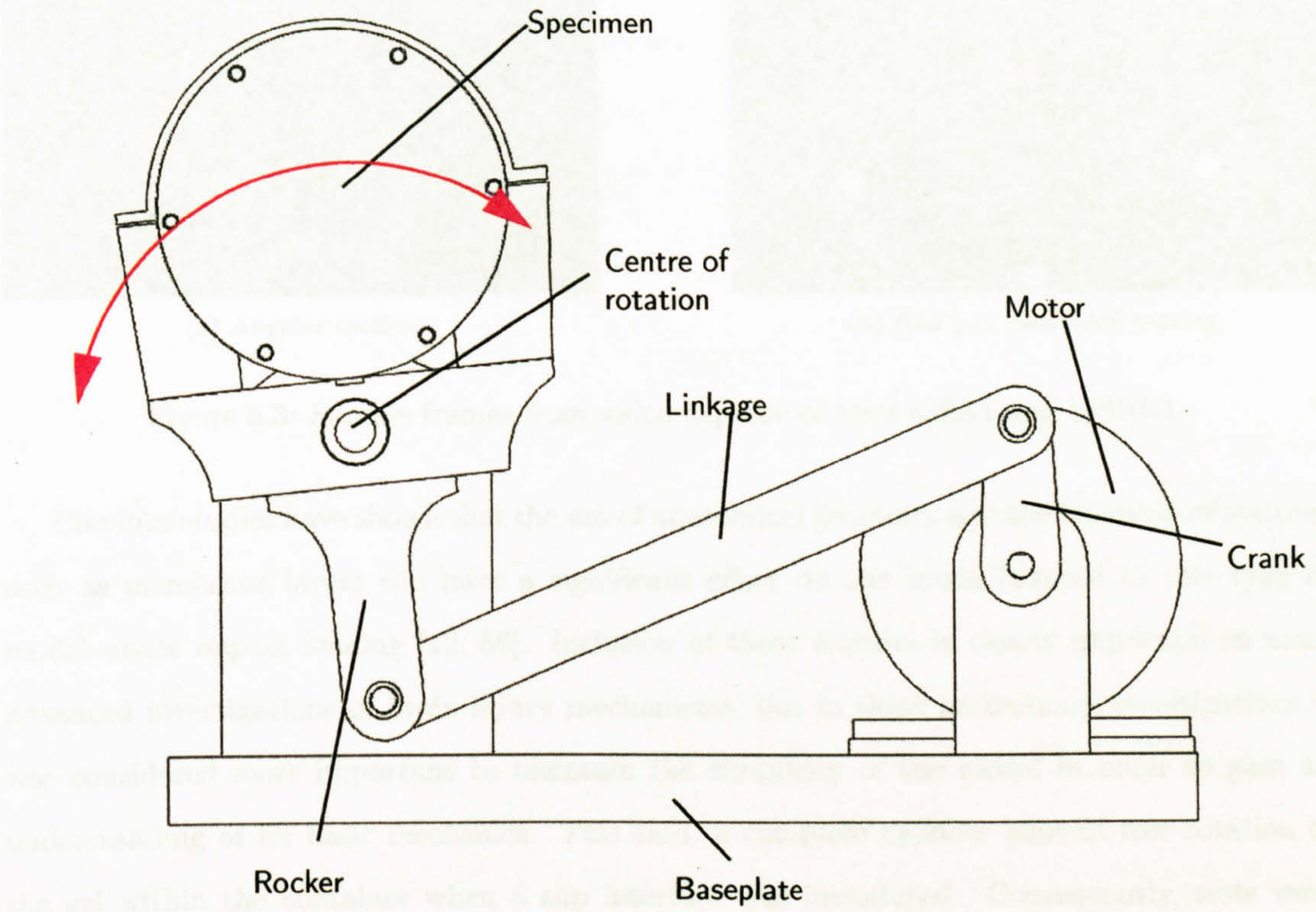

(a) Angular configuration

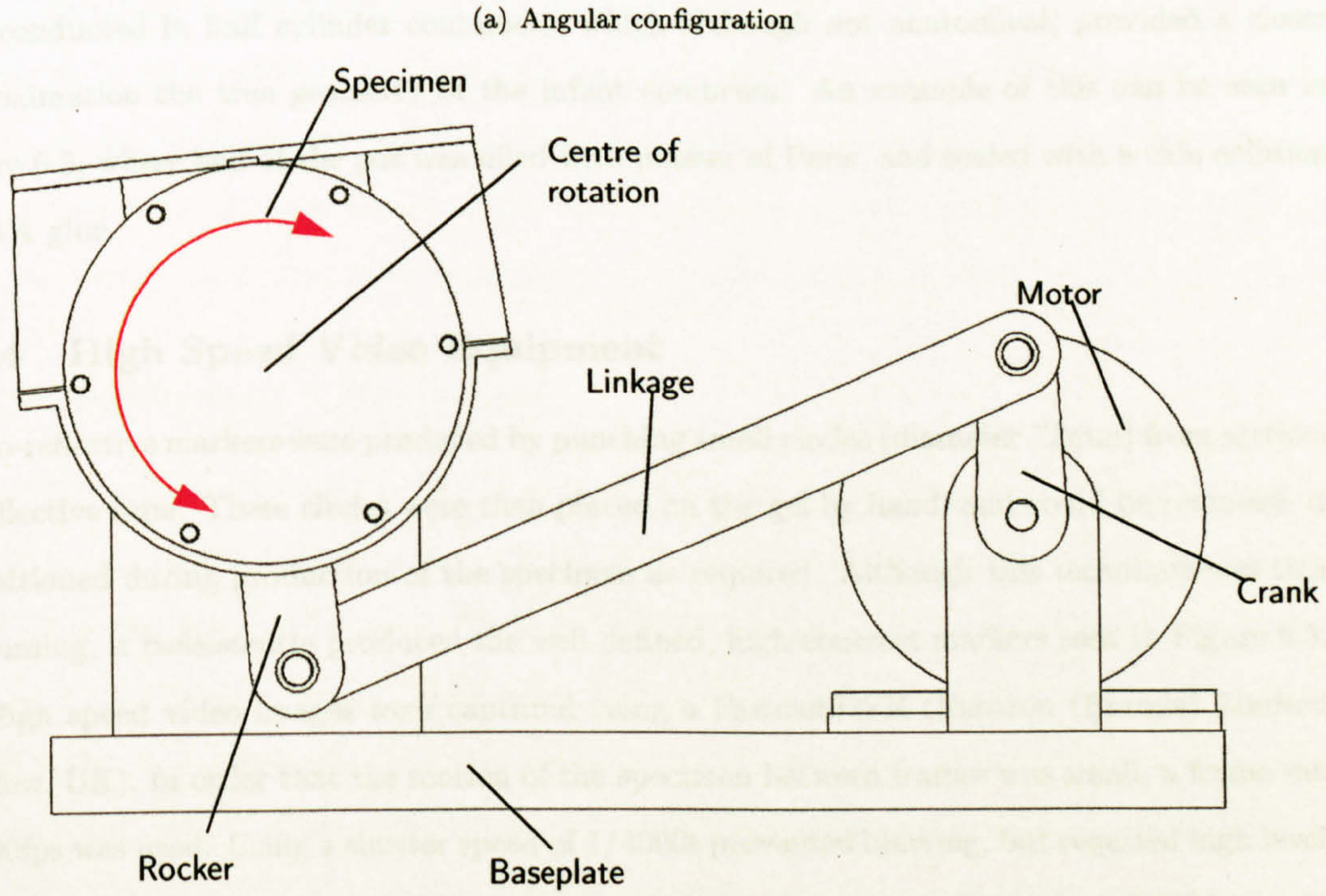

(b) Rotational configuration

Figure 6.2: Diagram of oscillation test rig. Red arrows indicae motion of test pot.

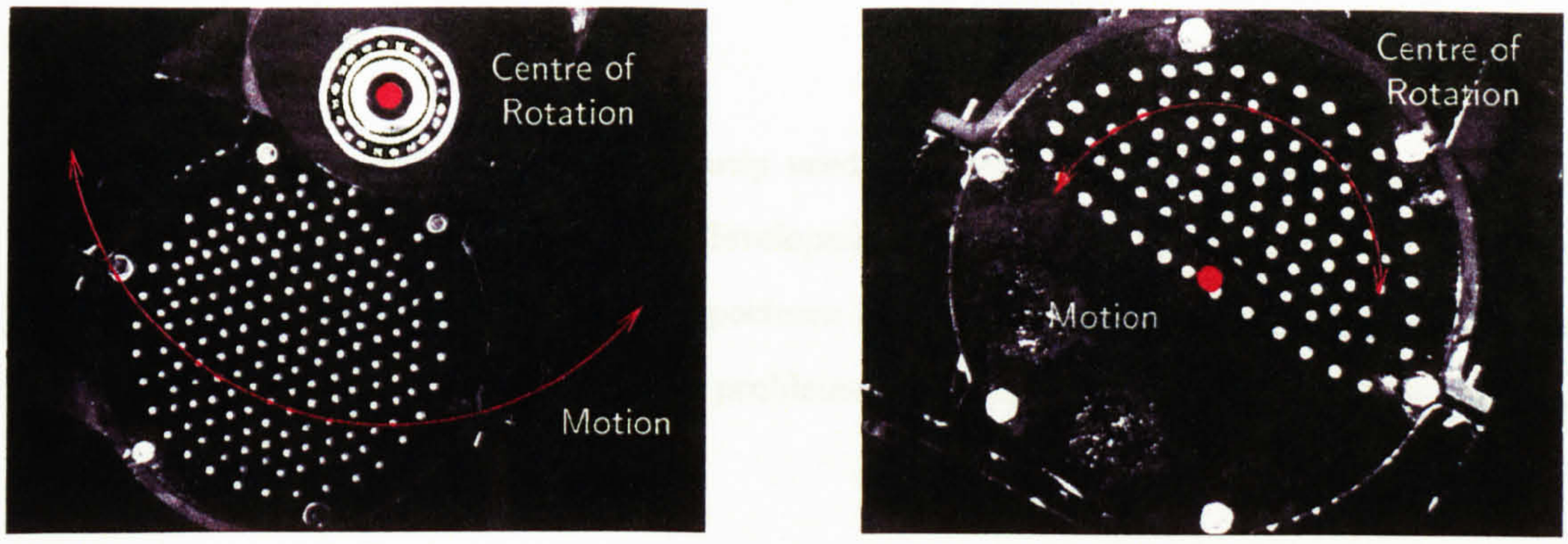

(a) Angular motion (b) Half pot, rotational motion

Figure 6.3: Sample frames from video capture of tests a)SA1 and b)SHR1.

Previous studies have shown that the use of anatomical geometry and the inclusion of features such as membrane layers can have a significant effect on the strain induced in this type of model under impact loading [12, 56]. Inclusion of these features is clearly important in more advanced investigations of brain injury mechanisms, but in these preliminary investigations it was considered more important to maintain the simplicity of the model in order to gain an understanding of its basic mechanics. This said, a complete cylinder allowed free rotation of the gel within the container when a slip interface was introduced. Consequently, tests were also conducted in half cylinder containers, which although not anatomical, provided a closer approximation the true geometry of the infant cerebrum. An example of this can be seen in Figure 6.3, where half of the pot was filled with plaster of Paris, and sealed with a thin solution of PVA glue.

6.1.4 High Speed Video Equipment

Retro-reflective markers were produced by punching small circles (diameter ~3mm) from sections of reflective tape. These circles were then placed on the gel by hand, and could be removed, or repositioned during production of the specimen as required. Although this technique was time consuming, it consistently produced the well defined, high-contrast markers seen in Figure 6.3.

High speed video images were captured using a FastcamDVR (Photron (Europe) Limited, Marlow, UK). In order that the motion of the specimen between frames was small, a frame rate of 500fps was used. Using a shutter speed of 1/4000s prevented blurring, but required high levels of lighting in order to capture a high contrast image. It was also necessary that the lighting did not result in shadowing within the container, so two 1000W and a single 500W floodlight were used to light the specimen from three angles.

6.2 Methods

Since these methods had not been previously used to investigate SBS all the equipment and experimental methods were designed and developed during the test process. Various problems were encountered both in perfecting the specimen preparation method, and obtaining images of high enough quality for analysis. These problems are discussed in Section 6.5; only the final techniques are described here.

6.2.1 Specimen Preparation

Q-Gel 310 is a two part silicone gel that was mixed in equal weights and degassed for approximately one minute before use. The containers were half filled with silicone gel, and allowed to cure for 24 hours. A layer of optical markers (diameter ~3mm) was then placed in a pattern of triads with spacing <10mm covering the surface of the gel. The spacing of these markers did not need to be precise, since the motion tracking and strain calculation techniques used the marker initial positions obtained from the first frame of video data. The pot was filled with a second layer of gel, adherent to the first and closed with a clear acrylic lid.

For the slip tests, the containers were lined with a 1mm spacer, and a layer of decalcomania paper(Twincal III, Tullis Russell Coaters, Stoke-on-Trent, UK). This allowed the cured gel and markers to be removed from the container, and the lining paper removed with water. Liquid paraffin oil was then poured into the container to create a slip condition. In addition to the markers used in the non-slip test, markers were also placed around the edge of the container, to allow the relative movement of the gel within the container to be measured.

6.2.2 Experimental Procedure

The test rig was mounted vertically on an anti-vibration block, and the camera positioned looking down on the specimen, as show in Figure 6.4. This orientation eliminated gravitational distortion of the gel in the plane of interest. Those faces of the rig that faced the camera were painted matt black to improve image contrast and reduce optical noise. The specimen was mounted in the rig, and the camera zoom and focus adjusted to view the plane of markers throughout their full range of motion. Lighting was adjusted so that the markers were not cast into shadow by the walls of the container, the camera was not obscured and there were no bright reflections.

The camera was primed, and the motor controller was turned on and set to the required speed. The camera was then triggered, and the motor started; motion was recorded for between 2 and 4 seconds, long enough to capture several cycles of motion. Video data was saved as uncompressed ".tiff" files and transferred from the camera controller to a PC for processing. Each specimen

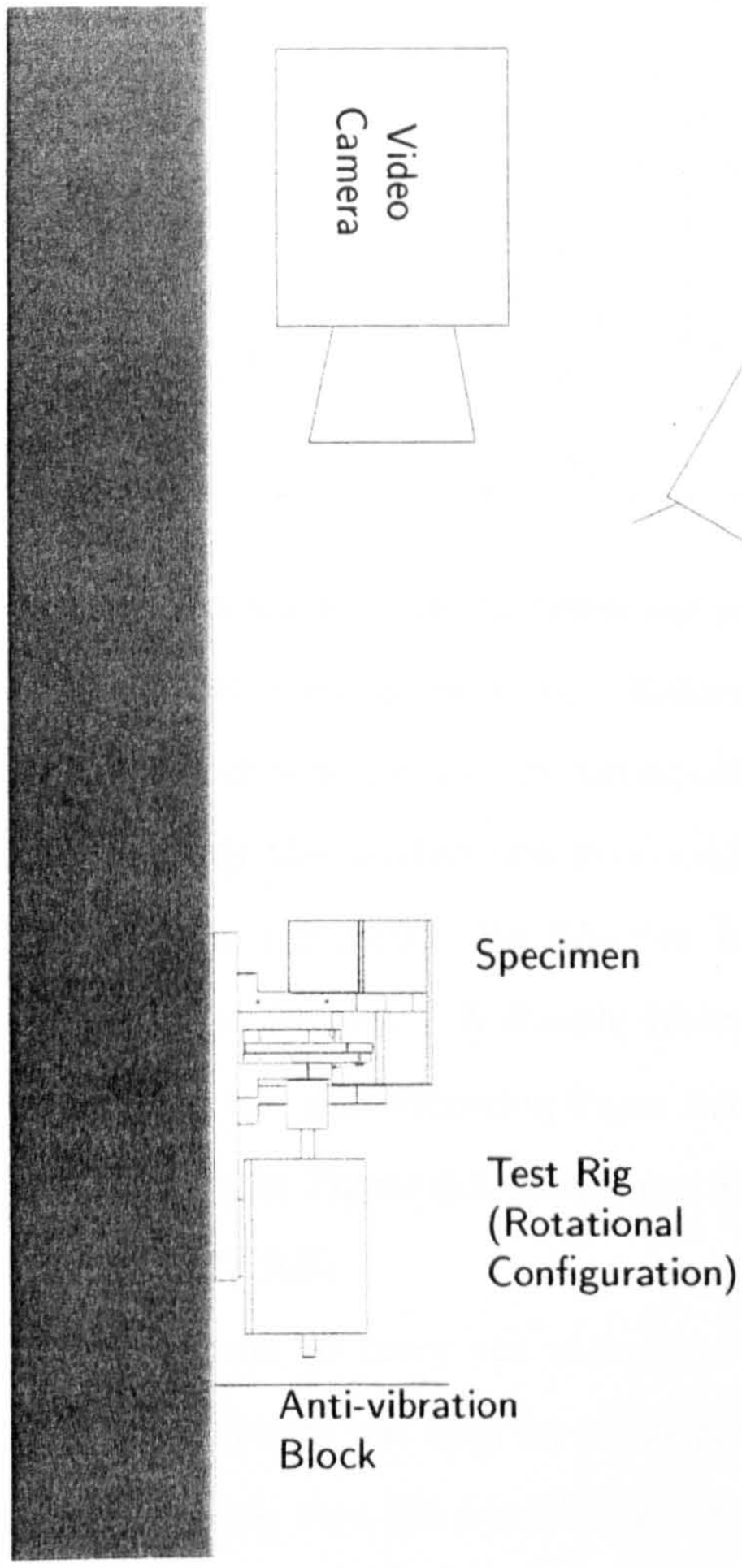

Figure 6.4: Video camera positioning

was tested in both angular and rotational configurations, at three nominal controller speeds; 1,2 and 3. This resulted in 24 speed-specimen combinations, described in table 6.1. Samples of the type of images captured are shown in Figure 6.3.

6.3 Analysis

As well as developing the experimental methods, motion tracking and strain calculation software also had to be written before strain data could be obtained from the experimental data. This required image processing, marker location and motion tracking to be performed before strain could be calculated.

6.3.1 Motion Tracking

In order to determine the distortion of the grid of markers in each frame it was necessary to know not only their current position but also their original position in the first frame. Simply

Table 6.1: Test configuration names used in physical modelling of SBS

Configuration	Speed	Non-Slip		Slip	
		Cylinder	Half-Cylinder	Cylinder	Half-Cylinder
Rotational	1	R1	HR1	SR1	SHR1
	2	R2	HR2	SR2	SHR2
	3	R3	HR3	SR3	SHR3
Angular	1	A1	HA1	SA1	SHA1
	2	A2	HA2	SA2	SHA2
	3	A3	HA3	SA3	HA3

locating the markers was therefore not sufficient; their motion between frames had to be tracked. This was achieved by means of a Kalman filter, as described in Section 2.5.1.

The track was initiated by thresholding and masking the first frame so that a binary image showing only the markers was produced. Due to the slight delay between triggering the camera and starting the motor, the first few frames of each video were static, so initial velocity was estimated to be zero. A Simple Kalman filter was then implemented for each dot, and its position in the next following frame determined. An example of the motion tracking from test A2 is shown in Figure 6.5, which was produced from preliminary motion tracking tests carried out in MATLAB.

A program to carry out this procedure was written in Visual C++. Intel's open source *"openCV"* library was used for image processing and the *"blobslib"* extension to detect the markers. A simple text file containing the Cartesian co-ordinates of each dot in each frame was produced, which was used to calculate strain.

6.3.2 Strain Calculation

Green-Lagrangian strain was calculated by tensor algebra from the track data using the methods described in Section 2.5.2. A MATLAB program was used to automate this process, utilising a Delaunay function to define a mesh of triads from the initial frame. The distortion of these triads was determined by comparing the position of nodes in the initial configuration of this mesh, with their position in the subject frame. Since the tracking procedure kept the node list in the same order, the transformation of the triad was not important; strain was determined from relative changes in position of the nodes within the triad (i.e the deformation tensor). In this manner, the strain within each triad of markers in a specimen was found for each frame of the video clip.

6.3.3 Acceleration

One of the primary controlled variables in these test was the speed of oscillation. Due to the design of the test rig, control of this variable was poor, with only arbitrary settings of the motor

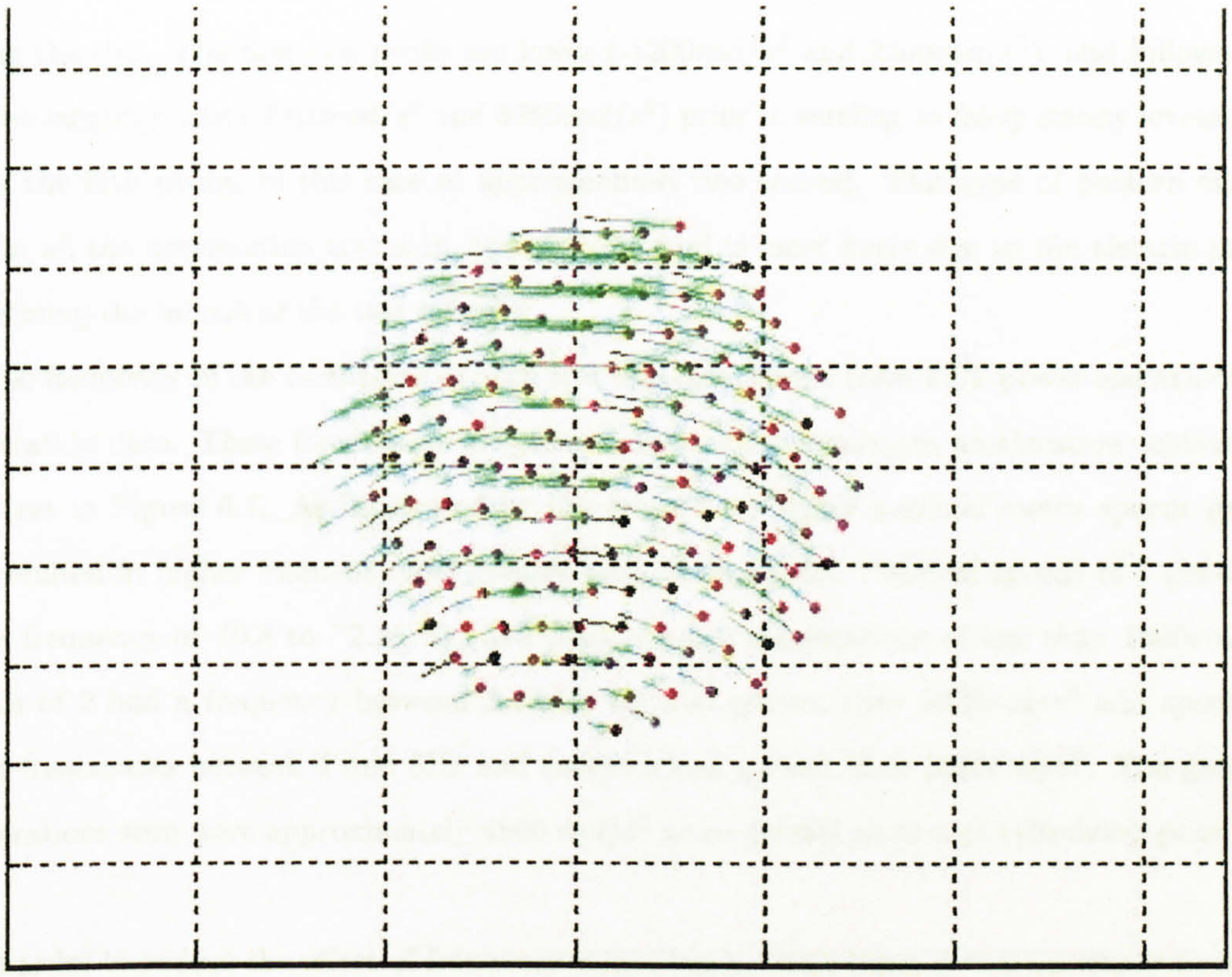

Figure 6.5: Example of motion tracking from A2 test. The red dots show the current position and the green lines the positions in the previous five frames.

controller available (i.e. 1, 2 and 3). It was therefore important to find the actual motion of the specimen in order to obtain results with physical meaning. To this end, a fixed point was selected on each specimen (i.e. a marker on the container, rather than within the gel) and its movement extracted from the track data. Using this data a MATLAB function was written to determine the angular acceleration of the specimen about its centre of rotation.

6.4 Results

Further to the analysis techniques used to track markers and calculate strain, various methods were used to summarise the data and evaluate their meaning. Two-dimensional strain maps provided good visualisations of strain distribution with the gel, and average strain data was used to examine temporal changes and the effect of experimental factors.

6.4.1 Acceleration

From the example trace shown in Figure 6.6, it can be seen that although the frequency of oscillation is fairly constant, the magnitude of acceleration is neither symmetrical, nor consistent. The positive angular acceleration is greater than the negative acceleration by approximately $1000 rad/s^2$ ($2800 rad/s^2$and $1800 rad/s^2$respectively) and the magnitude of acceleration changes

during the test. The first two peaks are lower (-1200rad/s^2 and 2200rad/s^2), and followed by the two largest peaks (-2300rad/s^2 and 3250rad/s^2) prior to settling to fairly steady levels after about the fifth peaks, in this case at approximately one second. This type of pattern can be seen in all the acceleration traces in Appendix H, and is most likely due to the electric motor overcoming the inertia of the test cylinder.

The frequency of the oscillation of each test was determined from FFT power spectra of the acceleration data. These frequencies are plotted against the maximum acceleration achieved in each test in Figure 6.7. As illustrated by the trend-line, higher nominal motor speeds generally resulted in higher frequency and greater peak acceleration. Nominal speeds of 1 generally had a frequency of ~0.8 to ~2.25 Hz, and peak average accelerations of less than 1500rad/s^2. Speeds of 2 had a frequency between 3 and 4 Hz and greater than 2000rad/s^2 and speeds of 3 had frequencies between 4 and 5Hz and accelerations greater than 3000rad/s^2. The greatest accelerations seen were approximately 4500 rad/s^2 in rotational motion of cylindrical pots with slip.

In order to reduce the effect of frequency variations in these tests, it was necessary to select a group of test with similar motion for further analysis. As with the selection of acceleration inputs for the computational modelling in Chapter 5, the capacity for injury was best assessed by selecting the worst-case data. This comprised the group of tests marked by a red ellipse in Figure 6.7 (a3, r2, ha3, hr3, sa3, sr3, sha3, shr3), acceleration traces for which are presented in Appendix H.

These tests had a average acceleration of 3495rad/s^2 and average frequency of 4.4Hz. This acceleration is higher than the greatest average head acceleration of 1034rad/s^2 from computational studies of neck stiffness found in Section 5.2, but the frequency is lower than the maximum shaking frequency of 5.5.Hz found in ATD tests in Chapter 4. Without the experimental facility to control these variable, it was felt that these data provided a suitable representation of worst case head motion during a shaking episode.

6.4.2 Strain

For each triad in the marked plane strain was calculated by tensor algebra, as described in Chapter 2. In calculating the strains using C++ six strain measures were generated for each of these triads: positive and negative principle strains, two identical shear strains, and X and Y strain.

Several of these measures have little physical meaning, and so are not used in further analysis: the two shear strains are identical, only one need be considered, and the X and Y strains are related to an arbitrary frame of reference. The principle strains however, describe the greatest

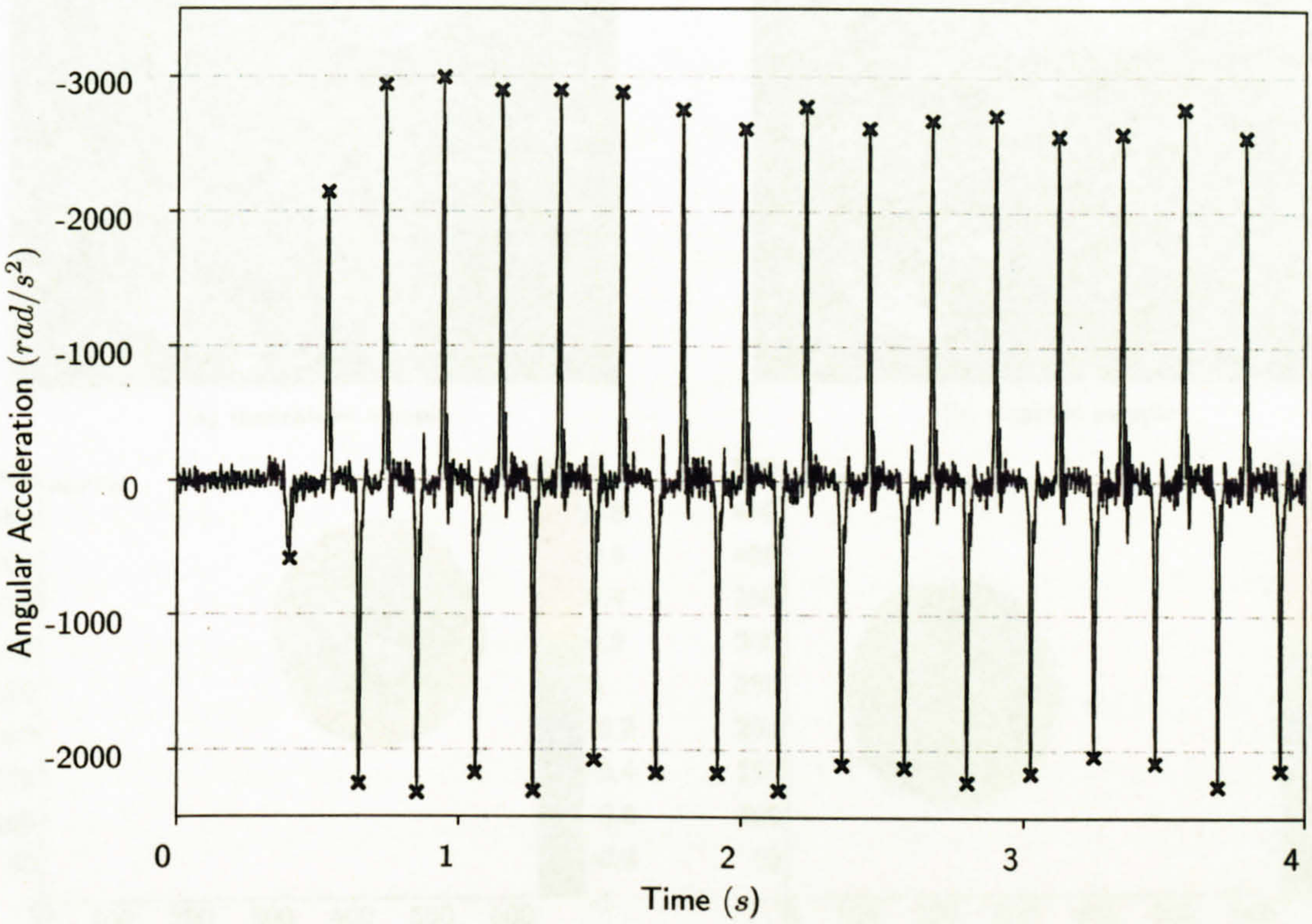

Figure 6.6: Example angular acceleration trace from A3 test; isolated peaks are marked by crosses.

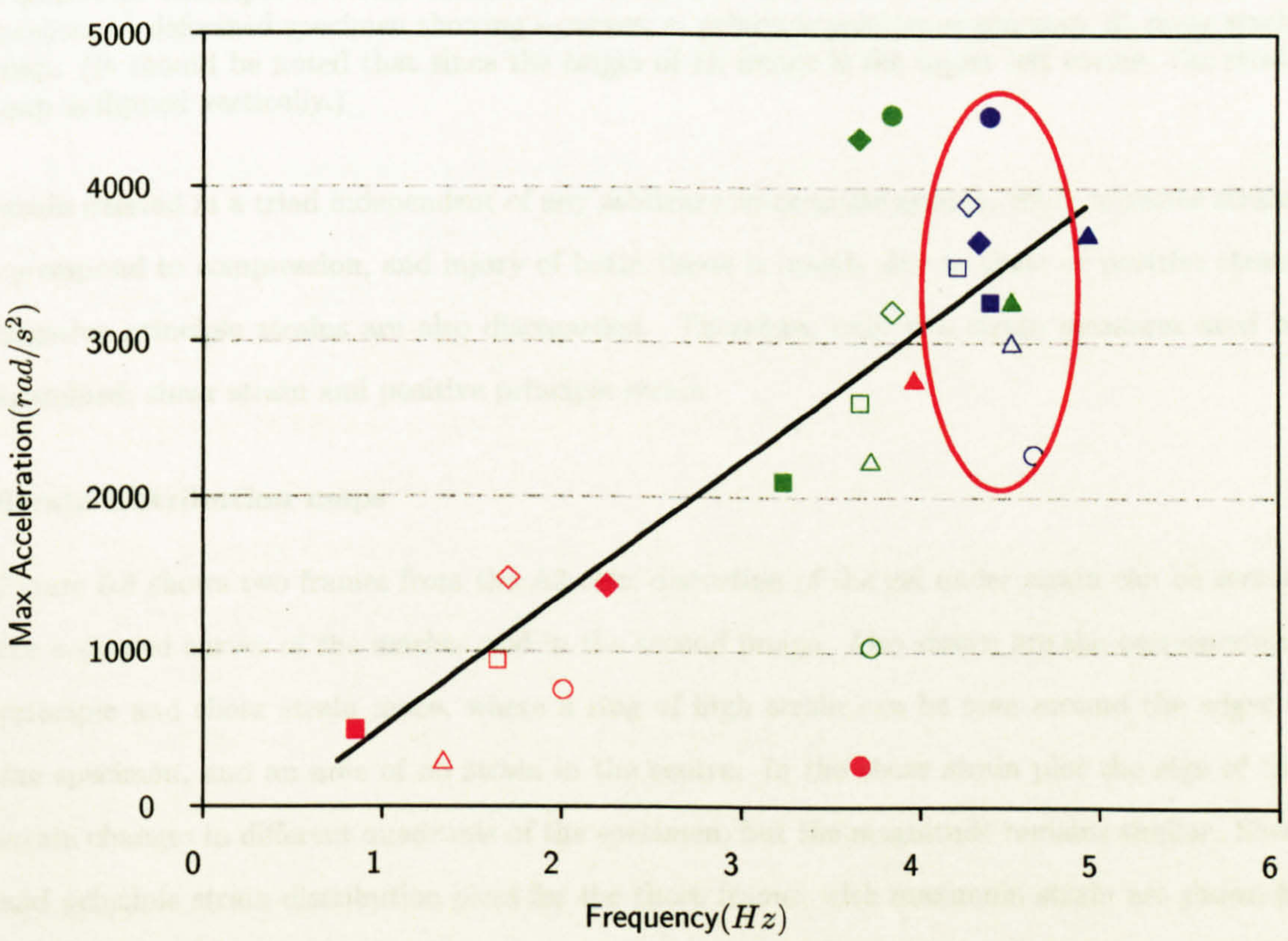

Figure 6.7: Summary of test frequencies and corresponding accelerations. The red ellipse marks those tests identified as representative of SBS. ■ a1, ■ a2, ■ a3, ▲ r1, ▲ r2, ▲ r3, □ ha1, □ ha2, □ ha3, △ hr1, △ hr2, △ hr3, ◆ sa1, ◆ sa2, ◆ sa3, ● sr1, ● sr2, ● sr3, ◇ sha1, ◇ sha2, ◇ sha3, ○ shr1, ○ shr2, ○ shr3.

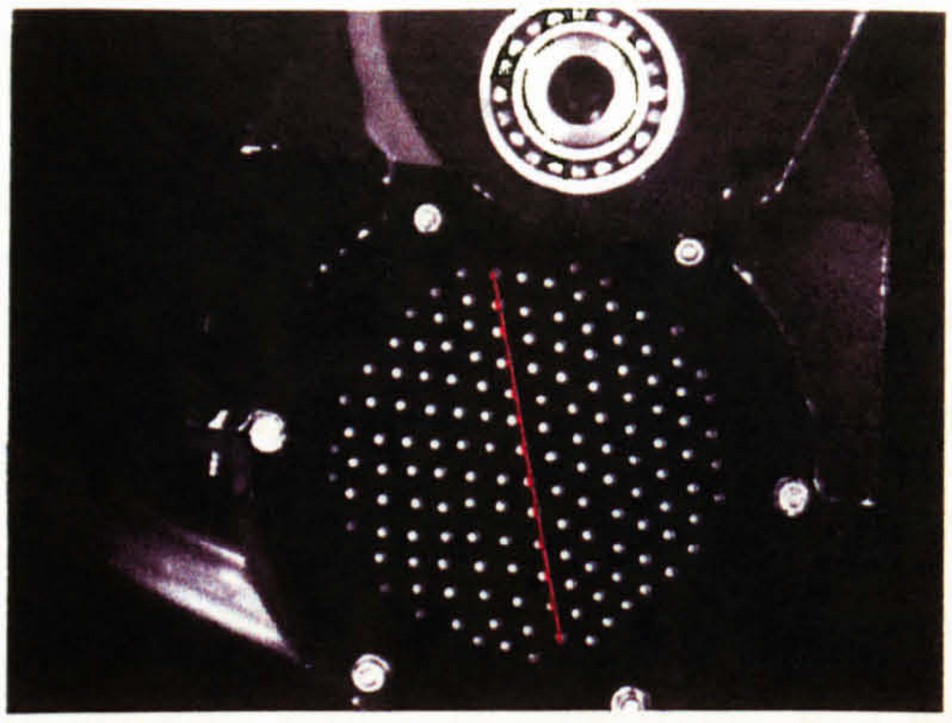

(a) unstrained sample

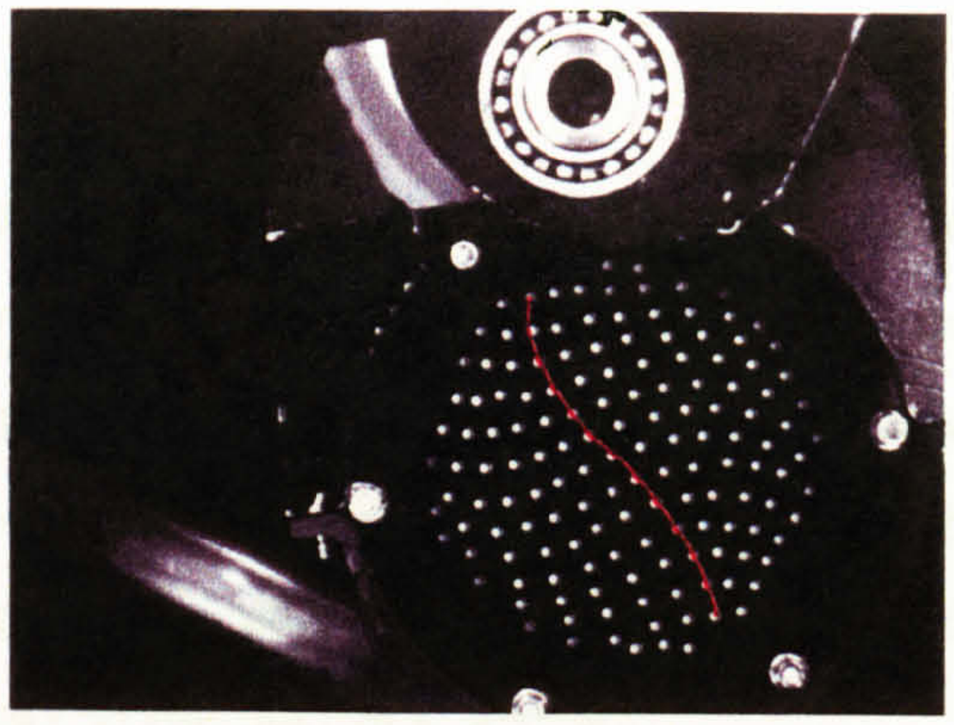

(b) strained sample

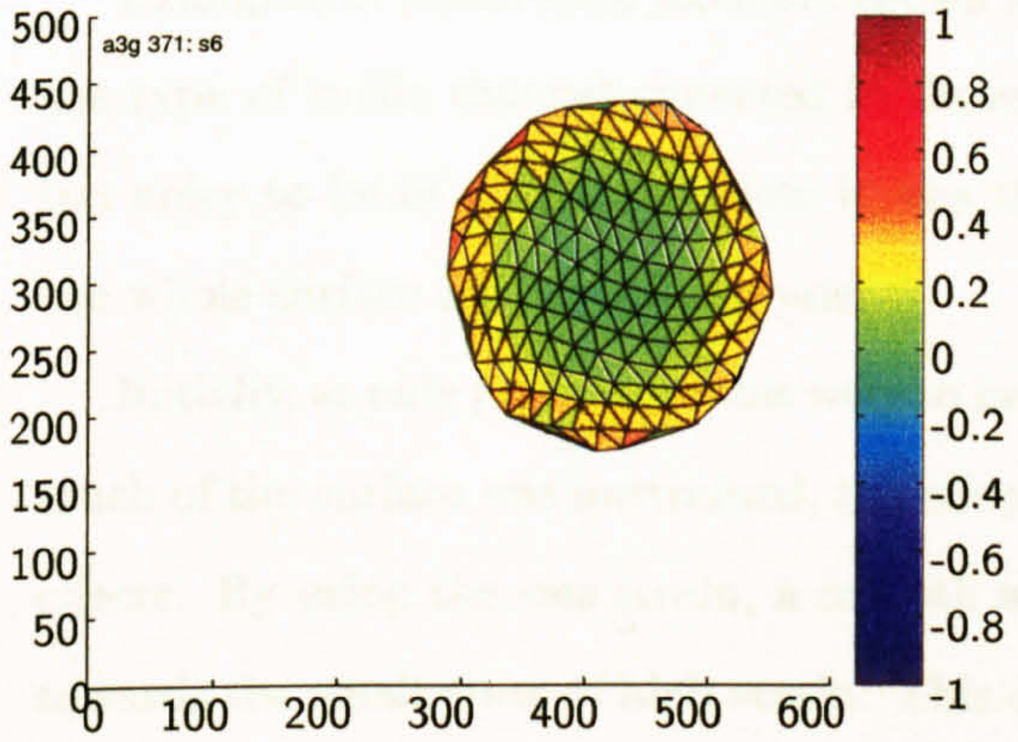

(c) principle strain map

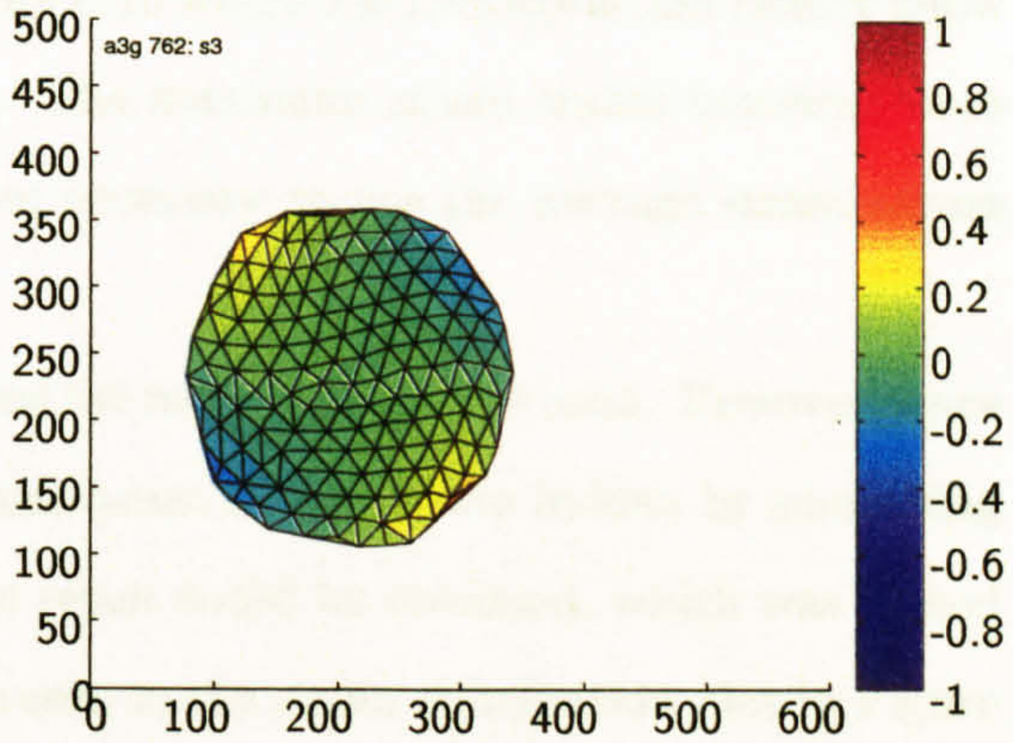

(d) shear strain map

Figure 6.8: Example of strain distribution analysis of A3 test: a) unstrained specimen before motion, b) deformed specimen showing s-curves, c) principle positive strain map, d) shear strain map. (It should be noted that since the origin of an image is the upper left corner, the strain map is flipped vertically.)

strain exerted in a triad independent of any arbitrary co-ordinate system. Since negative strains correspond to compression, and injury of brain tissue is mainly due to shear or positive strain, negative principle strains are also disregarded. Therefore, only two strain measures need be examined; shear strain and positive principle strain.

Strain distribution maps

Figure 6.8 shows two frames from the A3 test; distortion of the gel under strain can be seen in the s-shaped curves of the marker grid in the second image. Also shown are the corresponding principle and shear strain maps, where a ring of high strain can be seen around the edges of the specimen, and an area of no strain in the centre. In the shear strain plot the sign of this strain changes in different quadrants of the specimen, but the magnitude remains similar. Shear and principle strain distribution plots for the those frames with maximum strain are shown for selected tests in Appendix M.

Strain-time plots

Although strain maps provide useful visualisations of strain distribution, it was not practical to view the results of entire video clips containing thousands of frames of images in this fashion. By examining each triad within a specimen, it was possible to produce maximum, and average values of strain for each frame allowing simple one-dimensional plots of strain against time to be produced. As seen in the shear strain map in Figure 6.8, positive and negative strains could be achieved within the same frame, so it was necessary to use the r.m.s. average.

Examples of strain-time plots are shown in Figure 6.10 where the average strain clearly show the type of cyclic changes expected in these tests. The maximum strain traces however, were too noisy to be of analytical value; it was therefore necessary to use the average strain across the whole surface for further analysis.

Initially, as only positive strains were to be studied the mean average was used. However, since much of the surface was unstrained, the effect of small areas of high strain hidden by smoothing effects. By using the rms strain, a smooth average result could be obtained, which was biased towards the small areas of high strain. This can be seen in the strain distribution plot in Figure 6.9, where the frequency of strain levels for a single frame, with mean and rms averages are shown. More sophisticated methods for obtaining maximum strain data are discussed in Section 6.5.2, but this method was considered robust and could be easily incorporate into the analysis software already developed.

R.M.S. principle and shear strain traces for those data identified representative of SBS in Figure 6.7 may be found in Appendix I and Appendix J respectively. It is interesting to note from comparison of Figures 6.6 and 6.10 that the frequency of induced strain is twice that of acceleration, with a strain peak occurring at each change in direction; this can be seen in any pair of corresponding plots in Appendix H and Appendices I and J.

As with the example acceleration trace in Figure 6.6, the first strain peak was notably the lowest. This indicated a build-up of strain between cycles, apparently confirming the hypothesis that cyclic loading is a different mechanism to a series of separate loads. However, this build-up is consistent with the changes in acceleration levels observed in Section 6.4.1. It was therefore useful to normalise strain for fluctuations in acceleration in order to determine if this effect is real, or merely a result of experimental procedure.

Acceleration normalised strain plots

Although the irregular motion observed from acceleration traces is probably reflective of a shaking episode, it does not allow the effects of cyclic loading to be accurately investigated. In order to establish if the effect of a single loading cycle changes during shaking, strain was normalised

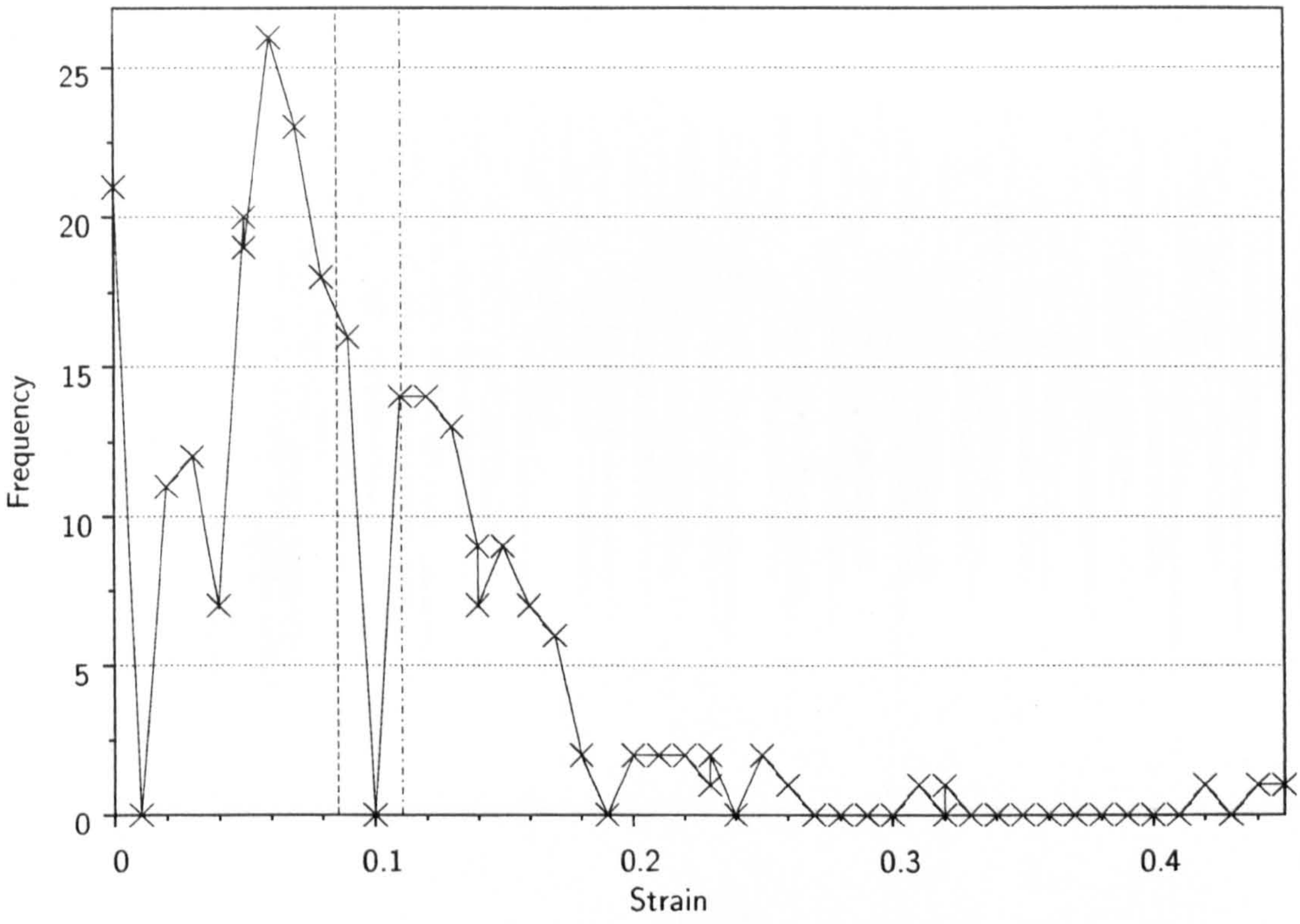

Figure 6.9: Stain distribution plot for principle strain in test SA3, frame 1814: - - - - mean average, -·-·-· rms average.

for angular acceleration. Having identified corresponding acceleration and strain peaks the strain per acceleration (i.e. strain/rads^{-2}) was calculated. The example in Figure 6.11 shows changes in sign, but the levels remain consistent throughout; there is no distinguishable trend away from a centre of zero and levels of $\pm 0.00005 s^2/rad$. Any trend would indicate a change in the effect of the same load between cycles and either a build-up, or dissipation of strain between cycles.

Normalised principle and shear strain plots for selected data are given in Appendix K and Appendix L respectively. Other than outlying initial peaks these traces are roughly symmetrical about zero and show no overall trends. There is therefore no evidence for a build-up in strain between cycles, independent of acceleration. The hypothesis that cyclic loading is distinct from a series of separate loads has not therefore been proved.

Summary of strain

Having identified the peaks in each average strain plot, they may be summarised to allow easier comparison between tests. Figure 6.12 shows plots of peaks in average principle and shear strains over time for those data selected as representative of SBS.

These data were selected to eliminate the effects of frequency on acceleration seen in Figure 6.7 and by zeroing the data this is confirmed by each test having 17-19 peaks in two seconds (i.e. ~4.5Hz). As with the example in Figure 6.10, the first strain peaks are lower than all subsequent

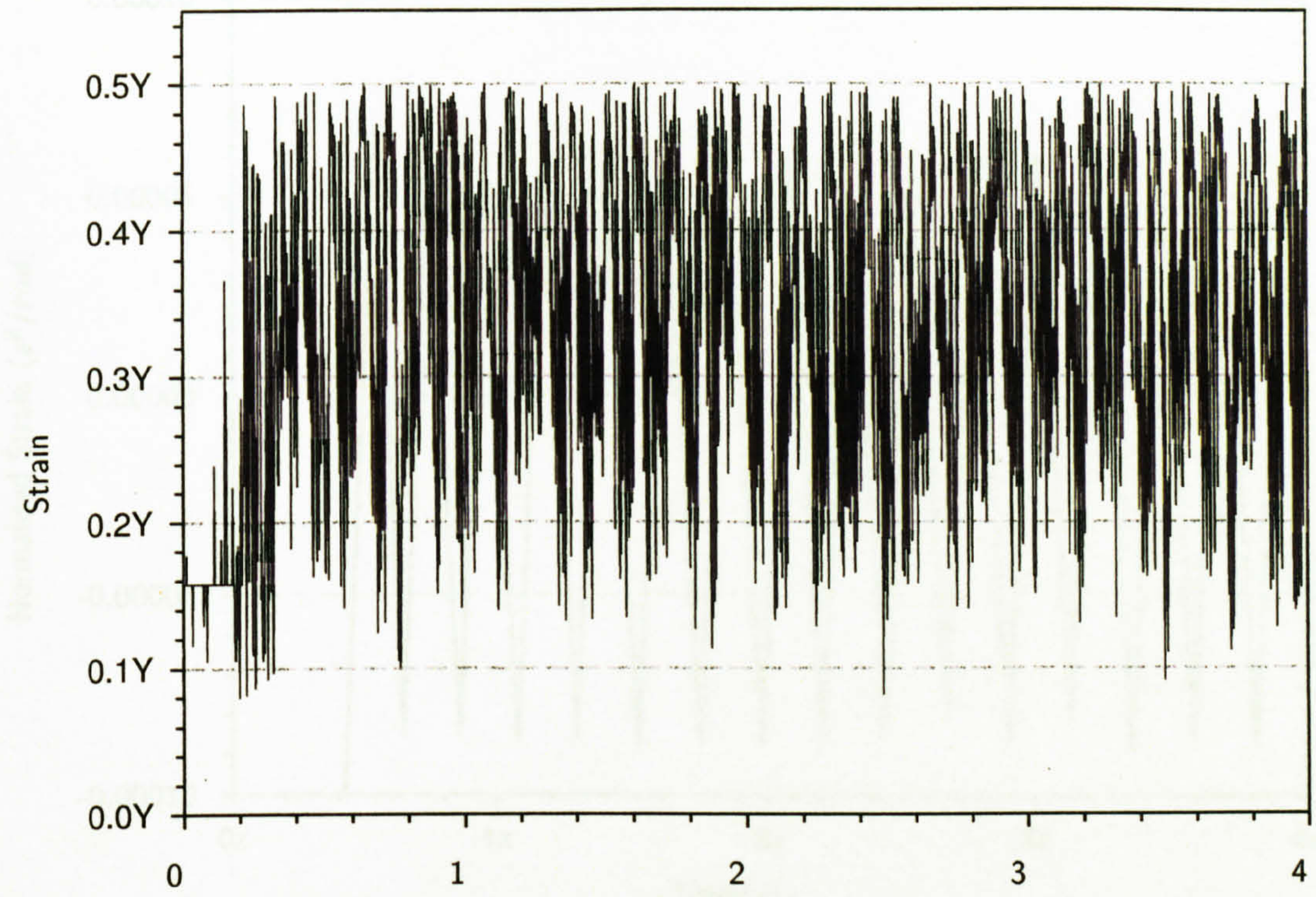

(a) max acceleration for frame

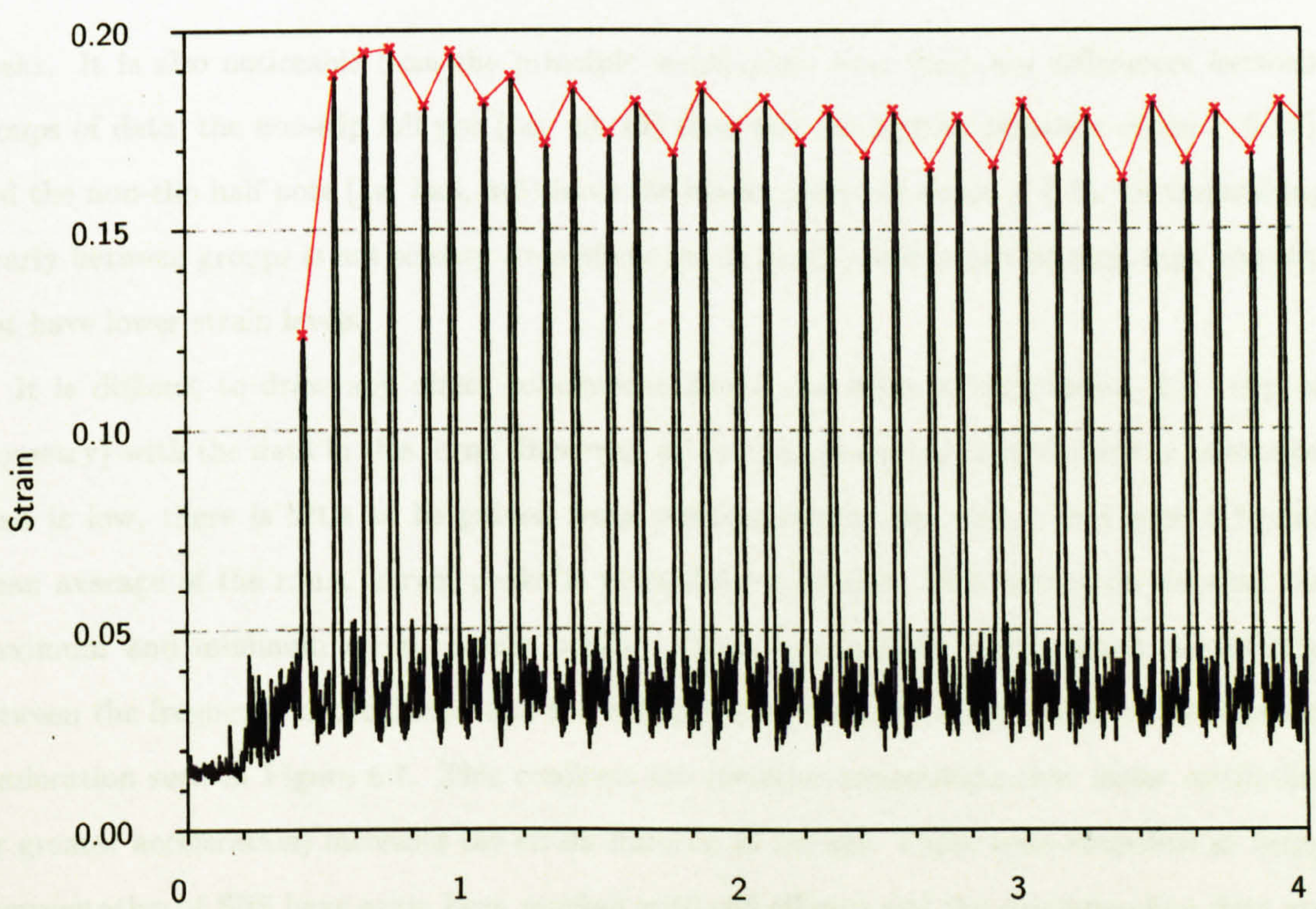

(b) average acceleration for frame

Figure 6.10: Example principle positive strain vs time plots for **A3** test. Where the maximum strain plot is too noisy to allow further analysis, the average strain plot clearly shows cycles in strain levels, allowing peaks to be isolated (here marked in red).

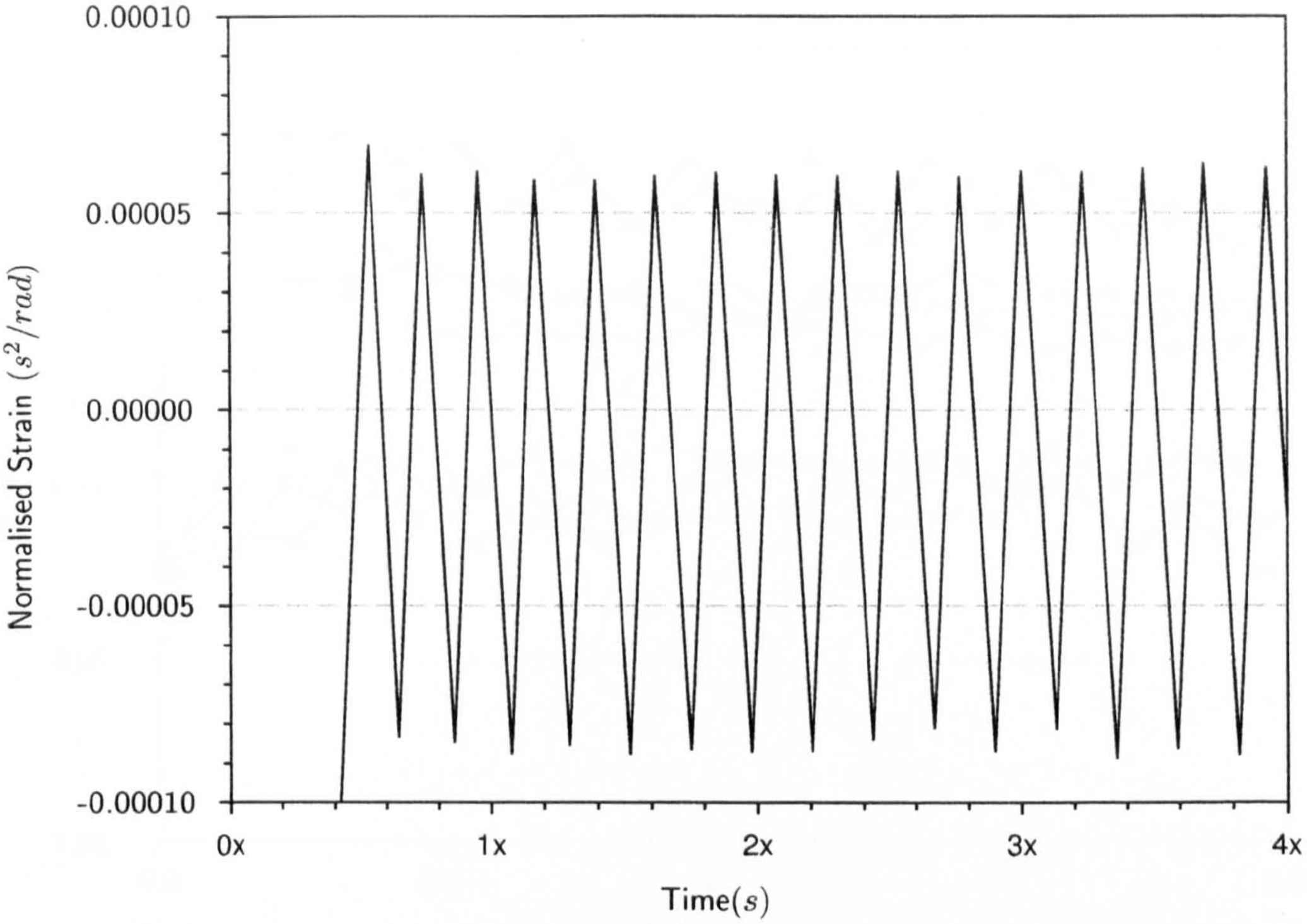

Figure 6.11: Example of normalised strain/acceleration plot for A3 test.

peaks. It is also noticeable from the principle strain plots that there are differences between groups of data; the non-slip full pot (i.e. a3, r2) have the the highest principle strain (~0.17), and the non-slip half pots (i.e. ha3, hr3) have the lowest principle strain (~0.1). Distinguishing clearly between groups is not so easy from shear strain results, but it can be seen that non-slip test have lower strain levels.

It is difficult to draw any direct conclusions about the effect of each factor (i.e. slip or geometry) with the data in this form. However, other than observing that the first acceleration peak is low, there is little to be gained from plotting strain over time. In Figure 6.13 the mean average of the r.m.s. strain peaks is plotted for each test, with error bars showing the maximum and minimum r.m.s. strain peaks. There is a broadly proportional relationship between the frequency of oscillation and the magnitude of strain consistent with the increase in acceleration seen in Figure 6.7. This confirms the intuitive expectation that faster oscillation (or greater acceleration) increases the strain induced in the gel. Those tests identified as being representative of SBS have again been marked with red ellipses and the corresponding data are given in Table 6.2. The same basic observations described above can be confirmed; a3 and r2 have the highest principle strain (0.196 and 0.201), ha3 and hr3 have the lowest principle strain (0.108 and 0.112). It is now also possible to make similar observations for shear strain; a3 and r2 have the highest shear strain (0.128 and 0.130), ha3 and sa3 have the lowest shear strain (0.072

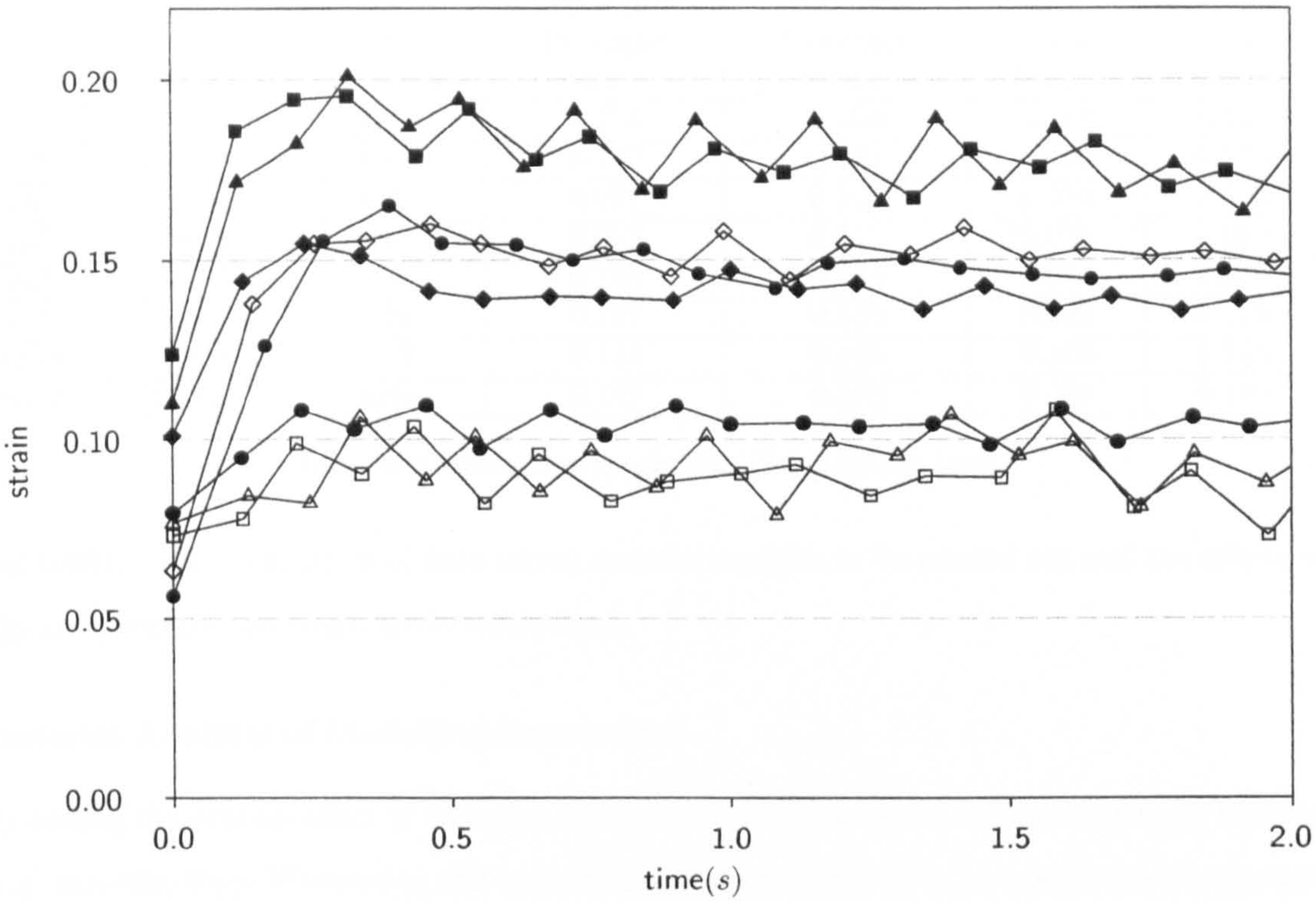

(a) principle strain

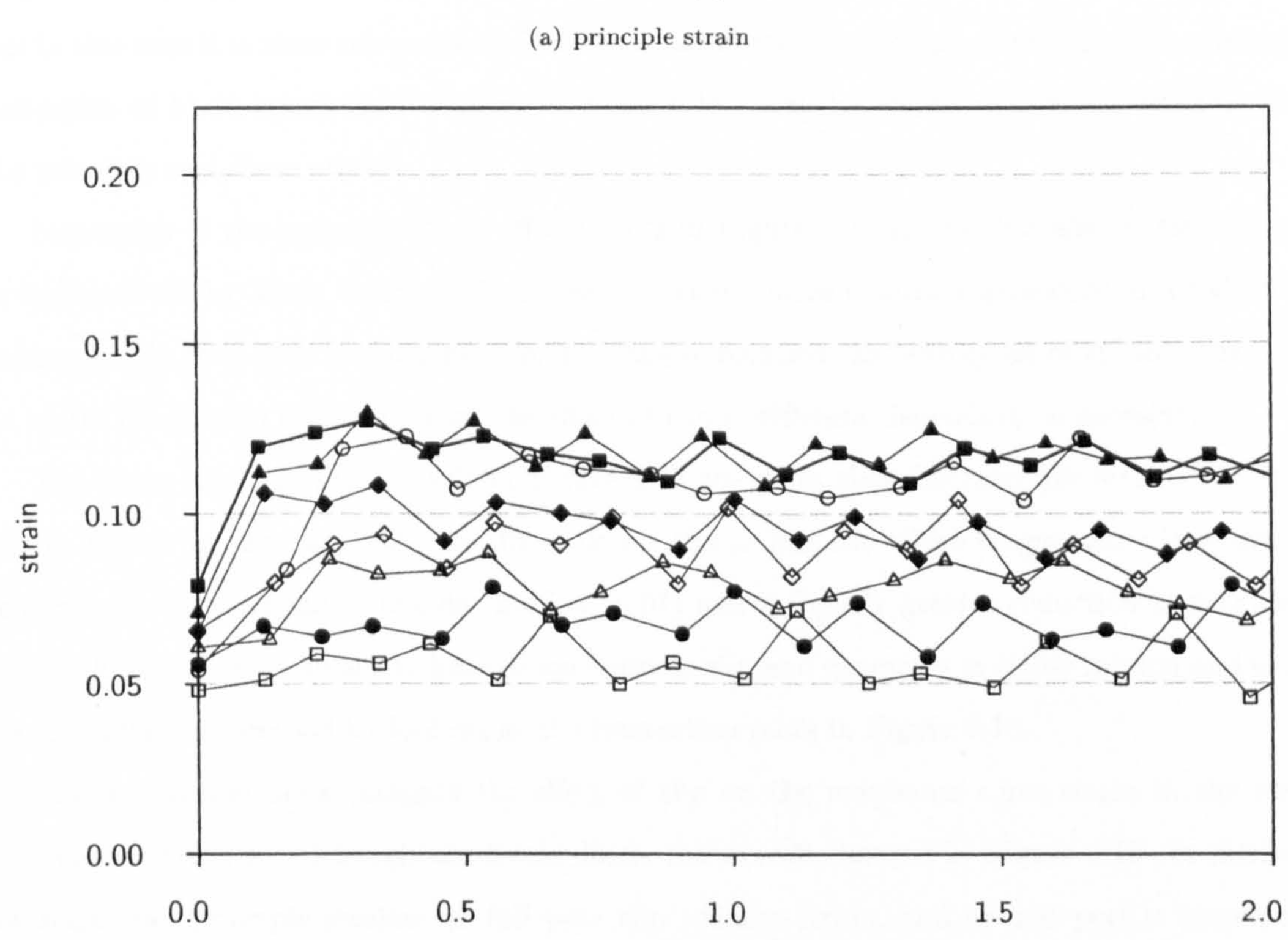

(b) shear strain

Figure 6.12: Peak average strain vs time plots for selected data sets (■A3, ▲R2, □Ha3, △Hr3, ●Sa3, ◆Sr3, ○Sha3, ◇Shr3). Time offset have been adjusted such that the first strain peak occurs at t=0, and the data are truncated at t=2.

Test	Acc. at max. strain rad/s^2	F at max. strain (Hz)	Mean rms Principle Strain	Max rms Principle Strain	Mean rms Shear Strain	Max rms Shear Strain
a3	3266.6	4.39	0.174	0.196	0.114	0.128
r2	3256.7	4.52	0.172	0.201	0.114	0.130
ha3	3491.0	4.21	0.087	0.108	0.056	0.072
hr3	2990.1	4.52	0.093	0.112	0.076	0.088
sa3	3658.0	4.33	0.105	0.114	0.687	0.081
sr3	4471.7	4.39	0.137	0.155	0.092	0.109
sha3	3900.8	4.27	0.143	0.165	0.108	0.123
shr3	2278.9	4.64	0.147	0.160	0.088	0.106

Table 6.2: Maximum strain data for selected tests.

and 0.081). This summation of data allows factorial analysis to be carried out and the effects of slip and geometry on strain levels determined.

Factorial Analysis of Modelling Parameters

By finding the average effect of changing a condition, the response to each factor can be isolated (e.g. non-slip/slip). When using this technique on statistical data it is normal to use the average, but in this case it is more relevant to look at the maximum r.m.s. strain since this gives a better indication of brain injury risk. Figures 6.14 and 6.15 show the results of factorial analysis for the principle and shear strains.

Inspection of the principle strain effects plots in Figure 6.14 shows that slip is effective in reducing strain by about 0.01 only in angular motion, where changing geometry to a half pot reduces strain by 0.02 in angular motion, and 0.04 in rotation. In both types of motion, there is an active interaction indicating that the effect of slip is different depending on geometry.

The shear strain response levels in Figure 6.15 are lower than for principle strain, but the effects shown are similar. Slip has little or no effect, but the effect of geometry is a small reduction in shear strain in angular motion (0.01) and a slightly greater reduction in rotation (0.02). Again, there is an active interaction between slip and geometry in either motion and this can be better understood by looking at the interaction plots in Figure 6.16.

The interaction plots compare the effect of slip on the maximum r.m.s strain in the two different geometries. Although the levels differ, the overall changes in Figure 6.16 are similar for shear and principle strains: in full pots slip reduces strain, and in half pots it increases strain. In angular motion, this interaction is complete with the crossing lines showing that the interaction is also active for geometry: without slip changing to a half-pot reduces strain, with slip changing to a half-pot increases strain. In rotation, the effect of slip is still dependant on geometry, reducing strain in full pots and increasing it in half-pots, but the interaction itself is slightly different: once a slip condition is in place, the effect of geometry is small.

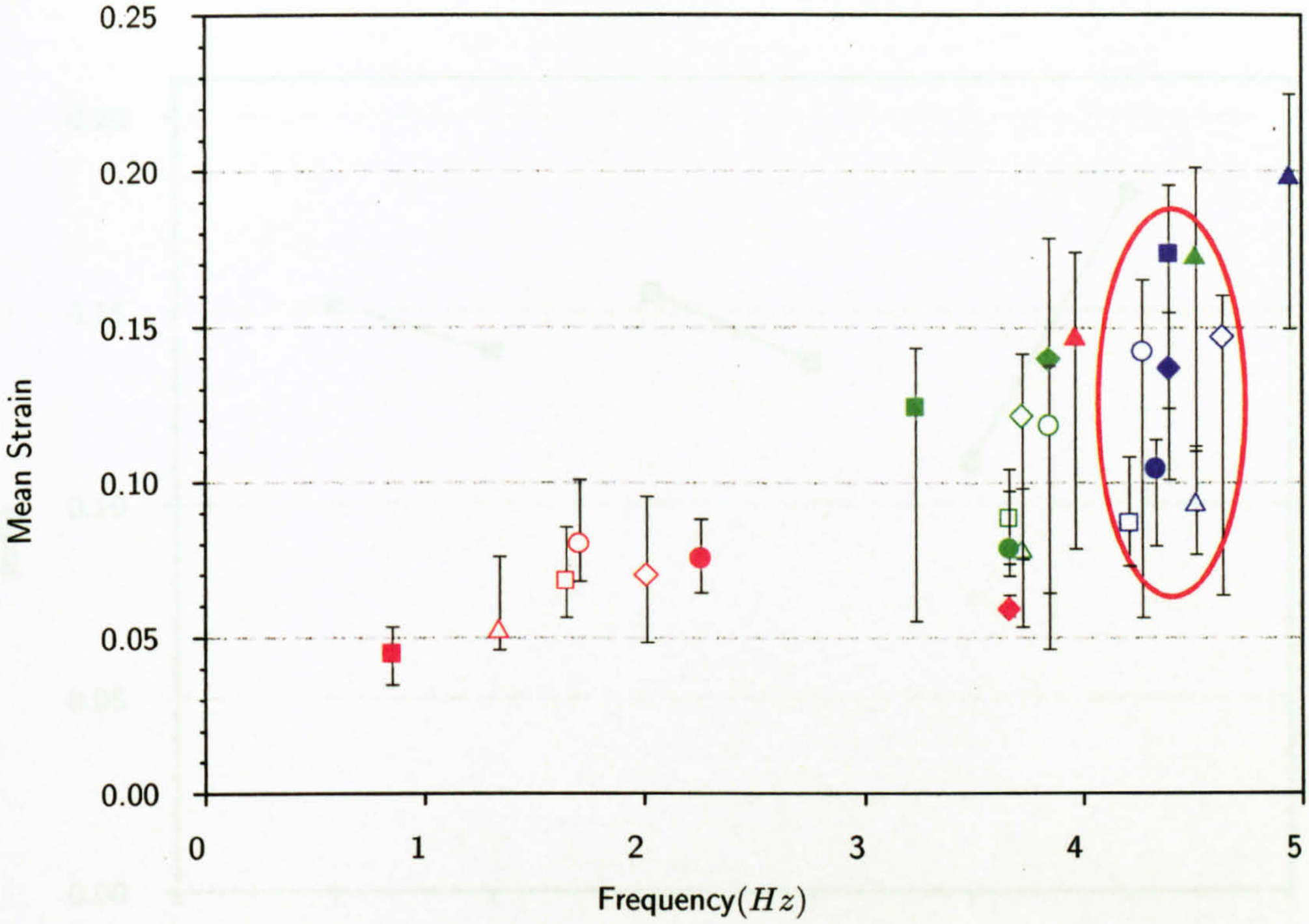

(a) Principle positive strain

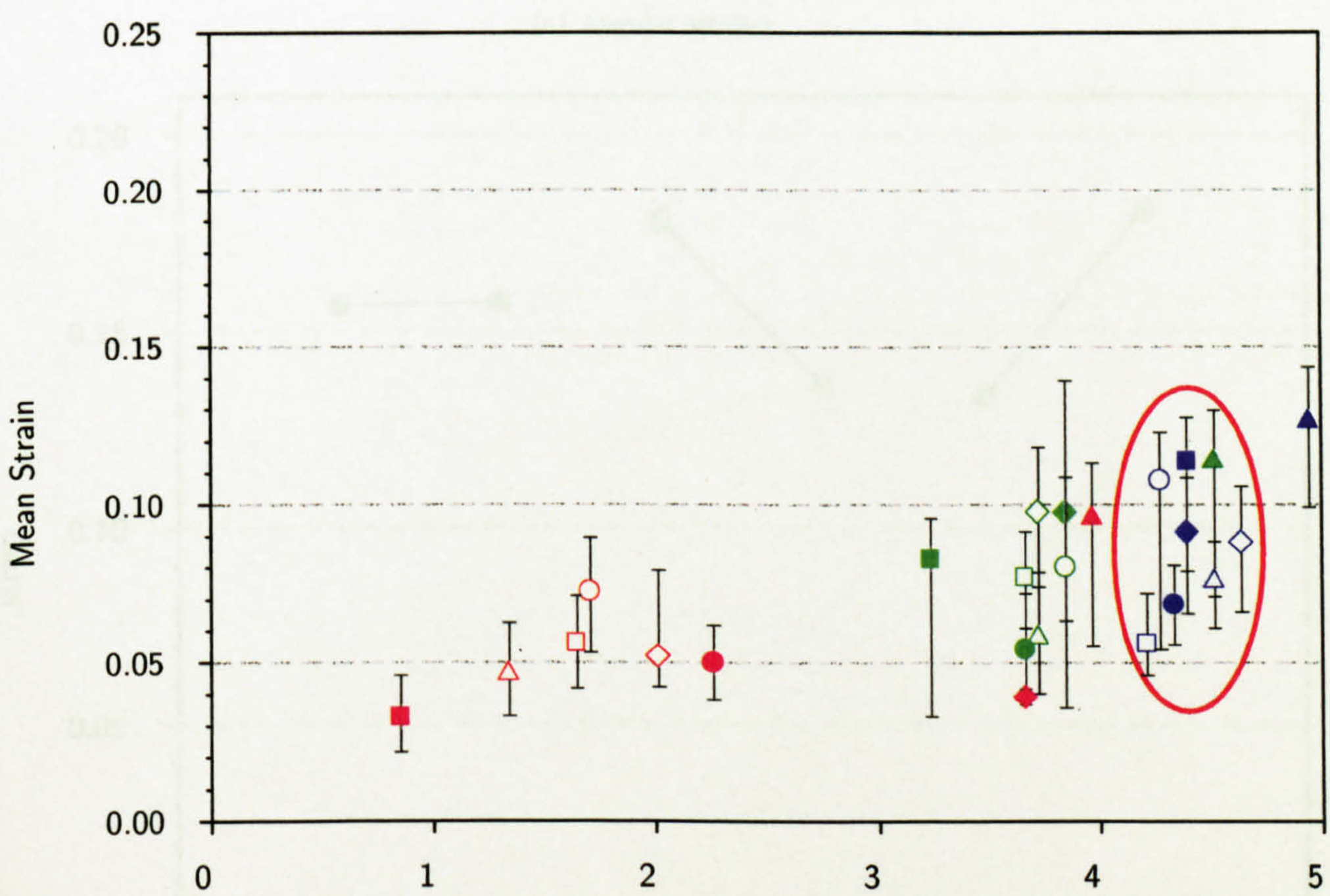

(b) Absolute shear strain

Figure 6.13: Peak average strain vs frequency summary plots. Markers denote mean peak strains and error bars max and min peaks. Red ellipse marks data selected as Representative of SBS. ■ a1, ■ a2, ■ a3, ▲ r1, ▲ r2, ▲ r3, □ ha1, □ ha2, □ ha3, △ hr1, △ hr2, △ hr3, ◆ sa1, ◆ sa2, ◆ sa3, ● sr1, ● sr2, ● sr3, ◇ sha1, ◇ sha2, ◇ sha3, ○ shr1, ○ shr2, ○ shr3.

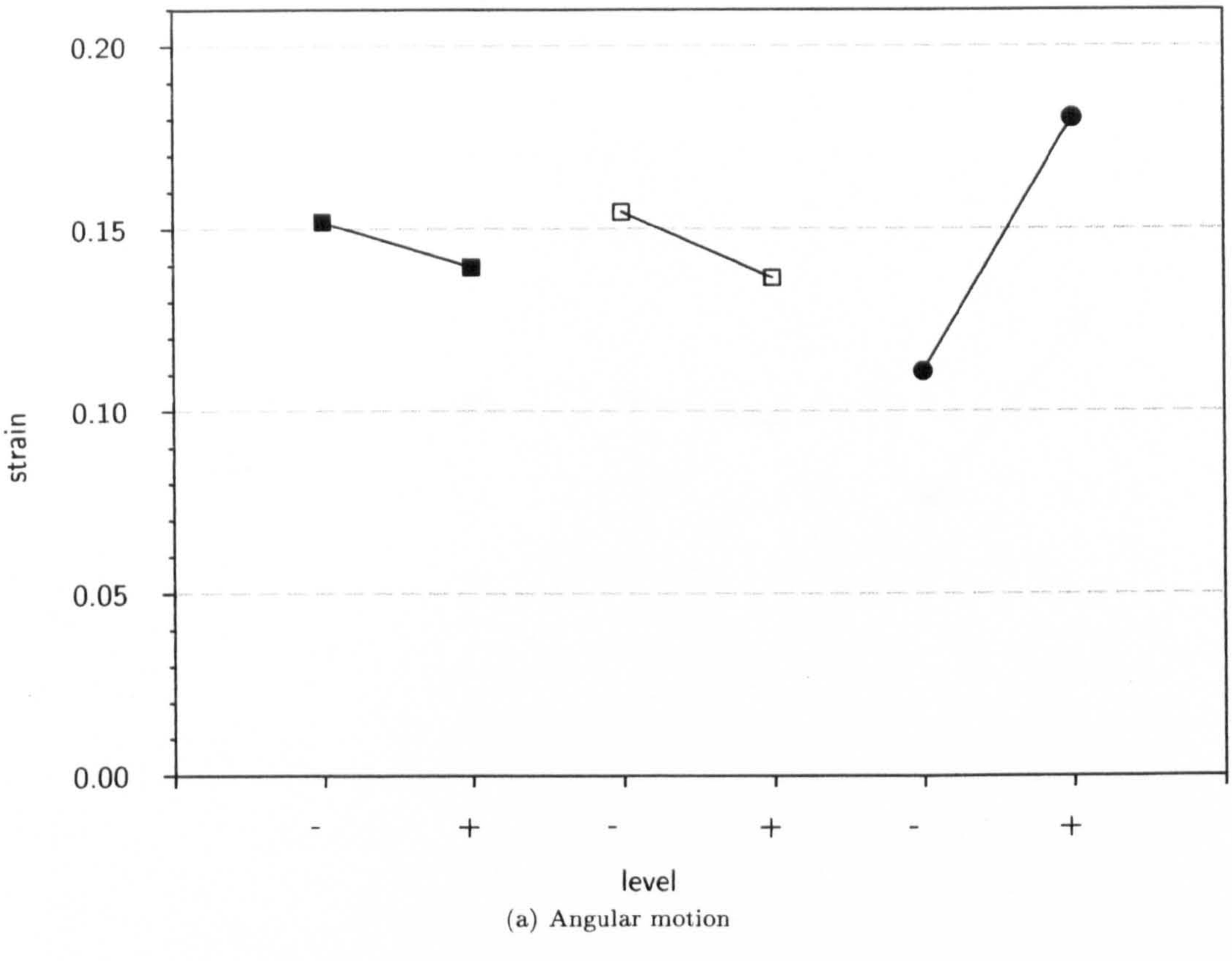

(a) Angular motion

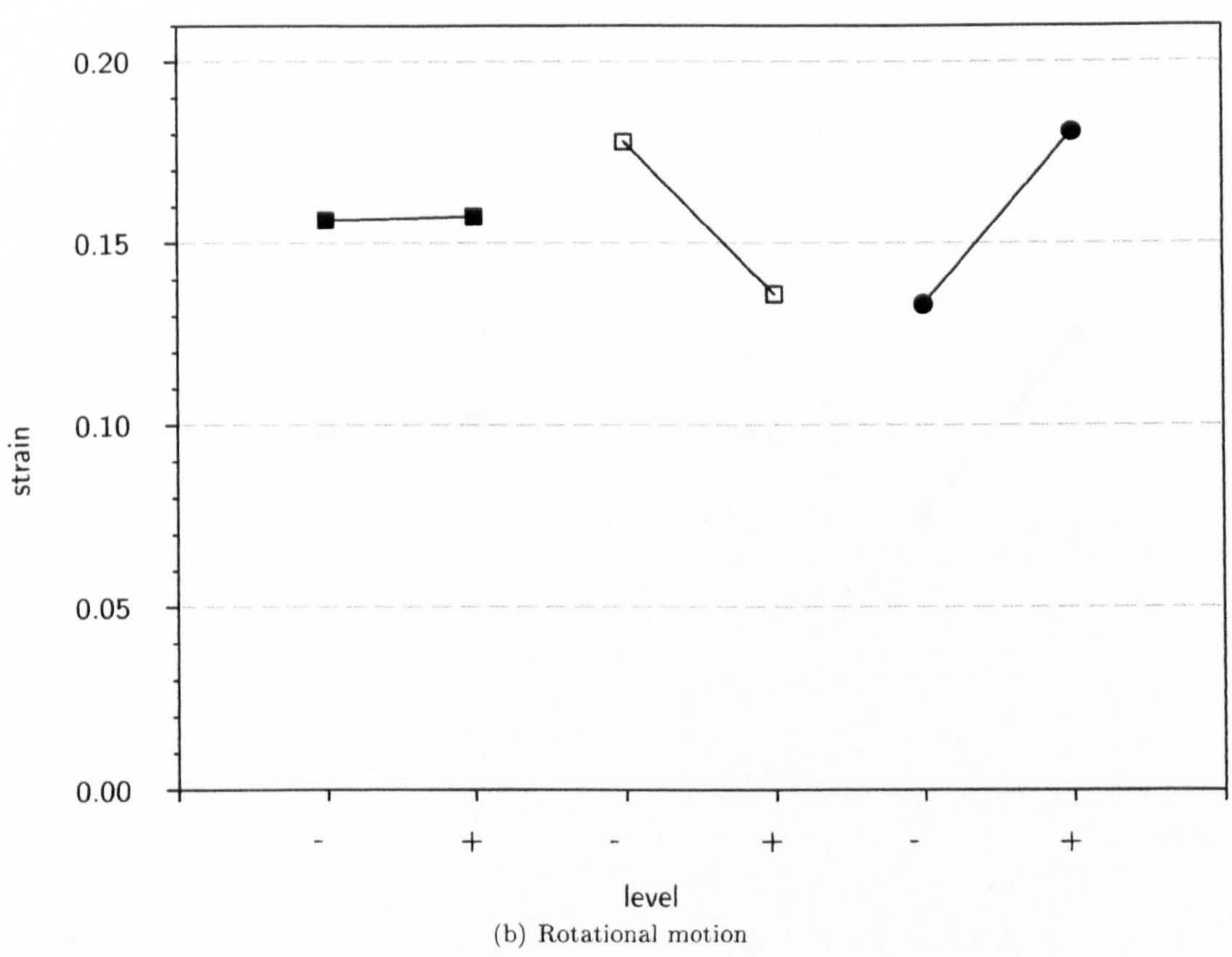

(b) Rotational motion

Figure 6.14: Factorial Analysis of Principle Strain. ■ Slip, □ Half Geometry, ● Interaction.

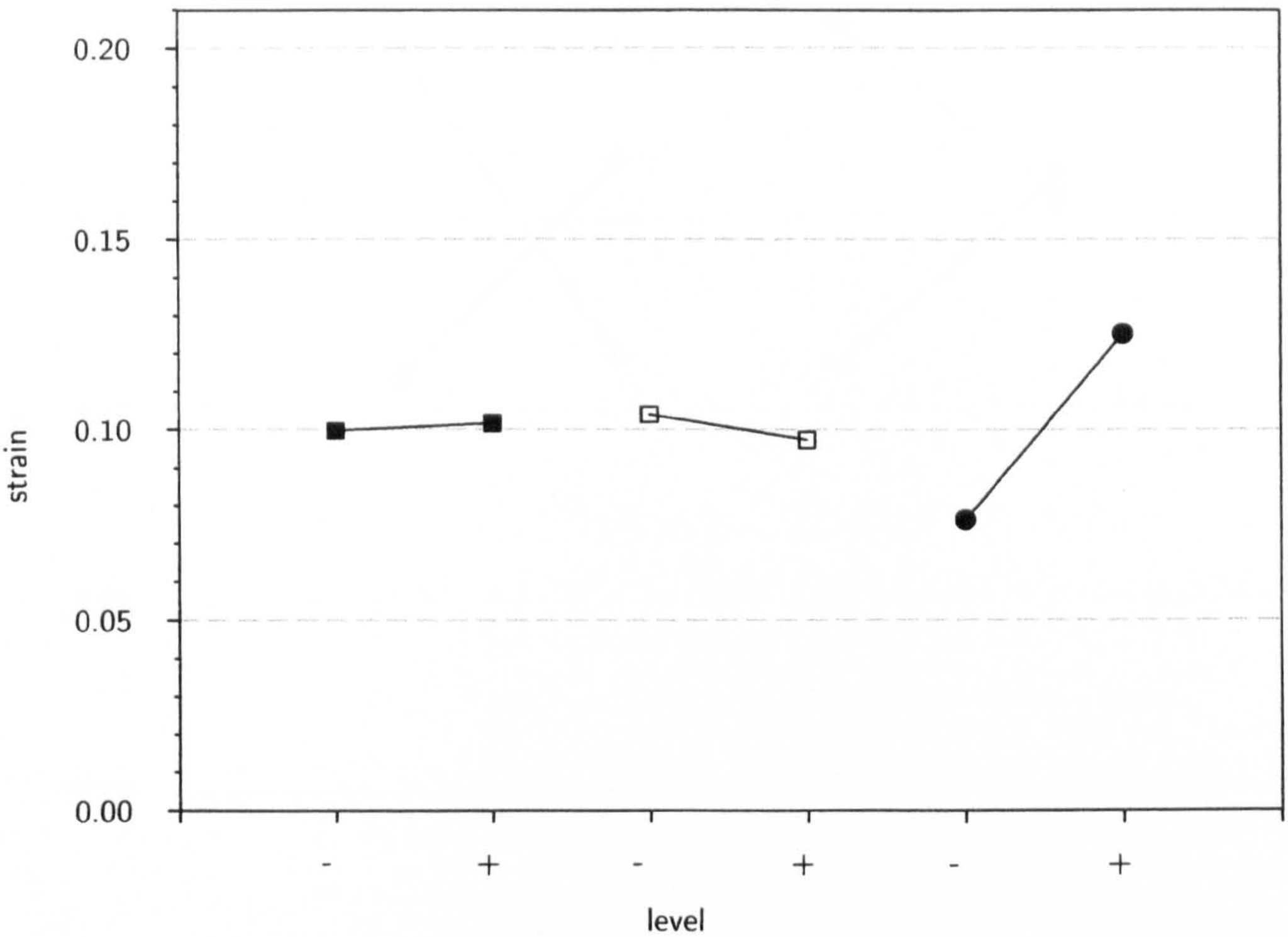

(a) Angular motion

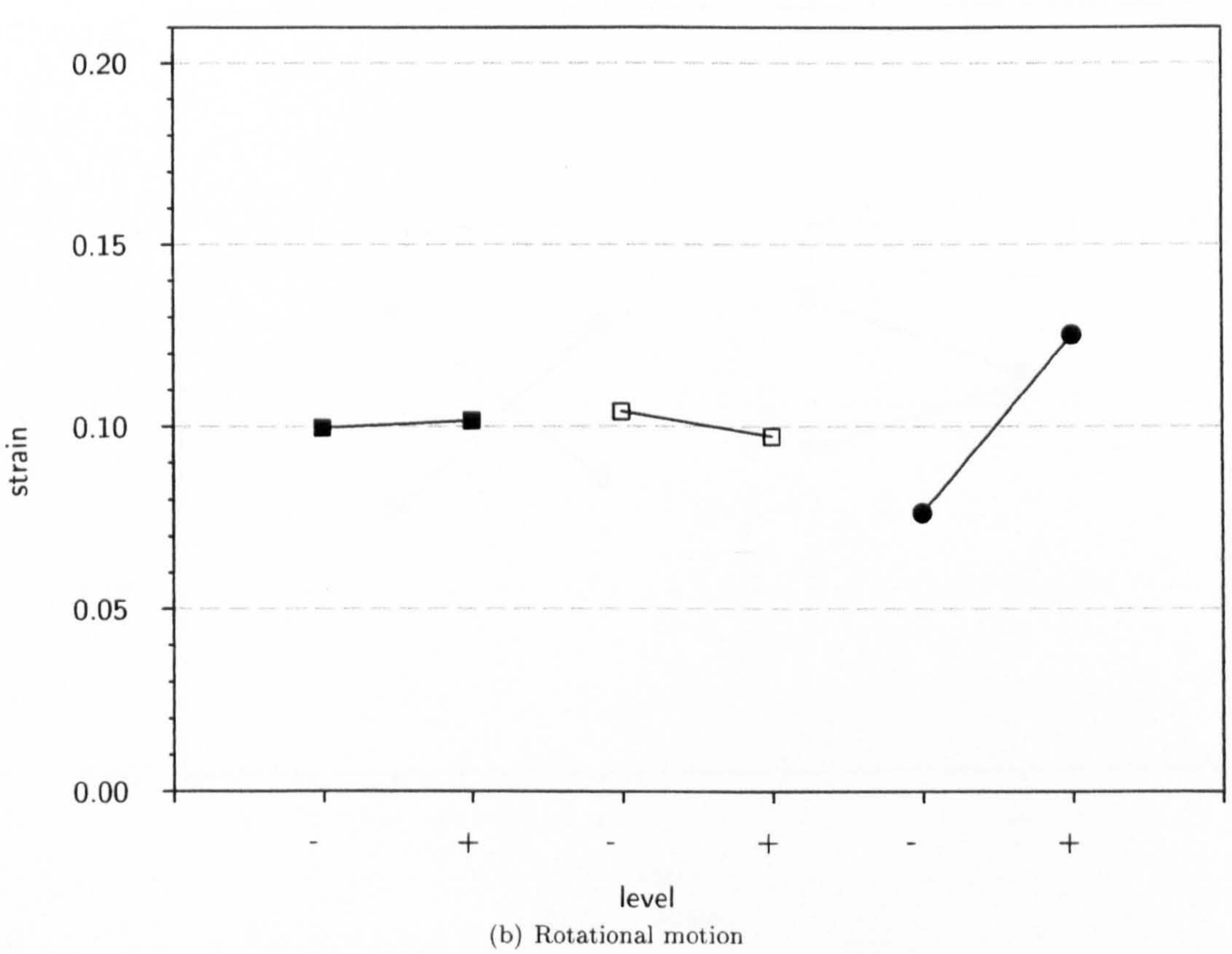

(b) Rotational motion

Figure 6.15: Factorial Analysis of Shear Strain. ■ Slip, □ Half Geometry, ● Interaction.

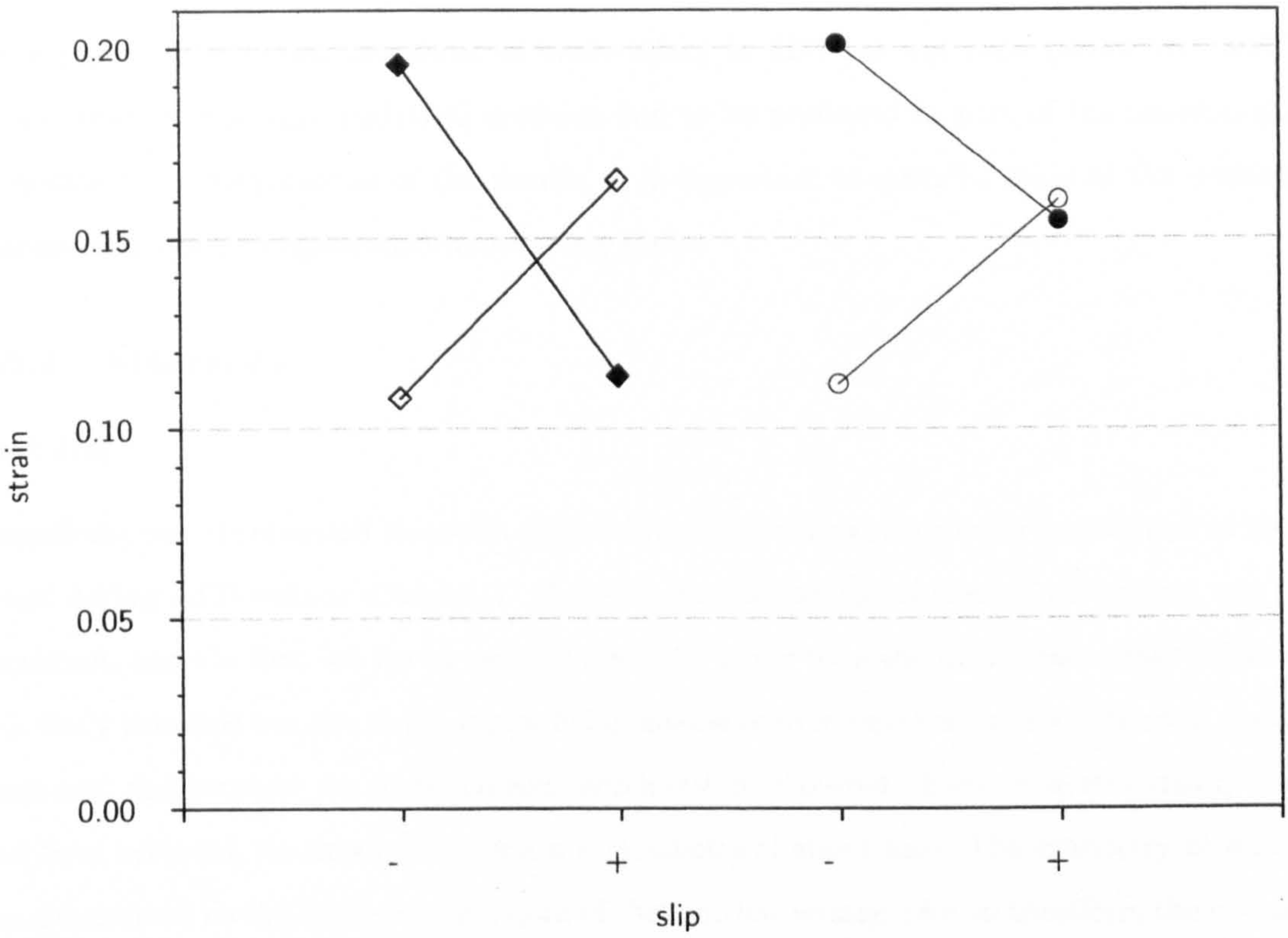

(a) Principle Strain

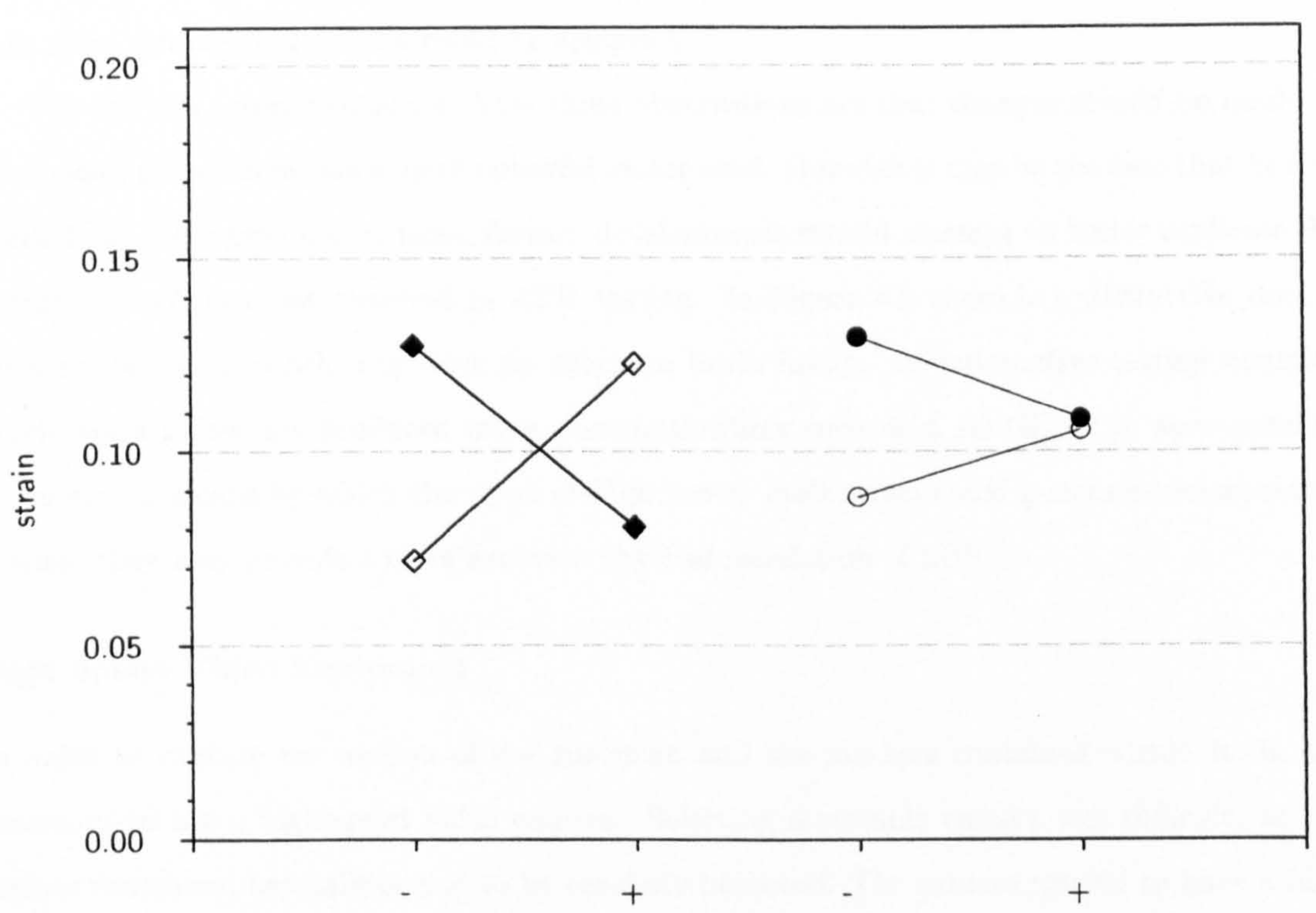

(b) Shear Strain

Figure 6.16: Interaction Plots. ◆Angular motion - full pot, ◇Angular motion - half pot, ●Rotaional motion - full pot, ○Rotational motion - half pot.

6.5 Discussion

Since physical continuum modelling of brain injury in SBS has not been carried out before, all the experimental and analytical methods had to be perfected as part of the investigation. In addition to interpretation of the results, it is important to describe some of the problems encountered and techniques used to overcome them.

6.5.1 Materials

Test Rig

Overall the test rig operated correctly, generating accelerations of a similar frequencies to those found during ATD tests in Chapter 4. However, the magnitude of these accelerations was not consistent, and the first few cycles were consistently lower than the final steady state achieved. It is likely that this was due to the motor being unable to overcome the inertia of the test rig and specimen, and produce the instantaneous accelerations required. Even once this steady state had been achieved, the acceleration was not symmetrical about zero. The symmetry of motion was determined by the relative proportions of the four bar linkage used to transform the rotation of the motor into the oscillatory motion of the test rig. By adjusting these proportions it is likely that more symmetrical motion could be achieved.

The obvious recommendations from these observations are that changes should be made to the linkage proportions and a more powerful motor used. However it may be the case that having carried out these preliminary tests, further developments should attempt to better replicate the pattern of accelerations observed in ATD testing. In Figure 4.2 there is a distinctive double acceleration peak, which may have an effect on brain injury. In automotive testing complex acceleration pulses are produced using pneumatic rams such as a HYGE. If it were possible to develop a means by which this type of high power mechanism could generate reciprocating motion, they may provide a more accurate physical simulation of SBS.

High Speed Video Equipment

In order to capture the motion of the specimen and the markers contained within it, it was necessary to use a high-speed video camera. Selecting a suitable camera was difficult, as the various functional capabilities had to be carefully balanced. The camera needed to have a high enough frame rate to capture motion as small movements, and a high enough shutter speed to eliminate blurring. However high frame rates and shutter speeds reduced the exposure time of the image, so either light levels had to be increased or a wider aperture lens used. Several cameras were trialled during preliminary testing, and a summary of the problems encountered

Camera	Comments
NAC 400 (NAC Image Technology, California, USA)	The mechanical shutter on this camera was unable to produce an adequately sharp image to allow clear identification of optical markers. Also, at 500fps it reduced light levels such that the image was unusable.
NAC 500 digital (NAC Image Technology, Califonia, USA)	Although this camera was able to produce a sharp and bright image at 500fps, the resolution was too low for close-up imaging, and the markers were not clear enough for motion tracking.
Motion Corder SR1000 (Kodak/Photron?)	The lenses available for this camera did not have a sufficiently large aperture to produce a bright enough image at high enough frame rate and shutter speed to capture a good enough image.
Fastcam DVR (Photron (Europe) Limited, Marlow, UK)	The Fastcam DVR was not only capable of capturing at a high frame rate, but also had a suitable lens to use a high enough shutter speed to give a sharp and bright image.

Table 6.3: Findings from trials of high-speed video cameras.

is given in Table 6.3. The camera used in final tests was a FastcamDVR (Photron (Europe) Limited, Marlow, UK), operating at 500fps with a shutter speed of 1/4000s.

Providing sufficient lighting without casting shadows within the pot was also a problem. Fluorescent or strobe lighting could not be used, as high frequency oscillations in light levels were captured by the video camera. Also, lights could not be positioned shining straight down into the pot, as this obscured the camera and caused reflections and glare. Two 1000W and a single 500W floodlight were sourced and used to light the specimen from three angles.

6.5.2 Methods

Optical Markers

Overall the preparation and test procedures were appropriate and successful, but there were some difficulties in producing the quality of images required for motion tracking. High contrast optical markers placed on a plane within the specimen were used to show the distortion of the gel. Initially black markers were produced by stenciling dots on the gel and the containers painted white to provide a contrasting background. It was found that in order for these dots to adhere to the surface of the gel, a silicone based paint was necessary which had to be thinned with white spirit. Thinning of the paint not only reduced the contrasts but often caused the paint to bleed beneath the stencil ruining the specimen. In addition to this, the black markers cast a shadow onto the white background, meaning that the shadow could be aliased for a marker. Changing to white markers against a black background solved the problem of shadows, but this method of producing markers was deemed unsuitable, as their quality was inconsistent, and paint bleeding required the whole specimen to be re-moulded. The hand-placed retro-reflective markers used in the final tests solved these problems.

Slip Boundary

Having developed a method for placing markers in the gel, there were further difficulties creating slip conditions between the pot and gel. Although the decalcomania paper allowed the cast gel to be freed from the pots, it proved impossible to prevent bubbles forming in the liquid paraffin. Automatically differentiating these from markers in the tracking program was not possible causing difficulties in the analysis of the video data. In addition to this, the bright lighting needed to illuminate the markers reflected off any grease on the lid of the specimen, also causing tracking errors.

6.5.3 Analysis

The analysis methods used to track markers and calculate strain were a core part of this research; beyond basic descriptions in the literature no details from previous work were available. Some of the more critical problems encountered were due to noise in original images, and producing a tracking regime capable of predicting cyclic motion.

Motion Tracking

This proved to be one of the greatest challenges in this study, and was fraught with problems throughout. Simple preliminary programming conducted in MATLAB was able to prove the principle that the images produced could be used to track markers between frames. However they initially relied on the motion of the markers between frames being smaller than the distance between markers. Although this was true for low speed rotational test, it was not the case at higher speeds or in angular motion.

Although tracking was improved by predicting position based on previous velocity, problems in specimen production caused further difficulties. If a bubble in the paraffin oil, or bright surface reflection passed near a marker the tracking program could incorrectly start to track its motion instead of that of the marker. A similar problem would occur if the motion was greatly different to that predicted, resulting in dot aliasing. Although this might be sustained for a few frames, it would eventually lead to a breakdown in the tracking procedure and an error in the program. Example images of tracking errors and the images that caused them are shown in Figure 6.17.

One solution to these tracking errors was to restrict the area within which marker detection was carried out which is a feature of motion tracking with a Kalman filter. Trials of the Simple Kalman filter method described in Chapter 2 were conducted using MATLAB. These functioned adequately, but since each marker had to be separately tracked in each frame processing times were too high to make its use practical. It was therefore implemented in visualC++ requiring MATLAB functions to be re-written prior to further development. Despite the improvements

(a) reflection

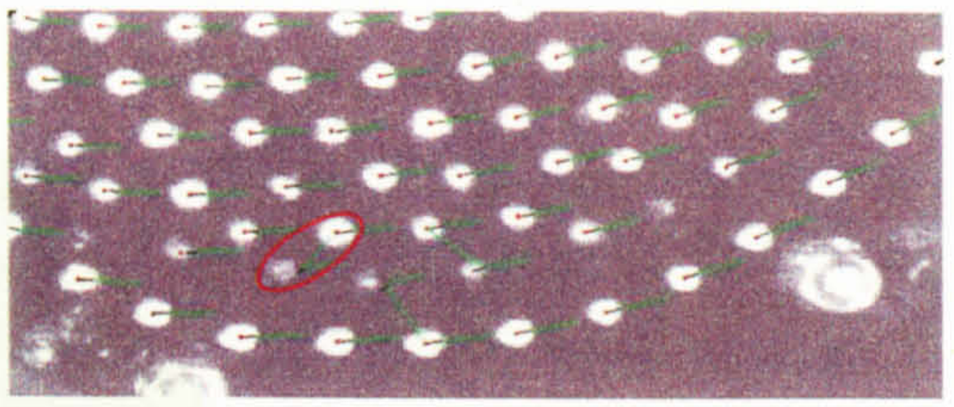

(b) dot aliasing

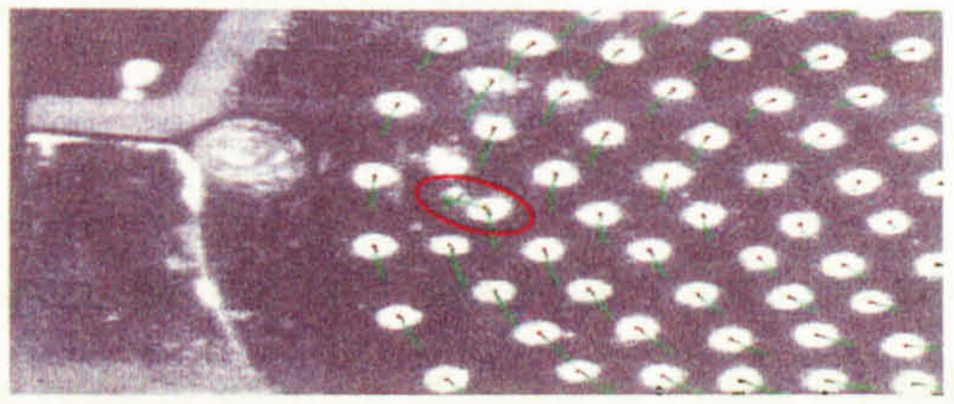

(c) bubble aliasing

Figure 6.17: Common imaging problems leading to track errors

from using this method there were still problems, the greatest of which was the rapid change in direction at the extremities of motion of the specimen.

The Simple Kalman filter is only able to predict relatively steady motion, so rapid changes in direction would again cause errors in the track. The Advanced Kalman filter is able to process more complex systems such as non-steady motion, but its implementation is more complex and requires good mathematical approximations of the system characteristics. Had the main aim of this project been to produce a stable and accurate motion tracking program for the experimental setup, it would have been appropriate to implement an Advanced Kalman filter. However, for the limited set of data it was deemed more suitable to work around this problem using the existing procedure.

Changes in direction were therefore predicted by slowing in the average velocity of the markers, and motion then tracked by assuming small motion between frames. In many cases this method was good enough to track motion throughout a data-set, but tracking errors or bubble aliasing would still cause occasional errors. The track was then restarted and if necessary, the original images manually edited to remove bubble reflections.

Despite providing accurate information on the position of all the markers in each frame, restarting the track caused further problems in data processing. The procedure used to detect markers in the image would scan through the image pixel by pixel, line by line from the origin (in image processing this is the upper left hand corner). This meant that on restarting the track, the order of the dots would be changed, effectively shuffling their positions in the full track data. A series of simple MATLAB functions were written to detect, and reorder this shuffle, producing consistent dot tracking throughout a video clip.

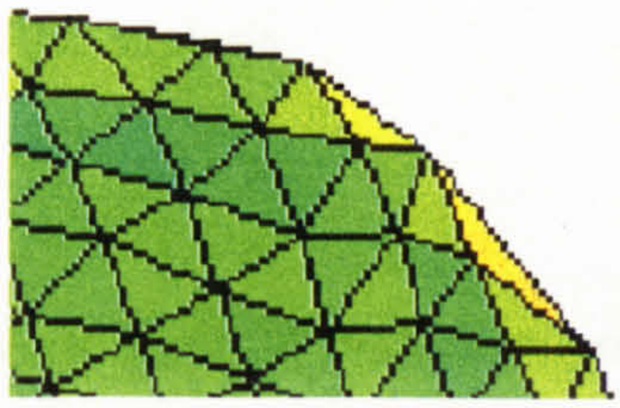

Figure 6.18: Irregular edge meshing leading to strain peaks.

Strain Calculations

The method used to calculate strain within the specimens was very successful. Since the deformations in each frame were determined from the relative position of markers within a triad and referenced to the first frame, the initial placement of the markers could be arbitrary. It was also not necessary to account for changes in the overall displacement and orientation of the specimen. The strain maps provided good visualisation of strain distribution and by averaging for each frame, strain-time data could be used to summarise the data. This method also generated principle strain data, independent of the arbitrary Cartesian co-ordinate system, which has more meaning in anatomical terms than X and Y strains.

Although the strain calculation method was good, deriving data on the maximum strain achieved in each frame would have provided better insight into injury risk. Simply extracting the maximum strain value for each frame produced data that was too noisy to be of analytical value, but it is possible that more sophisticated methods could produce useful data. In order to do so it would be necessary to identify sources of the noise. It is likely that the manner in which the triads were produced is one such source of noise. The MATLAB Delaunay function generated a mesh of the smallest triads possible from a network of points in the initial frame. In the centre of the gel this resulted in regular triads, but around the edge the shape and size of the triads was less consistent. This resulted in unrealistic strain being calculated in edge triads as illustrated in Figure 6.18. It is therefore unlikely that applying signal processing techniques to the maximum strain data currently available would produce useful data. Instead, smoothing the strain data between triads to produce a pixel dense estimate of strain distribution, and extracting maximum strain from this is more likely to produce useful data.

6.5.4 Results

Despite problems during the analysis of the high-speed video a full set of results was successfully generated for these tests including true acceleration information derived from track data. It was not possible to extract maximum strain data for each frame, so r.m.s. strain was used instead and compared to critical strains for neural damage. Examination of strain maps in Appendix M

is helpful in interpretation of factorial analysis.

Acceleration

Since the oscillation rig did not allow accurate control of motion, it was important to extract acceleration data from tracking of fixed points on the specimens. This allowed tests to be compared by their actual movement rather than arbitrary settings of the the motor controller. It was also possible to derive the frequency of oscillation using FFTs. Using this data it can be seen that there is correlation between frequency of oscillation and acceleration in Figure 6.7 with higher frequencies leading to greater acceleration.

By selecting a set of data with similar frequencies, the effects of slip and geometry could be studied in isolation from their nominal test speed. The data selected were a group with a frequency of about 4.5Hz, closest to the maximum shaking frequency of 5.5Hz (mean 3.5Hz) found for ATD tests in Chapter 4. Although within the range found in ATD test, this is a lower frequency than the maximum achieved as it was not possible to run the tests at higher nominal motor speeds. It is sensible to suggest that had these higher frequencies been achieved greater accelerations would have resulted.

Cyclic Loading

Table 6.4 summarises the results of some previous physical continuum models of brain injury. Although the peak accelerations achieved here are lower than in these other studies, comparable principle and shear strains were achieved. As well as providing some broad validation for the results found here, this suggests that high acceleration is not required to achieve high-strain, particularly since these data are surface averages, rather than maximum strains. Although maximum strain data would give better insight into injury risks the r.m.s. strain of each frame gave a good indication of the changes in strain over time.

A common feature observed in the strain-time data were fluctuations in strain levels over the first two or three cycles. This type of fluctuation was also seen in acceleration traces so strain data was normalised for acceleration to see if they were due to experimental variations or changes in strain response over several cycles. No trends were seen in this data, indicating that there was not a change in response and that these changes were due to the variations in acceleration. The main hypothesis that cyclic loading is distinct from a series of separate loads has therefore failed, and there is no reason to suggest that future studies need simulate shaking as opposed to a single cycle.

By summarising the r.m.s. strain-time plots general trends and the effect of the various experimental factors could be studied. Higher oscillation frequency gave higher strain and from

Author	Study	Acceleration	Strain
	This study	max: $4500 rad/s^2$	shear: 0.13
			principle: 0.20
Margulies [51] pp61	HYGE acceleration of non-slip gel cylinders	max: $9.01x10^4 rad/s^2$	Lagrangian 0.304
		min: $2.00x10^4 rad/s^2$	Lagrangian 0.070
Ivarsson [12]	Pendulum impacts with slip, anatomical geometry and strain relief from lateral ventricle and tentorium	$8000 rad/s^2$	shear: 0.2 principle: 0.4

Table 6.4: Acceleration - strain data from previous studies

the proportional relationship observed between frequency and acceleration this also implies that higher acceleration will cause higher strain. Had higher accelerations been achieved, it is reasonable to suggest that higher strain would have resulted.

Modelling Parameters

Factorial analysis of the maximum r.m.s. strain achieved in selected tests showed the overall effects of changing the boundary conditions and geometry. For both shear and principle strain it was found that the interactive effect between slip and geometry was most significant in both rotation and angular motion. With full pot geometry slip reduced strain, but with half pot geometry it increased strain. This interaction can be understand better by looking at the corresponding strain maps.

The figures in Appendix M show strain maps for those frames with the greatest r.m.s. strain for each data set. In non-slip tests with circular geometry there is a ring of high strain around the edge of the gel where it is firmly adhered to the container and no strain in the centre. Since the boundary conditions between the pot and gel are fixed, the forces caused by the rapid change of direction of the pot are applied to the edge of the gel, but the inertia of the gel acts to maintain its previous motion. At the edge, the external forces are high enough to deform the gel but in the centre its elasticity maintains the original shape.

When the boundary condition is changed to allow slip between the gel and pot, the external forces are transmitted only by the viscosity of the paraffin. This reduces the deformation at the edge of the gel, with only small areas of localised strain in both the angular and rotational tests. In the angular tests it is possible to relate these areas of high strain to the superior surface of the brain.

In non-slip tests, changing the geometry of the specimen from a full to half cylinder reduces r.m.s. strain in both angular motion and rotation. Changing the geometry in this way reduces both the volume of gel and the distance from the centre of the body of the gel to its edge. This

means that the inertia of the gel is reduced, and the distance from the edge of the pot to the centre is always small. The forces from the boundary are therefore large and it would require a large inertial force to induce strain in the gel. The strain maps of these test show low strain throughout, with only small areas of high strain.

In slip test with altered geometry the effect of the interaction can be seen. Although the volume and inertia of the gel are lower, the boundary conditions are free, so the gel is able to move and deform within the container. This enables localised areas of strain to build up. Although these strains are lower than those in full pot tests, they occur through a greater portion of the total volume of gel. This means that there is a smaller unstrained area and the average strain is higher. This interaction means that it is important that neither boundary conditions or geometry are altered in isolation, as their independent effect is to reduce strain, while their combined effect is to increase strain.

6.5.5 Tissue Damage

Brain injury criteria that relate head motion to clinical injuries are useful when the motion can be accurately measured or modelled, and the mechanisms of injury are well understood; in the case of SBS neither of these are true. Having developed a modelling method that describes the strain induced within the brain during shaking, it is of value to examine the findings in terms of tissue damage rather than injury. In coronal impact simulations Margulies *et al.* correlated strain in silicone gels with induced brain injuries in baboons [62]; critical shear strain of 0.094 was suggested as a threshold for DAI. Bilston *et al.* [63] suggest neural damage occurs at 15-20% tensile strain with strain rates of $< 5s^{-1}$. The maximum average strains achieved in the current study were in one of the least biofidelic models tested; model r2 used cylindrical geometry, had a no-slip boundary and was subjected to pure rotation. Principle strains reached 20% and average shear strains 13% both of which exceed the levels from brain tissue damage.

The most biofidelic model tested was sha3 which used half-cylinder geometry, incorporated a slip boundary and was subjected to angular motion of the type seen in shaking. In this test average principle strains of 16.5%, and average shear strains of 12% were achieved, again in excess of tissue damage levels. It can be reasonably assumed that had it been possible to study maximum strains, these values would have been considerably higher. This study therefore shows that shaking alone is capable of producing both shear and principle strains greater than published levels for brain tissue damage.

6.6 Conclusions

In this study a method for using silicone gel to investigate cyclic loading as a potential brain injury mechanism in SBS was developed. A simple mechanism was used to shake specimens in two loading modes, using two different geometries and boundary conditions. Programmes were written to track the motion of optical markers within the gel, and the data used to calculate Green-Lagrangian strain by tensor algebra. Average strain data were used to analyse the results, and the effects of geometry and boundary conditions assessed with factorial analysis.

No evidence was found to indicate a build up in strain levels between cycles, so the main hypothesis that cyclic loading constitutes a separate injury mechanism to a series of separate loads has not been proved. However, both principle and shear strains, averaged across the plane of interest, exceeded published thresholds for brain tissue damage [63, 62]. Had it been possible to study the maximum strains achieved within this surface, it can be assumed that they would be even greater. It has therefore been demonstrated that shaking alone is capable of inducing strains in excess of tissue damage thresholds of the type of injury associated with SBS.

Several further conclusions can be drawn from the development of this model. Intuitively, higher oscillation frequencies were found to result in higher accelerations and increased average strain. The effect of changing geometry from a full to half cylinder, or introducing slip boundary conditions, was to reduce strain. However, in combination, altered geometry and slip conditions increased strain, so it is important that these factors are not studied in isolation.

6.7 Recommendations and Future Work

Since tests of this kind had not been conducted previously there are several ways in which the materials and methods used here should be improved.

- Deriving maximum strains from the data obtained here, would give better insight into brain injury risks.

- The inclusion of anatomical features such as geometry and membranous layers have been shown to have a significant effect on strain levels in impact tests [12]. The effect of their inclusion in this model should be examined but the interactive effect of slip and geometry found here demonstrates the importance of careful analysis of the combined effect of modelling parameters.

- The efficiency of the analytical procedure would be greatly improved by perfecting the the motion tracking process; it is likely that this could be achieved by implementation of an Advanced Kalman filter.

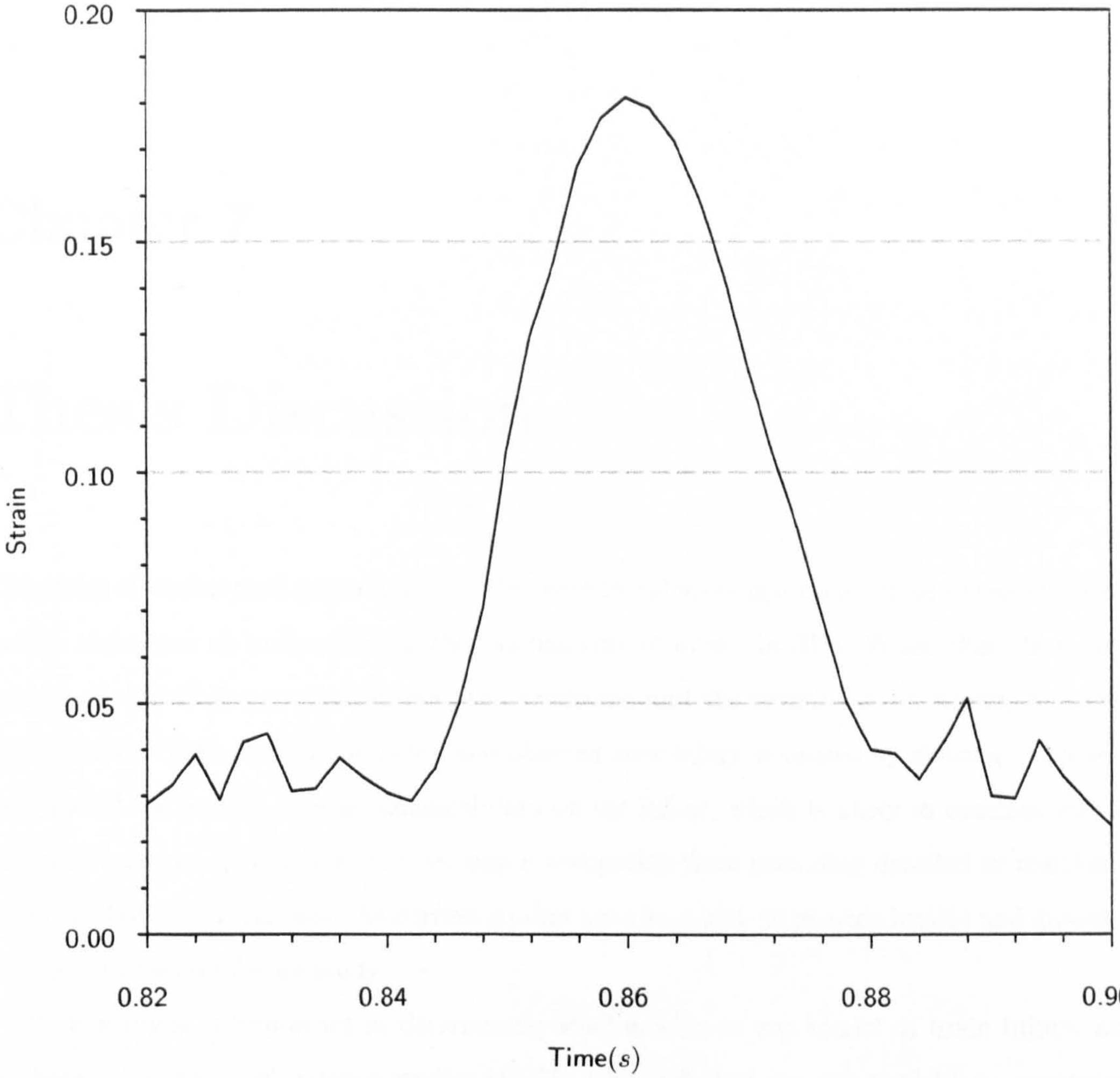

Figure 6.19: Individual principle strain peak from A3

Another important area not accounted for here is strain rate. Since brain tissue is visco-elastic the rate at which loading occurs can be critical in determining the level of damage. An estimated sample can be made from the individual principle strain peak shown in Figure 6.19.

If $\varepsilon_{t=0.845} = 0.03$

and $\varepsilon_{t=0.865} = 0.18$

then$\triangle t = 0.02$

and $\triangle\varepsilon = 0.15$

$\therefore \varepsilon^{\bullet} = \frac{0.15}{0.02} = 7.5s^{-1}$

Since strain rates of $< 5s^{-1}$ have been associated with brain injury, this estimate indicates that strain rates in excess of critical strains were also achieved in these tests [63]. Similar calculations could be applied to the data obtained here, to study this in more detail.

Chapter 7

Thesis Discussion

This series of studies used a combination of biomechanical investigation methods to assess various factors important in understanding the mechanisms of injury in SBS. While there is a large volume of clinical literature describing the syndrome and the severity of its effects, relatively little work has been carried out to try and discover how injury is caused by shaking. This is in part due to the paucity of biomechanical data on the infant, which is likely to continue for the foreseeable future. While this prevents any investigation from providing detailed or conclusive evidence about the syndrome, the current studies have been able to provide insight and guidance into useful areas for future study.

Neck stiffness is important in determining head motion in any model of brain injury, and has been a limitation of previous studies of SBS. Although data are not available to accurately model the infant neck, through a combination of ATD tests and RBM, a large parametric study was used to investigate its significance in assessing the injury capacity of SBS. As in previous work it was found that impact was required to exceed injury criteria for the syndrome, and neck stiffness had no significant effect on this. Although impact between the head-torso was found to be injurous, it did not exceed brain injury thresholds for SBS.

Since modelling of the head and neck did not appear to contribute new insight about injury in SBS, the methods for assessing the findings were re-examined. Through review of the literature, it was found that available brain injury criteria are derived from impacts, or single high-acceleration events. As this is a wholly different mechanism to shaking, the application of these criteria to SBS must be questioned. It was therefore hypothesised that shaking constituted a distinct injury mechanism that warranted separate study.

Derivation of full injury criteria is a large undertaking, and the lack of data and ethical considerations of infant research highly restrictive. Although work of this magnitude was beyond the scope of the present study, physical continuum modelling offered the opportunity to carry

out preliminary studies into shaking as an injury mechanism. By tracking the motion of optical markers placed within geometric silicone gel models of the infant brain, the strain induce during shaking was determined. While no evidence was found to indicate a build up of strain between cycles, relatively low accelerations were found to induced strains greater than critical levels for neural tissue damage. This shows that although shaking may not result in head motion exceeding injury criteria, it is capable of causing damaging tissue deformation.

During development of the model the effects of changing geometry and boundary conditions were also investigated. In isolation, introducing slip boundary conditions, or changing from a full to half-cylinder geometry were found to reduce strain. However in combination, they were found to have an interactive effect leading to increased strain demonstrating the importance of considering interactions when developing models.

7.1 Head Kinematics

In other studies of the biomechanics of SBS, ATDs were fitted with a small range of flexible neck forms and head acceleration data used to asses the injury risk of shaking [1, 2]. These studies were not able to demonstrate that shaking without impact is able to exceed injury criteria for SBS.

The kinematics of the neck are clearly critical in determining head motion, but since biomechanical data on infants are scarce, it is not possible to create a validated biofidelic infant neck form. The three forms used in the past studies described above were: a hinge allowing free motion, a thin-walled rubber hose allowing *"floppy"* motion and a thick-walled rubber hose allowing stiff motion.

This limited range of neck forms is a potentially significant source of error which warranted further investigation, but the construction of a biofidelic neck form would still be hampered by the paucity of biomechanical data on human infants. Since this type of accurate modelling would not be possible, a study to establish the significance of this potential error was designed instead. The requirements of constructing and testing enough physical models to create a reasonable study size was impractical. By using computational modelling, a greater number of neck forms could be tested, and the effect of neck stiffness on the capacity of shaking to exceed injury criteria established.

7.1.1 Acquisition of Torso Acceleration Data

In order to simulate shaking of computational models of infants in Chapter 5, it was necessary to obtain data on the kinematics of shaking. In Chapter 4 a simple, custom-build 6-month-old

ATD was used to obtain data on linear torso-acceleration during shaking. Unlike ATDs used in other biomechanical studies of SBS, this dummy was fitted with a rigid neck form and only torso acceleration was recorded.

Rather than construct a complete dummy, the ATD was adapted from a resuscitation training doll which was freely available for this project. It was ballasted to represent the total and body segment mass of a 6-month-old, and a uni-axial accelerometer placed within the torso. Volunteers then shook the dummy in an anterio-posterior direction for as long and hard as they were able.

The volunteers were able to shake the dummy for up to 22 seconds, and a maximum frequency of 5.5 Hertz. The maximum peak acceleration achieved was just over 11G, and the maximum average acceleration was 3G. These results were found to be comparable with previous studies, and exported to a format suitable for use with the computational models in Chapter 5.

In addition to this, an unexpected double peak was observed in the acceleration traces. Although this was not studied further here, it was speculated that this might due to hyper-extension of the arms caused by the inertia of the dummy. Without further investigation it is not possible to say what effect this might have on the injury capacity of the syndrome.

7.1.2 Computational Study of Neck Stiffness

The first hypothesis tested in Chapter 5 was that:

> *"Neck stiffness characteristics have a significant effect on the capacity of shaking to produce head motion exceeding injury criteria."*

Where previous studies had tested only three neck forms, here fifty neck form models were simulated in a parametric study. The aim of this study was to establish the significance of neck form design on the injury capacity of shaking. This required a suitable infant head and neck model to be developed, whilst overcoming the difficulties of obtaining suitable biomechanical data.

The development of accurate computation models of head injury is a complex task, usually utilising FE methods and requiring large amounts of input data. Anatomical geometry can be derived from clinical imaging like CT or MRI, and simulation input data such as forces or acceleration obtained from physical testing such as ATD tests. However, FE of modelling also requires material models, which more difficult to derive for biological material, particularly so for infants. Where this type of FE method can be viewed as a complex model constructed upon a large quantity of accurate data, RBM allows a simple model to be constructed with little data, and its complexity increased where necessary or when data become available. It was therefore more appropriate to use a rigid-body model for this task, thus reducing the complexity of the

model and allowing direct control of study parameters.

A standard ATD model was adapted for this task, and acceleration data from ATD tests in Chapter 4 used to simulate shaking; details of how this was carried out are given in Chapter 5. The results showed that while the majority of the neck forms tested did not lead to motion that exceeded injury criteria, several outliers from this group did tend towards, and even exceed, injury criteria. This appeared to confirm the hypothesis that neck stiffness was an important consideration in modelling SBS. In order to understand by what change in mechanism this injurious motion occurred, the specific neck forms were identified and all found to have end-stop stiffness characteristics. These stiffness characteristics were the extreme range of the parametric study, and did not lead to smooth biofidelic motion but to a repeated series of free motion and impacts. Therefore, instead of confirming the hypothesis, they appeared to confirm the assertion that impact is necessary to exceed brain injury criteria.

From these findings it was concluded that neck stiffness is not a significant factor affecting the capacity for shaking to exceed brain injury criteria in modelling SBS. The use of a small number of neck forms in the ATD modelling of Duhaime *et al.* and Cory *et al.* has not therefore been shown to be a source of error in these previous works[1, 2]. Considering the comprehensive examination of other modelling factors such as weight distribution by Cory *et al.* it appears unlikely that further head motion studies of SBS will offer insight into brain injuries without impact in SBS.

7.1.3 Computational Study of Head-Torso Impact

Cory *et al.* observed impact between the head and body during ATD studies of SBS, so an additional hypothesis was tested in Chapter 5 [2]:

> *"Head-torso impact leads to head motion exceeding injury criteria"*

Having constructed a working model of the infant head and neck, and successfully simulated shaking, few alterations were necessary to investigate the effect of impacts between the head and torso. The torso surfaces were re-included in the model, and the range of motion of the neck increased. The stiffness constraints of each of the neck joints were removed in turn, allowing free motion, first at the head-neck joint, then at the neck-torso joint. Finally, low stiffness constraints were placed on each joint, allowing near free movement at each. In each case, this resulted impact between the head and torso, but through slightly different paths of motion. Again, details are discussed in Chapter 5.

The size of the free radius of rotation of the head movement appeared to have an effect on the resulting head motion. Freeing the neck-torso joint created a larger radius of rotation

than freeing the head-neck joint, and resulted in head motion exceeding more injury criteria. In combination, freeing both neck joints reduced the effective radius of free rotation and gave the lowest peak angular velocity and acceleration. More importantly, although lower injury criteria for concussion were achieved, none of the criteria for SDH or DAI associated with SBS were exceeded. This study therefore showed that although head-torso impact might constitute an additional mechanism for more minor injuries during shaking, it did not lead to motion exceeding injury criteria for the more severe injuries associated with SBS

7.2 Brain Injury Criteria

The findings of Chapter 5 were that neck stiffness and head-torso impact were not significant in altering the capacity for shaking alone to exceed brain injury criteria. In fact, this work appeared to support the finding from Duhaime *et al.*'s first biomechanical study of SBS that impact is required to exceed these injury criteria. Between the work in Chapter 5 and published studies, the various factors affecting head motion in SBS have been comprehensively researched. The results have been broadly similar, and no evidence for shaking alone leading to head motion exceeding injury criteria has been found. Since head motion studies have been unable to provide an explanation for cases of SBS without impact, it was apparent that further research should focus elsewhere. Since all these studies have assessed their findings against available injury criteria, it appeared that a better understanding of the criteria and their meaning was required.

In Chapter 3, a review of the literature describing the derivation of brain injury criteria revealed that they are based on single high-energy insults, that might result from an indirect impact such as an automotive collision. Their application in SBS without impact, where cyclic low-energy loading is the only apparent injury mechanism, is therefore questionable. Indeed, a study by Raghupathi *et al.* where neonatal pigs were subjected to double, non-impact insults demonstrated that the second insult was more injurious than the first [49]. There is therefore great scope for advancement in the understanding of brain injury in SBS through the study of cyclic low-energy loading as a distinct injury mechanism.

7.2.1 Physical Continuum Modelling of Oscillatory Brain Injury

In Chapter 6 physical continuum models were used to study shaking as a brain injury mechanism. Currently available brain injury criteria have been derived from extensive long-term research in centres of brain injury specialism. Many are based on primate studies, and rely on scaling factors to estimate thresholds for man. The paucity of biomechanical data available for infants and the ethical constraints of expanding this data mean that compound scaling estimates are required

to derive infant injury thresholds. Deriving and validating an injury threshold for shaking was therefore beyond the scope of this investigation, but established modelling techniques offered an opportunity to conduct initial investigations, providing some insight into how shaking might constitute an injury mechanism.

By using physical continuum modelling, infant brain injury was studied without ethical restrictions. It offered the opportunity to investigate the type of cyclic low-energy loading seen in SBS as a brain injury mechanism. This had not been carried out previously, and no brain injury studies had been conducted at this research centre. The work was therefore based on published physical continuum studies of brain injury, and all materials and methods were developed during the investigation.

Optical markers were placed within silicone models of the brain, and their movement during shaking captured with high-speed video. The motion of the markers was tracked, and from their relative positions the strain within the gel was calculated. It has been shown that boundary conditions and geometry of physical models can have a significant effect on induced strain, so the model was developed to include these factors; complete and half cylinders were tested, with and without a slip interface between the gel and container. The design of the test rig also allowed two loading modes to be tested; rotational and angular motion. Since it was not possible to control the true speed of oscillation, three nominal speeds were used, and the acceleration of the specimen derived from its motion.

Cyclic Loading

Having constructed the model and developed the necessary methods and software to analyse the video output, the primary aim of the study was to test if cyclic loading constituted a distinct injury mechanism from a series of individual loads. The initial output from the analysis were strain distribution plots for each frame, of the kind seen in Appendix I, but in order to study strain over a period of many cycles, a single strain value was required for each time-step, or video frame. Since injury risk would be indicated by any area within the brain being strained above material thresholds, the best indicator for this would have been the maximum strain achieved in the surface at any time. Attempts to extract this maximum strain data did produce any meaningful results, but by averaging the strain for the entire surface useful strain-time plots were produced.

On initial observation, increases in strain during the first few cycles appeared to demonstrate a build-up of strain in the gel, independent of applied acceleration. If this could be verified, it would confirm that maximum strain levels were not achieved in a single cycle, but that many cycles need to be considered in developing injury criteria. Since the test rig could only

be controlled by a nominal speed, it was important to examine true acceleration in light of these findings. This was derived from the motion of fix points on the specimen and showed a corresponding build-up in acceleration. It is likely that this was because the motor was unable to instantaneously overcome the inertia of the test rig and meant that strain data needed to be normalised for fluctuating acceleration.

These normalised strain plots showed no build-up between cycles, indicating that the changes in strain in the first few cycles were directly attributable to fluctuations in acceleration. It was therefore not proven that oscillatory loading caused a build-up of strain between cycles, and does not constitute a distinct brain injury mechanism from single acceleration events.

Tissue Damage

Although the accelerations achieved during these tests were much lower than in previous continuum models of brain injury, comparable levels of strain were achieved. These results were therefore assessed in relation to published critical strains for tissue damage.

Where brain injury criteria relate head motion to induced injuries, critical strains define the deformation at which tissue is damaged. While these measures are less useful in ATD or whole body modelling, here they allowed the injury capacity of the strain induced by shaking to be assessed. Two published measures were used, critical shear strains of 0.094 for DAI and 15-20% tensile strain at strain rates of $< 5s^{-1}$ for "*neural damage*" [62, 63]. Both of these critical strain values were exceeded in these tests, with average principle strains of 16.5% and average shear strains of 12% using the most biofidelic of the models. Had it been possible to obtain maximum strain data, greater values could be demonstrated.

From these findings it can be concluded that shaking alone is capable of inducing strains that would damage brain tissue. This contradicts previous biomechanical studies of SBS that conclude that impact is required to cause the injuries associated with the syndrome. It can also be stated that the application of brain injury criteria derived from high-energy events to this syndrome is inappropriate. If the mechanisms of brain injury in this syndrome are to be understood, further research into the capacity for low-acceleration injuries needs to be conducted.

Modelling Parameters

During its development, the geometry and boundary conditions of the model were changed; full and half cylinders were tested, with and without slip condition at the gel-pot interface. The effects of these changes on strain were determined using factorial analysis, which also allowed the interactive effect of changing both boundary conditions and geometry together to be analysed.

It was found that changing from non-slip to slip boundary conditions caused a small reduction

in strain. Slip boundary conditions reduce the forces applied to the edges of the gel, and so the deformation within it. Changing geometry from a full to half-cylinder also reduced strain. The inertial mass of the gel is reduced, and the strong boundary conditions reduce the rotational torque. The combined effect of a slip boundary with a half-cylinder was to increase strain. In this case, although the mass of the gel is still small, the slip boundary means that it is free to move and deform within the pot, effectively increasing the torque.

Changing the geometry and boundary conditions of physical continuum models have both been shown to have an effect on strain in high acceleration studies [53]. By testing these parameters here, their effect has been confirmed in low-acceleration testing, and the nature of their interaction better understood. It is apparent that the effect of changing these parameters in isolation has the opposite effect to changing them in combination. It is therefore important that any future studies of this type include both a slip boundary and anatomical geometry, not one or the other.

7.3 Future Work

The work carried out here constitutes a series of investigations into various aspects of the biomechanics of SBS. Since many of the methods or applications were novel there are many improvements that could be made to them. However, while some avenues of investigation appear to offer opportunities to make a valuable contribution to the field, others appear to have been exhausted at this time.

7.3.1 Rigid Body Modelling of Head Kinematics

The studies in Chapter 5 extended the work of Duhaime and Cory to investigate the significance of neck kinematics and head-torso impact on head motion. Although it would certainly be possible to increase the level of detail of the models used, or extend the range of the parametric studies, it is unlikely that this would be of much value at this time. It is apparent from the work in Chapter 6 that the application of current head injury criteria to shaking is inappropriate. Until such time as more appropriate data are available, there is no way to assess data on head kinematics obtained from this type of work.

7.3.2 Physical Modelling

The physical modelling carried out in Chapter 6 was not able to establish that shaking constitutes a separate brain injury mechanism to a series of impacts. However, it was shown that low-accelerations could cause critical strains, and that interactions between modelling parameters can

have an important effect on model behaviour. Further research into this brain injury mechanism could begin to provide an understanding of how brain injuries are caused without impact in SBS. Various areas of research might be pursued, each offering different prospects for progress.

There is already some scope to further this work using the data already obtained in these studies. By developing the methods and software used in the analysis of high speed video, information on the maximum strains achieved during shaking may be obtained. This would prove better insight into the risk of injury than the surface average strains that it was necessary to use here. Further to this, it has already been seen in Section 6.7 that valuable data can be obtained by performing strain rate calculations. It is also important that some consideration is given to the limitation of this work.

It was shown from the motion of fixed points on the specimens that the accelerations achieved were not symmetrical, and increased as the electric motor overcame the inertia of the loaded test rig. If further simulation of shaking were to carried out, improvements should be made to the design of the test rig and specification of the driving motor. However, since no change in strain response was seen between cycles, oscillatory motion may not be necessary in physical modelling. The effects of repeated loading may not be seen in induced strain, but from biological studies such as that of Raghupathi *et al.* [49].

Having demonstrated that parameters such as boundary conditions and geometry have an effect in physical modelling of SBS, the inclusion of other anatomical features should be considered. The idealised cylindrical geometries used here could be developed to better represent the anatomy of the infant brain. This would require study of the development of intracranial membranes such as the falx and tentorium, and possibly the rigidity of the infant skull. These improvements are likely to be limited by the data available on infant tissue, and as shown in these studies their interactions as well as their independent effects should be considered.

7.4 Thesis Conclusions

At this time there is no clear explanation for how brain injuries are caused in cases of SBS without impact. This work has shown that little is to be gained through further study of the kinematics of the head and neck, and that better understanding of low-acceleration brain injury is required. Initial work to this end has demonstrated that shaking can cause deformation in physical models that would damage neural tissue. This work should be extended to examine maximum rather than average strains, and to improve the motion and physical model.

Bibliography

[1] A.C. Duhaime, T. A. Gennarelli, L. E. Thibault, A. B. Derek, S. S. Margulies, and W. Randall. The shaken baby syndrome: A clinical, pathological and biomechanical study. *Journal of Neurosurgery*, 66:409–415, 1987.

[2] C. Z. Cory and B. M. Jones. Can shaking alone cause fatal brain injury? a biomechanical assessment of the duhaime shaken baby syndrome model. *Med Sci Law*, 43(4):317–33, 2003.

[3] E. E. Conway. Nonaccidental head injury in infants:. *Pediatric Annals*, 27(10):677–690, 1998.

[4] R. G. Gedeit. The shaken baby syndrome: A multidisciplinary approach. chapter nine. medical management of the shaken infant. *Journal of Aggression, Maltreatment and Trauma*, 5(1):155–172, 2001.

[5] S. Ludwig and M. Warman. Shaken baby syndrome: A review of 20 cases. *Annals of Emergency Medicine*, 13(2):104–107, 1984.

[6] H. Hennes, N. Kini, and V. J. Pallusci. The shaken baby syndrome: A multidisciplinary approach chapter three; the epidemiology, clinical characteristics and public health implications. *Journal of Aggression, Maltreatment and Trauma*, 5(1):19–40, 2001.

[7] R. Alexander, L. Crabbe, Y. Sato, W. Smith, and H. S. Bennet. Serial abuse in children who are shaken. *American Journal of Diseases of Children*, (144):58–60, 1990.

[8] R. R. Seeley, T. D. Stephens, and P. Tate. *Anatomy and Physiology*. McGraw Hill, New York, 4th edition, 1998.

[9] K. D. Klinich, G. Auguste, S. Backaitis, and M. Kleinberger. Techniques for developing child dummy protection reference values. Technical report, NHTSA, 1996.

[10] M. Macmillan. Phineas gage information page. http://www.deakin.edu.au/hbs/GAGEPAGE/Pgstory.htm Jan 2006.

[11] Greg Welch and Gary Bishop. Introduction to the kalman filter. http://www.cs.unc.edu/ welch/kalman/kalmanIntro.html, April 2004.

[12] J. Ivarsson, D.C. Viano, P. Lovsund, and B. Aldman. Strain relief from the cerebral ventricles during head impact: experimental studies on natural protection of the brain. *Journal of Biomechanics*, 33:181–189, 2000.

[13] T. J. David. Shaken baby syndrome: Current controversies. In *Key Advances in Clinical Management: Shaken Baby Syndrome*, London, 2002. Royal Society of Medicine.

[14] A. N. Guthkelch. Infantile subdural haematoma and its relationship to whiplash injuries. *British Medical Journal*, (2):430–431, 1971.

[15] J. Caffey. On the theory and practice of shaking infants. *American Journal of Diseases of Children*, 124:161–169, 1972.

[16] J. Caffey. The whiplash shaken infant syndrome: Manual shaking by the extremities with whiplash-induced intracranial and intraocular bleedings, linked with residual permanent brain damage and mental retardation. *Pediatrics*, 54(4):396–403, 1974.

[17] R. Alexander, Y. Sato, W. Smith, and T. Bennet. Incidence of impact trauma with cranial injuries ascribed to shaking. *American Journal of Diseases of Children*, 144:724–726, 1990.

[18] W.J. King, M. MacKay, and A. Sirnick. Shaken baby syndrome in canada: clinical characteristics and outcomes of hospital cases. *CMAJ*, 168(2):155–159, 2003.

[19] K. M. Barlow and R.A. Minns. Annual incidence of shaken impact syndrome in young children. *The Lancet*, 356:15711572, 2000.

[20] H. Fischer and D. Allasio. Permanently damaged - long-term follow-up of shaken babies. *Clinical Pediatrics*, 33(11):696–698, 1994.

[21] C. Bonnier, M. C. Nassogne, and P. Evrard. Outcome and prognosis of whiplash shaken infant syndrome; late consequences after a symptom-free interval. *Developmental Medicine and Child Neurology*, 37:943–956, 1995.

[22] A.C. Duhaime, C.W. Christian, E. Moss, and T.S. Seidl. Long-term outcome in infants with the shaking-impact syndrome. *Pediatric Neurosurgery*, 24:292–298, 1996.

[23] R.F. Spaide. Shaken baby syndrome, ocular and computer tomographic findings. *Journal of Clinical Neuro-opthalmology*, 7(2):108–111, 1987.

[24] M.N. Hadley, V.K.H. Sonntag, H.L. Rekate, and A. Murphy. The infant whiplash-shake injury syndrome: A clinical and pathological study. *Neurosurgery*, 24(4):536–540, 1989.

[25] B. E. McGrory and G. M. Fenichel. Hangman's fracture subsequent to shaking in an infant. *Annals of Neurology*, 2:82, 1977.

[26] D. J. Pounder. Shaken adult syndrome. *Am J Forensic Med. Pathol*, 18(4):321–324, 1997.

[27] M. T. Prange and S. S. Margulies. Predictions of infant brain injuries in minor falls and inflicted events. In *IV World Congress of Biomechanics*, Calgary, 2002. Omnipress.

[28] M. T. Prange, B. Coats, A. C. Duhaime, and S. S. Margulies. Anthropomorphic simulations of falls, shakes, and inflicted impacts in infants. *Journal of Neurosurgery*, 99(1):143–150, 2003.

[29] S.H. Sinal, A.R. Petree, M. Herman-Giddens, M.K. Rogers, C. Enand, and R.H. DuRant. Is race or ethnicity a predictive factor in shaken baby syndrome? *Child Abuse and Neglect*, 24(9):1241–1246, 2000.

[30] A.C. Duhaime, T. A. Gennarelli, L.N. Sutton, and L. Schut. The 'shaken baby syndrome': a misnomer? *Journal of Pediatric Neuroscience*, 4:77–86, 1988.

[31] A.C. Duhaime, C.W. Christian, L.B. Rorke, and R.A. Zimmerman. Nonaccidental head injury in infants. *The New England Journal of Medicine*, 338(25):1822–1829, 1998.

[32] T. J. David. Shaken baby (shaken impact) syndrome: non-accidental head injury in infancy. *Journal of the Royal Society of Medicine*, 92(11):556–561, 1999.

[33] S. Lazortitz, S. Baldwin, and N. Kini. The whiplash shaken infant syndrome: Has caffey's syndrome changed or have we changed his syndrome? *Child Abuse and Neglect*, 21(10):1009–1014, 1997.

[34] M.G.F. Gilliland and R. Folberg. Shaken babies - some have no impact injuries. *Journal of Forensic Sciences*, 41(1):114–114, January 1996.

[35] H. Asamura, K. Yamazaki, T. Mukai, M. Ito, K. Takayanagi, M. Ota, and H. Fukushima. Case of shaken baby syndrome in japan caused by shaking alone. *Pediatr Int*, 45(1):117–119, 2003.

[36] J. F. Geddes, G. H. Vowles, A.K. Hackshaw, C. D. Nickols, I. S. Scott, and H. L. Whitwell. Neuropathology of inflicted head injury in children ii. microscopic brain injury in infants. *Brain*, 124:1299–1306, 2001.

[37] J. F. Geddes, R. C. Tasker, A. K. Hackshaw, C. D. Nickols, G. G. W. Adams, H. L. Whitwell, and I. Scheimberg. Dural haemorrhage in non-traumatic infant deaths: does it explain the bleeding in 'shaken baby syndrome'? *Neuropathol Appl Neurobiol*, 29(1):14–22, 2003.

[38] M. Donohoe. Evidence-based medicine and shaken baby syndrome part 1: Literature review, 1966-1998. *American Journal of Forensic Medicine and Pathology*, 24(3):239–242, 2003.

[39] P.E. Lantz, S.H. Sinal, C.A. Stanton, and R.G. Weaver. Perimacular retinal folds from childhood head trauma. *BMJ*, 328(7442):754–756, 2004.

[40] S. Kumaresan, N. Yoganandan, F. A. Pintar, D. J. Maiman, and S. Kuppa. Biomechanical study of pediatric human cervical spine: A finite element approach. *Transactions of the ASME*, 122:60–71, 2000.

[41] S. Kumaresan, N. Yoganandan, F. A. Pintar, and W. M. Mueller. Biomechanics of pediatric cervical spine: Compression, flexion and extension responses. *Journal of Crash Prevention and Injury Control*, 2(2):87–101, 2000.

[42] S. Kumaresan, N. Yoganandan, and F. A. Pintar. Age-specific pediatric cervical spine biomechanical responses: Three-dimensional nonlinear finite element models. *SAE Transactions*, 106(6(2)):3581–3611, 1997.

[43] S. Kumaresan, N. Yoganandan, and F. A. Pintar. Biomechanical responses of pediatric cervical spine using nonlinear finite element approach. Technical report, Dept. of Neurosurgery, Medical College of Wisconsin, 2002.

[44] Robert H. Pudenz and C. Hunter Shelden. The lucite calvarium - a method for direct observation of the brain. ii. crainial trauma and brain movement. *Journal of Neurosurgery*, 3:487, 1946.

[45] A. K. Ommaya, F. Faas, and P. Yarnell. Whiplash injury and brain damage. *The Journal of the American Medical Association*, 204(4):75–79, 1968.

[46] F. Unterharnscheidt and L.S. Higgins. Traumatic lesions of brain and spinal cord due to nondeforming angular acceleration of the head. *Texas Reports on Biology and Medicine*, 27(1):127–166, 1969.

[47] A. K. Ommaya and T. A. Gennarelli. Cerebral concussion and traumatic unconsciousness. *Brain*, 97:633–654, 1974.

[48] T. A. Gennarelli, L. E. Thibault, and J. H. Adams. Diffuse axonal injury and traumatic coma in the primate. *Annals of Neurology*, 12:564–574, 1982.

[49] R. Raghupathi, M. F. Mehr, M. A. Helfaer, and S. S. Margulies. Traumatic axonal injury is exacerbated, following repetitive closed head injury in the neonatal pig. *Journal of Neurotrauma*, 21(3):307–316, 2004.

[50] A. H. S. Holbourn. Mechanics of head injuries. *The Lancet*, 2:438–441, 1943.

[51] S.S. Margulies. *Biomechanics of traumatic coma in the primate.* PhD thesis, University of Pennsylvania., 1987.

[52] S.S. Margulies and L.E. Thibault. An analytical model of traumatic diffuse brain injury. *Journal of Biomechanics*, 111:241–249, 1989.

[53] J. Ivarsson. *Physical Modelling of Brain and Head Kinematics.* PhD thesis, Dept. of Machine and Vehicle Systems, Chalmers University of Technology, Goteborg, Sweeden, 2002.

[54] D.R.S. Bradshaw, J. Ivarsson, C.L. Morfey, and D.C. Viano. Simulation of acute subdural hematoma and diffuse axonal injury in coronal head impact. *Journal of Biomechanics*, 34(1):85–94, 2001.

[55] D.C. Ivarsson, J.and Viano and P. Lovsund. Influence of the anterior and middle cranial fossae on brain kinematics during sagittal plane head rotation. *Journal of Crash Prevention and Injury Control*, 2(4):271–287, 2001.

[56] J. Ivarsson, D.C. Viano, and P. Lovsund. Influence of the lateral ventricles and irregular skull base on brain kinematics due to sagittal plane head rotation. *Journal of Biomechanical Engineering -Transactions of the Asme*, 124(4):422–431, 2002.

[57] J. Ivarsson, D.C. Viano, P. Lovsund, and Y. Parnaik. Head kinematics in mini-sled tests of foam padding: Relevance of linear responses from free motion headform (fmh) testing to head angular responses. *Journal of Biomechanical Engineering - Transactions of the ASME*, 125(4):523–532, 2003.

[58] K. Schneider and R. F. Zernicke. Mass, center of mass, and moment of inertia estimates for infant limb segments. *Journal of Biomechanics*, 25(2):145–148, 1992.

[59] H. Sun and R. Jason. Body segment growth during infancy. *Journal of Biomechanics*, 27(3):265–275, 1994.

[60] R. K. Jensen. Body segment mass, radius and radius of gyration proportions of children. *Journal of Biomechanics*, 19(5):359–368, 1986.

[61] L. K. Thibault and S. S. Margulies. Age-dependent properties of the porcine cerebrum: effect on pediatric head injury criteria. *Journal of Biomechanics*, 31:119–1126, 1998.

[62] S. S. Margulies, L. E. Thibault, and T. A. Gennarelli. Physical model simulations of brain injury in the primate. *Journal of Biomechanics*, 23(8):823–836, 1990.

[63] L.E. Bilston and L.E. Thibault. Biomechanics of cervical spinal cord injury in flexion and extension: A physical model to estimate spinal cord deformations. *IJCrash*, 2(2):207–218, 1997.

[64] K. B. Arbogast, L. K. Thibault, B. S. Pinheiro, K. I. Winey, and S. S. Margulies. A high-frequency shear device for testing soft biological tissues. *Journal of Biomechanics*, 30(7):757–759, 1997.

[65] L. Z. Shuck and S. H. Advani. Rheological response of human brain tissue in shear. *ASME Journal of Basic Engineering*, 94:905–911, 1972.

[66] J. E. Galford and McElhaney. A viscoelastic study of scalp, brain and dura. *Journal of Biomechanics*, 3:211–221, 1970.

[67] G. T. Fallenstein, V. D. Hulce, and J. W. Melvin. Dynamic mechanical properties of human brain tissue. *Journal of Biomechanics*, 2:217–226, 1969.

Appendix A

ATD Torso Acceleration Traces

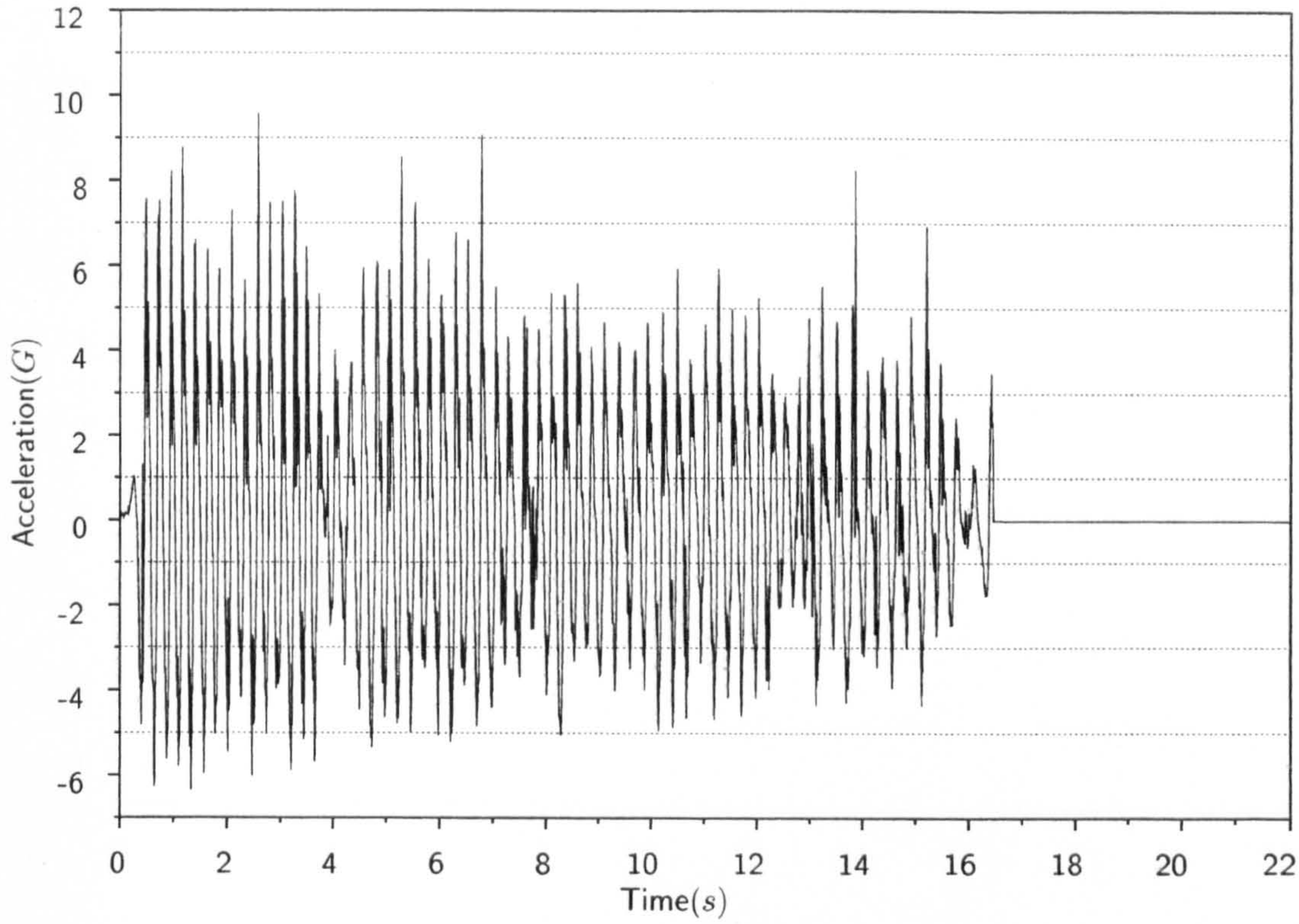

Figure A.1: Shake episode 1. Max rms shake used in Chapter 5.

Figure A.2: Shake episode 2. Max peak shake used in Chapter 5.

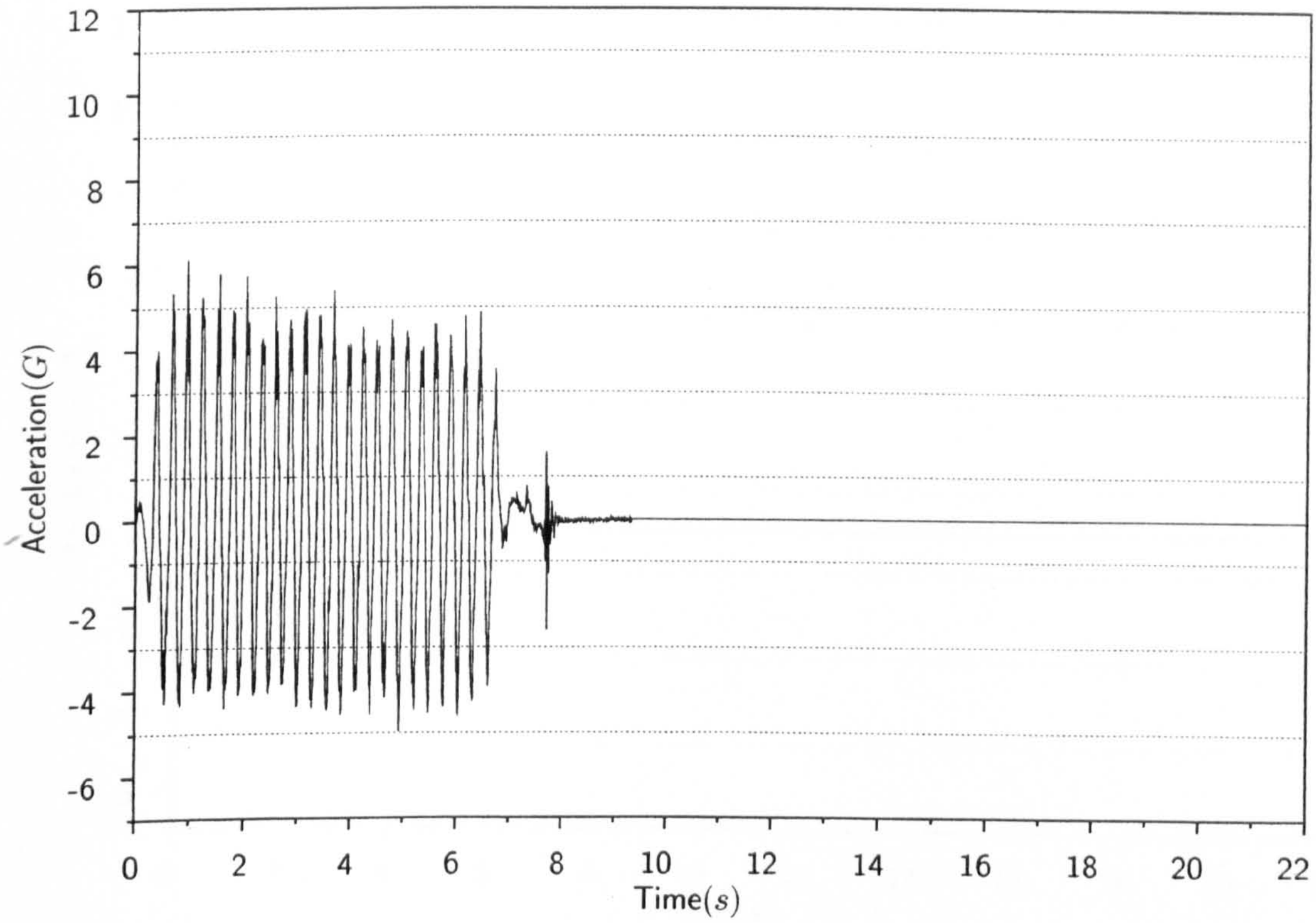

Figure A.3: Shake episode 3

Figure A.4: Shake episode 4

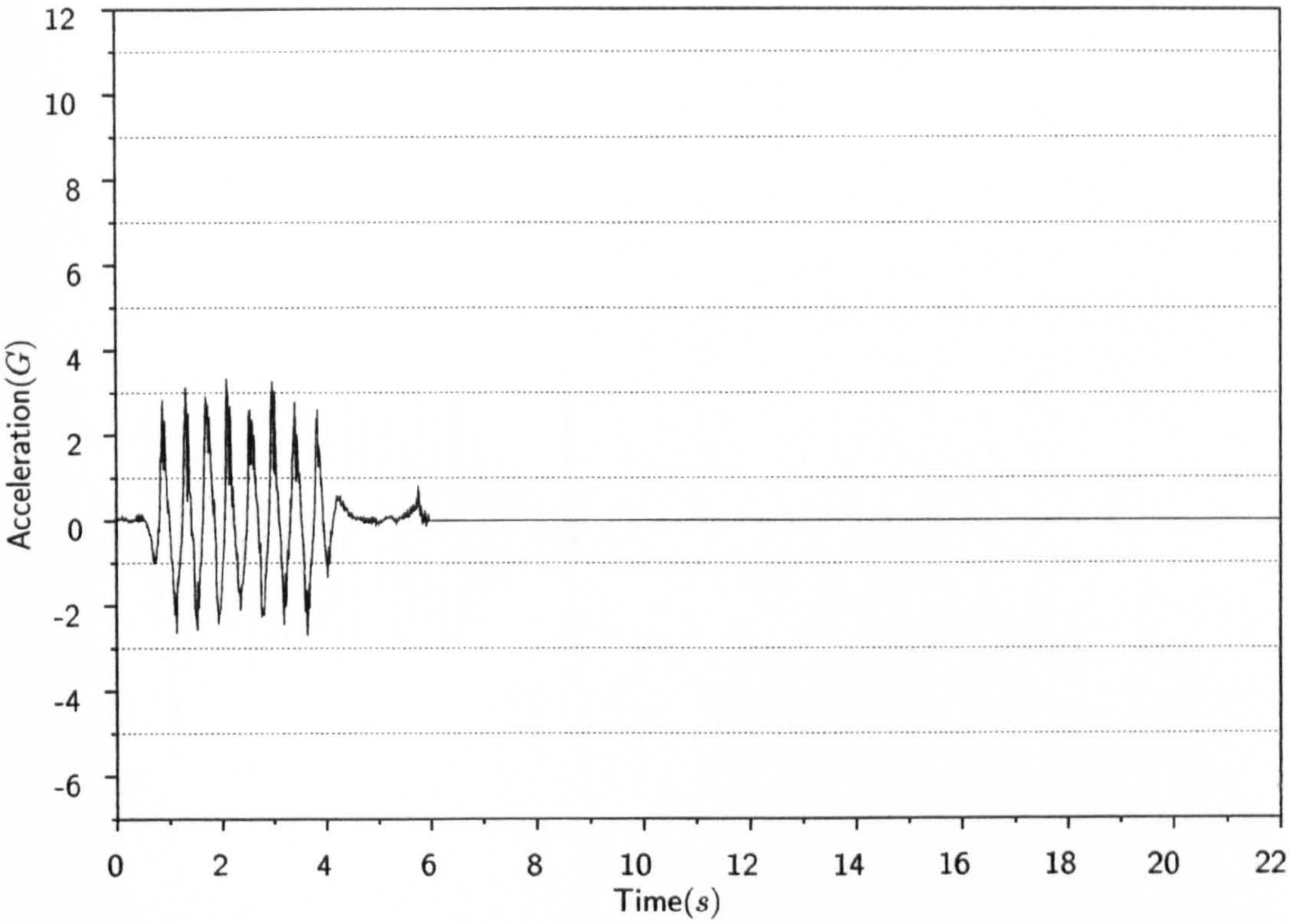

Figure A.5: Shake episode 5

Figure A.6: Shake episode 6

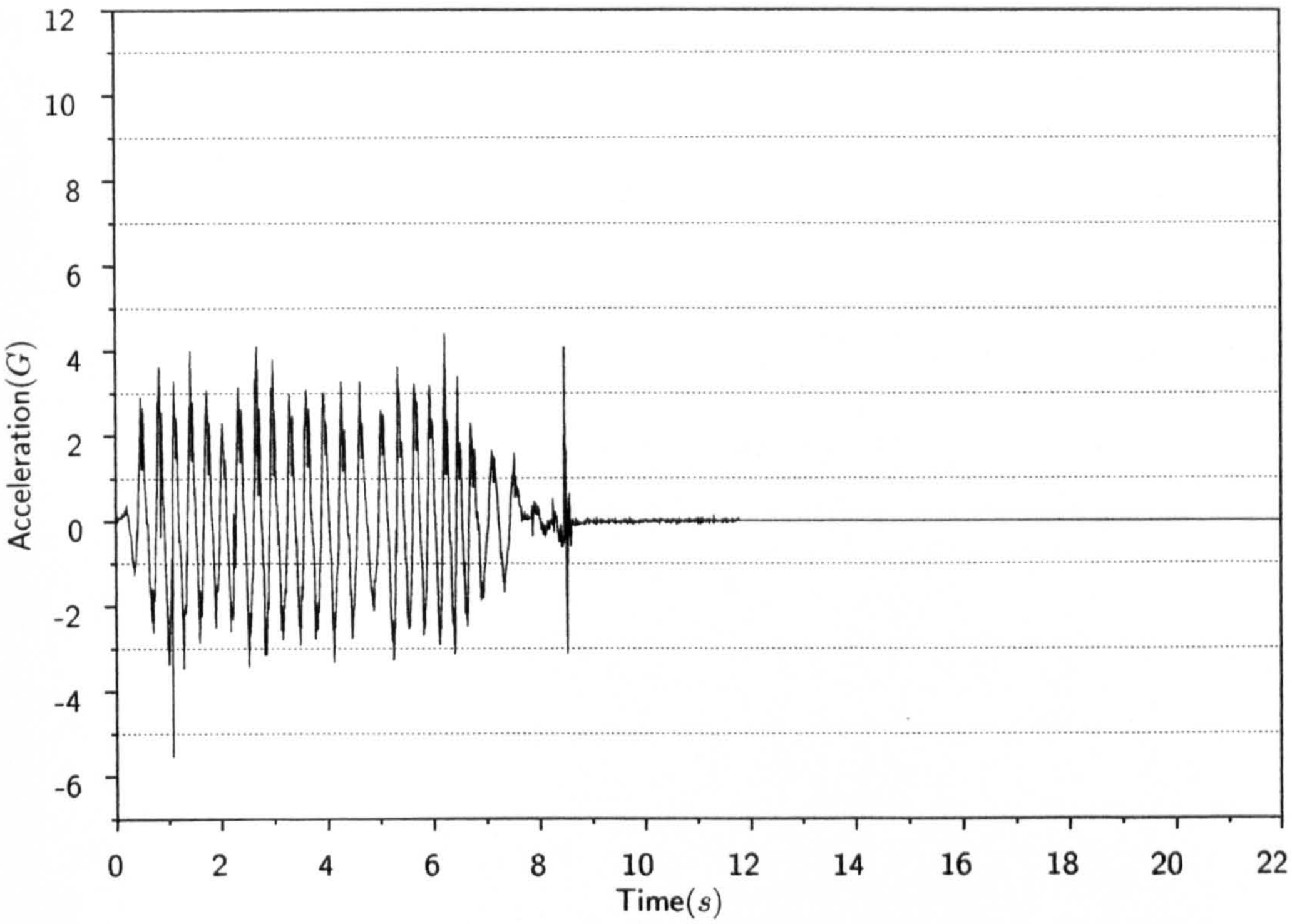

Figure A.7: Shake episode 7

Figure A.8: Shake episode 8

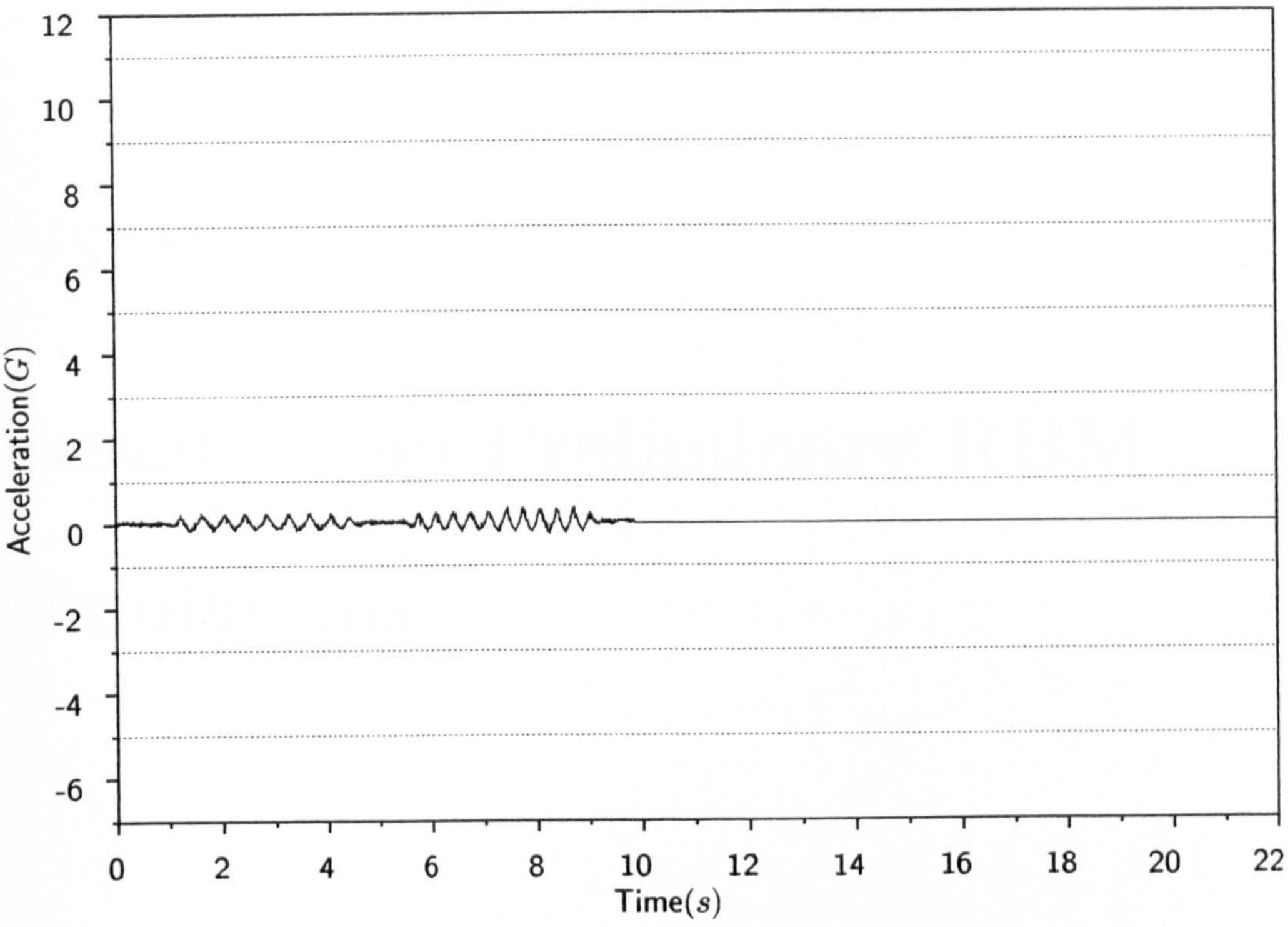

Figure A.9: Shake episode 9

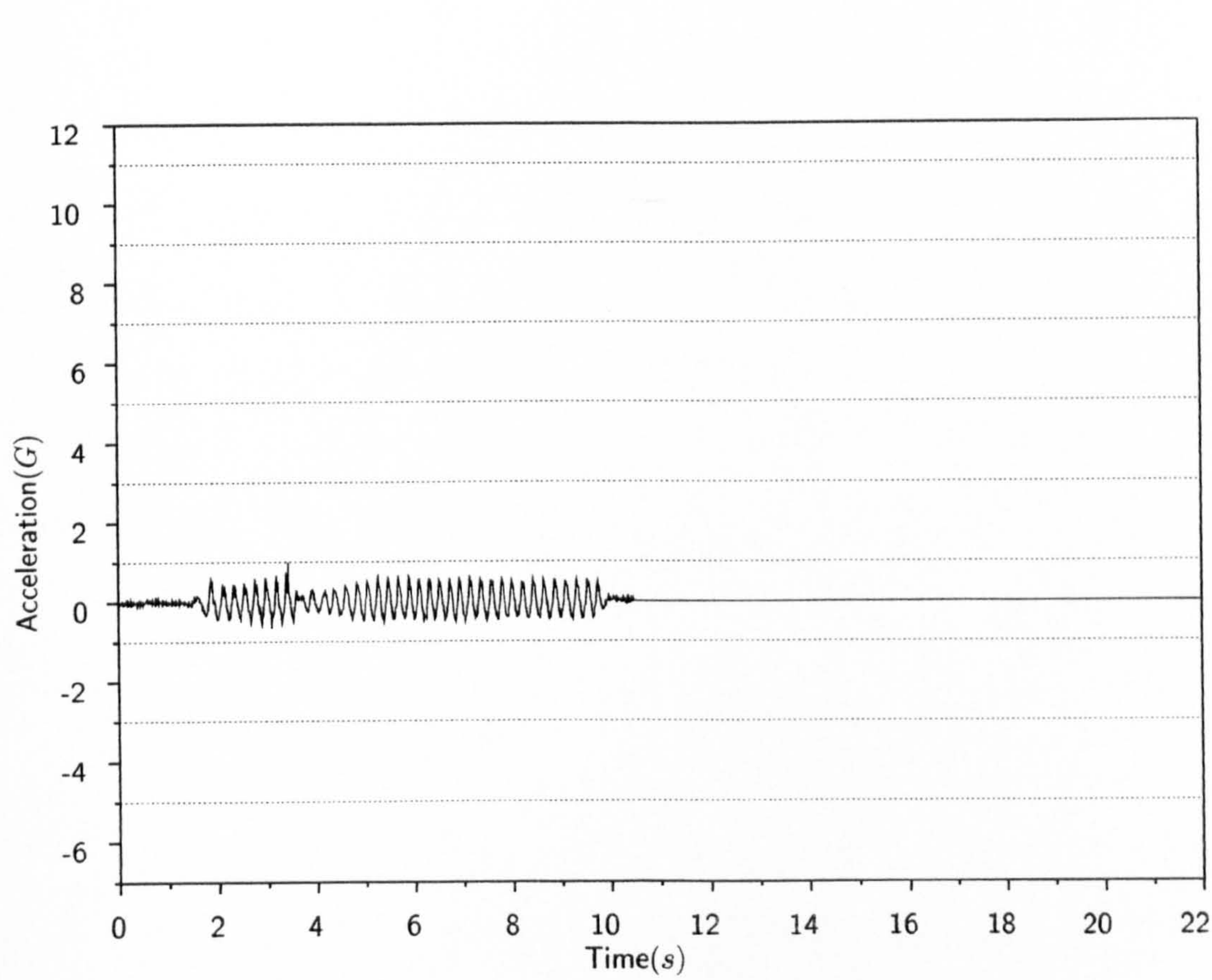

Figure A.10: Shake episode 10

Appendix B

Results from Preliminary RBM Simulations

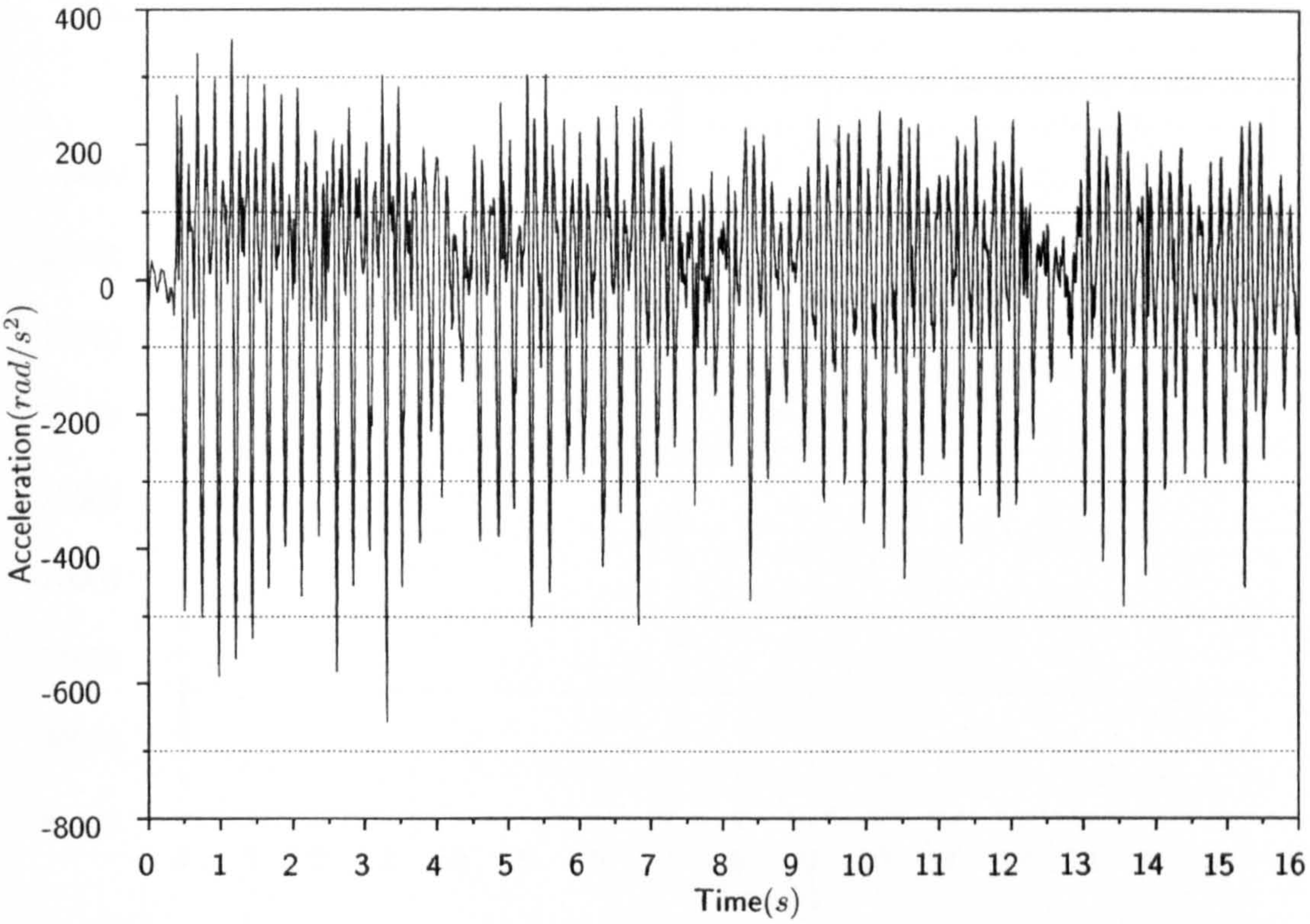

Figure B.1: Weight model, max rms shake

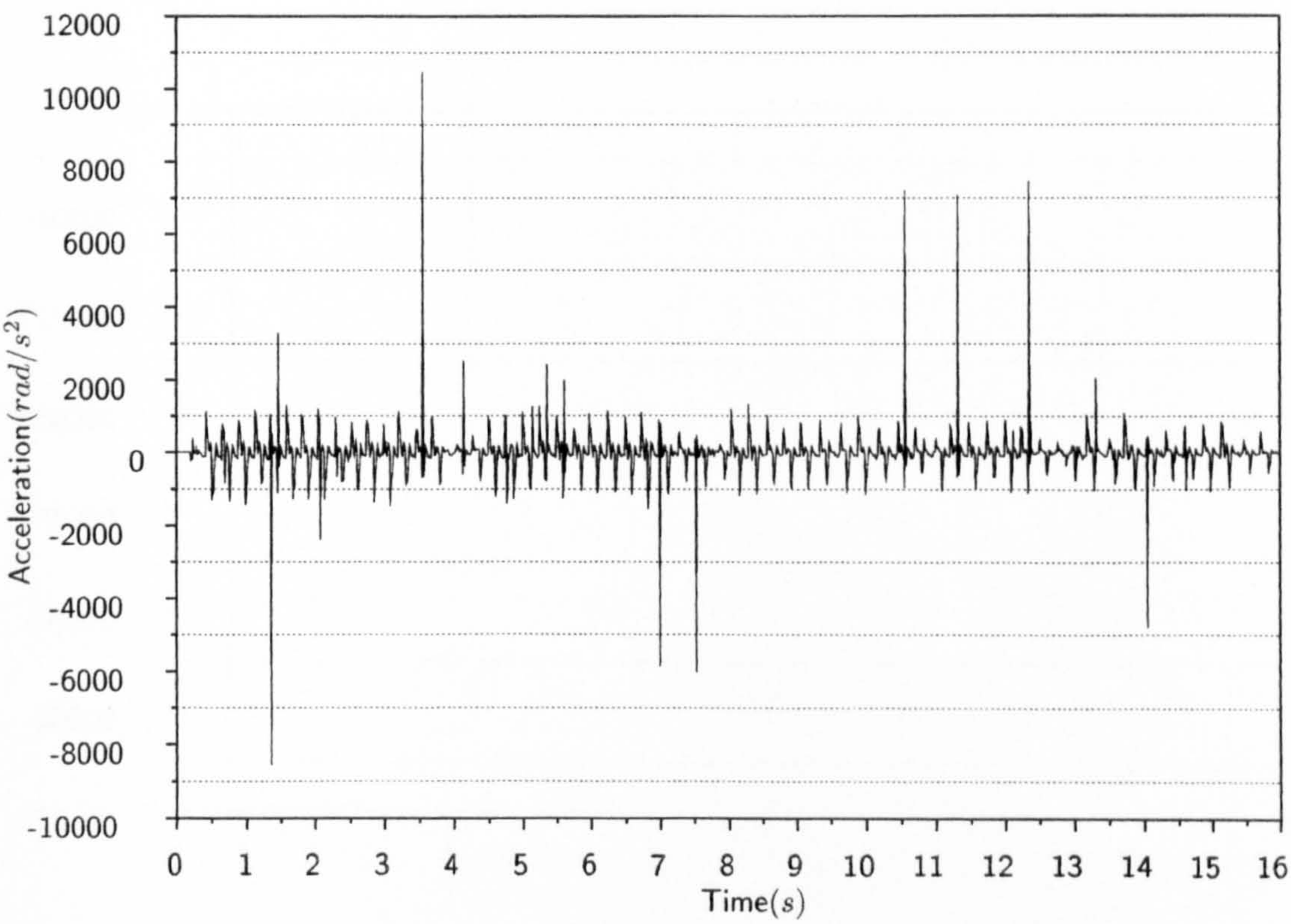

Figure B.2: Lower end-stop model, max rms shake

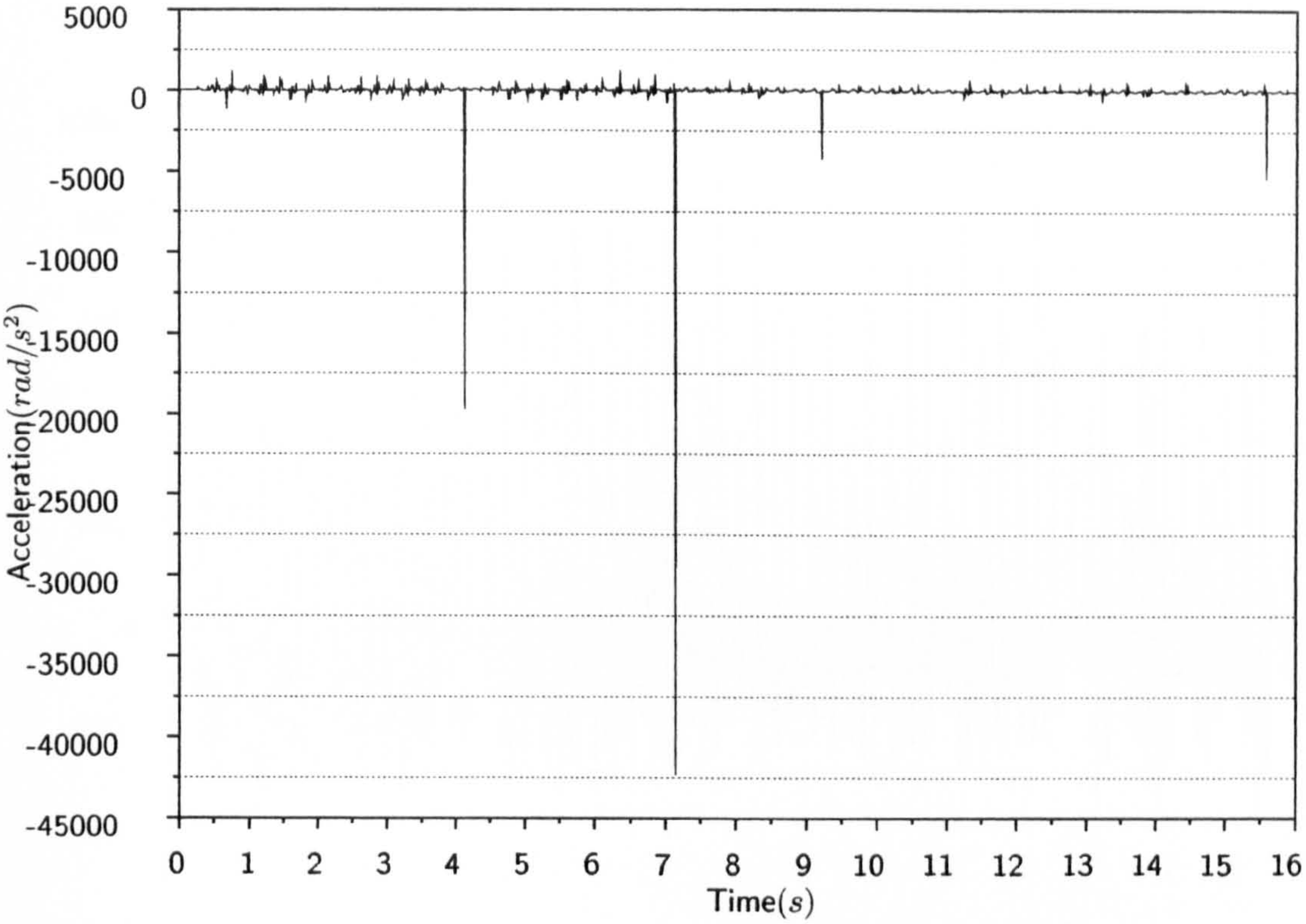

Figure B.3: Upper end-stop model, max rms shake

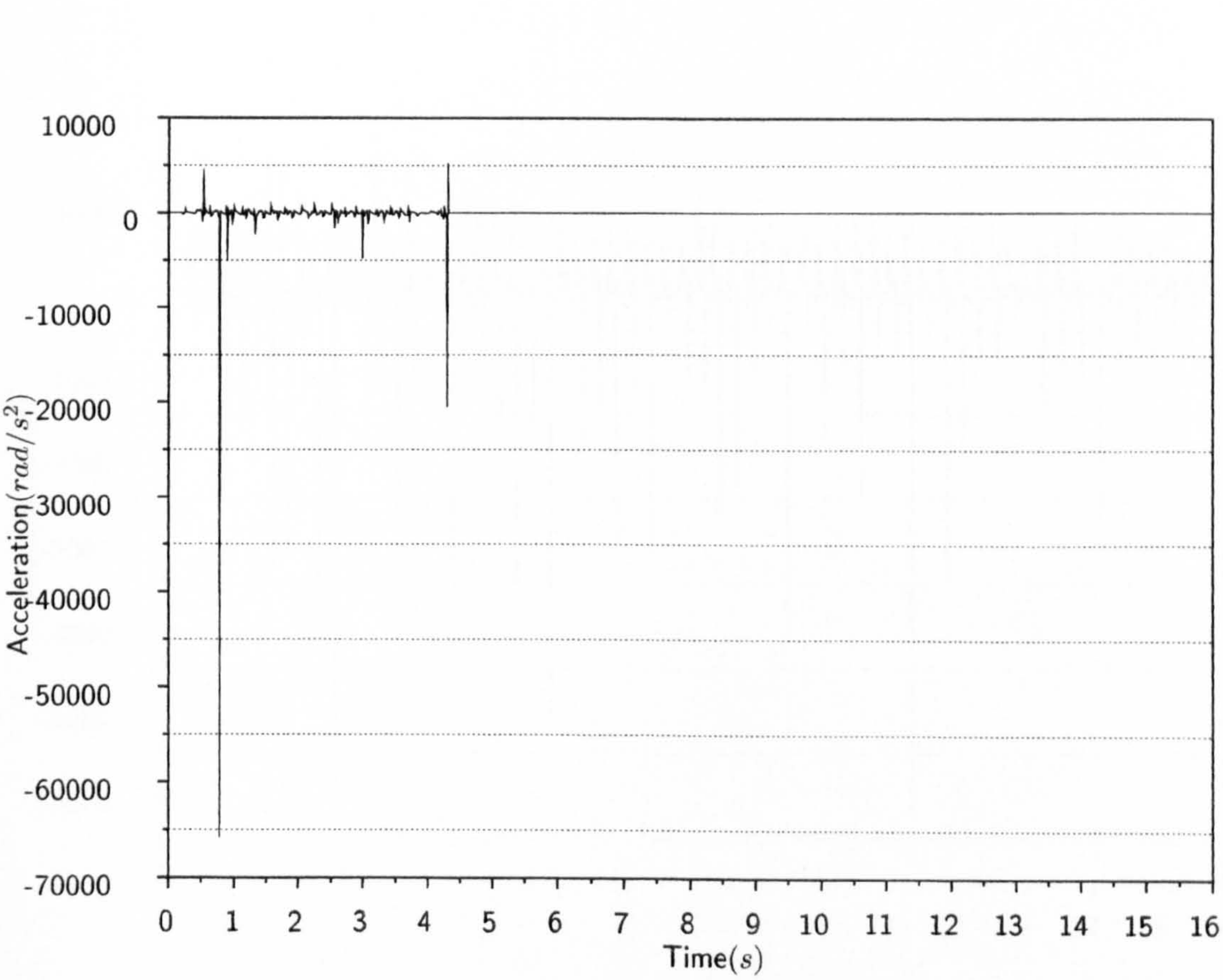

Figure B.4: Both end-stop model, max rms shake

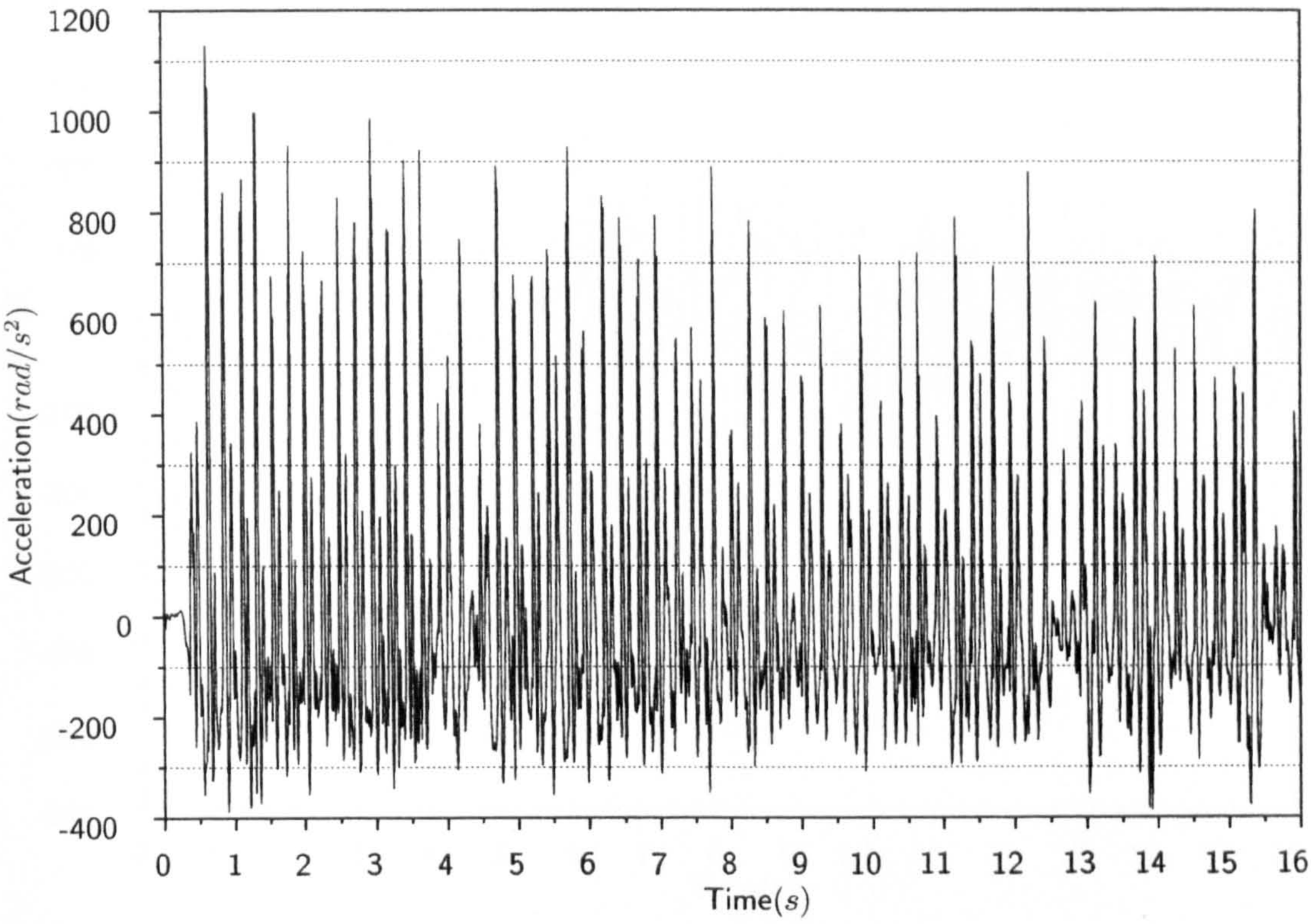

Figure B.5: Multi-segmented model, max rms shake

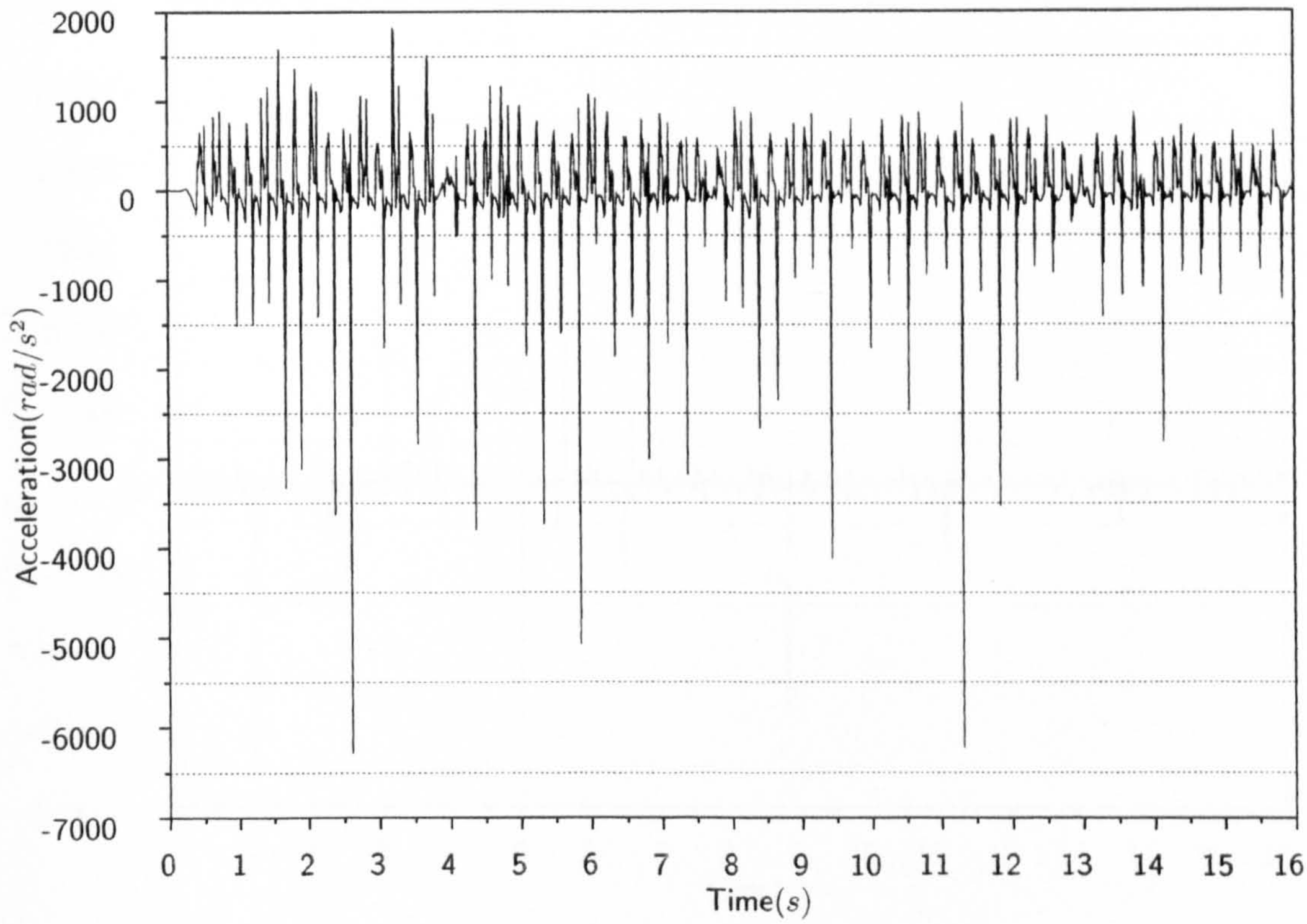

Figure B.6: Multi-segmented impact model, max rms shake

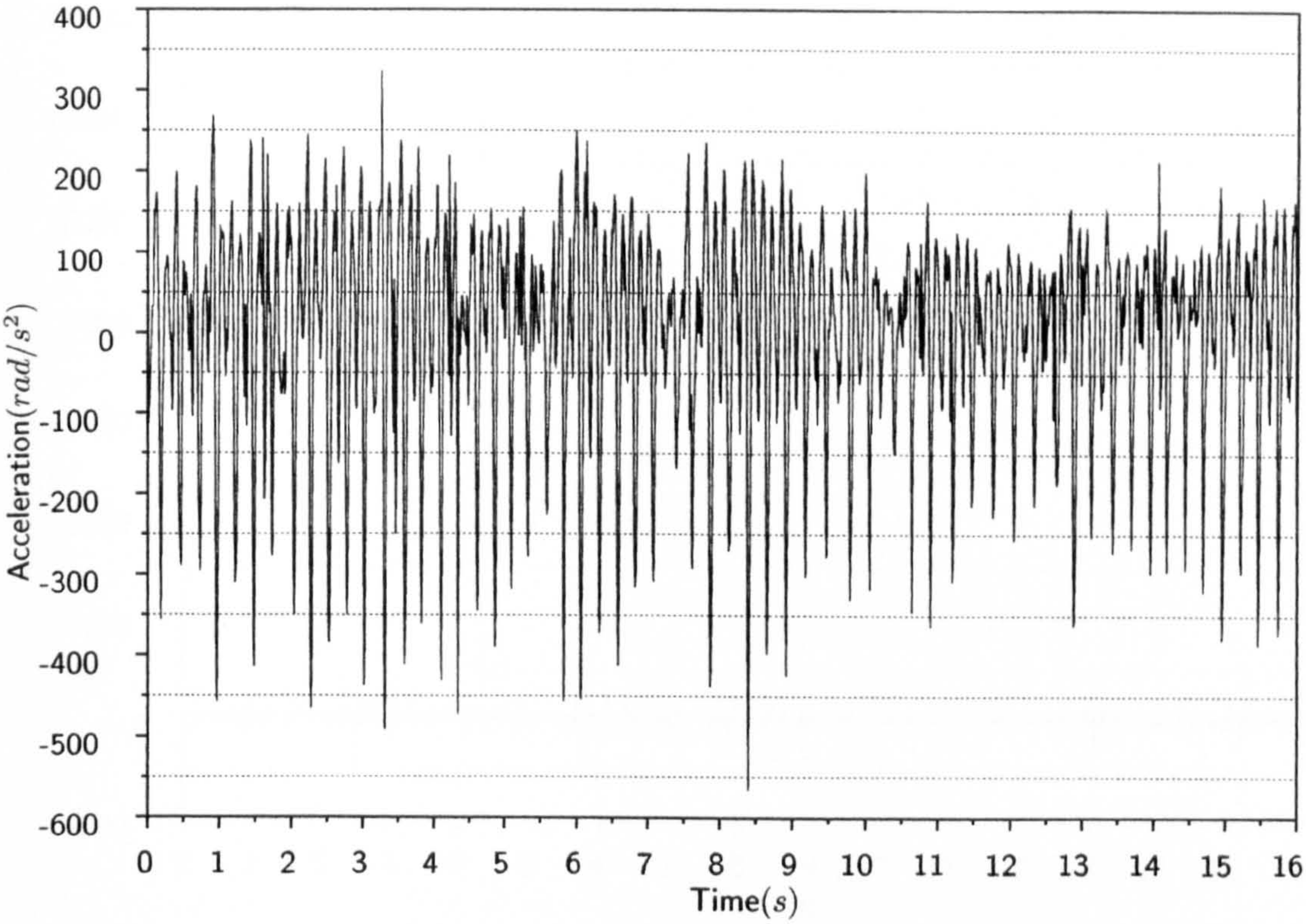

Figure B.7: Weighted model, max peak shake

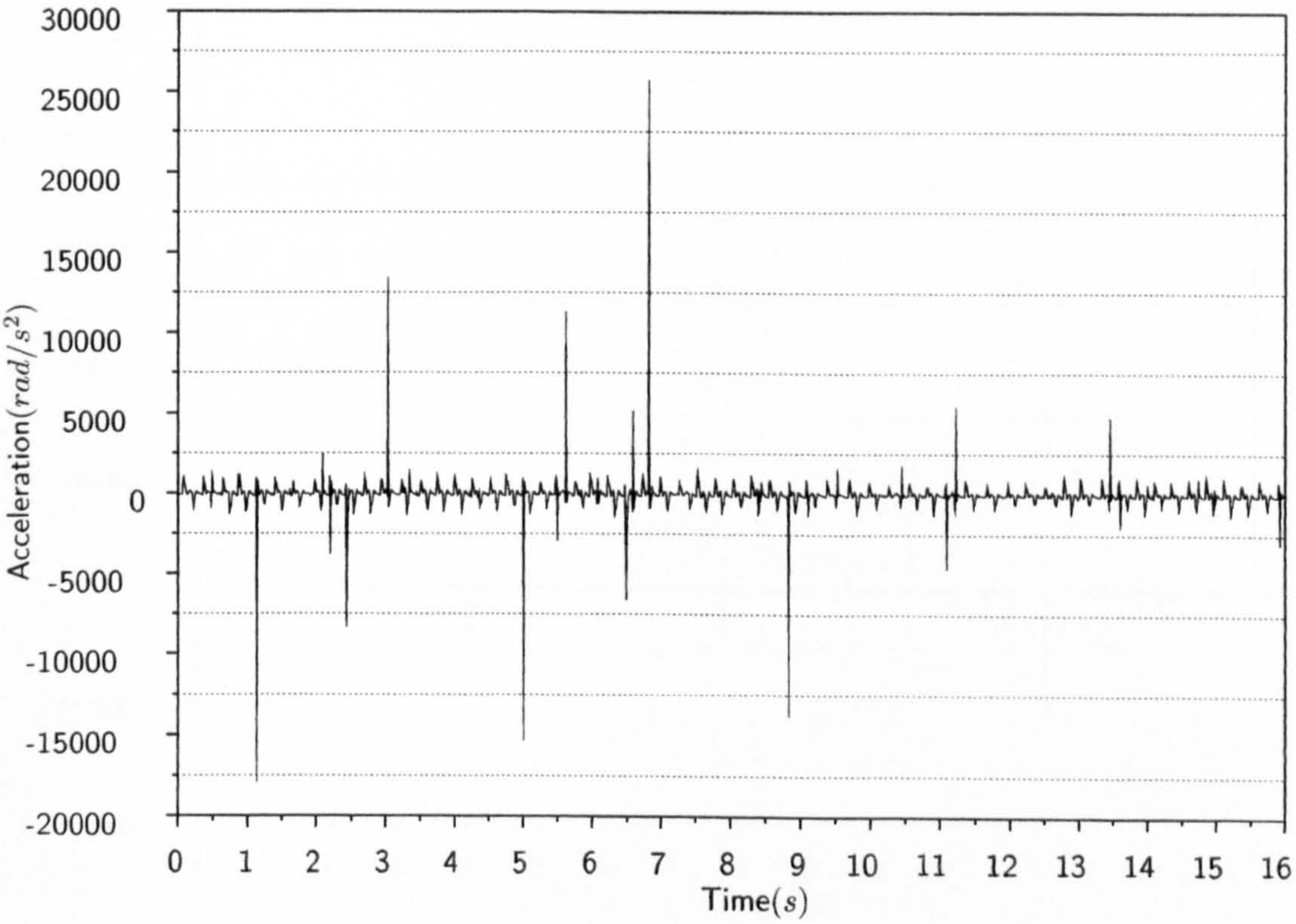

Figure B.8: Lower end-stop model, max peak shake

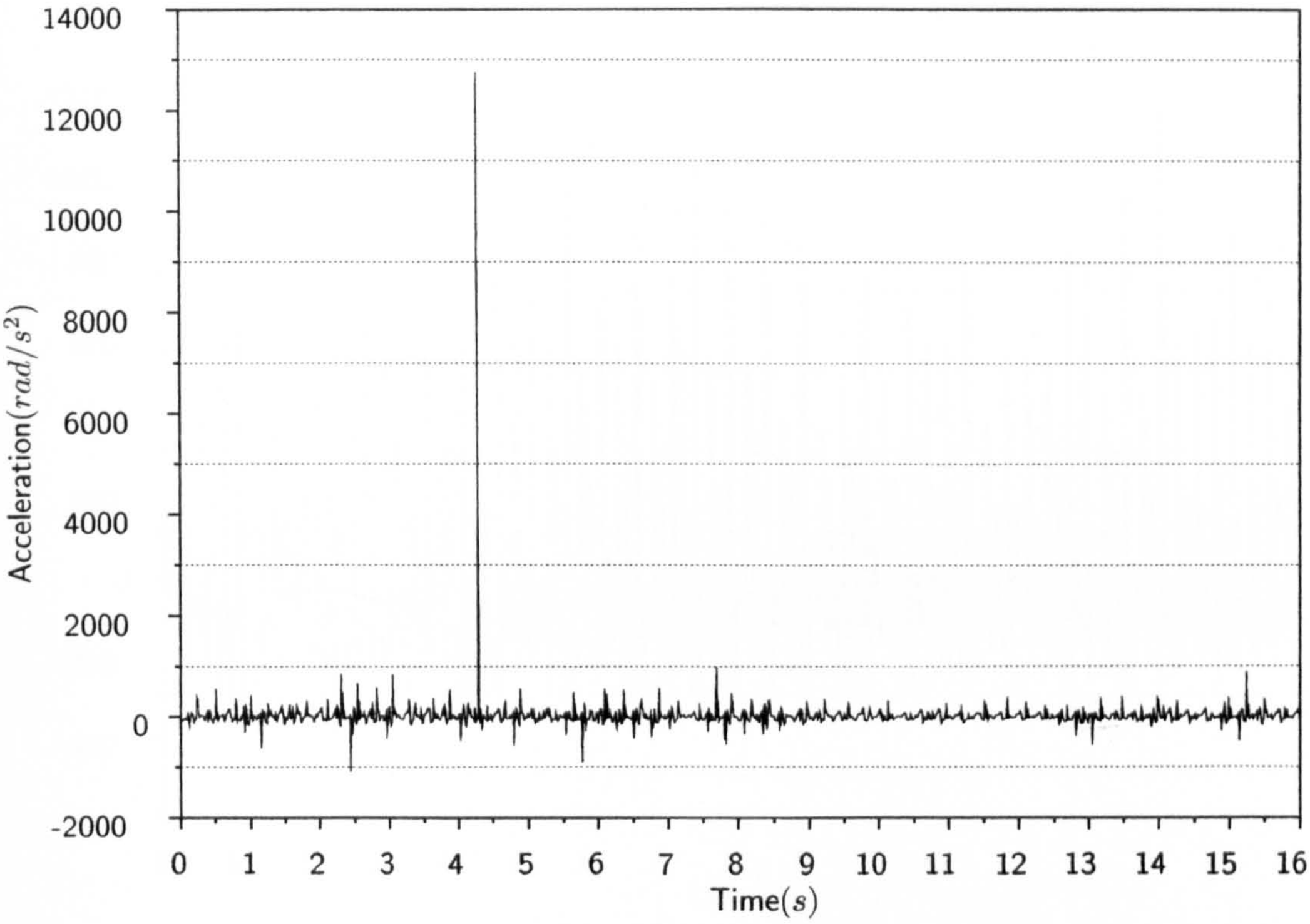

Figure B.9: Upper end-stop model, max peak shake

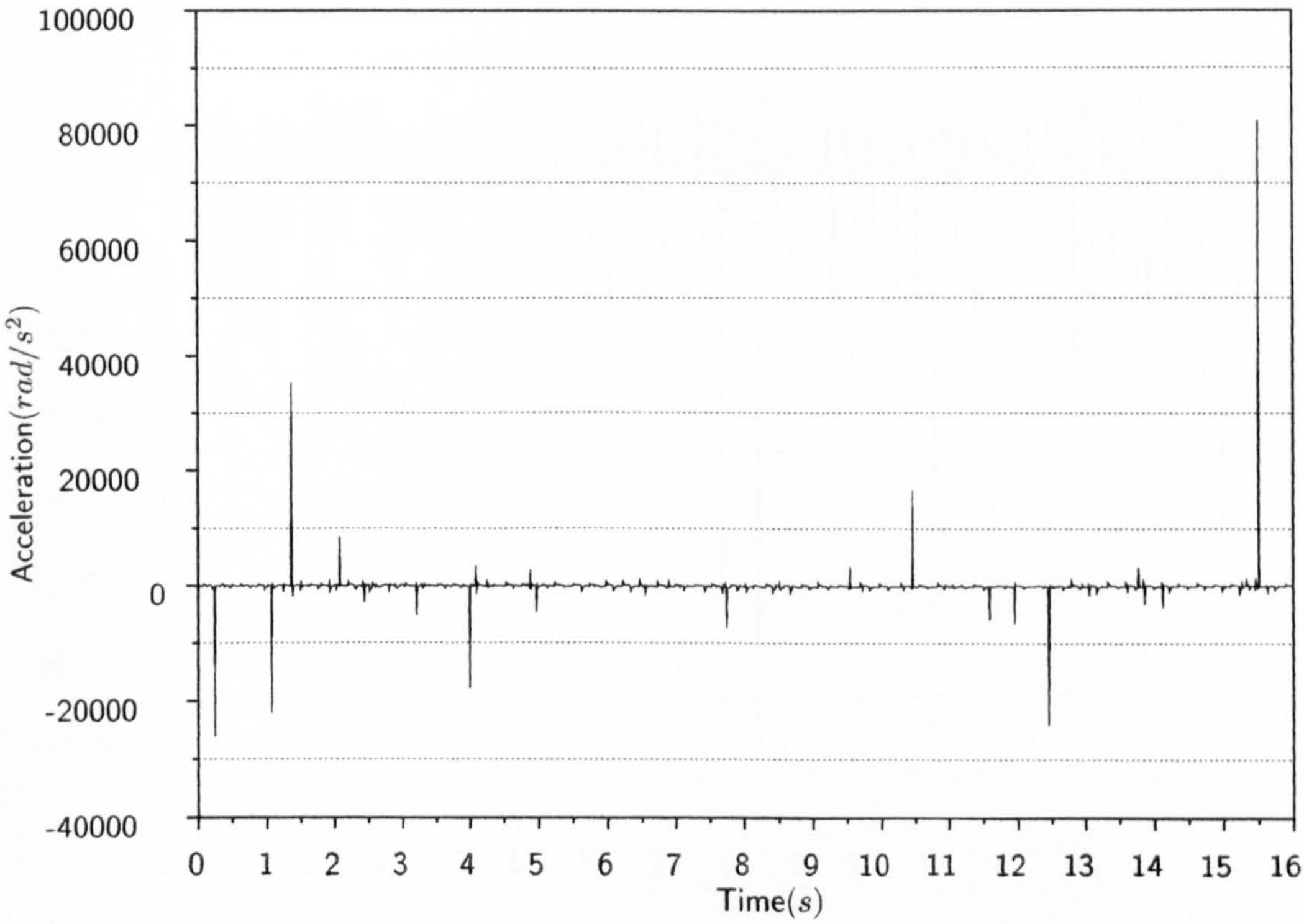

Figure B.10: Both end-stop model, max peak shake

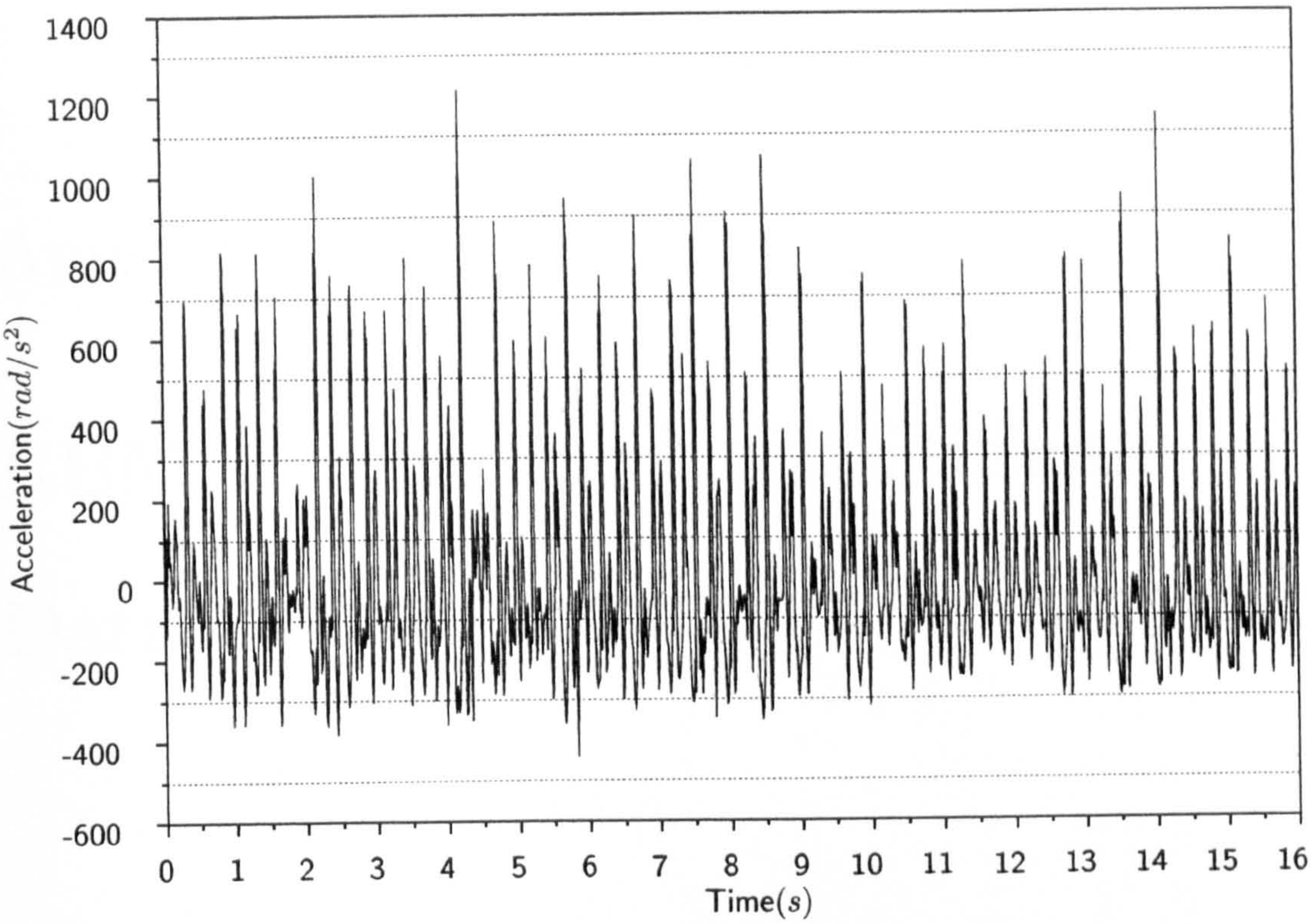

Figure B.11: Multi-segmented model, max peak shake

Figure B.12: Multi-segmented impact model, max peak shake

Appendix C

RBM Parametric Neck Stiffness Data

		Stiffness Charactersitics				
		Flexion			Extension	
Test		ROM	Free		Free	ROM
1	angle (rads)	-0.13	-0.13	0	0.4	0.4
	rot. Torque (Nm)	34.8	2.6	0	2.6	82.4
2	angle (rads)	-0.47	-0.13	0	0.4	0.71
	rot. Torque (Nm)	46.23	2.6	0	2.6	108.48
3	angle (rads)	-0.81	-0.13	0	0.4	1.02
	rot. Torque (Nm)	57.65	2.6	0	2.6	134.55
4	angle (rads)	-1.15	-0.13	0	0.4	1.33
	rot. Torque (Nm)	69.08	2.6	0	2.6	160.63
5	angle (rads)	-1.49	-0.13	0	0.4	1.63
	rot. Torque (Nm)	80.5	2.6	0	2.6	186.7
6	angle (rads)	-0.22	-0.22	0	0.49	0.49
	rot. Torque (Nm)	34.8	3.92	0	8.78	82.4
7	angle (rads)	-0.54	-0.22	0	0.49	0.77
	rot. Torque (Nm)	46.23	3.92	0	8.78	108.48
8	angle (rads)	-0.86	-0.22	0	0.49	1.06
	rot. Torque (Nm)	57.65	3.92	0	8.78	134.55
9	angle (rads)	-1.18	-0.22	0	0.49	1.35
	rot. Torque (Nm)	69.08	3.92	0	8.78	160.63
10	angle (rads)	-1.49	-0.22	0	0.49	1.63
	rot. Torque (Nm)	80.5	3.92	0	8.78	186.7
11	angle (rads)	-0.32	-0.32	0	0.58	0.58
	rot. Torque (Nm)	34.8	5.24	0	14.96	82.4
12	angle (rads)	-0.61	-0.32	0	0.58	0.84
	rot. Torque (Nm)	46.23	5.24	0	14.96	108.48
13	angle (rads)	-0.91	-0.32	0	0.58	1.1
	rot. Torque (Nm)	57.65	5.24	0	14.96	134.55
14	angle (rads)	-1.2	-0.32	0	0.58	1.37
	rot. Torque (Nm)	69.08	5.24	0	14.96	160.63
15	angle (rads)	-1.49	-0.32	0	0.58	1.63
	rot. Torque (Nm)	80.5	5.24	0	14.96	186.7
16	angle (rads)	-0.42	-0.42	0	0.66	0.66

Test		Stiffness Characteristics				
		Flexion			Extension	
		ROM	Free		Free	ROM
	rot. Torque (Nm)	34.8	6.57	0	21.13	82.4
17	angle (rads)	-0.69	-0.42	0	0.66	0.91
	rot. Torque (Nm)	46.23	6.57	0	21.13	108.48
18	angle (rads)	-0.96	-0.42	0	0.66	1.15
	rot. Torque (Nm)	57.65	6.57	0	21.13	134.55
19	angle (rads)	-1.23	-0.42	0	0.66	1.39
	rot. Torque (Nm)	69.08	6.57	0	21.13	160.63
20	angle (rads)	-1.49	-0.42	0	0.66	1.63
	rot. Torque (Nm)	80.5	6.57	0	21.13	186.7
21	angle (rads)	-0.52	-0.52	0	0.75	0.75
	rot. Torque (Nm)	34.8	7.89	0	27.31	82.4
22	angle (rads)	-0.76	-0.52	0	0.75	0.97
	rot. Torque (Nm)	46.23	7.89	0	27.31	108.48
23	angle (rads)	-1.01	-0.52	0	0.75	1.19
	rot. Torque (Nm)	57.65	7.89	0	27.31	134.55
24	angle (rads)	-1.25	-0.52	0	0.75	1.41
	rot. Torque (Nm)	69.08	7.89	0	27.31	160.63
25	angle (rads)	-1.49	-0.52	0	0.75	1.63
	rot. Torque (Nm)	80.5	7.89	0	27.31	186.7
26	angle (rads)	-0.61	-0.61	0	0.84	0.84
	rot. Torque (Nm)	34.8	9.21	0	33.49	82.4
27	angle (rads)	-0.83	-0.61	0	0.84	1.04
	rot. Torque (Nm)	46.23	9.21	0	33.49	108.48
28	angle (rads)	-1.05	-0.61	0	0.84	1.24
	rot. Torque (Nm)	57.65	9.21	0	33.49	134.55
29	angle (rads)	-1.27	-0.61	0	0.84	1.43
	rot. Torque (Nm)	69.08	9.21	0	33.49	160.63
30	angle (rads)	-1.49	-0.61	0	0.84	1.63
	rot. Torque (Nm)	80.5	9.21	0	33.49	186.7
31	angle (rads)	-0.71	-0.71	0	0.93	0.93
	rot. Torque (Nm)	34.8	10.53	0	39.67	82.4

		Stiffness Charactersitics				
		Flexion			Extension	
Test		ROM	Free		Free	ROM
32	angle (rads)	-0.91	-0.71	0	0.93	1.1
	rot. Torque (Nm)	46.23	10.53	0	39.67	108.48
33	angle (rads)	-1.1	-0.71	0	0.93	1.28
	rot. Torque (Nm)	57.65	10.53	0	39.67	134.55
34	angle (rads)	-1.3	-0.71	0	0.93	1.46
	rot. Torque (Nm)	69.08	10.53	0	39.67	160.63
35	angle (rads)	-1.49	-0.71	0	0.93	1.63
	angle (rads)	80.5	10.53	0	39.67	186.7
36	rot. Torque (Nm)	-0.81	-0.81	0	1.02	1.02
	angle (rads)	34.8	11.86	0	45.84	82.4
37	rot. Torque (Nm)	-0.98	-0.81	0	1.02	1.17
	angle (rads)	46.23	11.86	0	45.84	108.48
38	rot. Torque (Nm)	-1.15	-0.81	0	1.02	1.32
	angle (rads)	57.65	11.86	0	45.84	134.55
39	rot. Torque (Nm)	-1.32	-0.81	0	1.02	1.48
	angle (rads)	69.08	11.86	0	45.84	160.63
40	rot. Torque (Nm)	-1.49	-0.81	0	1.02	1.63
	angle (rads)	80.5	11.86	0	45.84	186.7
41	rot. Torque (Nm)	-0.91	-0.91	0	1.1	1.1
	angle (rads)	34.8	13.18	0	52.02	82.4
42	rot. Torque (Nm)	-1.05	-0.91	0	1.1	1.24
	angle (rads)	46.23	13.18	0	52.02	108.48
43	rot. Torque (Nm)	-1.2	-0.91	0	1.1	1.37
	angle (rads)	57.65	13.18	0	52.02	134.55
44	rot. Torque (Nm)	-1.35	-0.91	0	1.1	1.5
	angle (rads)	69.08	13.18	0	52.02	160.63
45	rot. Torque (Nm)	-1.49	-0.91	0	1.1	1.63
	angle (rads)	80.5	13.18	0	52.02	186.7
46	rot. Torque (Nm)	-1.01	-1.01	0	1.19	1.19
	angle (rads)	34.8	14.5	0	58.2	82.4
47	rot. Torque (Nm)	-1.13	-1.01	0	1.19	1.3

		Stiffness Charactersitics				
		Flexion			Extension	
Test		ROM	Free		Free	ROM
	angle (rads)	46.23	14.5	0	58.2	108.48
48	rot. Torque (Nm)	-1.25	-1.01	0	1.19	1.41
	angle (rads)	57.65	14.5	0	58.2	134.55
49	rot. Torque (Nm)	-1.37	-1.01	0	1.19	1.52
	angle (rads)	69.08	14.5	0	58.2	160.63
50	rot. Torque (Nm)	-1.49	-1.01	0	1.19	1.63
	angle (rads)	80.5	14.5	0	58.2	186.7

Appendix D

Results from Parametric Study of Neck Stiffness: Max. rms Acceleration Input

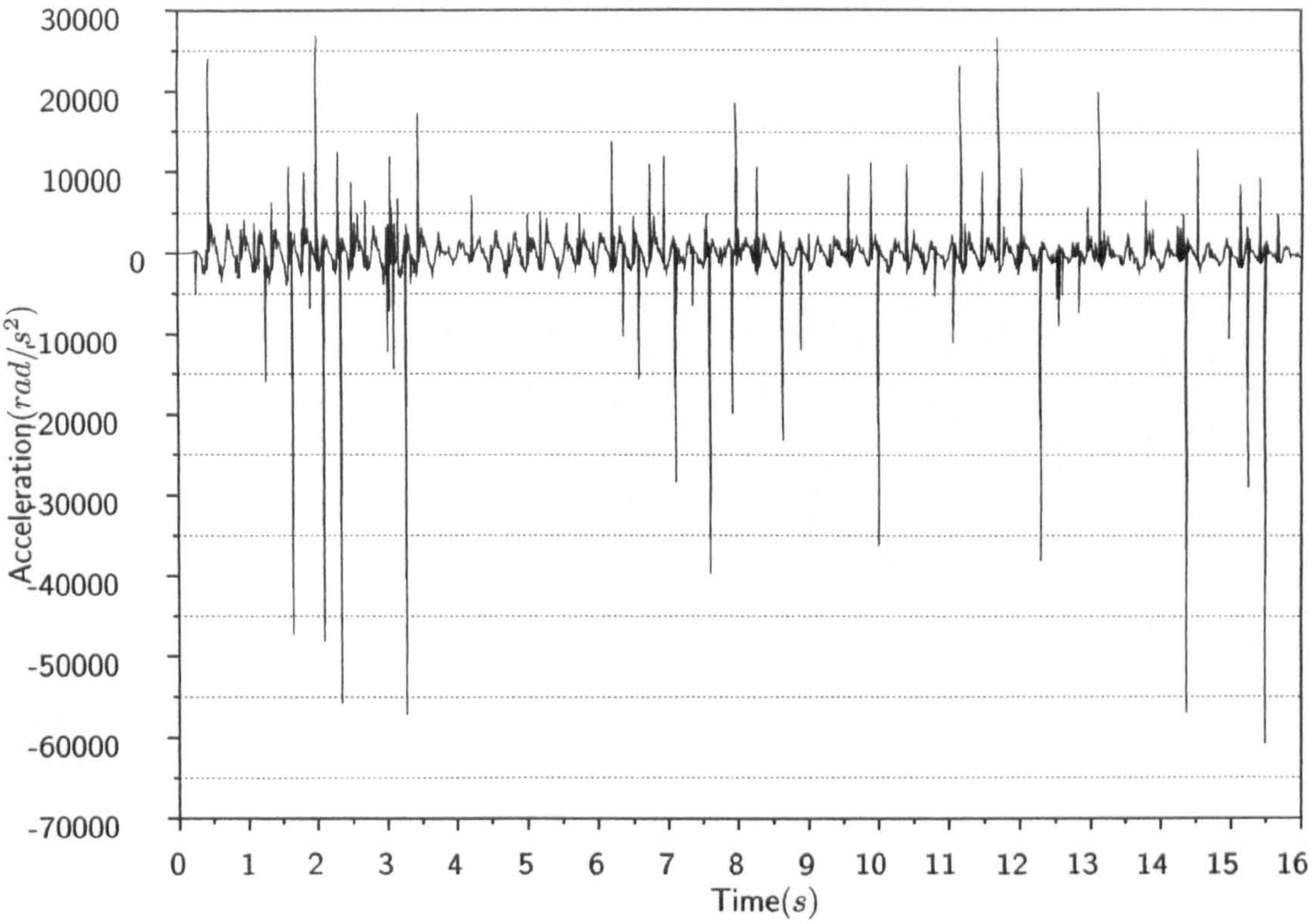

Figure D.1: Max rms acceleration, Model 1

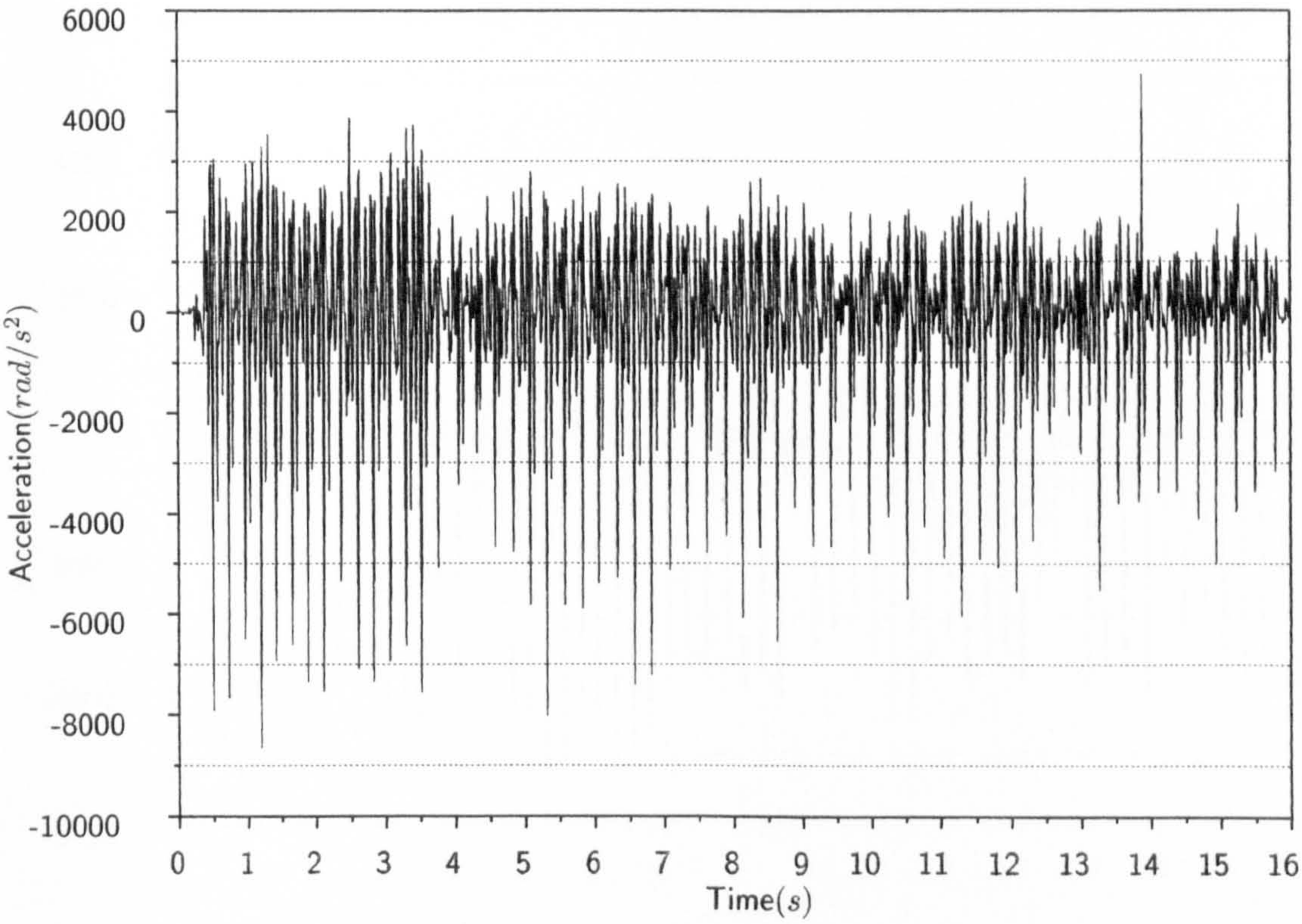

Figure D.2: Max rms acceleration, Model 2

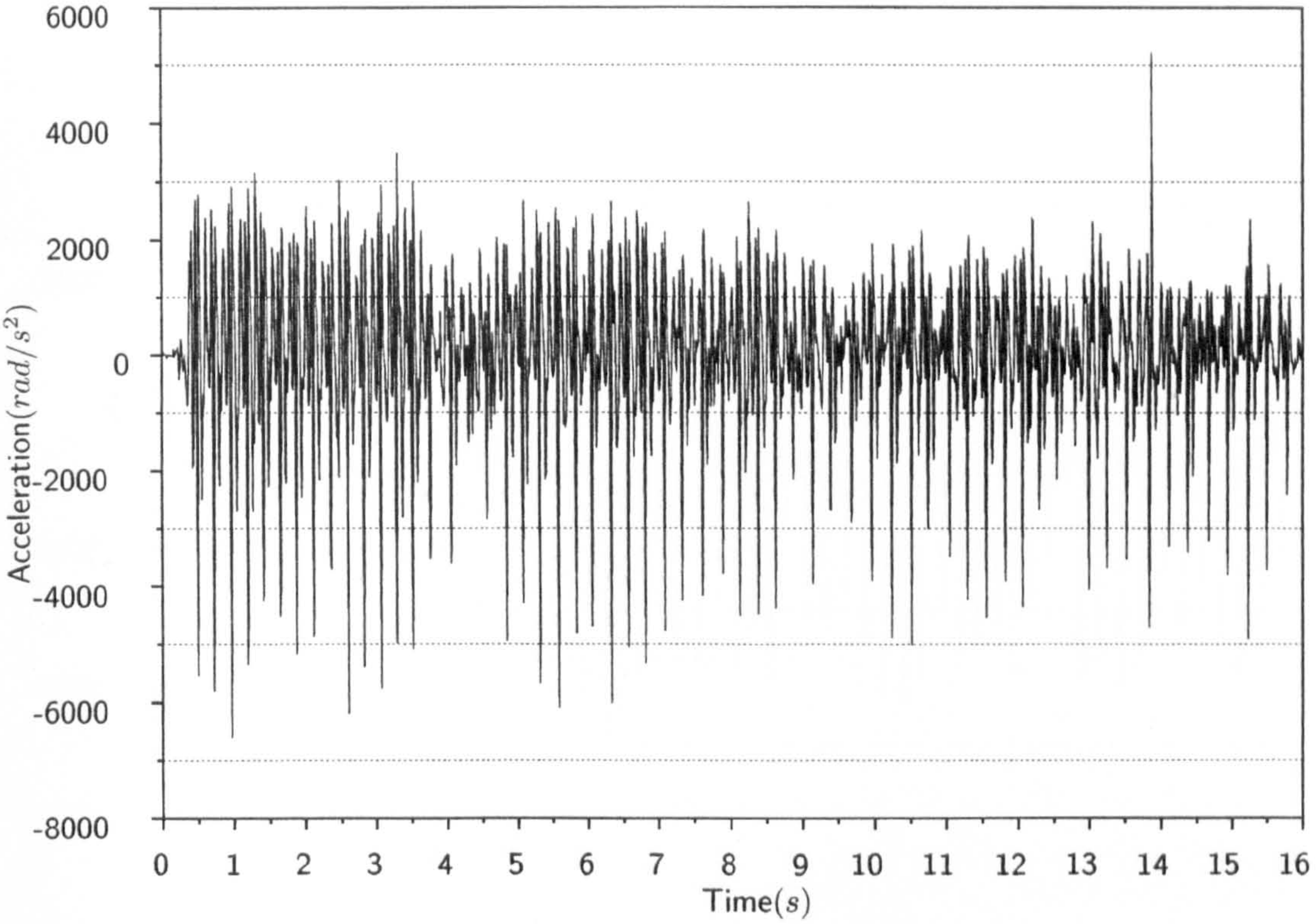

Figure D.3: Max rms acceleration, Model 3

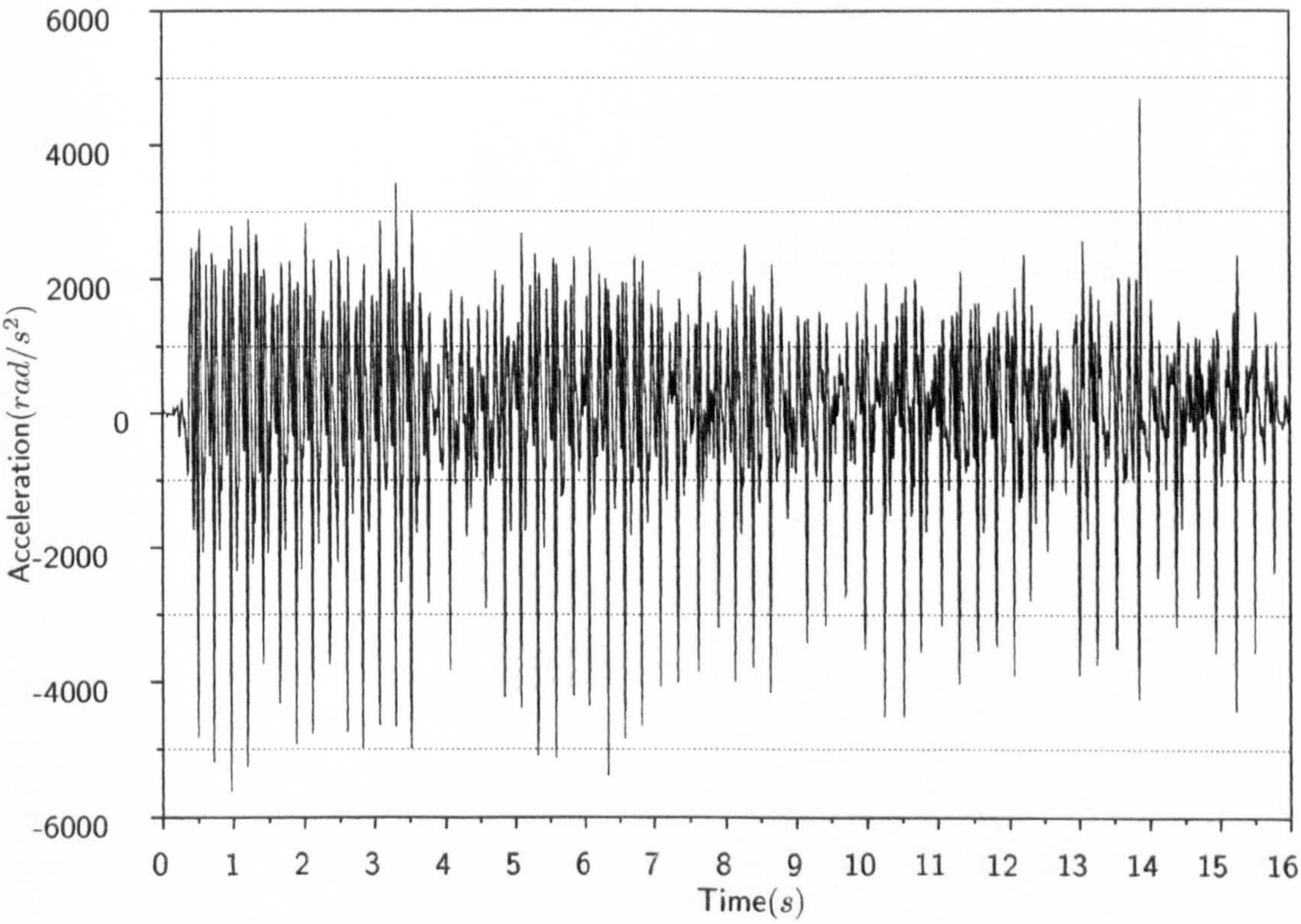

Figure D.4: Max rms acceleration, Model 4

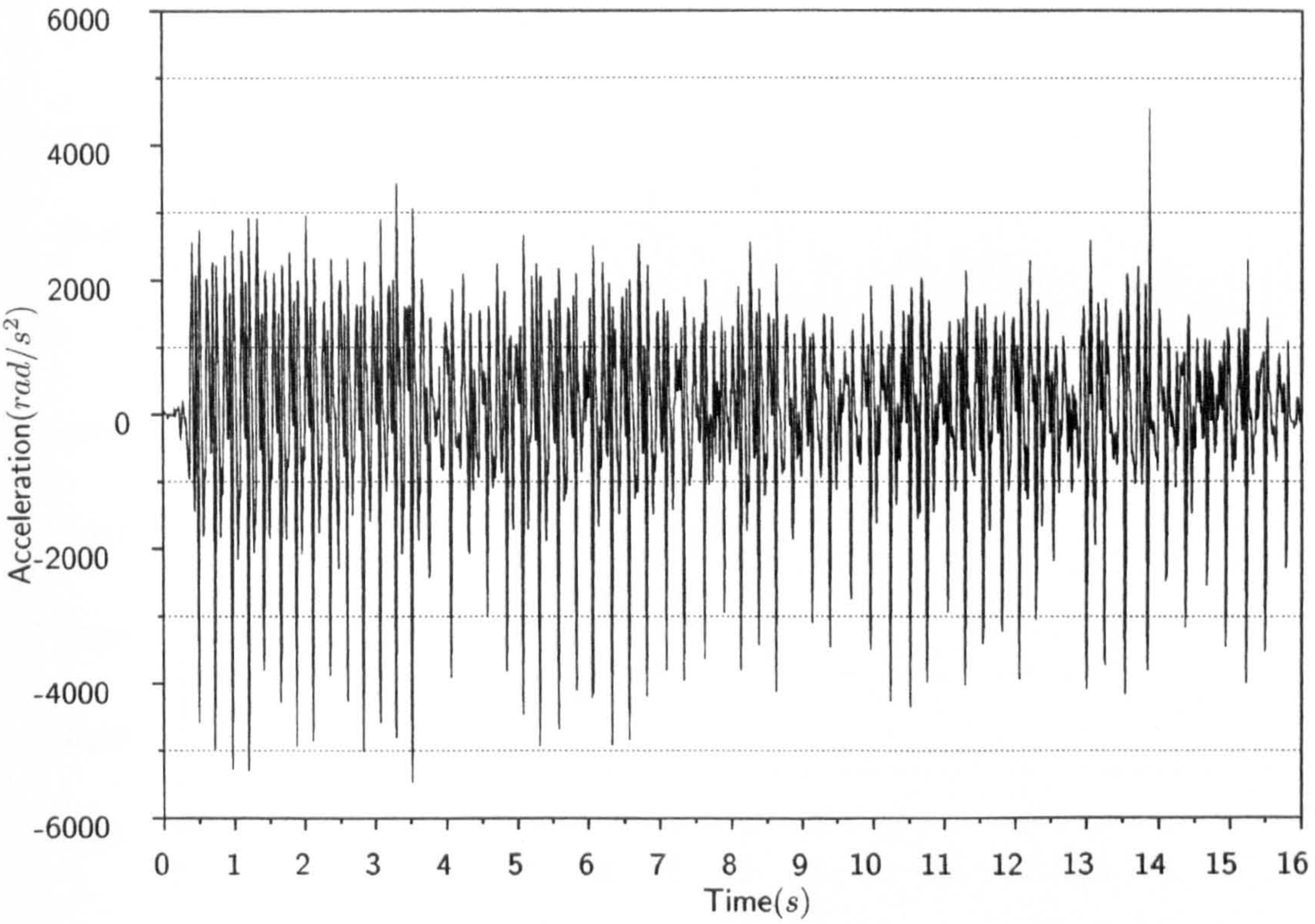

Figure D.5: Max rms acceleration, Model 5

Figure D.6: Max rms acceleration, Model 6

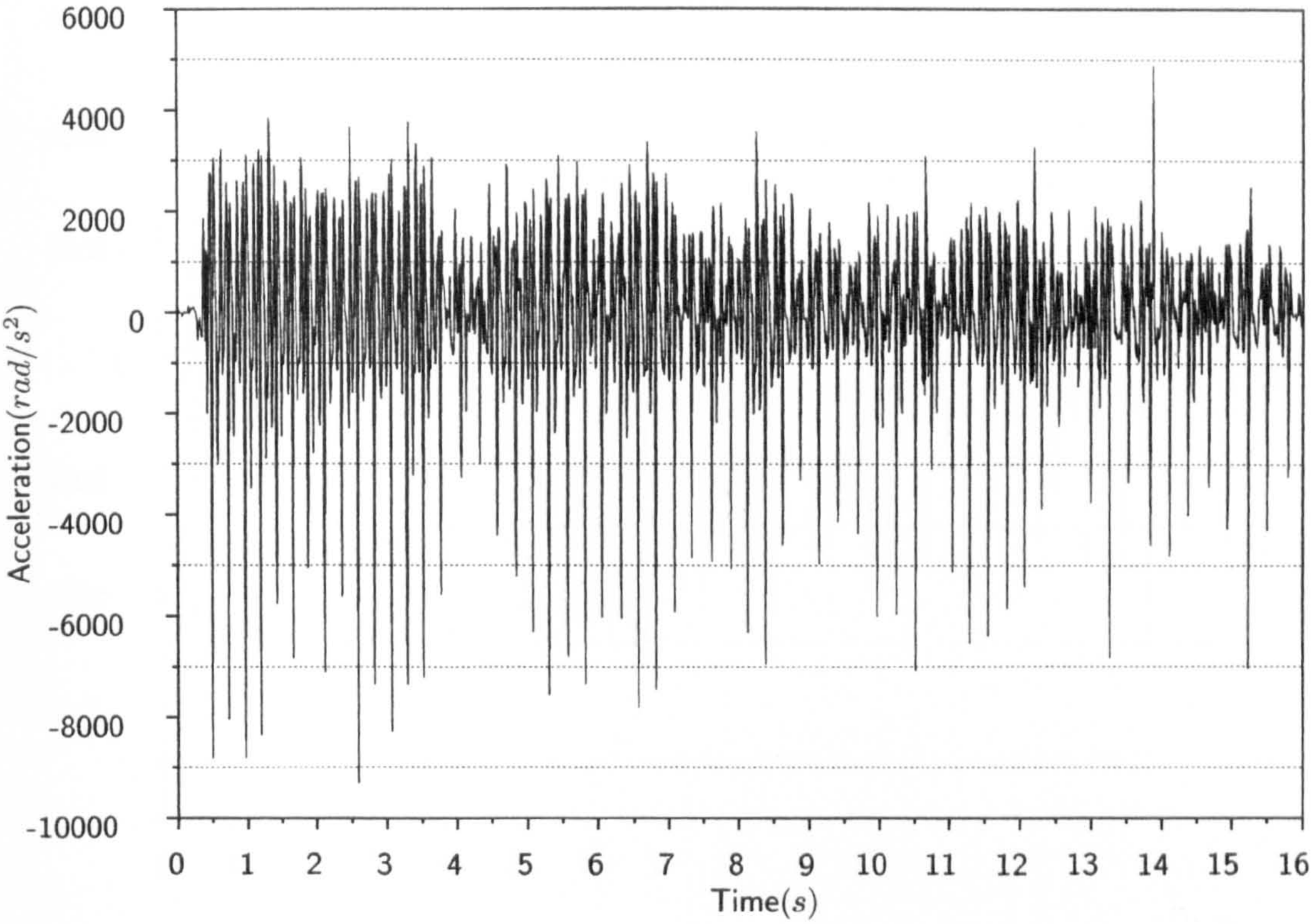

Figure D.7: Max rms acceleration, Model 7

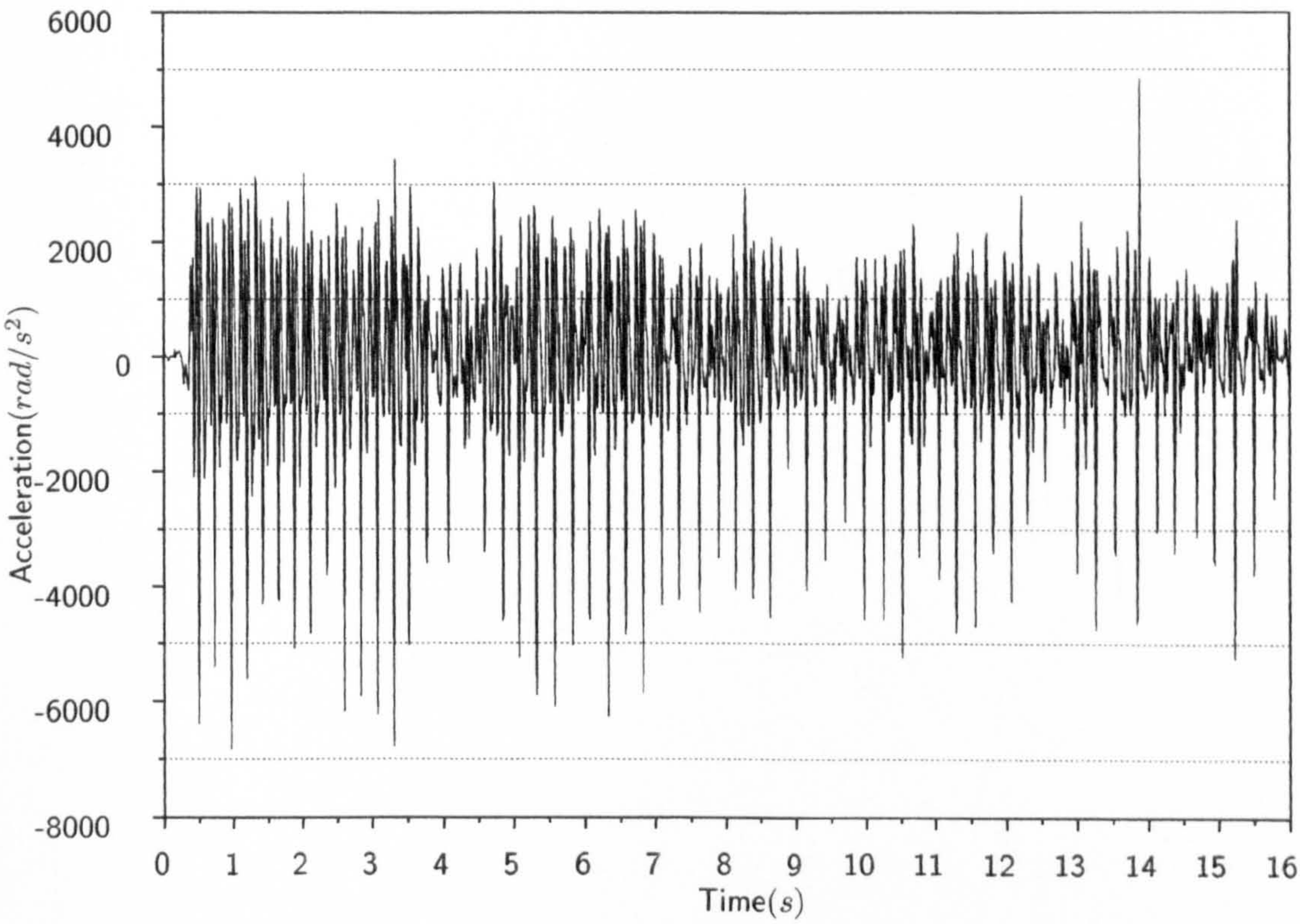

Figure D.8: Max rms acceleration, Model 8

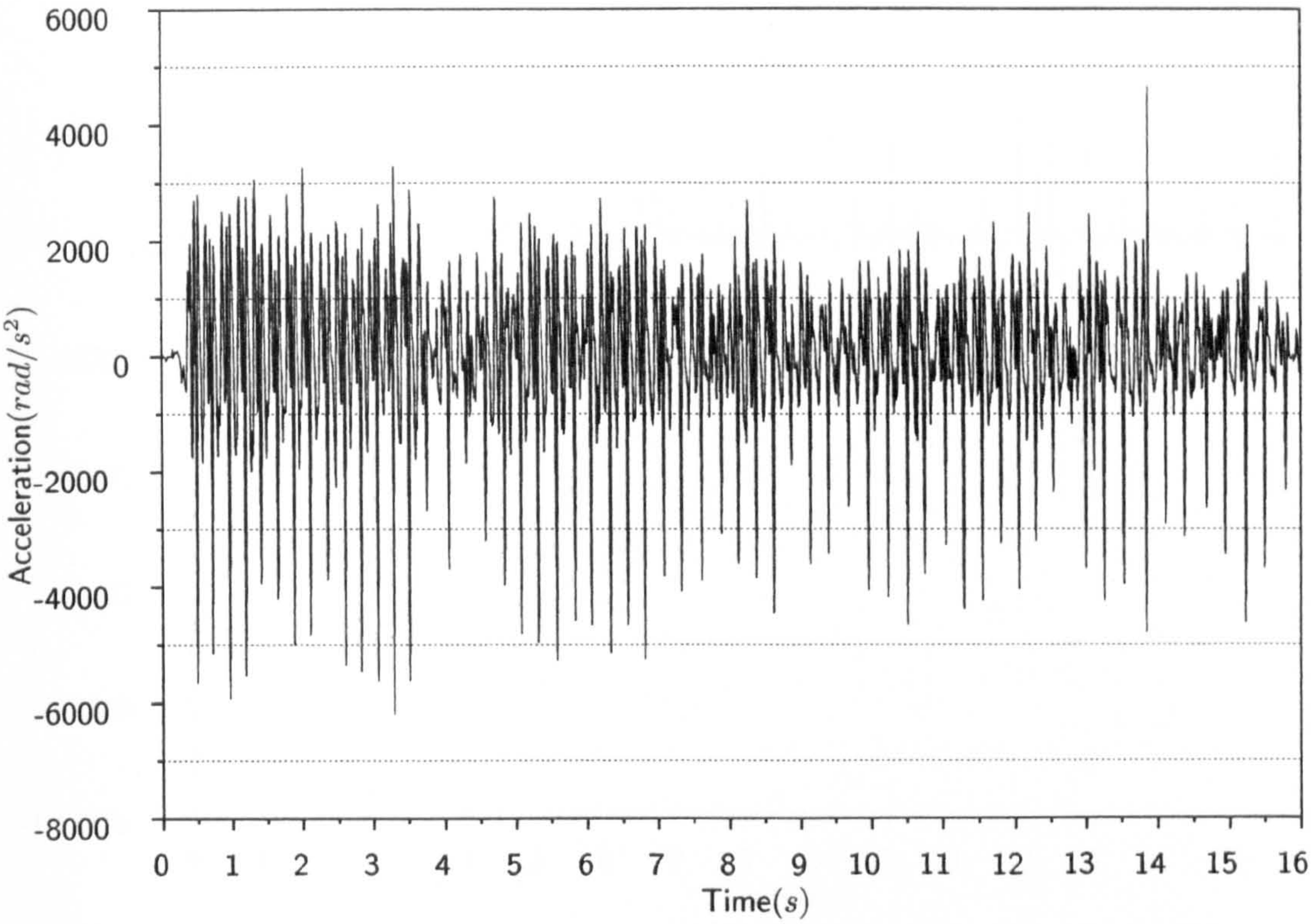

Figure D.9: Max rms acceleration, Model 9

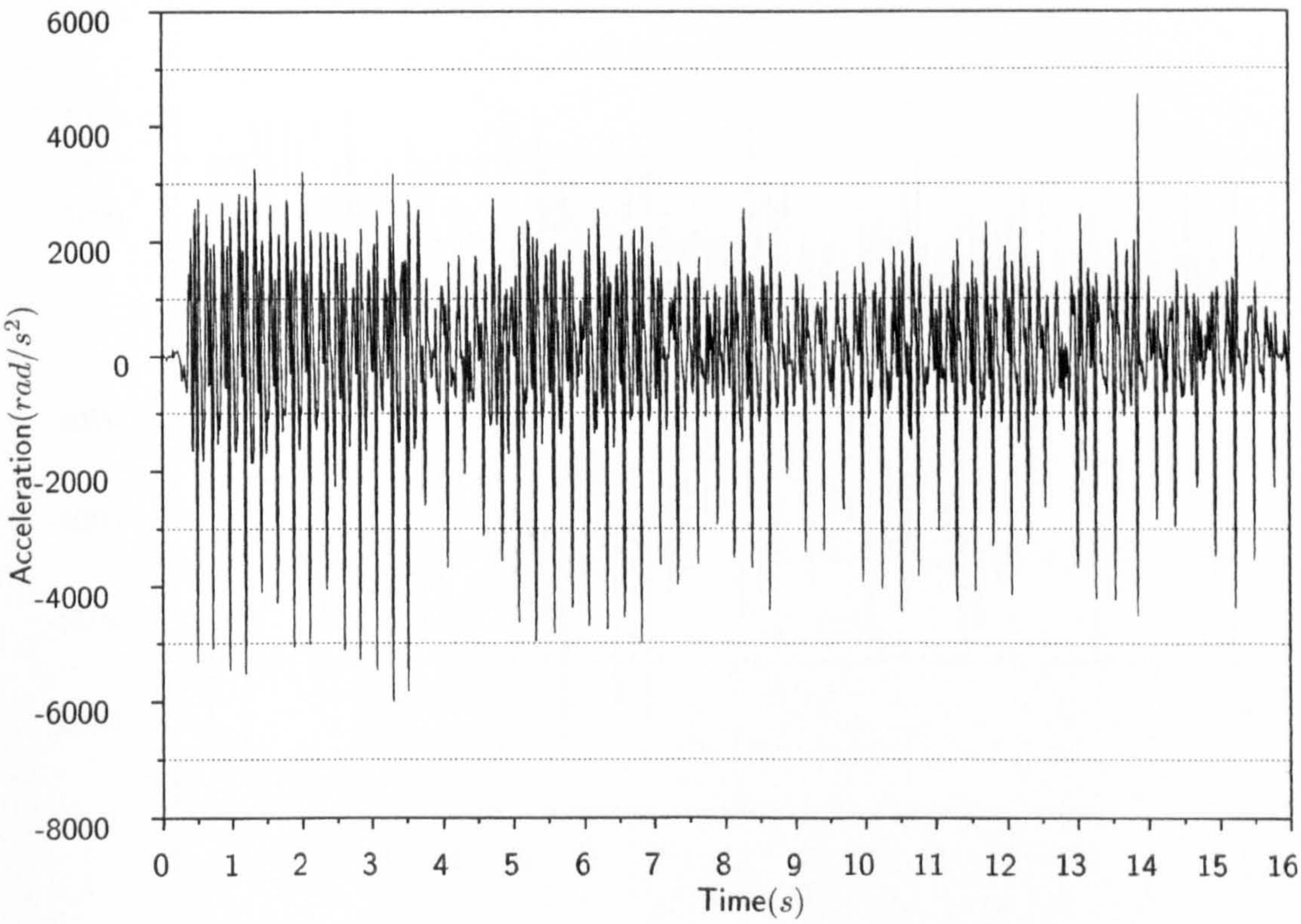

Figure D.10: Max rms acceleration, Model 10

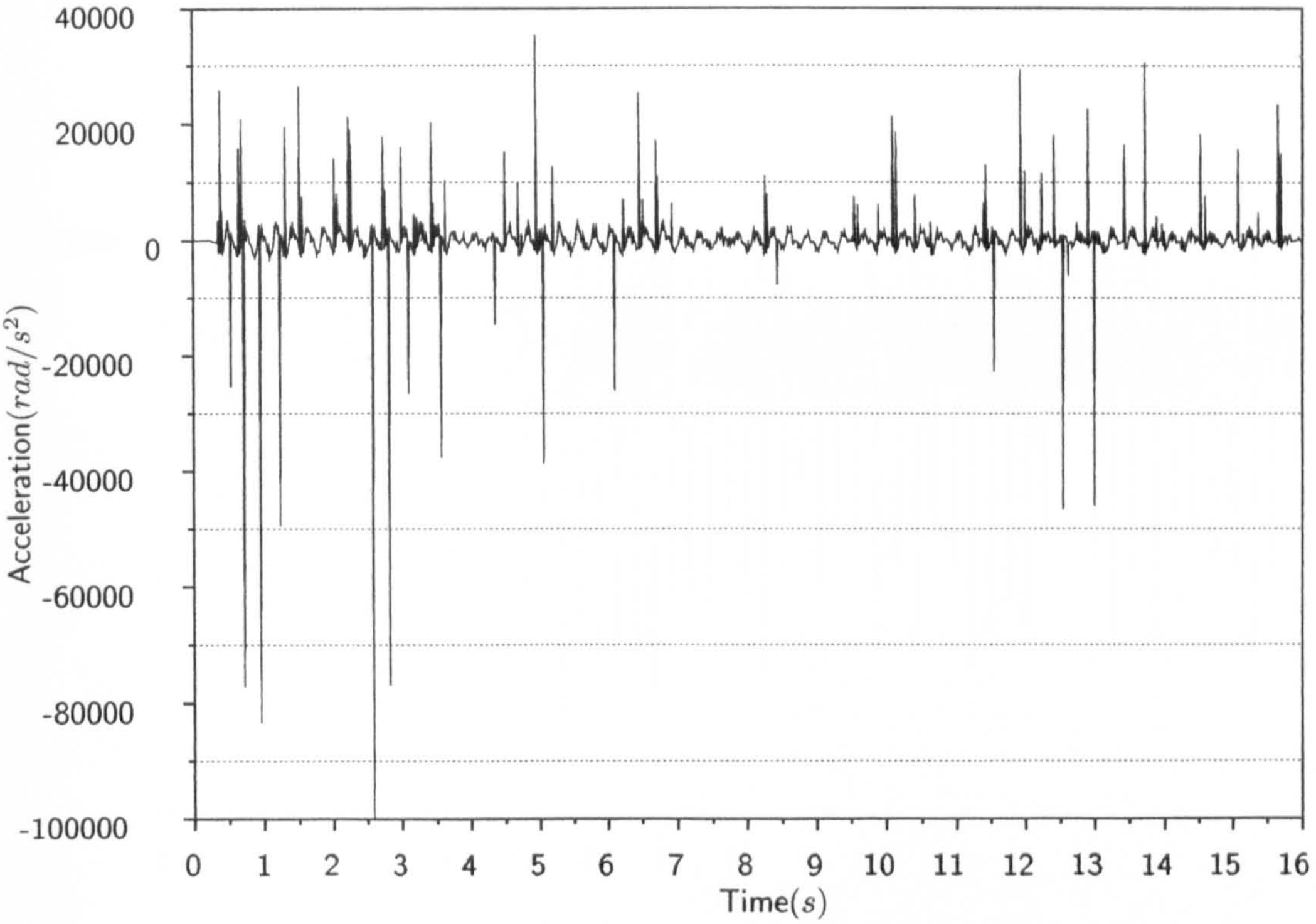

Figure D.11: Max rms acceleration, Model 11

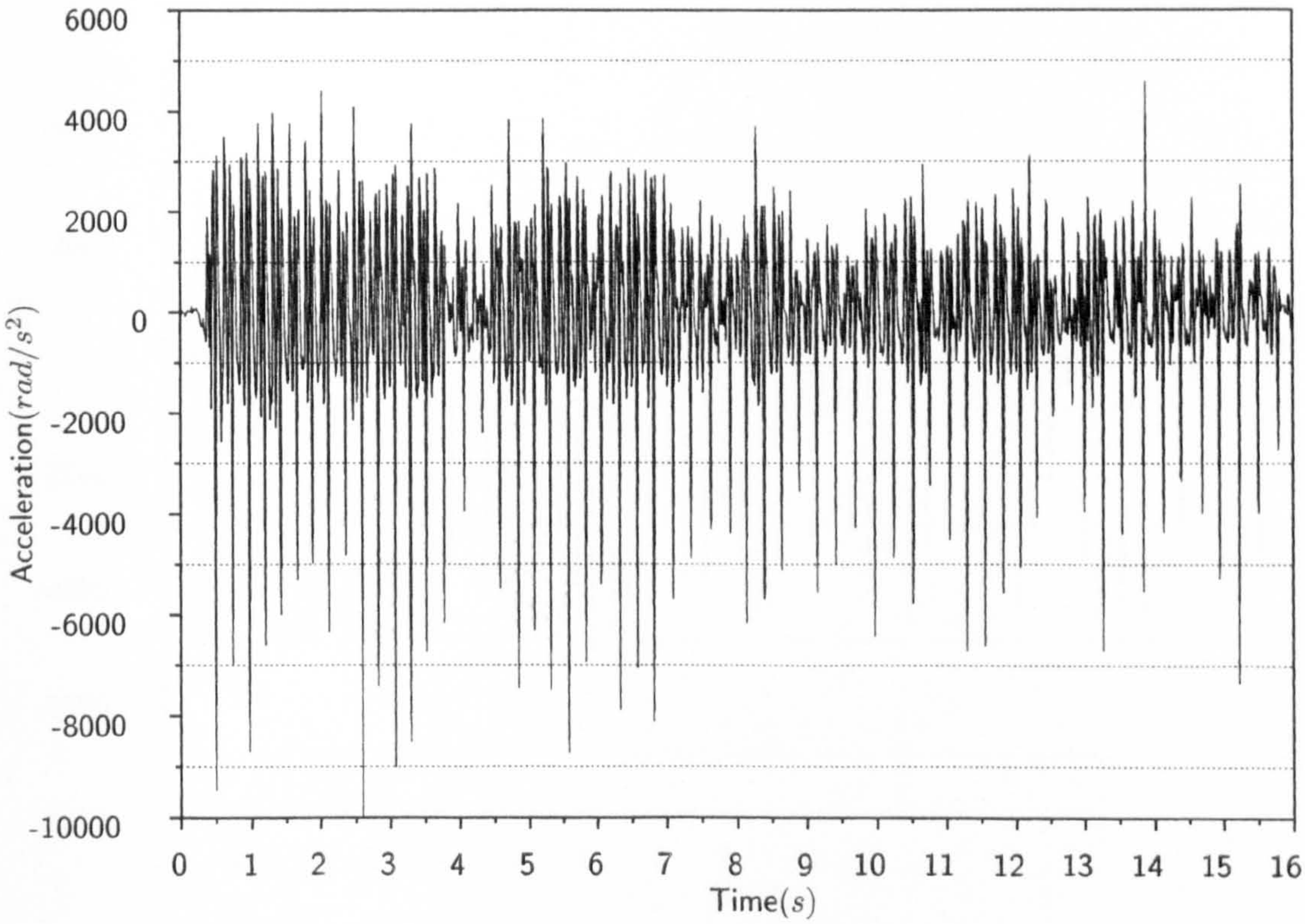

Figure D.12: Max rms acceleration, Model 12

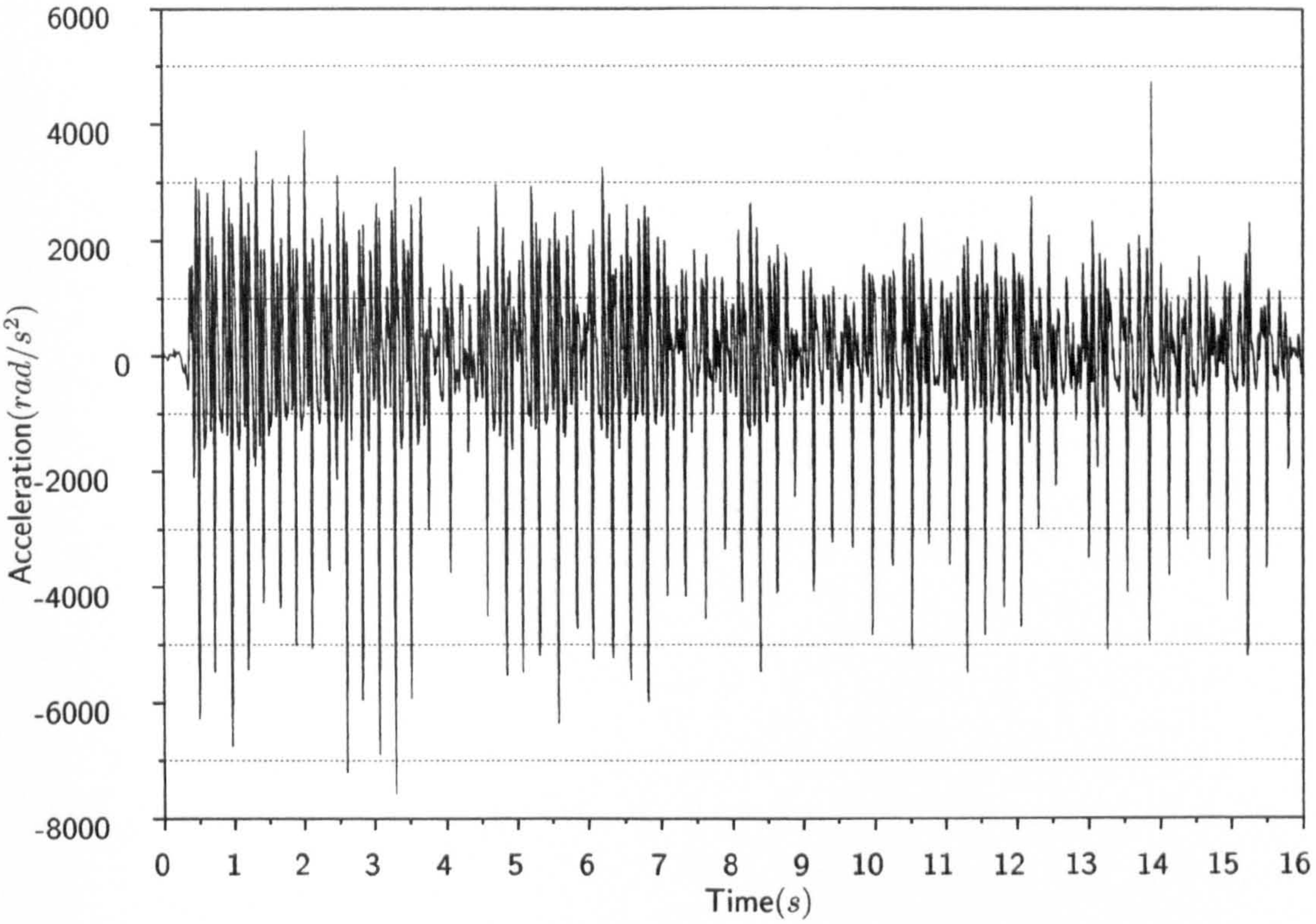

Figure D.13: Max rms acceleration, Model 13

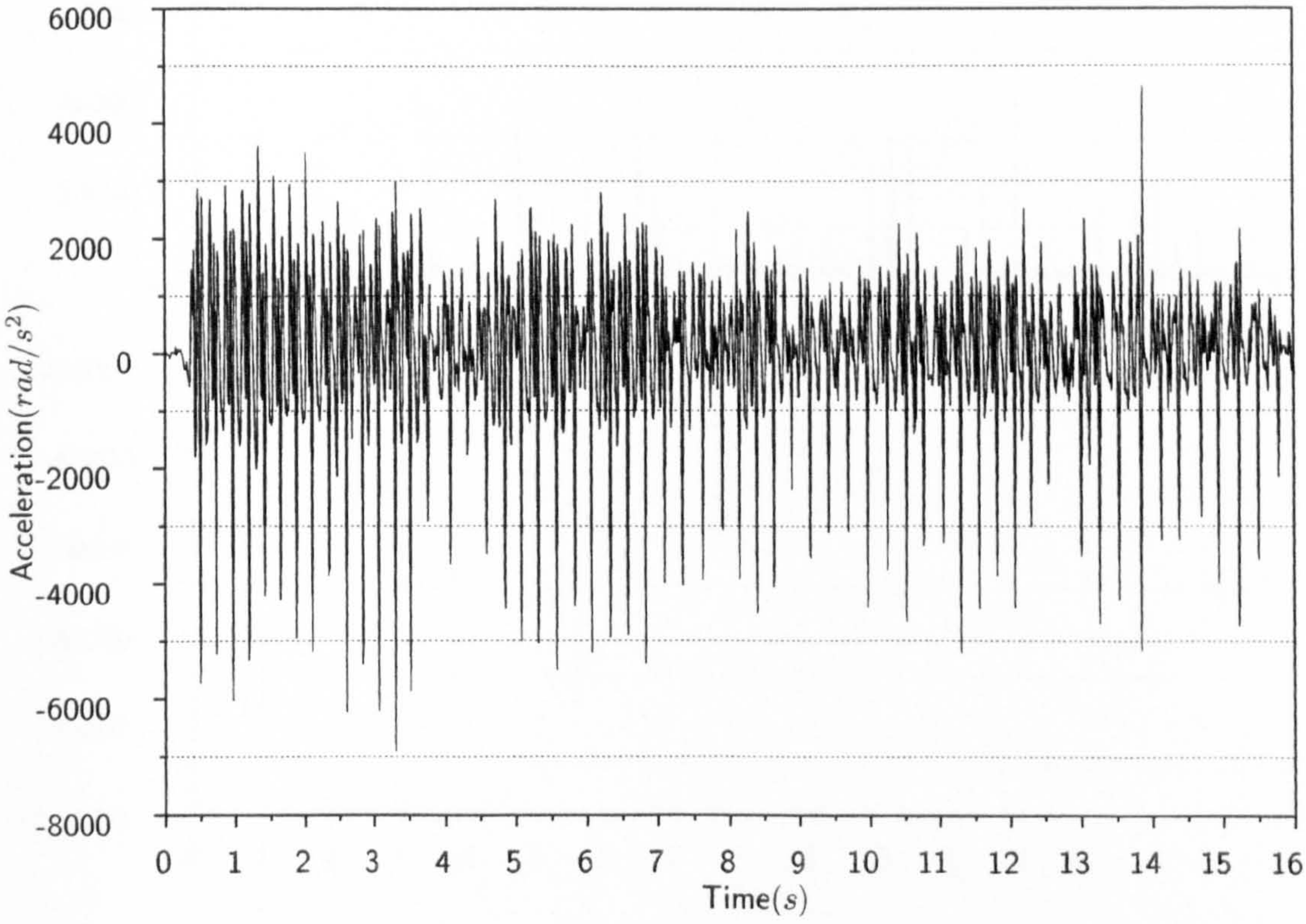

Figure D.14: Max rms acceleration, Model 14

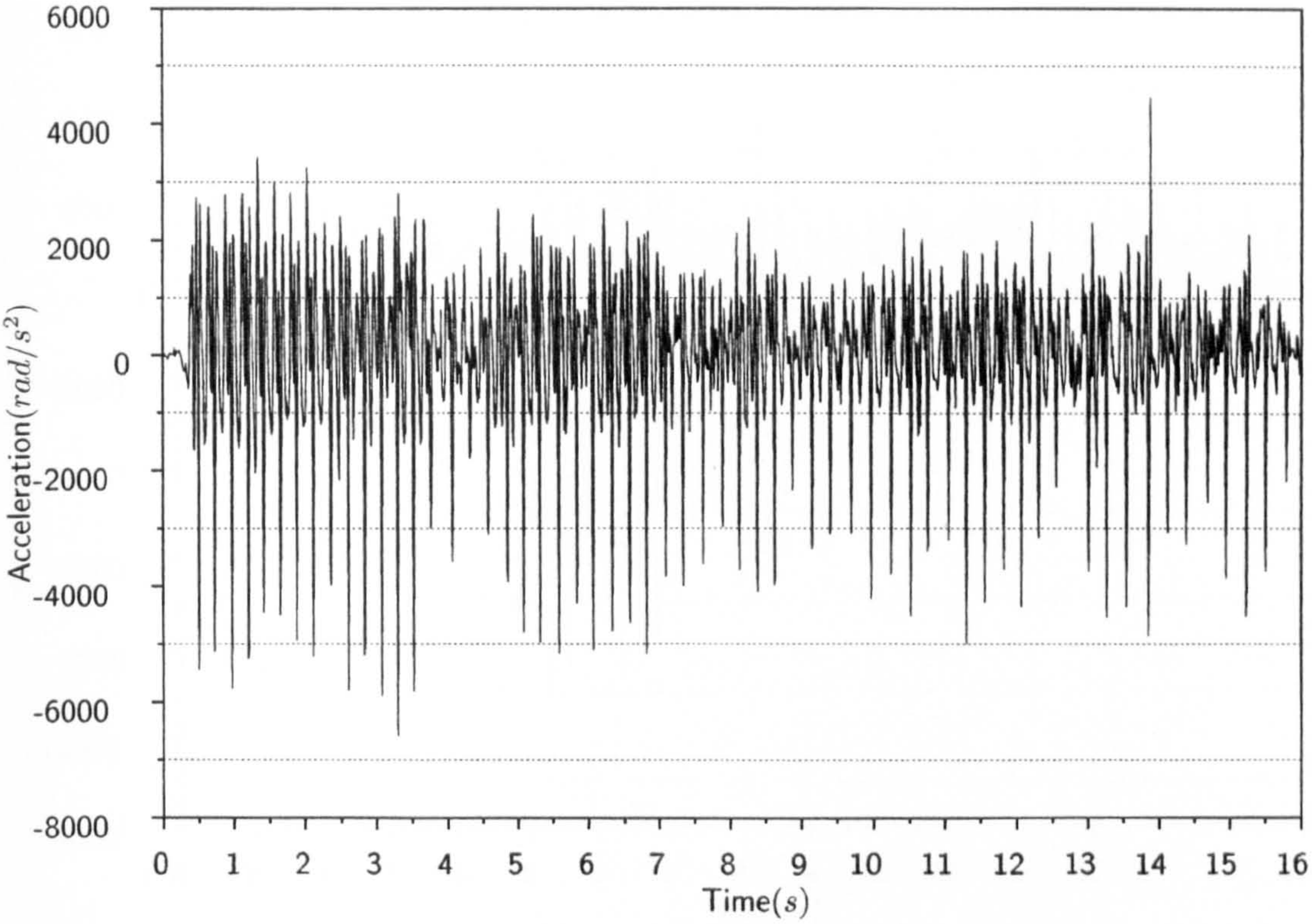

Figure D.15: Max rms acceleration, Model 15

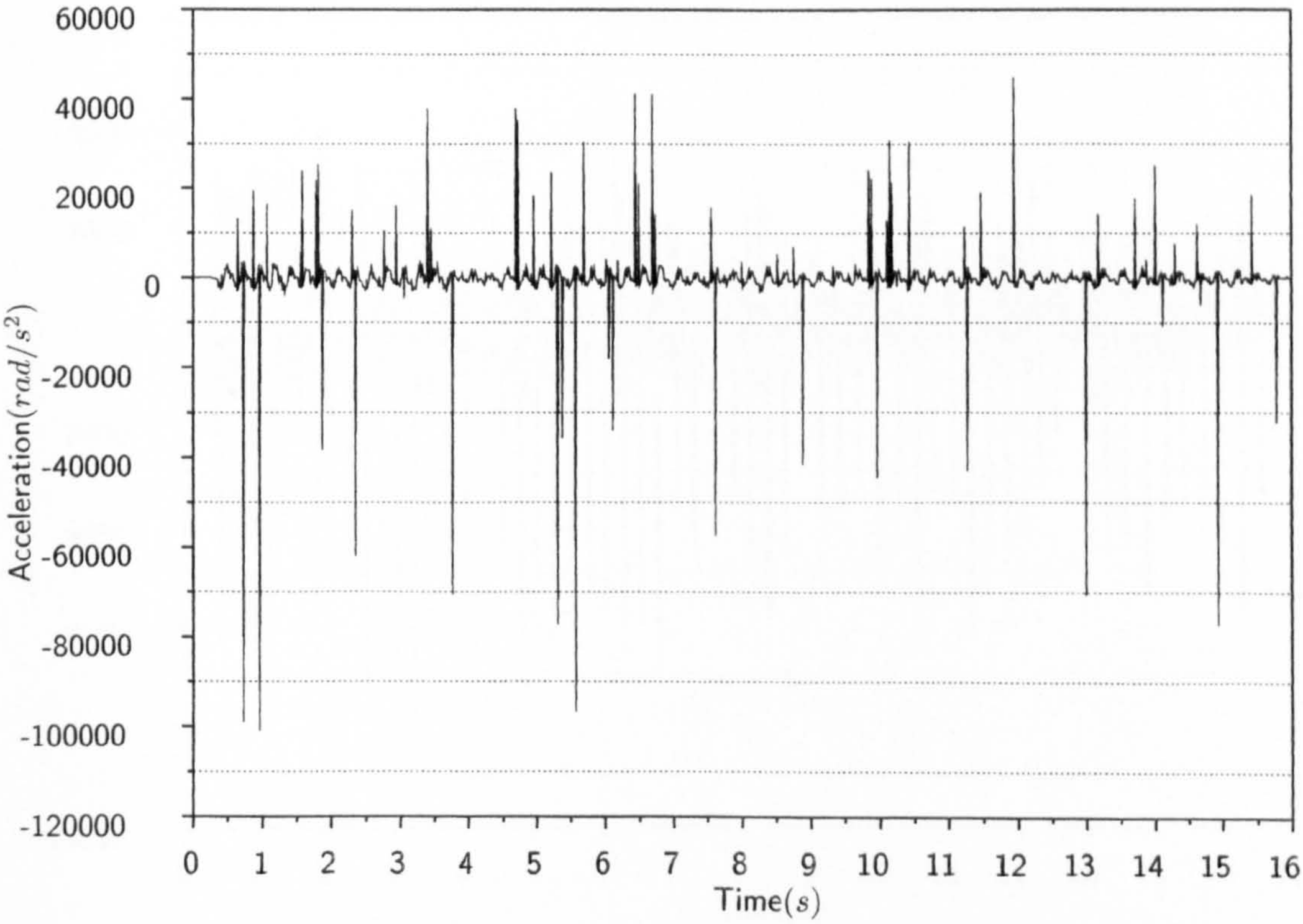

Figure D.16: Max rms acceleration, Model 16

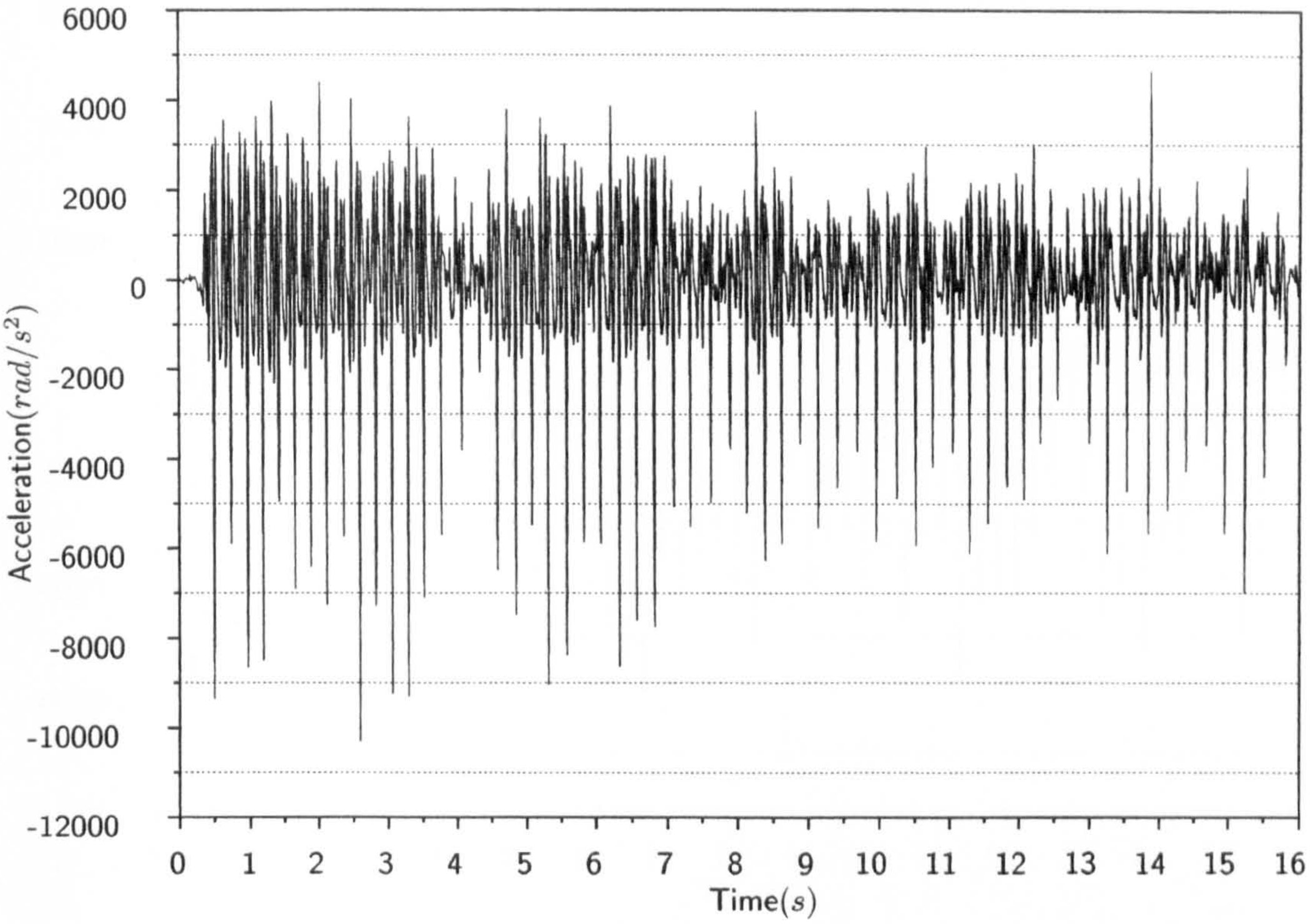

Figure D.17: Max rms acceleration, Model 17

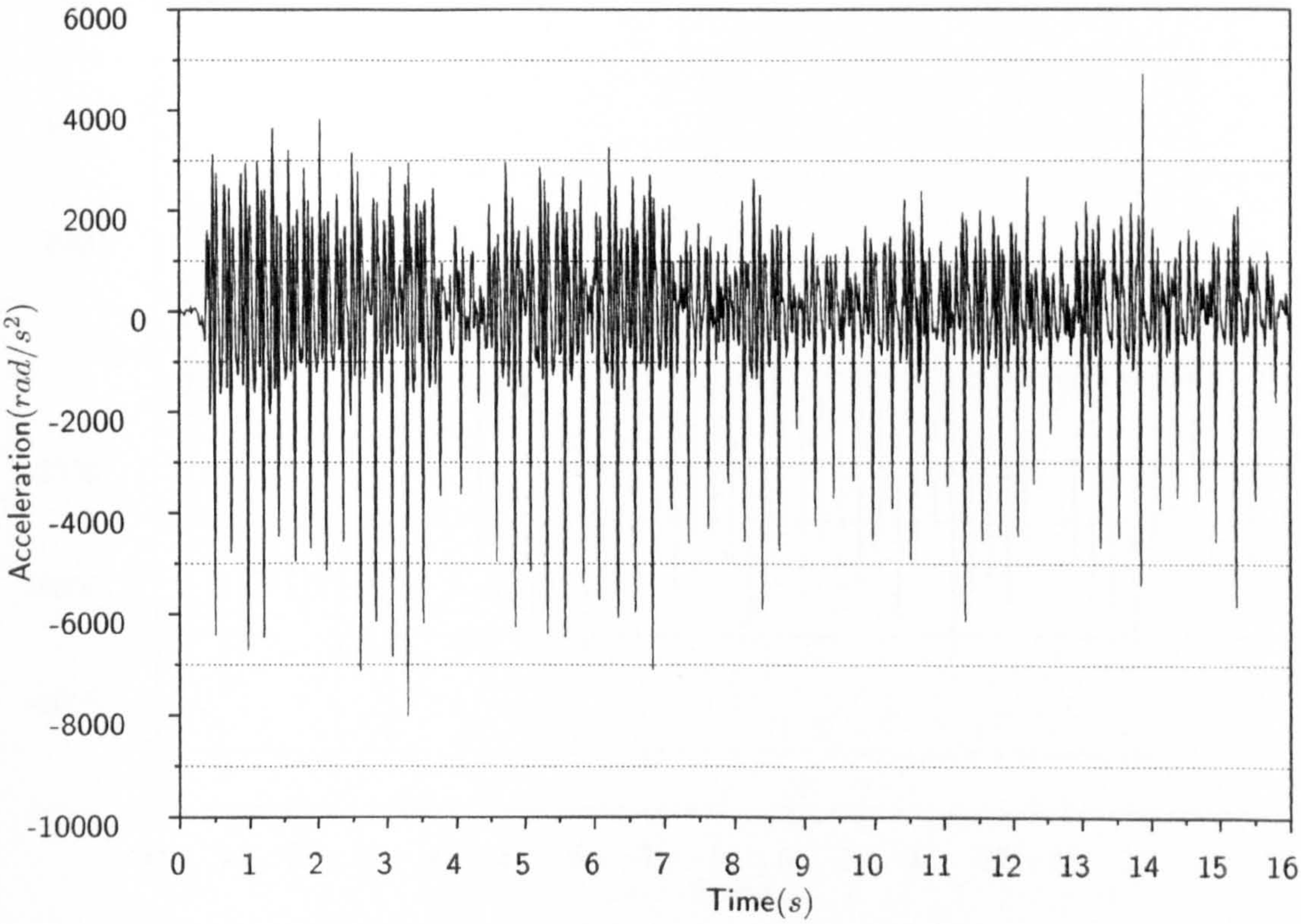

Figure D.18: Max rms acceleration, Model 18

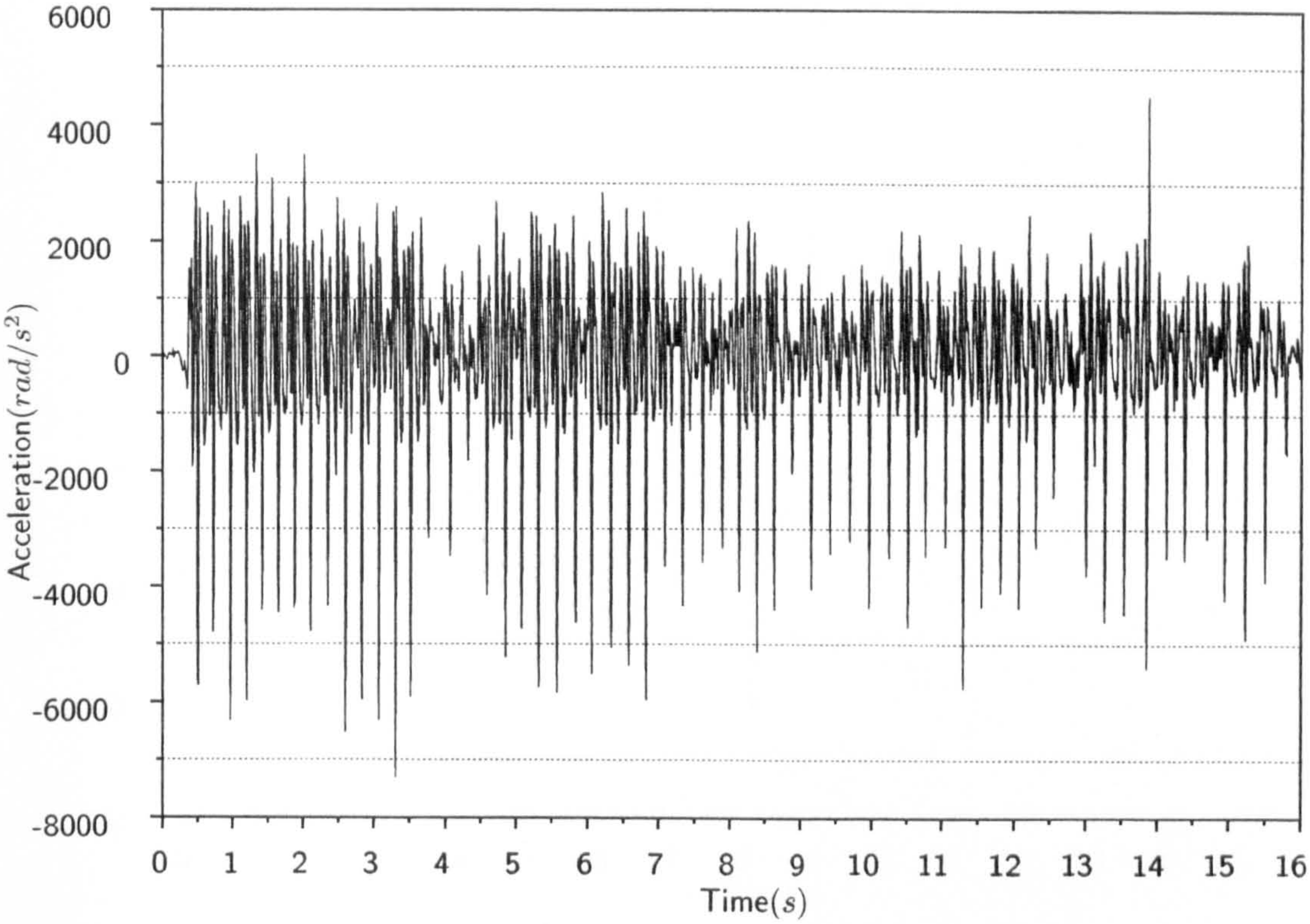

Figure D.19: Max rms acceleration, Model 19

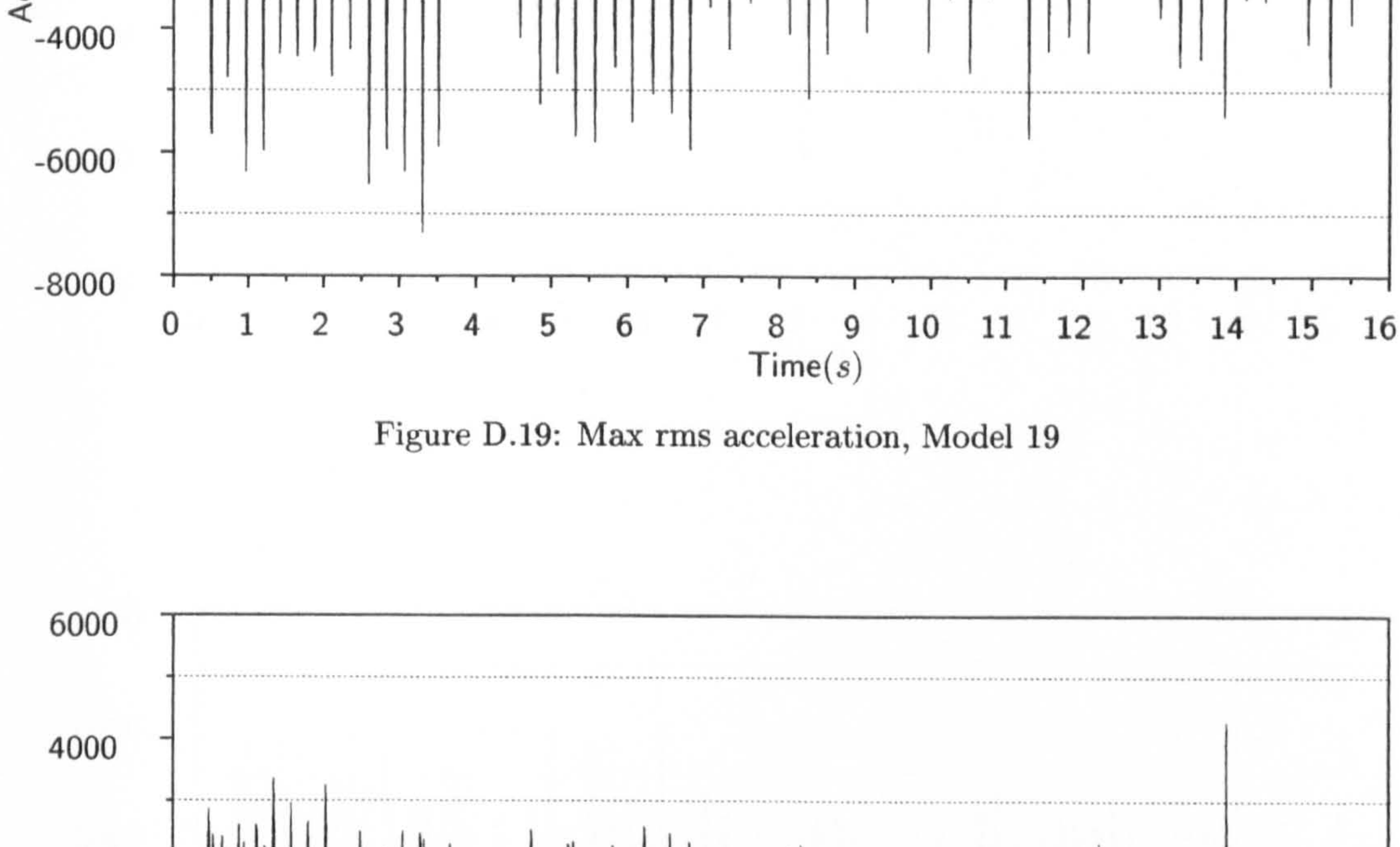

Figure D.20: Max rms acceleration, Model 20

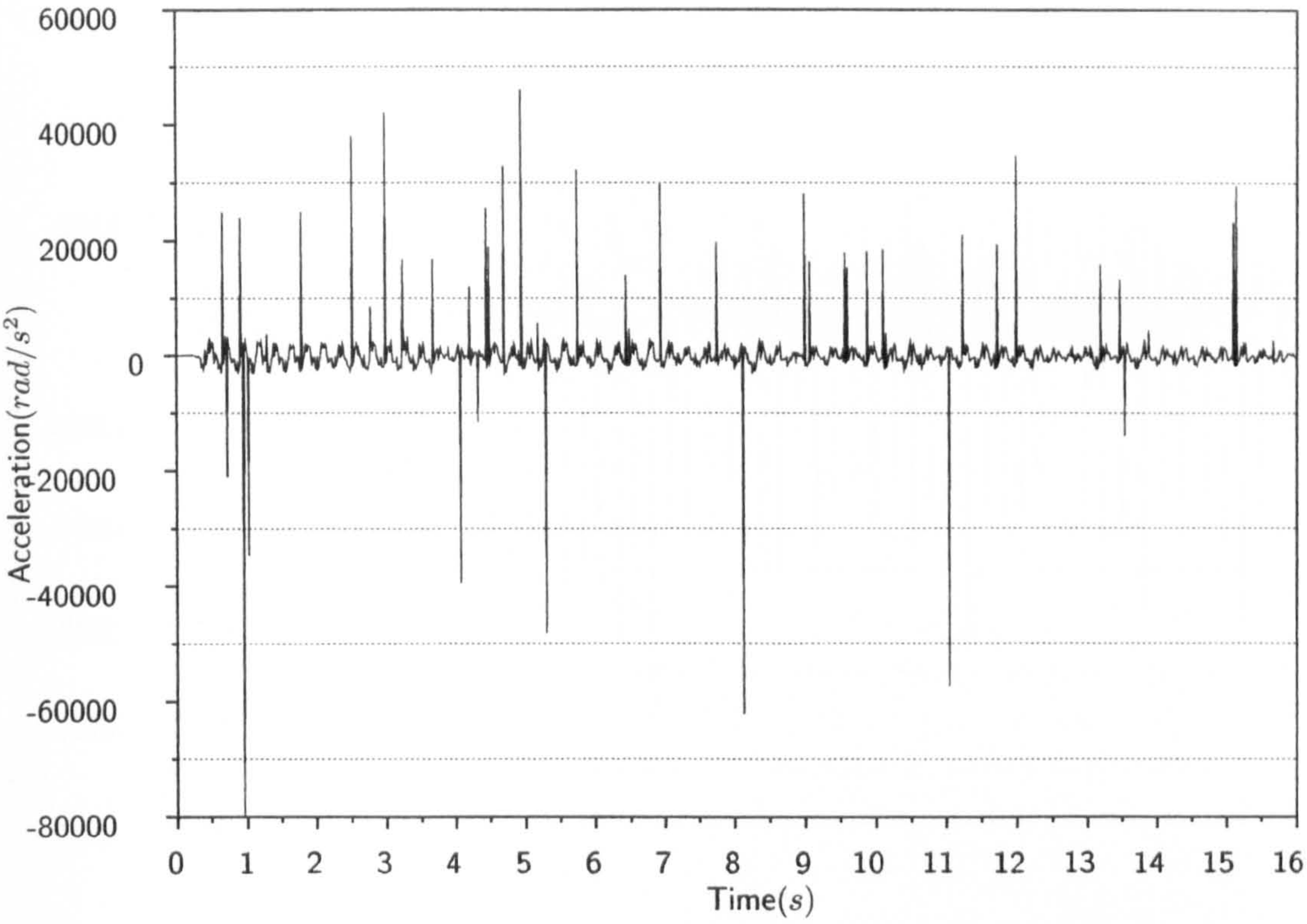

Figure D.21: Max rms acceleration, Model 21

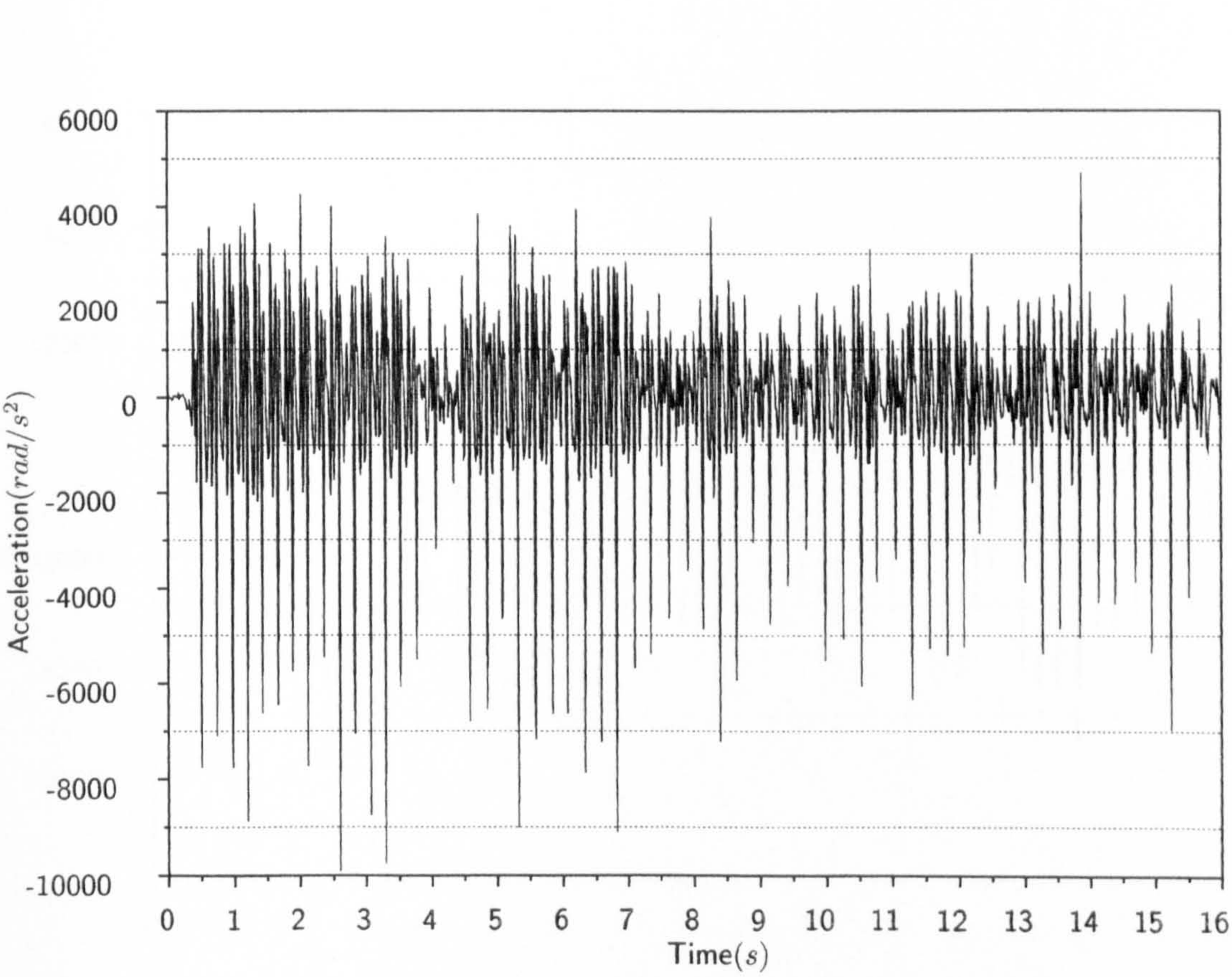

Figure D.22: Max rms acceleration, Model 22

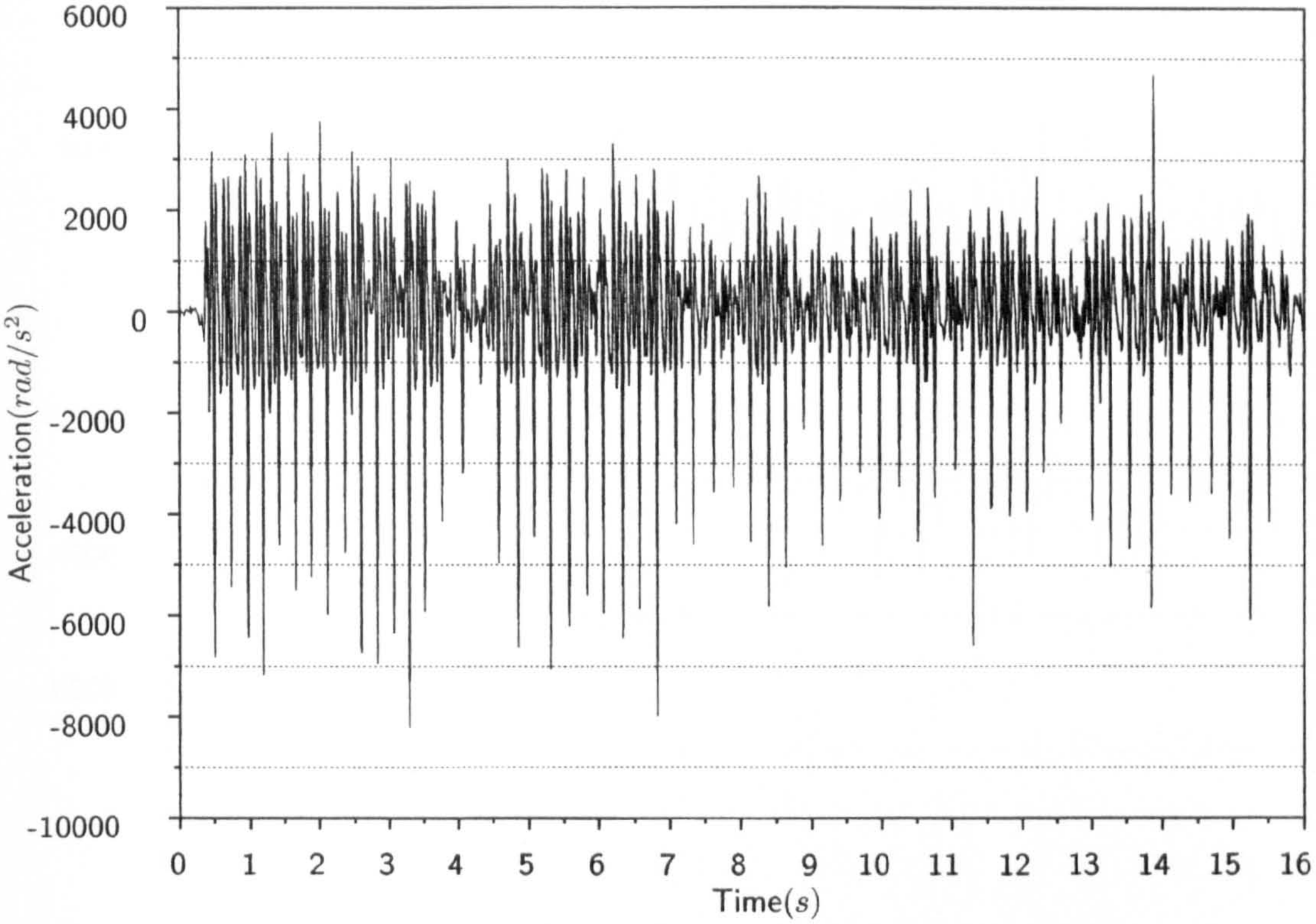

Figure D.23: Max rms acceleration, Model 23

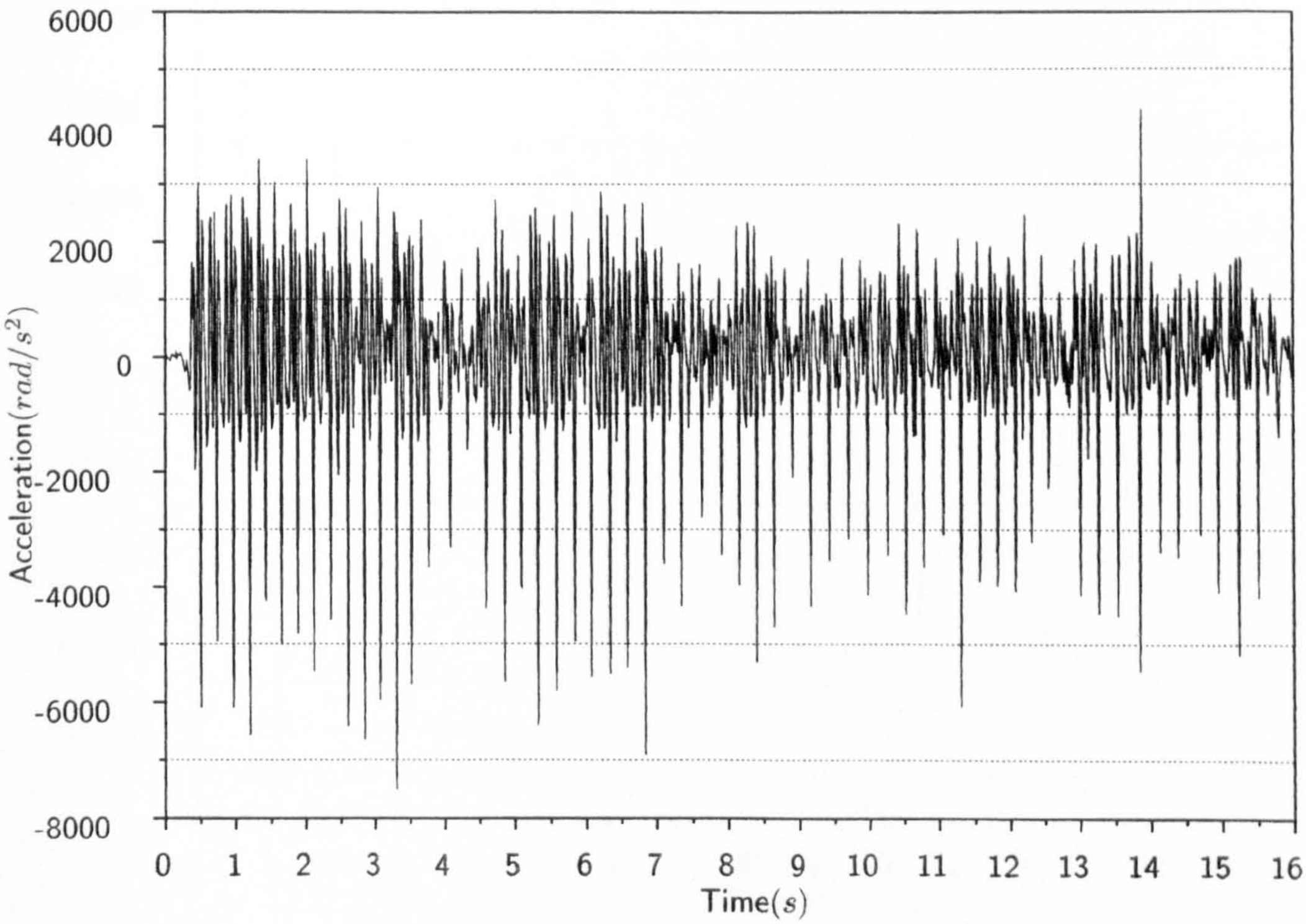

Figure D.24: Max rms acceleration, Model 24

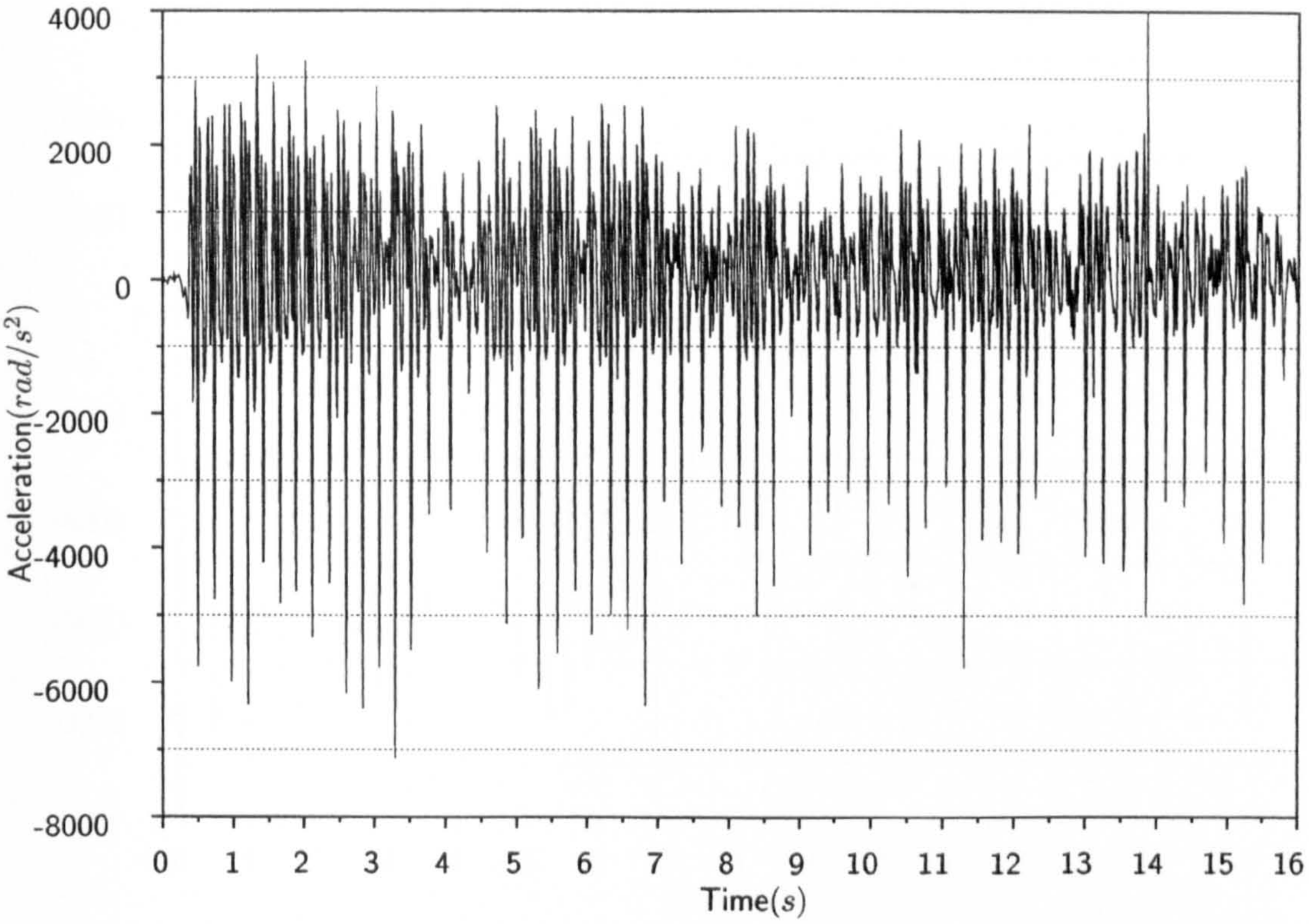

Figure D.25: Max rms acceleration, Model 25

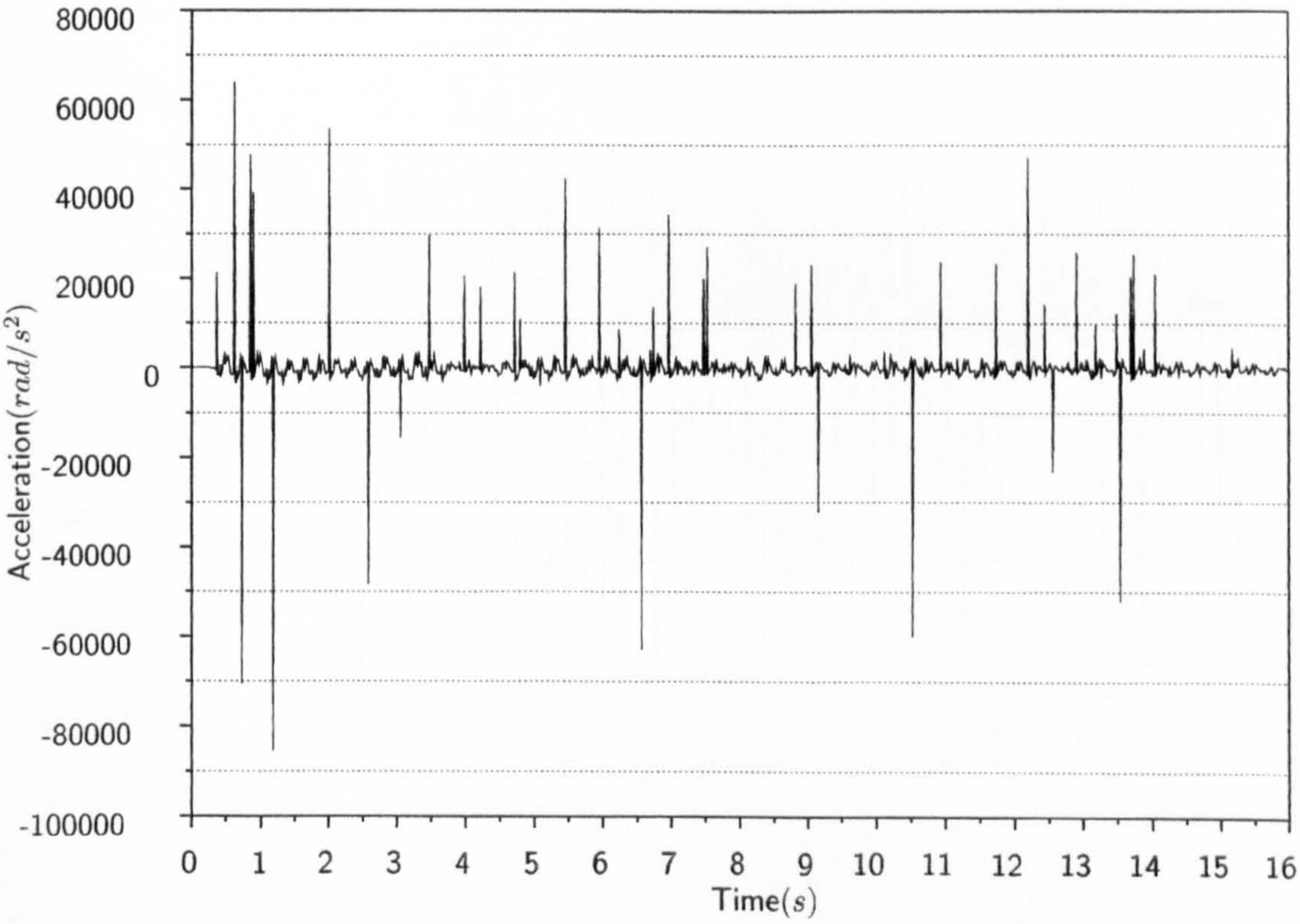

Figure D.26: Max rms acceleration, Model 26

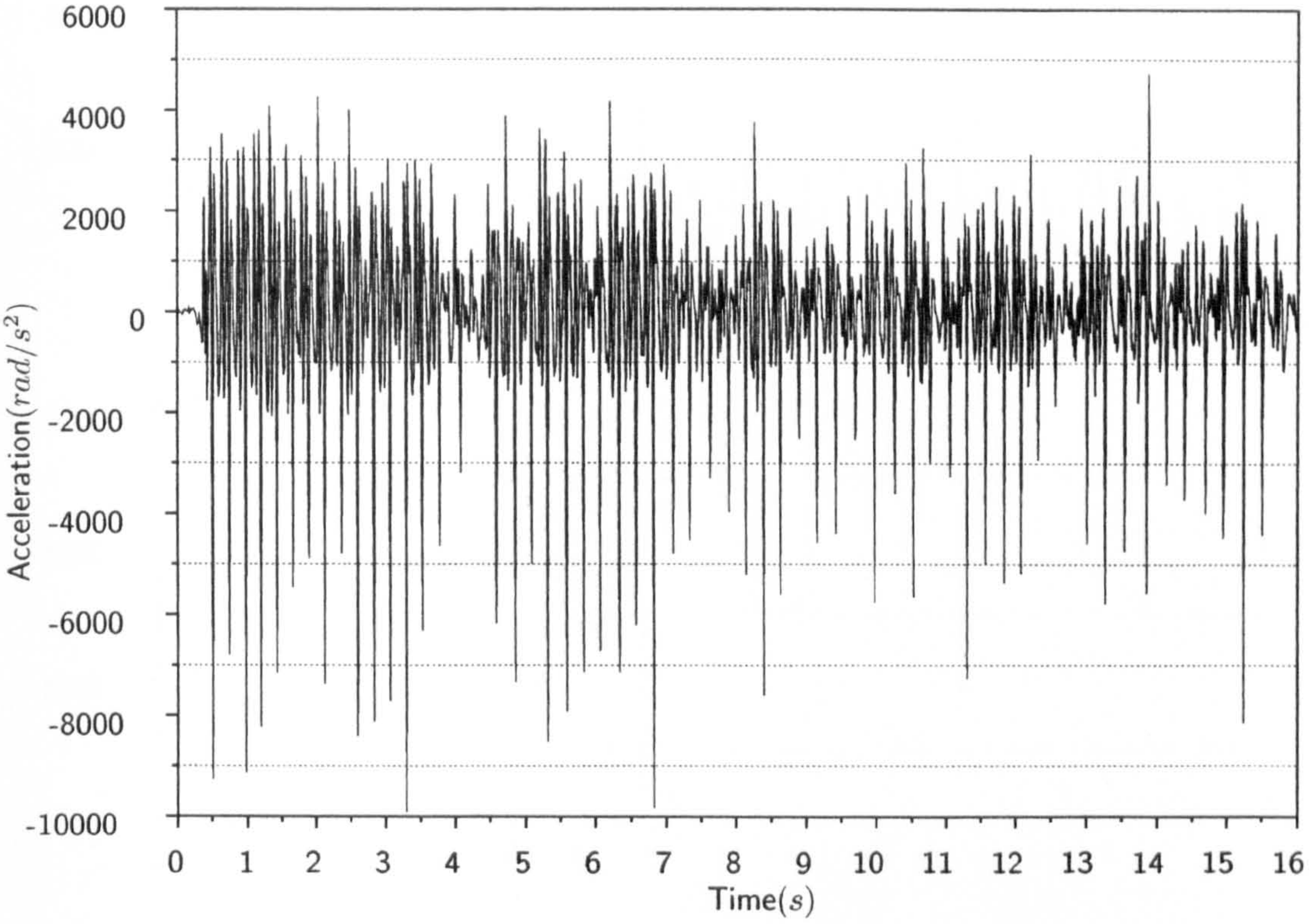

Figure D.27: Max rms acceleration, Model 27

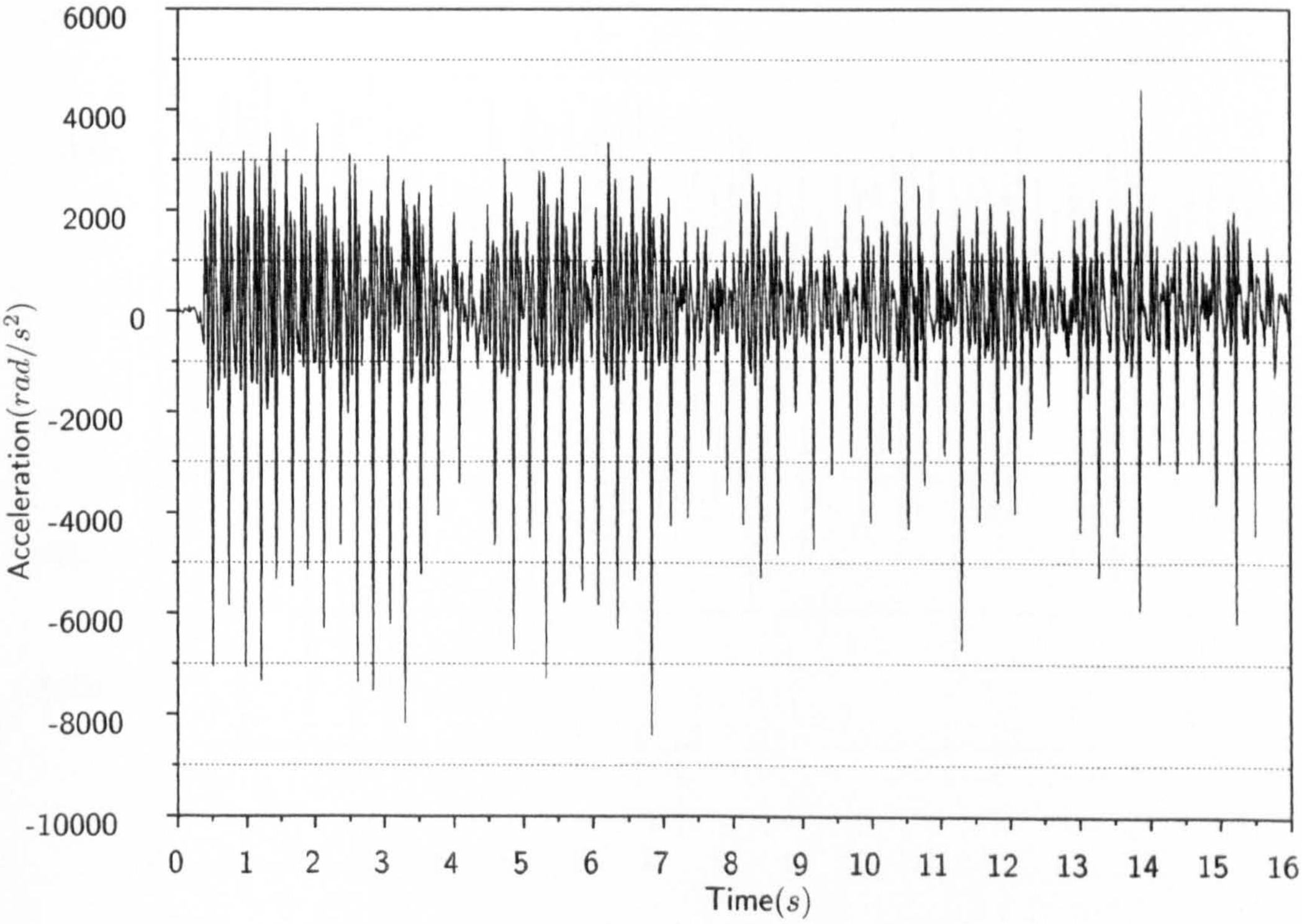

Figure D.28: Max rms acceleration, Model 28

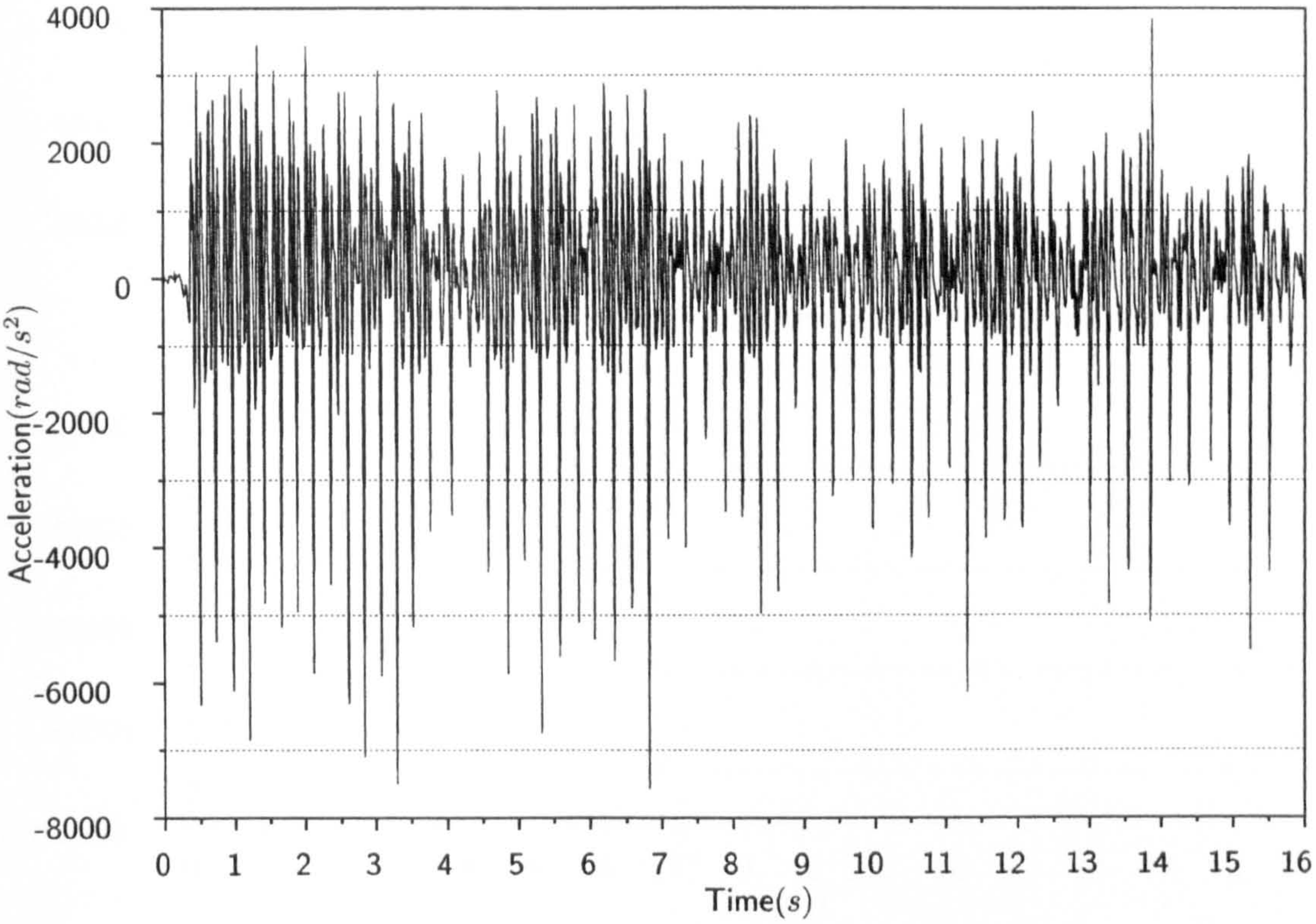

Figure D.29: Max rms acceleration, Model 29

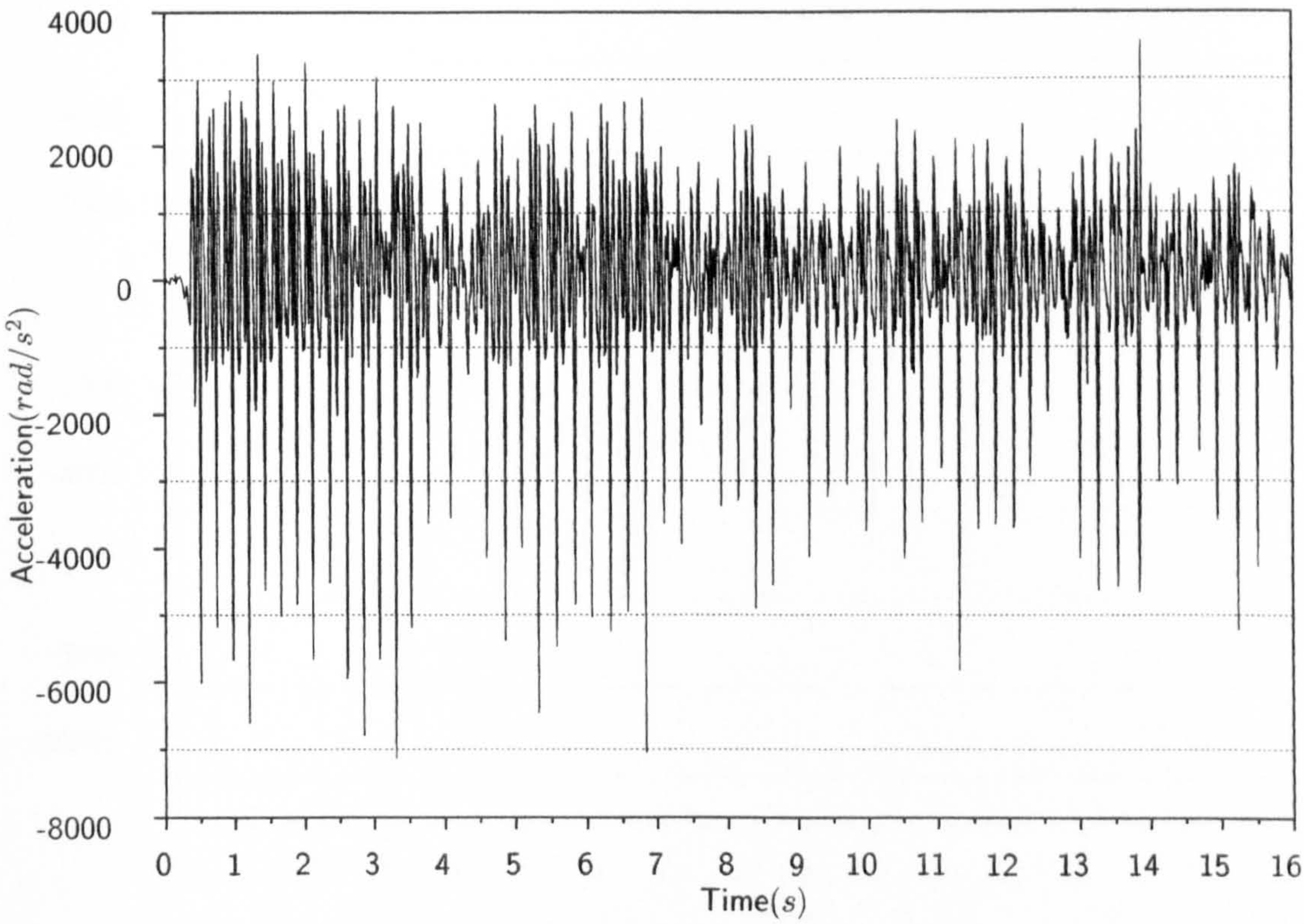

Figure D.30: Max rms acceleration, Model 30

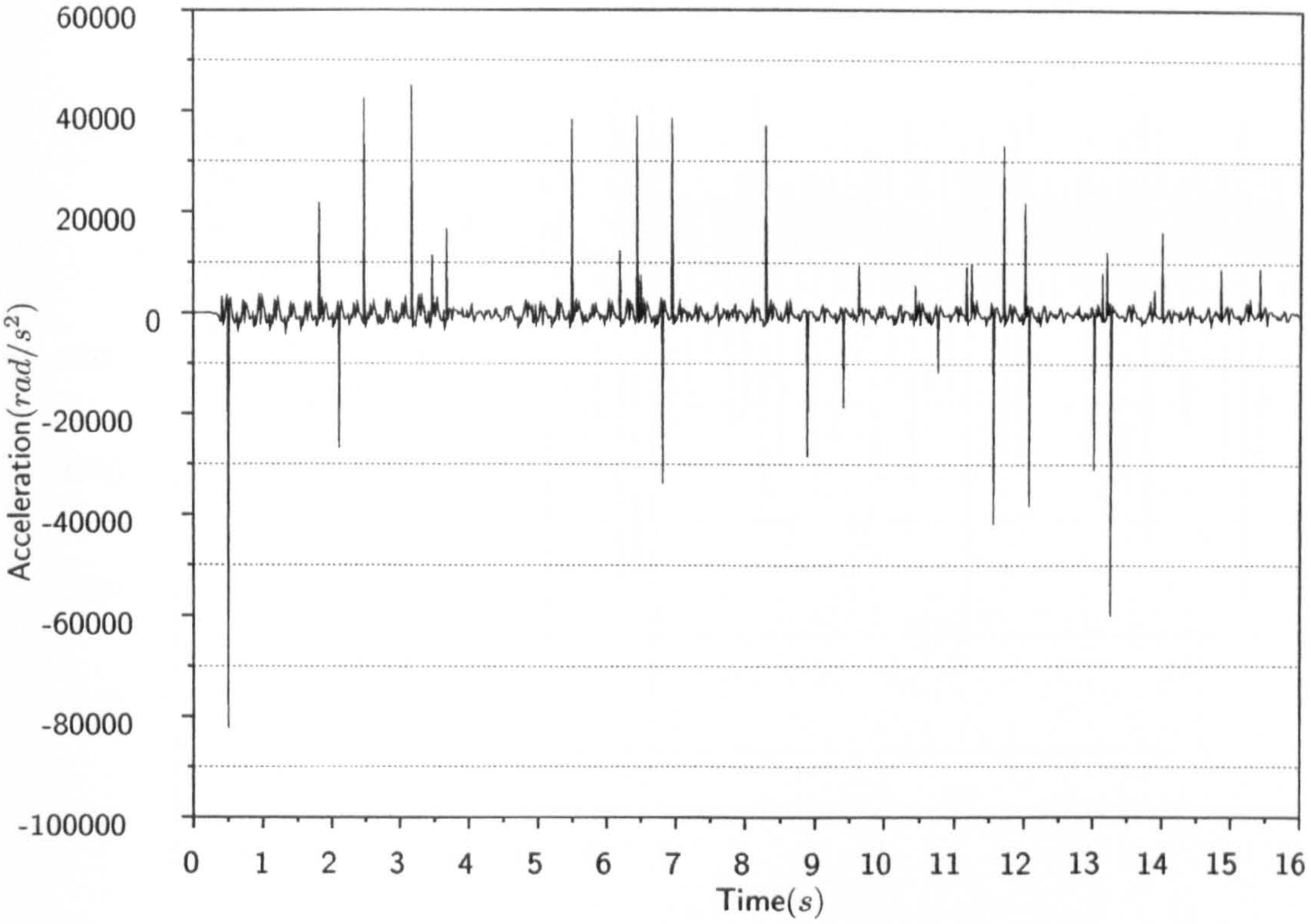

Figure D.31: Max rms acceleration, Model 31

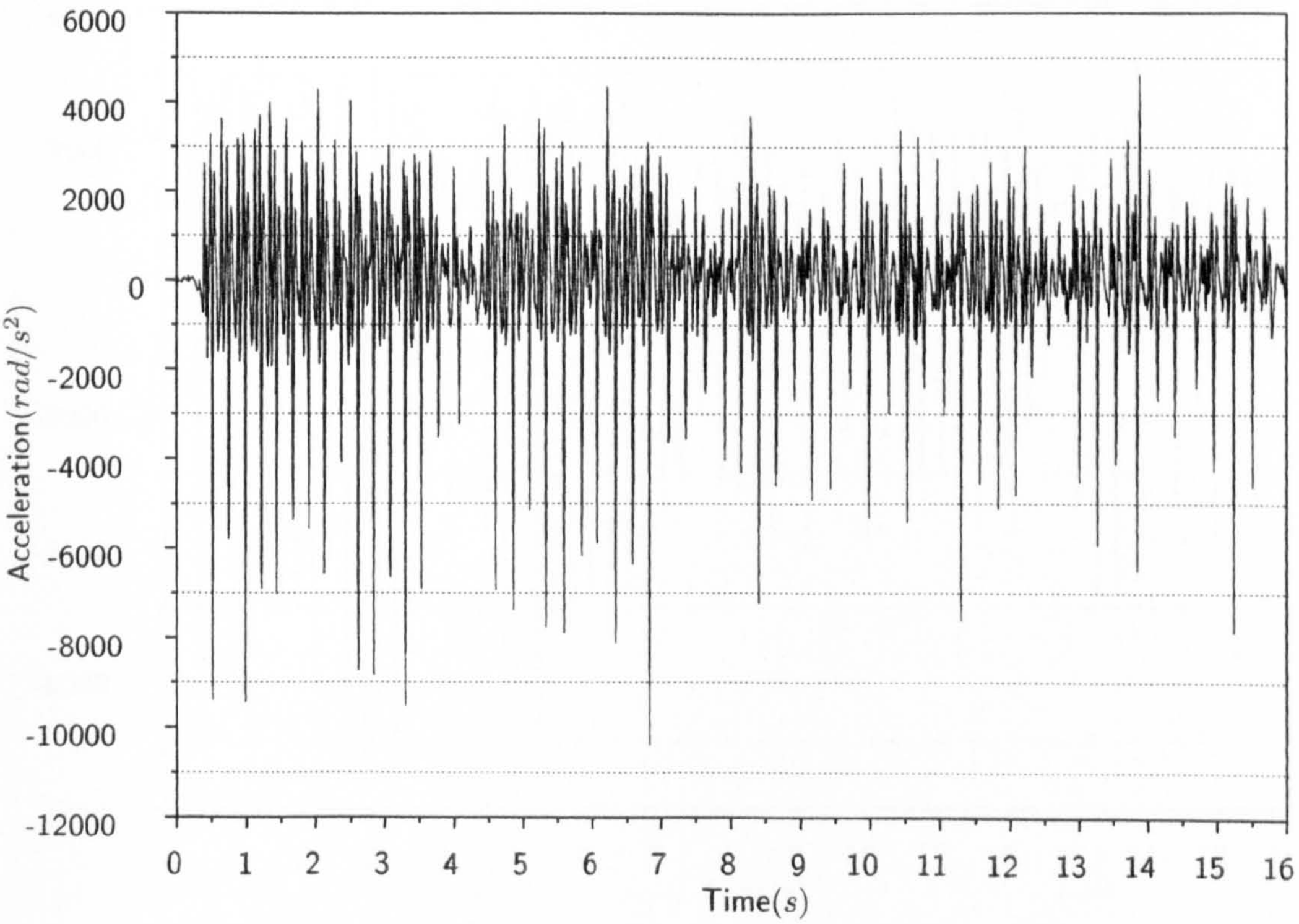

Figure D.32: Max rms acceleration, Model 32

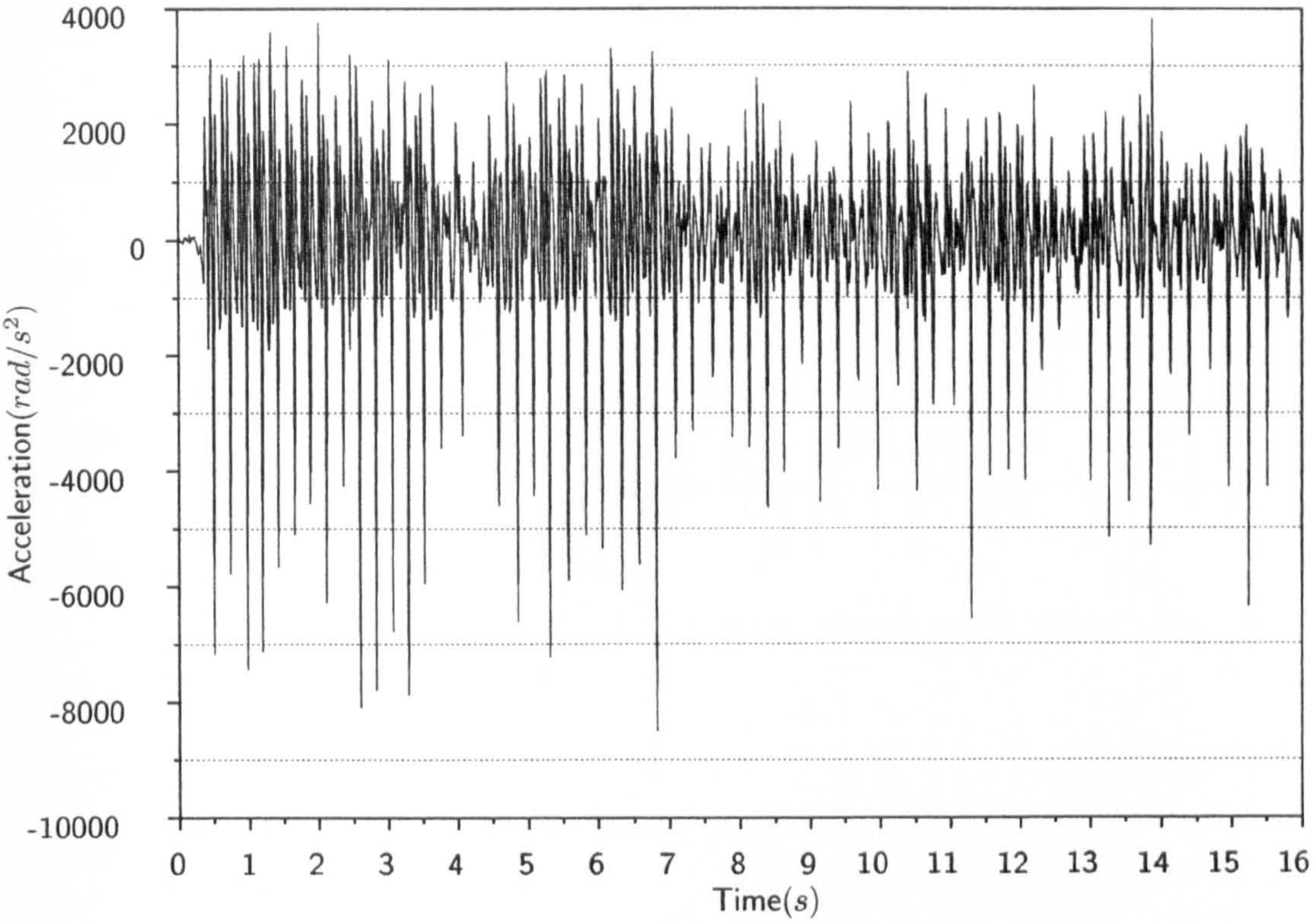

Figure D.33: Max rms acceleration, Model 33

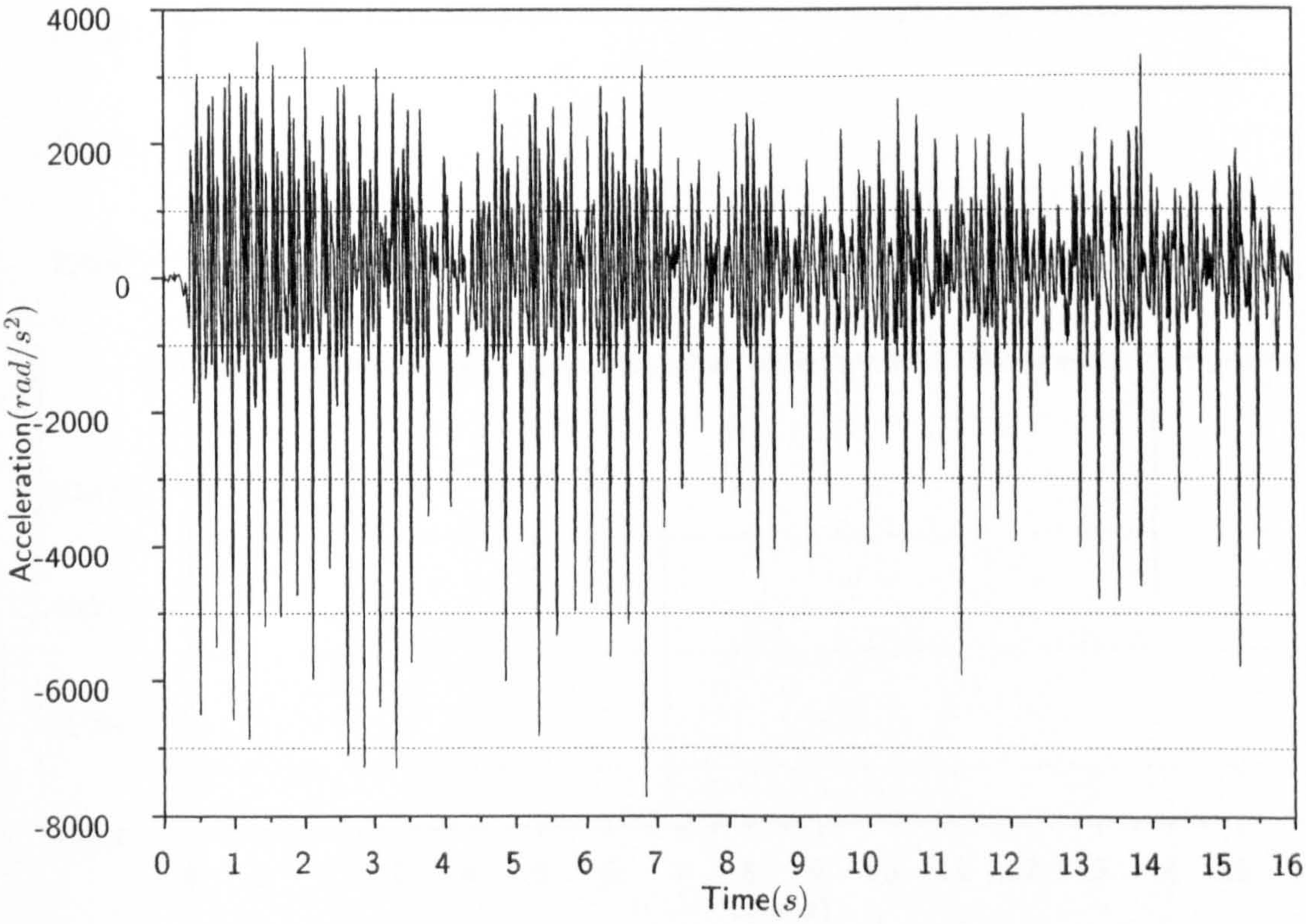

Figure D.34: Max rms acceleration, Model 34

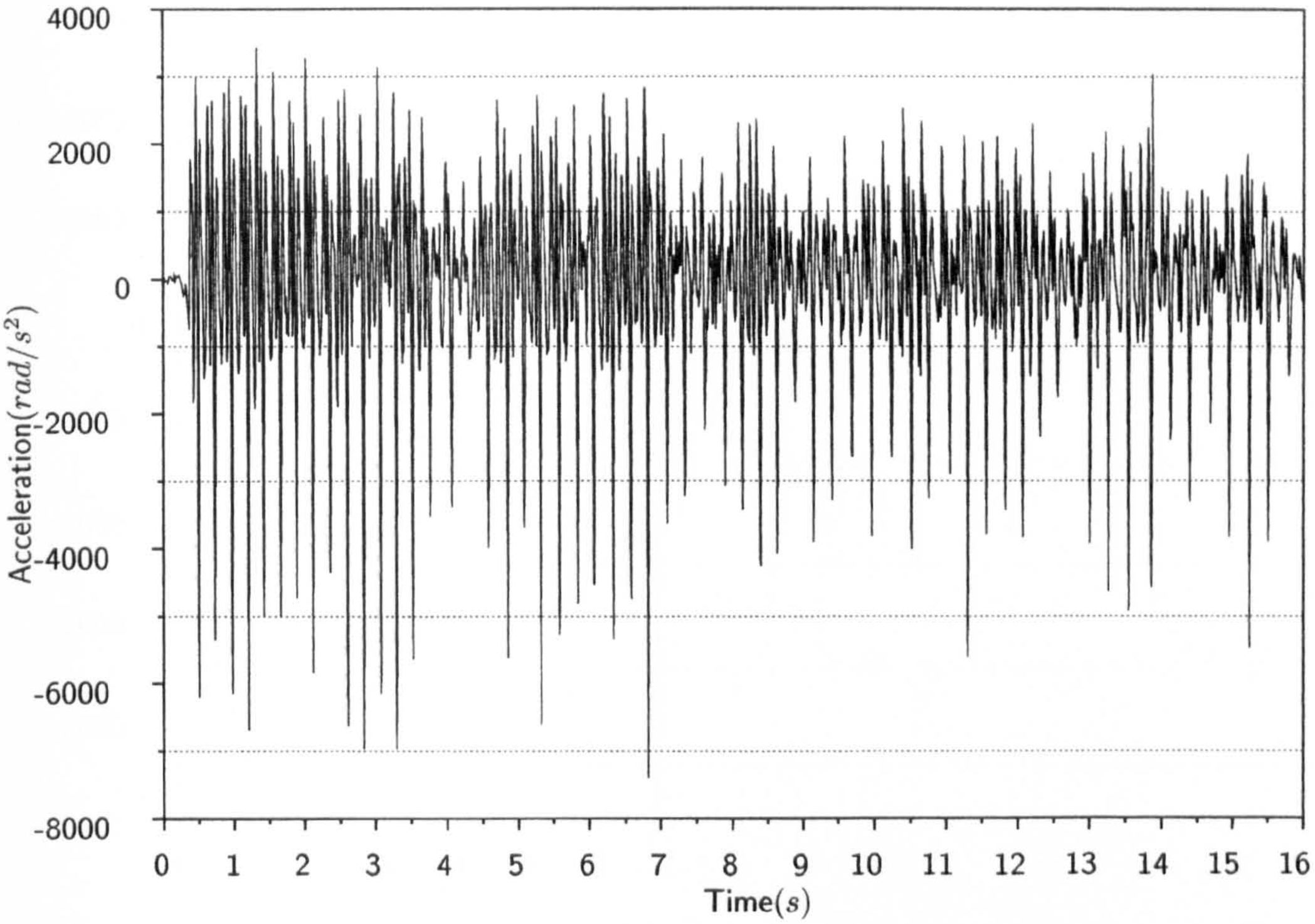

Figure D.35: Max rms acceleration, Model 35

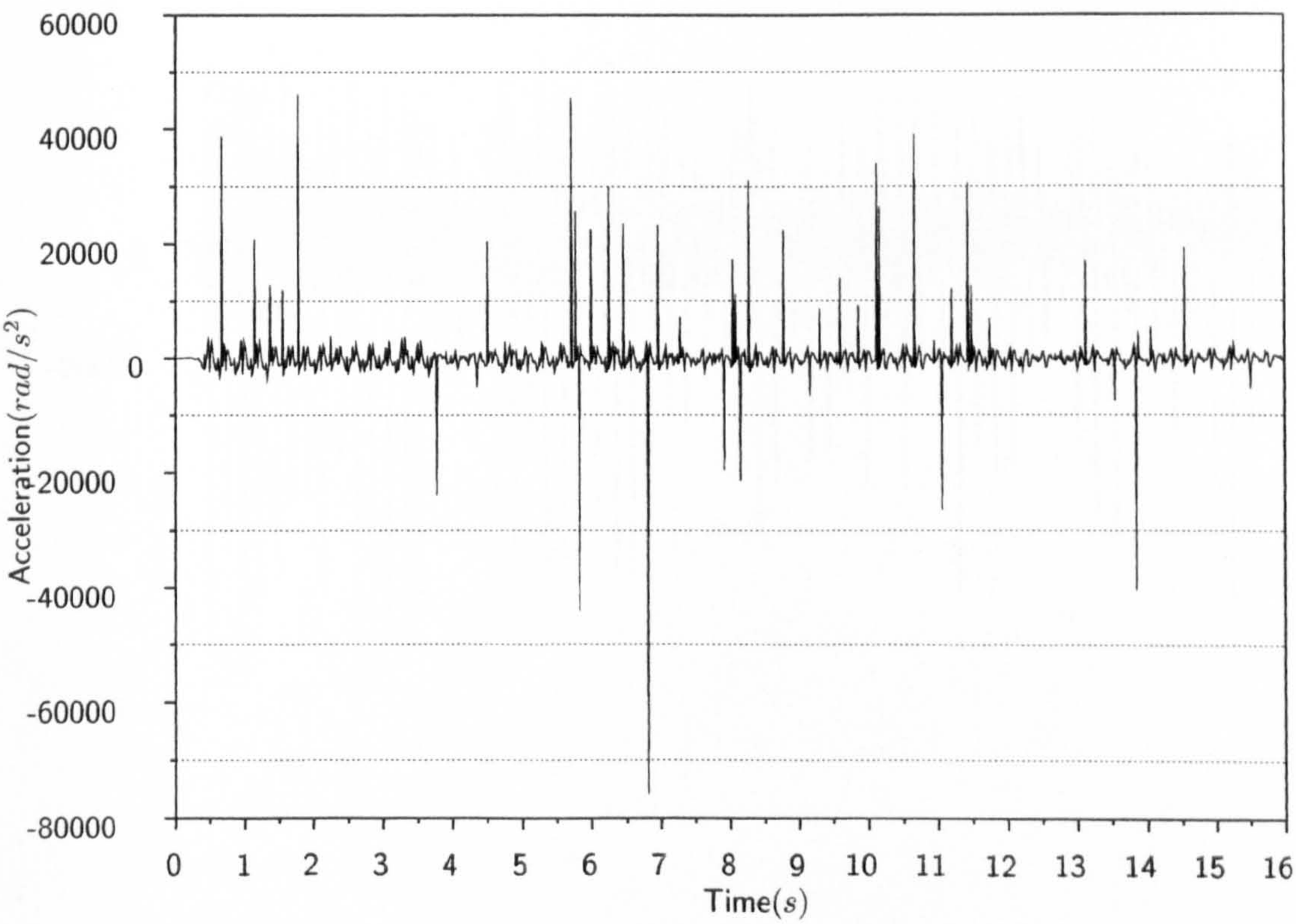

Figure D.36: Max rms acceleration, Model 36

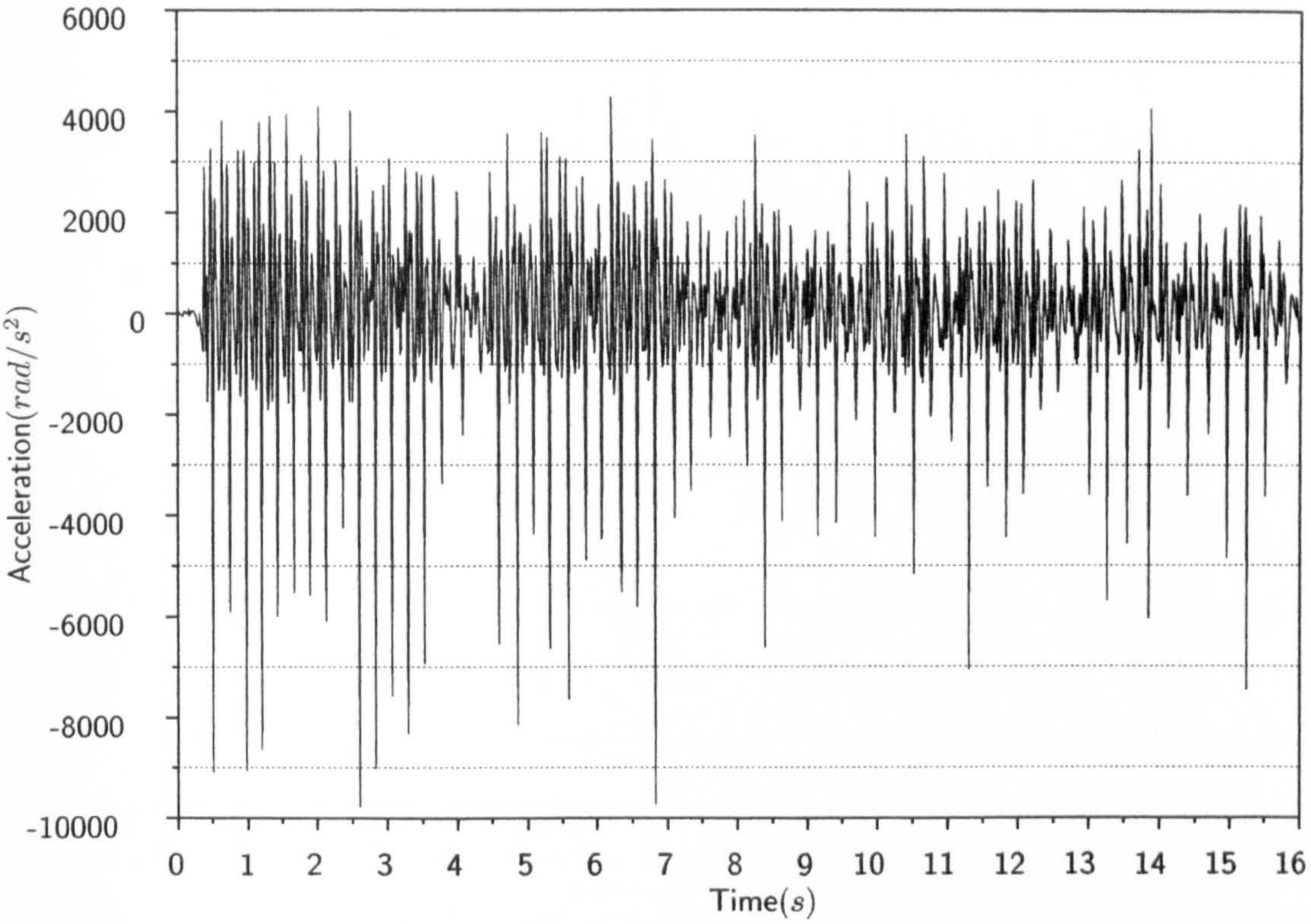

Figure D.37: Max rms acceleration, Model 37

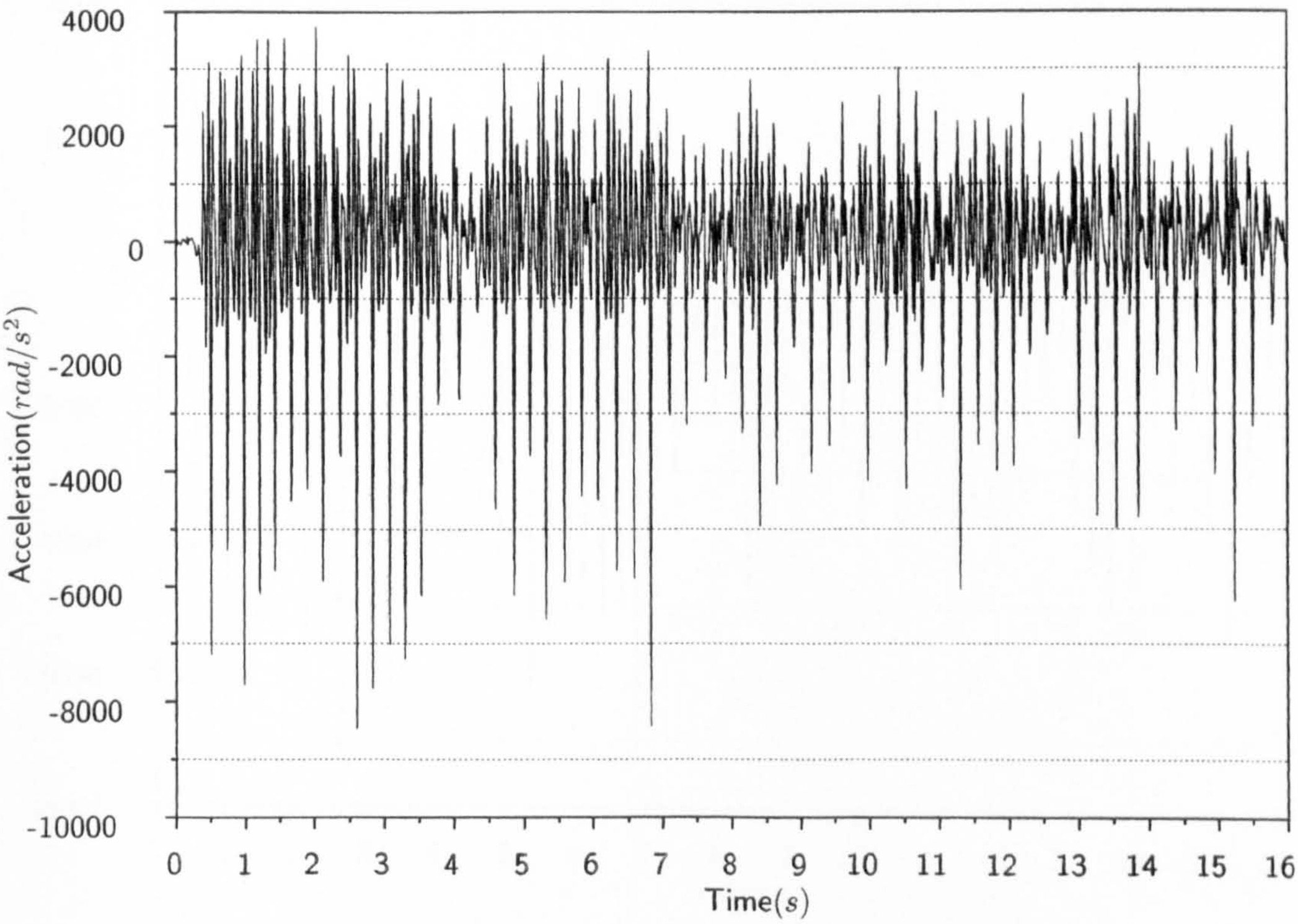

Figure D.38: Max rms acceleration, Model 38

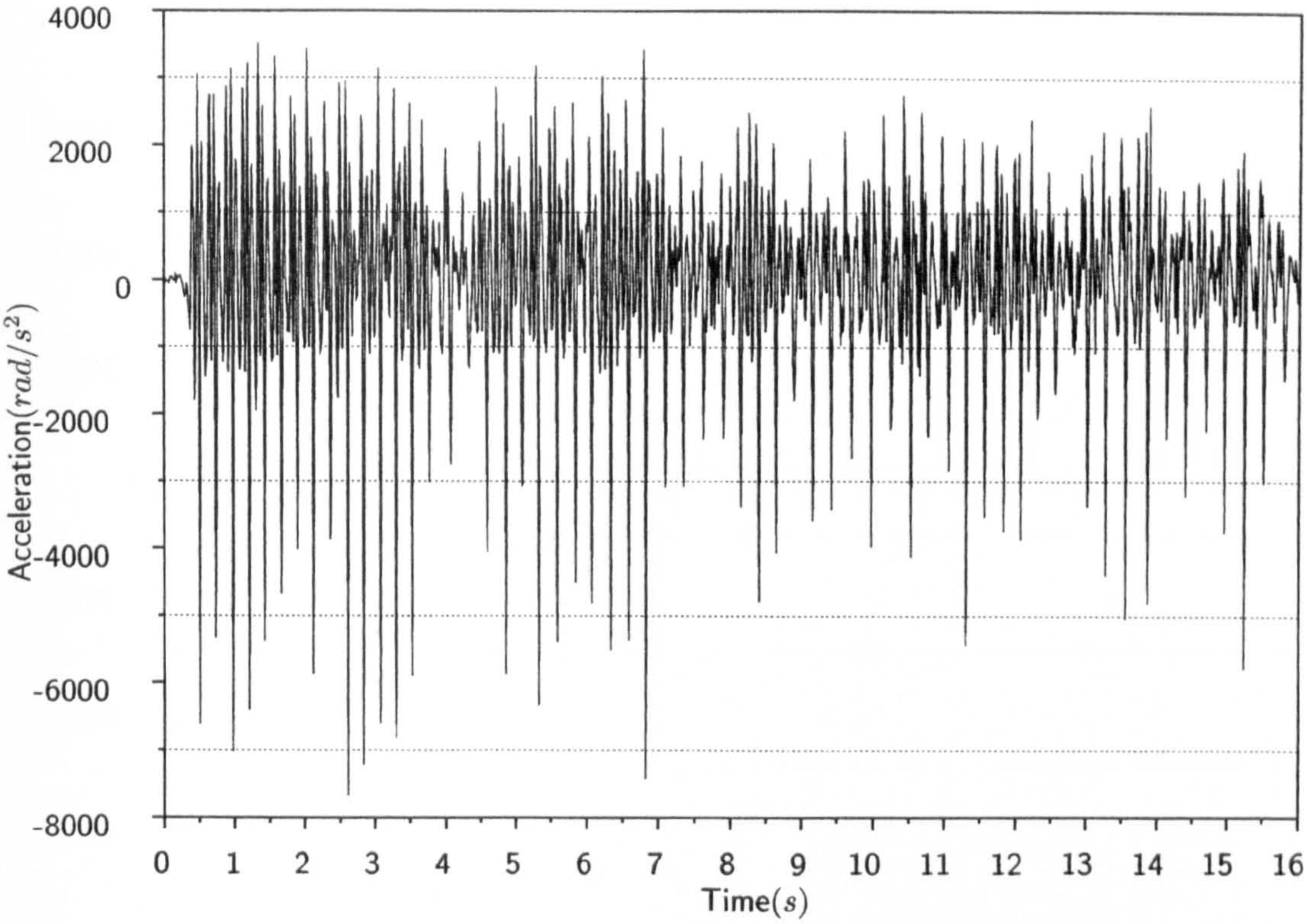

Figure D.39: Max rms acceleration, Model 39

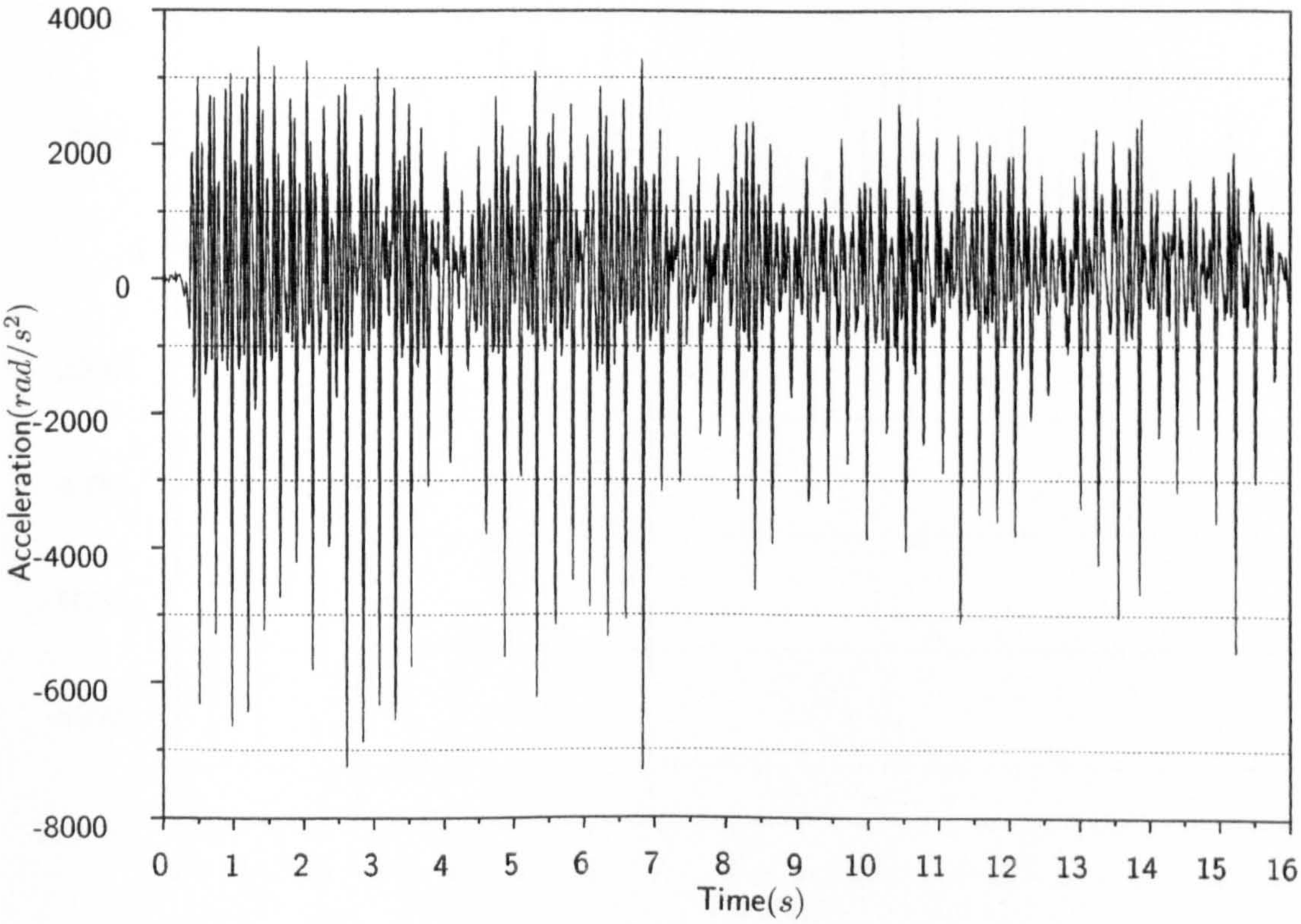

Figure D.40: Max rms acceleration, Model 40

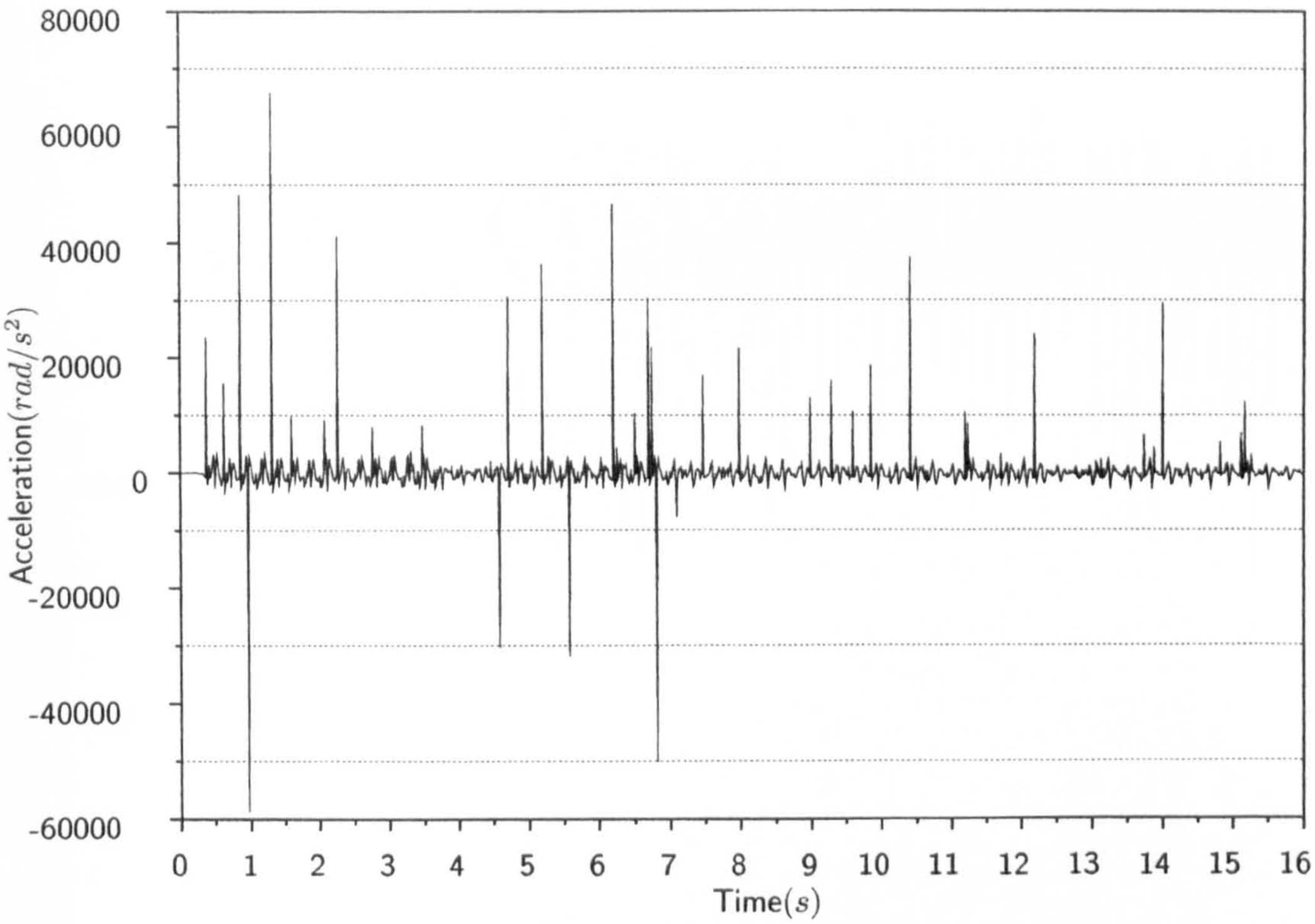

Figure D.41: Max rms acceleration, Model 41

Figure D.42: Max rms acceleration, Model 42

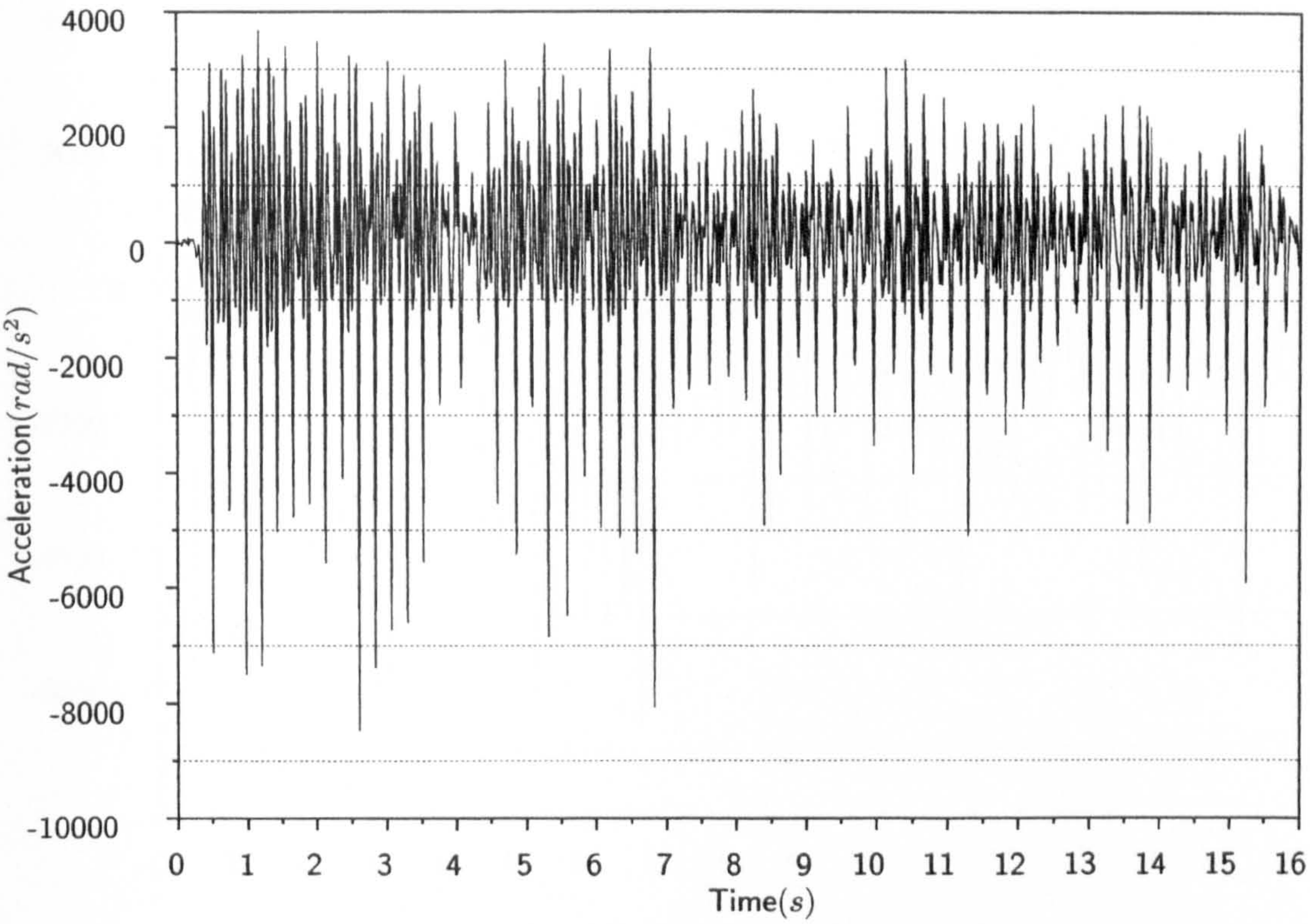

Figure D.43: Max rms acceleration, Model 43

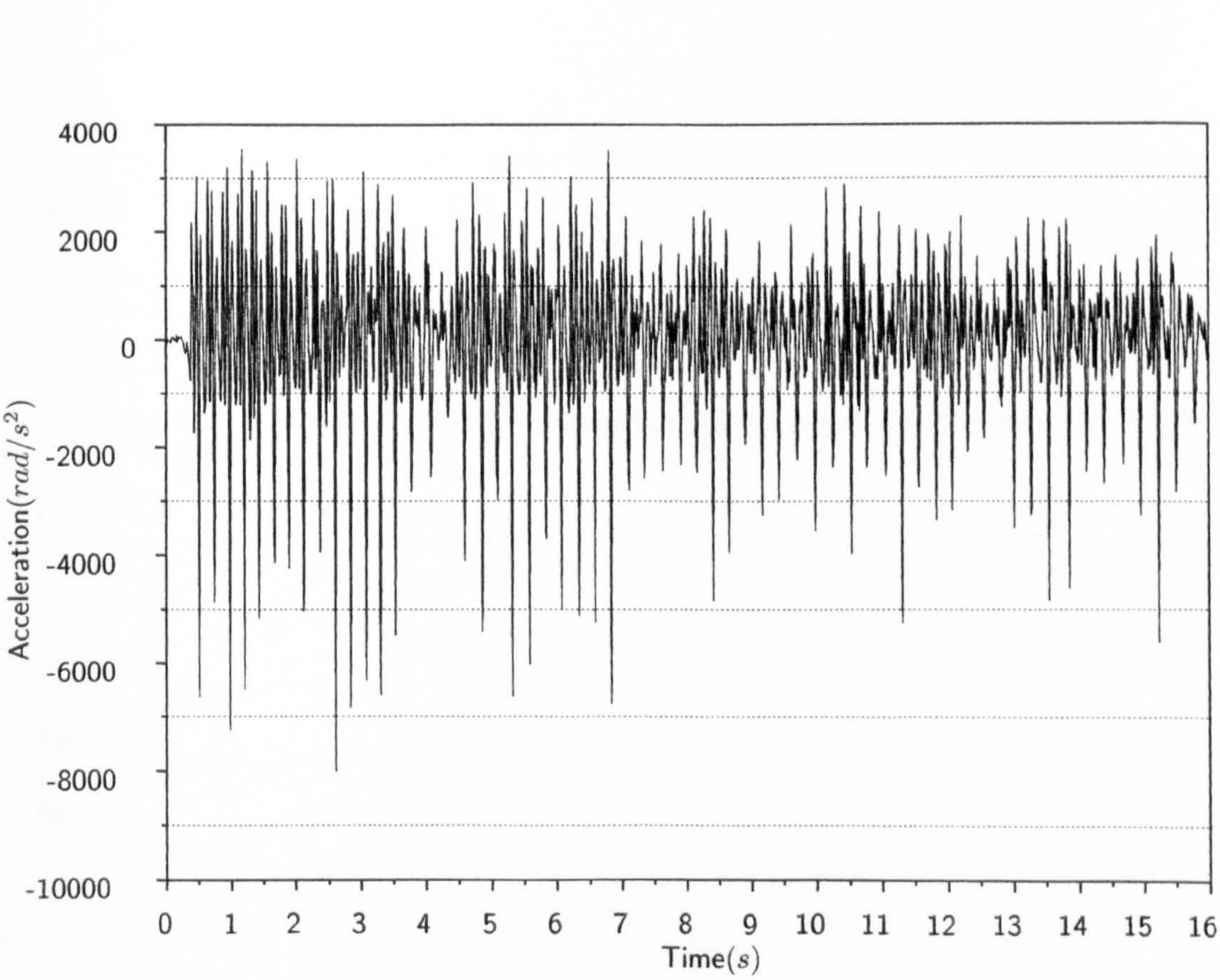

Figure D.44: Max rms acceleration, Model 44

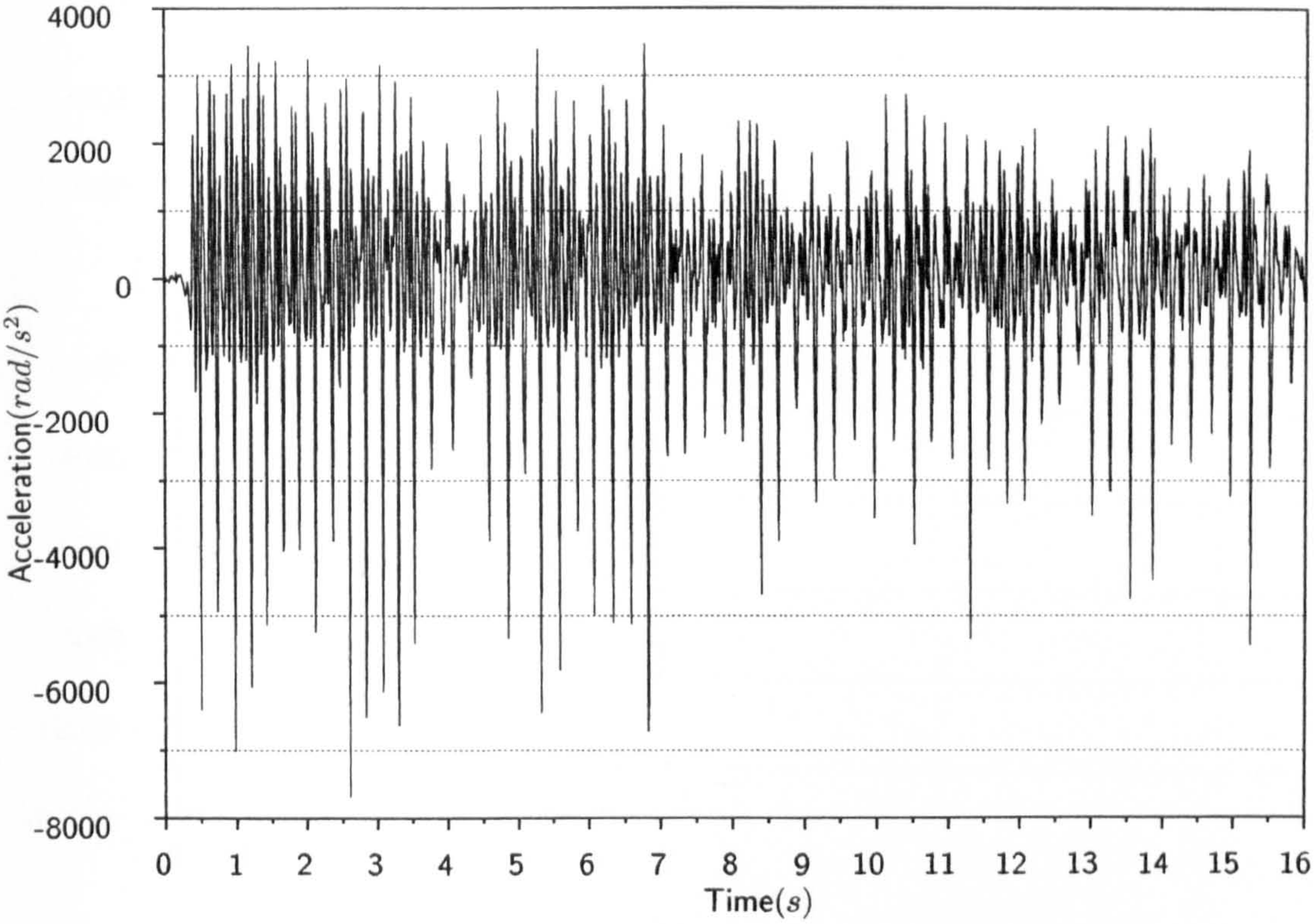

Figure D.45: Max rms acceleration, Model 45

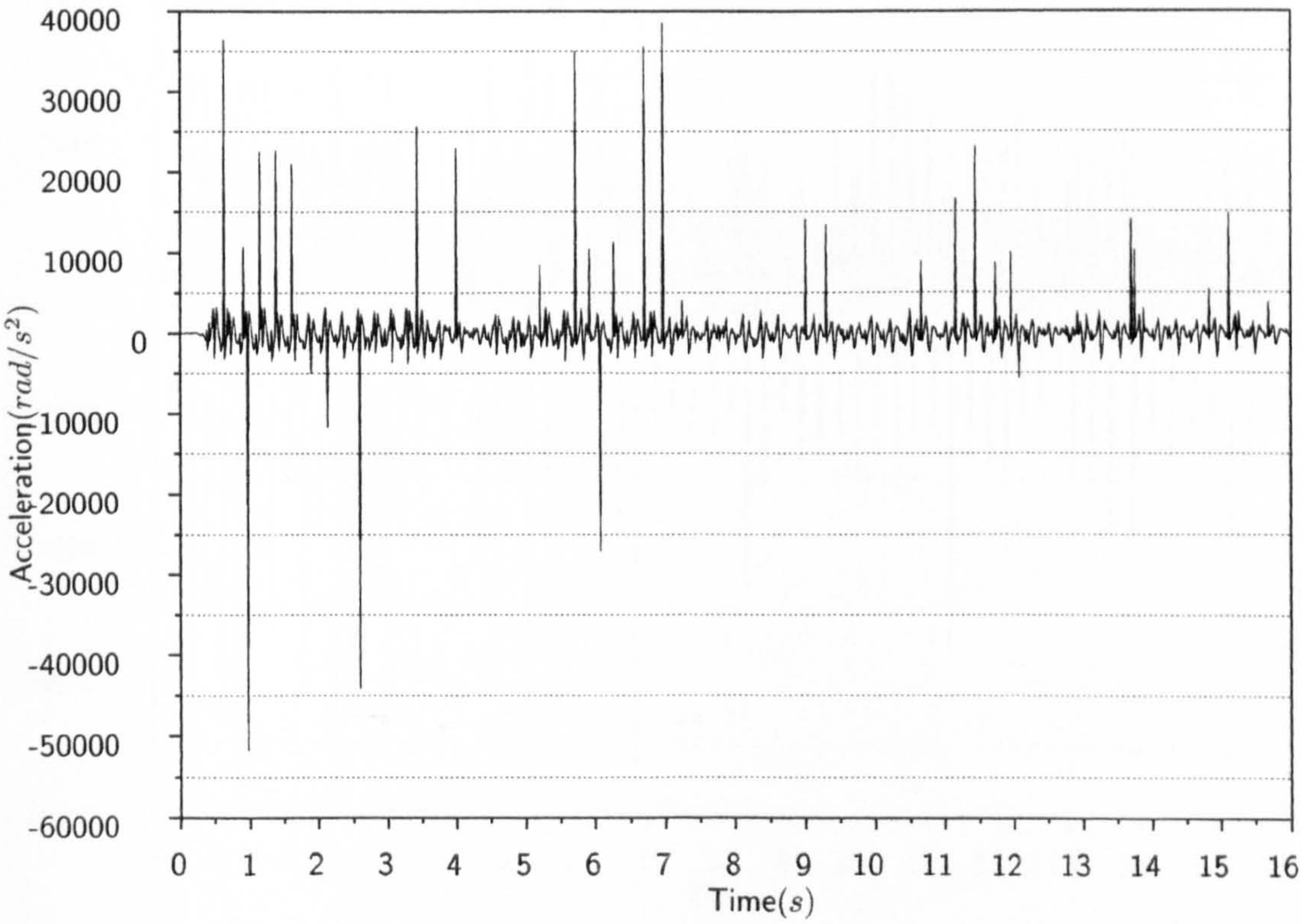

Figure D.46: Max rms acceleration, Model 46

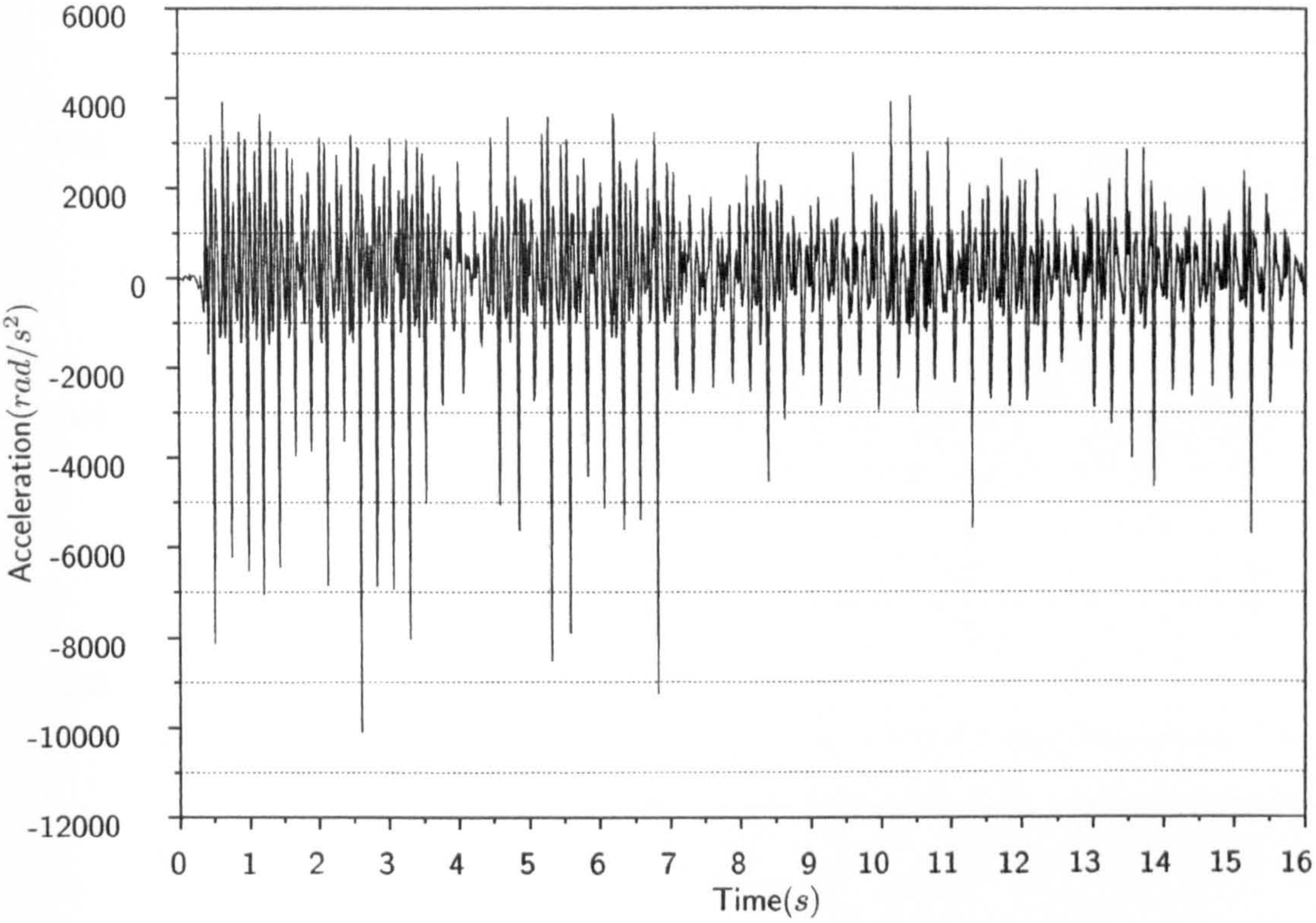

Figure D.47: Max rms acceleration, Model 47

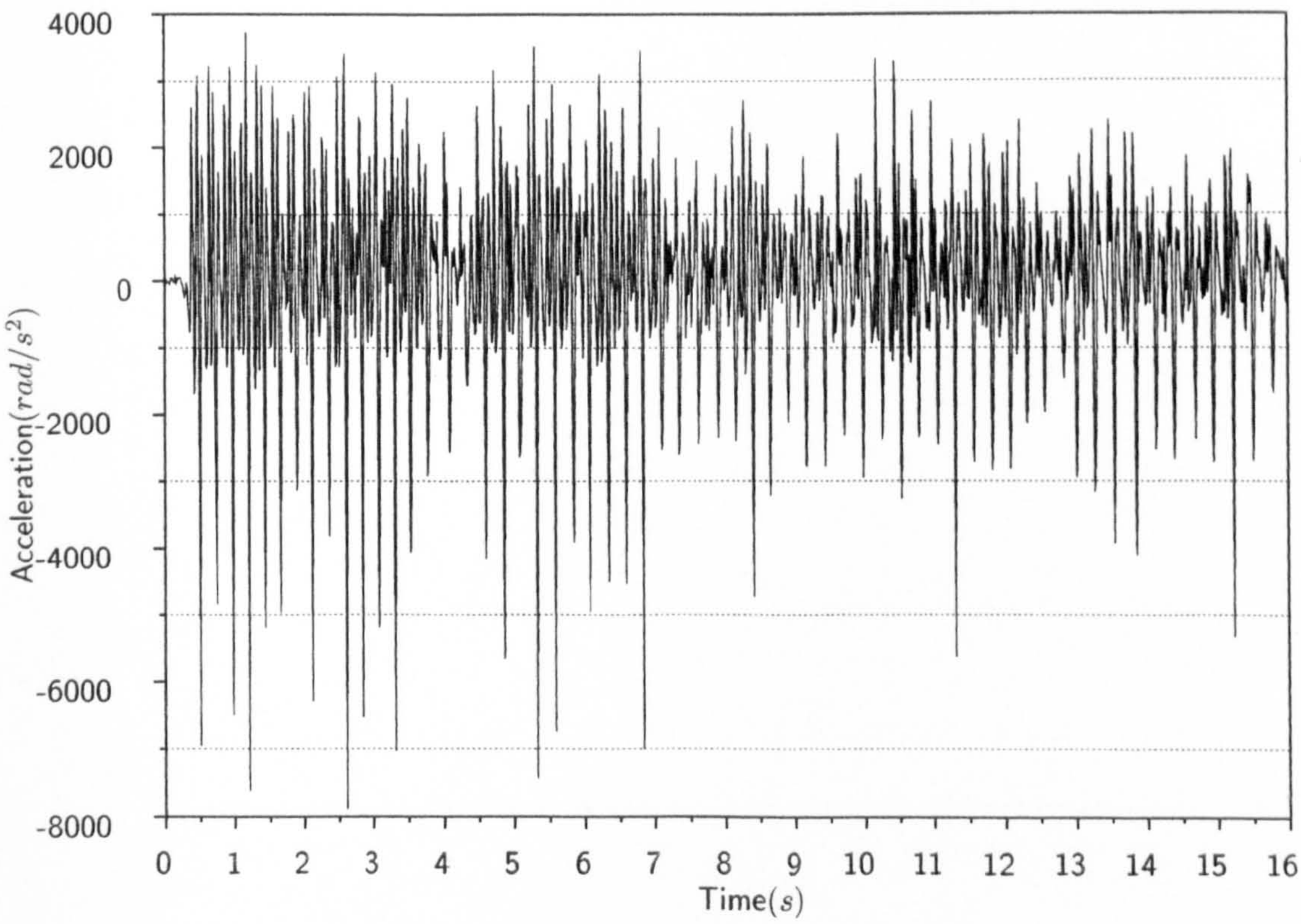

Figure D.48: Max rms acceleration, Model 48

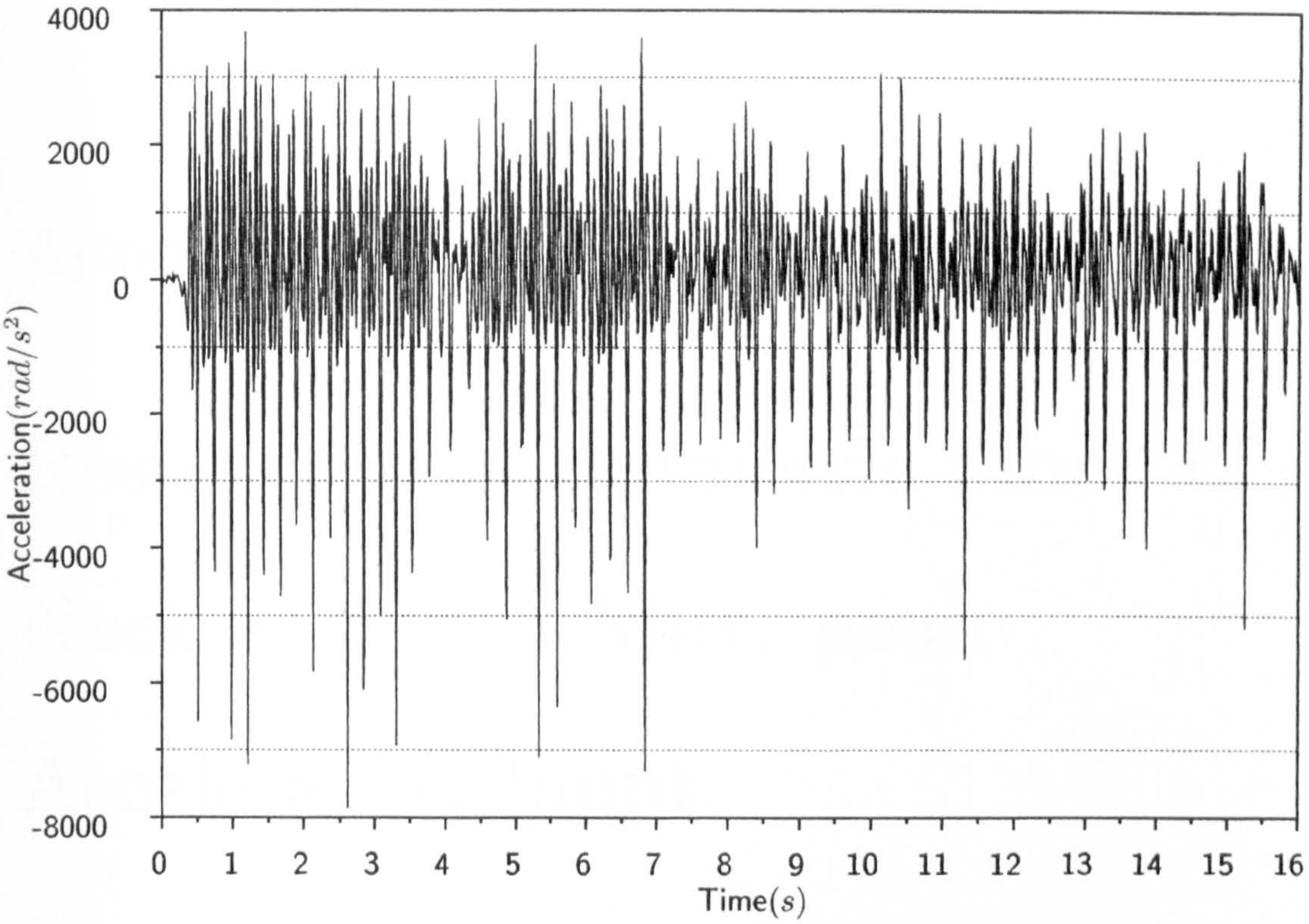

Figure D.49: Max rms acceleration, Model 49

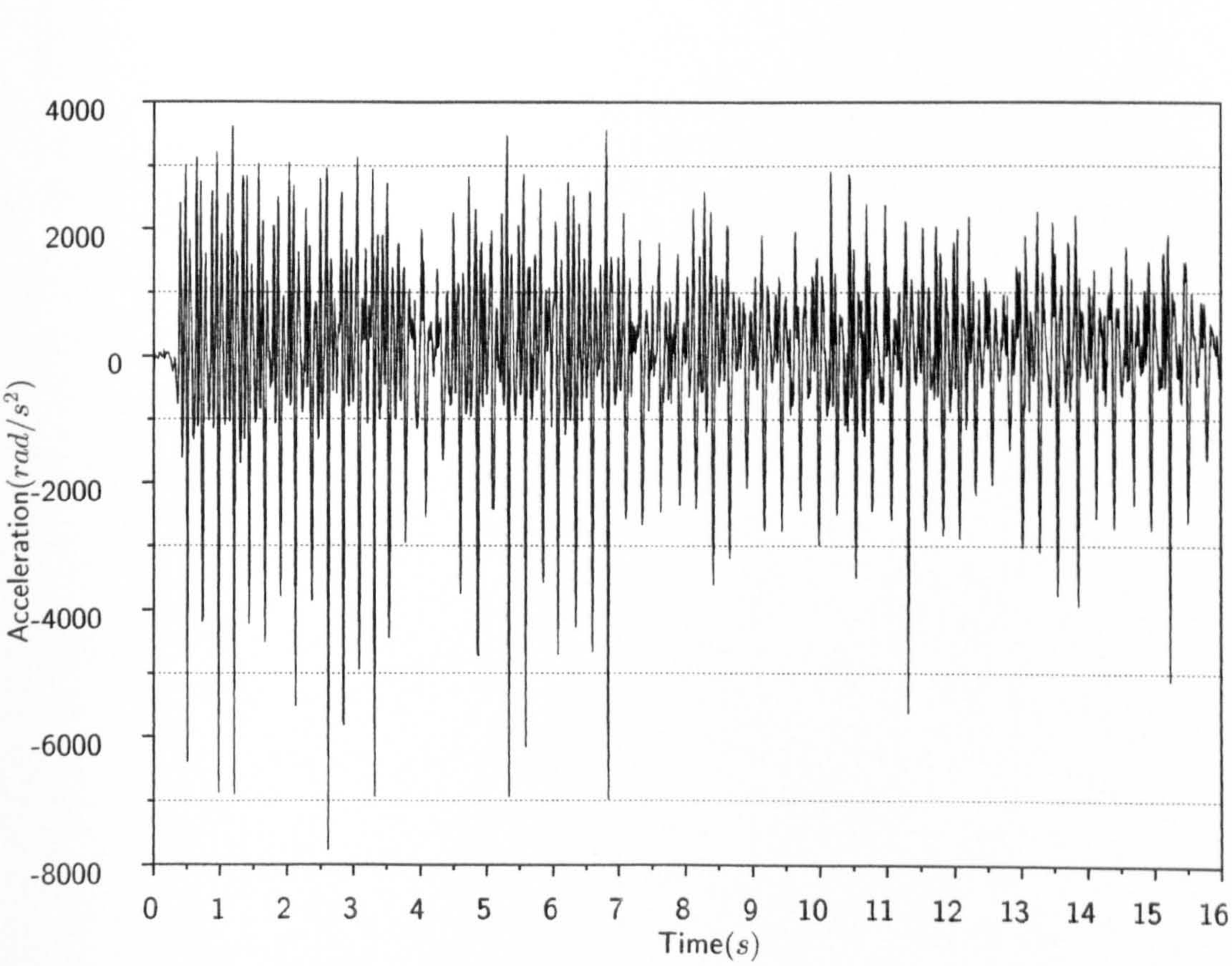

Figure D.50: Max rms acceleration, Model 50

Appendix E

Results from Parametric Study of Neck Stiffness: Max. peak Acceleration Input

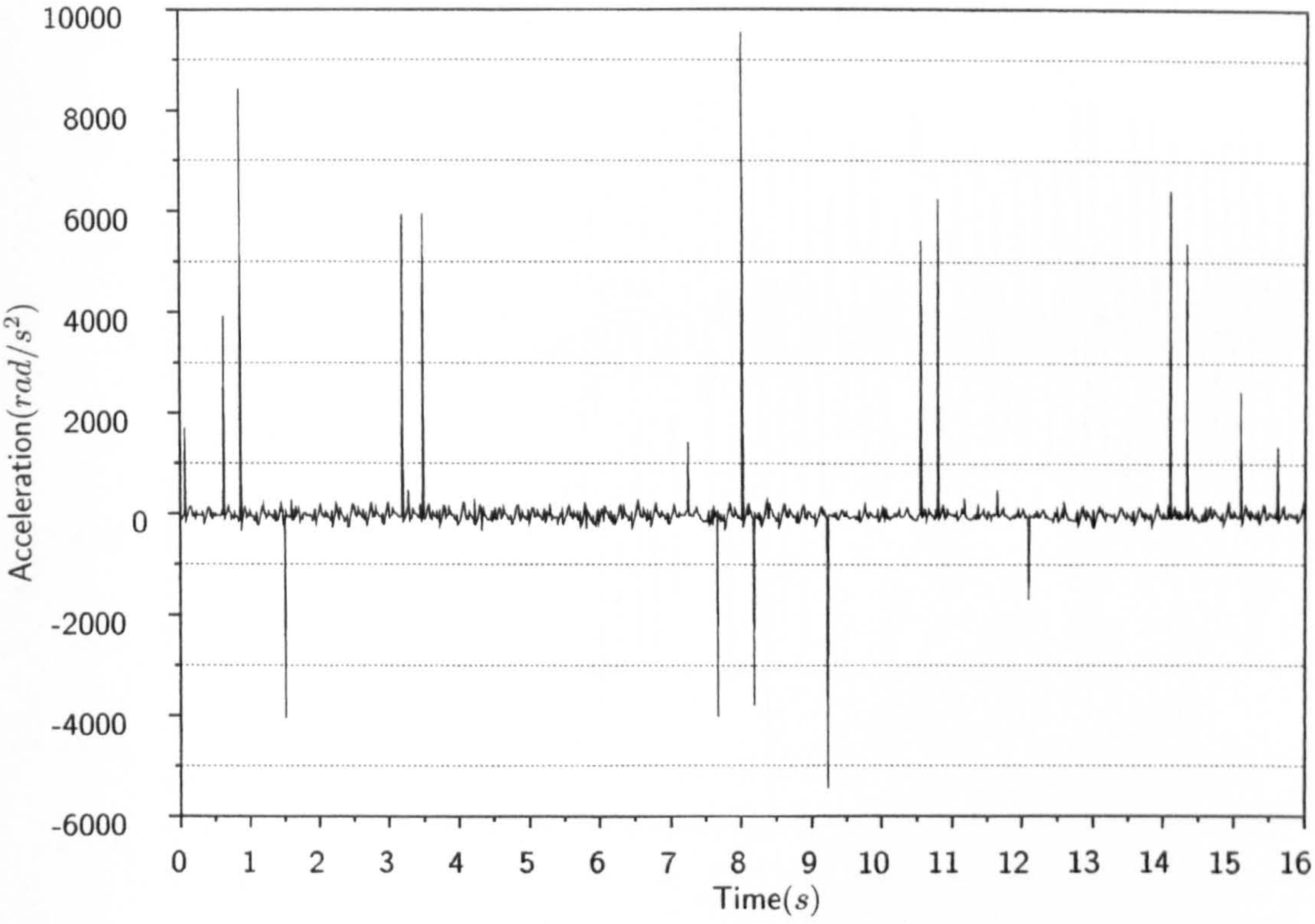

Figure E.1: Max peak acceleration, Model 1

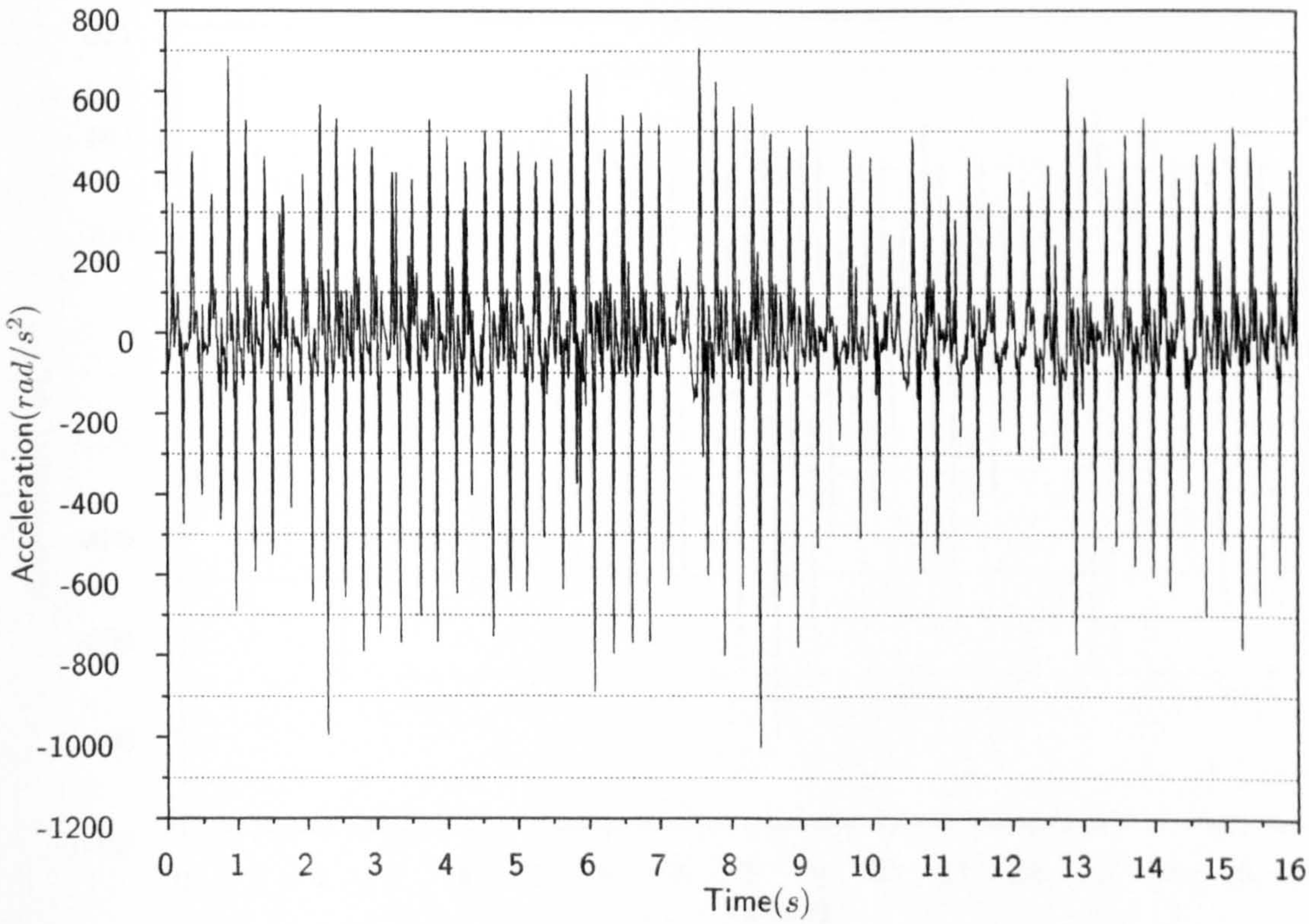

Figure E.2: Max peak acceleration, Model 2

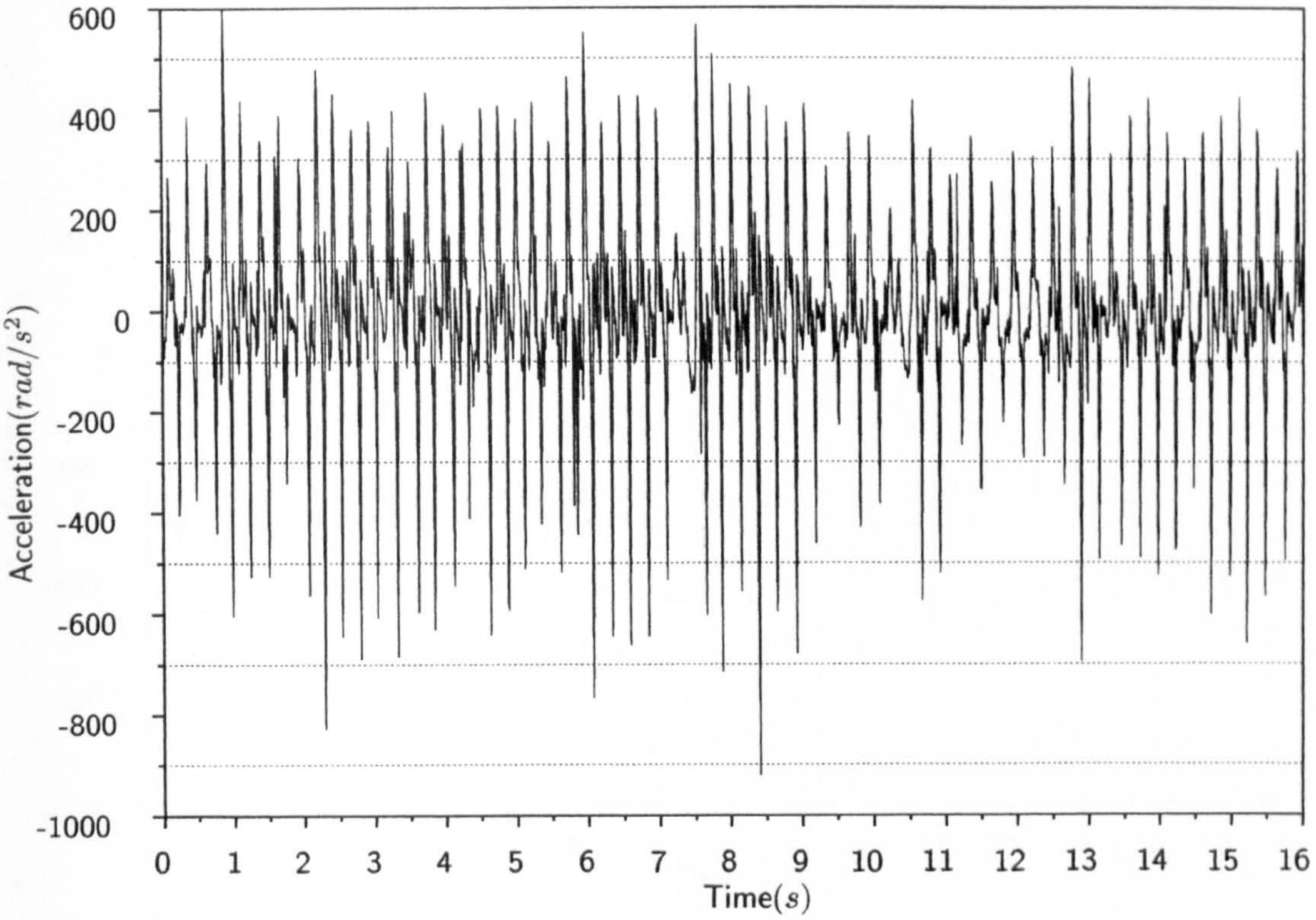

Figure E.3: Max peak acceleration, Model 3

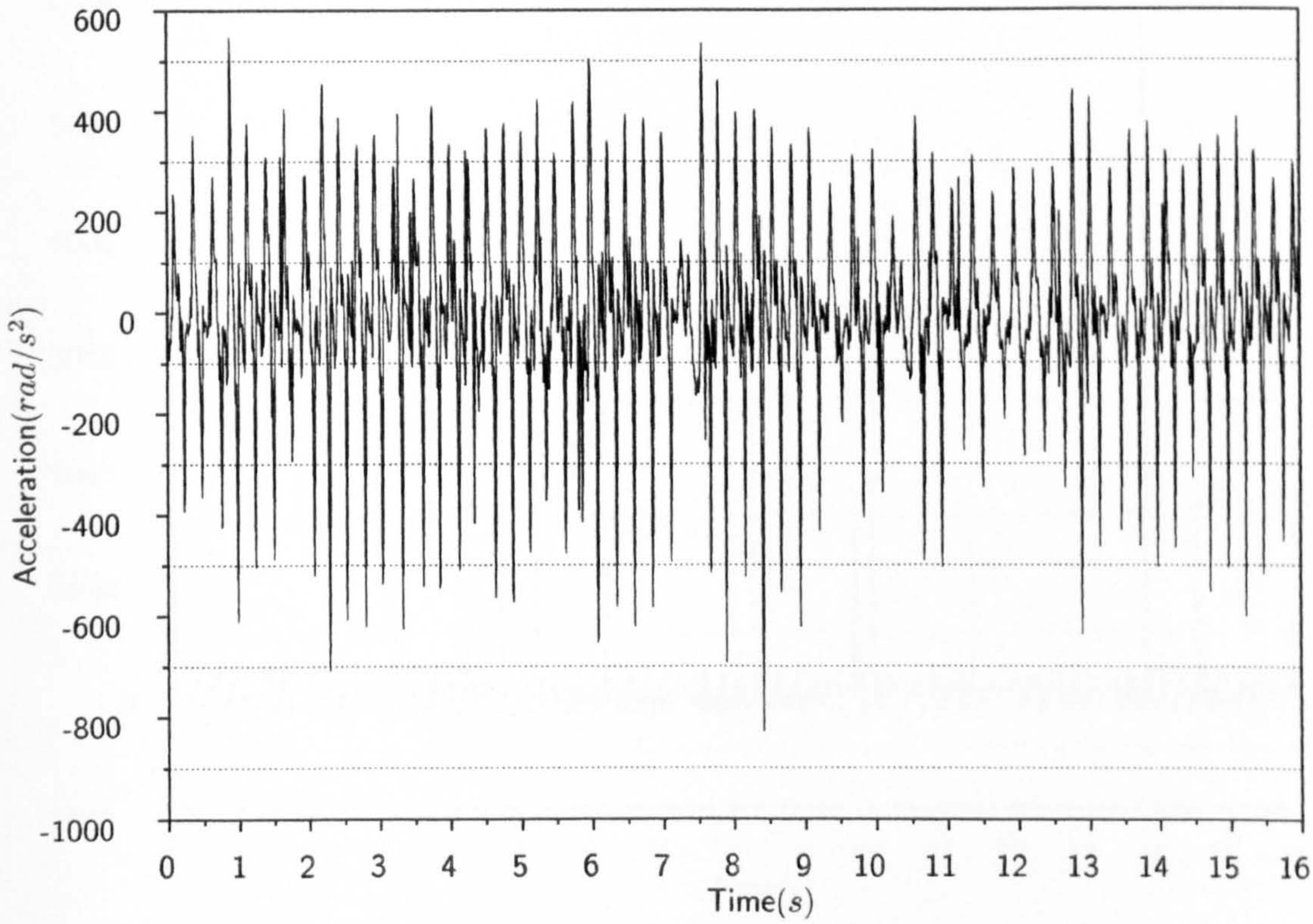

Figure E.4: Max peak acceleration, Model 4

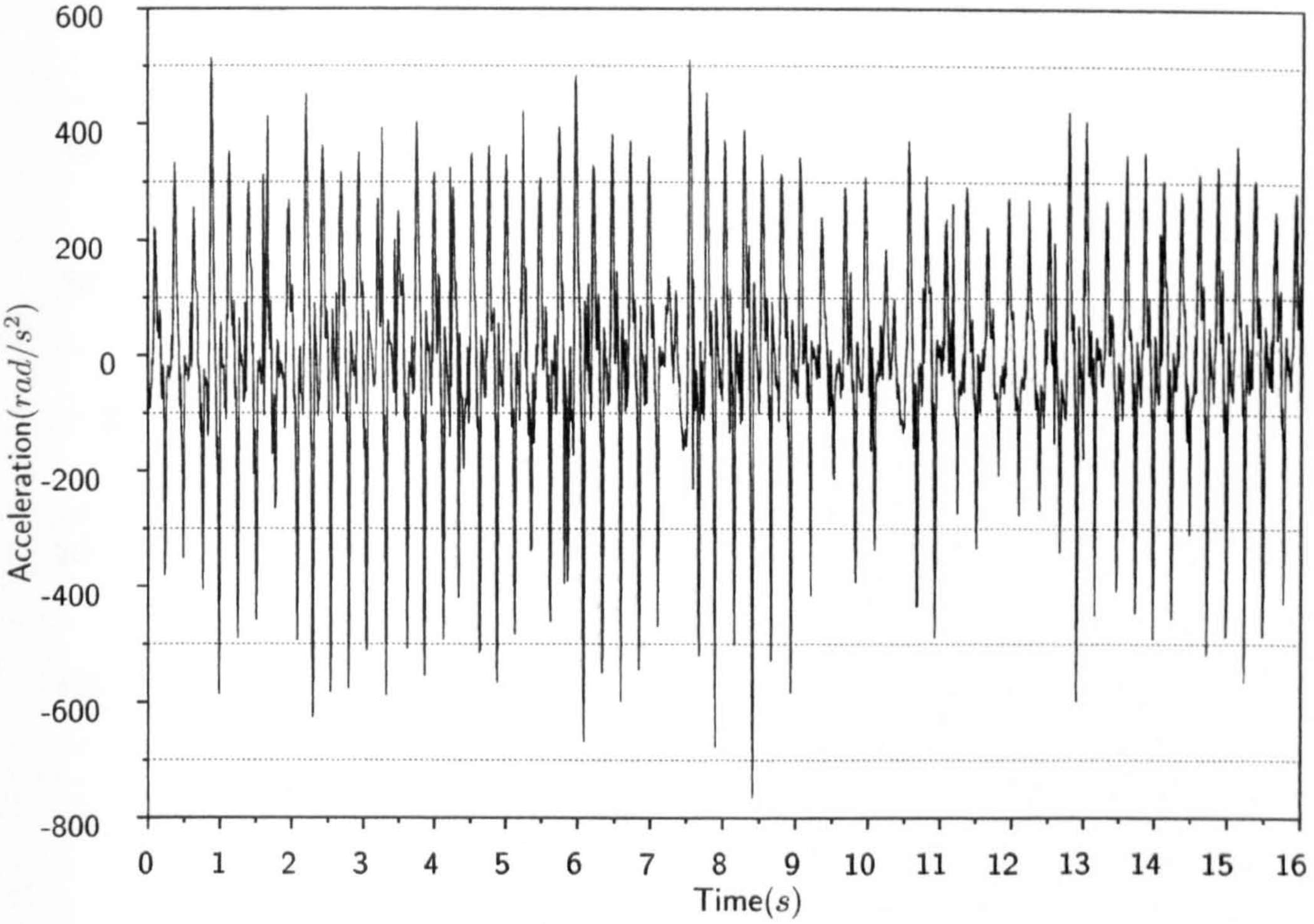

Figure E.5: Max peak acceleration, Model 5

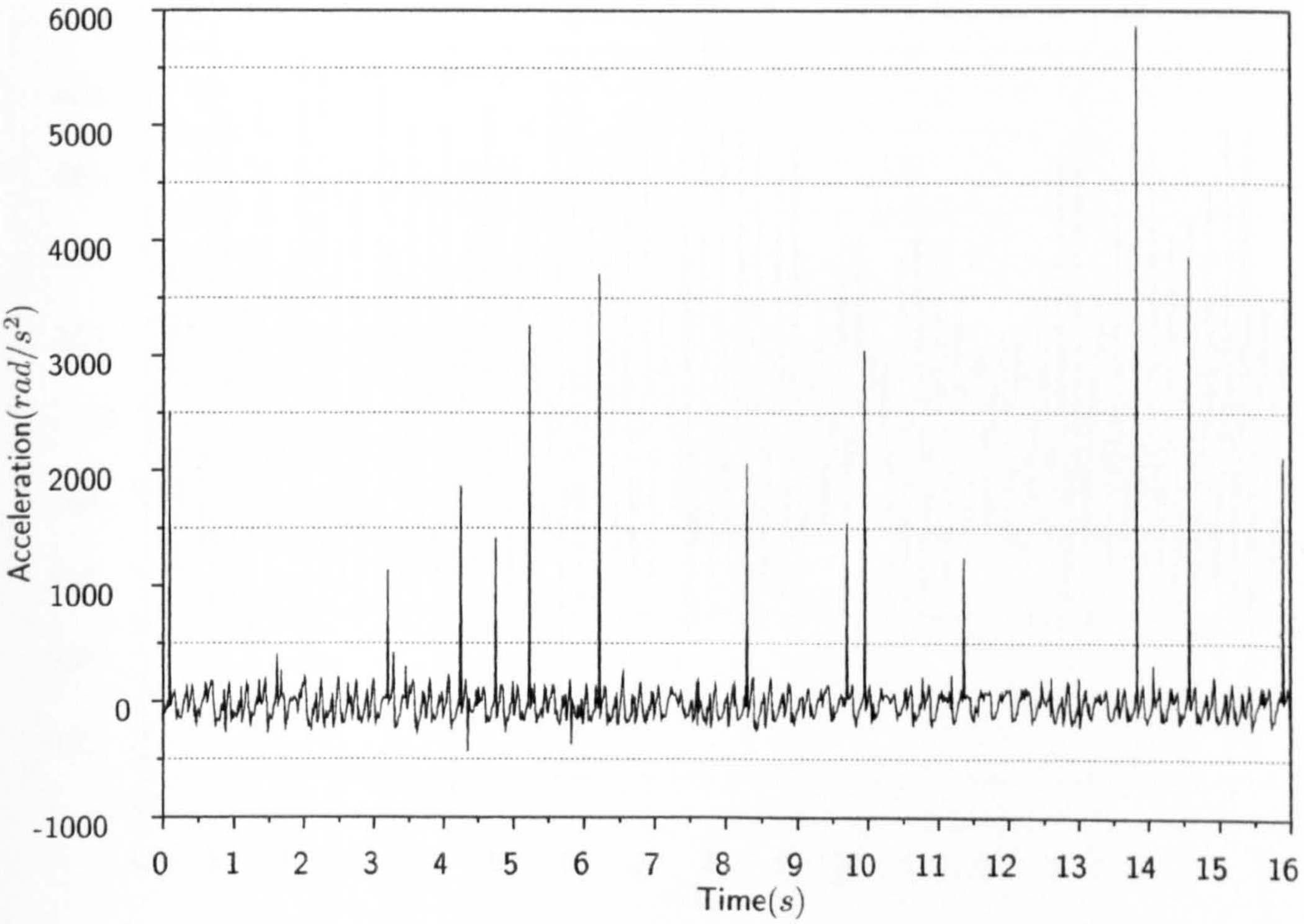

Figure E.6: Max peak acceleration, Model 6

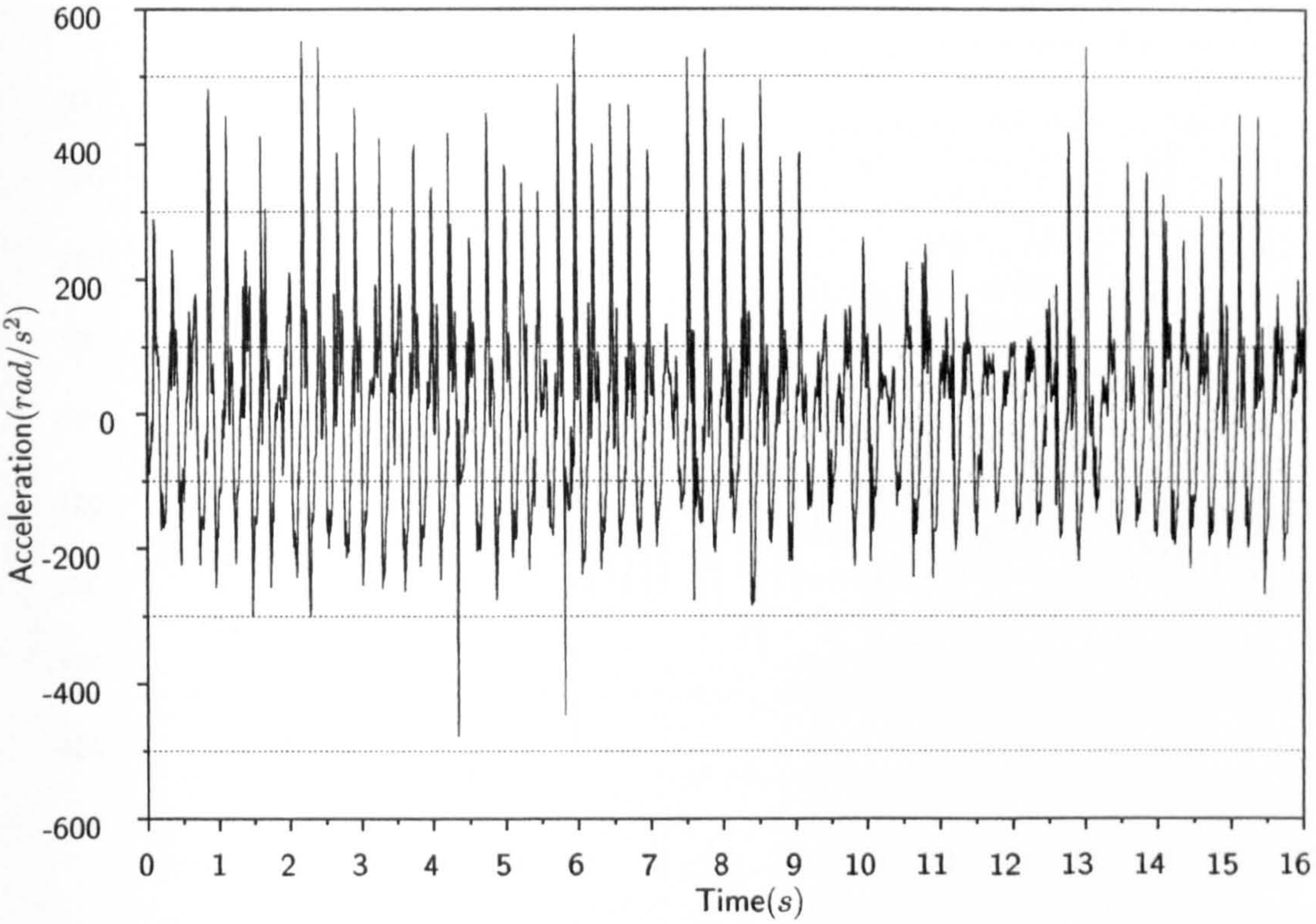

Figure E.7: Max peak acceleration, Model 7

Figure E.8: Max peak acceleration, Model 8

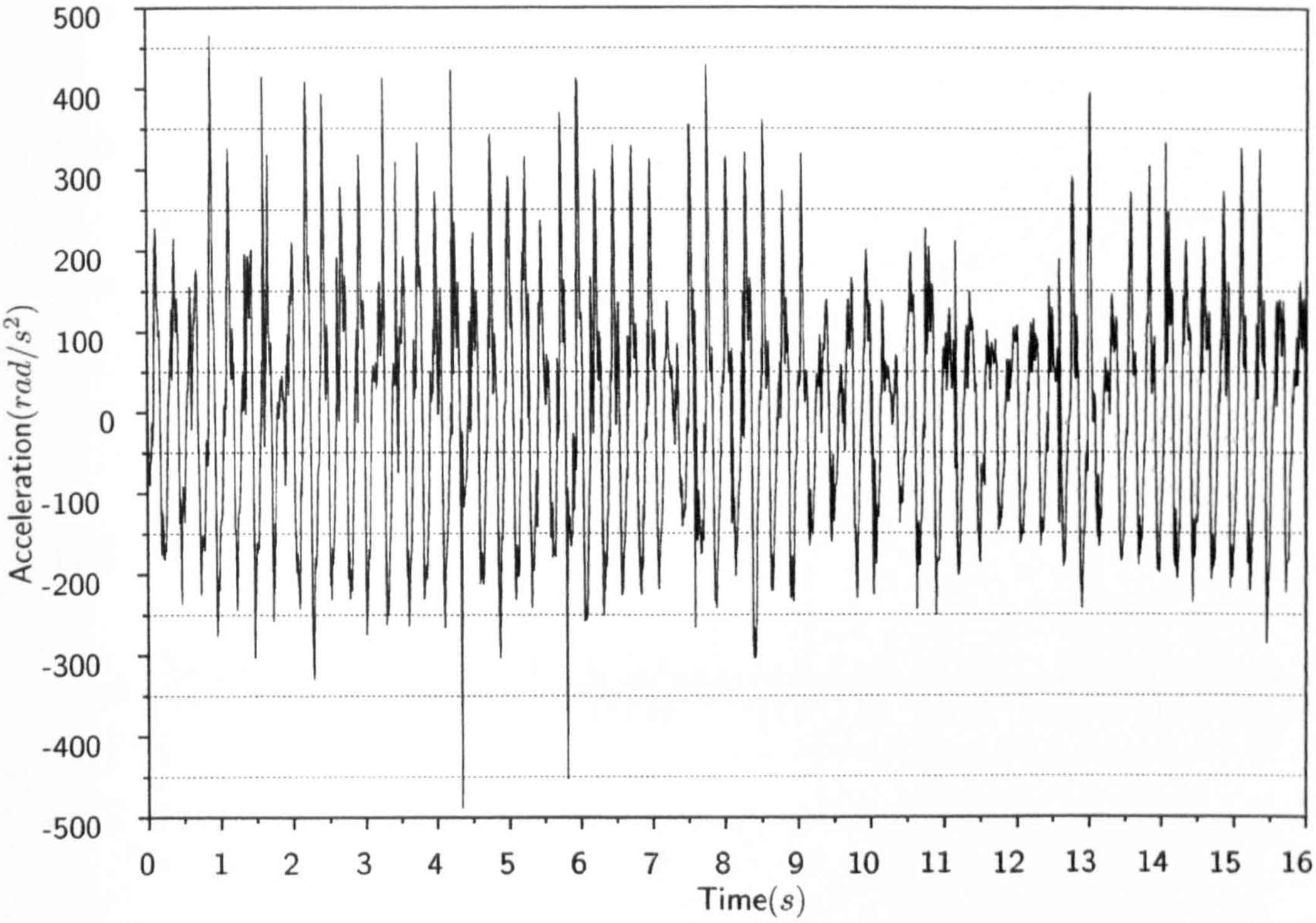

Figure E.9: Max peak acceleration, Model 9

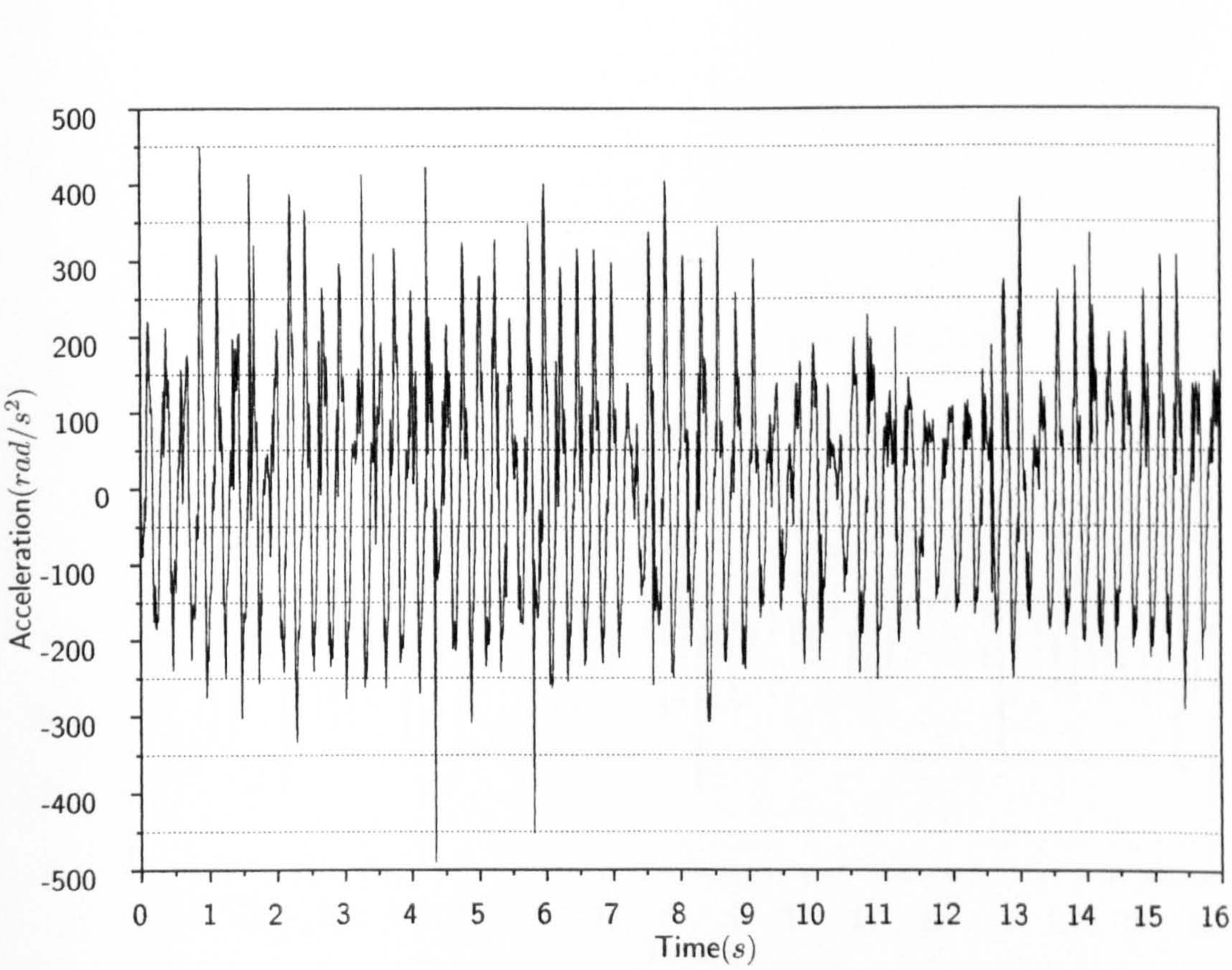

Figure E.10: Max peak acceleration, Model 10

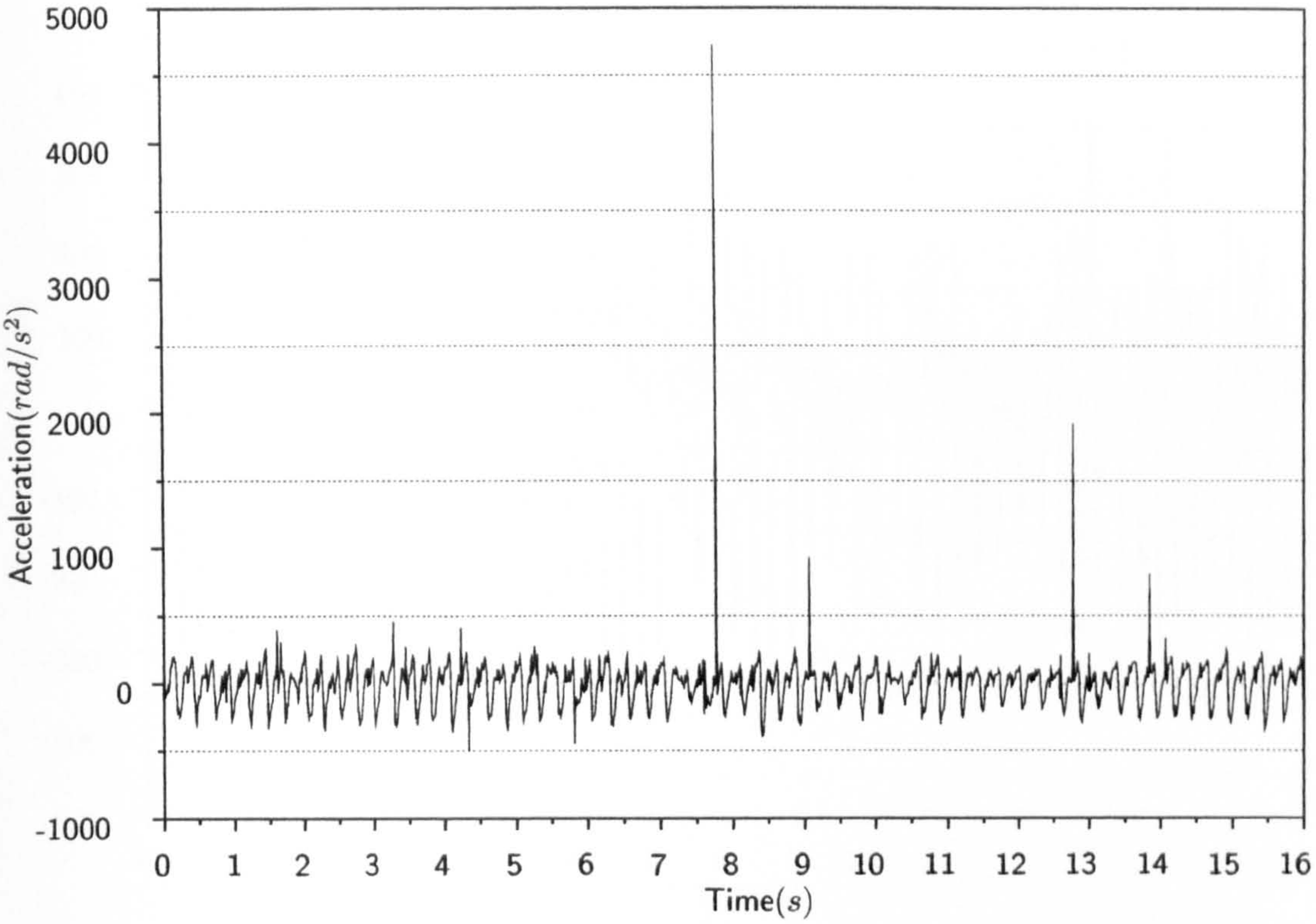

Figure E.11: Max peak acceleration, Model 11

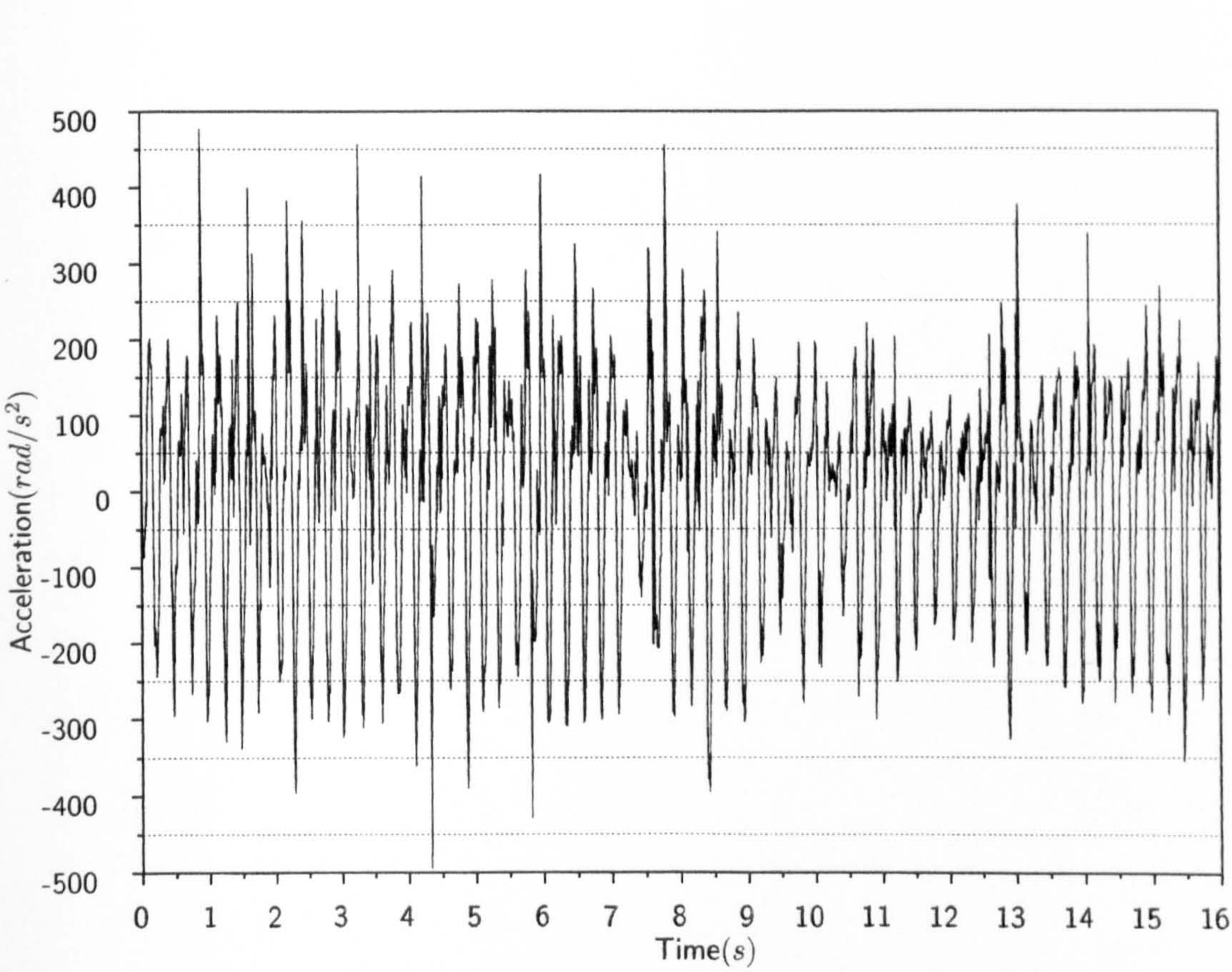

Figure E.12: Max peak acceleration, Model 12

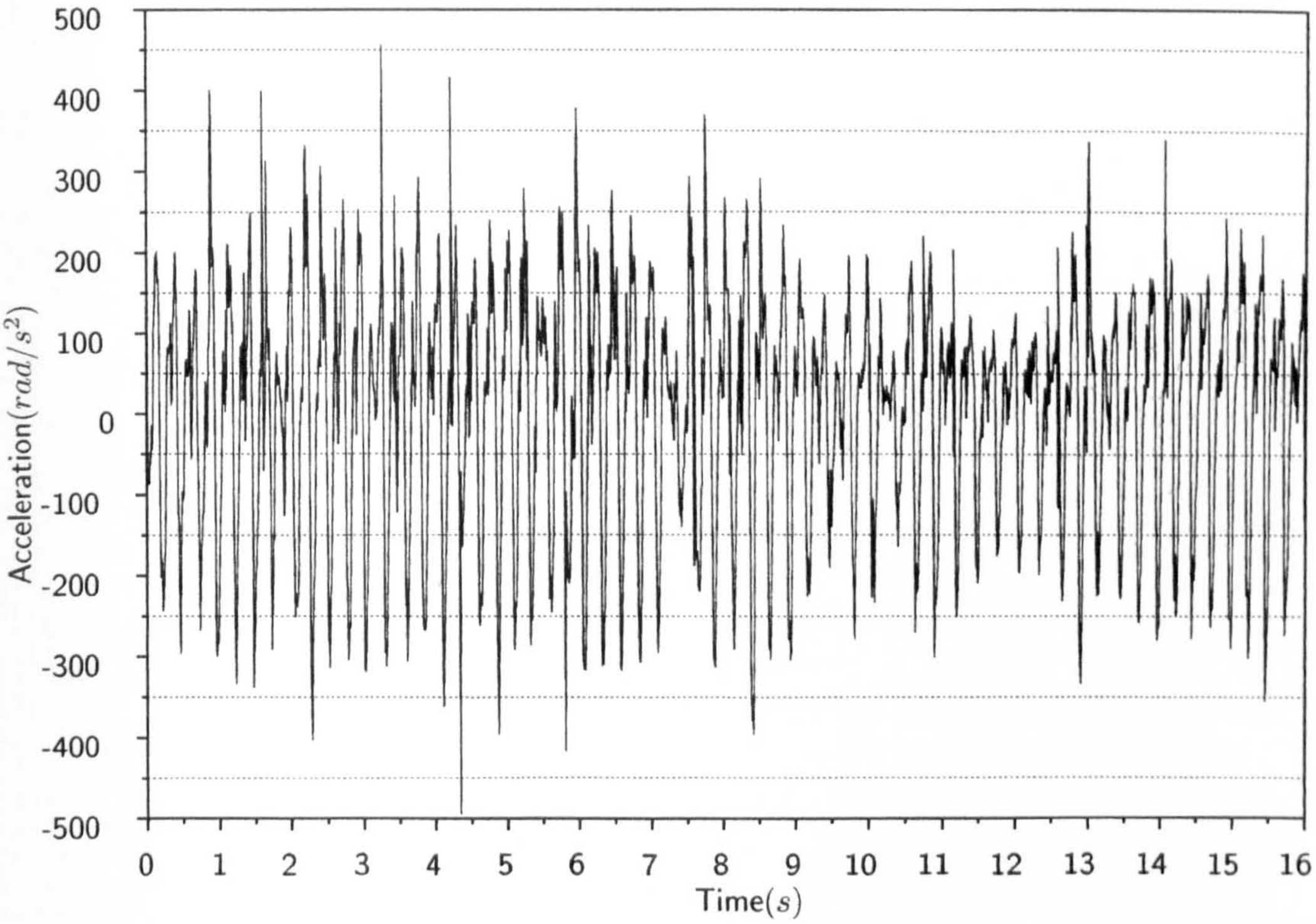

Figure E.13: Max peak acceleration, Model 13

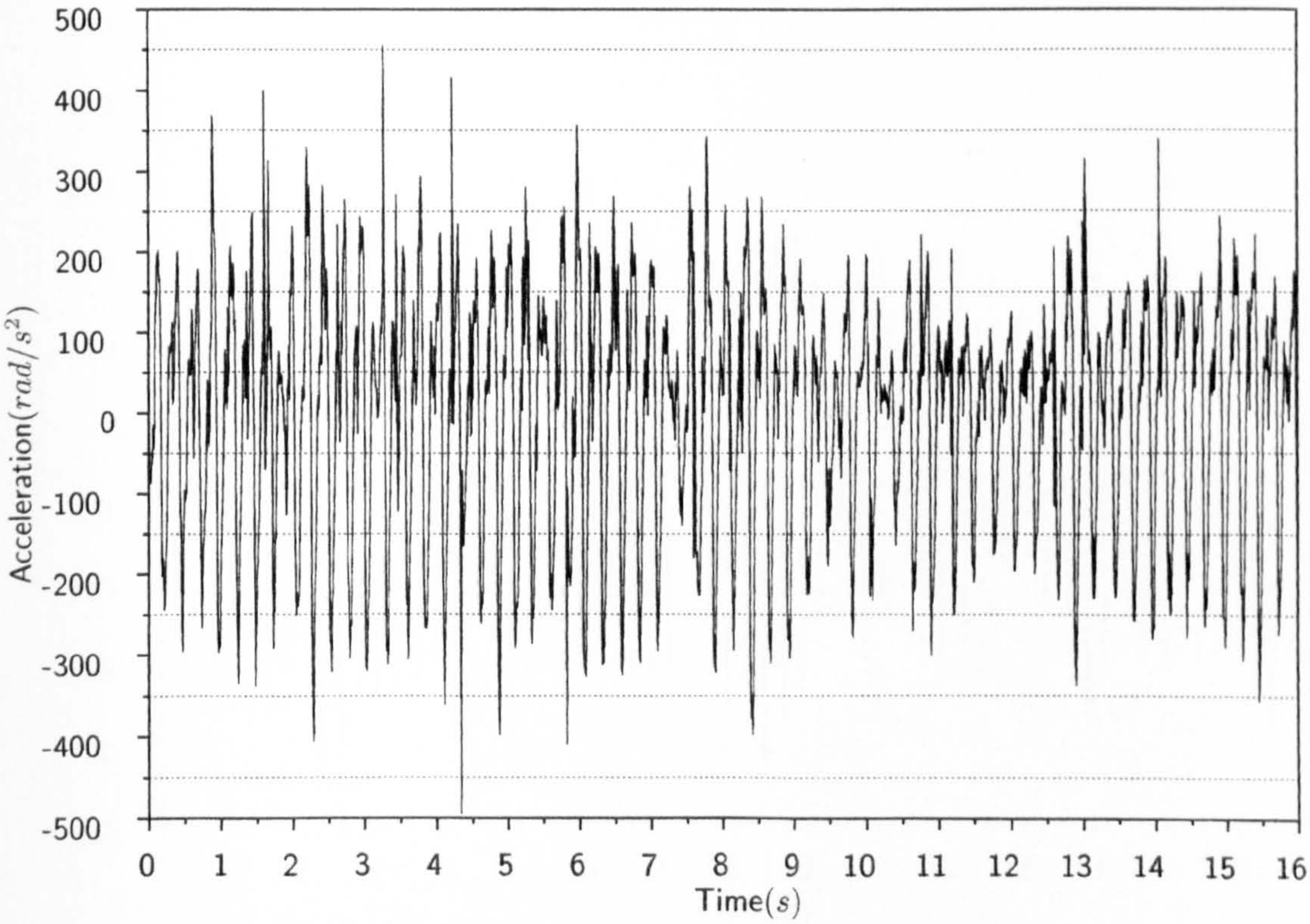

Figure E.14: Max peak acceleration, Model 14

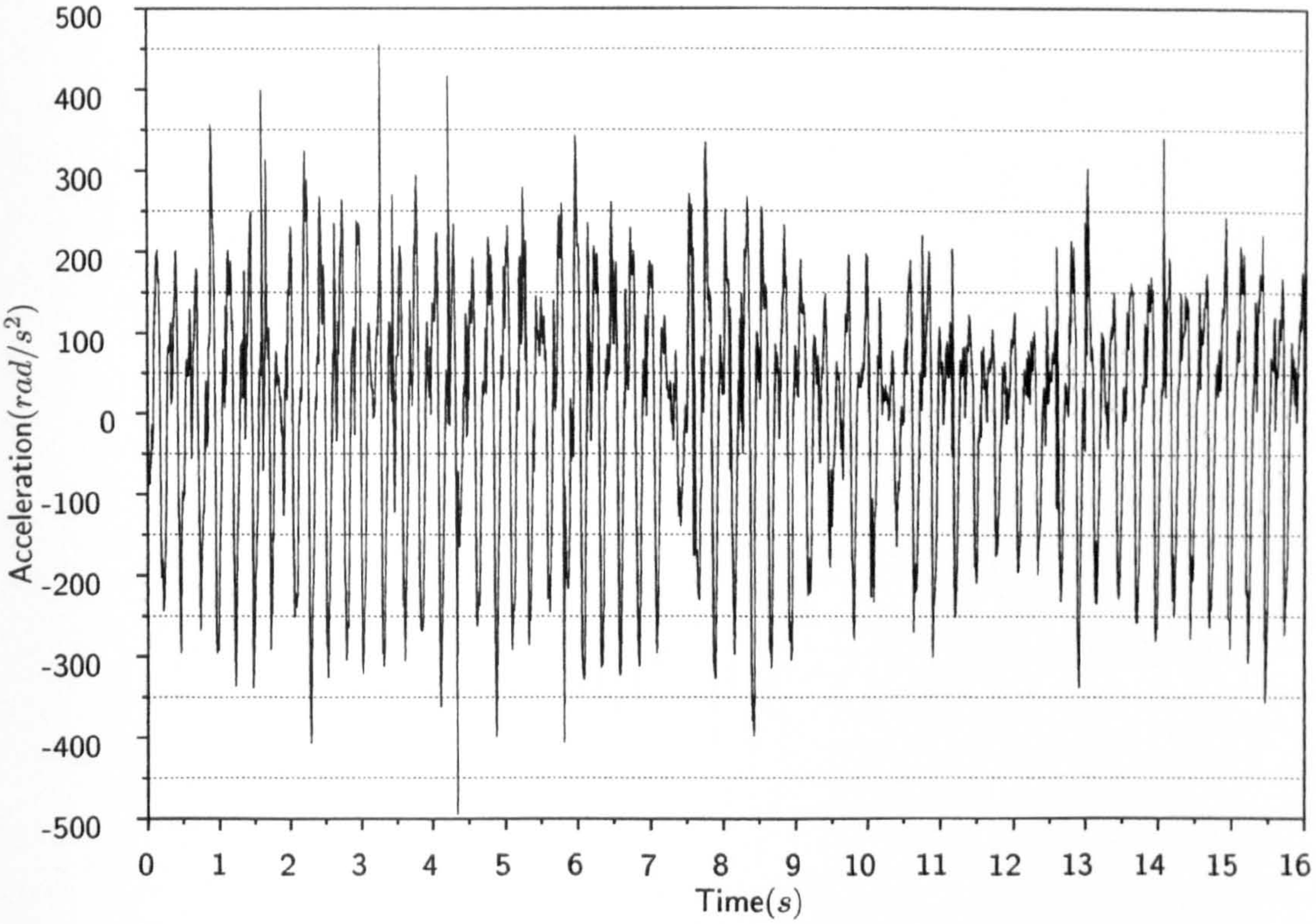

Figure E.15: Max peak acceleration, Model 15

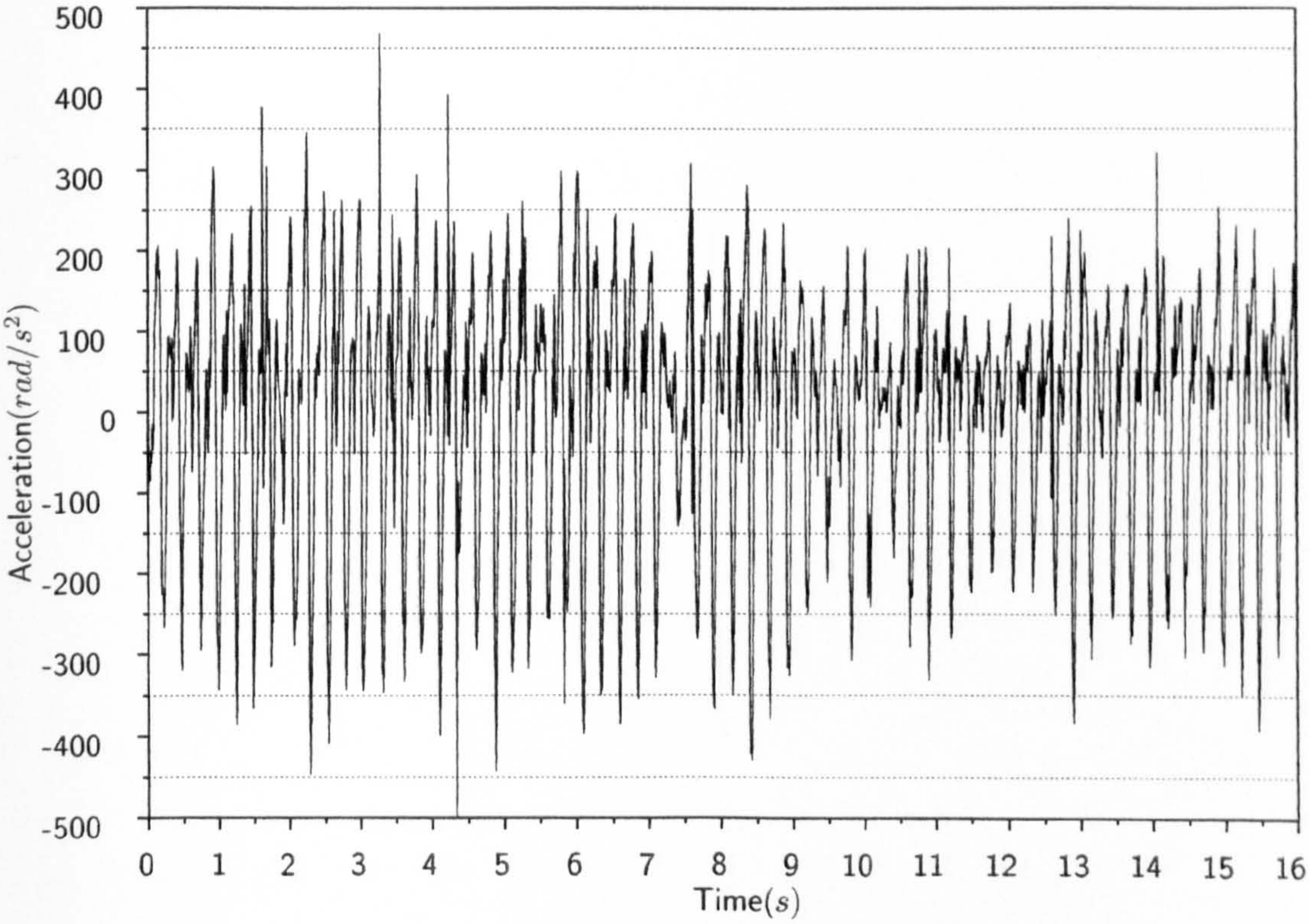

Figure E.16: Max peak acceleration, Model 16

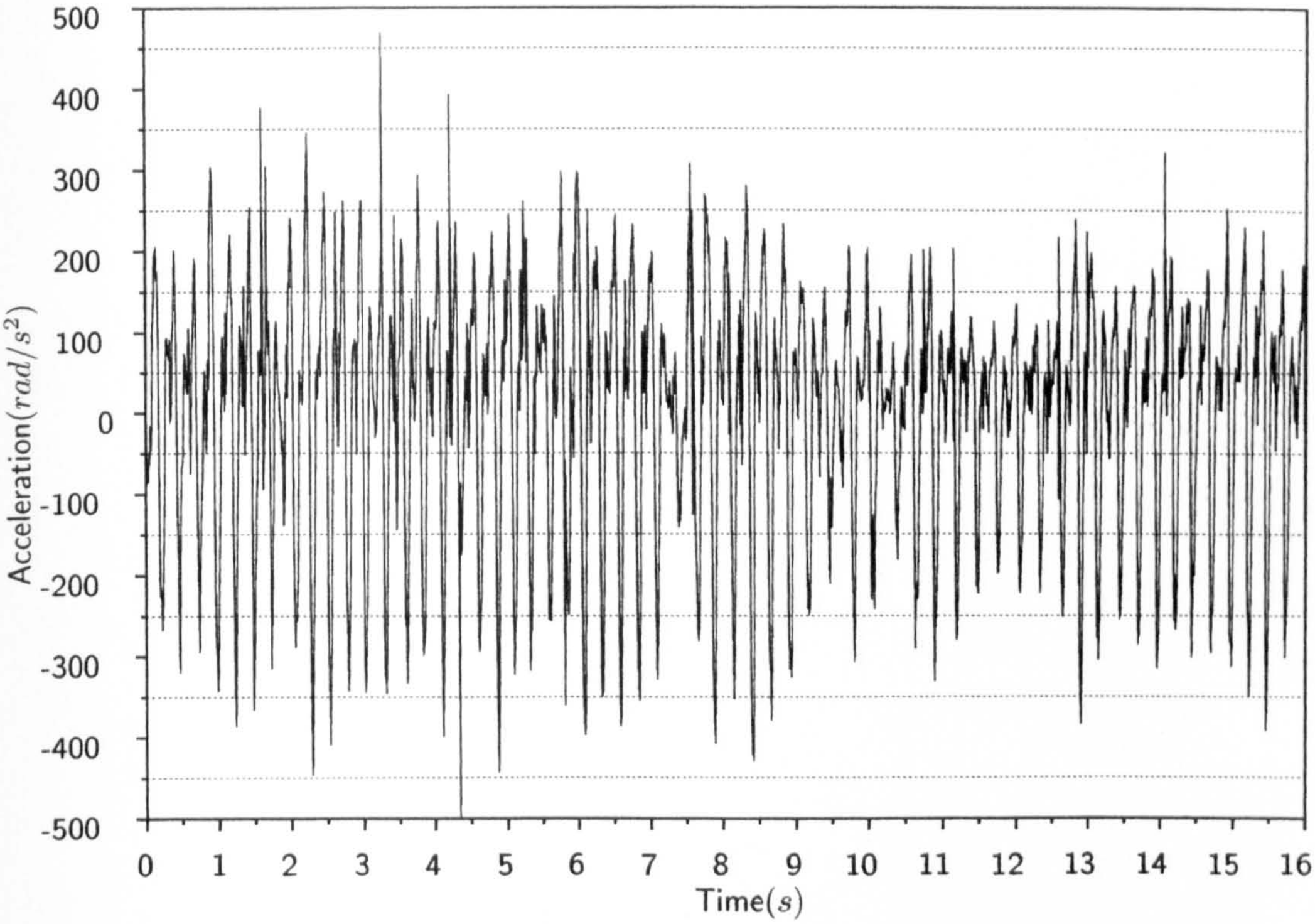

Figure E.17: Max peak acceleration, Model 17

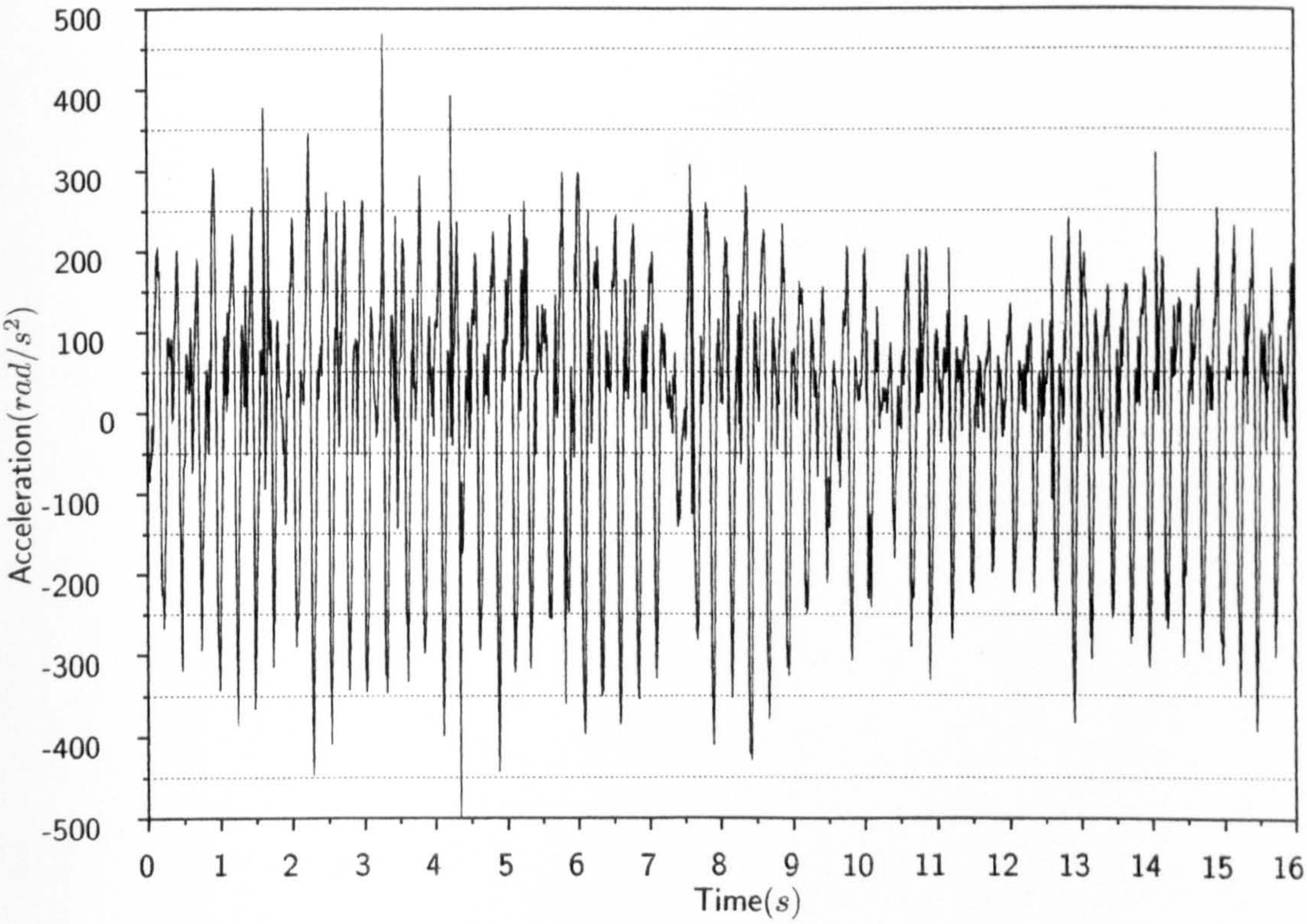

Figure E.18: Max peak acceleration, Model 18

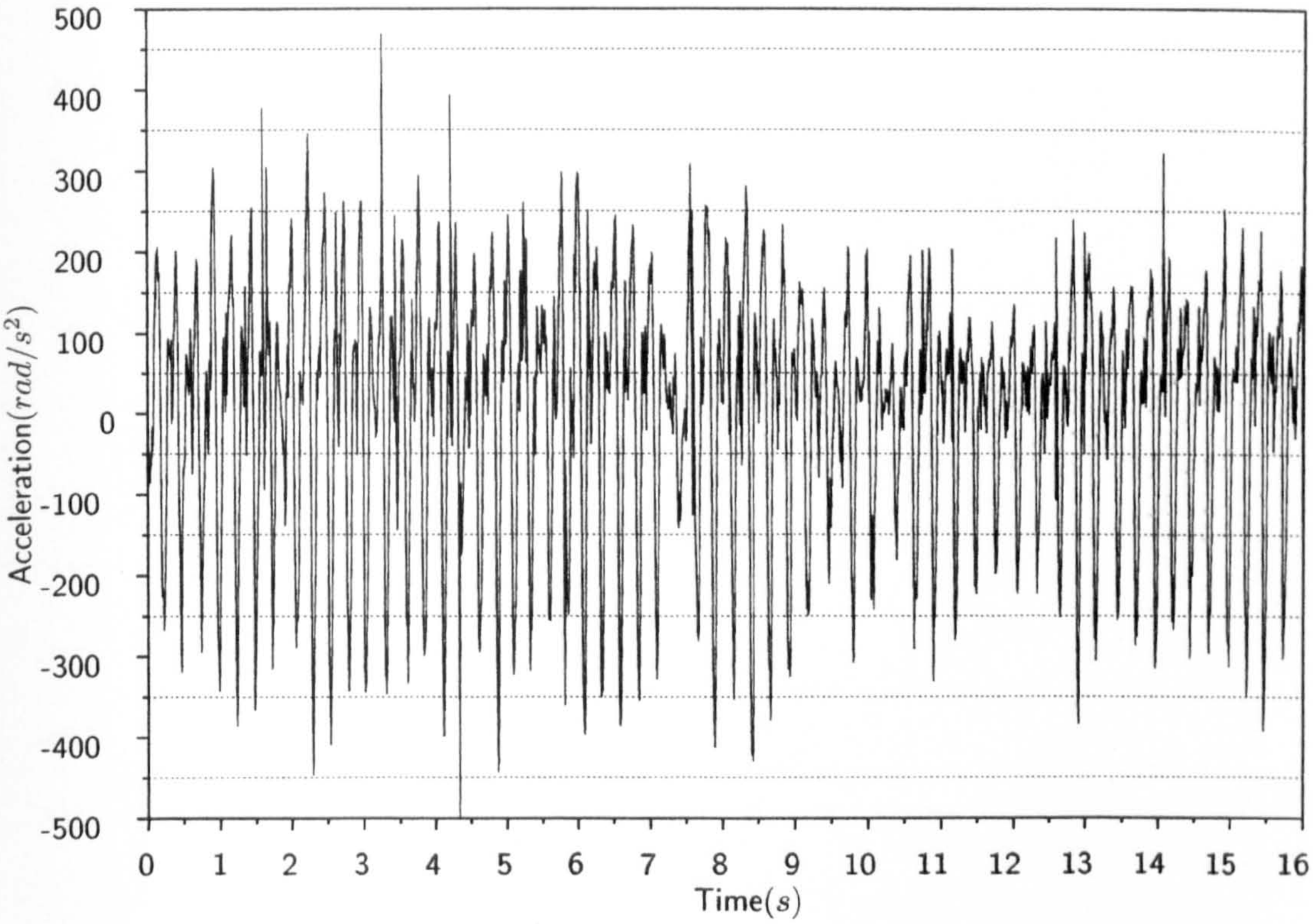

Figure E.19: Max peak acceleration, Model 19

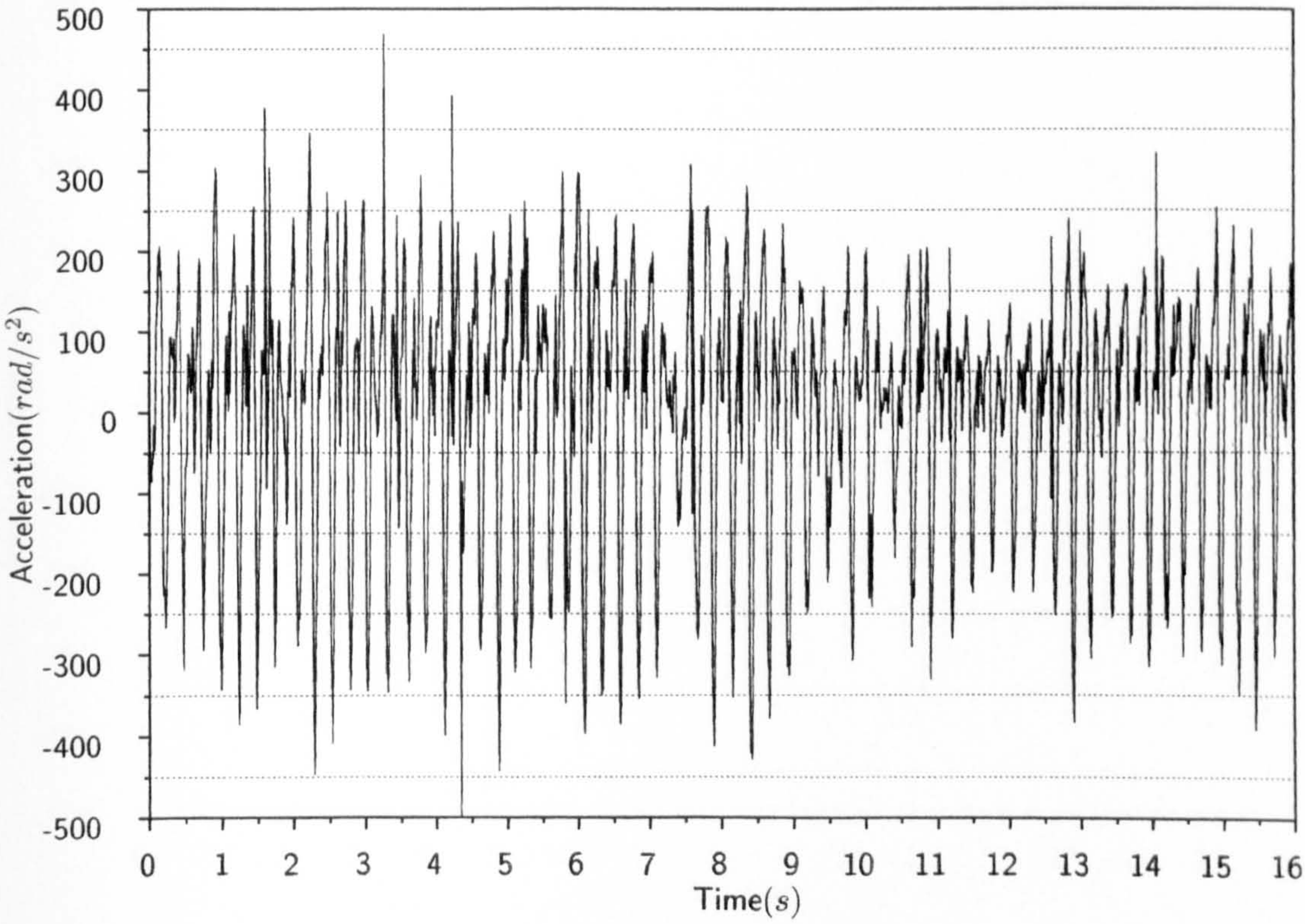

Figure E.20: Max peak acceleration, Model 20

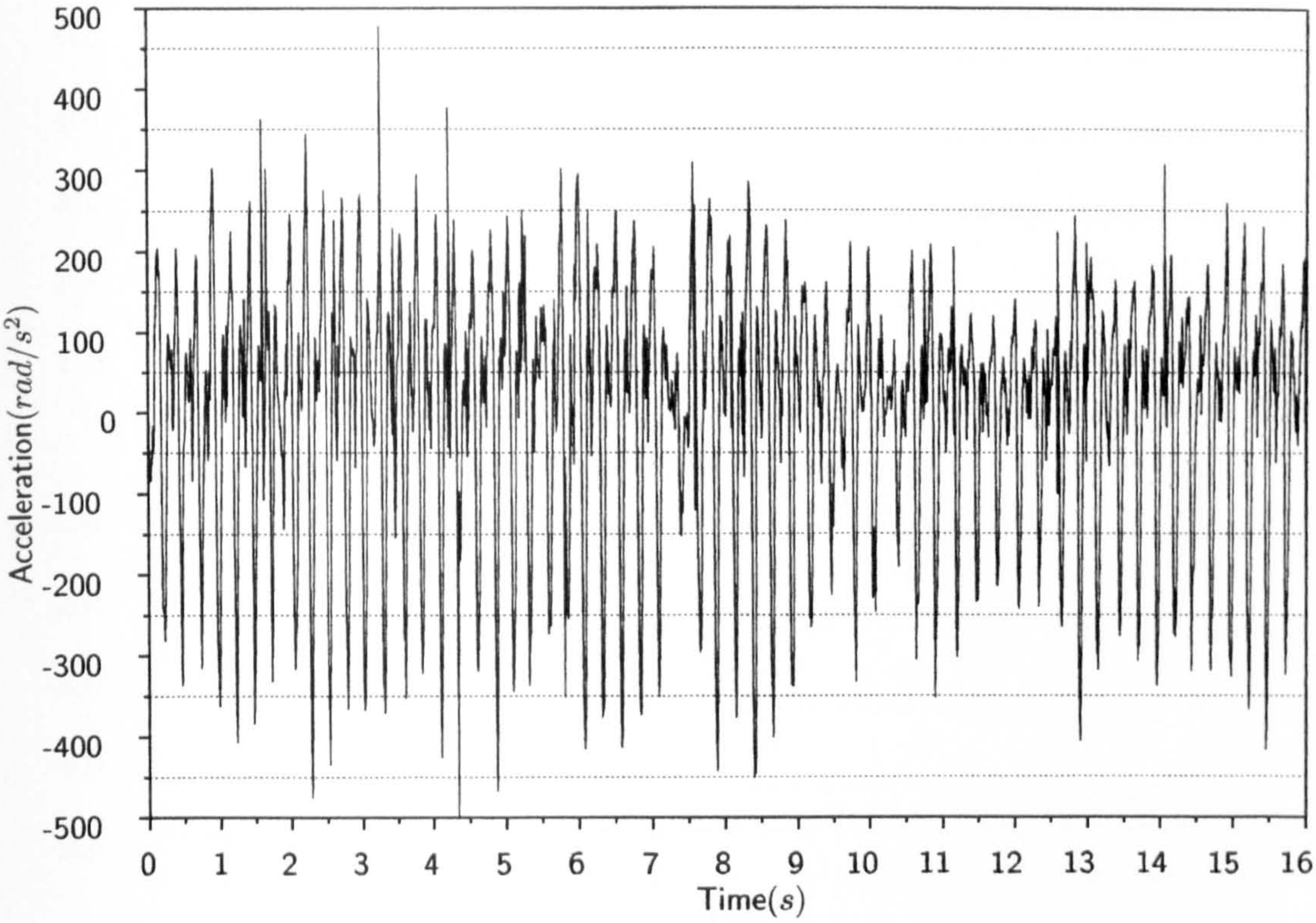

Figure E.21: Max peak acceleration, Model 21

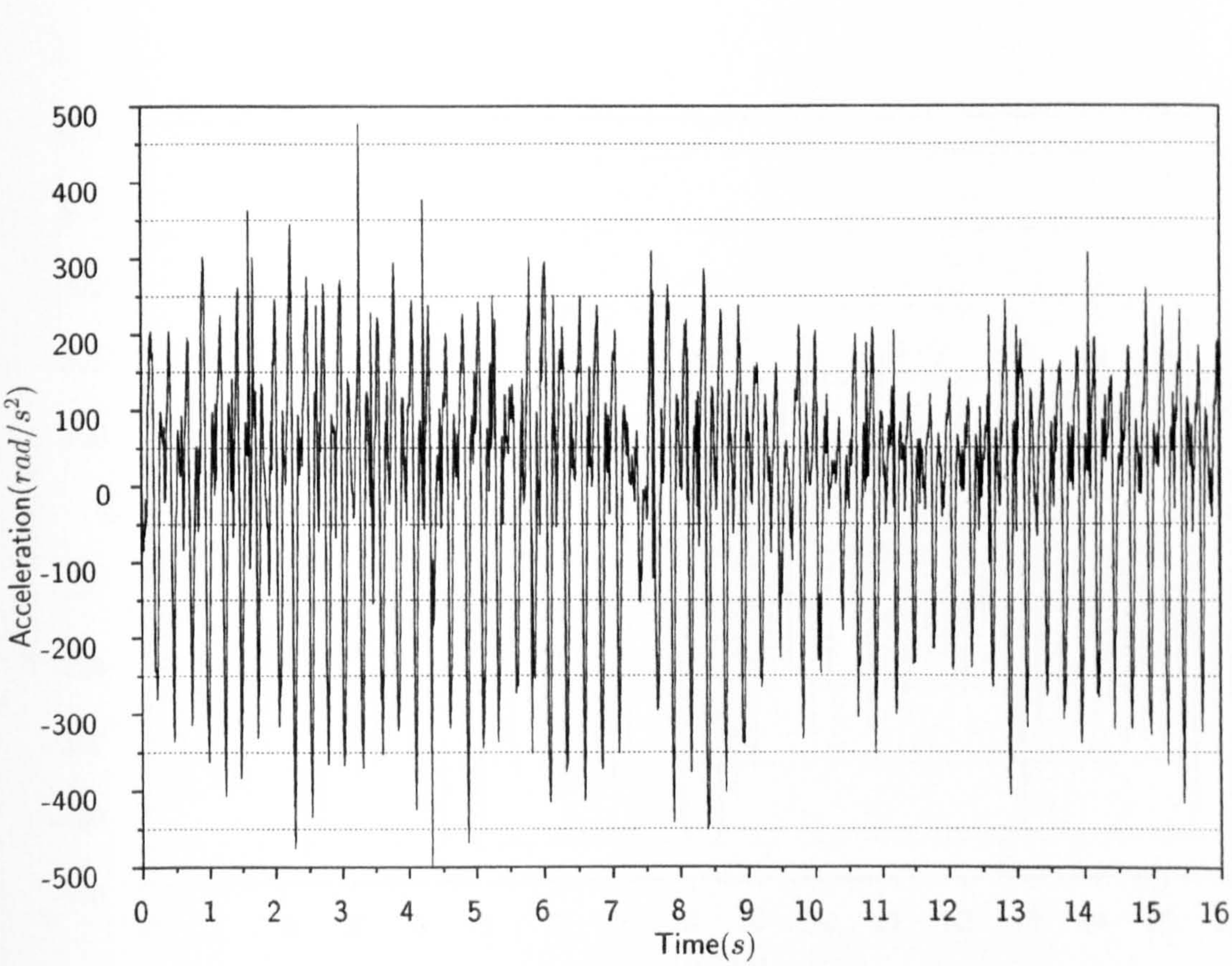

Figure E.22: Max peak acceleration, Model 22

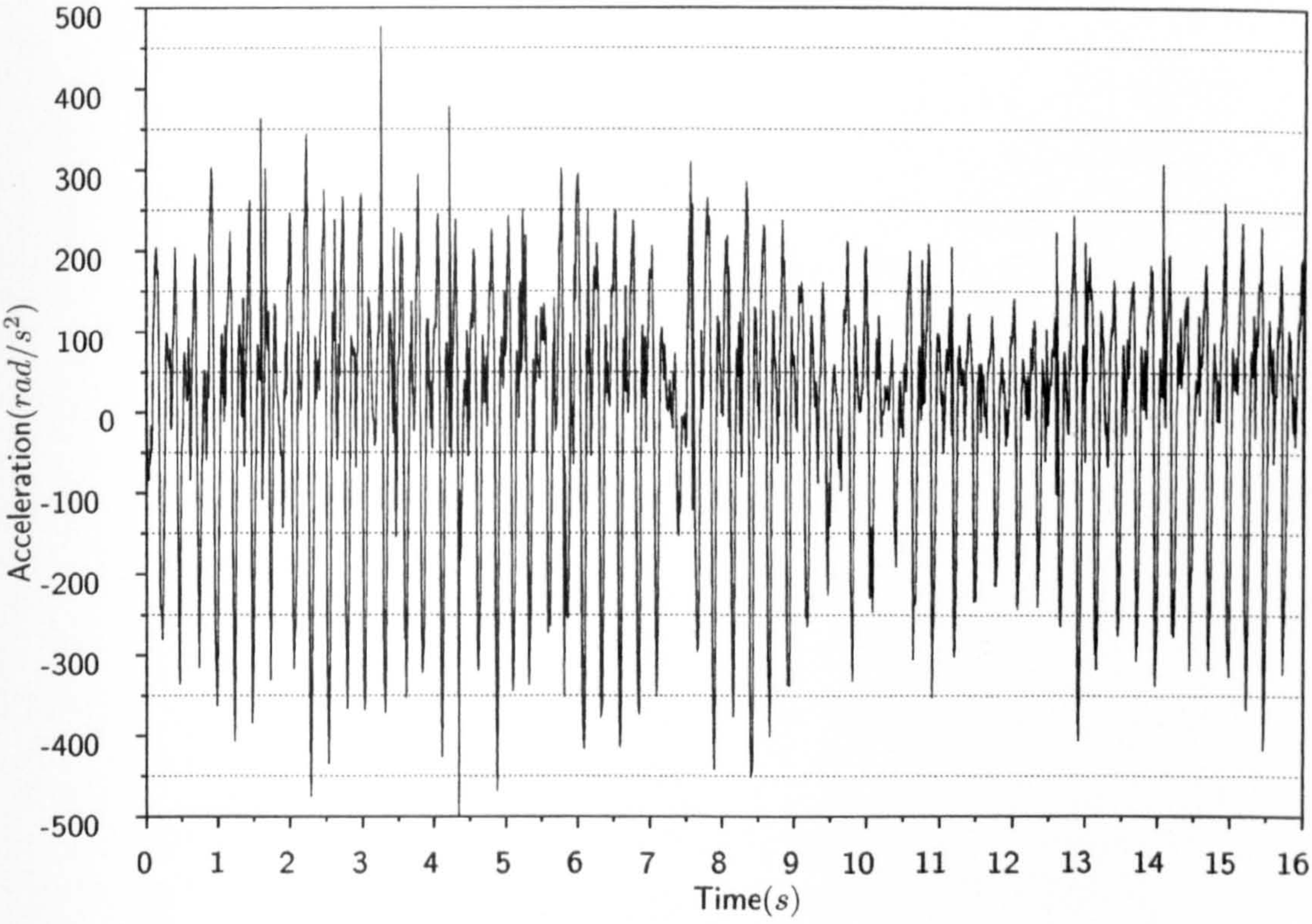

Figure E.23: Max peak acceleration, Model 23

Figure E.24: Max peak acceleration, Model 24

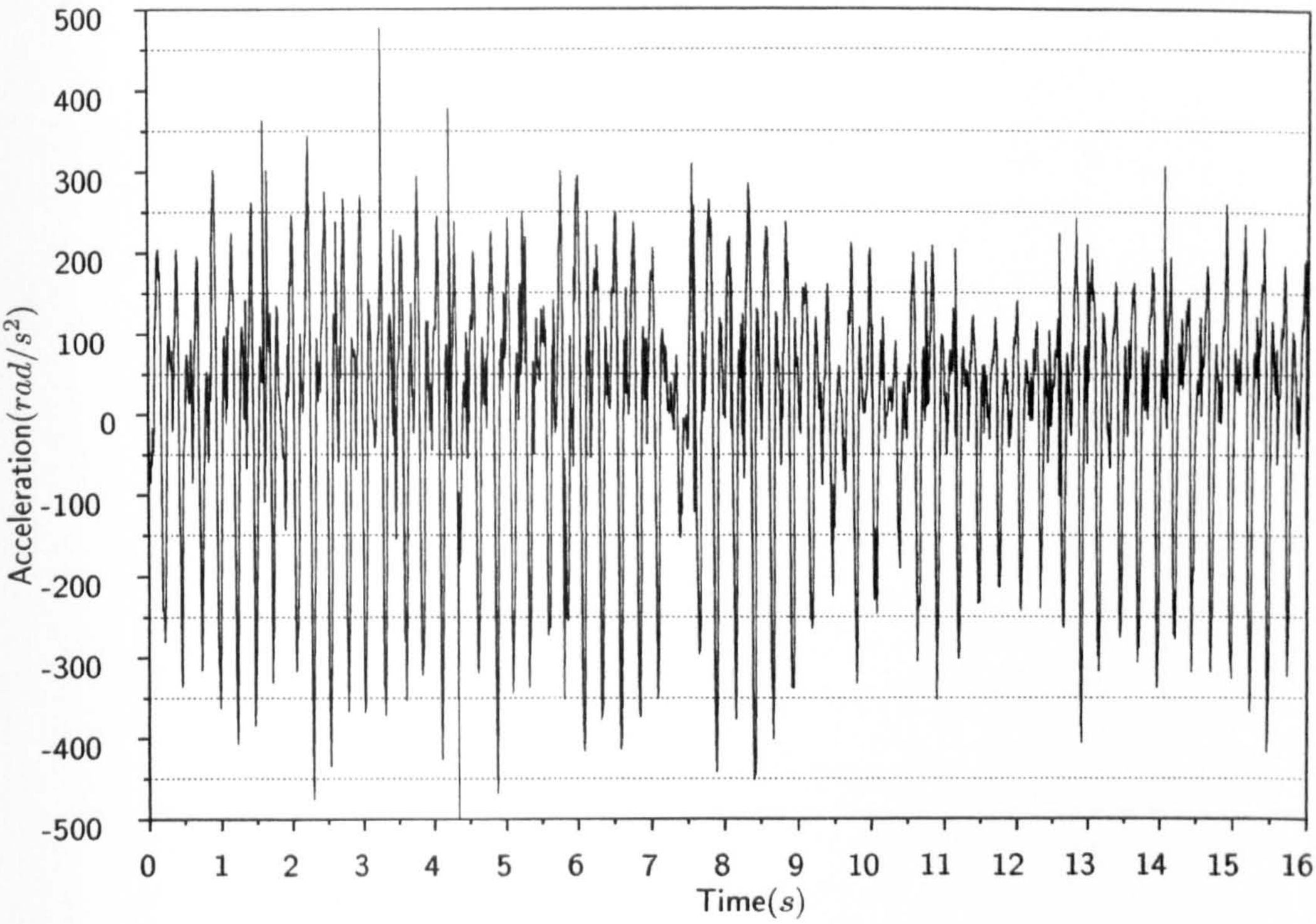

Figure E.25: Max peak acceleration, Model 25

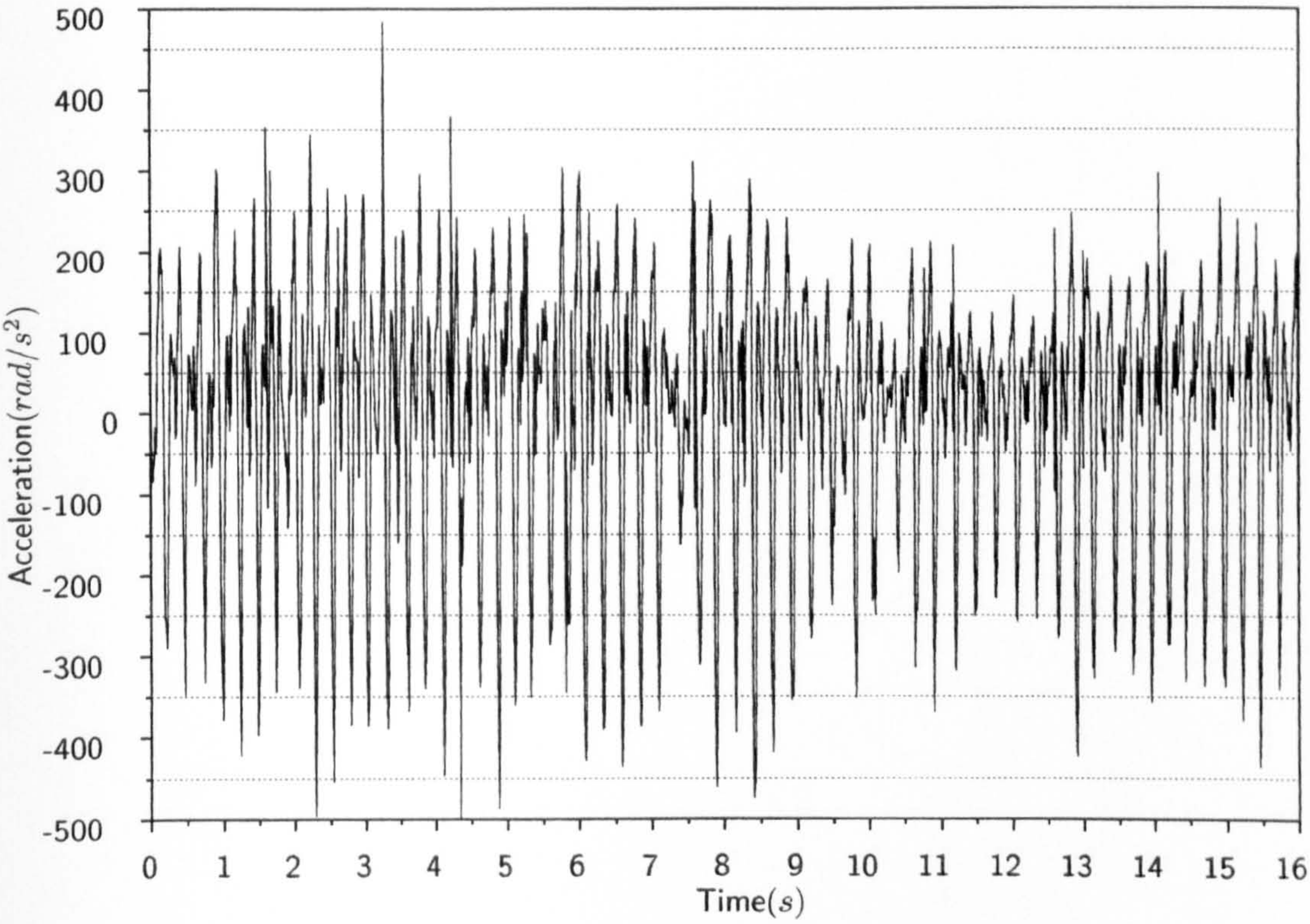

Figure E.26: Max peak acceleration, Model 26

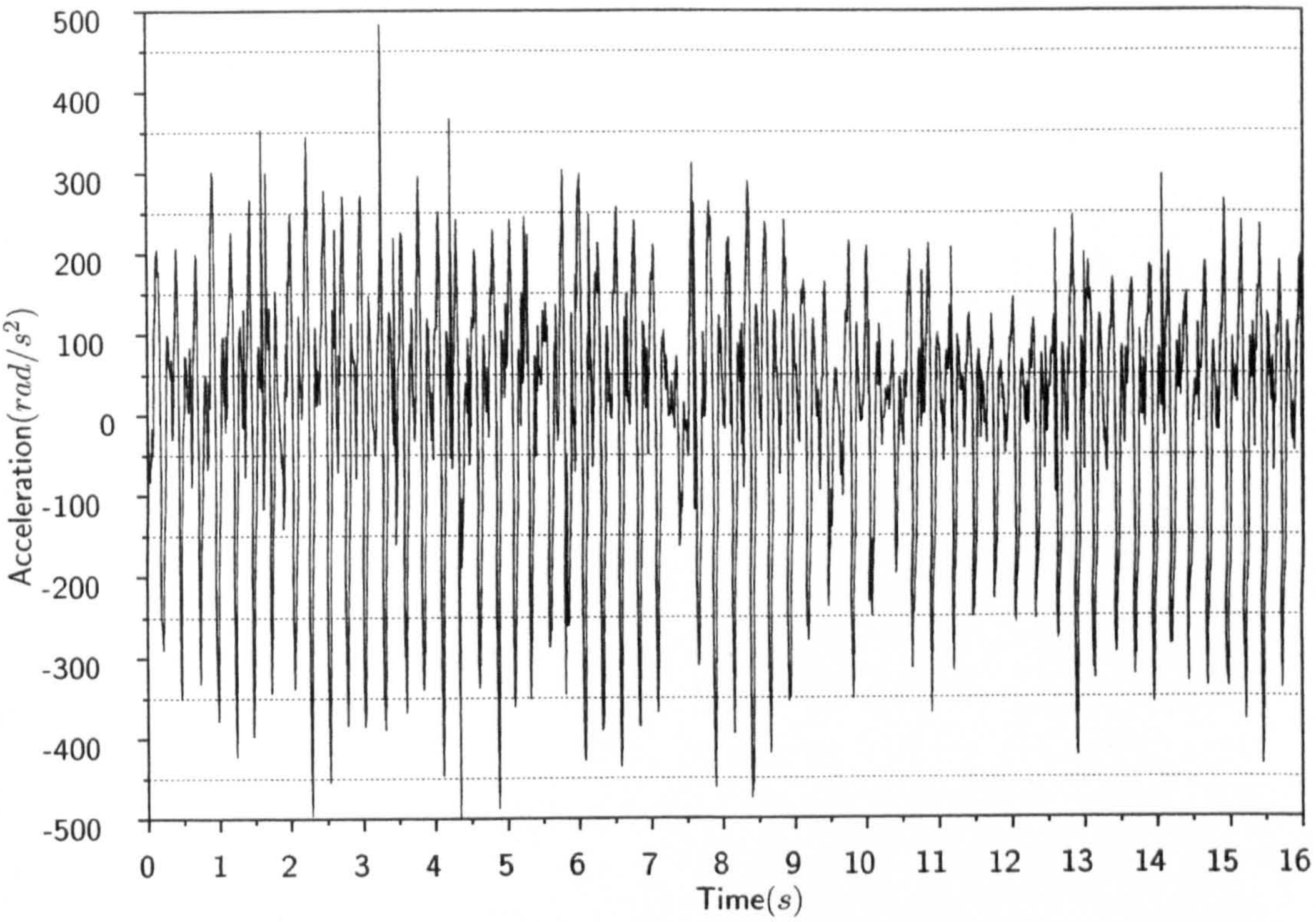

Figure E.27: Max peak acceleration, Model 27

Figure E.28: Max peak acceleration, Model 28

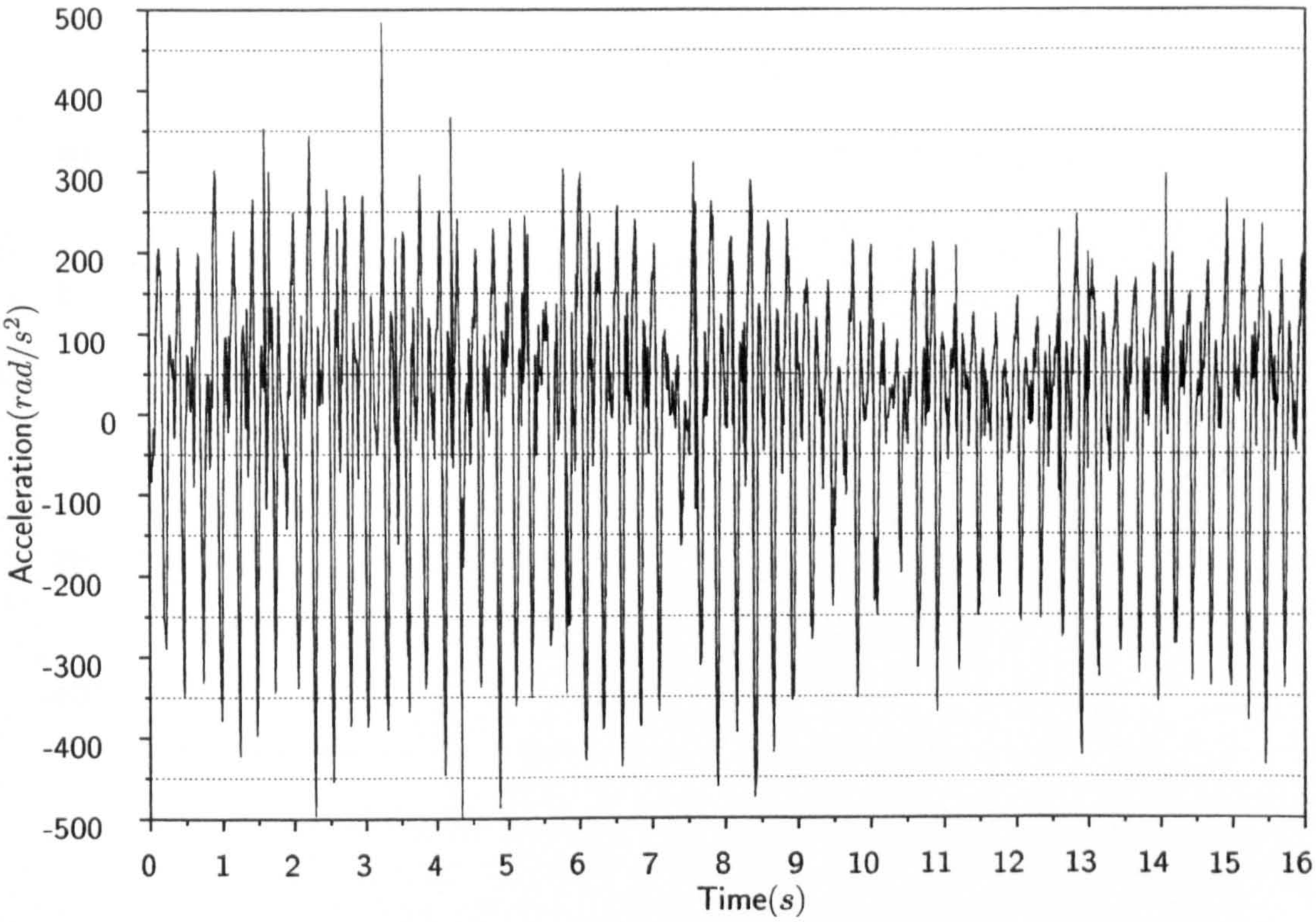

Figure E.29: Max peak acceleration, Model 29

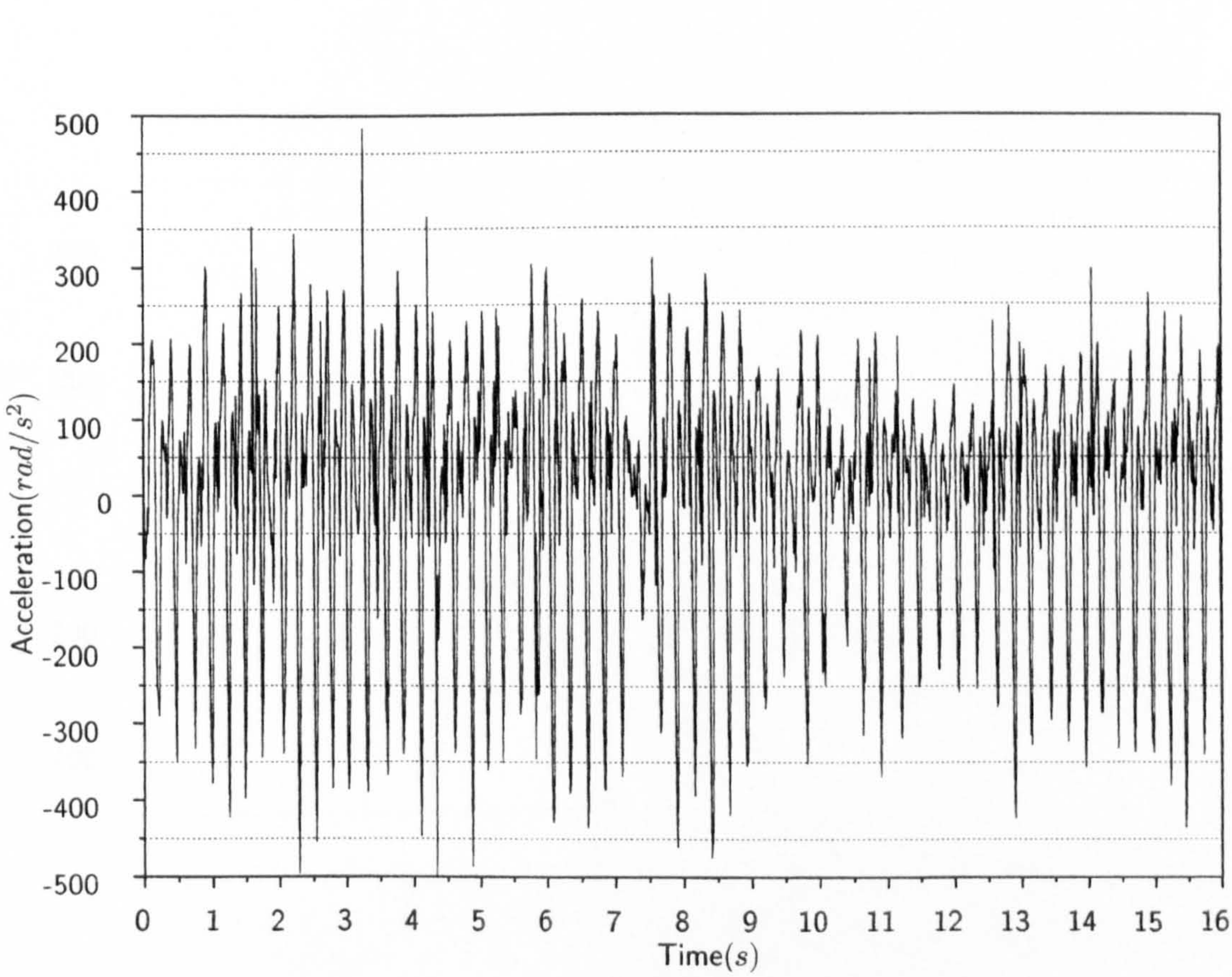

Figure E.30: Max peak acceleration, Model 30

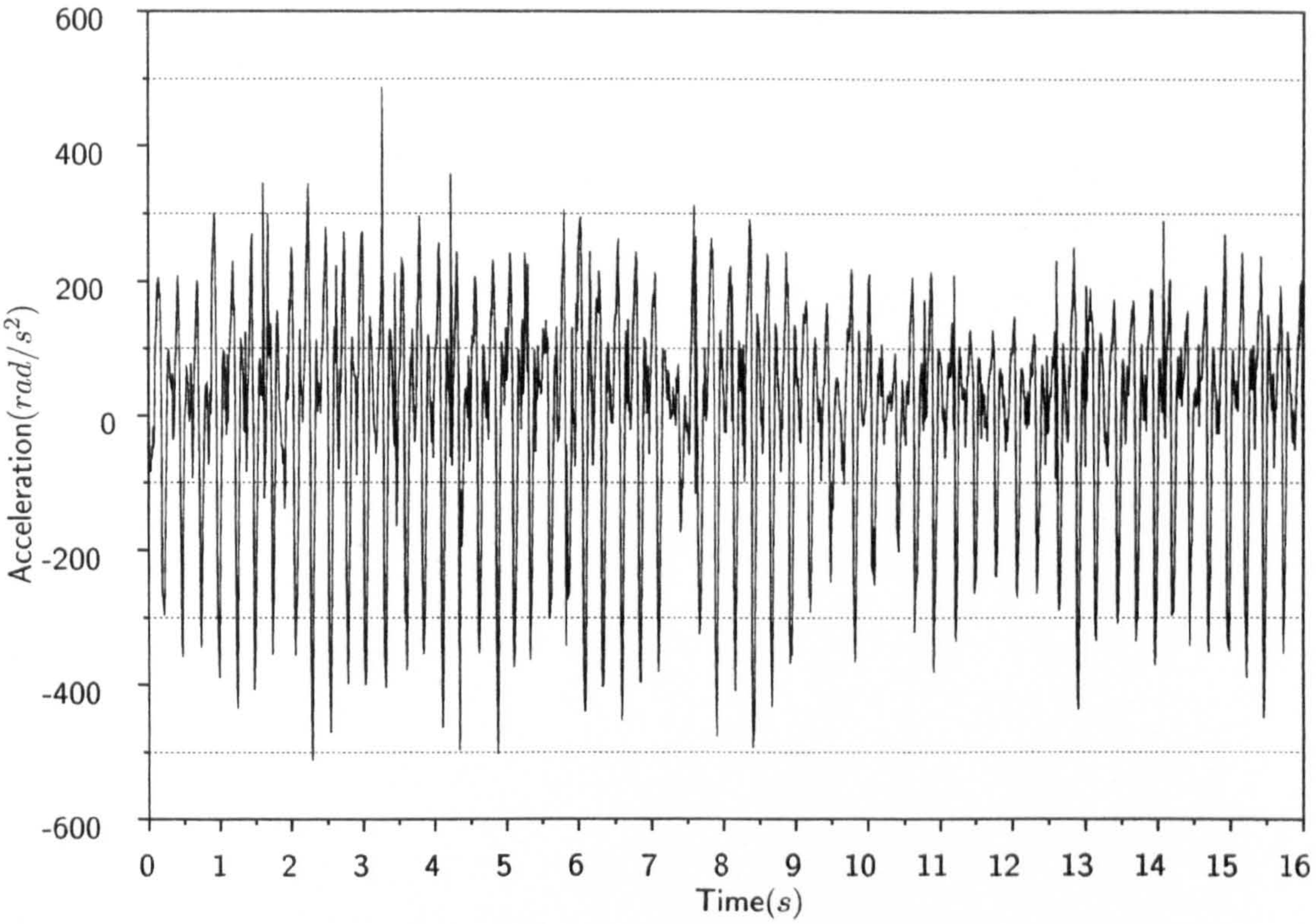

Figure E.31: Max peak acceleration, Model 31

Figure E.32: Max peak acceleration, Model 32

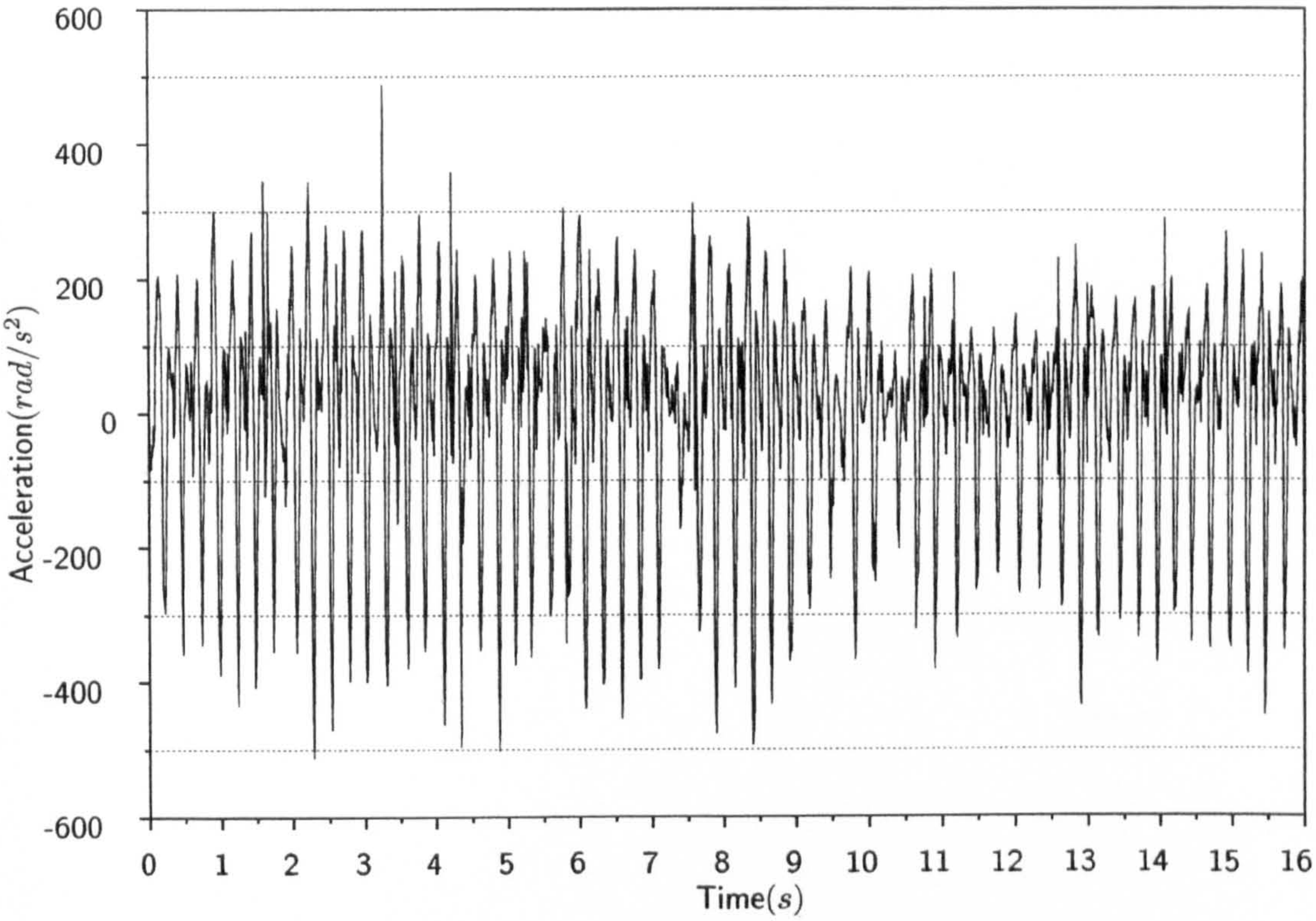

Figure E.33: Max peak acceleration, Model 33

Figure E.34: Max peak acceleration, Model 34

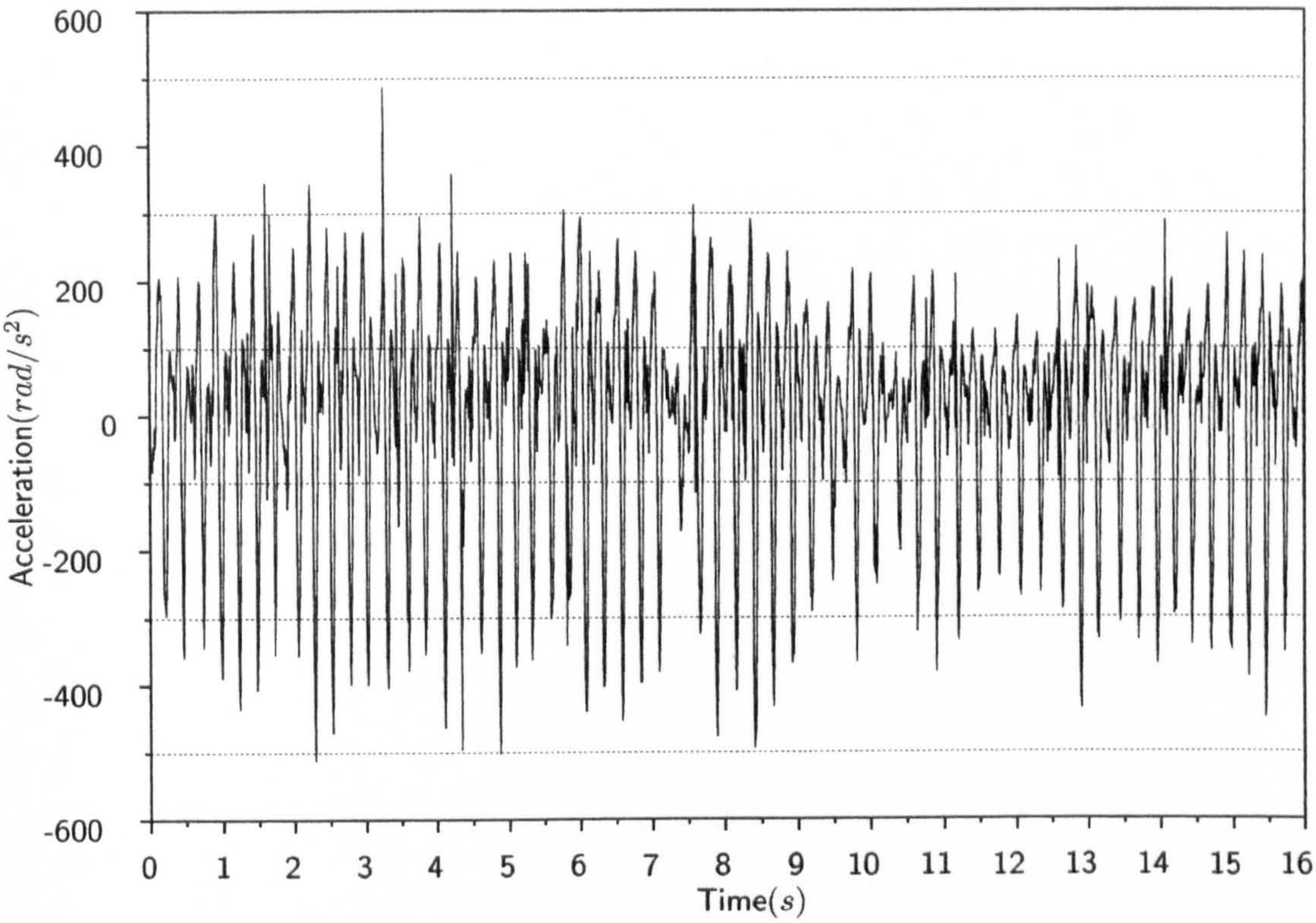

Figure E.35: Max peak acceleration, Model 35

Figure E.36: Max peak acceleration, Model 36

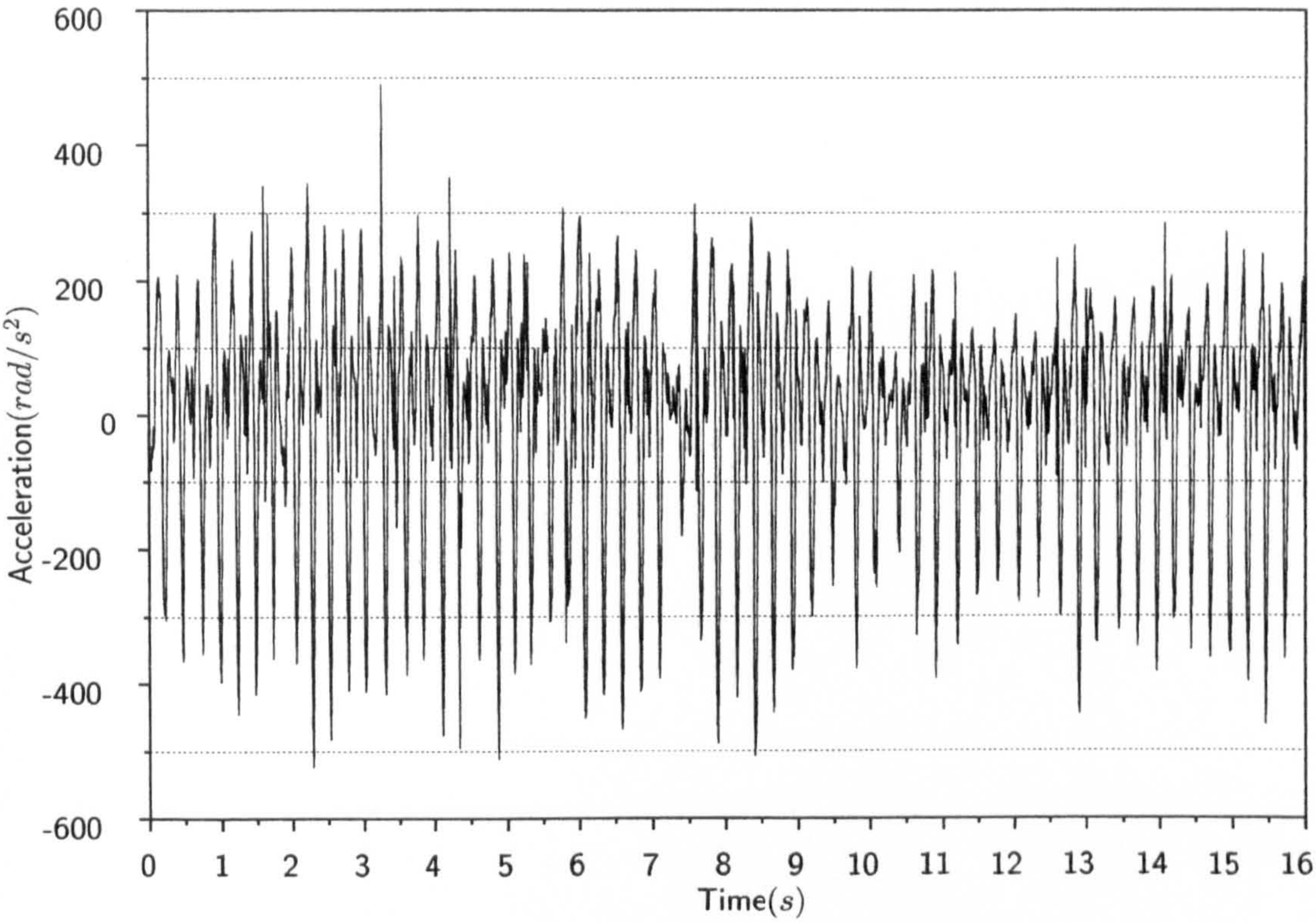

Figure E.37: Max peak acceleration, Model 37

Figure E.38: Max peak acceleration, Model 38

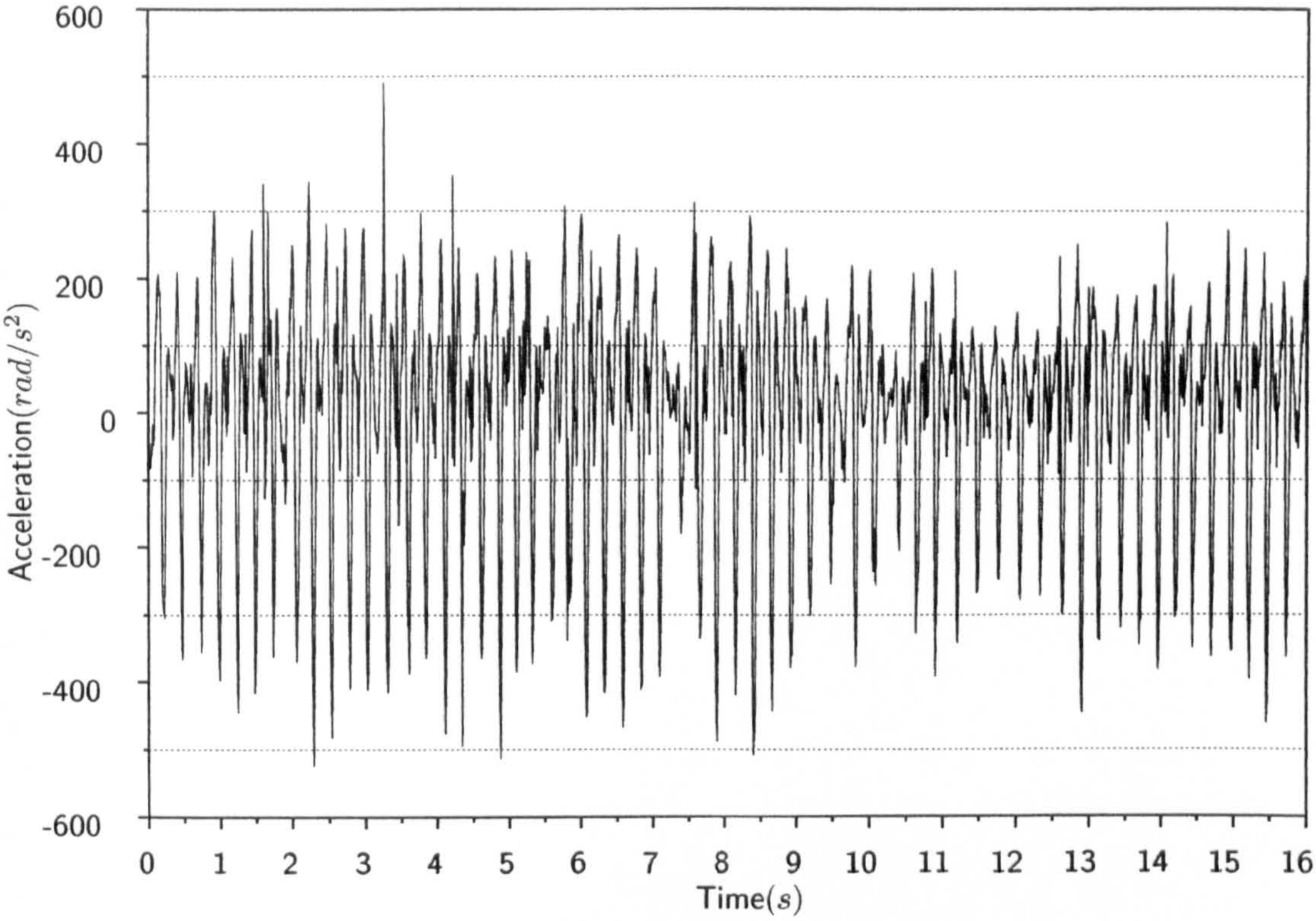

Figure E.39: Max peak acceleration, Model 39

Figure E.40: Max peak acceleration, Model 40

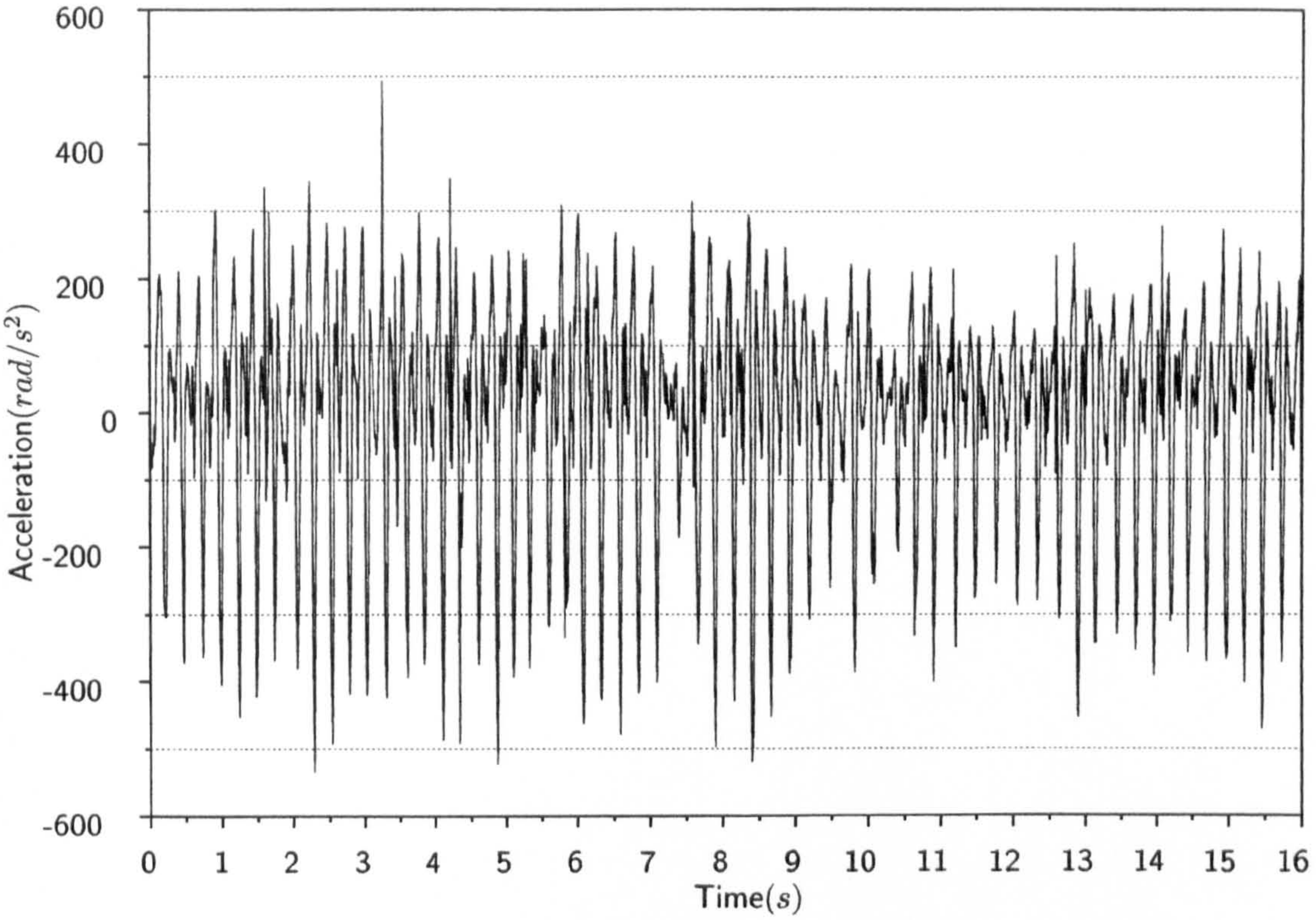

Figure E.41: Max peak acceleration, Model 41

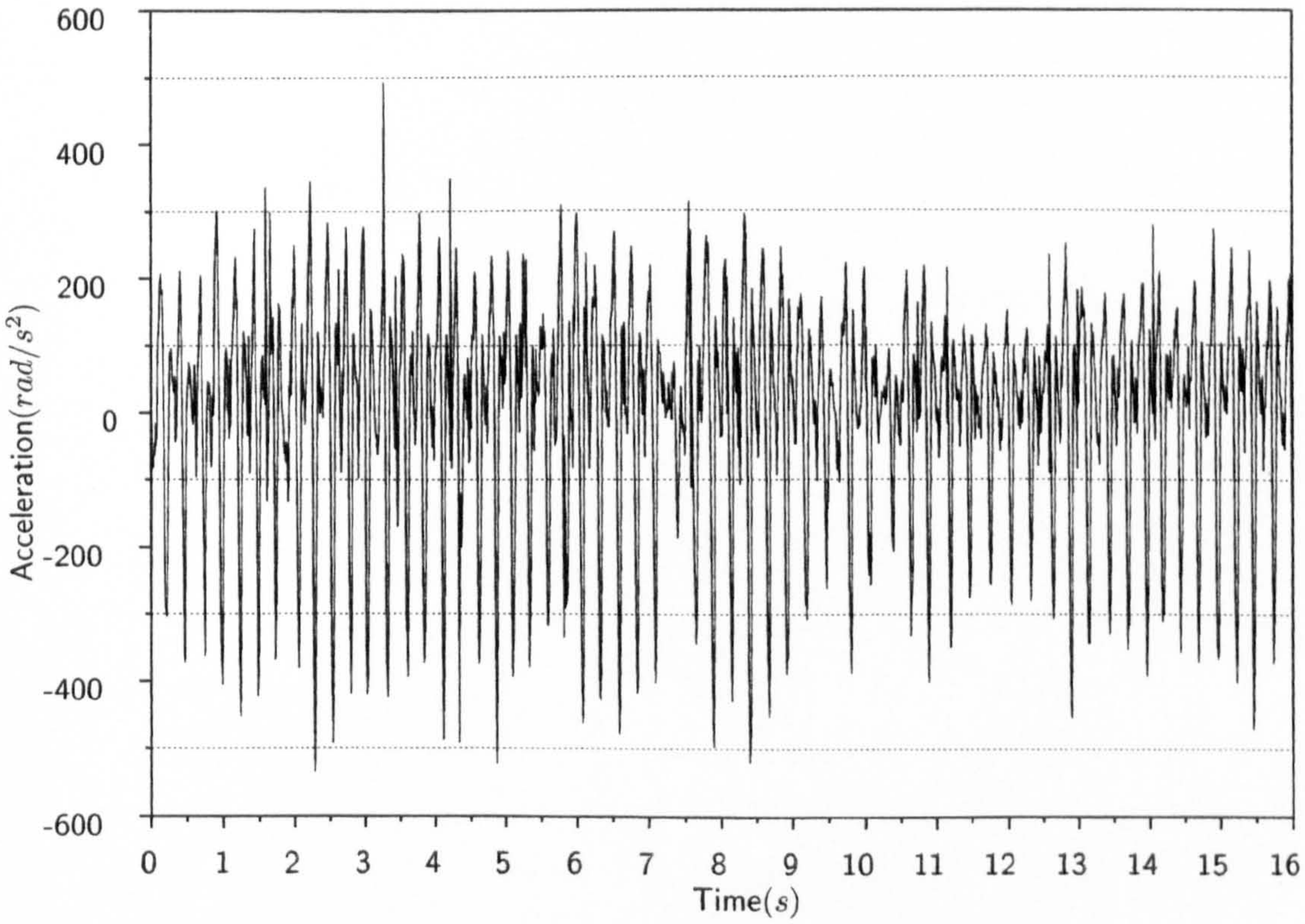

Figure E.42: Max peak acceleration, Model 42

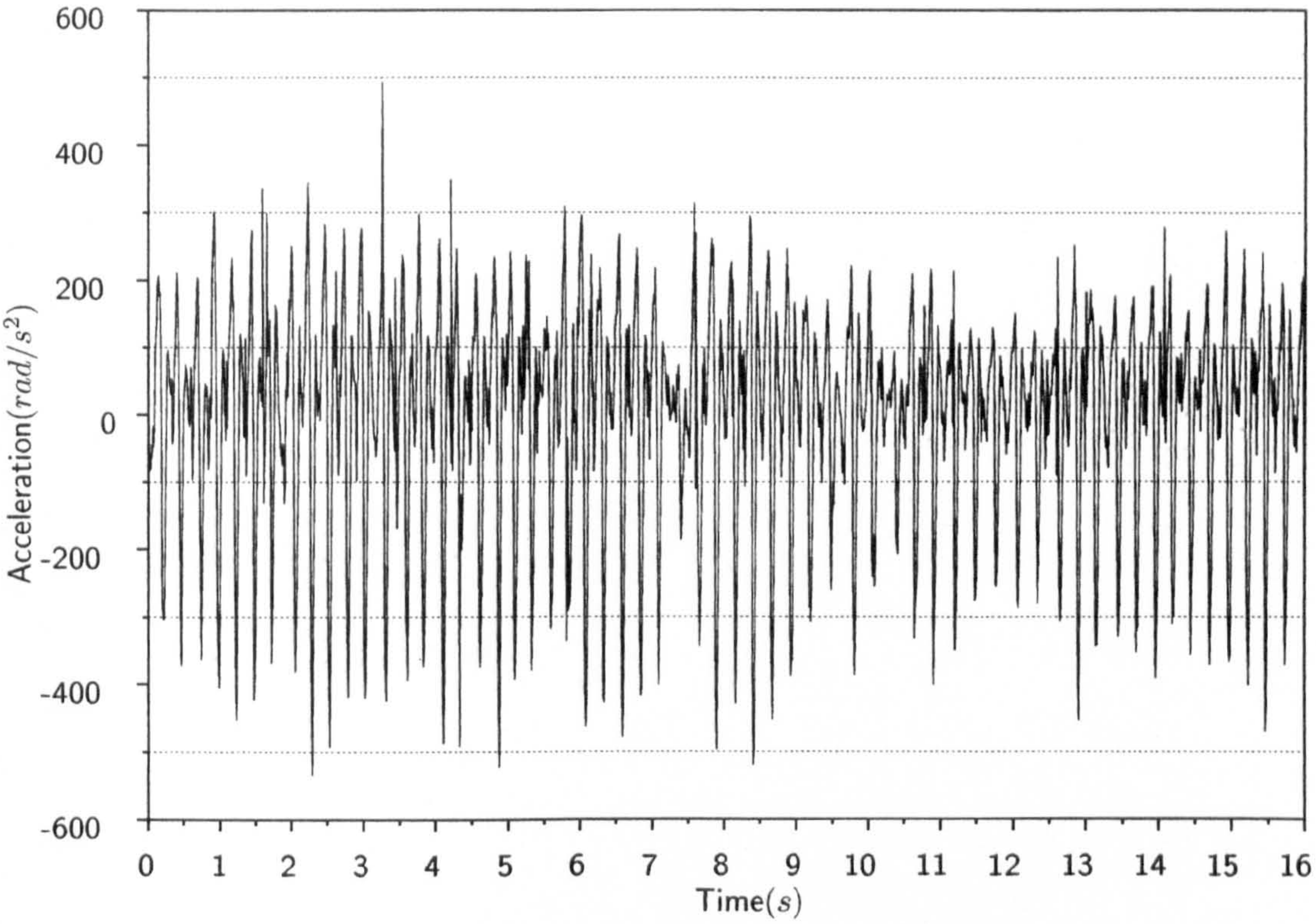

Figure E.43: Max peak acceleration, Model 43

Figure E.44: Max peak acceleration, Model 44

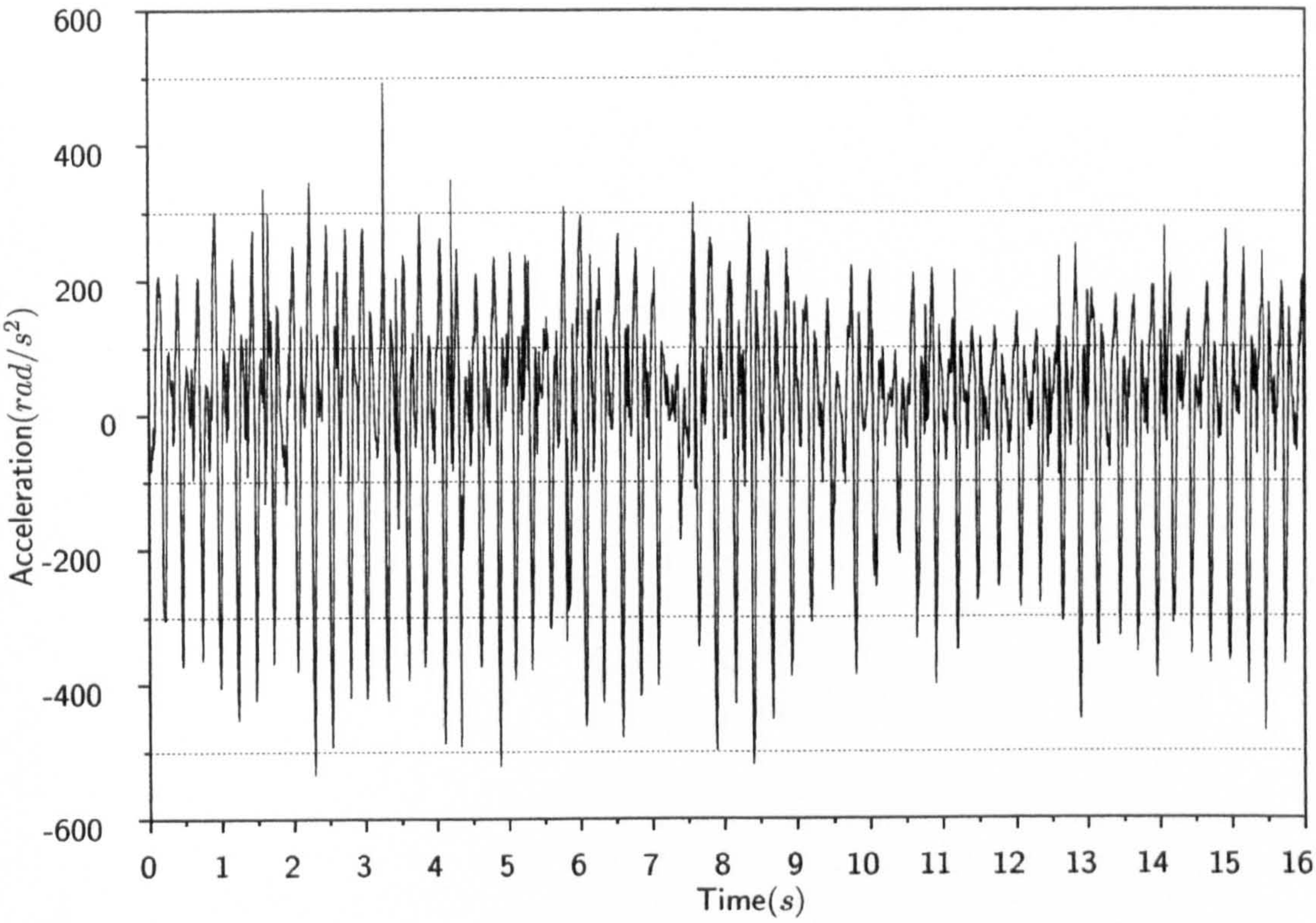

Figure E.45: Max peak acceleration, Model 45

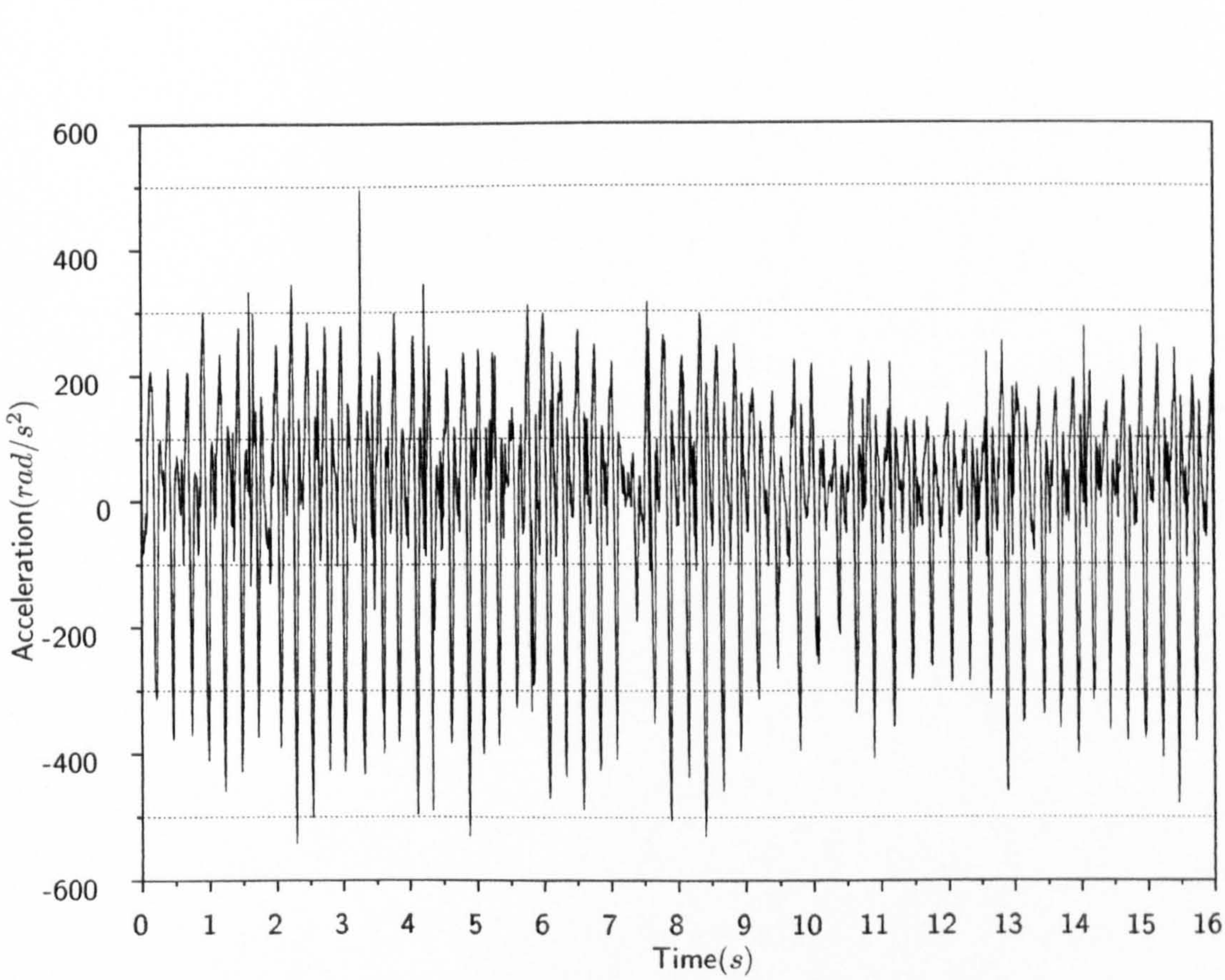

Figure E.46: Max peak acceleration, Model 46

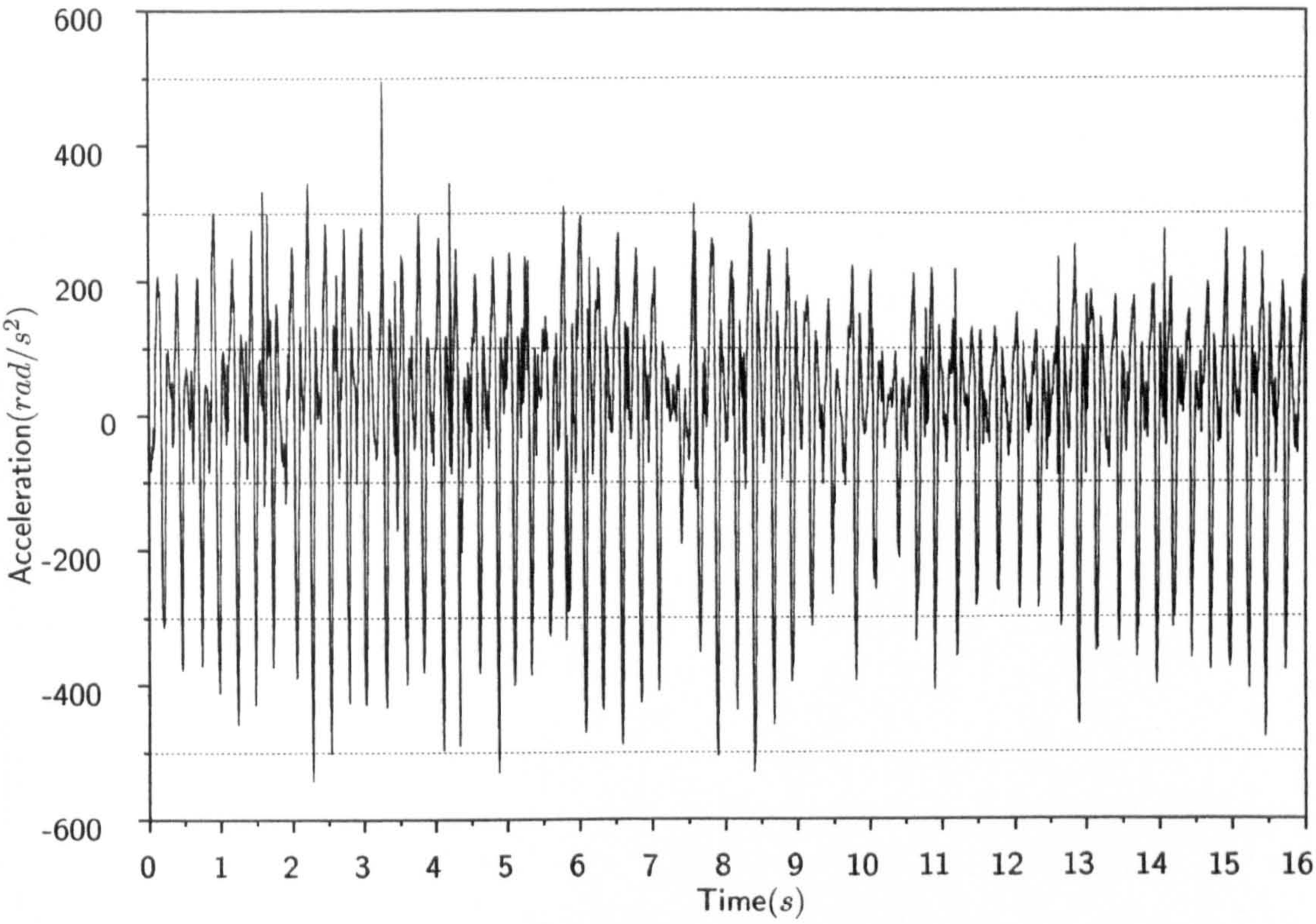

Figure E.47: Max peak acceleration, Model 47

Figure E.48: Max peak acceleration, Model 48

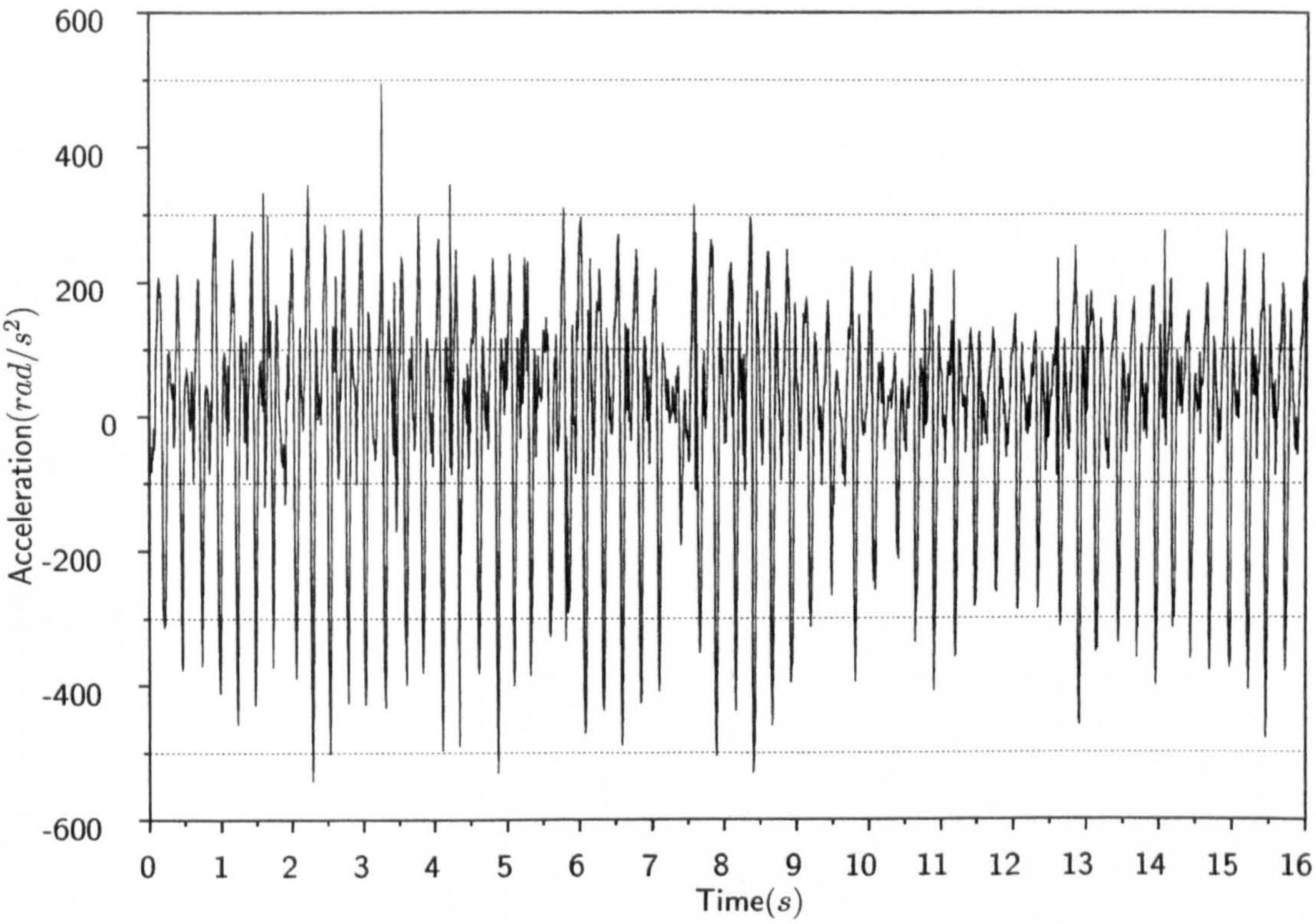

Figure E.49: Max peak acceleration, Model 49

Figure E.50: Max peak acceleration, Model 50

Appendix F

Results from Study of Head-Torso Impacts

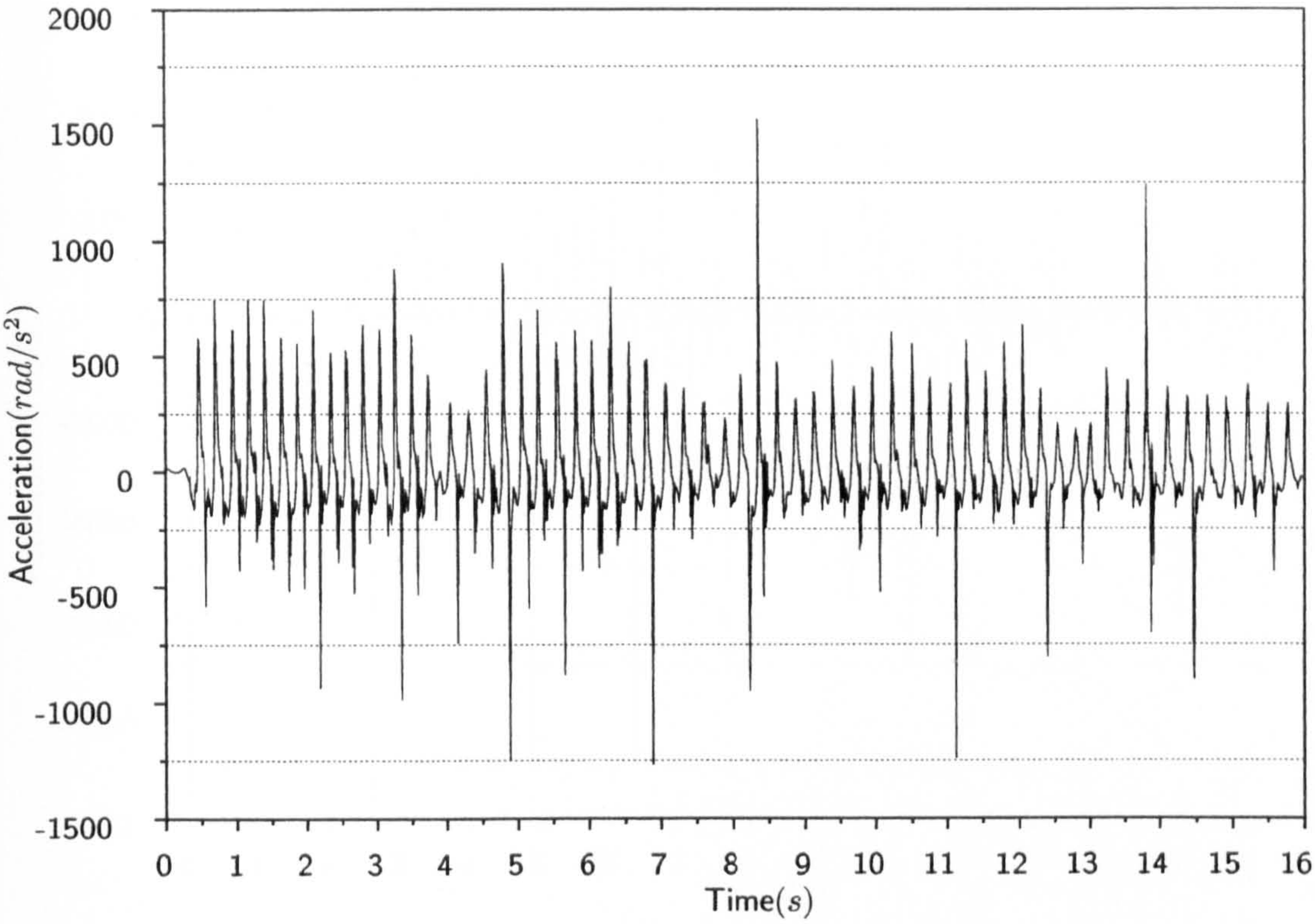

Figure F.1: Max rms acceleration, 2H Model

Figure F.2: Max peak acceleration, 2H Model

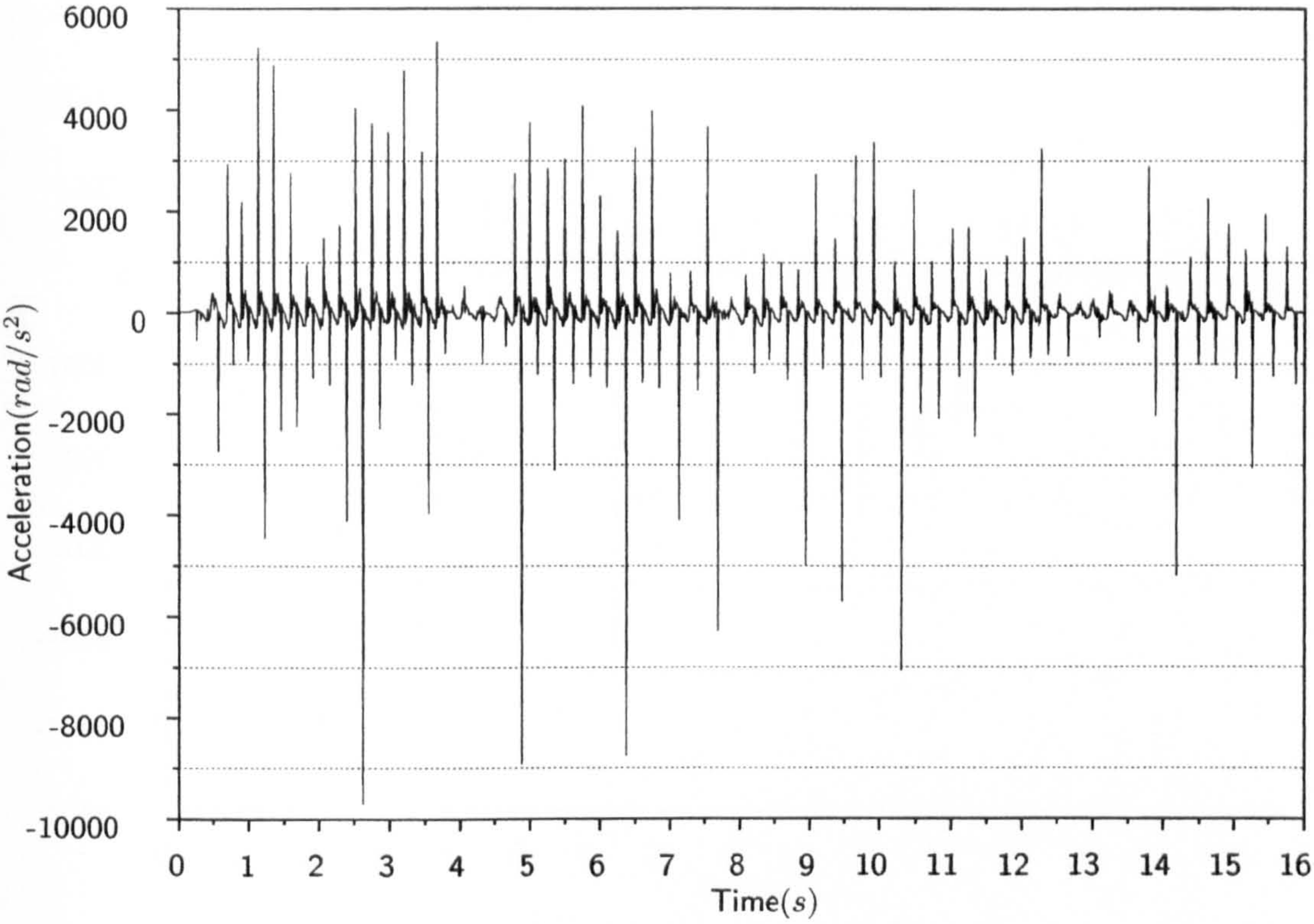

Figure F.3: Max rms acceleration, LH Model

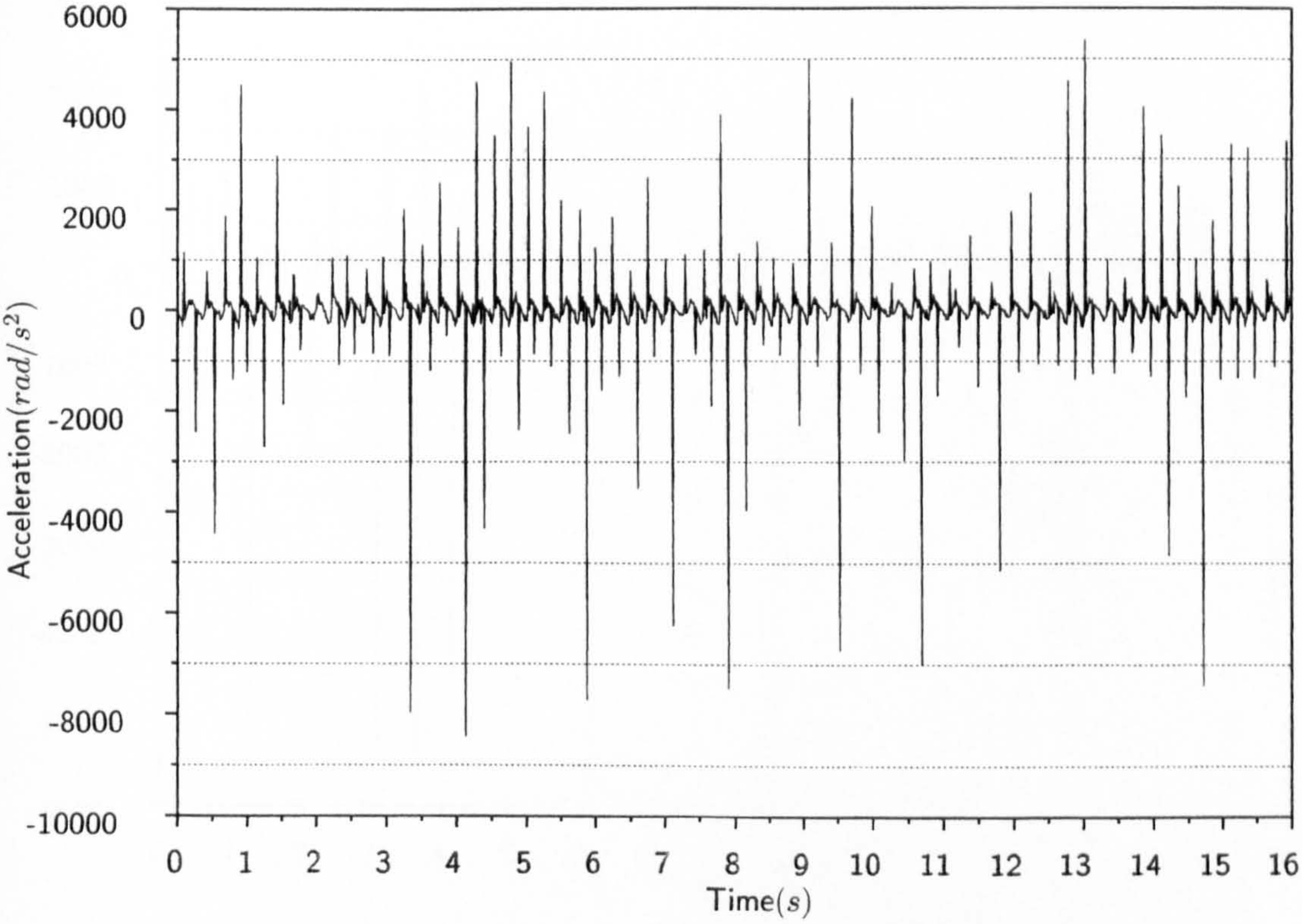

Figure F.4: Max peak acceleration, LH Model

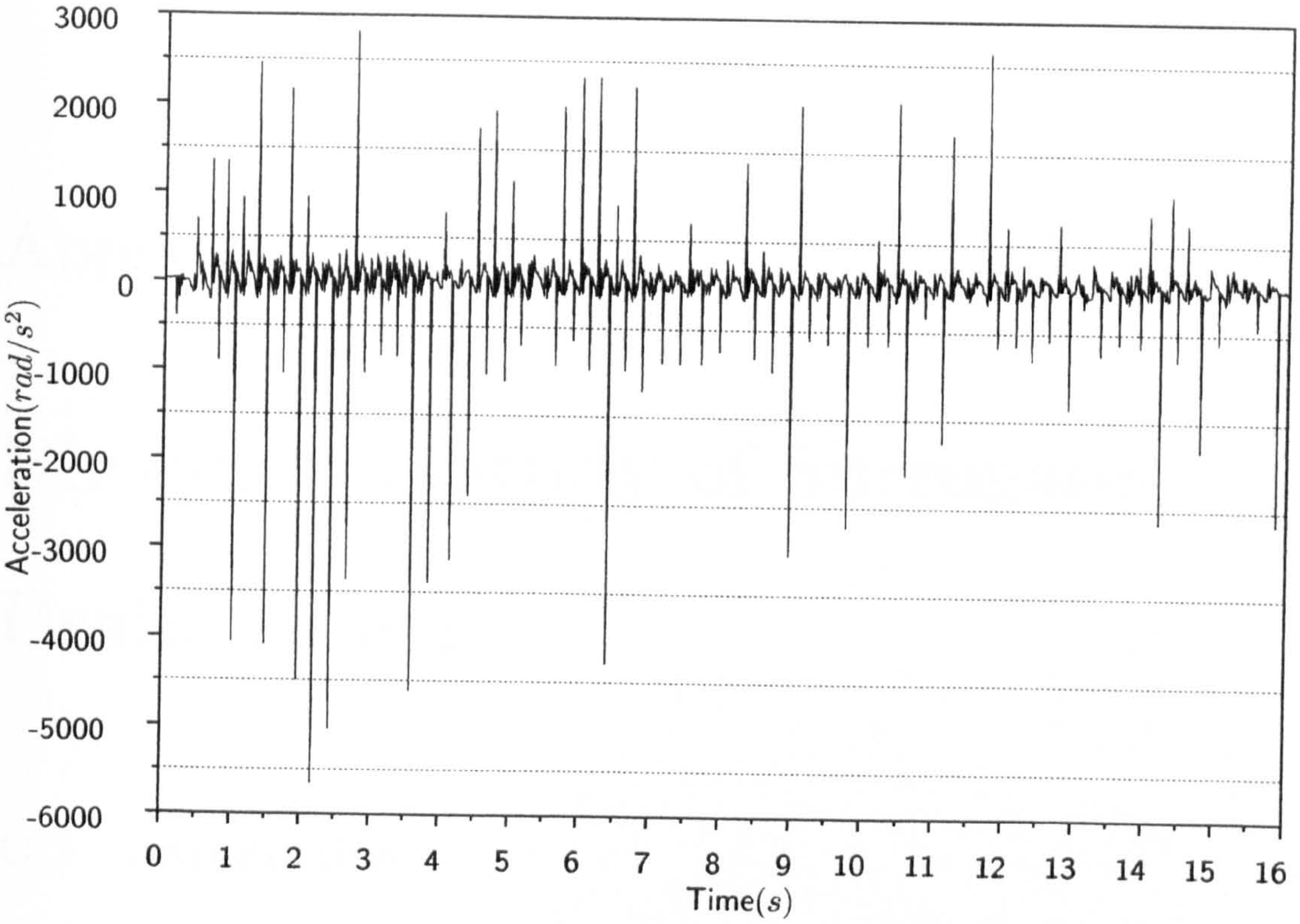

Figure F.5: Max rms acceleration, UH Model

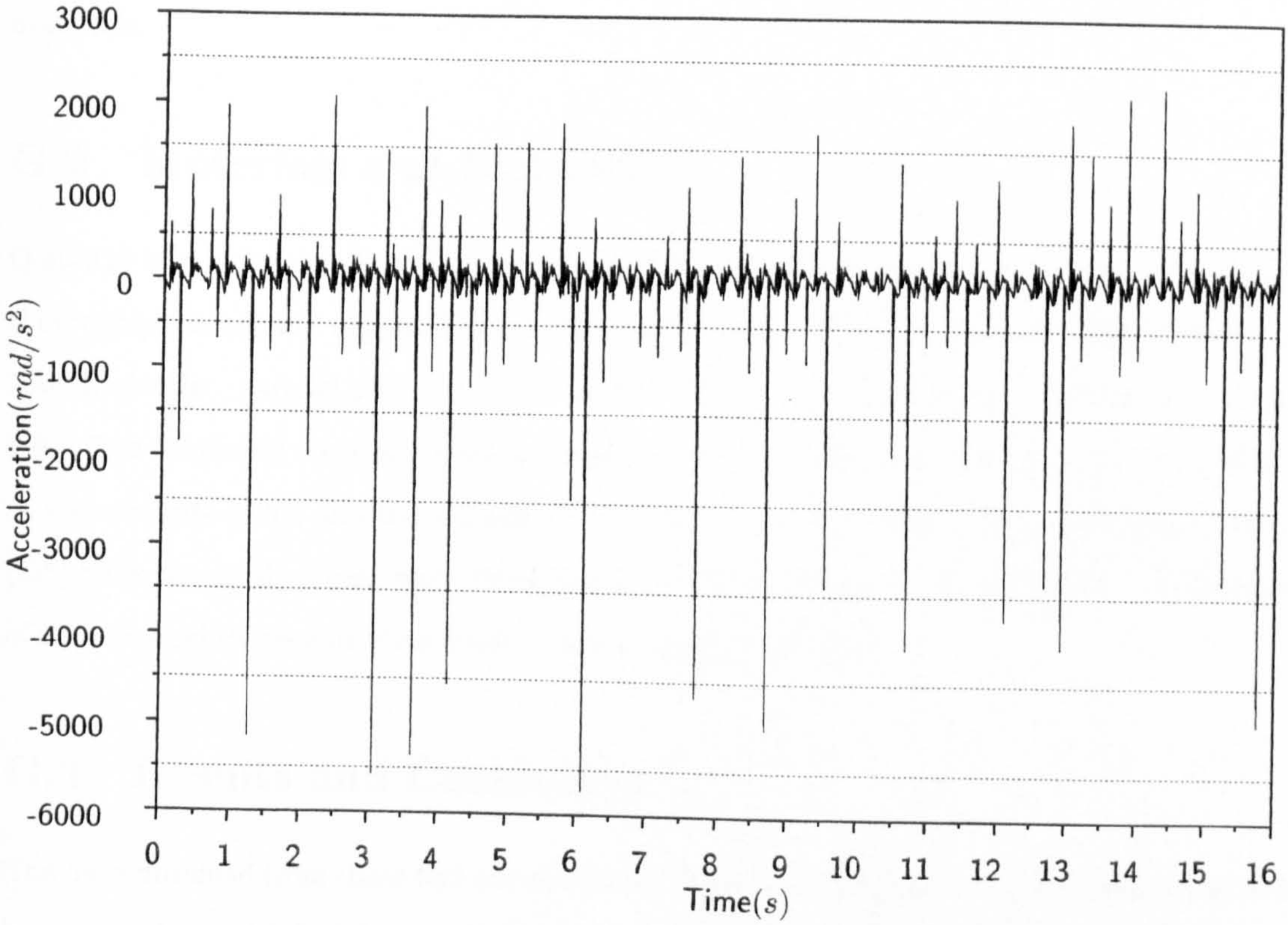

Figure F.6: Max peak acceleration, UH Model

Appendix G

Rheometric Study of Surrogate Brain Tissue

G.1 Introduction

In Chapter 6 Q-Gel 310 (ACC Silicones, Bridgewater, UK) is used as a surrogate brain tissue material in physical models of the infant brain. In order to validate its use, rheometric testing was conducted in order to compare the gel with published data on brain tissue and other surrogate materials.

G.2 Materials and Methods

Q-sil 310 is a two part silicone gel, so in order to prepare the specimines 5g of each part were thoroughly mixed, and degassed. A small amount was cured for one hour at $100°C$ between the 25mm, circular, parallel plates of a Bohlin C-VOR Rheometer (Malvern Instrument, Malvern, UK). The frequency response of the gel was tested for a range between $0.5rad/s$ and $6.5rad/s$, at a strain rate of 5% and the storage moudulus (G'), loss modulus (G") and complex modulus (G*) were obtained. These were compared to published data on the rheometric characteristics of neurological tissue and other brain tissue surrogate materials.

G.3 Results and Conclusion

The data obtained from these test are shown in Figure G.1. In Figure G.2, the complex modulus is compared to published data on brain tissue, and other brain tissue surrogates, and shows that Q-gel 310 is comparable to these other materials. It was therefore deceided that the gel was an

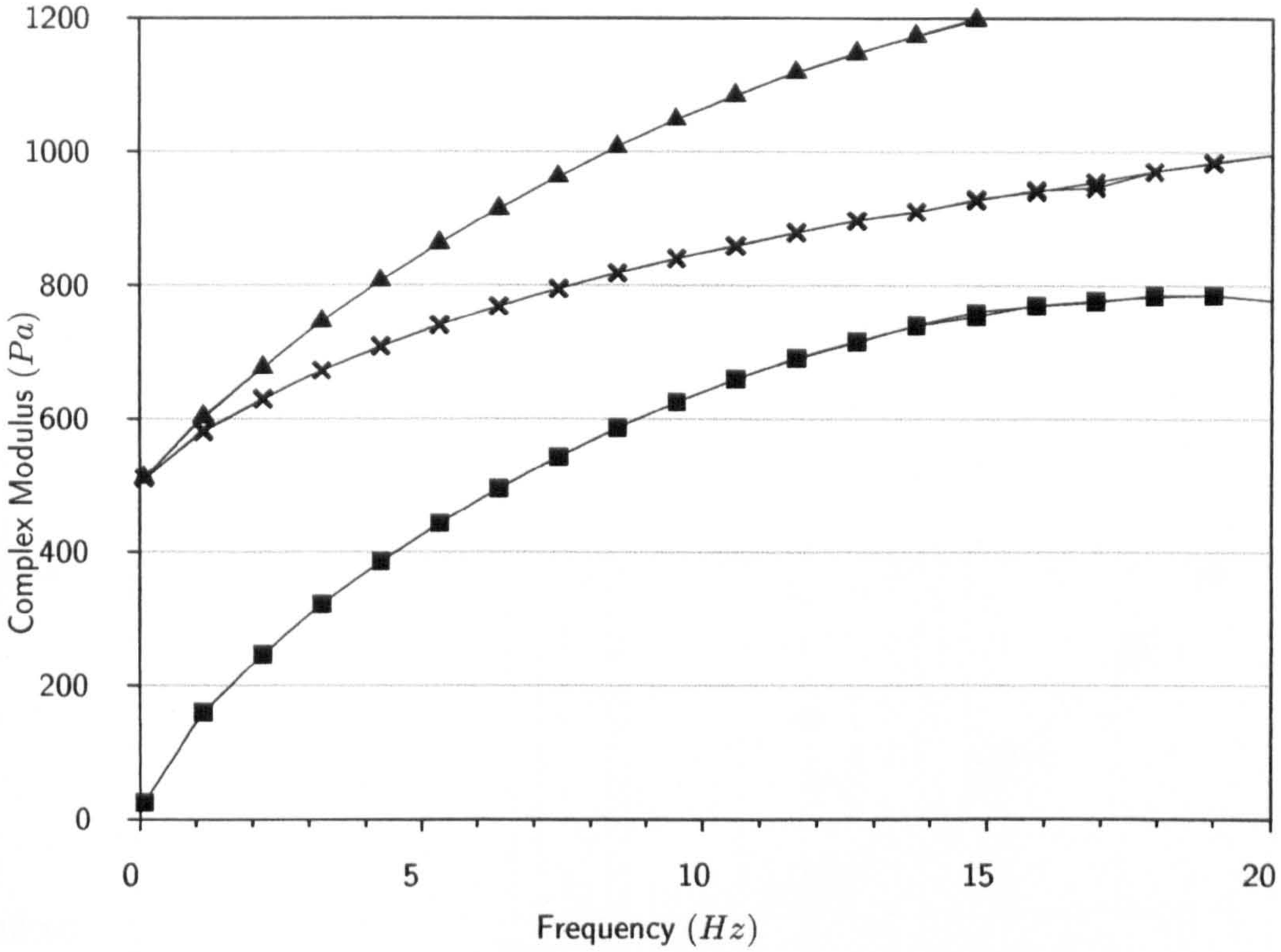

Figure G.1: Storage, loss and complex modulus results for Q-gel 310

G'

G"

Complex Modulus G*

appropriate material for use in the physical modelling carried out in Chapter 6.

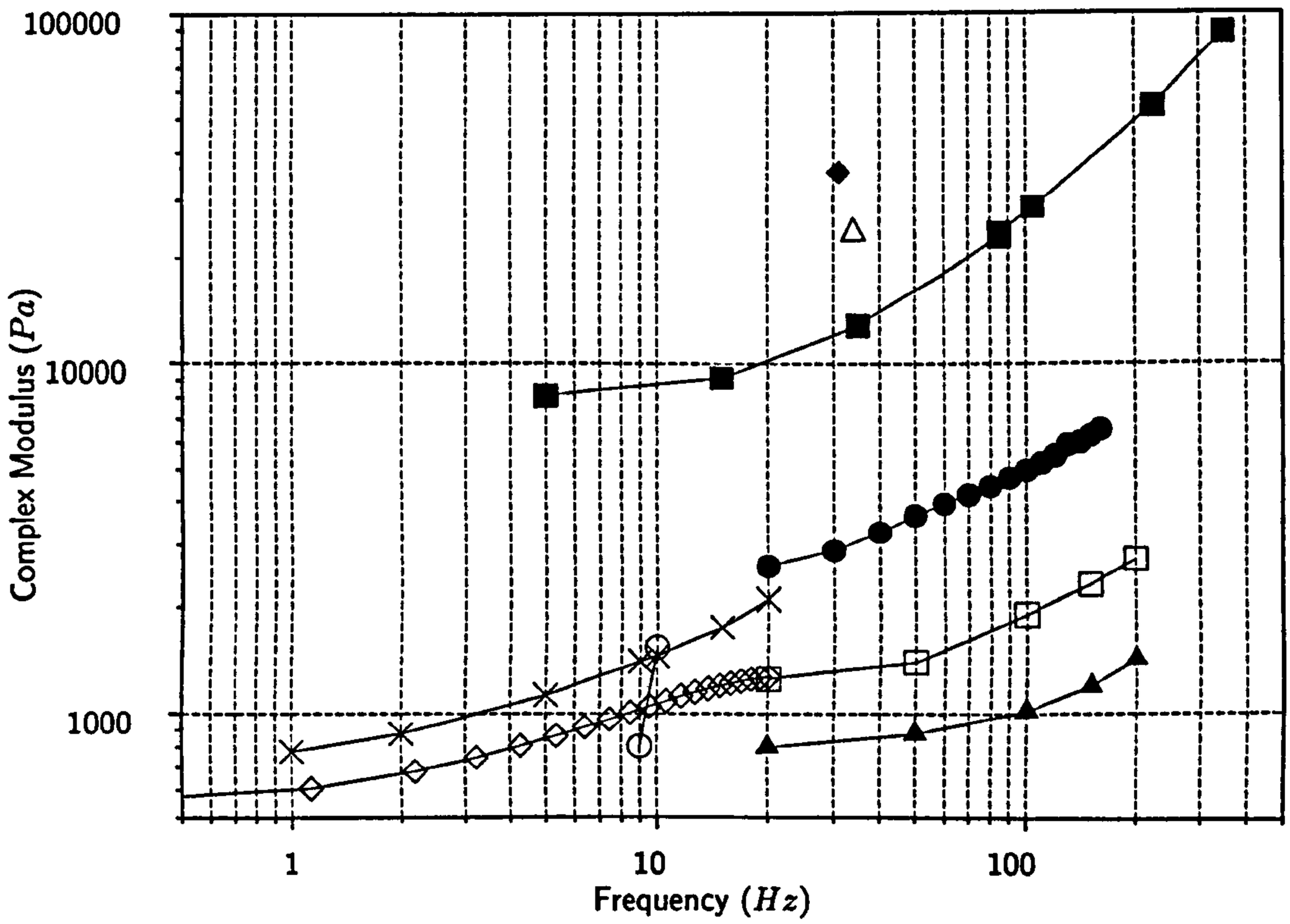

Figure G.2: Comparison of G* from rheometric testing of Q-Gel 310 and previous studies of brain tissue and brain tissue surrogates.
◇ Q-Gel 310 - pressent study, × Sylgard 527 silicone gel from [12], ▲ Infant porcine brain tissue from [61], □ Adult porcine brain tissue from [61], ● Sylgard 527 silicone gel from [64], ■ Human brain tissue from [65], ◆ Rhesus monkey brain tissue from [66], △ Human brain tissue from [66], ○ Human brain tissue from [67].

Appendix H

Acceleration Traces

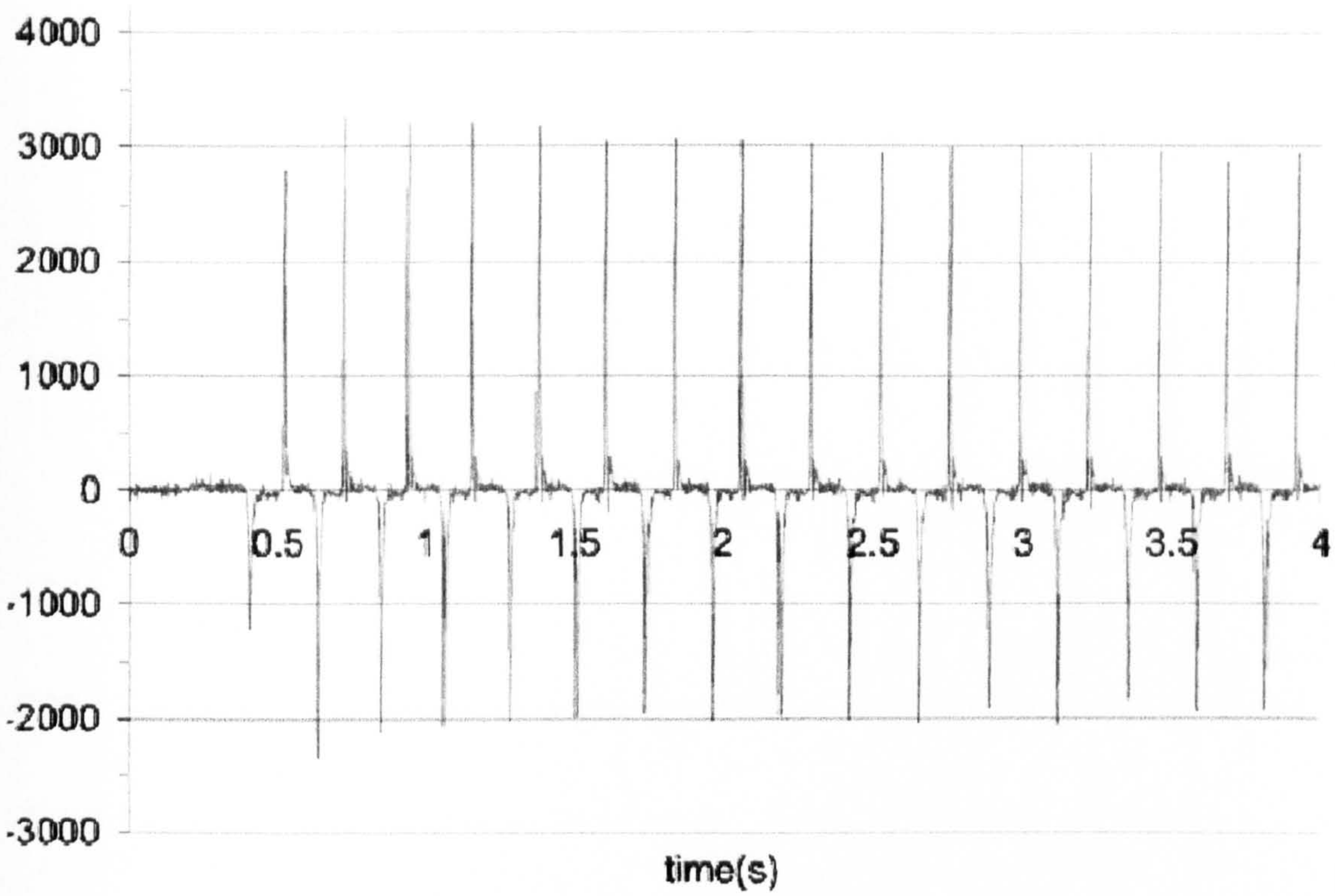

Figure H.1: A3 acceleration

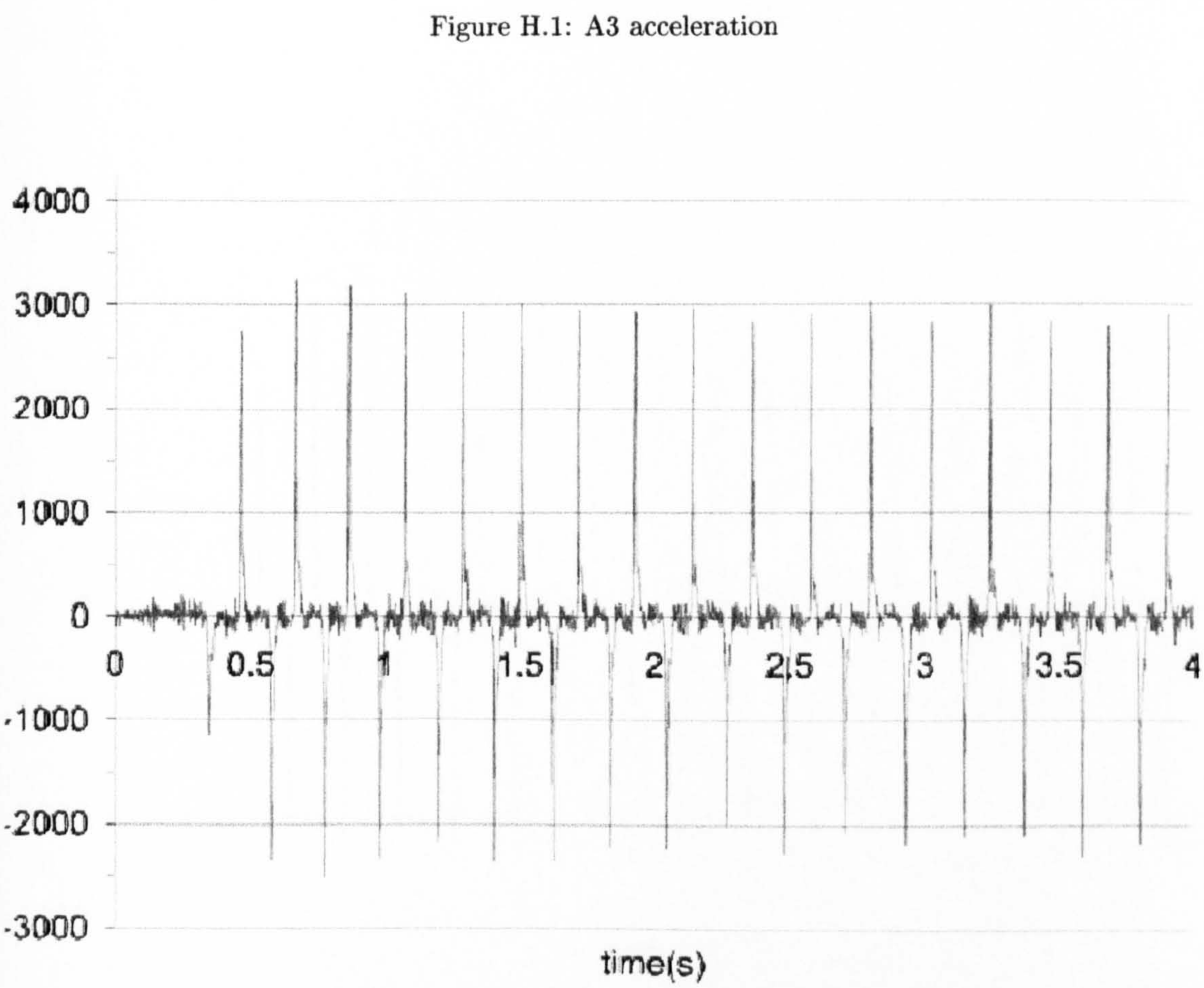

Figure H.2: R2 acceleration

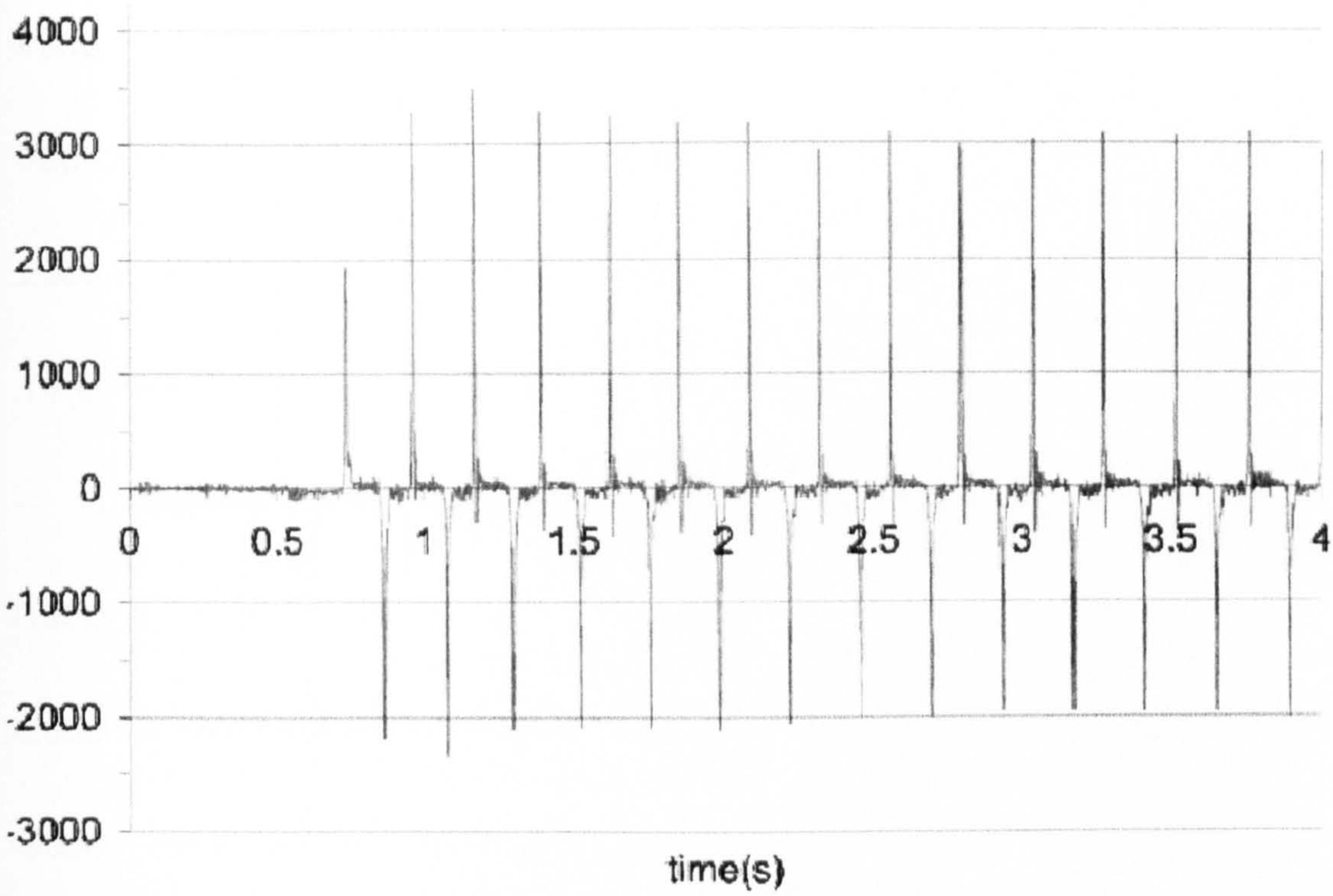

Figure H.3: HA3 acceleration

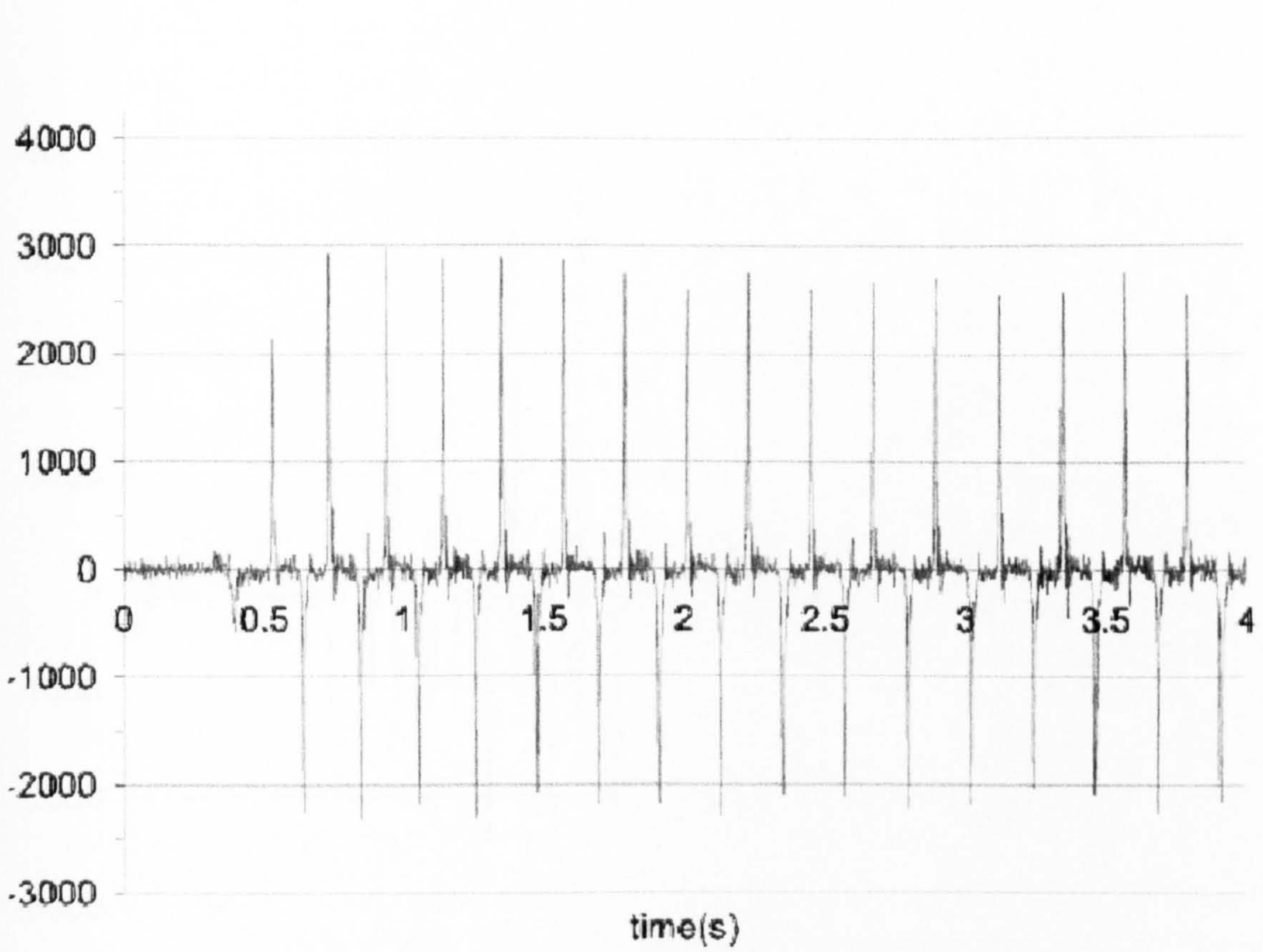

Figure H.4: HR3 acceleration

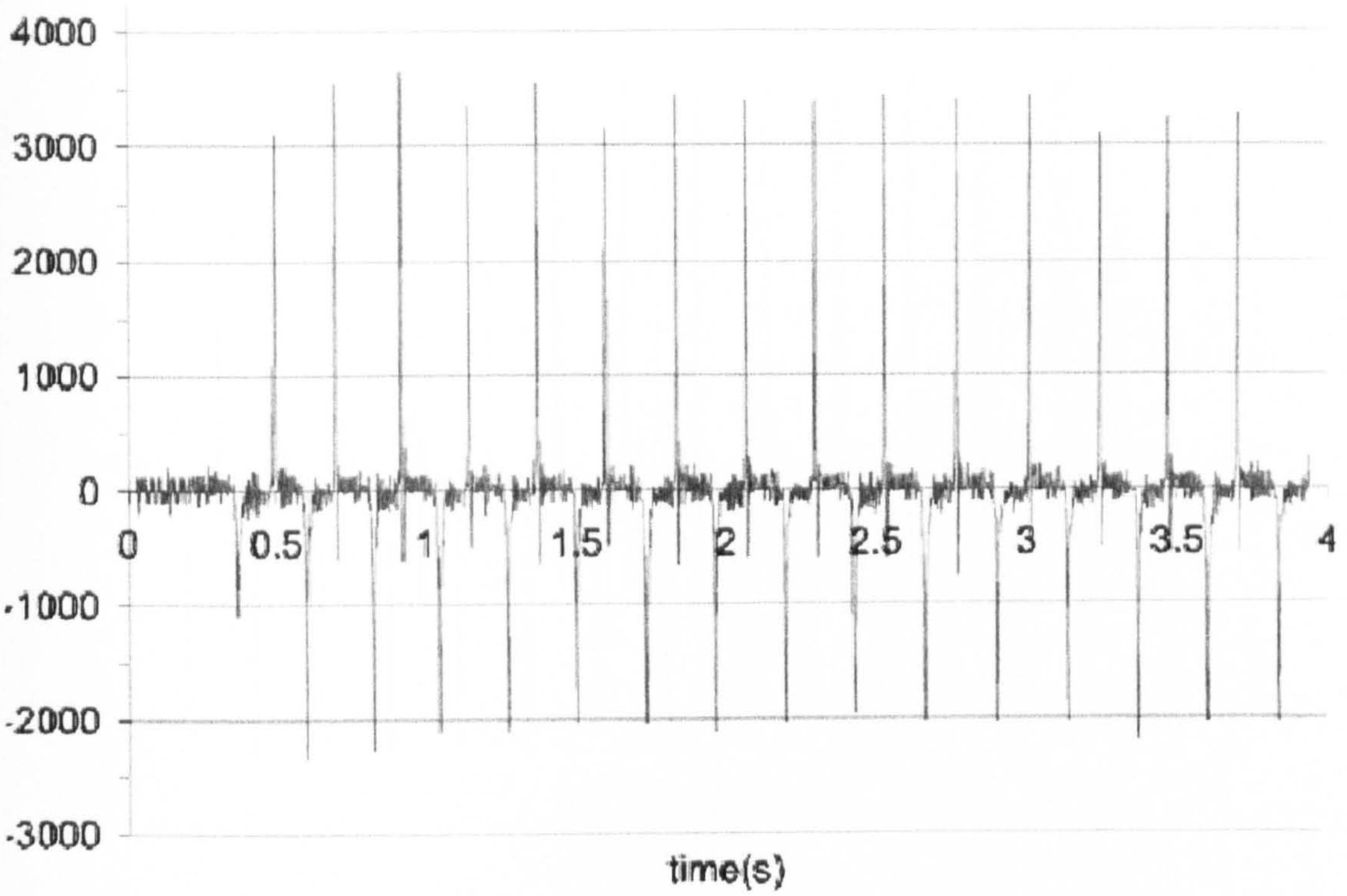

Figure H.5: SA3 acceleration

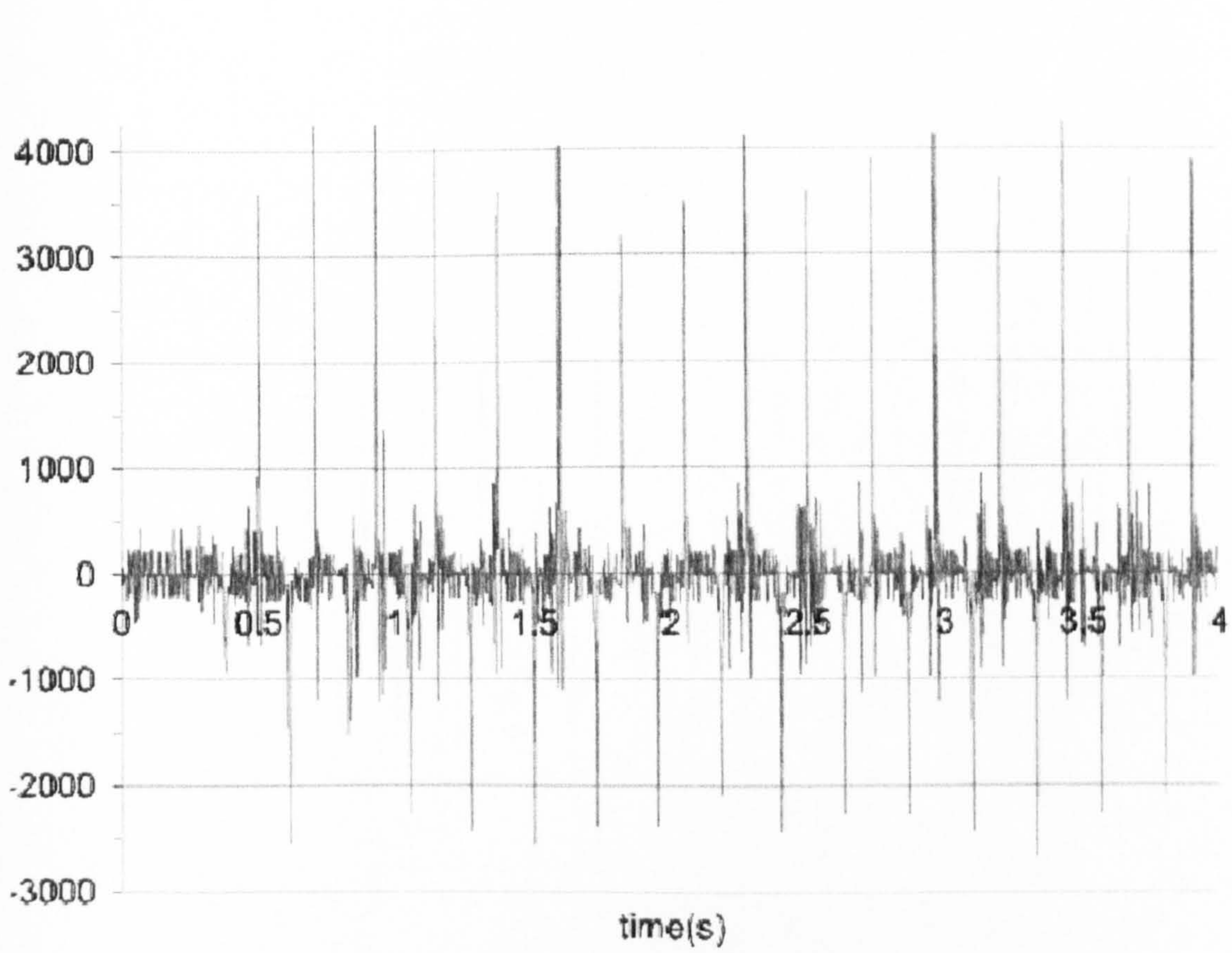

Figure H.6: SR3 acceleration

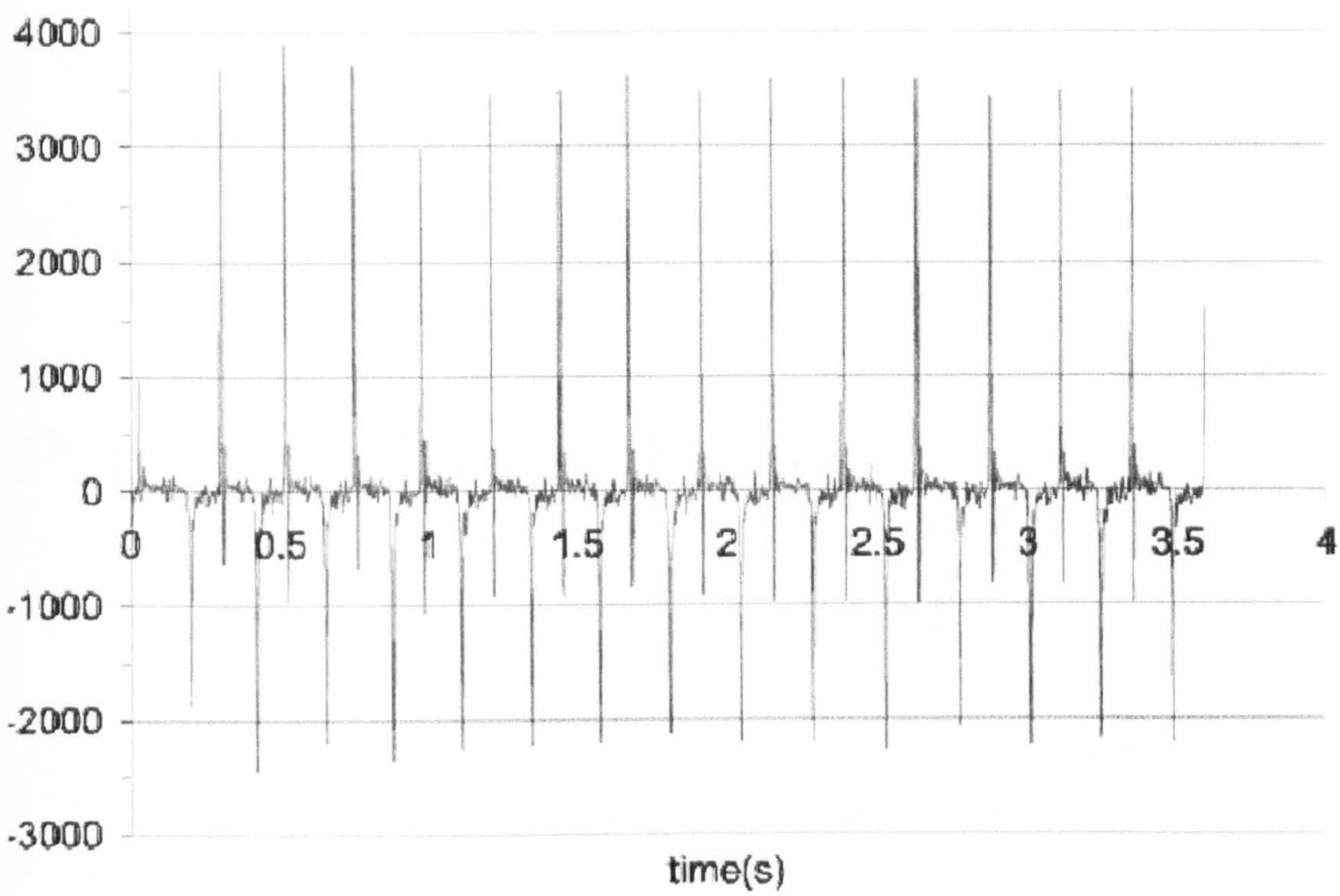

Figure H.7: SHA3 acceleration

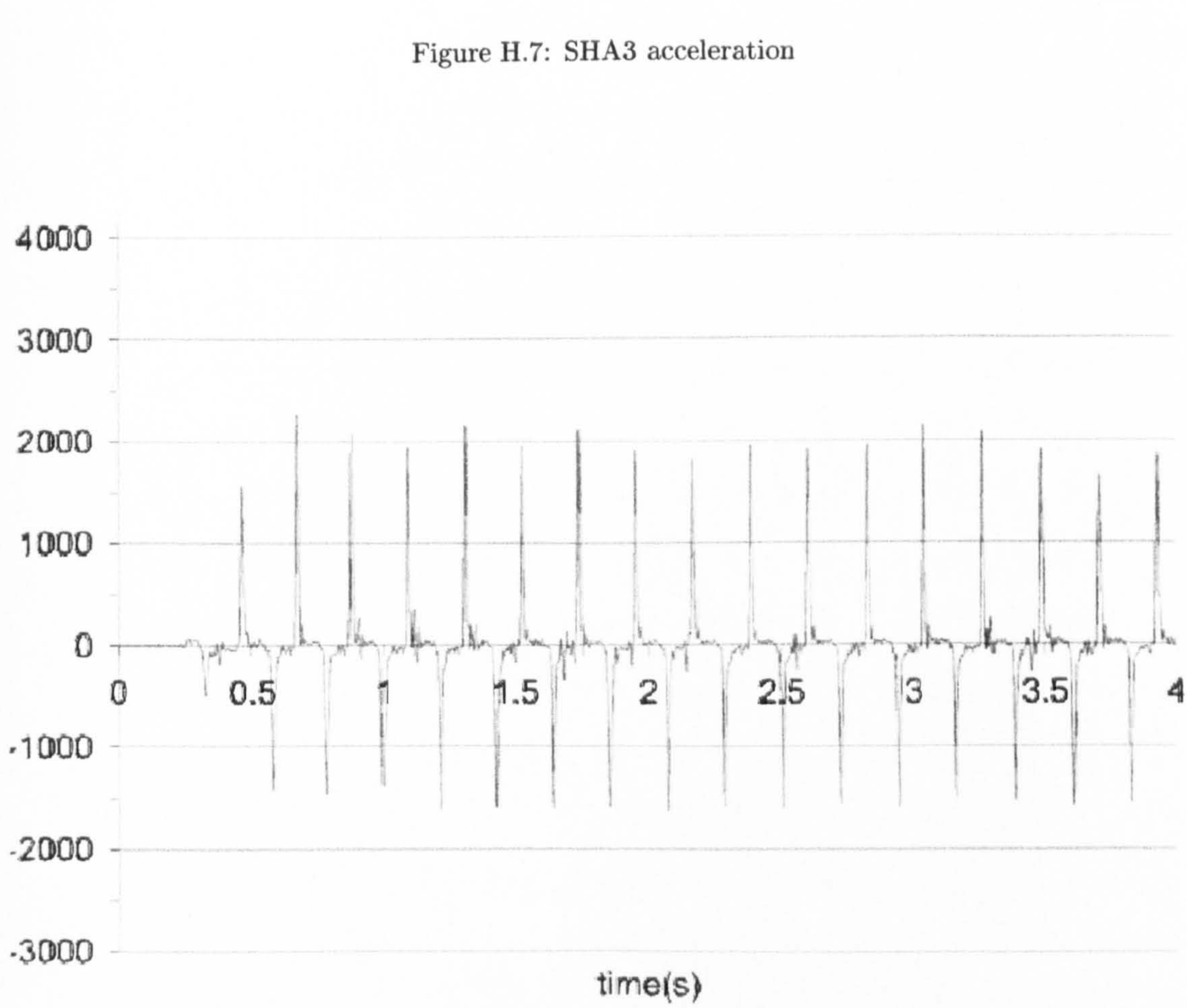

Figure H.8: SHR3 acceleration

Appendix I

Principle Strain Traces

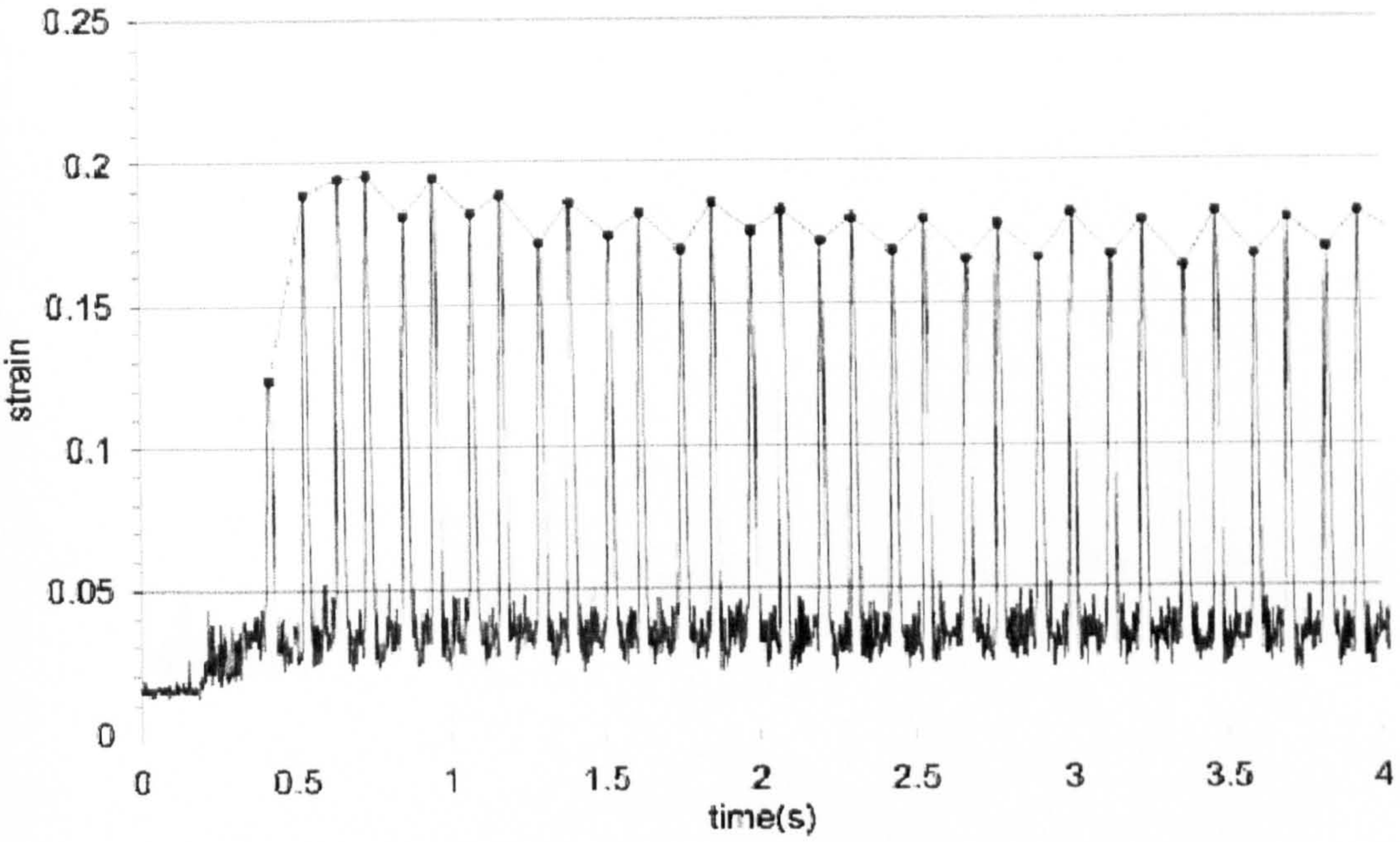

Figure I.1: A3 principle strain

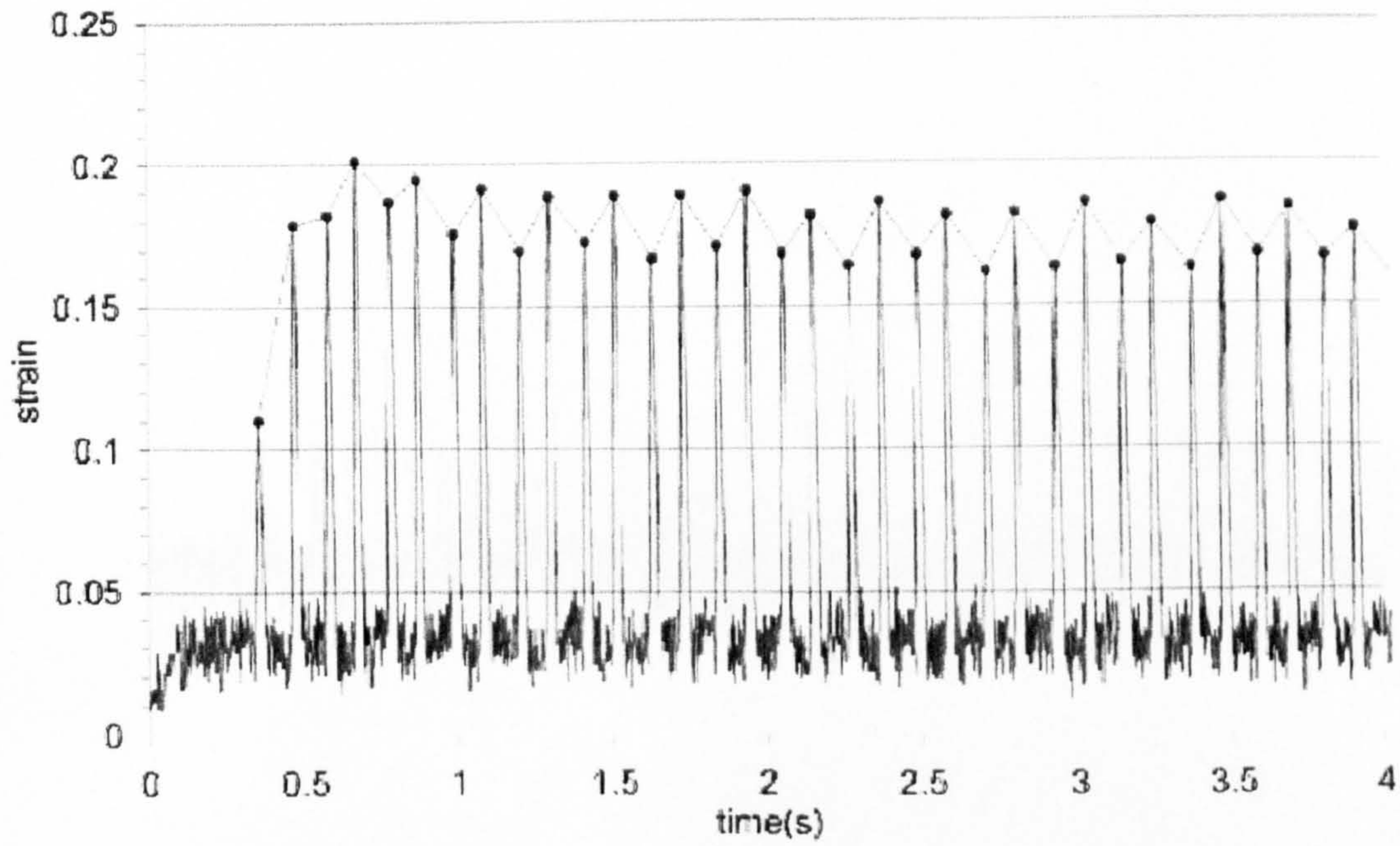

Figure I.2: R2 principle strain

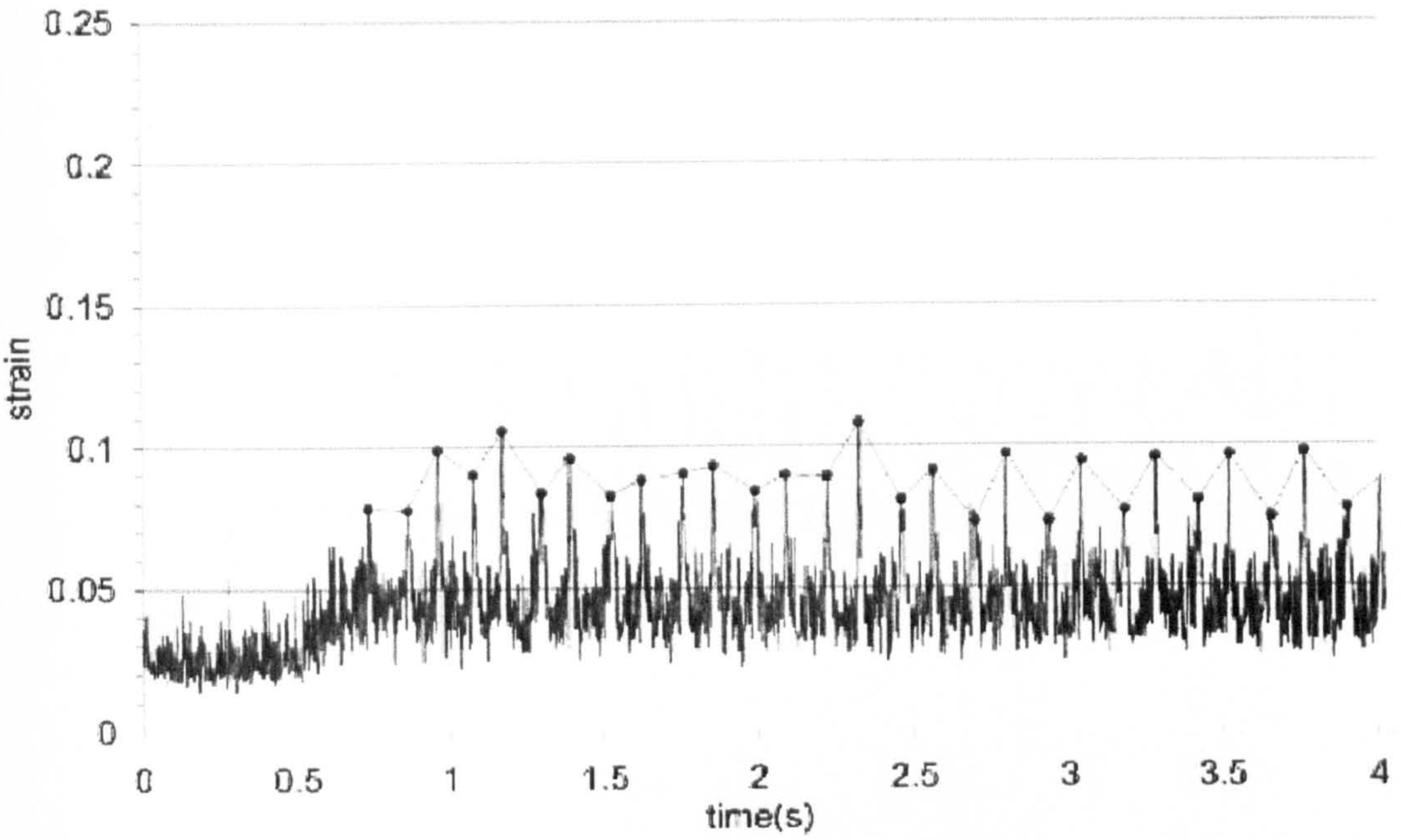

Figure I.3: HA3 principle strain

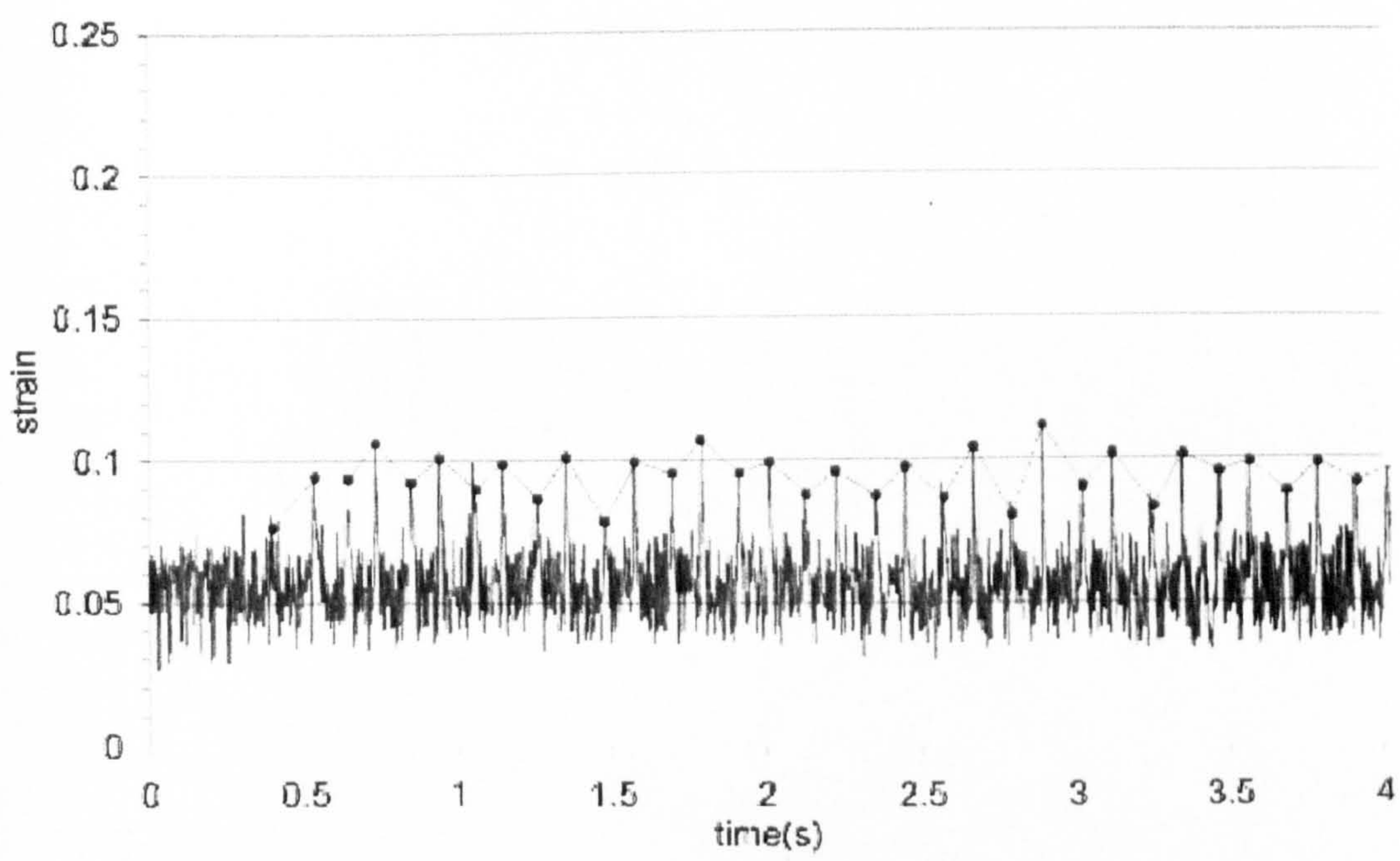

Figure I.4: HR3 principle strain

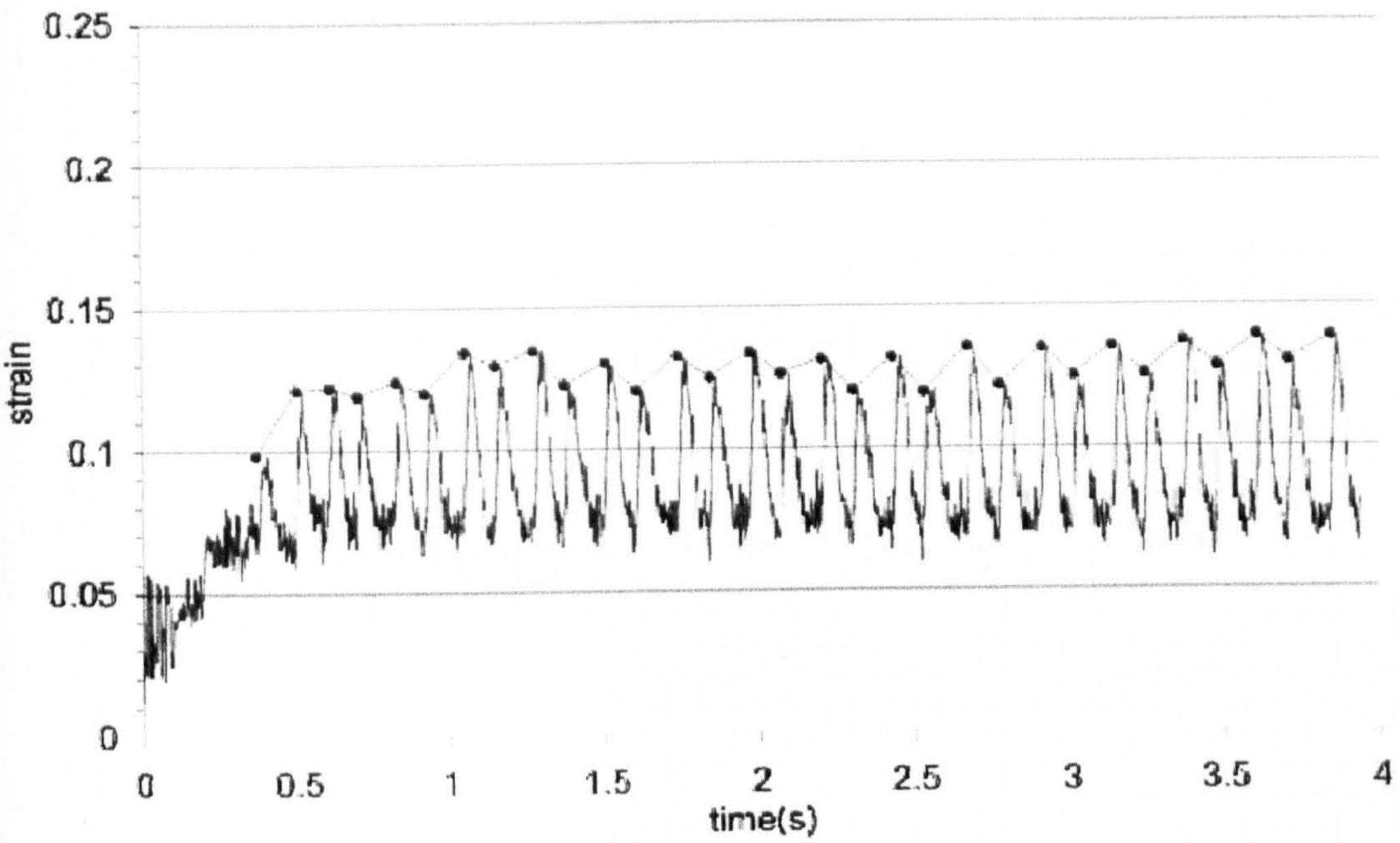

Figure I.5: SA3 principle strain

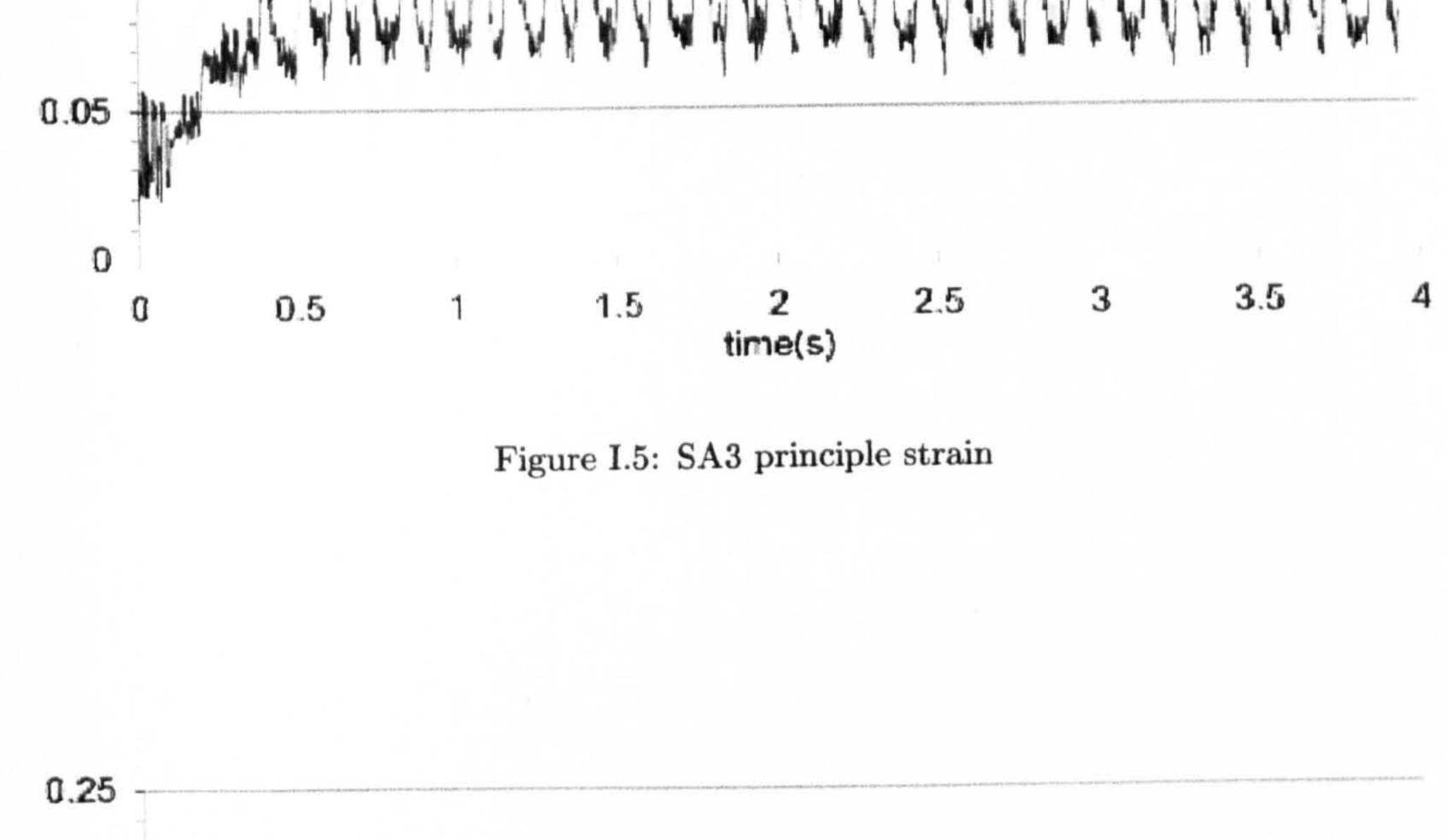

Figure I.6: SR3 principle strain

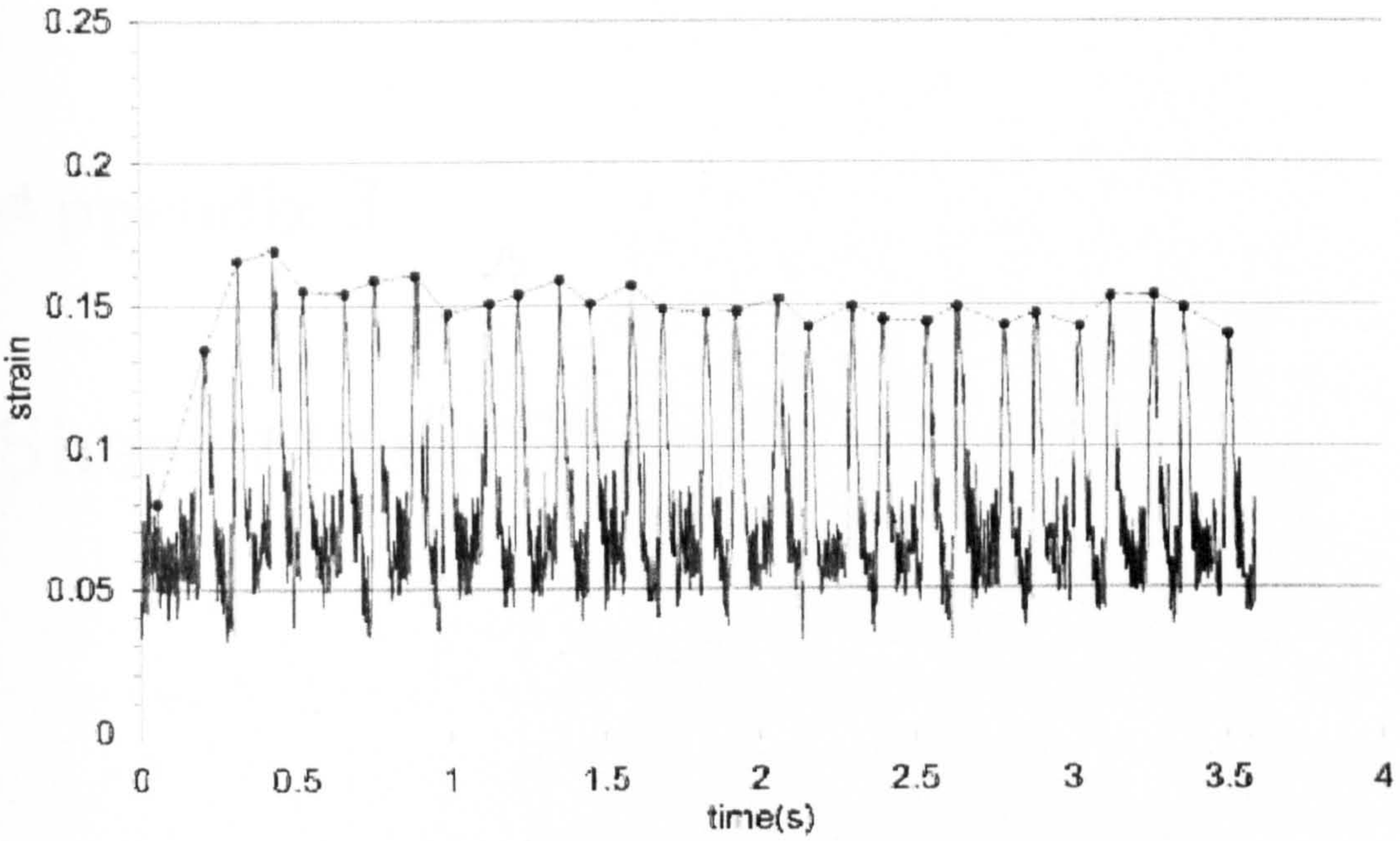

Figure I.7: SHA3 principle strain

Figure I.8: SHR3 principle strain

Appendix J

Shear Strain Traces

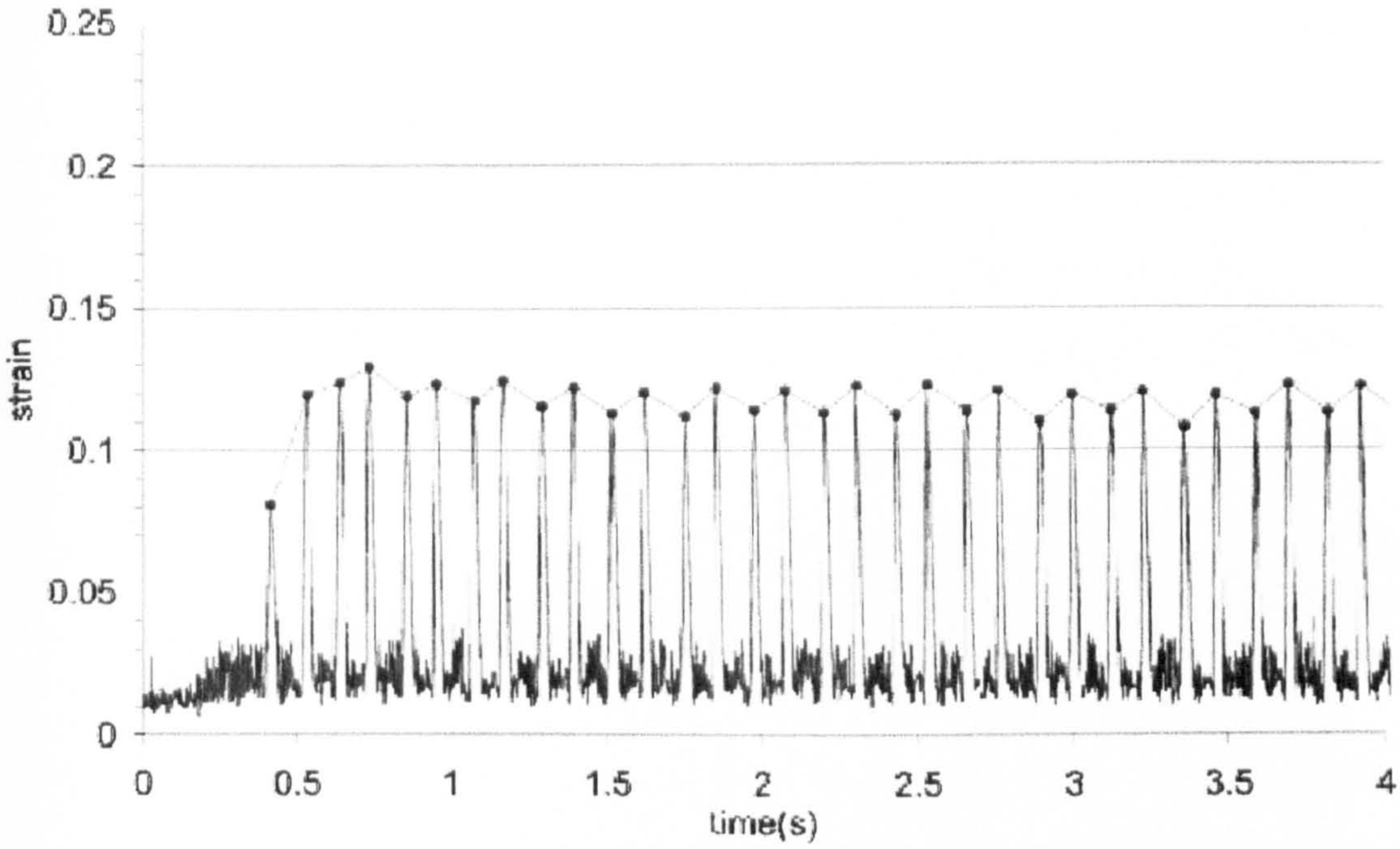

Figure J.1: A3 shear strain

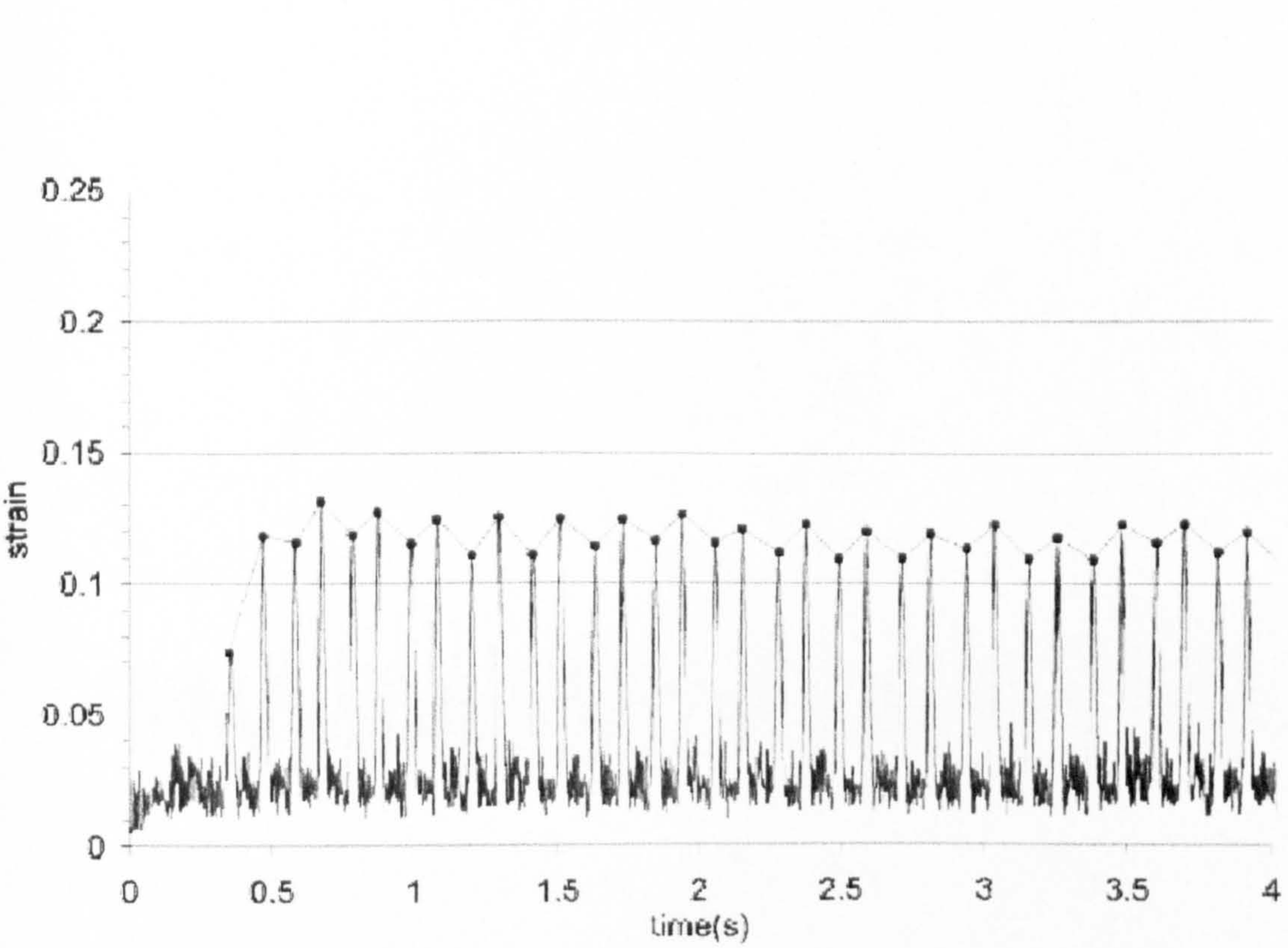

Figure J.2: R2 shear strain

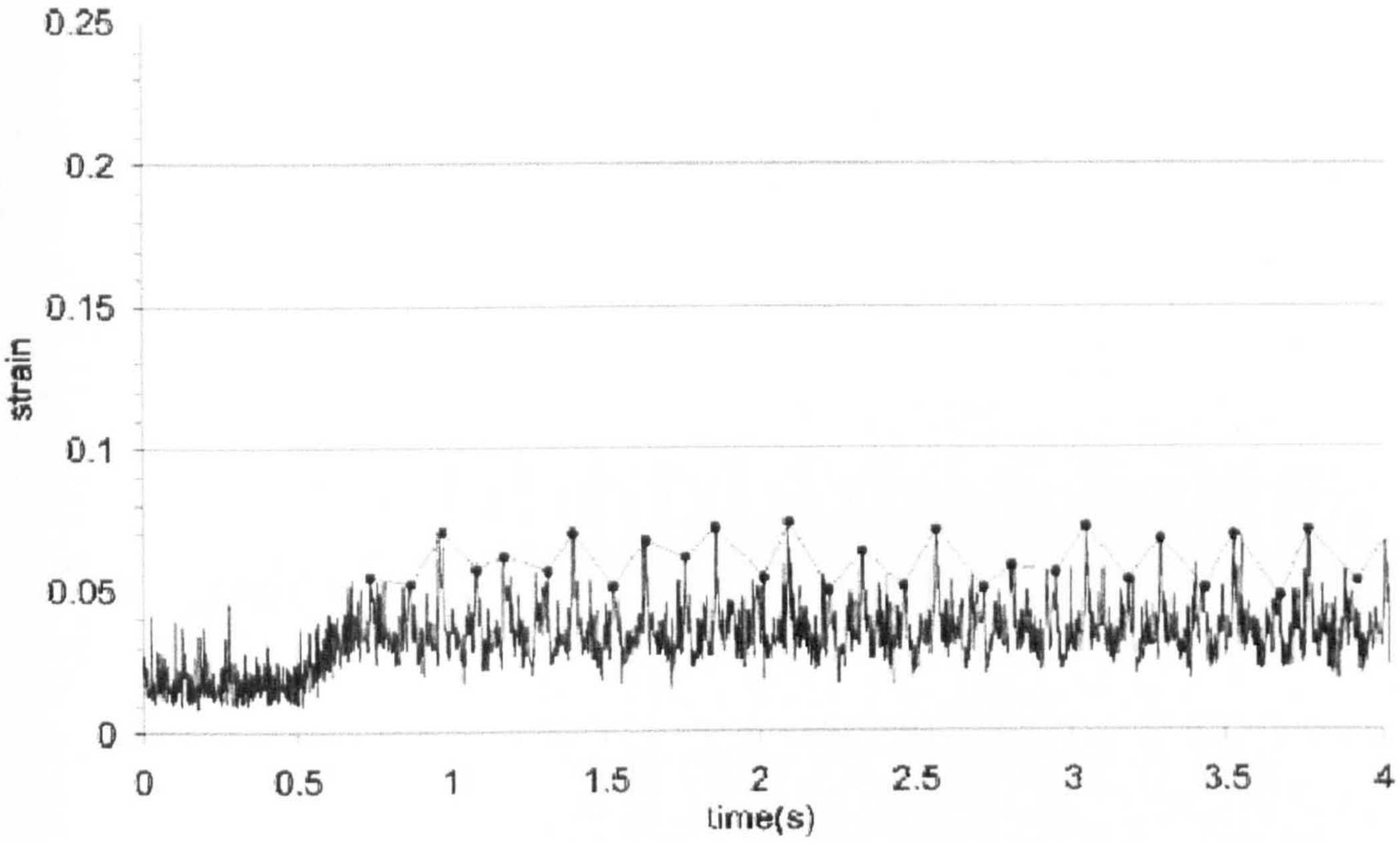

Figure J.3: HA3 shear strain

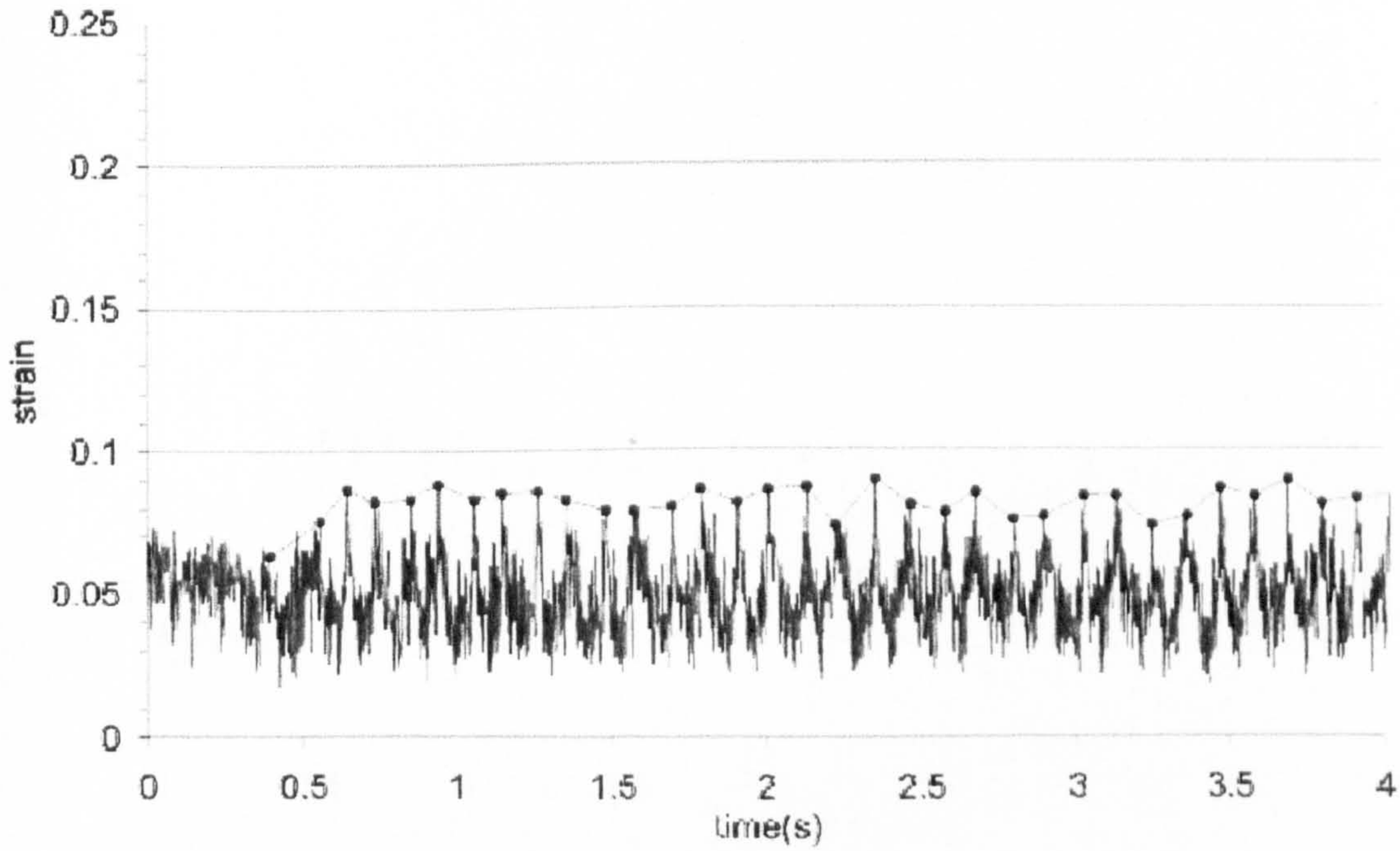

Figure J.4: HR3 shear strain

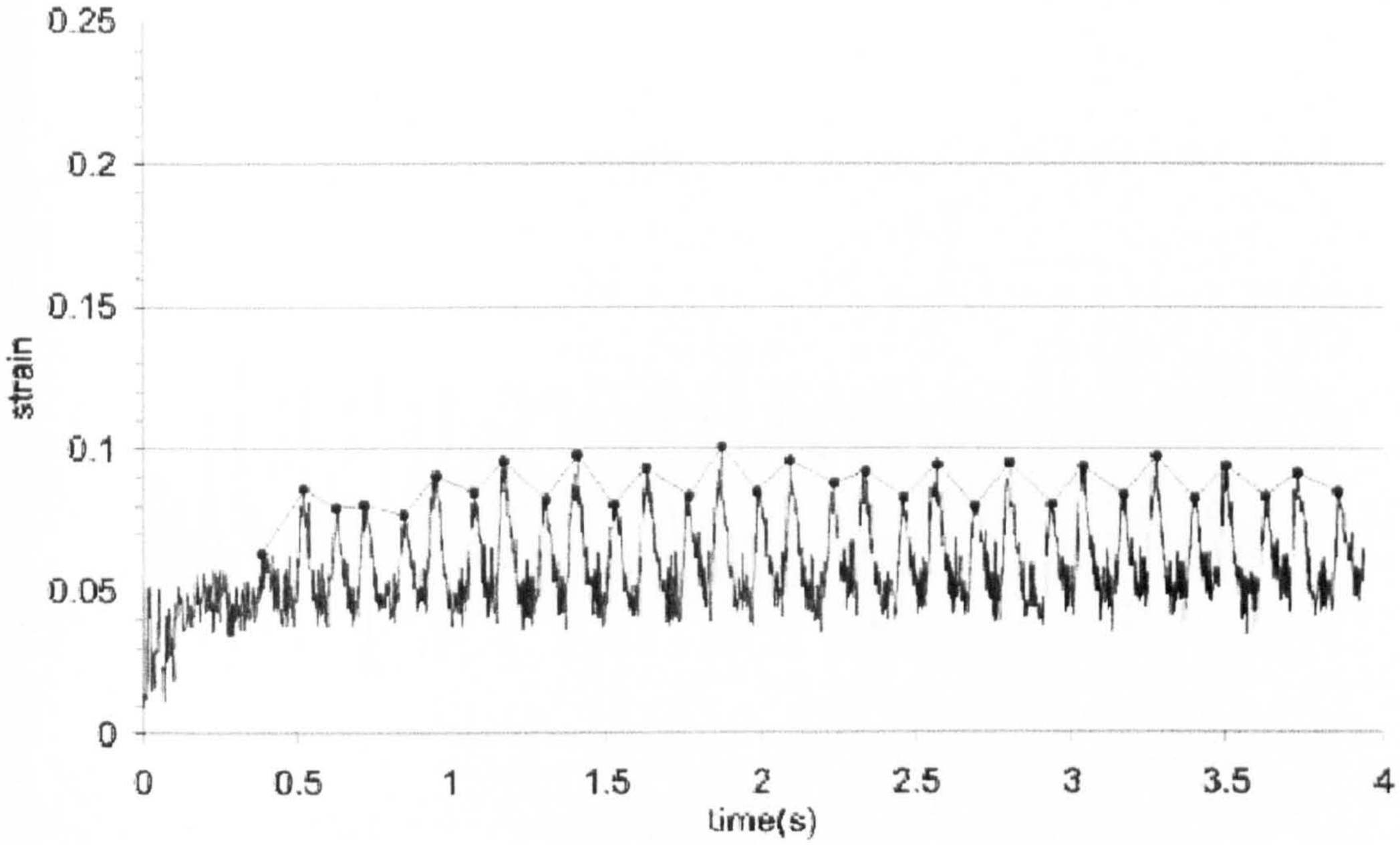

Figure J.5: SA3 shear strain

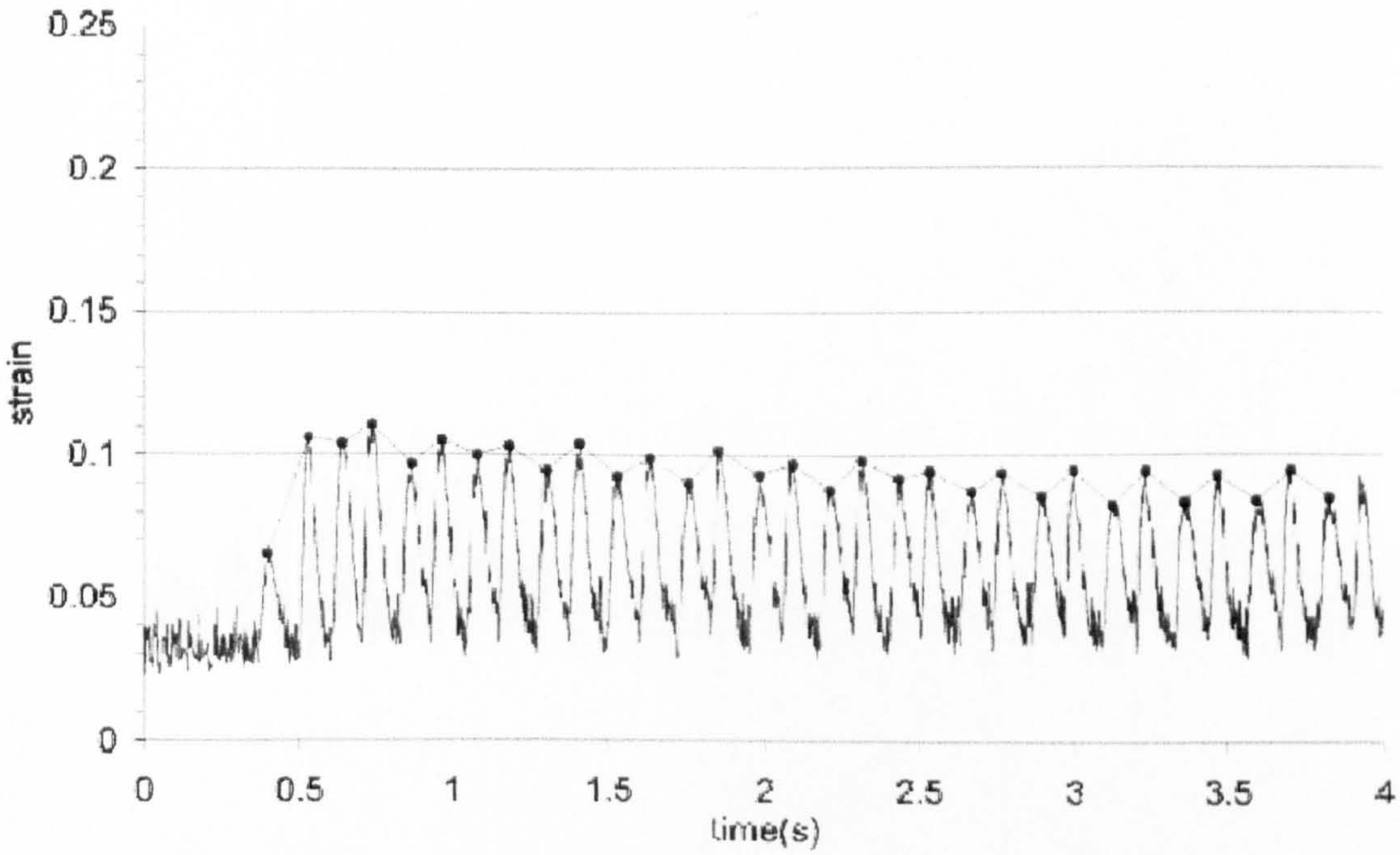

Figure J.6: SR3 shear strain

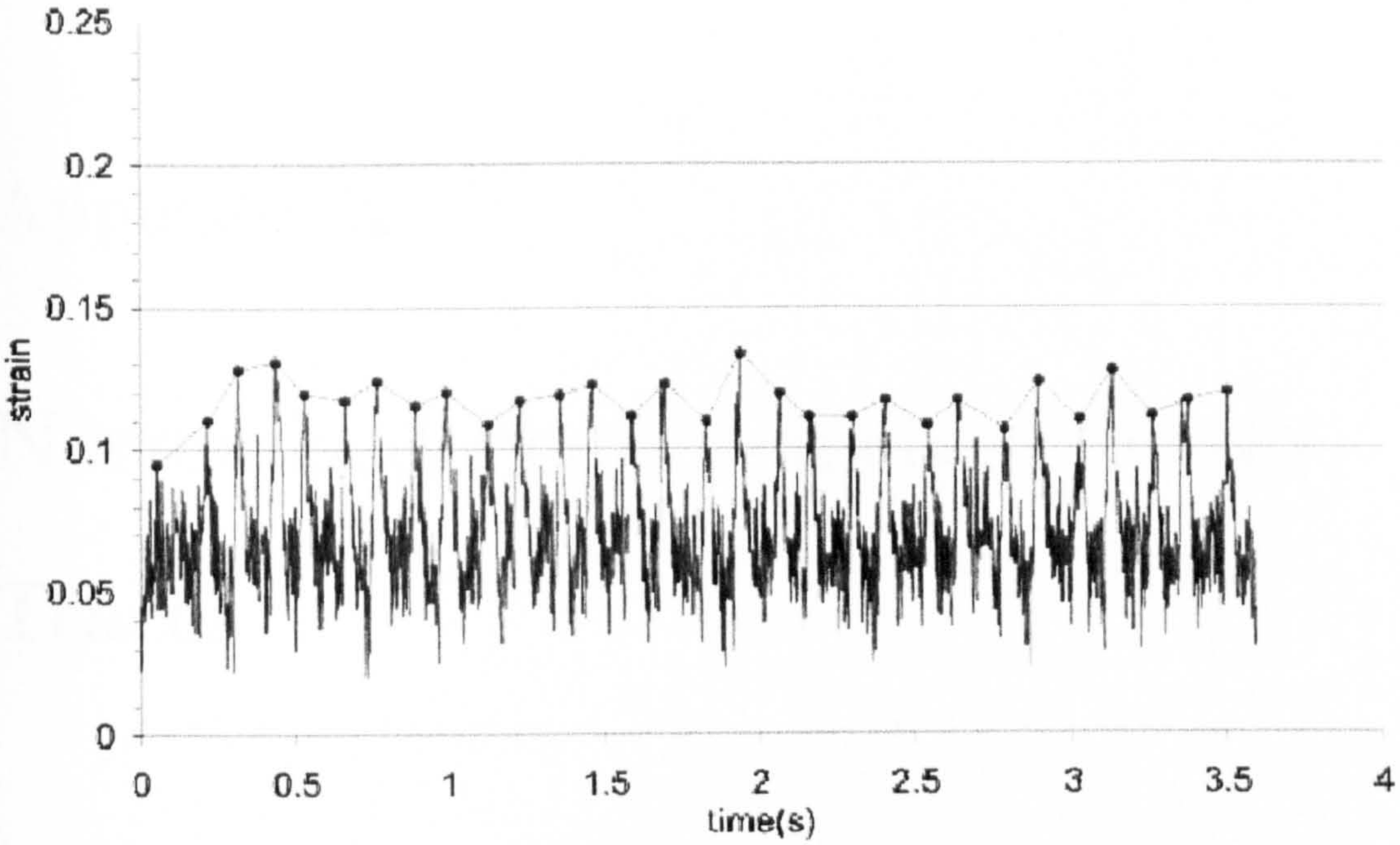

Figure J.7: SHA3 shear strain

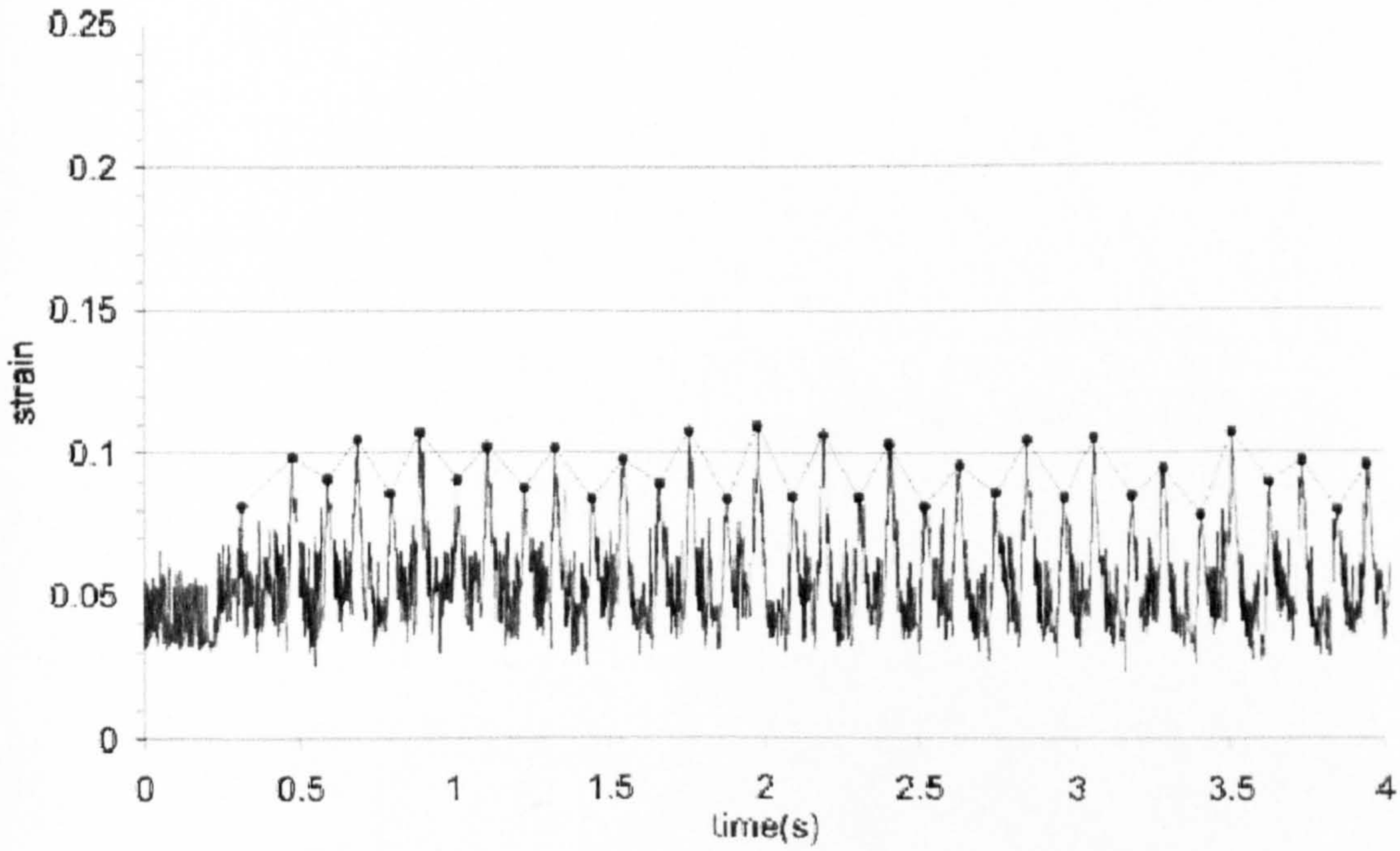

Figure J.8: SHR3 shear strain

Appendix K

Normalised Peak Principle Strain Traces

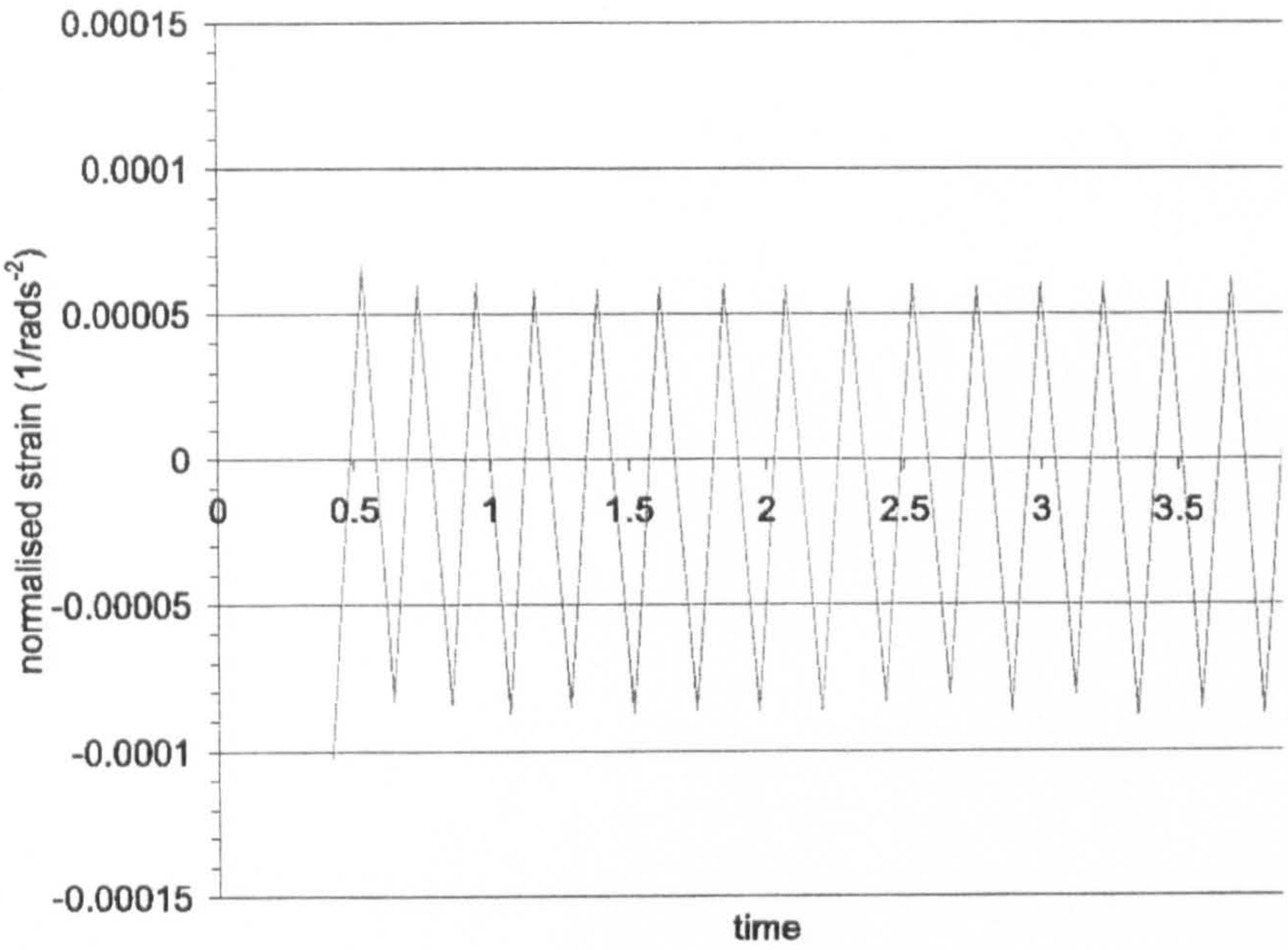

Figure K.1: A3 normalised peak principle strain

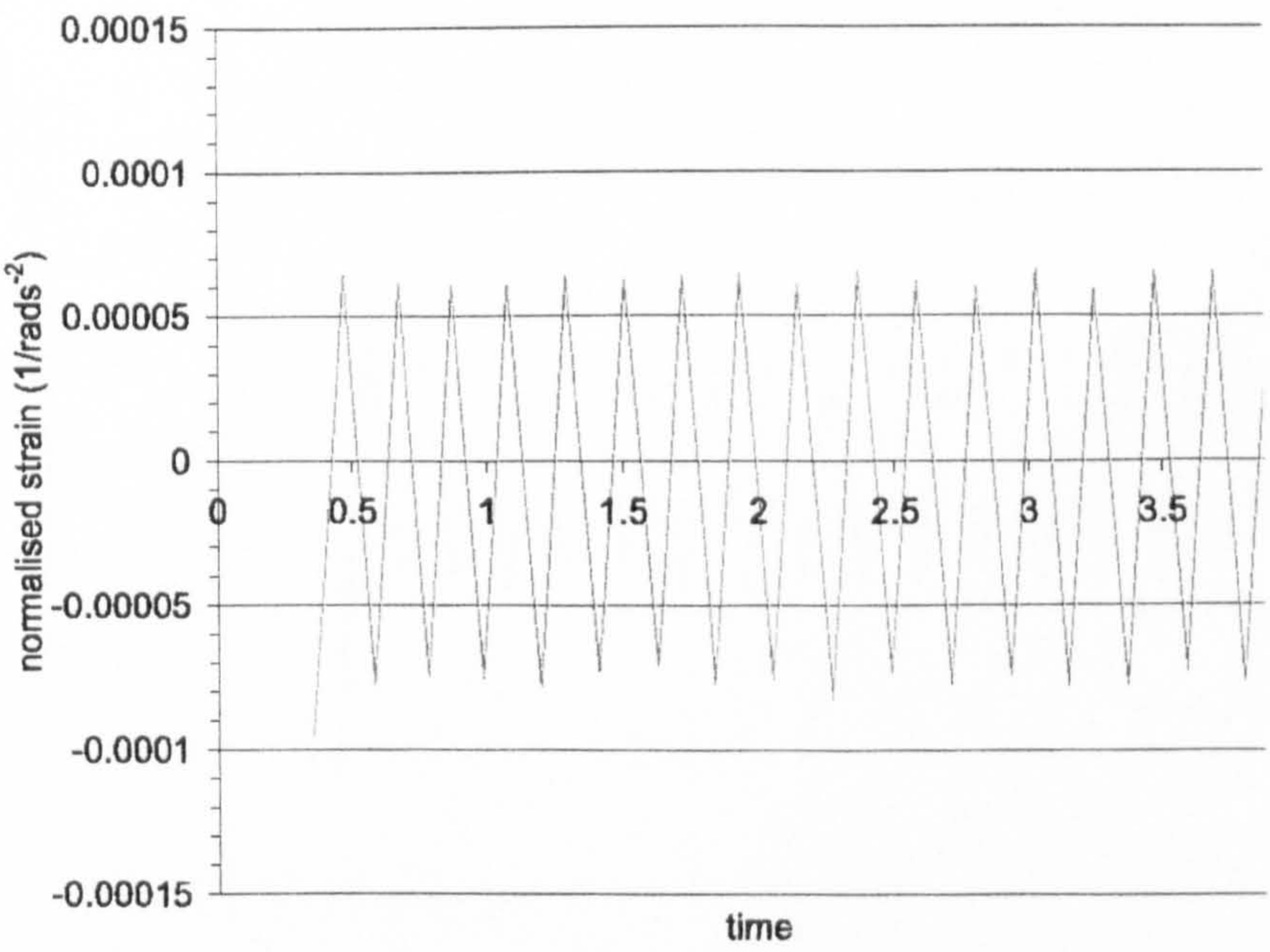

Figure K.2: R2 normalised peak principle strain

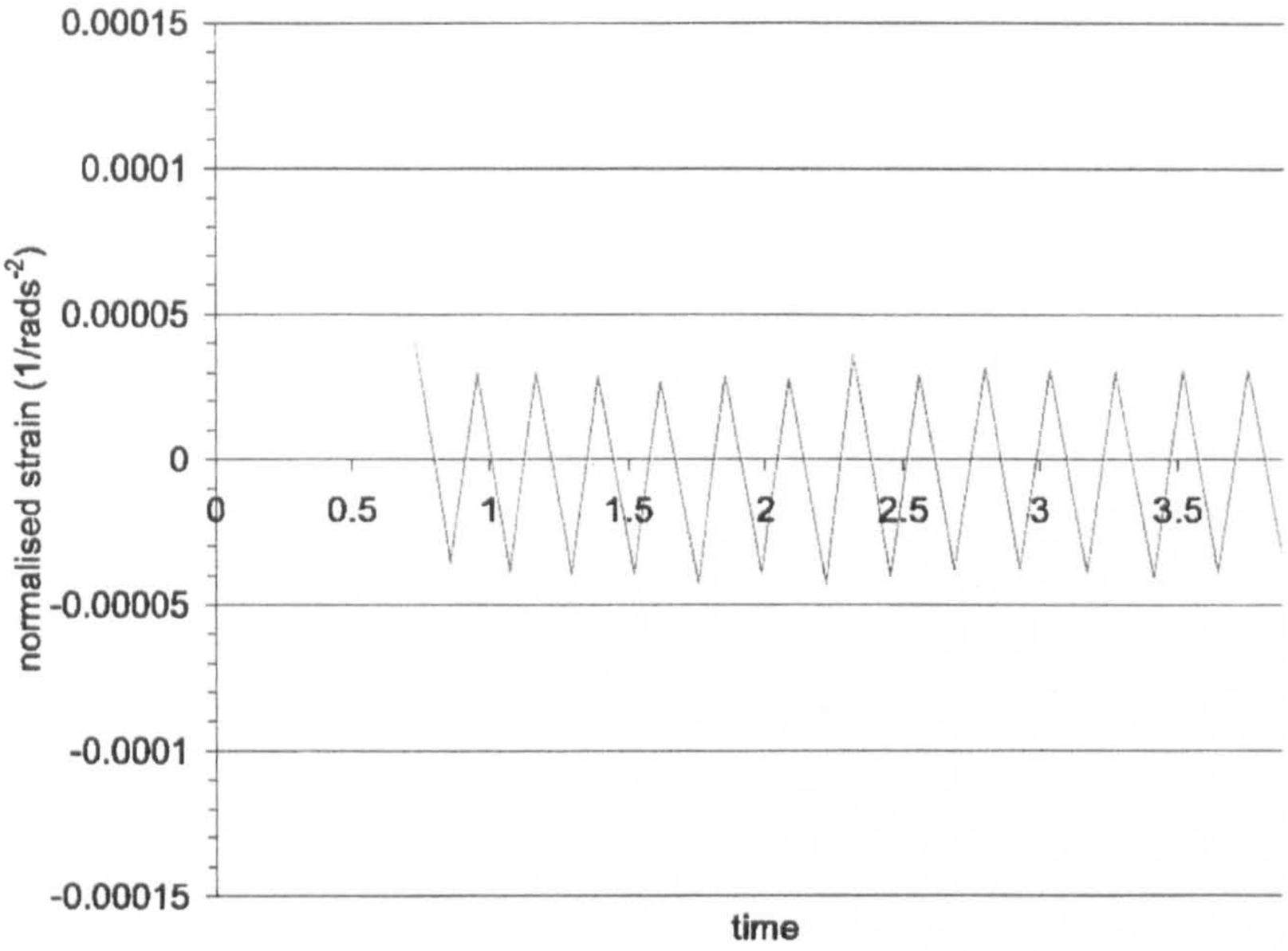

Figure K.3: HA3 normalised peak principle strain

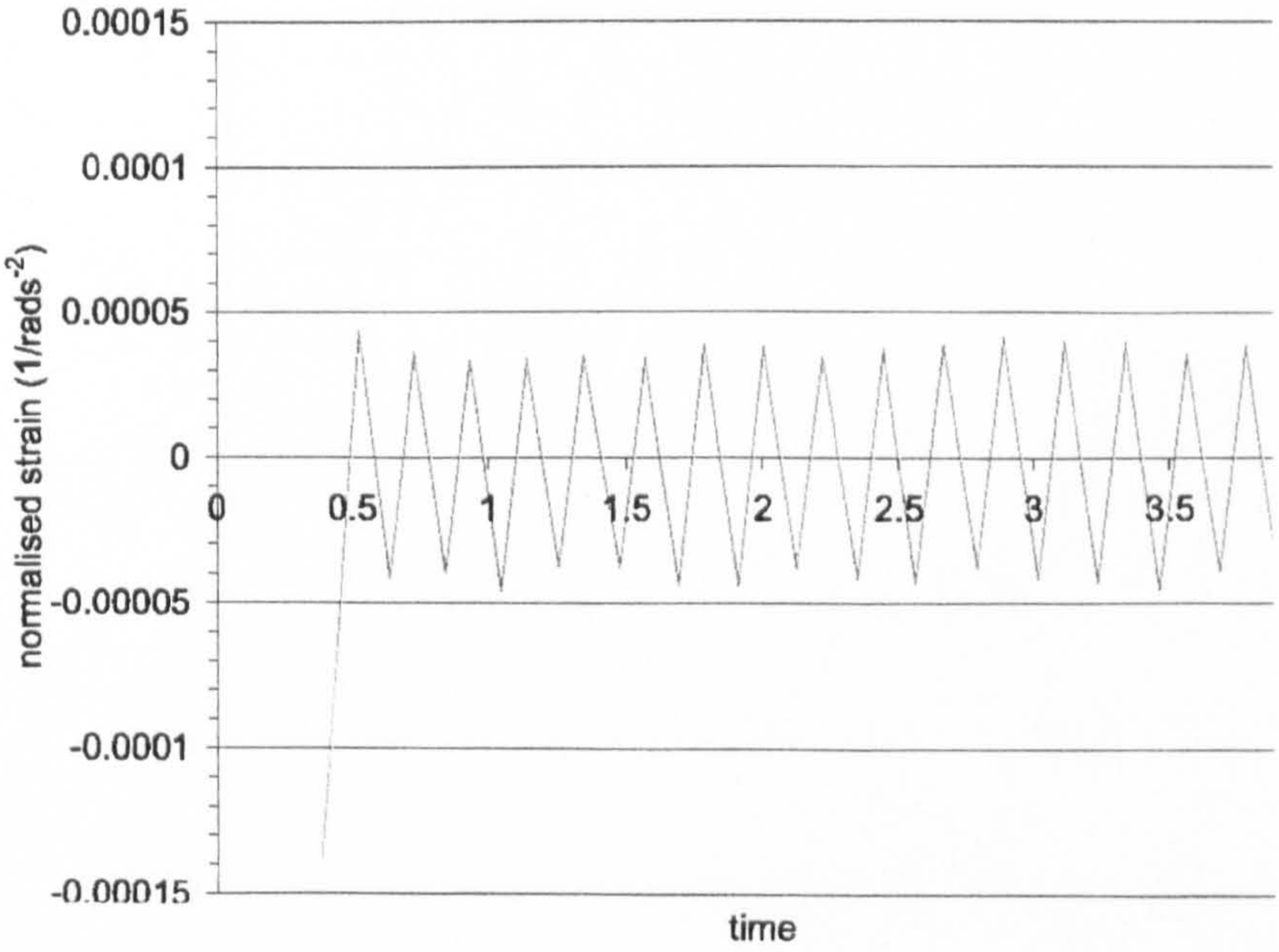

Figure K.4: HR3 normalised peak principle strain

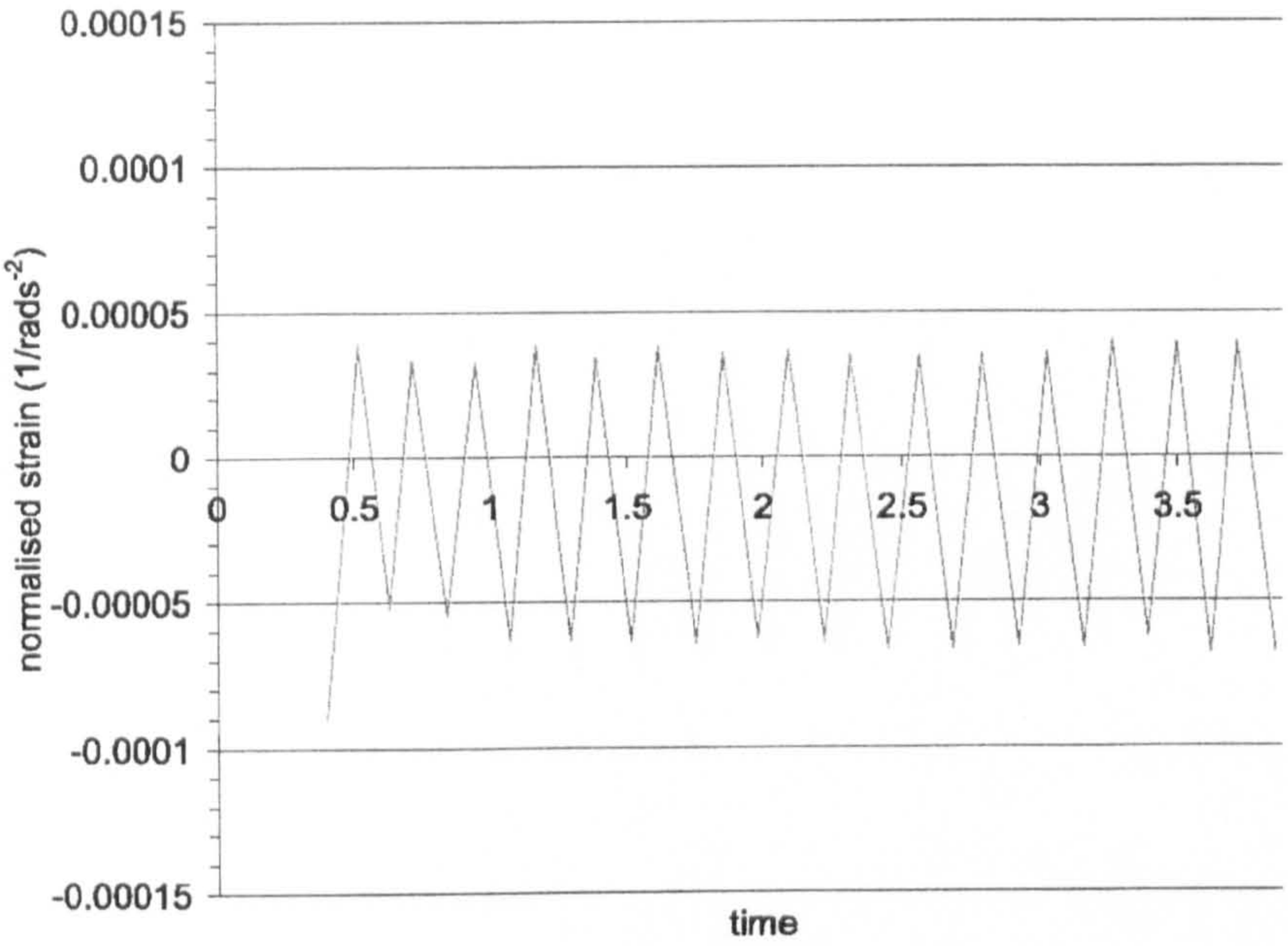

Figure K.5: SA3 normalised peak principle strain

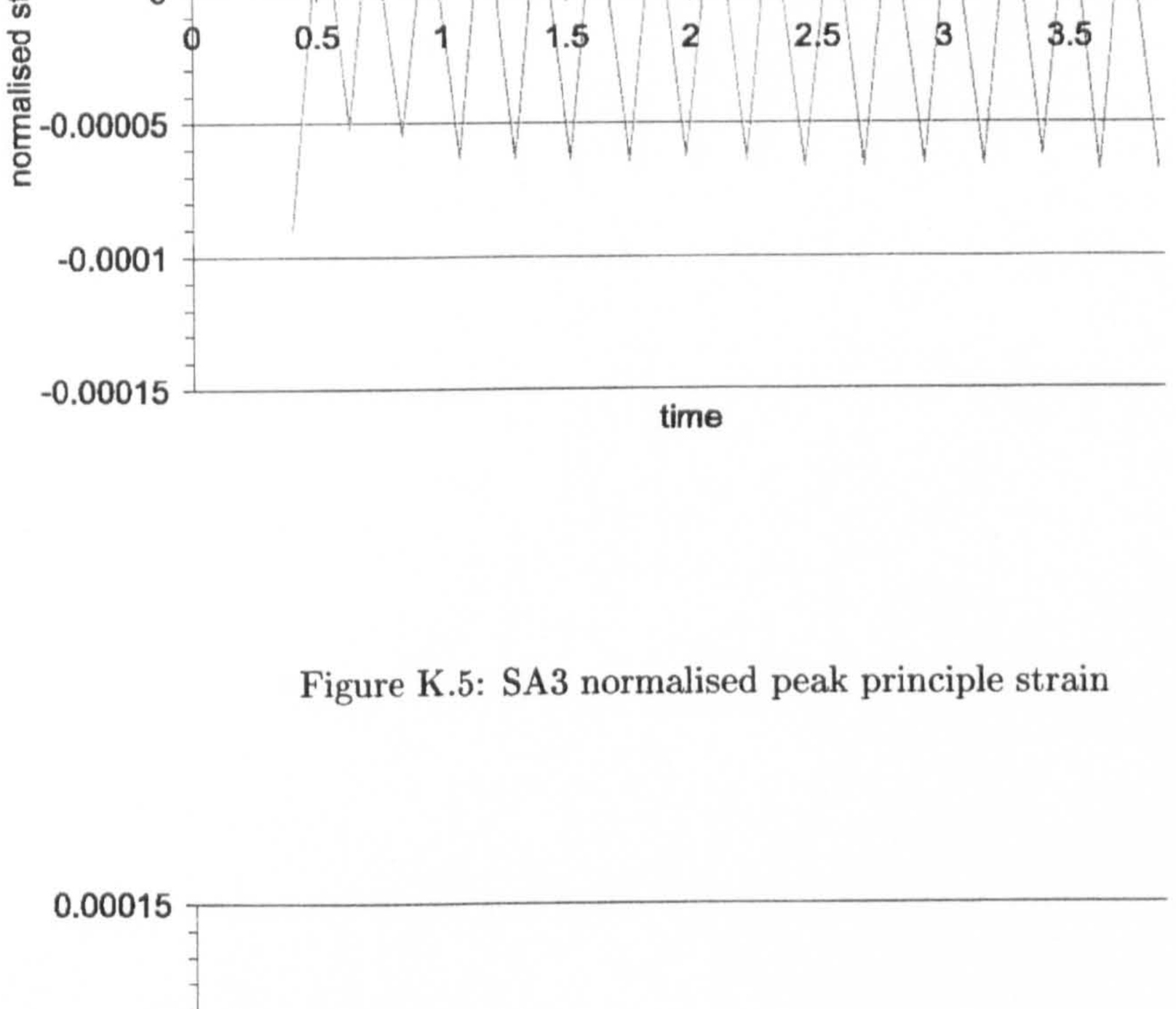

Figure K.6: SR3 normalised peak principle strain

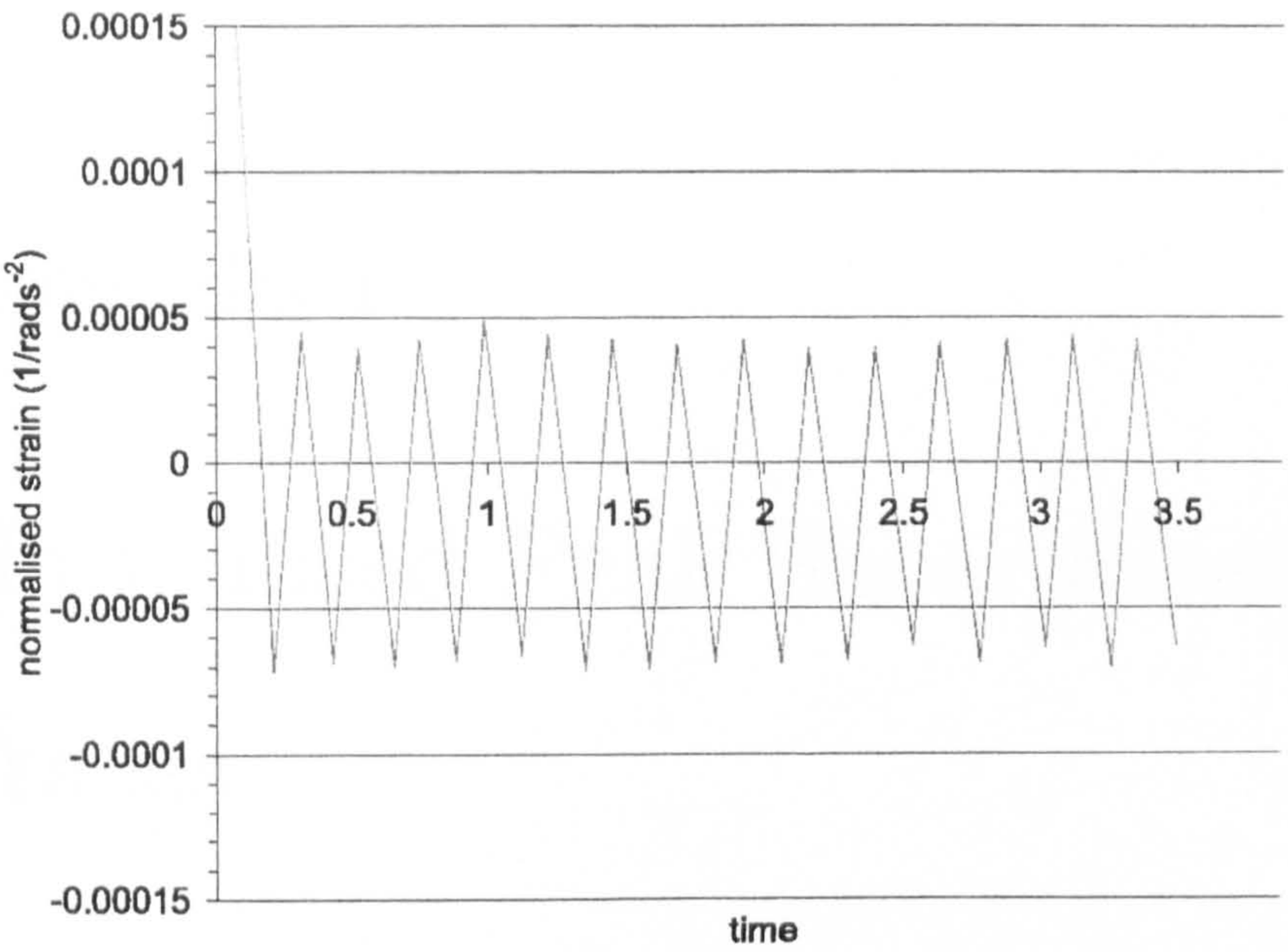

Figure K.7: SHA3 normalised peak principle strain

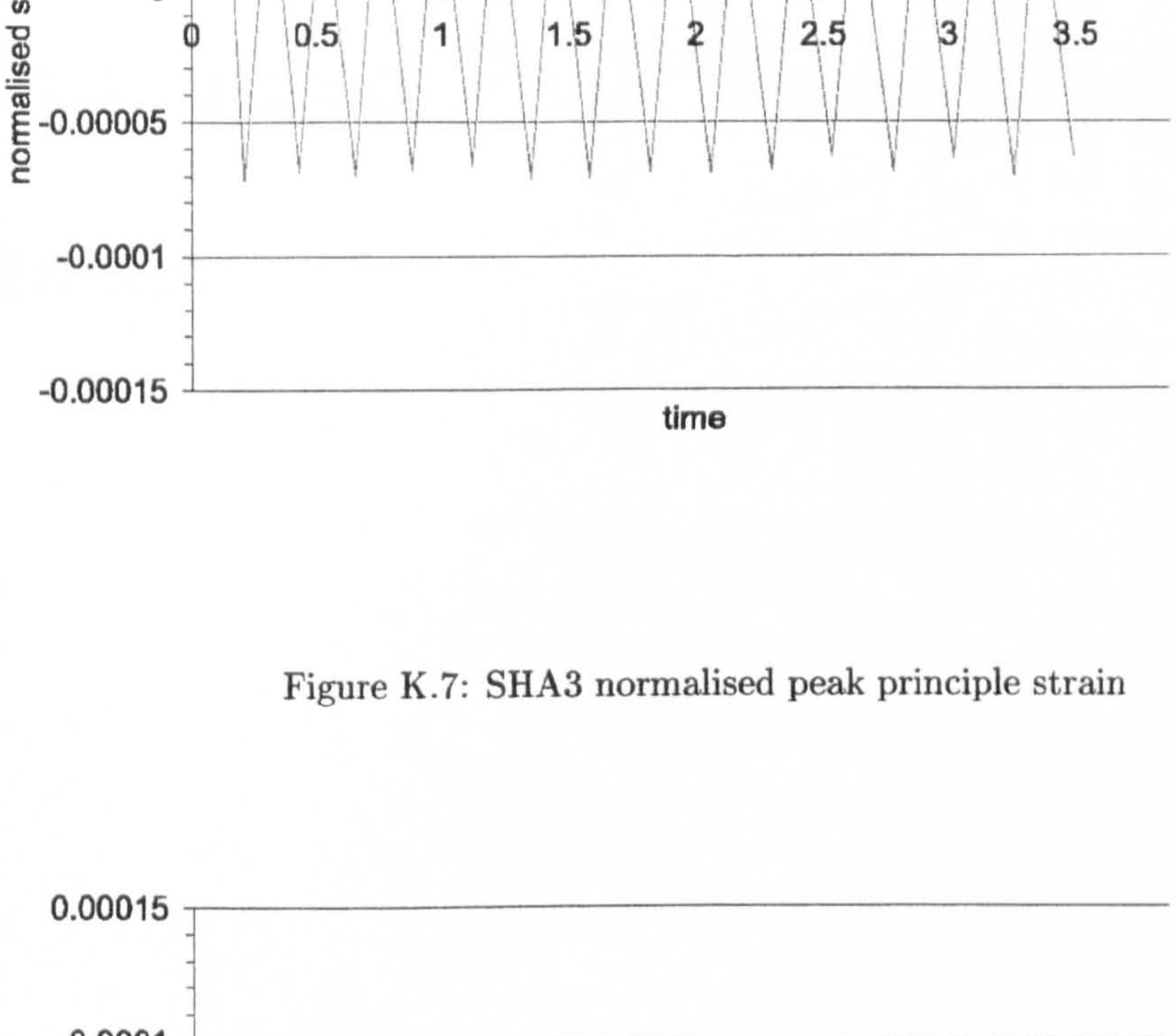

Figure K.8: SHR3 normalised peak principle strain

Appendix L

Normalised Peak Shear Strain Traces

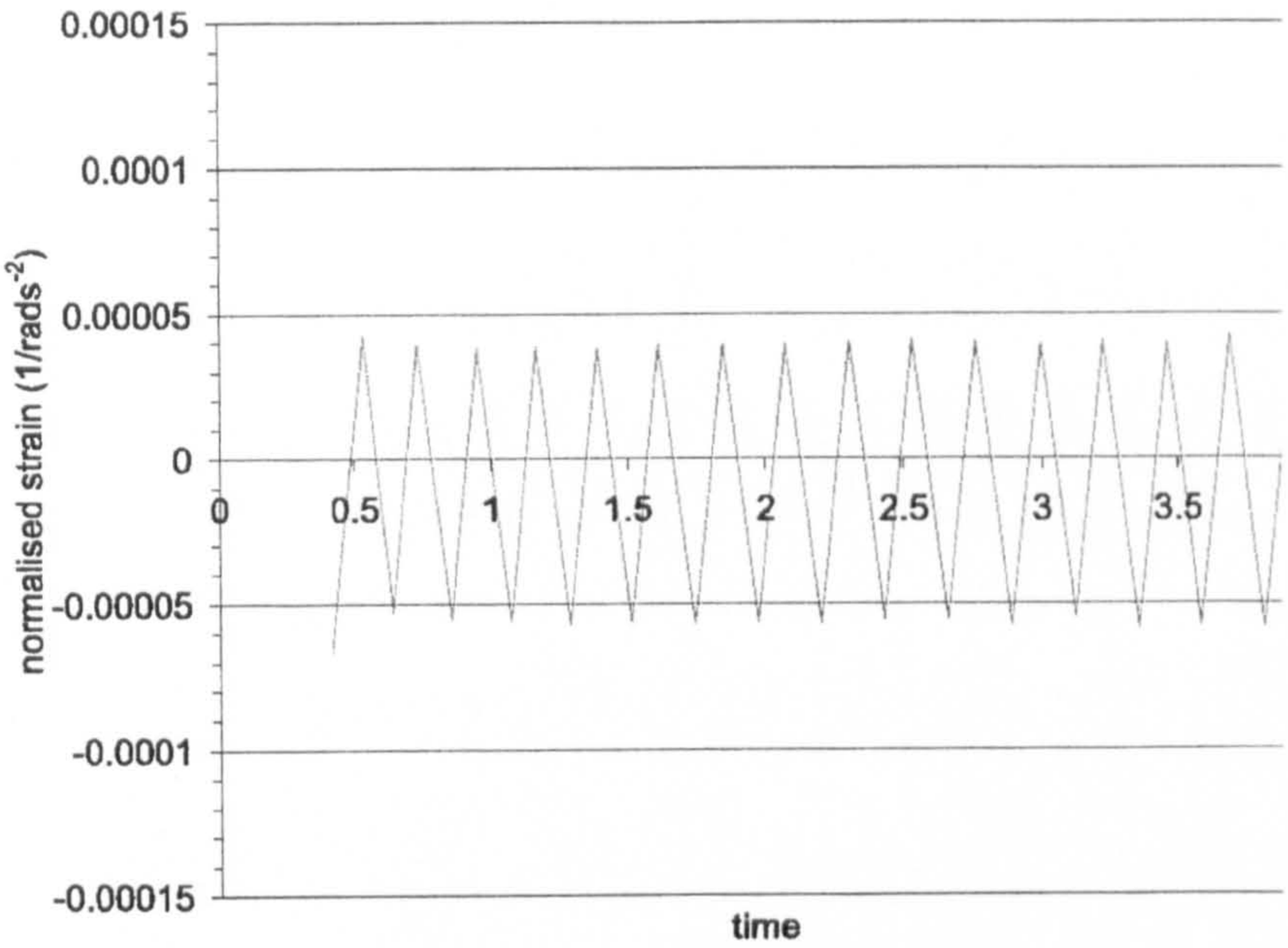

Figure L.1: A3 normalised peak shear strain

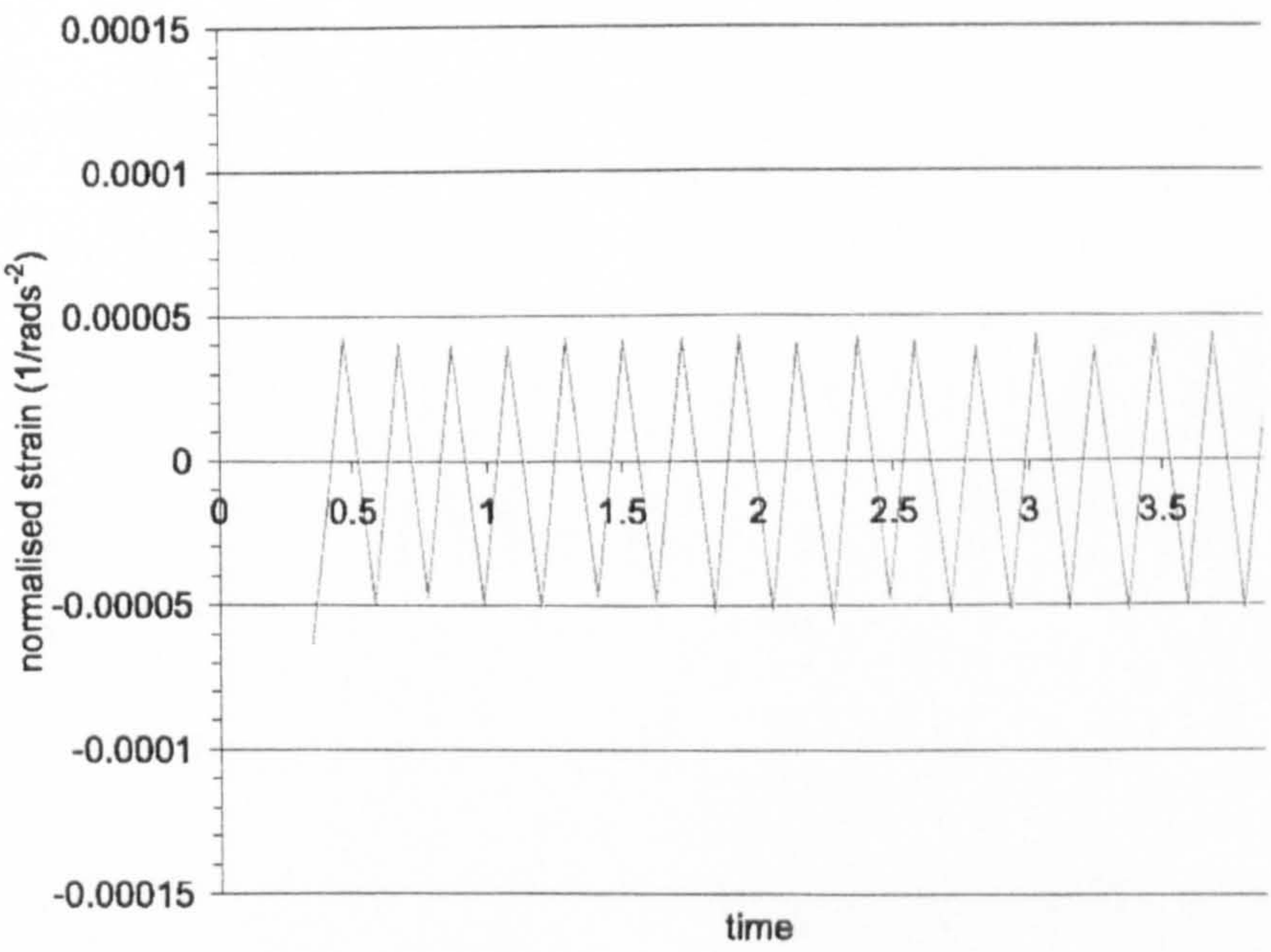

Figure L.2: R2 normalised peak shear strain

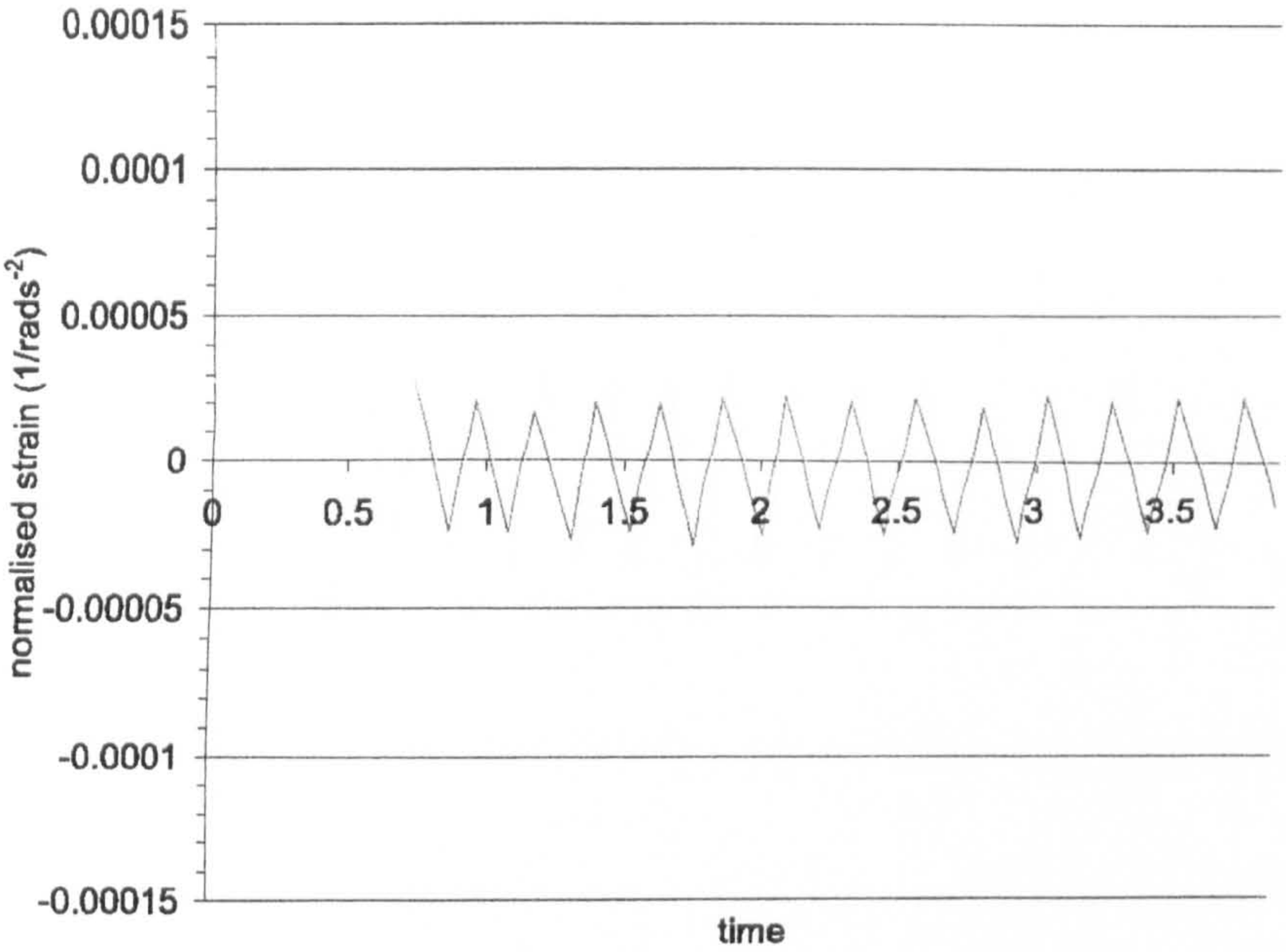

Figure L.3: HA3 normalised peak shear strain

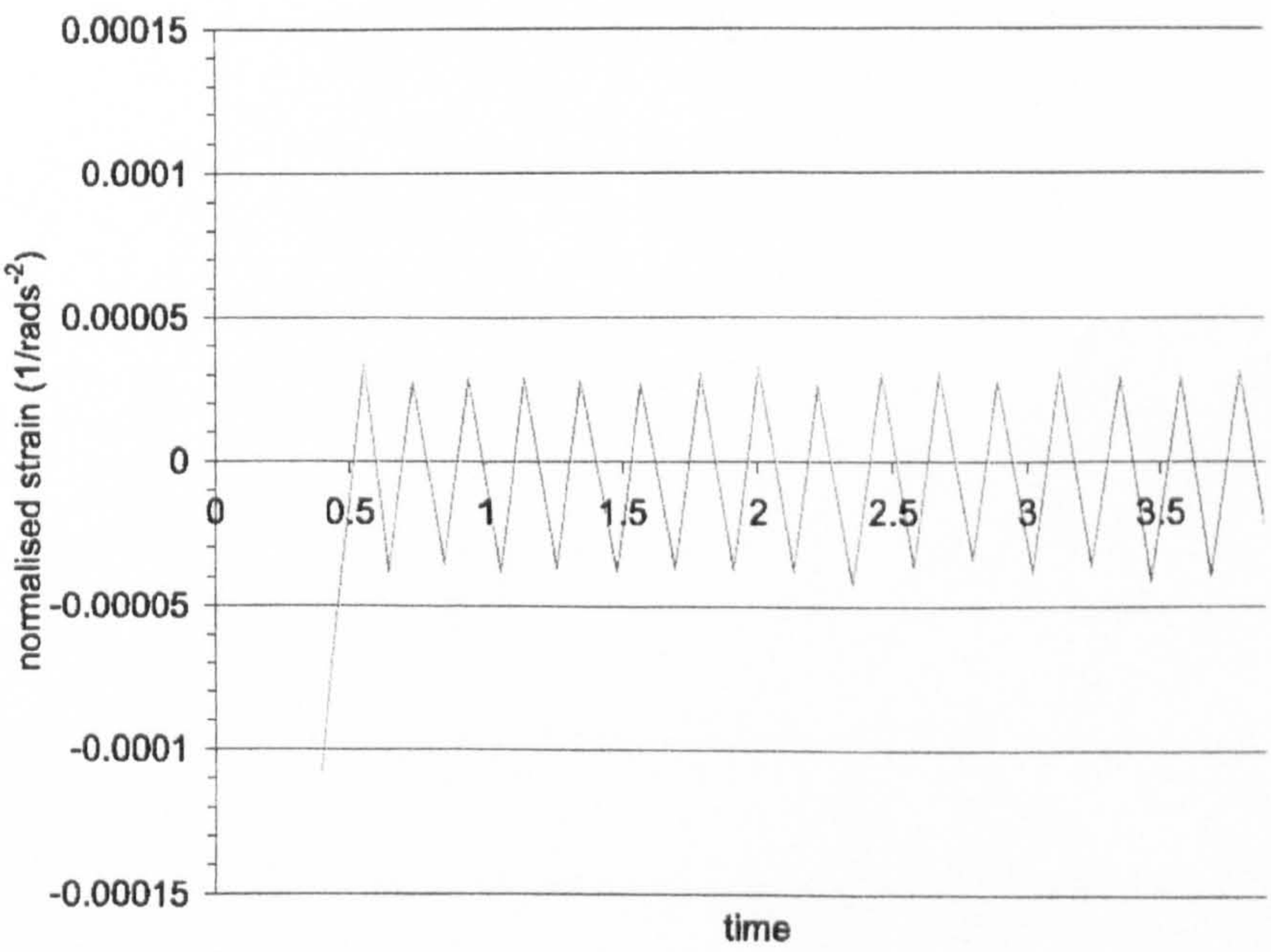

Figure L.4: HR3 normalised peak shear strain

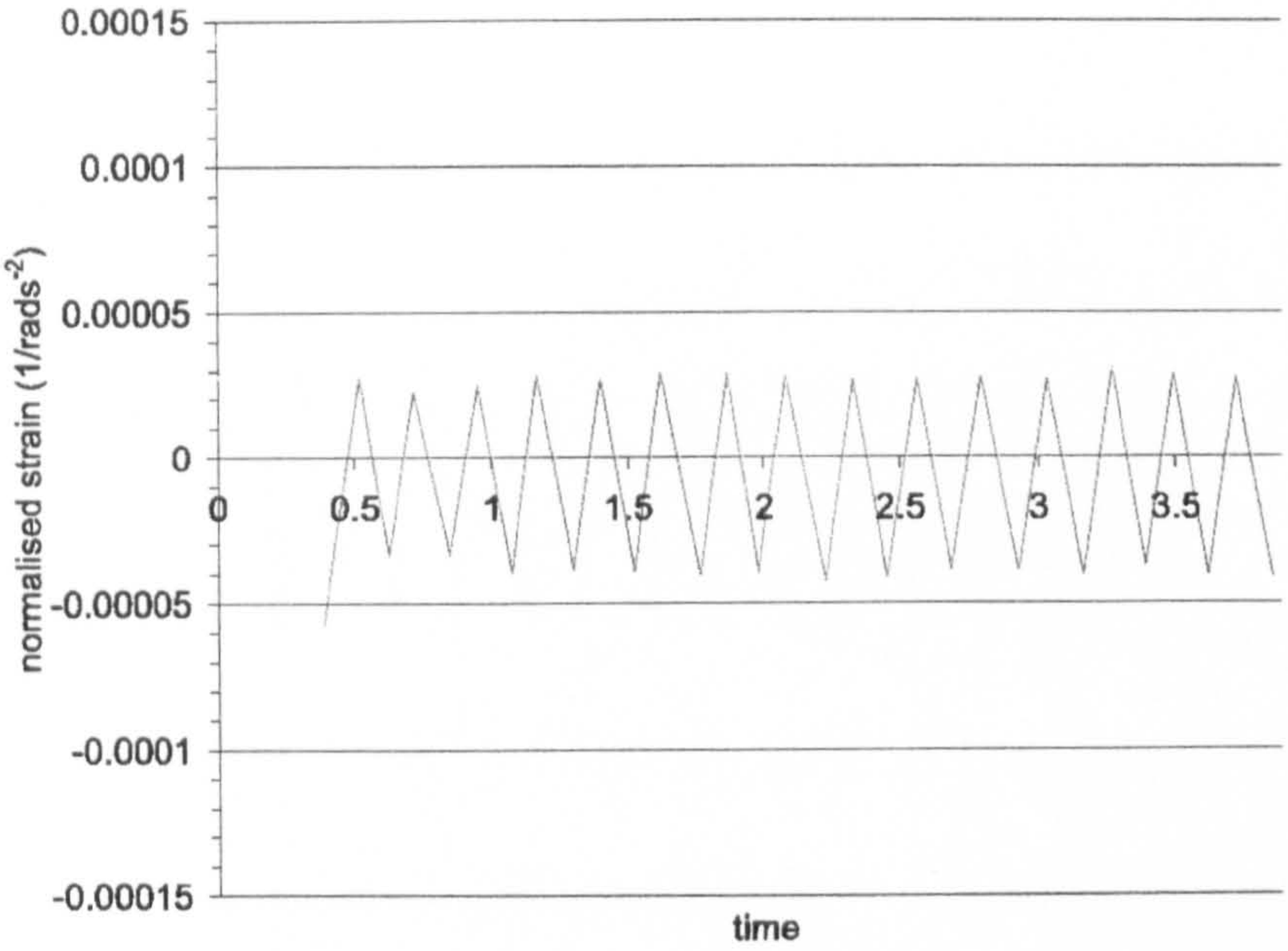

Figure L.5: SA3 normalised peak shear strain

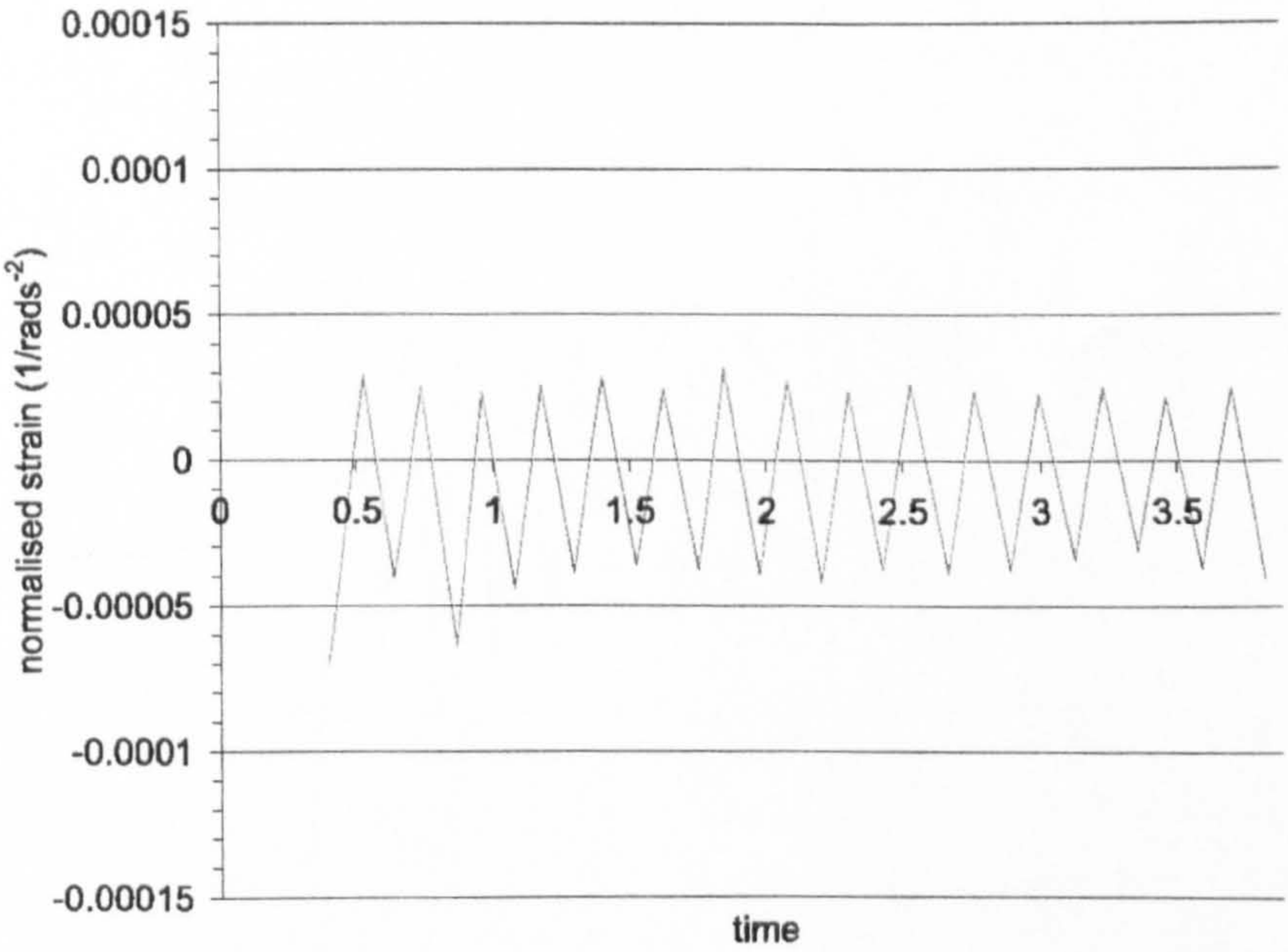

Figure L.6: SR3 normalised peak shear strain

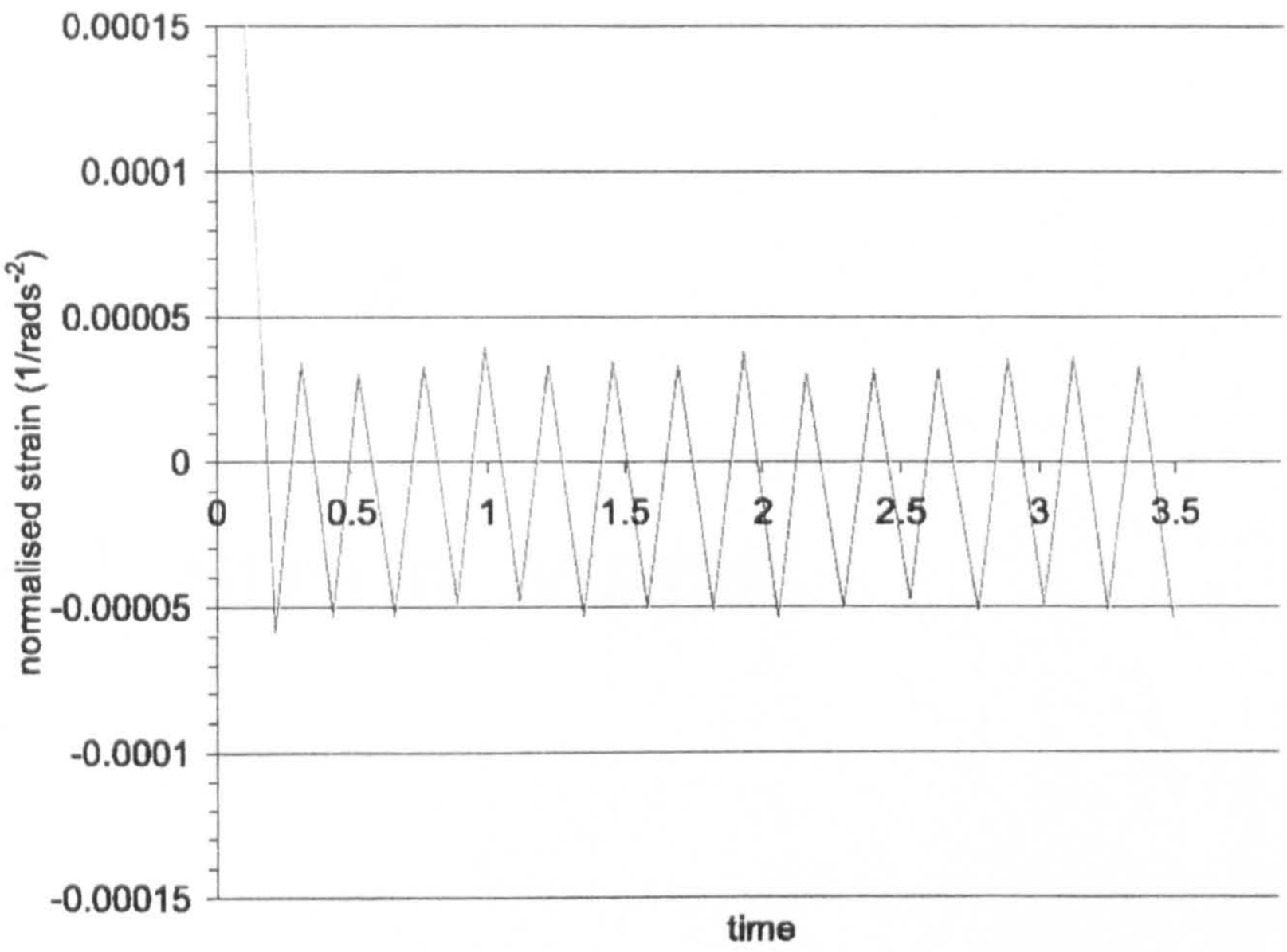

Figure L.7: SHA3 normalised peak shear strain

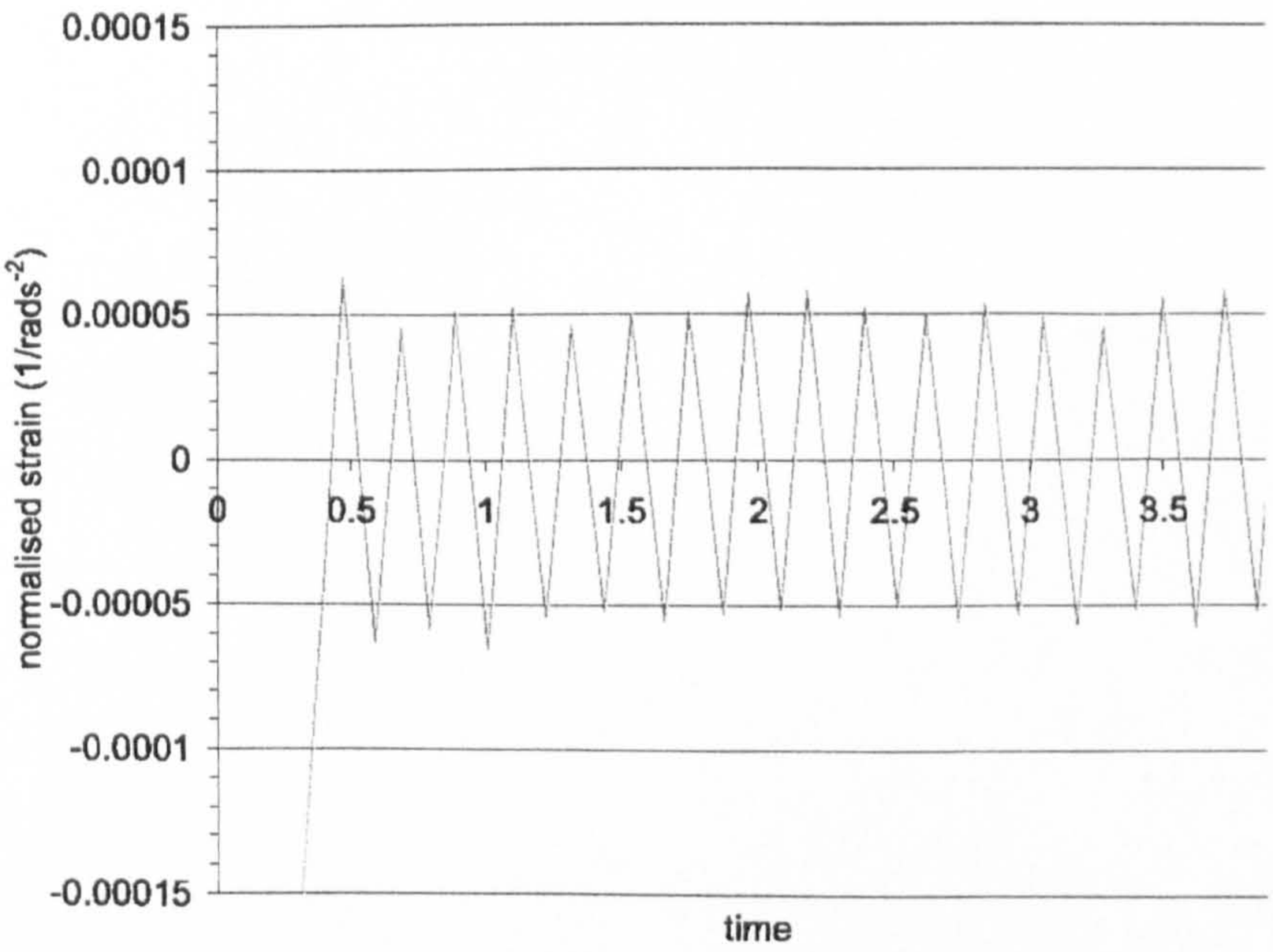

Figure L.8: SHR3 normalised peak shear strain

Appendix M

Peak Strain Maps

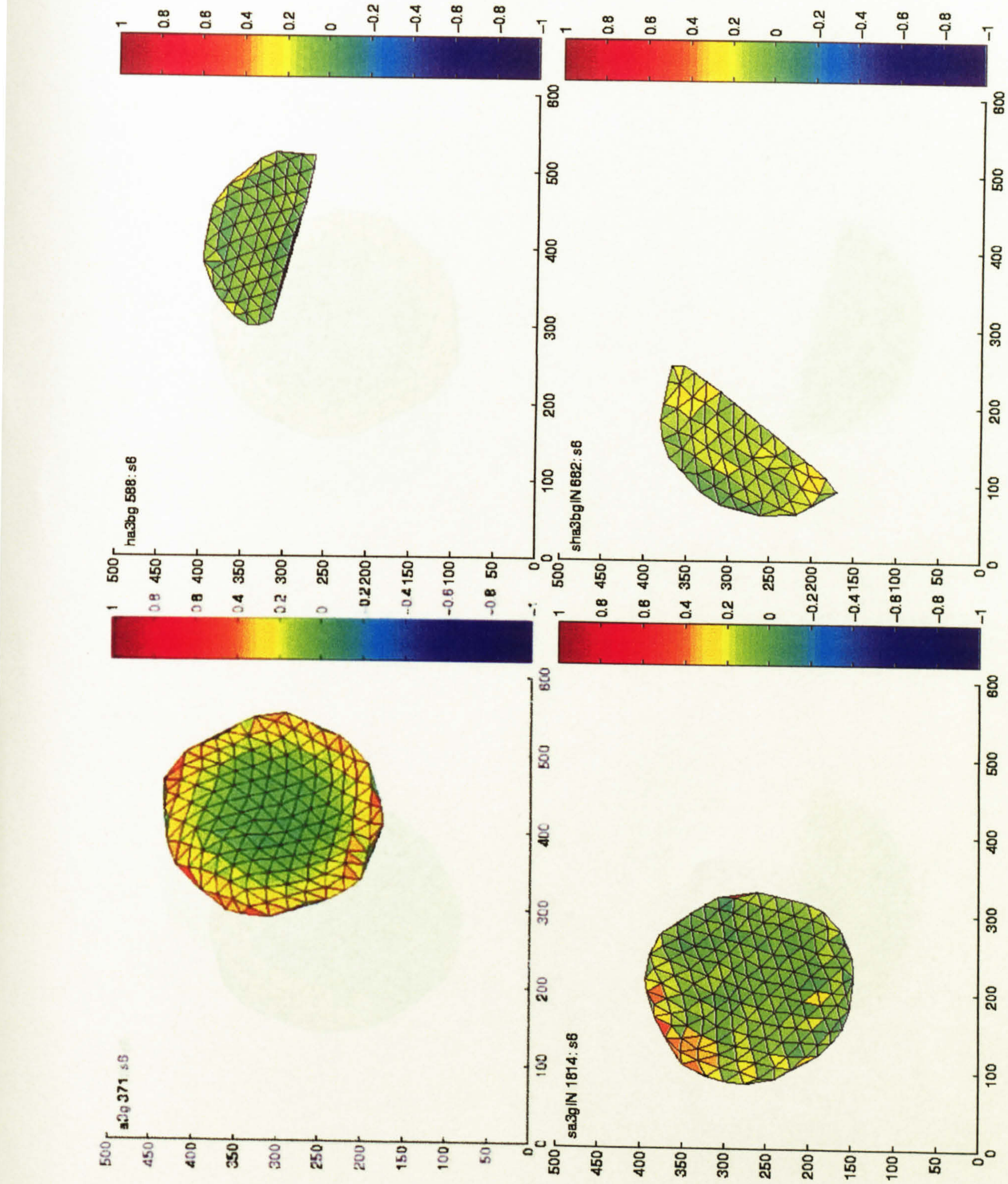

Figure M.1: Angular peak principle strain maps

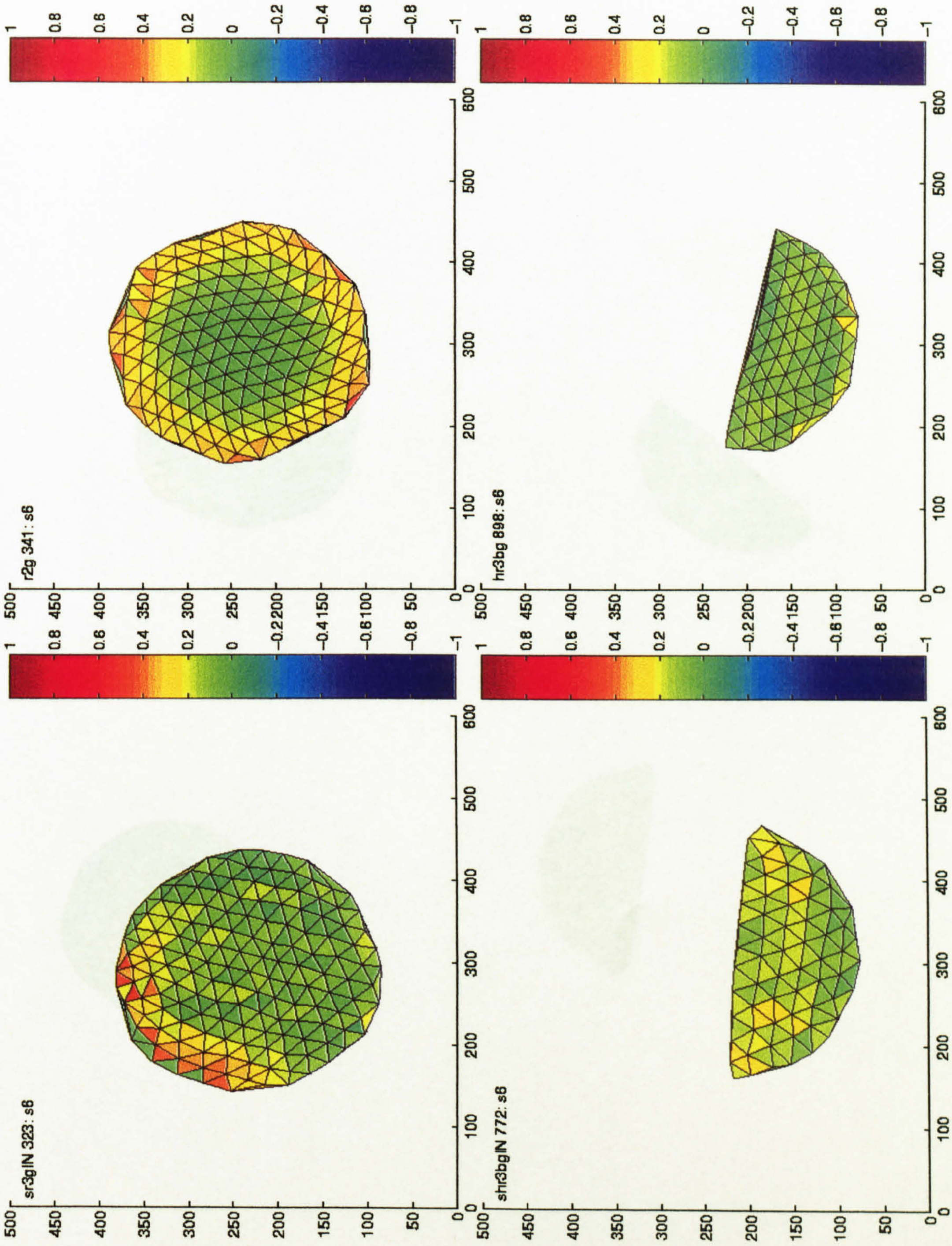

Figure M.2: Roatational peak principle strain maps

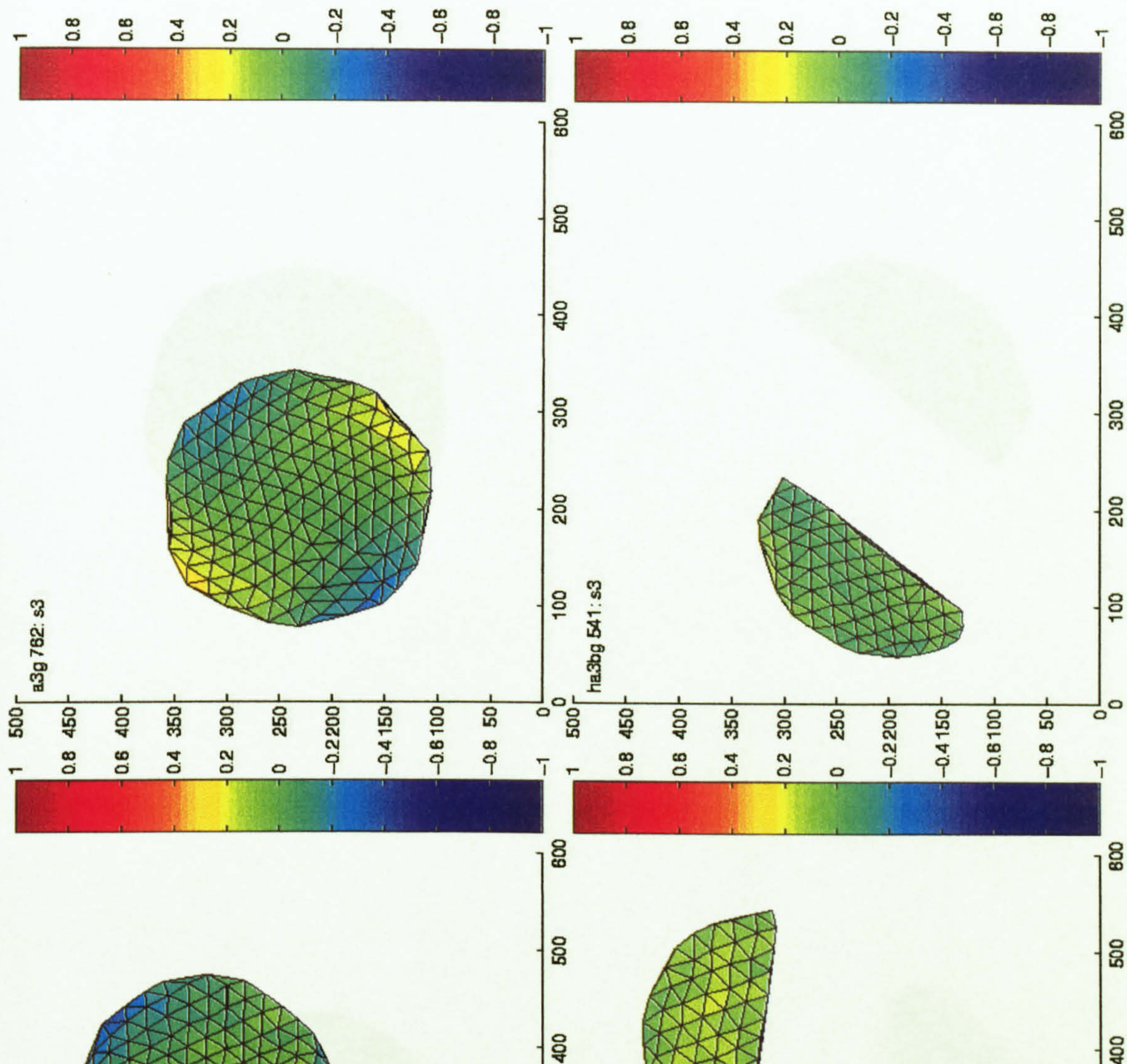

Figure M.3: Angular peak shear strain maps

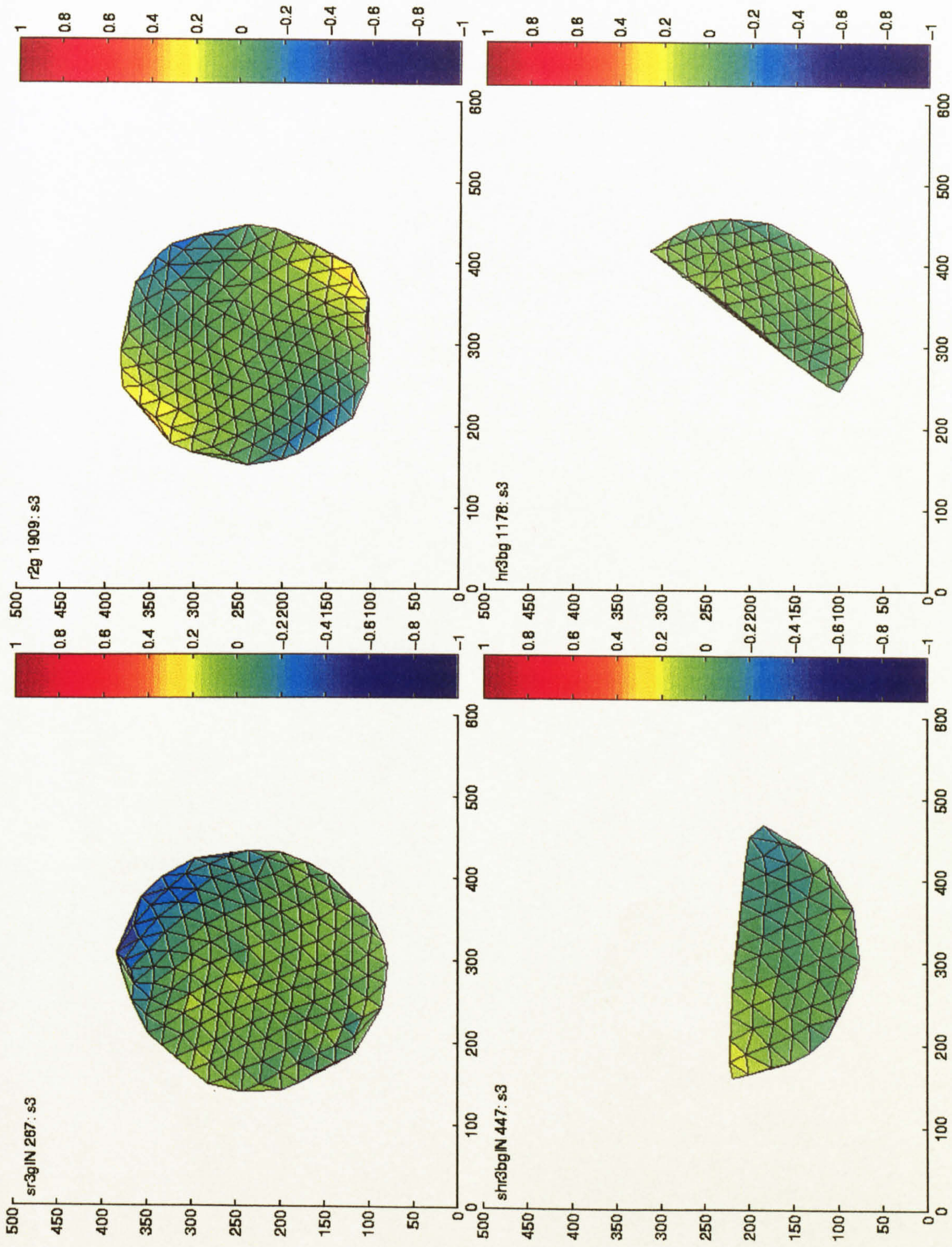

Figure M.4: Rotational peak shear strain maps